Final Scientific/Technical Report - Budget Period 2

Part I - Study Overview through Task 6.2

Federal Agency: **DOE EERE – Wind & Water Power Program**

Award Number: **DE-EE0005140**

Recipient: **Advanced Magnet Lab, Inc.** **DUNS Number: 94-374-8681**

Project Title: **A Lightweight, Direct-Drive, Fully Superconducting Generator for Large Wind Turbines**

Project Period: **10/1/2011 to 3/31/2015**

Principal Investigators:
Dr. Rainer Meinke, Senior Scientist
rbmeinke@amlsm.com (321) 728-7543
Mr. Darrell Morrison, Senior Principal Mechanical Engineer
Darrell.Morrison@Emerson.com (507) 345-2881

Report Submitted by:
Mr. Vernon Prince, Director
vprince@amlsm.com (321) 728-7543

Date of Report: March 31, 2015
Covering Period: October 1, 2012 to December 31, 2014

Working Partners:
Argonne National Laboratories, Dr. Jerry Nolen (630) 252-6418
Center for Advanced Power Systems (CAPS), Dr. Sastry Pamidi (850) 644-1447
Columbus Superconductor SpA, Dr. MatteoTropeano, Tel. 39.010.869.8100
Composite Material Technology Center (COMTEC), Dr. Keith Dennehy (507) 457-5276
Creare Inc., Dr. Tony Dietz (603) 643-3800 ext. 2310
Emerson Inc., Mr. Mike Sieberg (507) 345-2731
National Renewable Energy Lab (NREL), Mr. Derek Petch (303) 384-7012
University of Houston, Dr. Philippe Masson (713) 743-4605

Acknowledgment: "This material is based upon work supported by the Department of Energy's Office of Energy Efficiency and Renewable Energy Wind Water Power Technologies Office under Award Number DE-EE0005140."

Table of Contents – Part I

Study Overview through Task 6.2

List of Figures

TASK 4

TASK 5

TASK 6.1

This page removed due to Intellectual Property/Distribution Limitations

LIST of TABLES

Executive Summary

The U.S. National Offshore Wind Strategy [1] aims at creating an offshore wind energy industry in the United States, based on the facts that offshore wind energy can help the nation reduce its greenhouse gas emissions, diversify its energy supply, provide cost-competitive electricity to key coastal regions, and stimulate revitalization of key sectors of the economy.

Offshore wind turbines operate at higher capacity than wind turbines installed on land, and offshore wind speed profiles tend to correspond well to periods of high electricity demand by coastal cities. However, offshore wind installations have higher capital costs than land-based installations per unit of generating capacity because of required turbine upgrades for operation at sea and increased costs related to turbine foundations, system infrastructure, interconnection, and installation. To make offshore wind turbines cost competitive, a goal has been set to reduce the cost of all required components and aim for a total offshore wind deployment of 54 GW at a cost of energy (COE) of $0.07/kWh by the year 2030.

The current trend in the offshore wind turbine industry favors direct-drive generators based on permanent magnets, as they allow for a simple and reliable drivetrain without a gearbox. These generators, however, do not scale very well to high power levels beneficial for offshore wind, and their use in wind turbines over 6 MW is questionable in terms of mass and economic feasibility. Moreover, rare earth materials composing the permanent magnets are becoming less available, more costly and potentially unavailable in the foreseeable future. A stated goal of the DOE is a critical materials strategy that pursues the development of substitute materials and technology for rare earth materials to improve supply chain flexibility and meet the needs of the clean energy economy [2] .Therefore, alternative solutions are needed, in terms of both favorable up-scaling and minimizing or eliminating the use of permanent magnets. The generator design presented in this document addresses both these issues with the development of a fully superconducting generator (FSG) with unprecedented high specific torque. A full-scale, 10-MW, 10-rpm generator will weigh less about 150 metric tons, compared to 300 metric tons for an equivalent direct-drive, permanent magnet generator [3]. The developed concept does not use any rare earth materials in its critical drive components, but rather relies on a superconductor composed of mainly magnesium and boron (MgB_2), both of which are in abundant supply from multiple global sources [4].

As wind turbine technology continues to evolve in the areas of blade, tower and foundation design, larger turbines with power levels of 12 to 15 MW will become feasible. Such turbines will most likely rotate at speeds lower than 10 rpm and therefore operate with even higher torques. Scaling projections, comparing FSGs with other direct-drive generator technologies, including partially superconducting machines, show that at larger sizes and lower speeds the size and weight advantages of an FSG, and correspondingly COE differences, become even more pronounced.

As with any new technology, a fully superconducting generator has its specific technical risks that were identified in the first phase and systematically addressed in the second phase of this project. In the key technical risk areas significant advances have been made, which include the development of an appropriate MgB2 superconducting cable made of novel composite materials that are well matched in their thermal contraction to the metal of the conductor and accommodate the acting forces in the generator without fatigue. Of particular importance for the realization of the superconducting generator is AML's coil technology and the implementation of superconducting stator windings, offering the unique advantage of intrinsic fault current limitation, which significantly reduces the required mechanical strength of the generator drive train. Following multiple design iterations of the entire generator, a generator with unprecedented torque and power density has been developed. It is important to point out that independent of this project, newly developed cryogenic technology now can eliminate a major hurdle of large superconducting systems. Reversed-cycle, turbo Brayton cooling systems, originally developed in smaller scale for space applications [1], will be able to handle the heat load of the FSG and safely offer the reliability needed for power grid applications.

A conservative estimate performed independently by NREL shows that the FSG offers a lower COE than the competing technology that uses permanent magnets for a direct train. Based on the developments and achievements of the two phases of this project, the technology is ready for the next phase, which will be the construction and testing of a scaled-down version of an FSG. A 1.5-MW system as a replacement for existing wind generators is the proposed next step towards the U.S. National Offshore Wind Strategy.

1 Introduction

1.1 Project Overview and Objectives

The work described in this Final Report entails the development of a Fully Superconducting Generator (FSG) for wind turbines and a description of the work accomplished under Budget Periods 1 (BP1) and 2 (BP2) of DE-FOA-0000439. While the technology employed in this study can be applied to any type of wind turbine, land-based or offshore, this project proposes to apply the technology to reduce the cost of energy for offshore wind turbines.

As part of the proposal to the DE-FOA-0000439, deliverables were defined for BP1 and BP2 in the Statement of Project Objectives (SOPO) document. This report is a summary of BP1 accomplishments (SOPO Tasks 1.0 through 3.0), followed by a detailed description of the SOPO tasks completed for BP2 (Tasks 4.0 through 8.0), including:

- Task 4.0 – Advanced Modeling and Simulations
- Task 5.0 – Cost of Energy Model Update/Refinement
- Task 6.0 – De-risking Experiments
- Task 7.0 – Development of Commercialization Plan
- Task 8.0 – Project Management and Reporting.

1.1.1 Background and Motivation for Study

The current trend in the offshore wind turbine industry favors direct-drive generators based on permanent magnets, as they allow for a simpler and more reliable drivetrain without a gearbox. These generators, however, do not scale very well to increased power levels, and their use in wind turbines over 6 MW is questionable in terms of mass and economic feasibility. Moreover, the rare earth materials composing permanent magnets are becoming less available, more costly and possibly unavailable in the forseeable future. A stated goal of the DOE is a critical materials strategy that pursues the development of substitute materials and technology for rare earth materials to improve supply chain flexibility and meet the needs of the clean energy economy [2]. Therefore, alternative solutions are needed, in terms of both favorable up-scaling and minimizing or eliminating permanent magnets.

The generator design presented in this document addresses both these issues with the development of a very high specific torque, fully superconducting generator (FSG). A full-scale, 10-MW, 10-rpm generator will weigh less than 150 metric tons, compared to 300 metric tons for an equivalent direct-drive, permanent magnet generator [3]. The proposed system does not use any rare earth materials in its critical drive components, but rather relies on a superconductor composed of mainly magnesium and boron, both of which are in abundant supply from multiple global sources [4][5].

Ultimately, the system design and all associated choices and trades are driven by the goal of minimizing the levelized cost of the energy (COE) produced by wind turbines. In the National Offshore Wind Strategy Plan for the United States, published by the DOE [1], the COE targets for offshore wind power are $0.10/kWh by 2020 and $0.07/kWh by 2030. This report will show that the FSG, along with other technology improvements in wind turbines, has the potential to reach a COE of $0.077/kWh for a 10-MW turbine. In contrast, a direct-drive, permanent magnet generator of the same capacity would have a COE about $0.02/kWh higher than the FSG at current cost of rare earth materials.

Of equal importance as the potential to reach the targeted COE numbers, is the ability of this class of machines to scale beyond 10 MW in power output. As wind turbine technology continues to evolve in the areas of blade, tower and foundation design, larger turbines of perhaps 12 to 15 MW in size will become feasible. These turbines will very likely rotate at speeds lower than 10 rpm, operating with even

higher torques. Scaling projections, comparing FSGs with other direct-drive generator technologies, including partially superconducting machines, show that at larger sizes and lower speeds the size and weight advantages of an FSG, and correspondingly COE differences, become even more pronounced.

The design of the FSG presented in this report truly reflects a collaborative team effort and is a result of a pragmatic combination of existing methods of designing and manufacturing large-scale machinery with various innovations to achieve both performance and cost targets. Of particular importance is the application of AML's coil technology, which is an enabler for the superconducting coils used in these machines. The selected risk mitigation activities of BP2 represent the next logical step in the realization of low-cost, reliable superconducting generators. Of additional benefit is the fact that much of the progress made in the development of superconducting generators will translate into the maturation of other types of superconducting machines such as high-power motors with 99%+ efficiency and AC synchronous condensers. Considering the fact that motors of 1,000 HP or greater consume over 1/3 of the total electricity produced in the US [6], the cost savings in terms of efficiency improvement realized by such machines will be very significant.

1.1.2 Budget Period 1 Summary

The following summarizes work performed on the FSG project during Budget Period 1.

1.1.2.1 FSG Design

The fundamental design of the Fully Superconducting Generator follows a standard configuration of electrically excited field windings rotating within stationary armature windings surrounded by a magnetic ironshield. However, due to the many particulars of a superconducting machine significant differences to a conventional generator exist. The interconnect diagram shown in Figure 1.1.1 illustrates the principal system components of the superconducting generator system.

The use of superconductors in both the rotor, operating as a DC coil, as well as the stator, operating in AC mode, offers many advantages. Key features include lower mass and smaller size, favorable scalability to higher power, limitation of fault currents on the load side, elimination of rare earth materials, reliability, and lower cost. The conceptual design of the 10MW FSG was driven primarily from the need to carry a high level of torque (>10 MNm) through the structure, while at the same time minimizing thermal conduction between the cryogenic parts of the system and the surrounding room temperature. Additional design drivers were the containment of the relatively thin rotor and stator winding sections under load conditions and the rotary electrical and cooling interconnects.

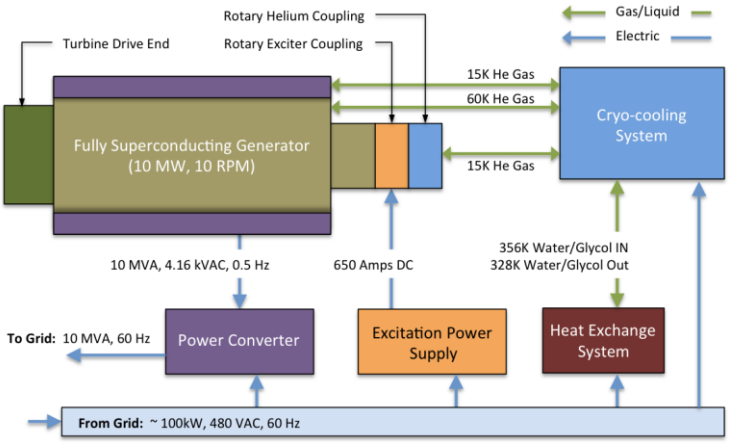

Figure 1.1.1. FSG Principal System Components

This page removed due to Intellectual Property/Distribution Limitations

This page removed due to Intellectual Property/Distribution Limitations

Table 1.1.1. FSG Specifications

System Parameters	**Value**	Unit	Parameter	Value	Unit
No Load Field	1.08	T	Power	10,000	**kW**
Synchronous Reactance	0.8	p.u.	Torque	9.54	**MNm**
Frequency	0.5	Hz	Specific Torque	65.3	**Nm/kg**
Number of Pole Pairs	3		Specific Power	0.068	**kW/kg**
Rotation Speed	10	rpm	Shear Stress	0.44	**MNm/m**
Efficiency	98.92	%			

1.1.2.1.3 Integration and Nacelle Interface

The 10-MW FSG will allow very large torque (9.54 MNm) relative to typical geared or direct-drive wind turbines of today. As a result of this higher torque capacity, a new up-tower design is needed. Figure 1.1.5 shows the FSG integrated in a turbine nacelle. This design was developed for the sole purpose of calculating the various mechanical loads on the system rather than the development of an optimized nacelle layout.

The higher specific torque capacity of the FSG allows operation with lower rpm for a given generator weight. At typical TSR (Tip Speed Ratio) this lower rpm translates to larger blade diameters and therefore increased power opportunity [8].

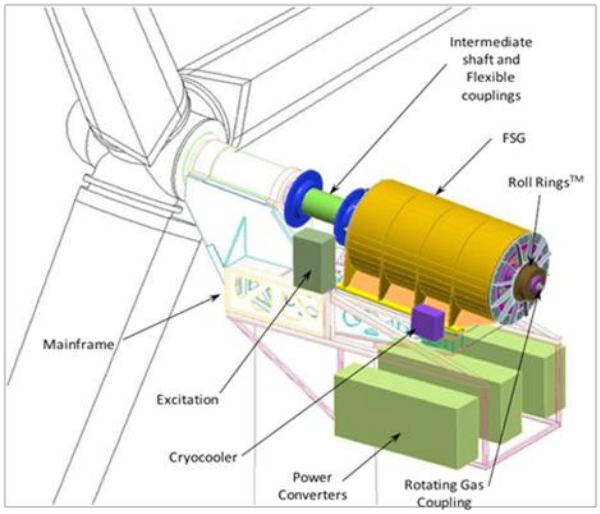

Figure 1.1.5. Turbine Nacelle with FSG

Flexible couplings are used in the design to prevent wind-load-related deflections from creating potentially harmful forces in the FSG. The FSG is aligned, shimmed and bolted to the mainframe to transfer the operational torque loads to the tower.

A key consideration in the design of blades, mainframe, tower and foundations is the ability to handle large fault torques. With the FSG, fault torques are greatly reduced, due to the current limiting feature of the superconducting stator windings, to a peak fault torque of less than 2 p.u. (1 p.u. equals rated conditions) as compared to typical copper-based systems with peak fault torques generally in the range above 5 p.u. [9].

1.1.2.1.4 Technology Readiness Level (TRL)

The DOE Technology Readiness Assessment Guide [7] was used to perform a TRL assessment of all the major subsystems of the FSG. Table 1.1.2 shows the outcome of this assessment.

Table 1.1.2. TRL Level Assessment Summary for the FSG Hierarchy

Subsystem	TRL	Subsystem	TRL
FSG	**3**		
Generator Electro-Magnetic Design	3		
Rotor Assembly	4	Stator Assembly	4
Active Section (Superconducting Coils)	4	Active Section (Superconducting Coils)	4
Cooling Network	4	Cooling Network	4
Power Network	7	Power Network	7
Shaft	7	Torque Tube	2
Cryostat/Vacuum Enclosure	7	Cryostat/Vacuum Enclosure	7
Frame	7	Excitation Power Supply System	7
Bearing System	7	Power Conversion System	7
Cryo-cooling System	4		

Generally, considering the state of the various subsystems, the FSG is assigned a TRL of 3. As a result of execution of the risk mitigation activities proposed for Budget Period 2, the TRL of certain subsystems such as the cryogenic cooling network and the stator torque tube will be raised. A significant increase of the TRL to a level of 6 will occur when a sub-scale version of the FSG is built and tested.

1.1.2.1.5 System Design Approach

The application considered is a superconducting (SC) direct-drive generator constituting the drivetrain of a 10MW wind turbine. At this power level, a very high specific torque is required to limit the total mass of the drivetrain, and a fully SC generator is therefore considered. Fully SC generators present the highest torque density possible in rotating machines, taking advantage of high current densities in both the rotor and stator. The design of SC generators progresses through several steps, starting from preliminary sizing to detailed simulations. The design involves different areas that, while coupled, are addressed separately as folllows:

Electromagnetic design. Analytical equations can be obtained from first principles to estimate the generated torque in rotating machines.The rotor and stator are composed of saddle coils. Because the stator is SC, the conductors need to be mechanically stabilized in an isolating substrate, such as composite materials, and a conventional distributed winding cannot be used. To support the superconductor stator windings adequately, a configuration of three (3) concentric cylinders is used, in which each phase is composed of a multipole winding.

Mechanical design. The main objective of the initial sizing is to define key dimensions that lead to a minimum mass of the generator. Once the initial dimensions are defined, optimization of the mechanical system is performed to reduce conduction heat leaks through torque tubes and to accommodate all required components for the machine including seals, cooling channels, multi-layer insulation (MLI) and other system components**.**

The initial design serves as starting point for the design optimization using high fidelity simulation tools. A major part of the optimization deals with the mechanical components that need to transfer large torque between cryogenic and room temperature with minimum heat loads.

1.1.2.1.6 Structural Design

The structural design of the Fully Superconducting Generator (FSG) was driven by four fundamental goals:

a. Reliably operate at the required high torque associated with the 10-MW, 10-rpm application.
b. Minimize the conductive thermal heat leak from the surrounding room temperature environment into the cryogenically cooled parts of the system.
c. Minimize the thermal stresses developed during cool-down from room temperature to nominal operating temperature (15 K).
d. Minimize the cost of the system while achieving all design and operational objectives.

A multi-phased design of the FSG was undertaken. The overall design evolution of the FSG was executed in three distinct design stages:

1. The **Primary Design** reflected the state of the design at the proposal stage, before Budget Period 1 funding. This configuration was primarily derived from a copper-based machine, with limited consideration concerning heat leaks, vacuum requirements, and cryogenic performance of the materials needed. The rotor consisted of a straight cylinder supported by two bearing systems in the generator frame, which also constituted the wind turbine mainframe. The armature was a hard-mounted, composite torque tube. The resulting machine needed additional length to accommodate rotary vacuum seals on the main shaft.

2. **DR1 (Design Revision 1)** was the first pass at a fully functional design with consideration of cryogenic requirements and material properties. The DR1 design generated a bill of materials needed for a cost of energy (COE) estimate. The machine evolved into a free-standing system, reducing the substantial stresses from supporting the turbine hub. Rotor and stator were equipped with re-entrant tubes at both ends to reduce the otherwise unacceptable heat loads. The rotor shaft center material was changed to titanium for reduced heat conductivity and less weight. The winding configurations for rotor and stator coils were changed from originally assumed “Double-helix” winding configurations to saddle coils for improved machine electrical performance. Cooling systems for conductor cooling and current leads were introduced into the design. Electrical connections with hermetic feed-throughs were developed. Titanium was considered for the stator torque tube to lower the thermal stresses in the stator, but discarded due to excessive AC losses in the metal. Titanium re-entrant ends were developed and added to the composite torque tube to reduce stress on the composite caused by thermal contraction. A separate cryostat concept for the rotor and stator was developed, which eliminated the need for vacuum shaft seals and constant vacuum pump operation. Compliant composite materials were introduced for the coil support substrates to reduce thermal stress during cool-down. FMEA techniques were applied to analyze potential failure modes needed for the COE estimates.

3. **DR2 (Design Revision 2)**: The overall design was improved by adding detailed cryogenic internal plumbing, facilitating access to the machine interior, and adding lift provisions. Vacuum valves, as well as shear disk torque transfer to the stator composite were added. Value engineering was performed to reduce system cost and thereby COE for wind generators. Pareto diagrams for the material and labor costs were used to identify cost drivers. Overall, the DR2 design reduced

the price of the FSG by over 40%, with insignificant performance loss. The DR2 configuration was used for risk assessment and planning de-risking tasks.

Figure 1.1.6 shows the developed concept of the FSG with exterior features and connections labeled.

1.1.2.1.7 Design Philosophy

The frame, core construction, bearings, and bearing support methods are all based on previous equipment design experience with successful operational history. FEA was used wherever needed to validate design performance

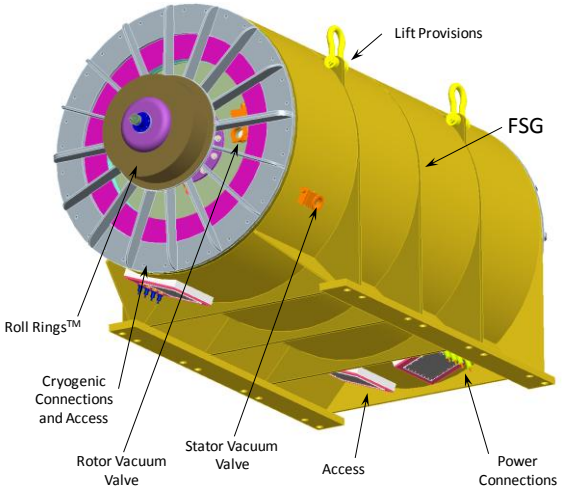

Figure 1.1.6. Fully Superconducting Generator

1.1.2.1.7.1 Fundamentals

The low rotational speed for the direct drive wind application makes it perfect for using grease-lubed, anti-friction, spherical roller bearings. They have very predictable life and minimal breakaway torque to allow blade rotation at very low wind speeds and less operational friction loss during operation. The non-drive-end bearing is insulated against shaft currents and has an additional slip plane added to accommodate the extra expansion/contraction of the cryogenically cooled rotor. The low rpm also allows using maintenance-free Roll-Rings™ to provide rotary coupling of excitation power to the rotor, which eliminates the frequent maintenance needed for brush wear and the cost/complexity of a brushless exciter.

1.1.2.1.7.2 New Aspects of the Design

Various novel design aspects were applied to meet some unprecedented requirements imposed by the FSG. These include:

- Existing superconducting coil technology, supported by composite substrates, are small in size and are able to sustain the high torque levels needed for the FSG.
- Constantly changing Lorentz forces acting on the superconductors of the coils require unprecedented fatigue life of the composite materials (*de-risking task proposed*).
- Accommodation of thermal stresses in a hybrid of metal and composite needed for the rotor to handle the required torque transfer (*de-risking task proposed*).
- A compliant composite support philosophy used for the rotor and stator. The required material properties are currently not qualified (*de-risking task proposed*).
- Novel cooling and winding configurations for the rotor and stator coils affecting coil support composites (*de-risking task proposed*).
- The stator active section is completely composite to avoid additional AC losses in the cryostat.
- Fault torque reduction caused by a transition from the superconducting to the normal conducting state of the stator winding (*de-risking task proposed*).
- The use of re-entrant configurations for the rotor and stator to reduce heat loads and accommodate thermal movements for the stator active section.

- An FSG of this large physical size requires hermetic cryostats designed to carry high torque loading. A double cryostat solution was introduced to avoid an extra seal between rotor and stator and constant operation of vacuum pumps.
- The torque levels delivered to this generator are beyond any existing wind application due to being direct drive with a higher power output and lower rpm.
- The system rotor dynamics are new due to being direct drive. The FSG rotor has very low inertia.
- The converter frequencies on the generator side are lower than converter manufacturers typically use.
- The use of electrical roll ring technologies for rotor field excitation.
- The mainframe for a 10-MW, 10-rpm direct drive FSG.
- The selection of 180 m blades to produce 10 MW at 10 rpm.

1.1.2.1.7.3 Design Procedure

The preliminary structural design used for the proposal was mainly based on solid experience with copper-based electrical machines. During Budget Period 1, design requirements resulting from superconductivity, cryogenic temperature operation, and special material properties were taken into account. Value engineering was performed to reduce system cost and to meet DOE's stated COE goals for offshore wind energy.

- **Conductive heat leaks.** Optimizations based on thermal FEA were performed, which produced the final design with significantly reduced heat loads. For the stator, which is subject to large AC losses, thermal intercepts were introduced using an intermediate stage of the cryocooler at 60 K to intercept the main heat load from AC losses at the higher temperature to improve efficiency.

- **MLI performance.** Large areas of the machine have to be insulated with MLI to achieve sufficiently low heat loads. MLI performance depends on low rest gas pressure in the insulation vacuum regions. The initial design used a single cryostat for the whole machine and shaft seals to provide the insulation vacuum. However, estimates of achievable leak rates from the shaft seals showed that constant operation of large vacuum pumps would be required to maintain the necessary vacuum level. Introducing separately sealed rotor and stator cryostats enabled elimination of shaft seals and the need for continuous vacuum pumping. The individual cryostats maintain sufficient vacuum levels for extended periods and require checks only during normal maintenance operations.

- **Heat load of current leads.** Current leads are routinely used for the operation of superconducting magnets and have been adapted for the FSG. For the stator coils, which operate at a higher current than the rotor, the load on the cryogenic system has been significantly reduced by intercepting the unavoidable heat conduction through the leads at an elevated temperature level of 60 K.

- **High torque levels.** Torque transfer in the FSG exceeds all existing wind turbines and extensive FEA calculations have been performed to verify the adopted torque transfer mechanisms. This includes analysis of the torque path from the drive end of the shaft through the active sections of the rotor and of the stator through the stator support to the machine mainframe. A splined shaft end with body-bound bolting between drive end shaft extension and the shaft center will be used. The OD of the shaft center will have a surface treatment, as defined in BP2, to sufficiently adhere to the active section composite. FEA studies of thermal stresses developed during cool-down to 15 K determined the need for a low modulus, compliant composite with matched Coefficient of Thermal Expansion

(CTE) to minimize induced stress levels from thermal contraction. The identified fiber material, while successfully used at room temperature, does not have measured material properties at cryogenic temperatures. The required data will be obtained during the proposed de-risking task.

- **Fault torque management.** Experience with copper-based designs, permanent magnet designs and partially superconducting designs shows fault torques in the range of 5–15 p.u., i.e., 5 to 15 times the rated torque. This requires that all components, including turbine blades, shaft, active sections, stator-frame, mainframe, tower, and foundation accommodate the increased fault torque. However, the superconducting armature of the FSG offers the unique advantage that the properly designed stator windings function as fault current limiters. This feature allows reducing the design requirement of the fault torque to less than 2 p.u., with significant effects on the overall system cost.

- **Thermal stress management.** Due to the large temperature range seen by various FSG components during system cool-down and warm-up, large thermal stress levels can occur. Differential expansion for the required temperature swing of about 285 K of the active FSG sections can develop large deflections. Assuming a conductor behavior equivalent to 304SS, a 4-m long coil winding will have shrunk by about 12 mm (0.47 inch) when it reaches 15 K. At a conductor diameter of 2.5 mm, the axial force developed, if fully restrained at the ends, would be 984 N (221 lbs), which would develop conductor stress of 1,333 MPa (193,408 psi). Matching of CTEs is therefore of utmost importance, and the issue will be addressed in one of the de-risking tasks.

- **High Lorentz forces.** The large current carrying capacity of superconductors enables the chosen rotor and stator currents in the range of 650 A and 1300 A, respectively. Due to these large currents, strong Lorentz forces act on the conductor, which must be supported by the composite matrix without degradation of the heat transfer interface bonds between conductor and composite. The combination of thermal stresses and magnetic loading stresses determines the requirements for the composite matrix. This issue is discussed in section 1.1.2.1.8.3 of this report.

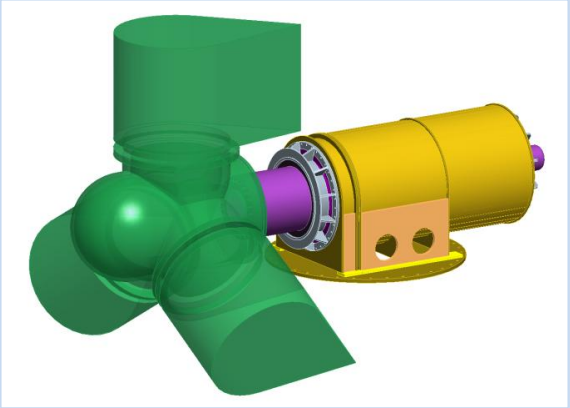

Figure 1.1.7. Primary Design Configuration

The effect of loading on all components of the FSG has been analyzed with FEA calculations. Many of these FEA studies had to be repeated for the major configuration changes during the design process. Examples include: change to the double re-entrant shaft ends, changing to the double vacuum containments (larger magnetic air gap), change of the shaft center using titanium for performance and change back to 304SS for reasons of cost, changing to stator titanium torque tube and back to composite, adding the re-entrant ends to the stator active section. As the design became refined, several analyses were repeated for the peak performance. The heat leak progression for the rotor is an important example of such a study.

1.1.2.1.7.4 Design Progression

The Primary Design shown in Figure 1.1.7 combined the mainframe, turbine rotor support and generator functions to minimize the tower top weight, part count and to maximize reliability. In this configuration, the system consists of only two bearings and a simple, straight, large-diameter non-magnetic cylindrical generator shaft, while supporting loads from the turbine. BEW examined the design and provided the expected loading for a 180-m diameter turbine. To allow turbine blade clearance to the tower, a large shaft extension was needed, creating an excessive bending moment on the shaft, and FEA results showed fatigue stresses well beyond the required life time.

Detailed calculations of the thermal heat leak due to conduction from the room temperature shaft ends showed unacceptable levels. The issue was solved with the implementation of a re-entrant shaft [10] which, however, is highly flexible. The combination of extreme bending moment capacity needed for turbine support and the weakening of the shaft for the necessary re-entrant ends to reduce conduction heat leak, forced a design change to a standalone generator configuration in DR1. The shaft bending stress was significantly reduced with the stand-alone design.

1.1.2.1.7.5 Rotor Heat Leak Progression

As the design progressed, several rotor configurations were developed which led to significant reductions in heat loads (Figure 1.1.8). However, the large amount of titanium needed for the shaft turned out to be unacceptable in cost. The solution was a rotor center section made of 304SS. Even with the weight increase from the larger sections needed for acceptable stresses and the higher density material, the rotor was roughly 1/6th the titanium cost, no longer being the most expensive material cost.

The final configuration, using the rotor center of 304SS, produces a conductive heat leak of 229 W, a significant reduction from 984 W of the Primary Design. The change from titanium to 304SS had no significant effect on the cryocooler size and cost and therefore led to a large improvement to the cost of energy.

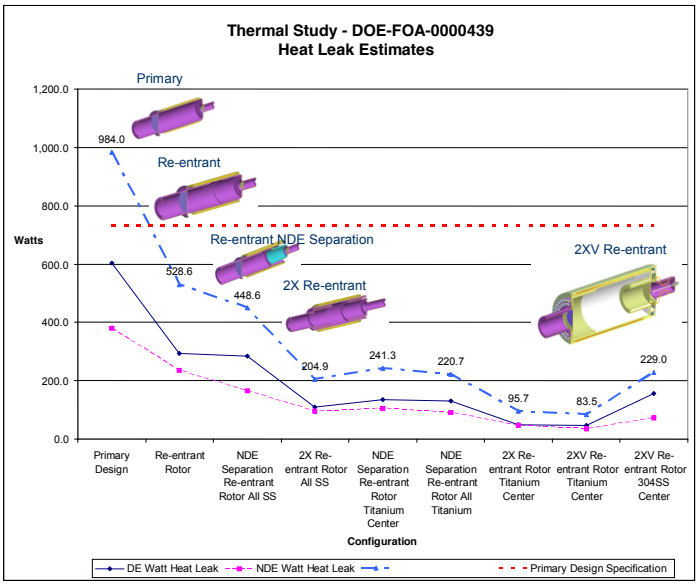

Figure 1.1.8. Rotor Conductive Heat Leak Progression

1.1.2.1.7.6 Stator Heat Leak Progression

As with the rotor, the stator progressed through several configurations and thermal performance levels before reaching the final design. A summary of the heat leak performance is shown in Figure 1.1.9.

The Primary Design stator was a straight composite torque tube with a flange on each end for mounting to the stator frame. Although the design showed an acceptable heat leak due to the long length of the active section, it was subject to high thermal stress caused by the high mounting rigidity.

This page removed due to Intellectual Property/Distribution Limitations

1.1.2.1.8.2 Rotor Coil Design Details

A detailed analysis of potential winding configurations for the rotor and stator coils showed that a Stacked Saddle Coil (SSC) constitutes the best choice for the FSG. An isometric view of SSC winding configuration is shown in Figure 1.1.10. An SSC coil is a multilayer saddle coil, in which the conductors of several layers are placed on top of each other in grooves precisely machined into a composite support cylinder. The designed rotor coil consists of 12-layers that are grouped in 3 "super-layers" consisting of 4 layers each. The coil design is shown in Figure 1.1.10 together with an enlarged view of the winding cross-section of such a winding configuration.

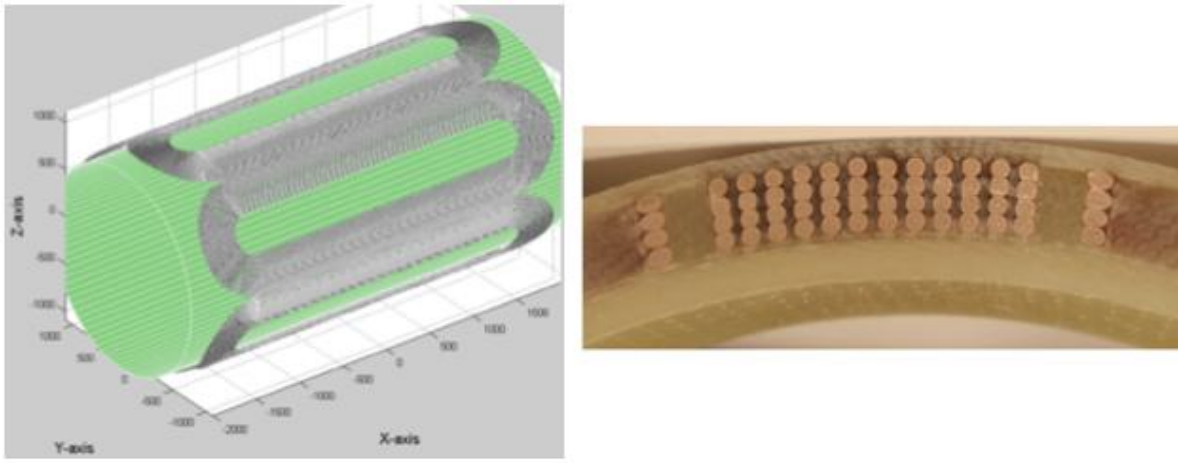

Figure 1.1.10. Left: Isometric view of rotor winding based on SSC consisting of 6 sub-coils. Right: Cross-section of an SSC winding section showing 4 conductors stacked in each support groove

1.1.2.1.8.3 Acting Lorentz Forces in Rotor and Stator Coils

A detailed understanding of the Lorentz forces acting in the rotor and stator coils is not only required for the design of the torque transfer mechanism of the machine, but also to develop requirements for the composite support structures of the SSC windings.

A detailed analysis has been performed, which determined the acting Lorentz forces on an individual conductor level. Lorentz forces depend on the current flowing through the conductor and the local field at each part of the conductor. Although a further optimization of field uniformity throughout the winding is possible, which will lead to unprecedented field uniformity throughout the winding, it has not been done, and the Lorentz forces presented below constitute conservative values, which during continued design work could be reduced. It is important to reemphasize that such an optimization hinges solely on the chosen SSC winding configuration developed at AML.

The Lorentz forces acting on the rotor and stator windings have two components. One component is due to the self-field of the coil, which creates a certain magnetic pressure; the second component is due to the rotor stator interaction. For the Lorentz forces presented below, it has furthermore been assumed that a fault conditions exists on the load side of the armature, and the armature currents have been increased to 1.5 times their nominal value. Although, Lorentz forces have been determined for all

parts of the rotor and stator windings, only forces for a few representative locations of the rotor winding are presented below.

The Lorentz forces acting in the central part (along the coil axis) of the stator winding are shown in Figure 1.1.11The maximum forces acting in the central part are about 125 Newton/cm of conductor length. The forces in all other conductors within the winding center cross-section are smaller than the ones presented in the figure.

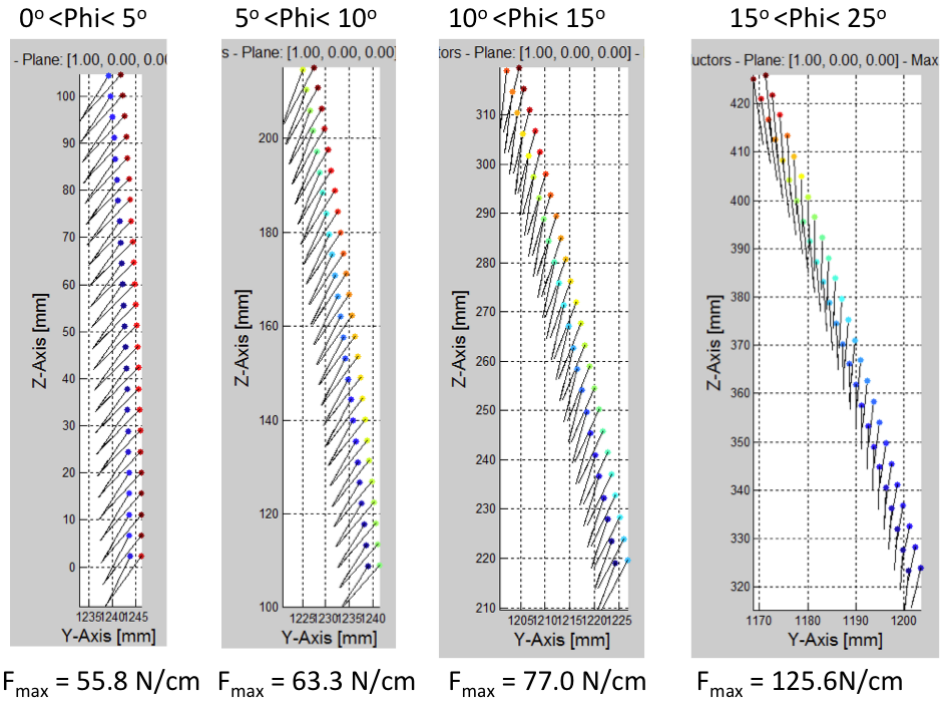

Figure 1.1.11. Lorentz forces acting on individual conductors of the innermost stator winding in Newton/cm of conductor length. The points indicate the conductors with color-coded field strength; the lines show the direction of the acting forces with the line length proportional to the force.

1.1.2.1.8.4 Models and Simulations

A large number of simulations were performed to evaluate several aspects of the FSG:

- The initial sizing of the generator was performed using 3D finite element simulations validating all electromagnetic parameters such as the peak field at the rotor and stator winding as well as the electromagnetic torque.
- Some fault conditions such as quench propagation in the rotor and stator winding, short circuit fault, and open phase conditions were simulated.

Numerical analyses using both AML's proprietary CoilCad and FEA software packages were used to optimize the FSG design, address some risk areas, and evaluate all operational parameters of the generator at all stages of the work.

1.1.2.1.8.5 Field Distribution in FSG

The electromagnetic design of the generator is the foundation for the mechanical design and cooling implementation. Extensive FEA simulations were performed to validate the preliminary sizing. 2D models were used to simulate the full load behavior and 3D simulations were used to validate the rotor design and the operating point of the superconductor. The field distribution at full load is very important to verify that the peak field at the rotor is acceptable and to determine the armature reaction field. Figure 1.1.12 shows the flux distribution at no load. Figure 1.1.13 shows the geometry implemented for FEA. The winding is approximated by solid components in which a uniform current density is applied. The rotor and stator saddle coils are represented with a constant cross-section and do not include any conductor placement optimization performed using CoilCad.

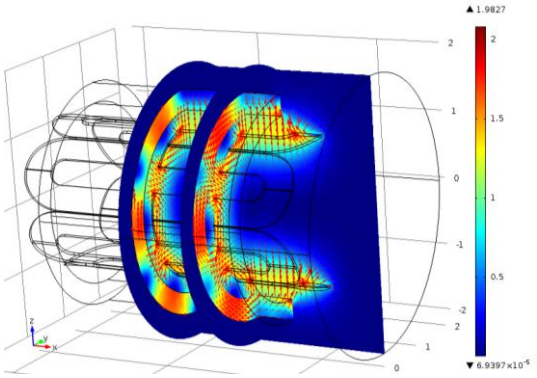

Figure 1.1.12. 3D No-load Flux distribution in FSG.

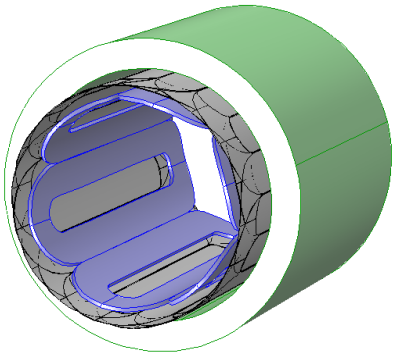

Figure 1.1.13. Geometry of active components as implemented

Fault Conditions and Electro-Thermal Instabilities

Dynamic simulations were performed to simulate two major types of fault conditions. The first type of fault is intrinsic to superconducting coils and is due to electro-thermal instabilities. Because of a local increase of temperature, part of the superconductor can become normal (i.e., non-superconducting), thus forcing the current to leave the superconducting filaments and flow in the resistive matrix leading to heat generation. Once a critical volume of superconductor is normal, a thermal runaway occurs, and a heat front propagates in the winding. It is paramount to understand the velocity of the normal zone propagation in the winding, the peak temperature, and the stability of the coils. In the case of the FSG, the conductor has been chosen to achieve very high operational margins of over 100% in the rotor and about 20% in the stator, making a quench highly unlikely. The electrical and thermal properties of MgB_2 conductors were provided by Columbus Superconductor. Figure 1.1.14 shows a typical MgB_2 conductor topology with fine filaments embedded in a resistive matrix. The conductors are embedded in a composite structure as shown in Figure 1.1.14. The heat transfer during a quench is progressing in 3 dimensions, and all the non-linear properties of the different materials were taken into account. While showingabout the same stability and temperature margin, the rotor and stator exhibit different quench behaviors, due mostly to their very different electrical conductivity of the chosen conductor matrix material. An example of such simulations is presented in Figure 1.1.15, showing the temperature distribution in a section of the rotor a few seconds after a quench was induced.

A second type of fault that can occur in all electric machines was also dynamically simulated; the stator can be subjected to a short circuit, or a phase can be open, leading to unbalanced operation. During a short circuit, the superconducting stator acts as a resistive fault current limiter by transitioning from superconducting to the resistive state as soon as the phase current becomes larger than the critical current. Due to the over-current the complete stator phase becomes simultaneously normal conducting and introduces a large impedance, thus limiting the current. During the quench of the stator phase winding, a large amount of heat is generated. The simulations performed confirmed that the fault current limiting regime is safe, with no expected degradation of the superconductor, since the maximum temperature reached after 1 second (time needed for the protection system to react) is only about 75 K.

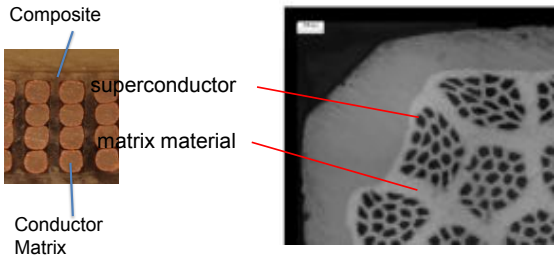

Figure 1.1.14. Winding configuration (left); MgB2 conductor topology

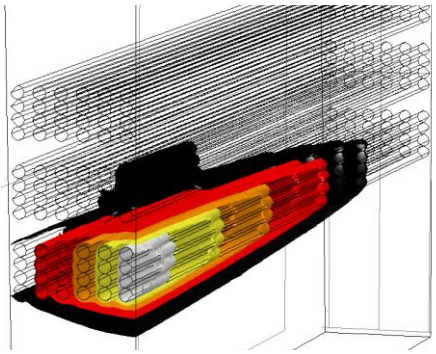

Figure 1.1.15. FEA model of a section of the rotor winding

The open phase condition represents several issues that need to be understood. These include induced currents in the rotor cryostat wall, causing fields that superimpose the rotor selffield, creating local Lorentz forces and AC losses in the rotor. The performed analysis shows that the forces applied on the cryostat wall are too low to be a concern, and the AC losses in the rotor lead to a very small temperature increase. In summary, the simulations confirmed that the FSG is intrinsically very robust against all the common types of generator faults.

1.1.2.1.9 Cryogenic Cooling System Design

This section is a summary of the cryogenic requirements and conceptual design of the stator and rotor cooling system, and the cryocooler developed during Budget Period 1.

1.1.2.1.9.1 Cryostat Design

Heat loads in the stator and rotor cryostats (loss analysis)

Based on several design iterations, the cryogenic heat loads in the rotor and stator cryostats for the present design concept are all below 18 K.

For the stator, it was decided to provide helium gas cooling at 15 K and additionally 60 K to reduce the load on the refrigerator. The largest heat load at 15 K is the heating of the stator coils caused by the rotating magnetic DC field of the rotor. This is a loss due to a hysteresis effect from the changing magnetic field in the superconductor and eddy current and coupling losses in the conductor matrix material. At 15 K, the next largest source of heat is the radiation through the multilayer insulation (MLI).

A conventional radiation shield operating at 60 K, as used in many superconducting magnets, is not feasible for the FSG, because eddy current heating in a metallic shield would be unmanagable. For the current leads, copper conductor is used above 60 K and high temperature SC leads below 60 K. 60-K thermal interceptsare used for the current leads and the torque tube to reduce the load on the cryogenic cooling system. Additionally, there are smaller heat loads from the cryo-distribution lines and penetrations into the cryostats.

For the rotor, only 15-K helium gas is used to avoid a more complex cold helium gas rotary feed-through system. The heat loads to the rotor are from heat conduction through the torque tube, radiation through the multilayer insulation, and the copper current leads.

The corresponding total heat loads that determine the size of the cooling system for the FSG **are 849 W at 15 K** (74 g/s at 2 K temperature rise) and **399 W at 60 K** (38 g/s at 2 K temperature rise).

Summary of helium gas cryocooler specifications (cooling system)

The design chosen for the cryocooler is based on a reverse Brayton cycle with two expansion turbines. As discussed below, this is an efficient solution using a relatively high helium gas pressure with a relatively large gas flow rate and low pressure drops and temperature rises in the cryostat cooling tubes. Given the above design heat loads, the cryocooler requirements for the two circuits are:

- Stator 15-K and 60-K circuits: 615 kPa pressure to the distribution system and cryostats, return pressure 20 kPa lower, temperature rise of 2 K. Total helium gas flow rates of 38 g/s and 74 g/s are required at 60 K and 15 K, respectively.
- Rotor 15-K circuit: 615 kPa pressure to the distribution system and cryostats, return pressure 20 kPa lower, temperature rise of 2 K, and a total gas flow rate of 38 g/s.

Given these parameters and the refrigerator efficiency, helium gas cooling tube configurations for the stator and rotor coils and the current lead heat exchangers have been developed and are described in the following paragraphs.

Helium gas cooling tubes and manifolds in the cryostats (cooling network sizing)

After several design iterations of the cooling tube configuration, a concept with both the rotor and stator coil packs being wrapped in stainless steel cooling tubes (6-mm OD and 5.5-mm ID) around the circumference in a helical path was chosen. With a pitch of 8 mm center to center and a total length of the coils of 4 m, the total tubing turn number is 500. To match the high helium gas flow rate and low pressure drop required by the refrigerator, the 500 turns are divided into 36 groups of parallel circuits. The circuits are fed from input and output gas manifolds from one end of the coil packs. The tubing is embedded in the epoxy/glass composite. An analysis of the temperature distribution within the composite was carried out for the stator with a finite element code STAR-CCM (Figure 1.1.16) to ensure that this configuration results in small thermal gradients within the composite structure. The analysis of the flow rates, pressure drops, and heat transfer coefficients was done using the properties of cold helium gas calculated with the program HEPAK [14].

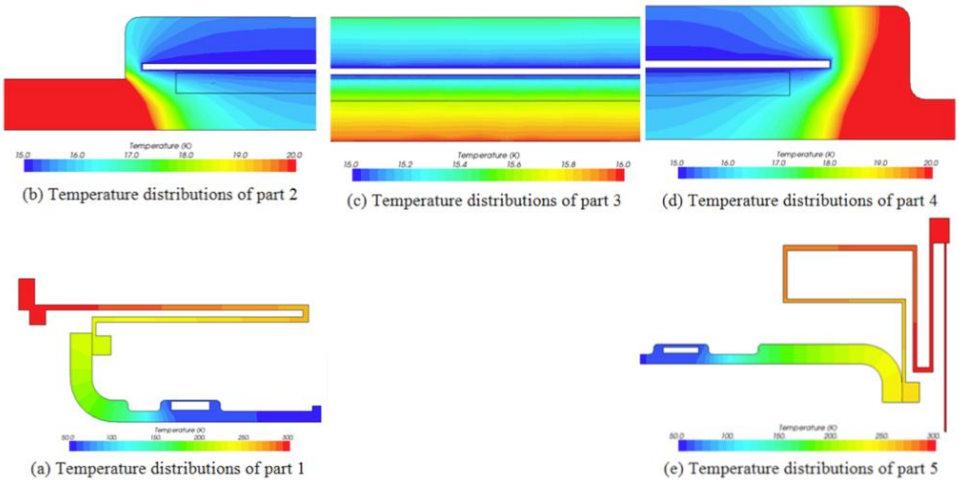

Figure 1.1.16. Temperature distributions in five regions of the stator (STAR/CD simulation)

In addition to the cooling of the coil packs at 15 K, a cooling circuit is required for the stator torque tube to provide the 60-K intercept discussed above. This heat load is taken by 2 turns of 17-mm OD stainless steel tubing.The helium gas is supplied at 60 K for the torque tube intercepts at both ends and the 4 current lead heat exchangers, which are all in series to avoid any issues of load balancing. Similarly, for both the rotor and stator, the 15-K cooling circuits for the coil packs and the current-lead heat exchangers are also in series.

Current lead heat exchangers helium cooling concept

The copper part of the current leads require heat exchangers at the cold ends. For the stator, three (3) heat exchangers are required, rated for the ~1000-A leads, and one heat exchanger for the 200-A neutral lead for intercepting heat at 60 K. For the rotor, two (2) heat exchangers for the 750-A leads at 15 K are required. A preliminary design of a micro-channel heat exchanger uses 100 small channels to yield the required small pressure drop and heat transfer with a small temperature difference between the lead heat sink and the helium gas. The details of the current leads, the conductor connections, and the voltage insulation are given in section 1.1.2.1.9.2. A budgetary cost estimate for the fusion bonding of the plates for these custom-made heat exchangers has been obtained from Refrac Systems in Arizona.

Radiation heat loads through the multilayer insulation

MLI is traditionally used in cryostats of SC magnets to reduce the thermal radiation heat transfer between room temperature and the cold surfaces inside the cryostat. A summary of many measurements of MLI shows an effective thermal conductivity, keff, of about 0.1 mW/m–K [15]. Based on these results and assuming a cold vacuum pressure of less than 10^{-4} Torr in nte insulation vacuum, a heat load of 1.2 W/m^2 for a 25-mm thick MLI blanket with perfect coverage is estimated. To allow for some leakage through the corners of the installed MLI, a more conservative value of 2 W/m^2 for the radiation heat loads has been assumed. A budgetary quote for the purchase of MLI per 1000 m^2 was obtained from CAD Cut (Middlesex, VT).

1.1.2.1.9.2 Cryocooler

Cooling system configuration

A two-stage turbo-Brayton cryocooler was selected to provide cooling helium gas flow to the superconducting rotor and stator coils. A schematic of the cooling system configuration is shown in Figure 1.1.17. The two-stage cryocooler provides active cooling at 60 K and at 15 K for the stator, and at 15 K for the rotor. The cooling cycle is continuous flow using helium gas as the cycle fluid. At the warm end of the cycle, four centrifugal compressors pressurize and circulate the cycle gas. The heat of compression is removed using intercoolers and an aftercooler heat exchanger, which reject heat through a liquid cooling loop. Recuperative heat exchangers (recuperators) are used to increase overall cycle efficiency by pre-cooling the high-pressure stream. The first-stage expansion turboalternator is used at the cold end of the first-stage recuperator to accommodate the ineffectiveness of this recuperator and to intercept thermal loads from the stator torque tube and current leads at 60 K. A second-stage turboalternator accommodates losses in the second-stage recuperator and parasitic heat loads at the cold end, and provides cooling to the superconducting stator coils, rotor coils, and rotor current leads at 15 K. Cooling to the rotor is provided through a rotary helium transfer coupling. The design ofthis coupling can accommodate only one cooling loop (one inlet and one return stream). For this reason, the 60-K flow is not used to intercept thermal loads on the rotor. The rotor and stator are each contained in separate vacuum-insulated cryostats. Thermal intercept heat exchangers are integrated into the stator current leads at 60 K and 15 K and into the rotor current leads at 15 K.

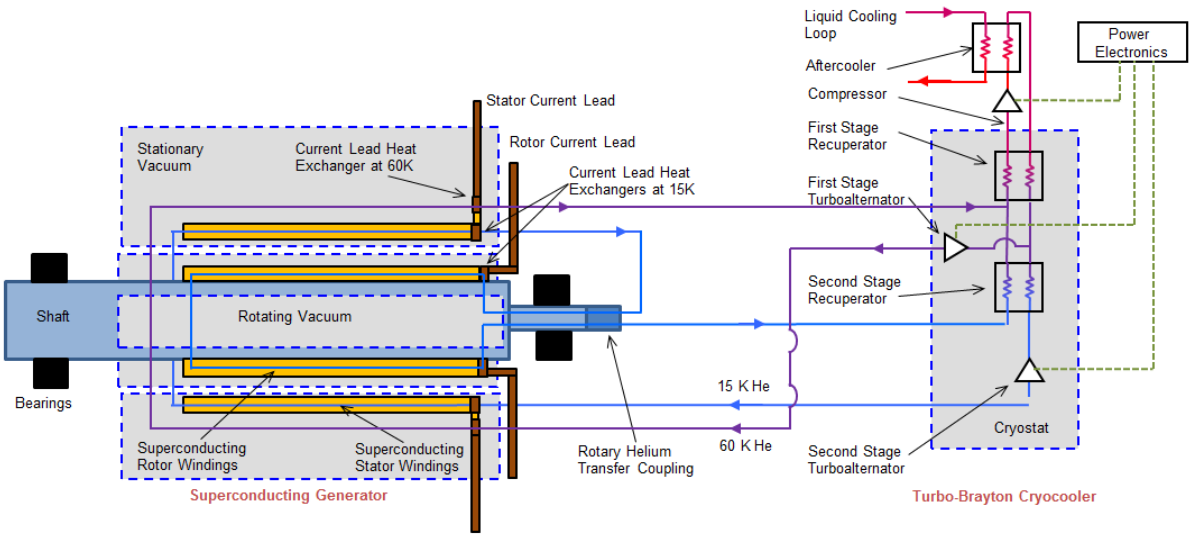

Figure 1.1.17. Cooling System Configuration with Separate Cryostats for the Rotor and the Stator

The cryocooler design point is 399 W of cooling at 60 K and 849 W of cooling at 15 K, with heat being rejected at 328 K. The efficiency of the cryocooler is projected to be 26% of Carnot. The cryocooler was optimized to minimize both unit cost and operating cost over a period of fifteen years.

Rotary helium transfer coupling

A rotary helium transfer coupling will be used to feed cryogenic helium gas from the stationary cooling circuit into the rotor. The FSG-specific design is based on a coupling that was built and tested

previously in Japan [16]. The coupling is built from a pair of concentric vacuum-insulated bayonet connectors, of the type commonly used in cryogenic transfer lines. The rotary connector is, in essence, a bayonet within a bayonet. A ferro-fluid seal (FerroTec Model HS-3000-SLFEC, Part # 133218) forms a helium-tight seal on the outer surface of the rotating connector. A labyrinth seal separates the inflow and outflow transfer lines.

Reliability

The reliability of Creare turbo-Brayton cryocoolers has been calculated for several space flight programs. The reliability of the cryocooler is governed by the control unit, which has a Mean Time Between Failure (MTBF) of 600,000 hours per MIL-HDBK-217 (MTBF of the mechanical hardware is 2.3 million hours). This is an order of magnitude greater than that of current commercial laboratory coolers, which have a reported MTBF of approximately 80,000 hours. The reliability of the rotating helium transfer coupling will depend on the bearings and seals. One manufacturer of ferrofluid seals lists an MTBF of 130,000 hours [17]. Given that the seals are rotating very slowly in the FSG application, this estimate is likely to be conservative.

1.1.2.1.10 Electrical Design

1.1.2.1.10.1 Design Details

The FSG converts mechanical energy into electrical energy; therefore, it needs to be able to connect to other devices such as power converters and be compatible with the other electric components of the wind farm electrical network.

Like all synchronous generators in wind turbines, the electrical load is a power converter rectifying the output of the generator to a regulated DC bus (Figure 1.1.18). The DC power is then inverted to the grid frequency and transmitted to the users. The FSG is based on an air-core design and, as a result, presents a large rotor inductance, making dynamic control of the excitation current challenging. However, the current can be adjusted slowly, based on wind conditions, to adjust to the operational power factor. As part of the electrical design, fault conditions are considered. One of the most important features of the FSG is its robustness to fault conditions and its intrinsic low short circuit power, while having a low synchronous reactance, contributing to an outstanding dynamic behavior. Indeed, the SC stator's capability of limiting fault currents has a significant positive impact on the mechanical design of the generator, the protection circuit breakers and on the wind turbine design. The connections to the converter and the excitation

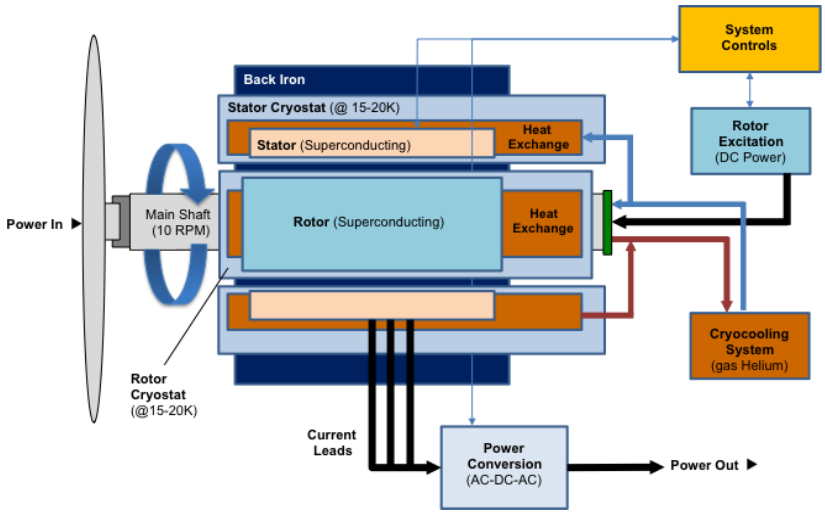

Figure 1.1.18. FSG Electrical Design

power supply are performed through optimized current leads designed to minimize the heat load at cryogenic temperature. The current interconnect design is based on a star configuration.

Short circuit fault and recovery

As mentioned, a short circuit fault leads to a transition of the stator winding from the SC to the normal conducting state. The protection circuit can interrupt the power within half a cycle. During the time of at most one (1) second, the stator winding heats up to about 75 K . The heat deposited into the stator winding will then have to be absorbed by the cooling system before the systems becomes operational again, which most likely will take several hours. The current change during limitation is limited by the EMF of the generator. Based on the current diffusion time constant, it takes only a fraction of a millisecond for the current to transition from the SC filaments to the resistive matrix. The current limitation feature of the phase windings is, therefore, almost instantaneous.

Converter configuration and specifications

The FSG is different from other wind generators in the sense that it is designed with a low number of poles. The low number of poles leads to a low frequency, which is needed to limit AC losses in the stator, but less advantageous in terms of power converter operation. Several high-power converters for wind turbines are commercially available; one of the largest one is manufactured by ABB and is rated to up to 9 MVA for operation in the frequency range 8-100 Hz, i.e., a much higher frequency than the FSG. After numerous discussions with ABB, it was concluded that their large converter with a power rating of 4.5 MVA would be able to operate at the FSG's frequency, with slight modifications. While operation at low frequency is interesting in terms of total harmonic distortion (THD), which will benefit the FSG, the low frequency leads to more heat generated in the solid-state switches. The thermal limitations of the converter components impose a de-rating to 3.3 MVA at 0.5 Hz. As such, three (3) converters must be operated in parallel to reach the 10-MVA rating of the FSG.

Rotor excitation

The rotor requires a DC current to generate the excitation field. In steady-state operation, the rotor winding, being superconducting, does not require any power, except minor losses due to the current leads. However, any change of the excitation current will lead to an inductive voltage and require power from the excitation power supply. In a synchronous machine the excitation current can be controlled to adjust the power factor during variable speed operation. The FSG rotor winding inductance is quite large at about 3.3 H, thus preventing any fast variation of current. Driving the current dynamically with a sub-second time constant would require a large amount of power and a significant cost increase for the excitation system. Operation at constant current is therefore recommended, with the possibility to adjust the current over long-time constants of several minutes.

1.1.2.1.10.2 Interconnects

Current lead design

The FSG uses conduction-cooled leads for both the rotor and stator coils. They operate essentially adiabatically with one end maintained at a cryogenic temperature, and the other end going to an external connection at room temperature. The cold end of each of the two rotor leads is attached to the coil lead; thus, it is necessary to use a heat exchanger at this location to keep the temperature of the superconductor below 20 K.

The armature, being composed of three-phase coils, requires four leads for the external connections, one for each phase main lead and one for a neutral connection between the three phases. In the case of the stator, a 60 K heat intercept is used on the torque tube to reduce the heat leak from

This page removed due to Intellectual Property/Distribution Limitations

1.1.2.1.11.2 Active Section Manufacturing

The active sections of the FSG refer to the assemblies containing the coil windings. The active section of the rotor consists of the rotor center section without the shaft ends. The torque tube for the rotor and stator active sections are shown in Figure 1.1.20 and Figure 1.1.21. The rotor active section lay-up of the composite will be using a low Young's modulus mat material at all metal interfaces to minimize thermally induced stresses. The lay-up process will be performed in multiple layers, where the mat is wound onto the rotor with the appropriate tension and weave angles to achieve maximum performance. That, in turn, is covered with a high strength retention layer. The stator active section will be manufactured from composite material only; consequently, a tooling mandrel must be used to achieve the proper geometry for the torque tube.

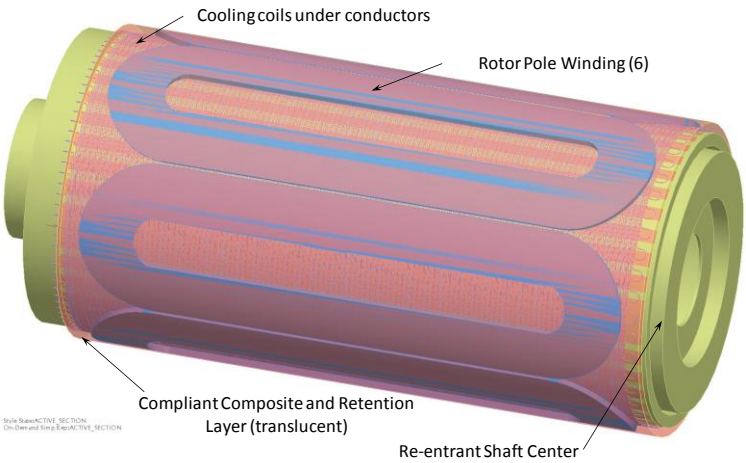

Figure 1.1.20. Rotor Active Section

The stator active section will consist of a composite torque tube with multiple layers of compliant composite for the cooling tubes and the windings. These, in turn, are covered with a high-strength retention layer.

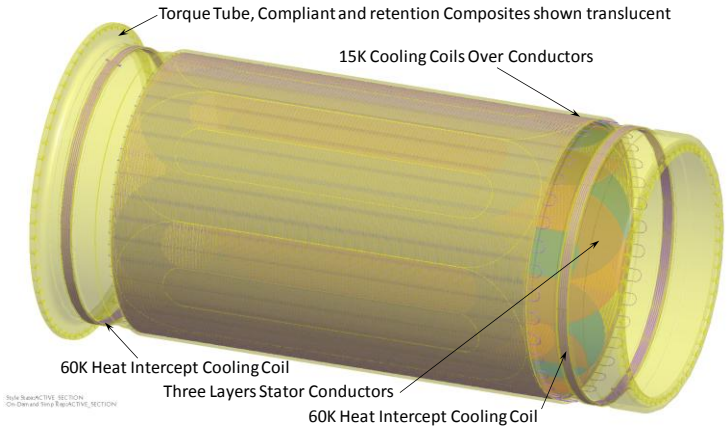

Figure 1.1.21. Stator Active Section

1.1.2.1.11.3 Bearing Arrangement

For this low-speed application with requirements for reliable, low maintenance capability, anti-friction bearings were chosen. Spherical roller bearings provide high load capacity and can be either grease lubed or used with an oil reservoir. The end-bell (bearing bracket) assemblies are typical configurations of standard construction components. Unique to the FSG is the introduction of an axial slip plane between the non-drive end insulated bearing housing and the outer race of the anti-friction bearing to better handle the larger axial relative movements between shaft end and housing without large forces.

1.1.2.1.11.4 Excitation Components

The conventional method for transferring current to the rotating field winding of a generator from a stationary power supply is to use brush rigging. The corresponding assemblies have stationary brushes sliding on rotating collector rings causing brush wear. These assemblies can require frequent

maintenance, such as brush replacement. To reduce maintenance, a new system, based on rolling contacts, using Roll-Rings™ was selected. These assemblies are reported to be maintenance free. The Roll-Ring™ configuration typically is similar to a typical exciter assembly, making its implementation rather straightforward. The configuration shown in the models represents a system that would be used for power generation applications. For the FSG however, the higher axial relative movement between rotating and stationary components requires a configuration where the Roll-Ring™ assembly will have self-contained bearings to allow the entire Roll-Ring™ assembly to "float" with the non-drive end of the FSG shaft.

1.1.2.1.11.5 Frame Construction

The frame assembly for the FSG is considered very conventional in the power industry. The laminated, low loss electrical steel will utilize standard die design techniques and ribbed frame support. Bored frame and dovetail keys are used to maintain radial location. The ribs will have an axial locating shoulder for the clamp plates. Through-bolting will clamp the laminations to the optimum pressure for minimized core loss. The stator frame will be stacked verticallyas in most large bore machines.

1.1.2.1.11.6 Frame Assembly

The non-drive end re-entrant end is mounted to a vertically placed generator frame with the frame NDE down. Placement of the frame is such that access to the non-drive end composite mounting interface is allowed. The composite active section with the drive end re-entrant end, cooling assemblies, current lead assemblies, etc., is lowered vertically into the stator frame and secured. Main leads, feed-through components, cooling connections and ID vacuum containment are added. The stator frame assembly is returned to horizontal for vacuum application and rotor insertion.

1.1.2.1.11.7 Rotor Insertion

Special tools for rotor insertion will be designed. The tools will be designed to allow crane picks from both ends of the stator frame. Turnbuckle "hangers" will be connected to provisions in the frame interior. The rotor is "threaded" into the stator, supported by the hangers and adjusted to proper concentricity. The bearings and end-bells are assembled and turnbuckles removed.

1.1.2.1.11.8 In-Process Testing

During the production of any electrical machine, in process inspections and non-destructive electrical testing are strategically placed in the process to catch errors in a timely manner in order to minimize lost effort and rework

1.1.2.1.11.9 Shipment

The machine has been kept to less than 12 feet in height and width to minimize shipping issues. Special trucks with higher axle count and low decks will allow minimal restrictions to travel to any coast for assembly to the mainframe and nacelle.

1.1.2.1.12 FSG Cost

A costed Bill of Materials was developed for the FSG based on the manufacturing processes described and quotes from various purchased components. Since reduced cost of energy is a primary mission for this project, Pareto diagrams for the part material costs and estimated labor hours was made for both the stator and rotor to help determine where DR2 effort on design cost reductions

should be focused. A summary of the system market pricing, based on estimated costs, is shown in Table 1.1.3.

Table 1.1.3. FSG Estimated Market Price, 2015 Dollars, Production of over 100 units/year

Item	Material ($)	Labor ($)	Total ($)
Generator Assembly			2,196,450
Stator	930,180	206,902	
Rotor	960,202	99,166	
Intermediate Shaft and Couplings	257,178	12,519	269,697
Excitation System			103,838
Roll-Ring (Exciter Connection)	43,930		
Excitation Power Supply	54,908		
Excitation Cabling	5,000		
Cryocooling System			434,316
Cryocooler	362,250		
Rotary Cryogenic Feed	30,000		
Heat Rejection System	42,066		
Power Conversion System			1,280,975
Power Converters (3 ea)	1,260,975		
Power Converter Cabling	20,000		
Total ($)	3,966,689	318,587	**4,285,276**

1.1.3 Project Overview and Objectives

The objectives of Budget Period 2 for the FSG project are mainly focused on de-risking the design produced in Budget Period 1. De-risking rationale and FSG design risk area assessments are discussed in section 3.1 of this report, together with the risk analysis process and risk mitigation plan.

Activities performed during BP2 for Task 4.0, Advanced Modeling and Simulation (section 3.2.1), include additional simulations and finite element analyses (FEA) of the results of the de-risking experiments.

Task 5.0, Cost of Energy Model Update/Refinement (section 3.2.2) is an in-depth technical analysis of the impact of the FSG on the turbine design and a refinement of the Cost of Energy (COE) model.

Task 6.0, De-risking Experiments (Part II, section 3.2.3), is a quarter-by-quarter description of the engineering activities performed for SOPO Sub-Tasks 6.1 through 6.6.

1.2 Project Participants

1.2.1 Participating Companies/Entities

Organizations participating as partners in the funded FSG project for BP2 are described below.

- ***Advanced Magnet Lab – Palm Bay, Florida***

(Project Lead)

The Advanced Magnet Laboratory (AML) is a research and development company with a wide range of design, manufacturing and testing capabilities. AML has designed, built and tested complex superconducting magnets for industry, accelerator applications and research for US and international Laboratories, NASA, DoD and others. The company holds numerous patents for cutting-edge technologies related to superconducting magnets. AML is located in Palm Bay, Florida in a state-of-the-art facility of about 10,000 sq. ft. The facility includes a fully equipped machine shop with 4-axis and 6-axis CNC machines, cryogenic, vacuum and leak testing equipment. High current, computer-controlled power supplies and test electronics enable performance and qualification tests of normal and superconducting magnets.

AML has all necessary software for the design of electromagnetic systems. AML uses COMSOL software for 3-D structural analysis, AMPERES and COMSOL for 3-D magnetic field calculations and multi-physics modeling and a proprietary coil design software package, CoilCAD®, which allows design, optimization and interface to CNC manufacturing of the most complex winding patterns. AML also has developed high fidelity sizing models for superconducting machines based on the patented Double-Helix™and Stacked Saddle Coil (SSC) coil packaging technology.

- ***Emerson Electric Company(Kato Engineering) Mankato, Minnesota***

Emerson Electric Company is a $21.8 B, diversified global technology company engaged in designing and supplying product technology, as well as delivering engineering services and solutions to various industrial, commercial, and consumer markets worldwide.

Concentrating in the 200 kW to 15 MW range, Leroy Somer North American (LSNA) - Kato Engineering, a subsidiary of Emerson Electric located in Mankato, MN, supplies custom engineered equipment for a variety of uses, including oil & gas, mining & manufacturing, military, transportation, wind generation, co-generation, computers and telecommunications. This broad product knowledge with the engineering flexibility needed for custom engineering, places Kato at or near the top of the list for capability to successfully develop new generator technology. Kato Engineering's equipment is manufactured in accordance with NEMA MG-1 and IEEE Std 115 and is compliant with many other industry certifications and standards.

Engineering Expertise: At its Mankato, MN, facility, all aspects of motor/generator design are fully supported. Designs are accomplished using ProE 3-D modeling and FEA simulation using ANSYS Multi-Physics or Pro-Mechanica. Advanced simulation capabilities include non-linear stress, electromagnetic using EMAG, CFD using CFX, heat transfer, as well as fracture mechanics. The company holds many patents for motor and generator technologies.

Insulation Expertise: Kato Engineering has developed many proprietary insulation systems for our products of Class F or Class H insulation using vacuum pressure impregnation (VPI) cycle.

Field Excitation Systems Expertise: Kato Engineering designs and builds custom, brushless excitation and voltage regulation systems.

Manufacturing Expertise: At its Mankato, MN, facility, Leroy Somer North America ("LSNA"), Kato Engineering has 300,000 square feet and 360 employees using connected processes for rapid throughput. State-of-the-art equipment and processes have been optimized for a complete line of precision-engineered, top quality AC generators, motor-generator sets and controls for prime, standby, and peak-shaving power generation equipment.

➢ *Argonne National Laboratory – Chicago, Illinois*

Argonne National Laboratory seeks solutions to pressing national problems in science and technology. The nation's first national laboratory, Argonne conducts leading-edge basic and applied scientific research in virtually every scientific discipline. Argonne researchers work closely with researchers from hundreds of companies, universities, and federal, state and municipal agencies to help them solve their specific problems, advance America's scientific leadership and prepare the nation for a better future. With employees from more than 60 nations, Argonne National Laboratory is managed by "UChicago Argonne, LLC" for the U.S. Department of Energy's Office of Science.

Argonne brings extensive experience in the development of superconducting magnets and cryogenics methods for a wide variety of applications to instrumentation and facilities for basic research in nuclear physics and also has a very strong simulation group available to provide medium to very large-scale thermal, fluid, and mechanical analysis on a variety of computer clusters up to the peta-flop scale if necessary. This group extensively uses both commercial packages such as Star-CD/CCM+, as well as the in-house developed large-scale code Nek5000. In Budget Period 2, the appropriate test facilities and expertise at the Argonne ATLAS superconducting linear accelerator will be used to perform experimental measurements to validate the performance of a cryogenic in Task 6.4.

➢ *Creare Inc. – Hanover, New Hampshire*

Creare Inc. is an engineering research and development firm located in Hanover, New Hampshire, an Ivy League college town in the heart of New England. Founded in 1961 to allow innovative engineers the freedom to expand the boundaries of their engineering disciplines, Creare continues this tradition of innovation and exploration today. Members of the senior staff are leaders in their fields and current areas of research and development are at the cutting edge of technological and scientific development. Typical end products of Creare's work include analytical techniques and results, experimental data, engineering models, design recommendations, software, numerical solutions, prototype hardware, and hardware designs.

Creare has developed turbo-Brayton cryocooler technology that is well suited to superconducting applications. Our technology has its heritage in a space-qualified cryocooler that was developed by Creare and installed on the Hubble Space Telescope. Our coolers rely on miniature turbomachines operating at high speeds in non-contract bearings that result in very long component lives with no maintenance requirements. The components are small, light-weight, and may be configured in separate modules, facilitating integration into compact systems and allowing components to be situated in thermally sensible locations, reducing parasitic heat loads and insulation requirements. Distributed cooling is provided through the compressor-driven cycle gas, eliminating the need for an additional circulator and heat exchanger, and the machines may be multi-staged to provide cooling at multiple

temperatures. Furthermore, because the system relies on high- speed turbomachines, the system efficiency and system mass scale favorably at high capacities. This is not the case for regenerative coolers, such as the Gifford McMahon or Stirling systems that are commercially available today.

➢ *Columbus Superconductors - Genoa, Italy*

Columbus Superconductor SpA is a world leader in cutting-edge magnesium diboride (MgB_2) technology and the transformation of this superconducting material into long, versatile and highly reliable superconducting wires. The company is vertically integrated, from R&D to applications and from production to sales.

Columbus Superconductors was established in Genoa in 2003 following successful cooperation involving ASG Superconductors, CNR-INFM (the Italian National Research Council) and a group of researchers. The company was among the first to develop long wire prototypes and in 2005 set the world record with the first 1.6 km MgB_2 tape. This milestone event paved the way to industrial applications for MgB2-based wires and their large-scale production.

Columbus Superconductors manufactures superconducting wires using the so-called Powder in Tube (P.I.T) ex-situ process, which is a very effective way of producing uniform, strong, long-length conductors. During the initial chemical phase, the fine MgB_2 powders are obtained from a controlled solid-state reaction between boron and magnesium. During the second metallurgical stage, the powders produced by the reaction are packed inside a metal tube, which then undergoes several drawing and rolling processes to produce a monofilament MgB_2-based wire with the desired cross-section. A variable number of monofilament wires, possibly combined with additional wire constituents, are packed inside a second tube which is then subjected to a similar manufacturing process in order to obtain the desired cross-section, length and shape. The production process is completed by a heat treatment that delivers the final transport properties of the wire. The entire production process is managed using state-of-the-art process control techniques involving both skilled engineers and modern technology.

➢ *The University of Houston - Houston, Texas*

The University of Houston is the leading public research university in Houston and the third largest university in Texas. Classified by the Carnegie Foundation as Tier One in its national research-focused designation, the university conducts nearly $130 million annually in research, and operates more than 40 research centers and institutes on campus. Interdisciplinary research includes superconductivity, space commercialization and exploration, biomedical sciences and engineering, energy and natural resources, and artificial intelligence. The University's Texas Center for Superconductivity-Applied Research Hub (TcSUH-ARH) works with industry to advance high-temperature superconductivity (HTS) applications in energy. A major interest is in the manufacture of superconducting wire for use in cable and other related products that are expected to play a major role in improving the electric power grid, of vital importance for the transmission and distribution of electricity from renewable sources such as wind and solar.

➢ *National Renewable Energy Laboratory Golden, Colorado*

The National Renewable Energy Laboratory (NREL) is the U.S. Department of Energy's primary national laboratory for renewable energy and energy efficiency research and development. NREL develops renewable energy and energy efficiency technologies and practices, advances related science and engineering, and transfers knowledge and innovations to address the nation's energy and environmental goals.

The National Wind Technology Center (NWTC) at NREL has unique research capabilities, experienced staff, and specialized state-of-the-art equipment to provide its industry partners with the technical support they need to take their projects from the design table to the marketplace.

Research at the NWTC covers a wide spectrum of engineering disciplines that are applicable to both land-based and offshore wind energy, including: atmospheric fluid mechanics and aerodynamics; dynamics, structures, and fatigue; power systems and electronics; and wind turbine engineering applications for wind turbines with capacity ratings of a few hundred kilowatts to several megawatts. The center's unique capabilities include:

- Design review and analysis
- Computer-aided engineering tools
- Systems Engineering
- Controls Analysis
- Testing
- Transmission grid integration
- Wind resource assessment and mapping.

➢ *Center for Advanced Power Systems – Tallahassee, Florida*

The Center for Advanced Power Systems (CAPS) is a multidisciplinary research center, located on the campus of the Florida State University, organized to perform basic and applied research to advance the field of power systems technology. CAPS emphasis is on application to electric utility, defense, and transportation, as well as, developing an education program to train the next generation of power systems engineers. The research focuses on electric power system modeling and simulation, power electronics and machines, control systems, thermal management, high temperature superconductor characterization, and electrical insulation research.

With support from the U.S. Navy, Office of Naval Research (ONR) and the U.S. Department of Energy, CAPS has established a unique test and demonstration facility with one of the largest real-time digital power system simulators along with 5 MW AC and DC test beds for hardware in the loop simulation. The center is supported by a research team comprised of dedicated and highly skilled researchers, scientists, faculty, engineers, and students, recruited from across the globe, with strong representation from both the academic/research community and industry.

CAPS is dedicated to creating the focus and resources needed to develop and implement an overall Systems Driven Strategy focused on the high level system issues of power distribution, system control, performance and component needs of tightly coupled power systems typical of advanced transportation power systems.By concentrating on broad industry objectives, CAPS provides the

mechanism for government and industry to capitalize on a joint infrastructure to produce advanced power systems and components.

- ***Composite Analysis Design and Test*** -

Winona State University was first founded in 1858 for the purpose of educating teachers. Since then, the university has gone through four name changes. The Board of Directors adopted the current name in 1976.

The university mission statement says "to educate and enlighten our citizenry at a distinctive institution: a community of learners dedicated to improving our world." It is classed as a Master's College and University I by the Carnegie Institute.

WSU offers more than 80 major programs of study and 10 pre-professional programs. In addition to the Bachelor of Arts and Bachelor of Science degrees, academic programs include four Special Licensure Programs. The University includes five colleges: Business, Education, Liberal Arts, Science & Engineering, and Nursing & Health Sciences.

- ***Composite Technology Development Layfayette, Colorado***

Composite Technology Development, Inc. (CTD) specializes in developing state-of-the-art materials and products for extreme conditions and demanding applications. Since its founding in 1988, the company has built a diverse portfolio of sophisticated engineering solutions, as well as a reputation for innovative problem solving and outstanding customer service and communication.

CTD has over 20 commercial resin systems that are sold worldwide for a variety of specialty applications:

- NANUQ® Electrical Insulation is used to insulate many of the world's highest performing magnets.
- CTD has licensed radiation resistant cryogenic insulation for the ITER fusion device to LORD Corporation.
- CryoCoat™ Thermal Insulation materials are formulated to provide excellent thermal and mechanical properties at cryogenic temperatures.
- CryoBond™ Adhesives are compatible with a wide variety of substrates and are formulated to withstand thermal cycling to cryogenic temperatures.
- KIBOKO® Resin Systems are used in composite tanks and structures that operate at cryogenic temperature.

CTD offers engineered composites such as KIBOKO® all-composite (or linerless) tanks and pressure vessels and Portable Array Modules (PAM™) that provide reliable solar power for expeditionary forces and remote operation. PAM™ has been licensed to Nishati, Inc. for manufacture and commercialization.

In addition to its technology offerings, CTD provides engineering services including cryogenic mechanical testing and thermo-mechanical design.

1.3 Research Summary

Developing a Fully Superconducting Generator (FSG) with its anticipated benefits constitutes an ambitious R&D project, and the success of this endeavor requires advancements in several technologies. A fully superconducting rotating machine has characteristics that significantly differentiate it from conventional machines and, consequently, there are risks in achieving commercializing of such systems. During Budget Period 1 of this project, three categories have been identified as the main contributions to technical risk. These are: MgB_2 Superconductor Development, Structural Issues related to cryogenic operation, and Coil Performance Issues. The most important characteristics in each of these categories, which affect commercialization, are Cost, Performance and Reliability. De-risking of the main technical issues was the main goal of Budget Period 2 and the substantial achievements can be summarized as follows.

1.3.1 MgB_2 Mini-cable Development and Qualification

MgB_2 superconductor constitutes a brittle conductor and accordingly has significant bending radius limitations. With increasing wire diameter, larger and larger bending radii have to be accommodated. Given the bending radius requirements of the rotor and stator coil for the FSG, a mini-cable consisting of several wires is needed that has sufficient current carrying capacity and, due to the individual thin wires, enables the required bending radii. Additionally, some modest increase in current carrying capacity is needed to allow for sufficient operational margin in the rotor winding. For the stator winding, a conductor with smaller superconductor filaments in needed to reduce AC losses in the stator winding, which are proportional to the filament diameter.

In collaboration with Columbus Superconductor from Genoa, Italy, a 6-around-1 mini-cable, consisting of sufficiently thin individual wires, has been successfully developed, that shows no cable degradation and enables the required bending radii. At the same time, progress has been made in critical current performance that meets the requirements of the rotor windings. Progress has also been made in the reduction of filament size; however, the original goal of 10-micron filament diameters has not yet been achieved. This shortcoming in the currently available MgB_2 conductor would lead to larger losses in the stator windings, which can be accommodated with additional cooling. The conductor development by Columbus was performed on an industrial scale and no further development is needed for large-scale production. The projected cost of the MgB_2 superconductor is estimated to reduce significantly for larger production runs and would meet the cost goals developed during Budget Phase 1.

1.3.2 Structural Composite Analysis

A very large temperature range exists between manufacturing (~ 300 K) and operation (15 K – 20 K) of the rotor and stator assemblies of the FSG. Many different materials are used in these assemblies and differential thermal expansion/contraction of materials can easily develop damaging high stresses, if not properly addressed. It is therefore a design criteria of utmost importance that all active section materials need to be closely matched in their thermal expansion. The superconductors of the rotor and stator windings carry much higher currents in a much smaller conductors than in copper-based designs. The local forces developed are therefore much higher than in copper-based machines. To support the superconductors dielectric, non-magnetic, non-conductive, high thermal conductive materials are required that are strong enough to support the superconductor at cryogenic temperatures without allowing potential quench-causing micro-movements.

A Compliant Composite (CC) material to thermally match the metal structures with the lowest possible Young's modulus was developed to meet these requirements. Using the CC material, metals

are allowed to expand or contract with minimal structural stress occurring from differential thermal expansion/contraction. As required, the developed CC materials are electrically non-conductive, and their Young's modulus is much lower than the superconductor, the cooling tubes, and the rotor torque tube. Additionally, the thermal conductivity is relatively high. The CC material is dielectric and strong enough to provide support for the superconducting windings. The concept of a Compliant Composite to meet the special requirements of the FSG has been achieved.

1.3.3 Conductor Containment Fatigue Test

The FSG rotor and stator coils are embedded in the newly developed Compliant Composite Matrix (CCM), which matches the CTE of the coil support structure to the CTE of the MgB_2 conductor. A close match in CTE values of the two components is essential to avoid excessive build-up of mechanical stress during cool-down and warm-up, which could exceed material strengths and cause failure modes. Additionally, Lorentz forces acting between the rotor and stator coils are constantly changing during machine operation and mechanical fatigue could occur in the coil assemblies. This could lead to a de-bonding of the superconductor from the surrounding CCM material and allow conductor movements and premature quenching of the conductor. For the stator windings, such de-bonding could lead to reduced heat transfer needed to accommodate the AC losses in the winding.

A special superconducting test coil was built using the newly developed CCM and a Kapton-wrapped mini-cable as foreseen for the FSG. The coil underwent a large number of current cycles in a high background field at cryogenic temperatures. The resulting Lorentz forces acting on the conductor were representative of the forces acting in the FSG under full load. The coil showed no signs of fatigue, de-bonding or micro-cracks.

1.3.4 Subscale Torque Tube Temperature Cycling

Thermal cycling of the active FSG components could lead to delamination of the superconducting mini-cable from the surrounding composite material. Such delamination could lead to microscopic conductor movements and premature quenching of the superconductor, or in case of the stator windings, to a decreased heat transfer from the superconductor to the cooling tubes. Specific test setups consisting of an embedded conductor, a cooling tube and multiple precise temperature sensors were built and thermal cycling tests have been performed. No detrimental effects from thermal cycling were found.

1.3.5 AC Loss Measurement

A detailed understanding of the AC losses in the stator winding is needed for the design of the FSG. An accurate calculation of the resulting AC losses in a superconductor stator winding is rather complex. Existing models of AC losses in superconductors are only qualified for the loss calculation for pulsating magnetic fields. In a synchronous machine the situation is more complicated, since the superconductors in the stator windings experience pulsating as well as rotating fields, while simultaneously carrying AC currents with certain phase shifts relative to the changing magnetic fields.

A special experimental setup has been designed and built to measure AC losses in superconductors under the conditions seen in synchronous machines. The test setup measures AC losses of a given superconducting test coil, which is inserted in a surrounding background field. A calorimetric measurement of AC losses for a coil consisting of a certain superconductor can be performed as a function of operational temperature, as well as strength and frequency of the background field. The unique test setup, which was only possible by using additional funding sources from other projects with the same goals, is fully operational at the Center for Advanced Power Systems, located at the Florida

State University campus in Tallahassee, Florida. Measurements of various MgB_2 conductors have been performed and analyzed. Based on the measurements, the University of Houston, another collaborating partner for Budget Period 2, is developing models that allow prediction of AC losses in synchronous machines under the various operational conditions.

1.3.6 Fault Current Limitation

A generator operating at a grid has to be designed to accommodate potential short circuits on its output. Under such fault conditions the currents in the stator windings become very large and significant torques act on the rotor and stator windings. To safely handle such fault conditions, the support structures of the coils and the rotor shaft have to be over-designed. The FSG offers the unique feature of intrinsic fault current limitation. If a certain current limit is exceeded in the superconducting stator winding, the conductor quenches, leading to a substantial increase in the resistivity of the winding and thereby an automatic fault current limitation.

Using the test setup developed for AC loss measurements, the expected fault current limitation resulting from a quenching MgB_2 coil has been experimentally verified. An MgB_2 coil with a high resistivity matrix material was operated inside of the background field magnet. With an alternating field of the background magnet, a voltage and current is induced into the MgB_2 test coil. Introducing a short circuit at the output of the test coil leads to a rapid increase in the current, causing a quench of the superconductor. Due to the sudden increase of resistivity of the test coil, the induced current is rapidly reduced to a save level. The performed quench tests verified the intrinsic fault current limitation of an FSG.

2 Program Plan and Execution

Table 2.1 shows a summary of the overall program plan for BP2. The table also shows a high-level schedule for the various activities, along with the budgets for the cost-sharing team members: Advanced Magnet Lab Inc. and its collaborators, Emerson Electric Corporation (Kato), Columbus Superconductor, and the Center for Advanced Power Systems (CAPS).

Table 2.1. Budget Period 2 Program Plan and Schedule

SOPO Tasks for Budget Period 2 - Revision 8	Total Budget ($)
Updated 7/2/2014	
4.0 Modeling and Simulations	**119,777**
U of Houston - Analysis/Dynamic Simulations	
AML - Coil Design	
Kato - Analysis/Re-modelling	
5.0 COE Update with BP2 Results	**57,450**
NREL - COE Analysis	
6.0 De-risking Experiments	
T1. MgB2 Mini-Cable	**276,691**
AML - Analysis	
Columbus SC - Wire/Cable Build and Test	
T2. Structural Composite Analysis	**449,660**
Kato - Analysis and Test	
AML - Analysis	
T3. Conductor Containment Fatigue	**281,437**
Kato - Analysis	
AML/Winona - Manufacture	
AML/NHMFL - Test	
T4. Sub-Scale Torque Tube Temperature Cycling	**218,856**
Kato - Analysis	
AML - Manufacturing	
Argonne National Lab - Testing	
T5. AC Loss Measurement	**945,188**
AML - Design and Manufacture	
Creare - Cryogenic Cooling System	
CAPS - Testing	
T6. Fault Current Limitation Measurement	**38,000**
AML - Design and Manufacture	
CAPS - Testing	
7.0 Commercialization Plan	
Plan Development	**39,040**
8.0 Management, Reporting and Documentation	**49,985**
Final Report	
	Budget
Total	**2,476,084**
Federal Share	**1,485,650**
Recipient Cost Share (40%)	**990,434**
% of Budget Spent	

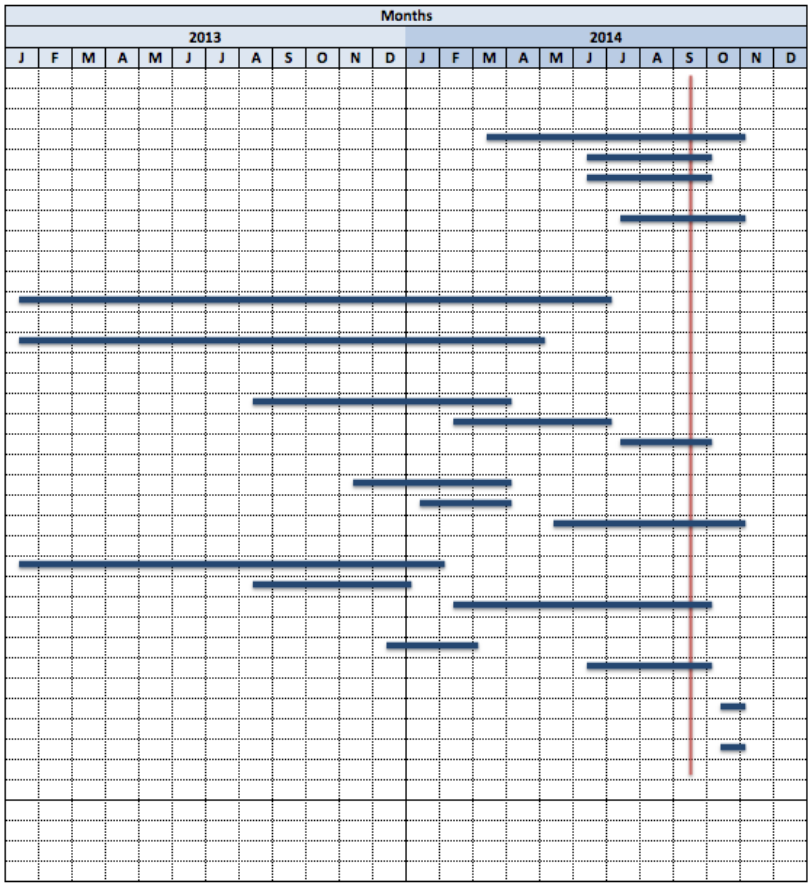

2.1 Statement of Project Objectives

As part of the proposal to the DE-FOA-0000439, deliverables were defined for Budget Periods 1 (BP1) and 2 (BP2) in the Statement of Project Objectives (SOPO) document. Having met the objectives of Tasks 1.0 through 3.0 during BP1, SOPO Tasks 4.0 through 8.0 were completed during BP2. Short descriptions of Tasks 4.0 through 8.0 are presented in the following section.

2.1.1 High-Level Task Descriptions and Assignments

Budget Period 2 tasks are summarized as follows:

- **Task 4.0 Advanced Modeling and Simulations**

  As part of this task, AML and Emerson will perform additional finite element analysis (FEA) and special purpose simulations using data obtained from the various de-risking experiments. The scope of the simulations will include both the structural and electro-magnetic design. The outcome of this activity will be a better understanding of the FSG performance and help define the next round of development.

- **Task 5.0 Cost of Energy Model Update/Refinement**

  This task will be performed in two parts: (1) The team will use the results of the risk mitigation activities to improve the assumptions in the areas of reliability, cost and performance portions of the COE model; (2) The existing COE model will be enhanced through a potential consulting engagement with NREL. NREL's know-how in turbine design and scaling will be used to better analyze and interpret the impact of the various unique features of the FSG on the COE.

- **Task 6.0 De-risking Experiments**

  This task consists of execution of the various de-risking activities (T1 through T6) described in section 23.1 of this report. The objective of this task is to better understand the key risk elements of the FSG and to elevate the TRL level of certain key subsystems. The tasks and topic areas of the experiments performed under BP2 and described in this report are:

  6.1 (T1) MgB_2 mini-cable Build and Test
  6.2 (T2) Structural Composite Analysis
  6.3 (T3) Conductor Containment Fatigue Analysis
  6.4 (T4) Sub-scale Torque Tube Temperature Cycling
  6.5 (T5) Characterization of AC losses in MgB_2 Superconductor
  6.6 (T6) Fault Current Limitation Measurement.

- **Task 7.0 Development of Commercialization Plan**

  This task consists of the development of commercialization plan, which will address the various aspects of manufacturing and sourcing of various subsystems, system test and qualification, and integration with other turbine components.

2.1.1.1 Project Team Members

The project team for BP2 was enhanced with the addition of new team members to support the specific technical objectives. Table 2.1.1 lists the team members along with their specific areas of responsibility.

Table 2.1.1. FSG Team Members and Assignments for Budget Period 2

Team Member	Area of Contribution
Advanced Magnet Lab	Project lead, Co-PI, Electromagnetic design, Execution of de-risking tasks T1, T3, T5 & T6.
Emerson Electric (KATO)	Co-PI, Structural/Mechanical design, Execution of de-risking tasks T2 & T4. Analysis support for T3
Argonne National Lab	Test site for de-risking task T4, cryogenic consulting
Creare	Developer of cryogenic cooling system for FSG and for de-risking tasks T4, T5 & T6
University of Houston (UH)[1]	Modeling and Analysis of FSG Electro-Magnetic design. Analysis support for T5 & T6
Columbus Superconductor[2]	Development of fine filament MgB_2 superconductor wire and cable (de-risk task T1)
Center of Advanced Power Systems (CAPS)[2]	Test site for de-risking tasks T3, T5 & T6
National Renewable Energy Lab (NREL)[2]	Assessment of influence of FSG features on turbine design (blade, tower foundation) and performance. Analysis of resulting impact on COE
Composite Technology Development	Physical property and fatigue performance testing of developed composites

[1] AML contributor now at UH
[2] New to FSG team for Budget Period 2

2.2 Program Budget

Table 2.2.1 shows the budget for the SOPO tasks in Budget Period 2.

Table 2.2.1. FSG Program Budget for Budget Period 2

SOPO Tasks for Budget Period 2 - Revision 8	Total Budget ($)	Total Spent ($)	% of total	Team Members/Subs										
				AML	Kato	Columbus	Argonne	UHouston	Creare	Winona	Dennehey	CTD	CAPS	NREL
Updated 7/2/2014														
4.0 Modeling and Simulations	**119,777**		**4.8%**											
U of Houston - Analysis/Dynamic Simulations		**19,054**		31,626										
AML - Coil Design		**11,480**						38,151						
Kato - Analysis/Re-modelling					50,000									
5.0 COE Update with BP2 Results	**57,450**		**2.3%**	9,283	9,600									
NREL - COE Analysis		**38,567**												38,567
6.0 De-risking Experiments														
T1. MgB2 Mini-Cable	**276,691**		**11.2%**											
AML - Analysis		**30,691**		30,691										
Columbus SC - Wire/Cable Build and Test		**246,000**				246,000								
T2. Structural Composite Analysis	**449,660**		**18.2%**											
Kato - Analysis and Test		**442,594**			184,032					84,708	59,909	91,351		
AML - Analysis		**29,660**		29,660										
T3. Conductor Containment Fatigue	**281,437**		**11.4%**											
Kato - Analysis		**83,734**			32,000									
AML/Winona - Manufacture		**68,880**		249,437										
AML/NHMFL - Test		**91,840**												
T4. Sub-Scale Torque Tube Temperature Cycling	**218,856**		**8.8%**											
Kato - Analysis		**71,772**			108,856									
AML - Manufacturing		**11,480**		25,000										
Argonne National Lab - Testing		**85,000**					85,000							
T5. AC Loss Measurement	**945,188**		**38.2%**											
AML - Design and Manufacture		**711,760**		686,888										
Creare - Cryogenic Cooling System		**109,800**							109,800					
CAPS - Testing		**44,607**											148,500	
T6. Fault Current Limitation Measurement	**38,000**		**1.5%**											
AML - Design and Manufacture		**57,400**		12,000										
CAPS - Testing													26,000	
7.0 Commercialization Plan														
Plan Development	**39,040**		**1.6%**	19,840	19,200									
8.0 Management, Reporting and Documentation	**49,985**	**149,240**	**2.0%**	49,985										
Final Report														
	Budget	**Spent**		**AML**	**Kato**	**Columbus**	**Argonne**	**UHouston**	**Creare**	**Winona**	**Dennehey**	**CTD**	**CAPS**	**NREL**
Total	**2,476,084**	**2,303,559**		**1,144,410**	**403,688**	**246,000**	**85,000**	**38,151**	**109,800**	**84,708**	**59,909**	**91,351**	**174,500**	**38,567**
Federal Share	**1,485,650**	**1,382,136**												
Recipient Cost Share (40%)	**990,434**	**921,424**		**319,836**	**424,720**	**98,400**	**0**	**0**	**0**	**0**	**0**	**0**	**147,478**	**0**
% of Budget Spent		**93%**												

3 Tasks

3.1 Task Motivation

3.1.1 BP1 De-risking Rationale

Ambitious technology projects are typically characterized by a combination of the exciting prospect of advancing the state-of-the-art, with new levels of cost/performance and the reality of a wide range of execution risks. Executing the task of delivering the benefits of a Fully Superconducting Generator (FSG) is no exception. In addition to the risks associated with building large-scale machines, other risks exist, which stem specifically from the nature of SC machines. When considering the topic of "de-risking", it is most important to understand the relevant risks and the sources thereof. This understanding will come only from experience with machines of this scale and type. Specific to our funded project, the AML team has the benefit of having team members with a longstanding business in large electrical machines (Emerson Electric) and large-scale SC systems (AML, Argonne National lab). Utilizing this broad base of experience, the risk analysis of the Fully Superconducting Generator was performed.

3.1.1.1 Superconducting Rotating Machine Risks

SC rotating machines have several characteristics that significantly differentiate them from conventional machines. Consequently, the risks in achieving commercialization of such systems are also different. In order to better understand these risks, one can classify them in three categories: the superconductor, cryogenic cooling, and FSG system design. The most important characteristics in each of these categories, which affect commercialization, are: cost, performance and reliability. Given the above classification and categorization of risk, one can begin to analyze what the current state of the risk is in each area and where to focus de-risking (Table 3.1.1).

Table 3.1.1. Risk Area Assessment for the Fully Superconducting Generator

	Superconductor (MgB_2)	**Cryogenic Cooling**	**Generator Design**
Working	Multiple suppliers are on favorable cost reduction trajectory New applications provide additional drivers for scale increase and cost reduction **Risk: Low**	Chosen cooling technology (Turbo Brayton Cycle) provides best $/Watt performance at operating points. Scales very favorably as we move to turbines beyond 10 MW Projected costs deemed reliable (based on scaling current systems and meet COE targets **Risk: Medium**	Majority of design methods and selected materials have been used before on this scale. Some uncertainty in cost of manufacturing composite winding structure at this scale **Risk: Medium**
Performance	Suppliers demonstrating quick response to application driven performance needs. Manufacturing in sufficient lengths (100's of km) with consistent quality is key. **Risk: Medium**	Performance has been demonstrated at smaller scale in low volume applications. Up-scaling projects are currently in process, with federal and private funding. **Risk: Medium**	Various new technologies at a larger scale than previously demonstrated Most areas validated through FEA and simulations so risk areas are understood. **Risk: High**

Table 3.1.1. Risk Area Assessment for the Fully Superconducting Generator			
Reliability	Lifecycle data is limited due to lack of long term performance data in industrial applications Conductor failure risk is minimized through conservative design of magnet coils. **Risk: Low**	Most reliable, "no-maintenance", cryo-cooling technology available. **Risk: Low**	Various new technologies at a larger scale than previously demonstrated Most areas validated through FEA, remaining uncertainty due to potential material fatigue. **Risk: High**

3.1.1.1.1 MgB2Superconductor

Performance, availability and cost of the conductor are obviously key elements of successful commercialization of the FSG. Over the past several years, AML scientists have worked very closely with two of the leading MgB_2 manufacturers, Hyper Tech Research from Ohio, USA and Columbus Superconductor from Genoa, Italy. Both of these manufacturers are on the leading edge of the field and have invested significant funds in both performance improvement of the conductor as well as development of manufacturing processes and capacity to deliver the wire in the quantities required for commercial use. Columbus Superconductor is currently producing wire for MRI systems, billet induction heating systems, and has recently entered into a contract to deliver cables for the Large Hadron Collider in Switzerland. The company recently announced that they have succeeded in improving critical current density in MgB_2 by a factor of 5 over present commercial superconducting MgB_2 wire for lengths of 1-10 m.

At the present time, both suppliers project to have a conductor available within 2 years that will meet FSG requirements. As part of the de-risking process the AML team will continue discussions with both suppliers, including possible factory visits, to closely monitor progress. Additionally, Columbus Superconductor offered a cost-shared R&D program that addresses the specific needs of the FSG, and some of the de-risking tasks will use wire supplied by Columbus Superconductor.

The allowed bending radius of MgB_2 conductor depends on the strand diameter and, as a rule of thumb, the minimum bending radius is about 150 times the strand diameter. While the required bending radius for the full-size FSG is about 200 mm, much smaller bending radii are required for small-scale prototype machines during continued FSG development. However, smaller bending radii can be achieved by using mini cables, and the development of such multi-strand conductors is planned. As part of the de-risking tasks, the team will engage Columbus Superconductor in the manufacture and test of a 6-around-1 cable consisting of 0.8-mm diameter MgB_2 strands. Since Columbus is already manufacturing stranded cable, the activities will focus on the qualification of a cable with specific electrical and mechanical characteristics for the FSG. Details of this activity are described in Section 3.2.3.2.

3.1.1.1.2 Cryogenic Cooling System

Low cost and high reliability are the most important requirements for a cryocooler for the FSG in an offshore wind turbine. The FSG requires an operating temperature of about 17 Kelvin at a total heat load of about 800 Watts. Only Reverse Turbo-Brayton Cycle (RTBC) cryocoolers can meet the cost and reliability requirements. Creare, Inc., a team member on the FSG project, has built RTBC cryocoolers, including systems for ultra-high reliability applications such as the Hubble Space

Telescope. The main risk for required cooling systems comes from the up-scaling requirement to meet absorption of 800 W of heat. Similar to the superconductor manufacturers, the AML team will continue to have discussions with Creare, Inc. and other suppliers to closely monitor their progress towards the FSG requirements.

3.1.1.1.3 FSG System Design

A variety of configuration choices exist when designing a superconducting (SC) machine. These choices range from partially SC, where only the machine rotor is SC, to machines, in which the field windings are stationary and the armature windings are rotating and coupled to a power converter through the use of slip-rings. Our team chose a fully SC generator design that provides significant advantages, as outlined in detail in the FSG Design section (1.1.2.1). Table 3.1.2 outlines the key innovation areas, along with the advantages provided and associated risks.

Table 3.1.2. FSG Design Innovation Areas and Associated Risks

Innovation	Advantage	Risk
Fully SC Generator, i.e., SC rotor and stator	A fully superconducting generator is smaller and lighter as compared to partially superconducting configurations.	AC losses in the SC stator, strongly depending on conductor design, have to be absorbed at cryogenic temperatures. Uncertainties in the estimate of AC losses affect cryocooler requirements .
Stator acts as fault current limiter	Limiting fault currents significantly reduces fault torques, which in turn imposes much lower constraints on the structural design of all wind generator components and thereby reduces cost.	The fault current limitation has to be well understood and the various properties of the stator and superconductor that limit the torque have to be examined and validated.
SC coils made from conductor embedded in composite	The use of composites as the substrate for the SC rotor and stator coils provides large flexibility in coil manufacturing as well as advantages in the integration of cooling.	The physical properties of various composites at cryogenic temperatures are not fully characterized. Quantifying these properties is essential for performing accurate FEA analysis. Additionally, the structural requirements of the composite as a retention system for the conductor under high operating forces have to be validated.
Stator torque tube made from composite	Avoid eddy current losses caused by the varying flux introduced by the rotor.	The composite torque tube has to transmit the full system torque and also interfaces with various other non-composite system components. Validation of the various composite properties and structural limits of the various interfaces has to be validated across the full temperature range.

3.1.1.2 Risk Analysis Process

Risk mitigation activities performed during BP1 were chosen in two specific areas: (1) Structural Design under various operating conditions and (2) Rotor and Stator Coil Performance. Under each area, specific experiments were designed to provide better fundamental properties that would be used to perform higher fidelity analysis and simulations and to provide experimental validation of the calculations performed during the design stage. Figure 3.1.1 shows an overview of the FSG risk

focus areas, along with the specific activities to be performed under each area. Details of the activities in each area are presented in Part II, section 3.2.3 of this report.

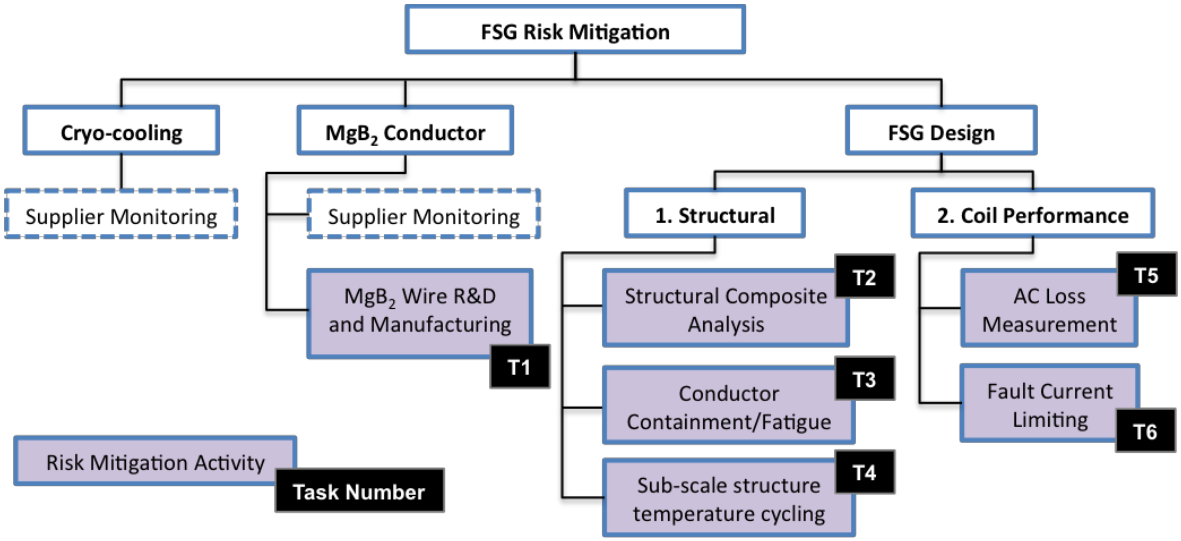

Figure 3.1.1. FSG Risk Mitigation Areas

3.1.1.2.1 Structural Design De-risking

As discussed in the Design section (1.1.2.1) of this report, direct-drive generators at low rpm have to handle very large torques, not only as a result of steady-state conditions, but also due to possible transients caused by system faults. For the FSG additional design, considerations are: operation at cryogenic temperatures, minimization of thermal heat leaks, containment of the SC windings under large forces, and minimization of eddy current losses in metallic components. As a result, various combinations of metal and composites are needed to meet these requirements. The de-risking approach for the structural aspects of the system starts with obtaining fundamental properties of key materials, which can then be used in high fidelity FEA, which finally affect the construction and testing of representative, sub-scale portions of the system.

3.1.1.2.2 Coil Performance De-risking

The performance of MgB_2 as a superconductor for magnets with operating currents and background fields as present in the FSG, are well qualified, for example in large MRI systems based on Columbus Superconductor wire [19]. However, the FSG imposes two specific performance requirements on the conductor that were not present in existing applications, which need to be qualified in realistic tests. One of these areas relates to the AC losses in SC coils. It is critical that these losses are validated, since they directly impact the size of the cryogenic cooling system. The second issue relates to the fault current limitation of the stator coils. Limitation of these currents and the resulting fault torque reduction to about 1.5 times the nominal torque is an important feature of the FSG, which favorably impacts the design of various turbine components.

3.2 Statement of Project Objectives (SOPO) Tasks

Work completed under BP2 for the following SOPO tasks is detailed below in the format of progress reports by task and sub-task as submitted quarterly to the DOE under the requirements of the Statement of Project Objectives document :

- Task 4.0 – Advanced Modeling and Simulations
- Task 5.0 – Cost of Energy Model Update/Refinement
- Task 6.0 – De-risking Experiments

3.2.1 Task 4.0 - Advanced Modeling and Simulations

3.2.1.1 Summary

A fundamental design philosophy for the FSG is minimization of thermal stresses by thermal matching of the materials used. This is needed due to the large range of temperatures seen by the FSG. The planned operation temperature is more than 280 Kelvin below room temperature. Even minor thermal expansion differences cause high thermal stresses with such a large range. By minimizing the thermal stresses, more stress margin becomes available for electromagnetic loading, faults, etc. Task 6.2 effort was used to develop and obtain tested performance data for two cryogenically capable, thermally matched composites.

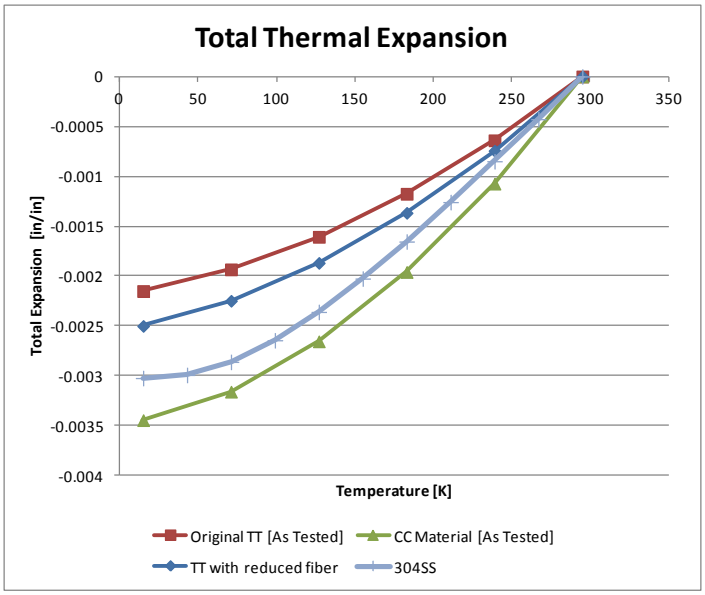

Figure 4.1. Composite Total Thermal Expansion Compared to 304 SS

The primary mission of Task 4.0 is to assess the success of Task 6.2 in achieving thermal matching of the materials developed for the FSG. Tested material properties for the Compliant Composite (CC material) and the Torque Tube material (TT) were used as inputs for FEA thermal and structural analyses of the FSG components. Limits found during composite testing at a full range of temperatures were then used to assess the results of the development efforts (Figure 4.1).

The configuration of the validation models used for Task 4.0 represents geometry developed at the end of BP1. The conductor is a 6-around-1 cable with an overall diameter of 2.5 mm.

The cable will be overlaid with 1 half-lapped layer of Kapton. The insulated conductor is embedded in the CC material with a retention layer applied for containment. Delays in revising the electromagnetic design precluded full analyses of the final BP2 configuration. The results from the analyzed geometry, however, should represent achieved risk reduction with the development of the new, thermally matched composites.

The basis for thermal matching in the FSG is the rotor torque tube made of 304 series stainless steel. Strength needs for the rotor dictates metal use. 304SS was selected because it is non-

This page removed due to Intellectual Property/Distribution Limitations

model used the 6-around-1 cable wrapped with Kapton. Four materials for the conductors were examined: Copper, 304SS, Monel and Titanium. Each has different thermal expansion properties. Monel is the closest to the planned and developed conductor at Columbus (Figure 4.3).

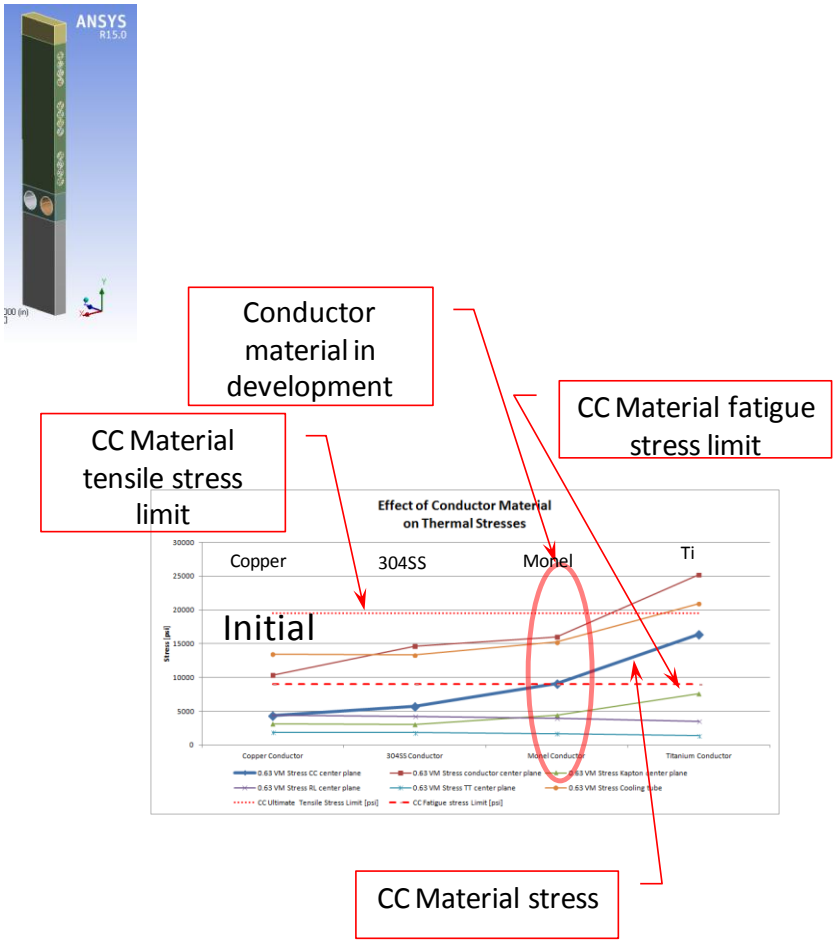

Figure 4.3. Effect of Conductor Material on Rotor Local Stress [Initial]

The results showed thermal stresses in the CC material high enough to be concerned about the long term life for the rotor due to fatigue. The Monel induced thermal stress in the CC material is close to the estimated fatigue limit for the CC material, leaving little, if any, margin for electromagnetic loading. Although the rotor current is DC, the variability of loading during wind turbine operation creates a significant fatigue type loading.

The stresses focused heavily on the thin CC material between radial adjacent turns.

The concern for possible fatigue related shortcomings triggered investigation of the effect of conductor radial spacing. The results were quite successful, reducing rotor thermal stress in the CC material over 29% (Figure 4.4).

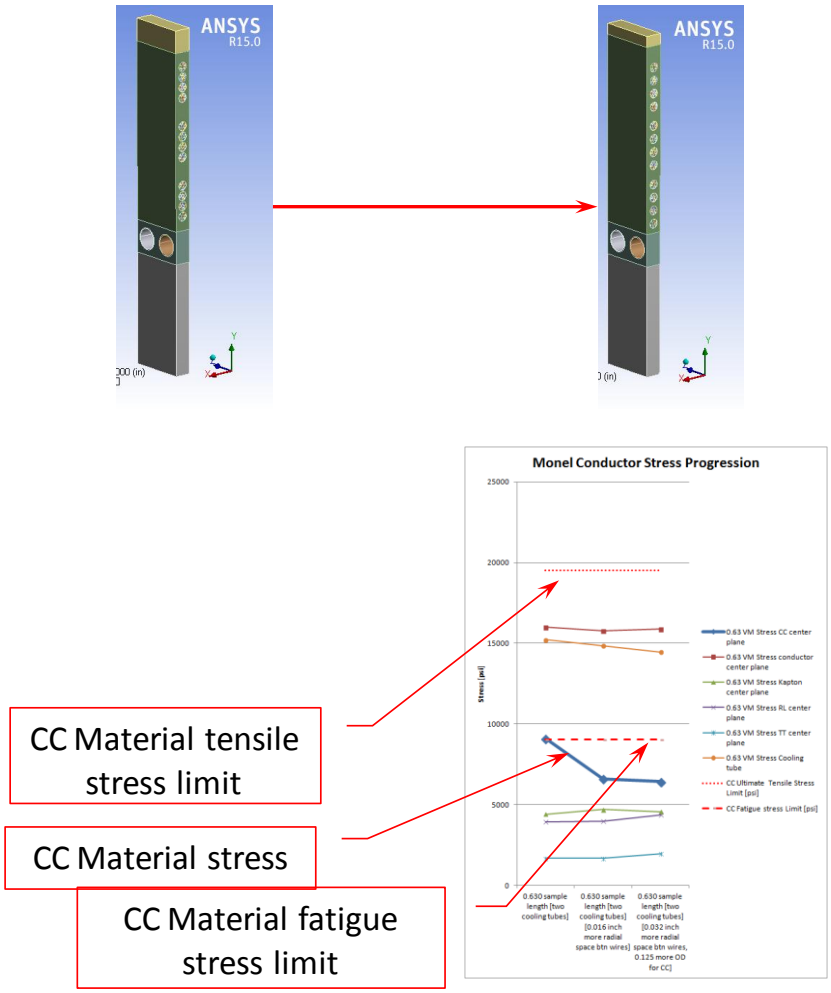

Figure 4.4. Rotor Thermal Stress Reduction Effort

After the thermal stresses were reduced, the effect of conductor material was revisited. The results show acceptable margin for the Monel conductor. They also show the potential benefits of using sheath materials of copper or 304SS (Figure 4.5).

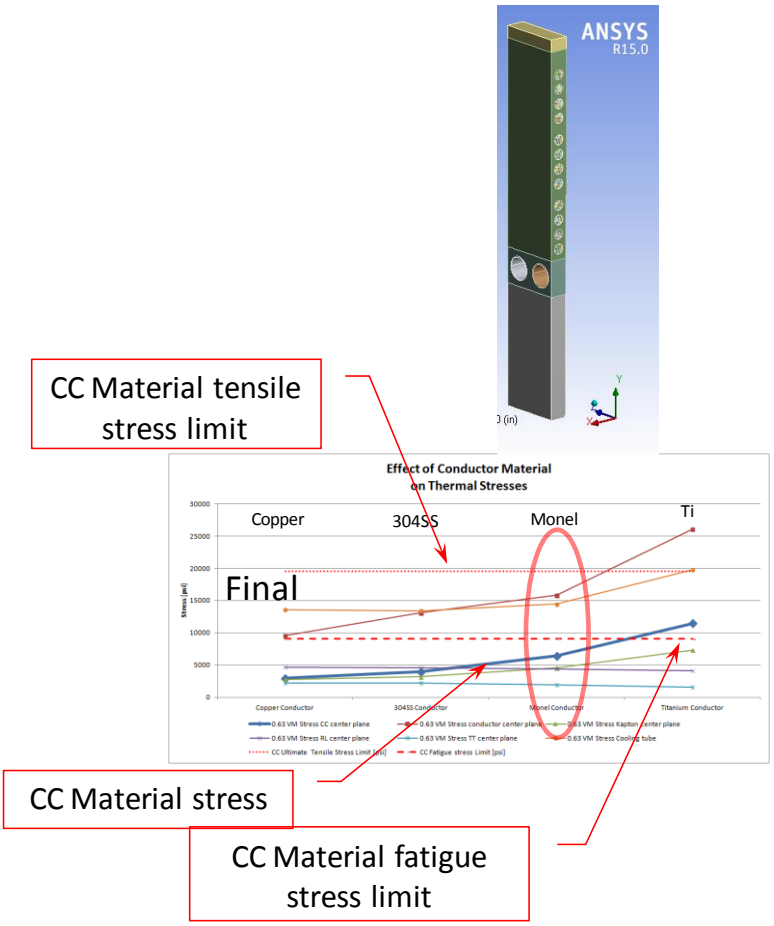

Figure 4.5. Effect of Conductor Material on Rotor Local Stress [Final]

During these calculations, the axial deformations were found to be a good indication of the thermal matching success (Figure 4.6).

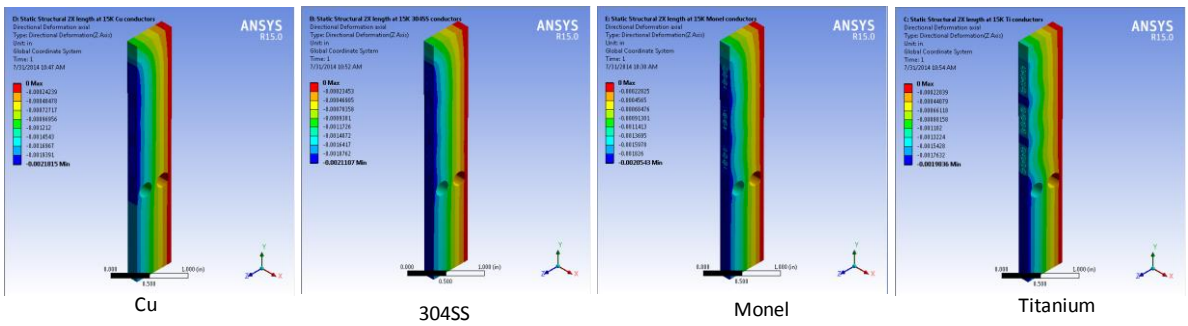

Figure 4.6. Initial Axial Deformation Plots

The final rotor axial deformation plots show smoother axial movement in the radial locations (Figure 4.7).

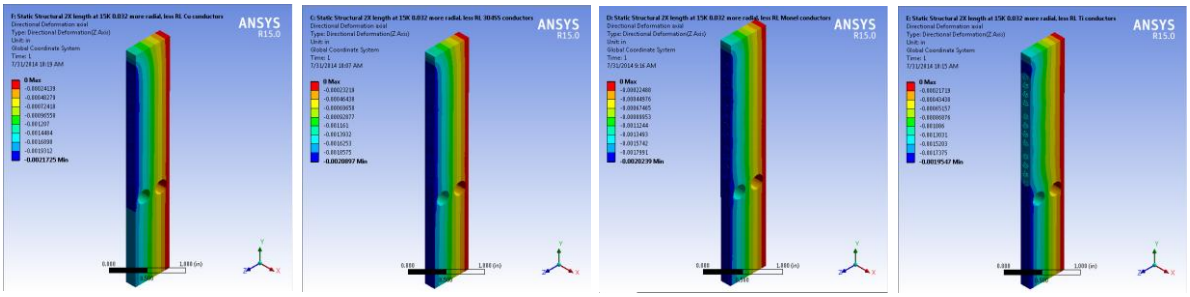

Figure 4.7. Final Axial Deformation Plots

3.2.1.2.1 Electromagnetic Design, Revision 2 Rotor Effects

Late in the BP2 timeframe, a revision of the FSG design, with the goal of reducing the total amount of superconductor in the machine to reduce the FSG cost was completed. The design still uses saddle coils, but slightly increases the stator shield OD and length.

A primary goal of the original frame size was to stay less than 12 feet wide to allow overland travel with minimal difficulty with permits, etc. This goal is met with the revised design, although the machine will need to be shipped rotated to achieve the width constraint.

The increased size of the machine lowers the magnetic effort needed, which lowers the magnetic field, reduces the shield cross-section and the amount of conductor needed. In fact the Revision 2 design only uses 37% of the original design's total superconductor length with minimal weight effect. The same quench philosophies used for the original design are maintained for Revision 2. The windings have higher current, but far less conductors so the electromagnetic loading will be higher, locally, but lower, globally. This should allow the knowledge gained and conclusions from the original design to carry forward to the Revision 2 design (Figure 4.8).

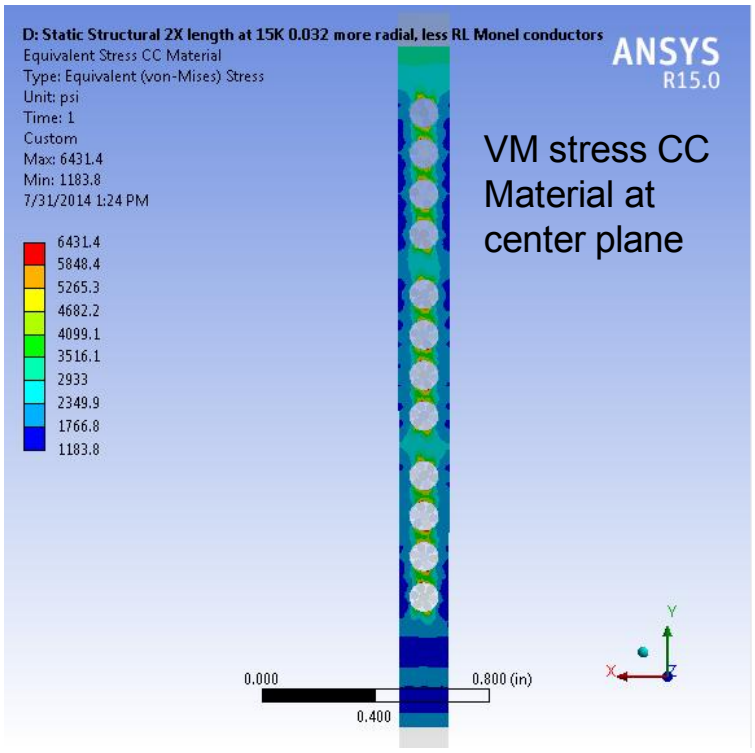

Figure 4.8. Final Rotor CC Material Thermal Stress

3.2.1.3 Stator Analyses

Initial stator CC material thermal stresses were found surprisingly high. The source of the elevated stresses was tracked to a poor TT material expansion match to the CC material. The greater strength TT material forced high hoop stress in the CC material, concentrating at the conductors. Increased conductor spacing and increased TT material expansion using a tweak of the TT material design reduced the stator thermal stresses to acceptable levels.

A model of the stator active section was used to examine the increased cross section torque tube and retention layer stresses and found acceptable for both.

The stator geometry is for the FSG configuration at the end of BP1 (Figure 4.9).

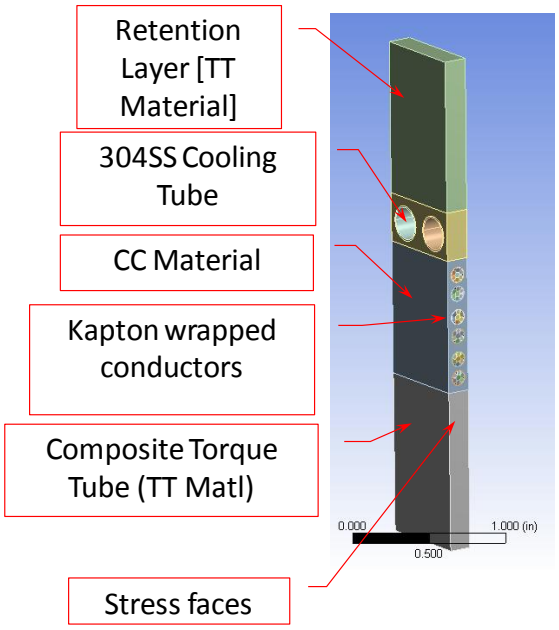

Figure 4.9. Stator FEA Geometry

The stator studies primarily focused on Monel conductor material, although 304SS conductors were also examined to show potential stress improvements with closer thermal property matching. It was found that the TT material, as tested, is not well matched to the CC material, causing surprisingly high thermal stresses in the CC material. The stator geometry has the CC material, containing the stator windings, sandwiched between two substantial thicknesses of TT material. The TT material has significantly lower expansion properties than the CC material, causing thermally induced hoop stress in the CC material.

TT material expansion behavior was changed to match 304SS and the CC material thermal stress reduced to about half. Dr. Dennehy was consulted and a “tweak” to the TT material design was developed. The volume fraction of the fiber was reduced to increase the expansion properties by 16%. The result was an improved thermal stress about 40% less than the as tested TT material (Figure 4.10).

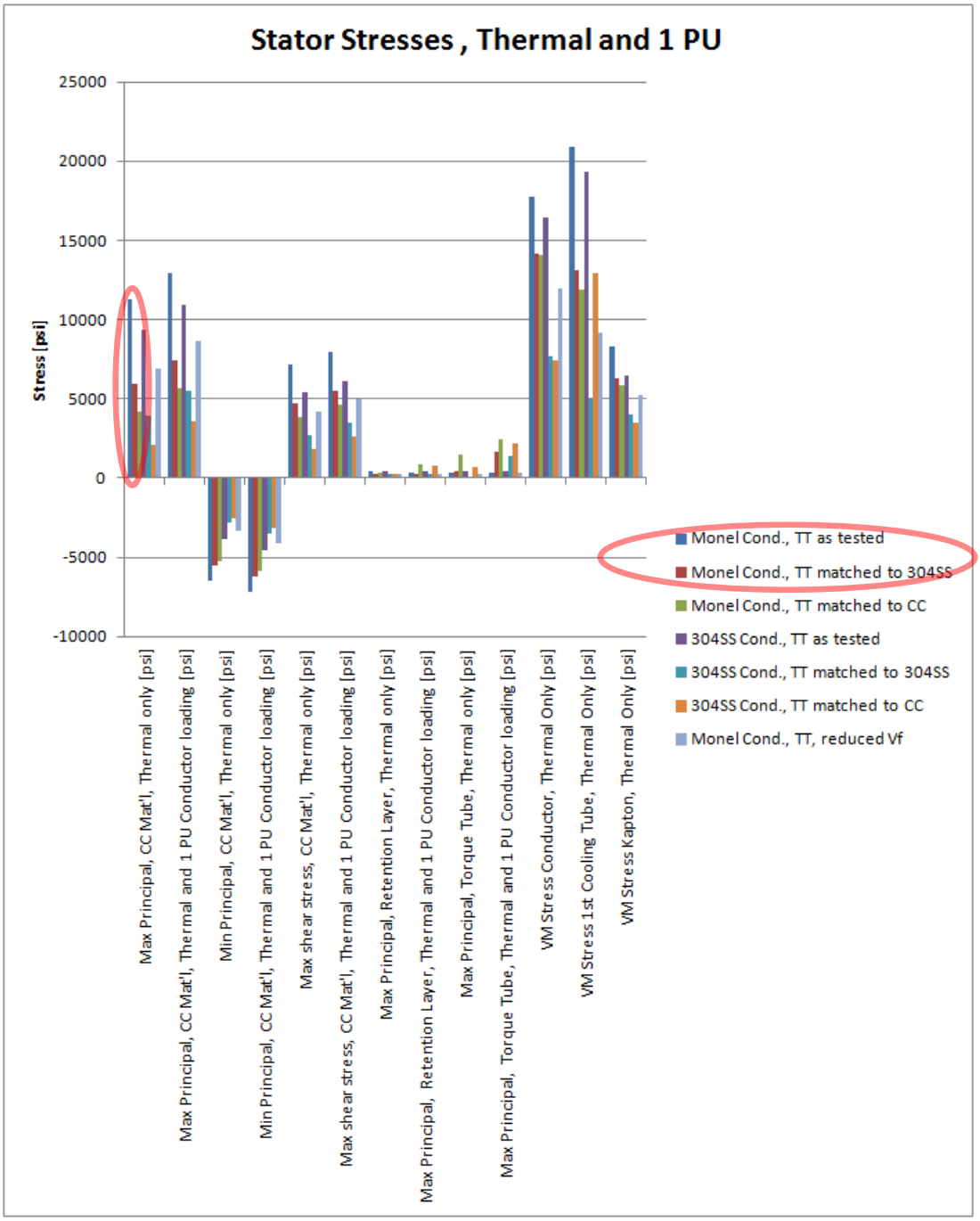

Figure 4.10. Thermal Stress Results

Similar to the rotor results, the axial deformation can be used to indicate the level of matching for the materials (Figure 4.11).

Thermal Only Axial Deformation Plots

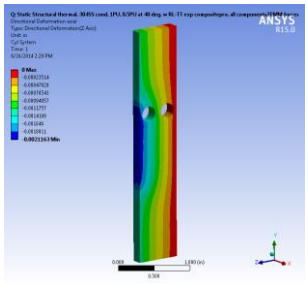

304 SS Conductor,
TT as tested

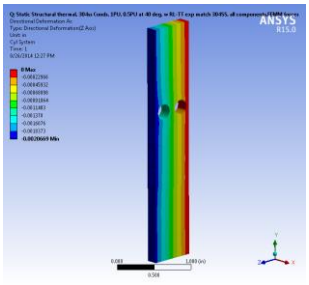

304 SS Conductor,
TT matching 304SS

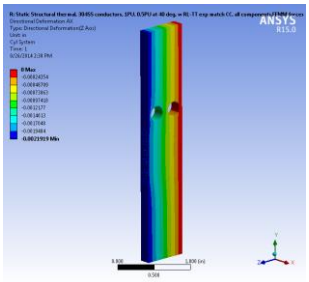

304 SS Conductor,
TT matching CC

Thermal Only Axial Deformation Plots

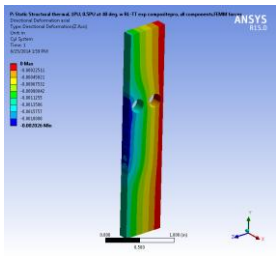

Monel Conductor,
TT as tested

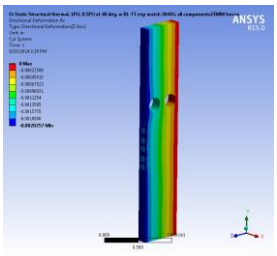

Monel Conductor,
TT matching 304SS

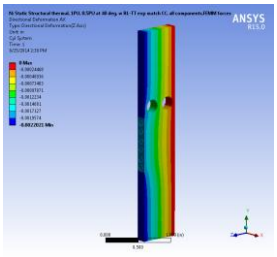

Monel Conductor,
TT matching CC

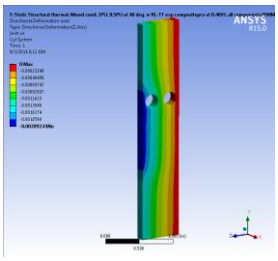

Monel Conductor,
TT reduced Vf

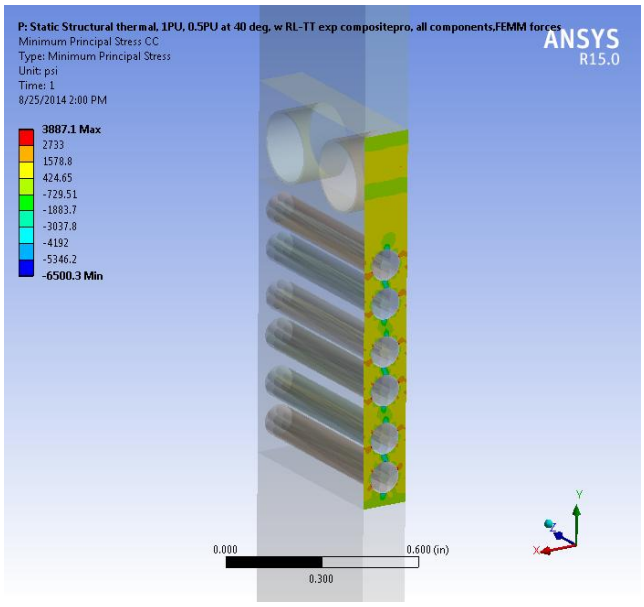

Figure 4.11. Thermal and Electromagnetic Stator Stress

A global stator active section model (Figure 4.12) was used to determine the effect of electromagnetic loading on the torque tube. The cross-section of the torque tube was increased due to the weakening effects of reduced fiber volume needed for thermal expansion improvement.

The torque tube was clamped tangentially at the ends with the center plane clamped axially. Thermal loading and then electromagnetic [applied to the windings] plus thermal was applied to the model. A load combination subtracting the thermal case from the electromagnetic plus thermal case isolated the effects of electromagnetic loading only (Figure 4.13 throughFigure 4.19).

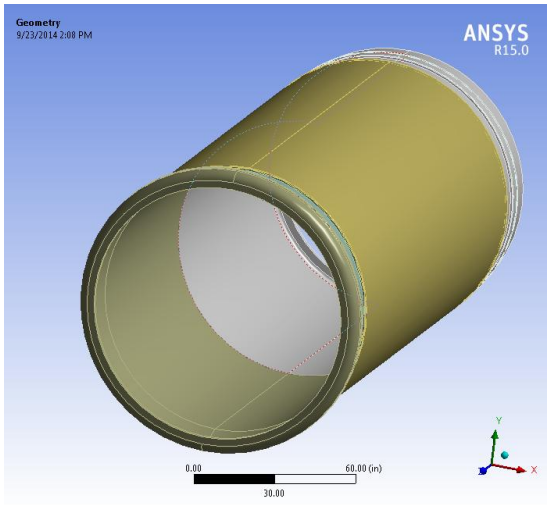

Figure 4.12. Stator Active Section Model

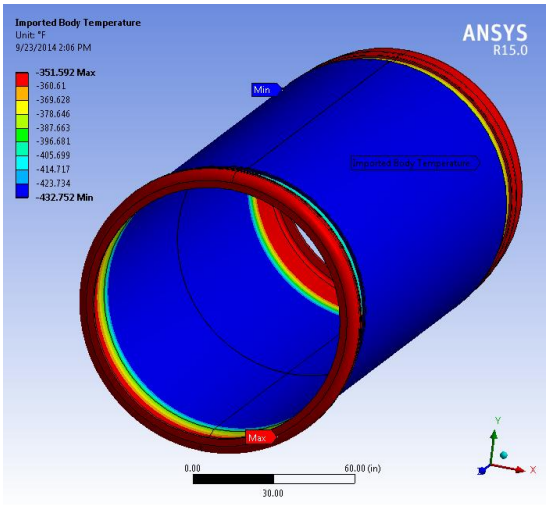

Figure 4.13. Stator Imported Temperatures for Structural FEA

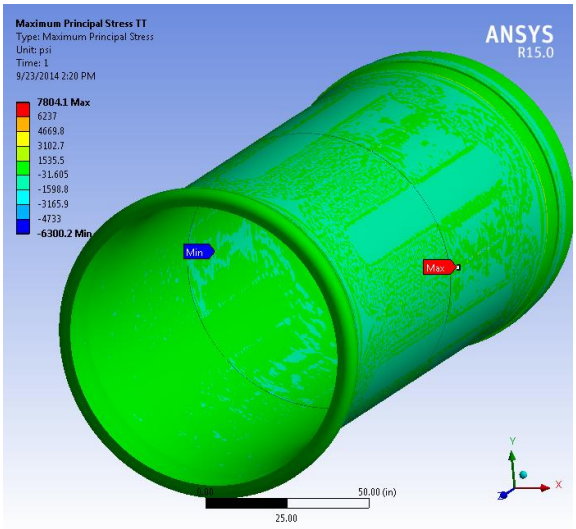

Figure 4.14. Torque Tube Thermal Stress

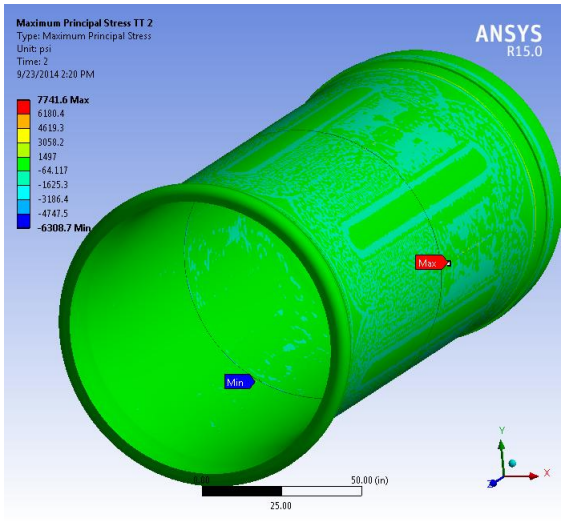

Figure 4.15. Stator Torque Tube Thermal and Electromagnetic Loading

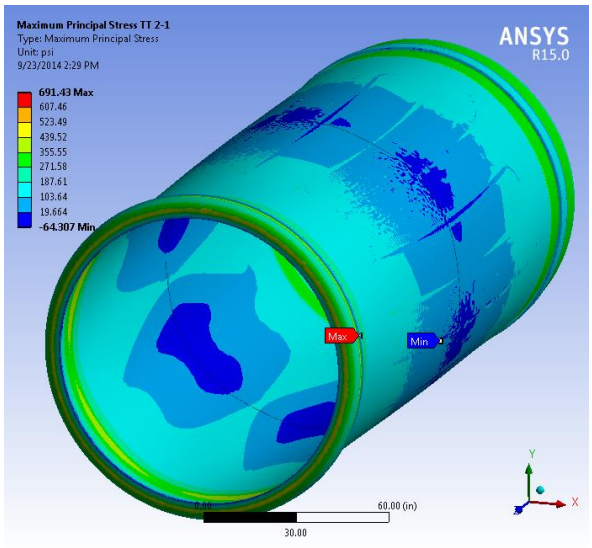

Figure 4.16. Stator Torque Tube, Just Electromagnetic Loading

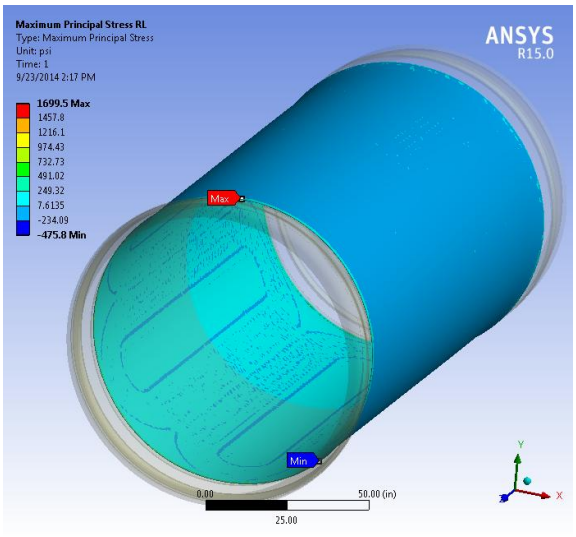

Figure 4.17. Stator Retention Layer Thermal Only

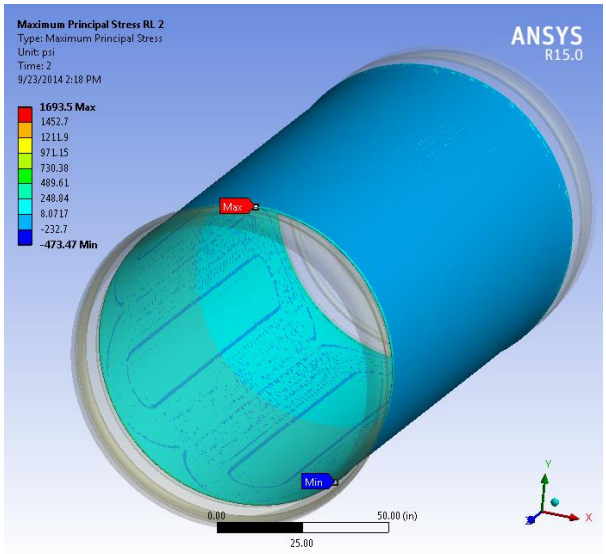

Figure 4.18. Stator Retention Layer Thermal and Electromagnetic Loading

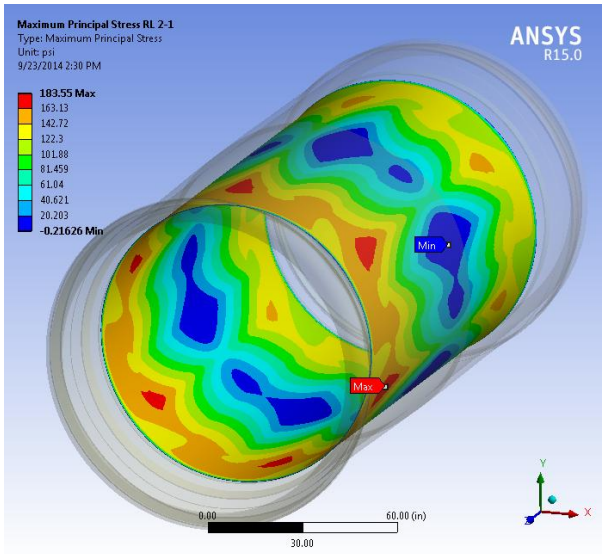

Figure 4.19. Stator Retention Layer, Just Electromagnetic Loading

3.2.1.3.1 Electromagnetic Design, Revision 2 Stator Effects

As in the rotor, the stator for Revision 2 has much fewer conductors with higher currents. The electromagnetic loading generated small additional stresses, relative to the thermal stresses seen in the FEA studies. The knowledge and conclusions from the original design are therefore transferrable to the Revision 2 design.

A secondary mission of Task 4.0 is analyses supporting FSG/mainframe configuration design related to estimation of tower head mass to facilitate proper comparisons to a DTU benchmark design. This is related to COE calculations (Figure 4.20).

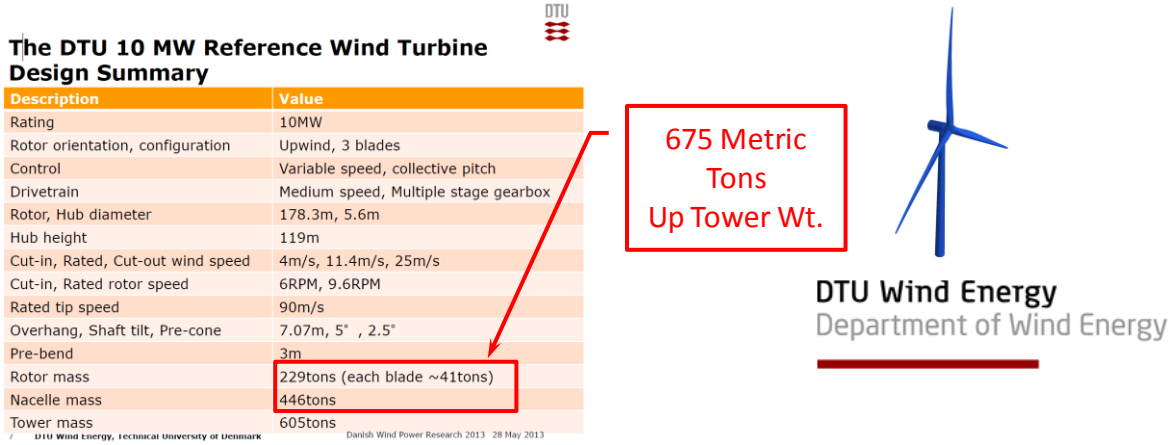

Figure 4.20. NREL Recommended Benchmark Turbine

The development of a rotor configuration utilizing a center shaft capable of turbine hub support required extensive FEA for the sizing of the shaft. The resulting configuration, where the FSG rotor is also the turbine rotor, blurs the separation of the mainframe and FSG. They become intertwined, requiring large combined FEA models to assess the configuration capabilities for the wind application.

An evolution of the FSG configuration has occurred during this development:

In BP1, the configuration used a fabricated mainframe assembly with separate turbine and FSG shaft, linked with an intermediate shaft and two flexible couplings. The FSG rotor had no capability for external moments (Figure 4.21).

This page removed due to Intellectual Property/Distribution Limitations

■ If the speed of rotation and the load are variable, the service life is calculated for each level of use, then the duration is weighted for the cycle as a whole.

▸ Variable load and speed of rotation

Weighted duration $L = (t_1 / L_1 + t_2 / L_2 + \ldots + t_z / L_z)^{-1}$ with $\sum_{i=1}^{z} t_i = 1$

with:
t_i Duration of use
N_i Speed of rotation for duration of use t_i
P_i Load for duration of use t_i
L_i Service life for duration of use t_i
n 3 for ball bearings and ball thrust bearings
n 10/3 for roller bearings and roller thrust bearings

Main Brg Life

Col 1	Col 2	Col 3	Col 4	Col 5	Col 6	Col 7	Col 8	Col 9	Col 10	Col 11
Wind speed	Hours at WS	Radial load	Axial load	Y1	rpm	C	Equiv load	Reliability	Hours Life	Time fraction / Col 10
[m/s]	[hrs]	[kN]	[kN]				[kN]	[%]	[hrs]	
4-6	25,734.7	4499	358.5	0.72	6.00	34,700	4757.12	99	439,071	3.65262E-07
6-8	25,528.7	4499	646.3	0.72	6.14	34,700	4964.312	99	372,161	4.27483E-07
8-10	26,086.5	4499	1017.4	0.72	7.23	34,700	5231.528	99	265,579	6.12129E-07
10-12	23,759.5	4499	1341.3	0.72	8.82	34,700	5464.76	99	188,089	7.87219E-07
12-14	19,647.0	4499	1106.9	0.72	9.60	34,700	5295.968	99	191,901	6.38028E-07
14-16	14,903.0	4499	894.5	0.72	9.60	34,700	5143.04	99	211,590	4.38934E-07
16-18	10,435.9	4499	777.1	0.72	9.60	34,700	5058.512	99	223,607	2.90847E-07
18-20	6,774.6	4499	699.7	0.72	9.60	34,700	5002.76	99	232,022	1.81959E-07
20-22	4,088.9	4499	643.2	0.72	9.60	34,700	4962.128	99	238,416	1.06879E-07
22-24	2,299.3	4499	600.7	0.72	9.60	34,700	4931.48	99	243,391	5.88724E-08
24-26	1,206.6	4499	575.0	0.72	9.60	34,700	4912.964	99	246,462	3.05094E-08
Total Op Hrs =	160,465							Total Op Hrs fraction divided by life at load =		3.93812E-06
		Estimated bearing life hrs =		253,928						
		Estimated bearing life yrs =		**29.0**						

Figure 4.24. Main Bearing Life Calculation

FEA was used to examine the mainframe, FSG stator and FSG rotor stresses for the effects of gravity and rated torque (Figure 4.25 throughFigure 4.31).

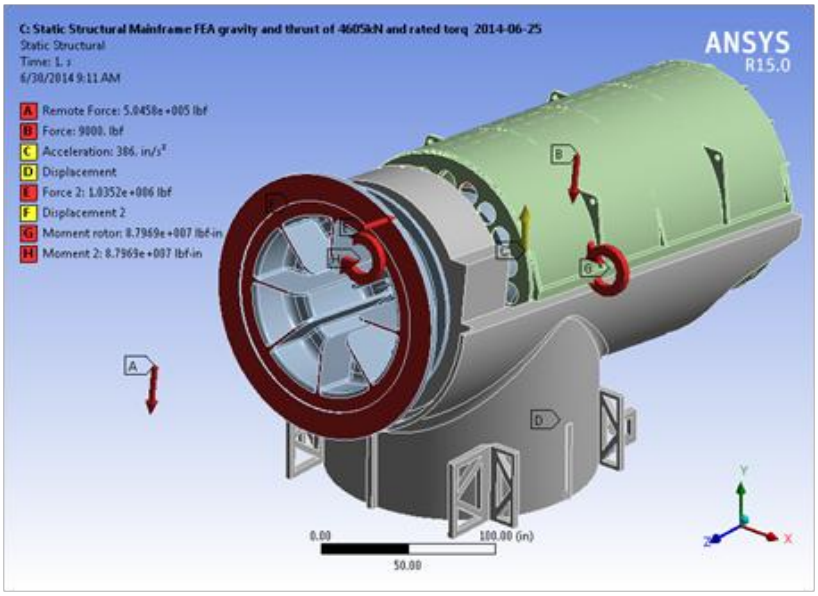

Figure 4.25. Mainframe Assembly Model

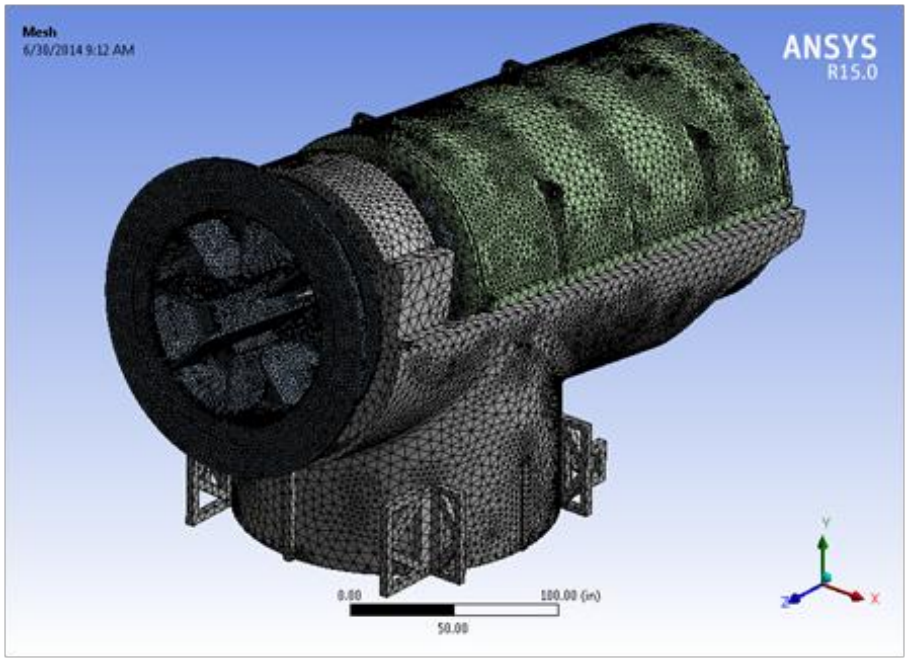

Figure 4.26. Mainframe Assembly Mesh

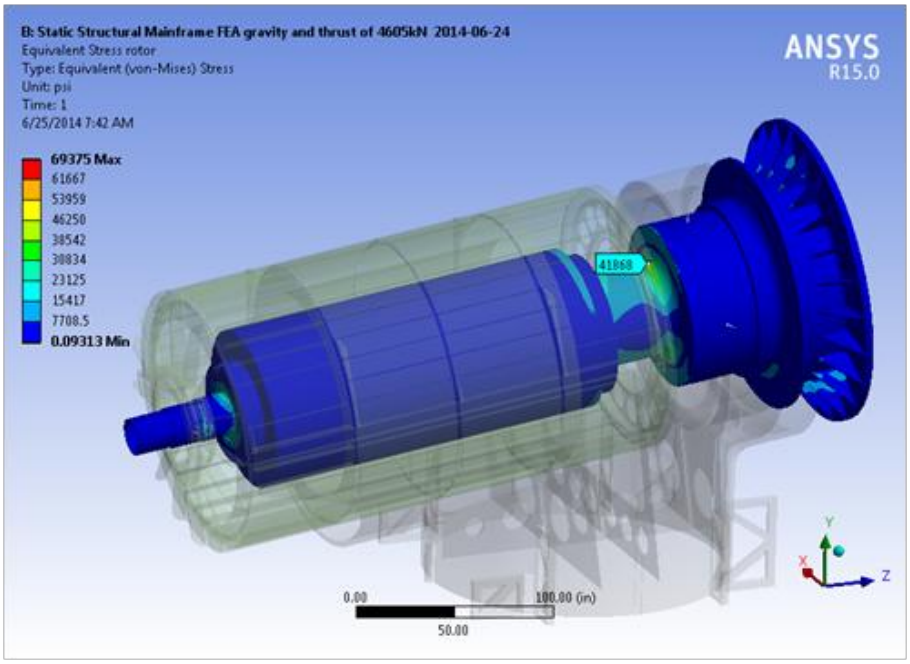

Figure 4.27. Example Rotor Stress from Gravity and Thrust

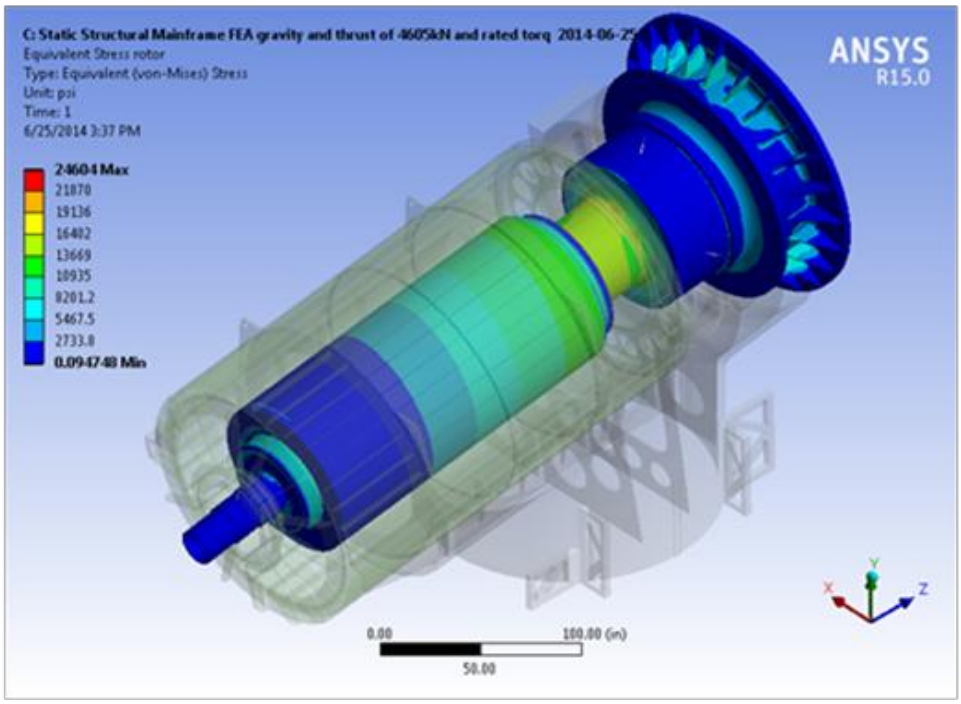

Figure 4.28. Example Rotor Stress from Gravity, Thrust and Rated Torque

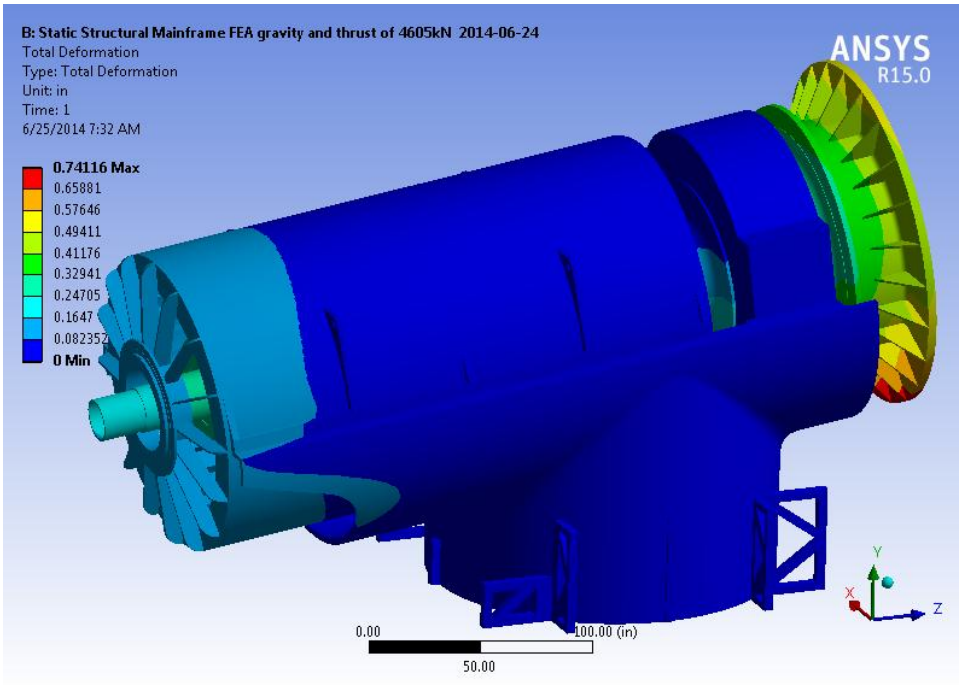

Figure 4.29. Example Total Deformation from Gravity and Thrust

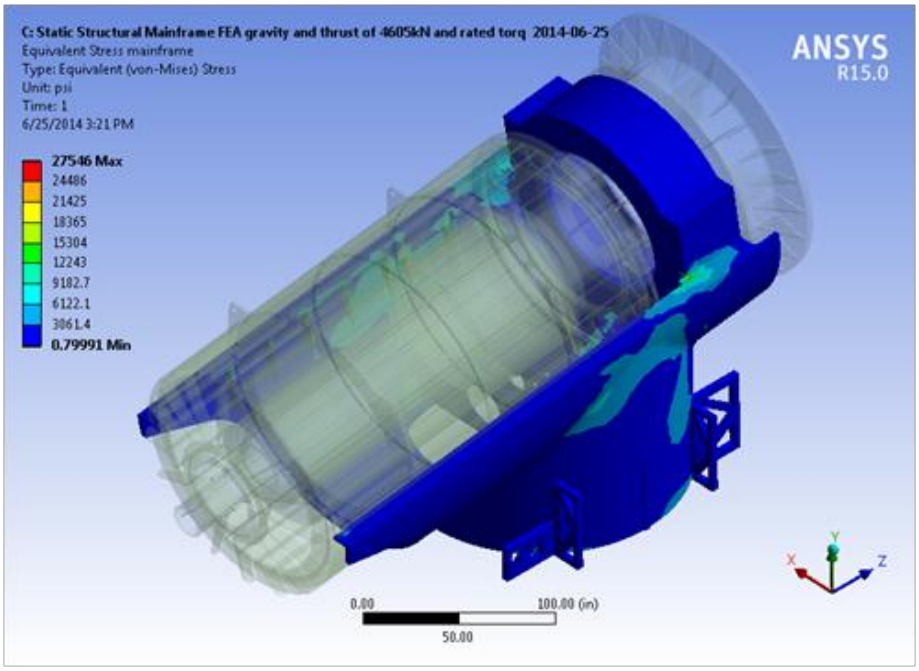

Figure 4.30. Example Mainframe Stress from Gravity, Thrust and Rated Torque

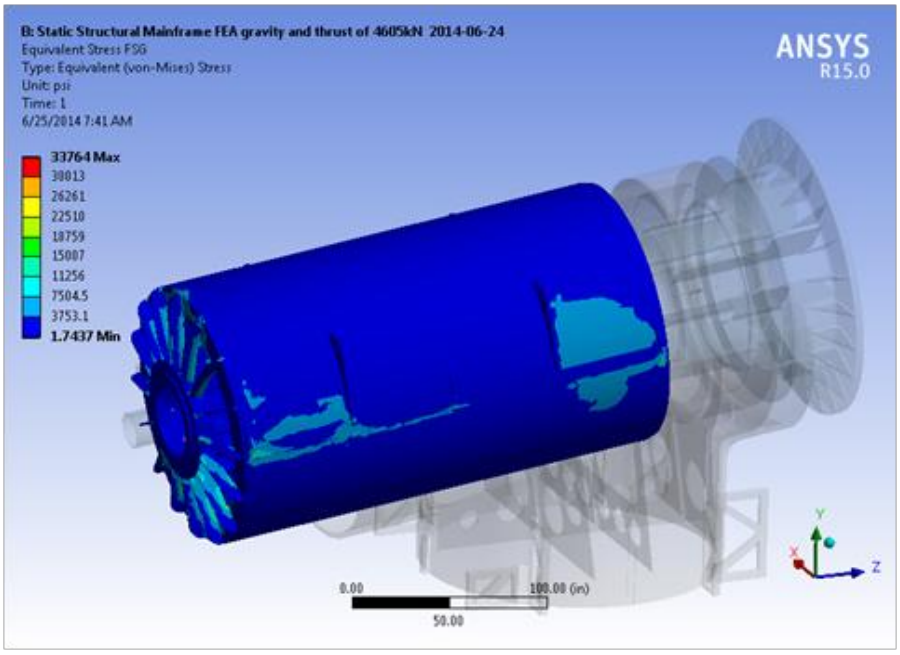

Figure 4.31. Example FSG frame Stress from Gravity, Thrust and Rated Torque

This page removed due to Intellectual Property/Distribution Limitations

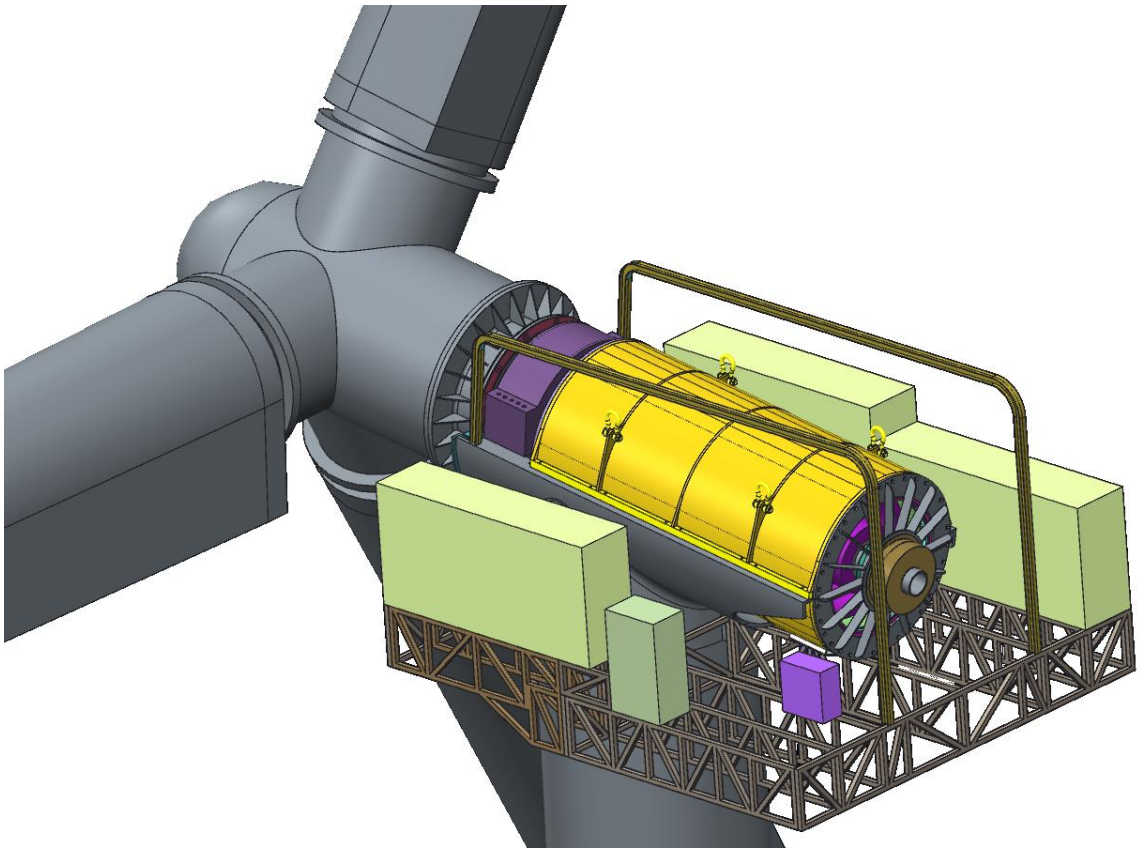

Figure 4.33. General Assembly for Revision 2 Design

3.2.2 Task 5.0 - Cost of Energy

This task consists of the evaluation of the levelized cost of energy (LCOE) for the current design of the FSG and all its attributes. During BP1, DNV (formerly BEW Engineering) assisted the team in determining the LCOE for the then current system. The details of this analysis were included in the BP1 final project report. For BP2, the goal is to perform a deeper analysis of the impact that the specific features of the FSG have on the overall turbine and accurately reflect this in the LCOE analysis.

3.2.2.1 COE- Rationale

BEW was tasked with developing an estimate of the Cost of Energy (COE) for a 10-MW wind turbine utilizing the Fully Superconducting Generator (FSG) in place of other existing transmission and electricity generation systems. The following two turbine configurations are considered in this analysis:

- 300-MW wind farm, 10-MW turbines, Permanent Magnet Direct Drive (PMDD) generators, 172-m rotor diameter
- 300-MW wind farm, 10-MW turbines, FSG, 172-m rotor diameter.

The aim of the analysis is to identify whether the 10-MW FSG drivetrain provides a cost advantage compared to the 10-MW PMDD drivetrain; if cost advantages were identified, they have been quantified in terms of their potential impact on the cost of energy. Other types of drivetrains, such as those involving gearboxes and high-speed generators were excluded from this analysis, as they are not yet considered feasible with the high torques involved at 10 MW.

It should be emphasized that several potential cost reductions of the FSG are not included in the presented COE comparison between the FSG and the PMDD, due to uncertainties in quantifying the impact of these features. These areas are:

- Lower cut-in speed of the FSG
- Reduced top weight of the FSG
- Significant future increase current carrying capacity of MgB2 conductor (up to 5 times; see Part II, section 3.2.3.2.1).

The COE model developed by BEW consists of a Capital Expenditure (CAPEX) model, an Operation & Maintenance (O&M) model, an Annual Energy Production (AEP) model, and a set of financial inputs (Figure 5.1). The cost inputs for the models are based on publicly available information, while estimated reliability figures for existing wind turbine components (excluding the FSG components) are based on experience from previous projects. The following sections describe the models developed, the data input, the current results, and what they mean in terms of the potential of the FSG drivetrain.

3.2.2.1.1 CAPEX Model

The CAPEX model is made up of two parts—the Turbine Capital Cost, and the Balance of System Cost. The Turbine Capital Cost includes the main components of the wind turbine itself, and this cost is evaluated on a ‘per turbine’ basis. The Balance of System costs include costs for transportation, installation, civil works, electrical transmission system, permitting, and insurance. Many of these costs are spread among all the turbines in a farm.

The estimates of component costs for the 10-MW turbines were taken from the NREL report Wind Turbine Design Cost and Scaling Model (December 2006) [20], the NREL report Comparative Assessment of Direct Drive High Temperature Superconducting Generators in Multi-Megawatt Class Wind Turbines (October 2010) [21], and, where possible, compared against data from the UpWind project [22].

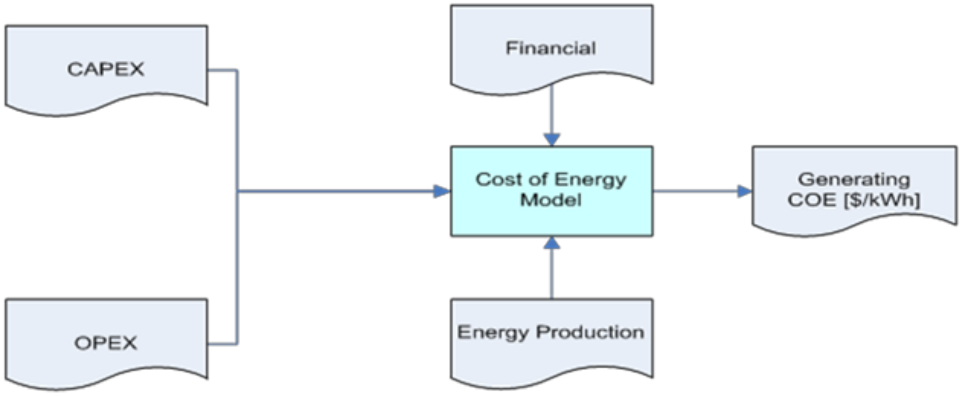

Figure 5.1. Cost of Energy Model Inputs and Outputs

The costs for the Balance of System are also estimated from the NREL report with the exception of offshore installation and transportation costs. There have been significant steps forward in the transportation and installation of offshore wind turbines in recent years with the development of bespoke Wind Turbine Installation Vessels such as the MPI Resolution, and the new MPI vessels Adventure and Discovery. Estimates for the transportation and installation costs are based on a day-rate for a jack-up vessel in 2002 in the NL7 Wind Farm O&M report [23] and time requirements for installation of wind turbines reported for offshore wind farms in the UK

3.2.2.1.2 Operation and Maintenance (O&M) Model

3.2.2.1.2.1 General

The aim of the O&M model is to estimate all costs associated with operation and maintenance of a wind farm over its design lifetime. The cost components included in the model are:

- Staff costs
- Consumables costs
- Access system costs
- Components and materials costs.

Additionally, the model will estimate the downtime and average availability for use in the AEP model. In the current model, the design lifetime is assumed to be 20 years, which is consistent with many current offshore wind farm projects.

The O&M model uses the same system breakdown as given in the NREL scaling document [20]. For each component entered in the model a number of possible failure modes was examined The assumed failures may require different costs in order to repair the turbine, principally due to the size of vessel required. Vessels vary from a small personnel transfer vessel for minor repairs to a large jack-up vessel with heavy lift crane for the heaviest components. The different vessels also have different associated downtimes for the turbine due to variations in mobilization time

3.2.2.1.2.2 Access Systems

Four different access systems were identified based on lifting limitations.

3.2.2.1.2.3 Results

The O&M results for the two different turbines show that the FSG offers a significant reduction in O&M costs over the lifetime. The principal reason for this in the current study is that the FSG components have a lower capital cost than those in the PMDD system. Due to the low operating temperature inside the FSG, there is the potential for high downtimes when failures occur, due to the amount of time required to warm up and cool down the generator. For this reason, considerable effort was made to ensure that the least reliable components (generally mechanical components) were moved outside of the low temperature zone into more accessible locations. This has allowed the FSG to achieve a similar availability over the lifetime as the PMDD (98.4% for the FSG versus 99.1% for the PMDD). These availability results are considered to be well within the uncertainty margins of the input data, so this difference has not been taken into account in the Annual Energy Production model.

3.2.2.1.3 Annual Energy Production (AEP) Model

3.2.2.1.3.1 General

The AEP model is used to estimate the number of kilowatt-hours produced by the turbine over the course of a year, taking into account the following aspects:

- Incident wind resource
- Rotor power curve
- Generator power curve
- Other energy losses.

Generic data have been entered for all of these aspects based on experience from previous projects. The incident wind resource, and other energy losses remain constant for all configurations of wind turbine in this comparison study, while the drivetrain losses and generator power curve are expected to vary.

The resource used in the current COE model is based on the resource suggestion from the DOE funding opportunity for this project, using an average wind speed of 8.8 m/s:

- Rotor diameter: 172 m
- Cut-in speed: 3.5 m/s
- Rated speed: 12.0 m/s
- Cut-out speed: 25.0 m/s

The FSG lower rotor weight and use of anti friction bearings could potential result in a lower cut-in speed, which would improve the AEP. **However, this assumption was not included in the AEP analysis.**

3.2.2.1.3.1 Generator Power Curve

The generator power curve provides data on the efficiency of the generator at different power levels. Losses are estimated based on inefficiencies in the generators, friction, inverter, and parasitic losses such as power required for cooling systems and rotor excitation. This provides a kW output for the turbine for different wind speeds.

3.2.2.1.3.2 Other Energy Losses

BEW has used general loss assumptions similar to the values that would have been used on standard energy estimates. For the losses that are site-specific, due to the location and layout of the

turbines not being determined, BEW has used the average value of the loss estimated from a large number of earlier projects.

3.2.2.1.4 Financial

Financial aspects impacting the cost of energy are assumed to be those defined by the Department of Energy. The following aspects are included:

- Fixed Charge Rate (FCR) of 14%.
- Levelized Replacement Cost: This is the cost of planned overhauls of the wind turbine, and is assumed to be 65% of the total parts replacement cost
- O&M tax reduction: The Levelized O&M cost (minus Levelized Replacement Cost) is reduced by 40%.

3.2.2.1.5 Impact of FSG on System

An important aspect of the FSG's value proposition is its impact on the other components in the wind turbine. In this respect the FSG offers four significant advantages over the PMDD drivetrain:

- Reduced weight due to increased torque-to-weight ratio
- Reduced short circuit fault torque
- Reduced reliance on rare earth materials
- Reliability/Reduced maintenance.

These are discussed further below.

3.2.2.1.5.1 Effect of Weight Reduction

The FSG system offers a total tower-top weight reduction of 27%, compared to the PMDD system (including the effects of torque reduction described below). This would result in an improved dynamic response of the system, with the primary impact being on the natural frequency of the tower. The major influence on tower and foundation design is still the overturning moment from the rotor thrust, and while the reduction in tower top weight is likely to improve the COE results, the scope of the current project does not allow for a robust quantification of this effect at this time. A further advantage of the reduced tower top weight is in any potential life extension to the turbine. By reducing some of the fatigue loading amplitude on the tower, it is likely that less refurbishment work will be required in order to achieve life extension of the system. Again, this effect is not quantified in the present study due to the complexities of the life cycle analysis comparisons, but extensions to lifecycle with limited costs are the 'holy grail' of improvements to wind energy economics at present, and wind turbine developers are seeking weight reductions in any areas for this reason as well as to achieve the potential reductions in tower weight.

The significant reduction in tower top mass also has a potential impact on the O&M cost and the installation cost if it allows the use of a smaller vessel for turbine installations. The present O&M analysis does not have the sensitivity to quantify this effect, but its impact can be only positive.

3.2.2.1.5.2 Effect of Short Circuit Fault Torque Reduction

It has been estimated that the FSG system reduces the Short Circuit Fault Torque from 5 times nominal torque (assumed for the PMDD system) to less than 2 times nominal torque. It has been suggested that this reduction will have an impact on the following components: mainframe; low speed shaft; tower; foundation; blades.

The mainframe and low speed shaft are normally designed based on the maximum fault torque, so it has been assumed that their cost will be reduced in the same proportion as the reduction in fault torque from the values given by the NREL scaling model. For the tower and foundation, the effect of a short circuit fault event during normal operation has been estimated, and the reduction in the maximum stress in this case is of the order of 1.5% for the foundation and 3% for the tower. Finally, for the blades, the fault torque is likely to have some impact, but as blade design is primarily fatigue driven due to the high number of weight loading cycles experienced the actual impact of fault torque is difficult to quantify in the present study and has been left out of the results.

3.2.2.1.5.3 Effect of Reduced Reliance on Rare Earth Materials

Rare earth materials, as used in PMDD systems, have exhibited large fluctuations in their pricing since the NREL scaling report, which was based on 2002 costs [20]. For this reason, the cost of the permanent magnet generator has been revised from the original estimate assuming the material cost has increased from $10/kg in 2002 to $85/kg in 2012. The price of rare earth materials appears to be decreasing at present, but it is difficult to estimate where the price may stabilize in the coming years. Rather than predicting the price of the materials, an assessment of the effect of rises or drops in the price on the cost of energy for the PMDD has been developed, assuming that rare earth materials account for 50% of the cost of the PMDD generator in 2012. This chart shows that, for the current estimates of all other costs, the cost of energy from the PMDD will never decrease enough to achieve the same COE as the FSG system.

3.2.2.1.5.4 Reliability/ Reduced Maintenance

SC windings are kept at a constant low temperature, except for a few maintenance cycles throughout the lifetime of an electrical machine. Electrical fatigue of conductor insulation, which in conventional normal conducting coils tends to lead to electrical breakdowns in the coil windings, is almost completely eliminated in a SC coil. An additional increase in reliability related to electrical break downs stems from the applied stacked saddle coil windings, in which insulated conductors are inserted in machined grooves of an insulating composite. Although, a cryocooler system is needed to keep the SC coils at the required operational temperature, it is stated by Creare that their Turbo-Brayton system has an expected MTBF of 600,000 hours. A further advantage in expected reliability in comparison to a PMDD generator is the reduced fault torque in the FSG, which leads to significantly reduced peak loads on various components of the whole wind turbine.

3.2.2.1.6 Cost of Energy Results

Table 5.1 shows the breakdown of results for the FSG system, compared to the 10-MW PMDD system. The table shows the results for the FSG including the effects of the limited fault torque. The results show that the FSG has a better cost of energy result than the PMDD system at the present pricing of rare earth materials, with all the conservative assumptions for the FSG outlined above.

This shows that, using the same method for estimating the capital costs, and all of the other assumptions outlined in the sections above, the estimated cost of energy for the FSG is 1.77 c/kWh lower than for the PMDD at the same MW capacity, which is a 12.7% reduction. The FSG offers a large reduction in capital cost over the PMDD system, as well as reductions in Balance of System cost, increase in energy produced and a further reduction in COE due to the reduced fault torque.

Table 5.1. Cost of Energy Results	10 MW PMDD	10 MW FSG	% Difference
Turbine Capital Cost ($ per Turbine)	17,930,312	14,961,667	-16.6
Balance of System Cost ($ per Turbine)	14,123,958	13,589,602	-3.8
Operation and Maintenance Cost ($/kW/year)	34.35	30.33	-11.7
Annual Energy Production (kWh/turbine/year)	34,076,552	34,708,415	+1.9
Total COE (cents/kWh)	13.98	12.21	-12.7

A further study was done to allow comparison with the DOE's strategy for offshore wind [1], which targets a COE of 10c/kWh in 2020 (using 2009 USD). The NREL paper on Technology Improvement Opportunities [24] was used to extrapolate future costs for the different technologies incorporating all the potential cost reductions in the wind turbine system due to further product development. The result is that the FSG could achieve a Cost of Energy of 7.67 c/kWh if all of the stated reductions are achieved.

In addition to these results, weight reduction should also be noted. A 27% reduction in the tower top weight of the turbine is likely to enable a further reduction in the COE in several areas – including capital cost, O&M cost and life extension – which would be likely to significantly strengthen the already positive comparison of the FSG against the PMDD system.

3.2.2.2 Levelized Cost of Energy (LCOE) Analysis

3.2.2.2.1 Report period: April 1, 2014 to June 30, 2014 (Q8)

Introduction

This task consists of the evaluation of the levelized cost of energy (LCOE) for the current design of the FSG and all its attributes. During BP1, DNV (formerly BEW Engineering) assisted the team in determining the LCOE for the then current system. The details of this analysis were included in the BP1 final project report.

For BP2, the goal is to perform a deeper analysis of the impact that the specific features of the FSG have on the overall turbine and accurately reflect this in the LCOE analysis.

NREL Technical Support Agreement (TSA)

After a number of meetings and agreement on a scope of work, NREL (Derek Petch) provided AML with a TSA for the work to be performed. AML reviewed the TSA, approved it and provided NREL with a purchase order and full payment in order to commence the work.

The NREL TSA Statement of Project Objectives (SOPO), which contains all the pertinent information regarding the work to be performed, is presented below.

NREL Statement of Project Objectives (SOPO) in Support of Advanced Magnet Lab's Innovative Drivetrain DOE Award for Budget Period 2 (Ends 9/30/14)

Background

Advanced Magnet Lab (AML) has a 10-MW, 10-rpm, fully superconducting generator (FSG) concept that it is developing as part of the DOE innovative drivetrain FOA. Their proposed generator concept is substantially lighter than the mass of a conventional geared drivetrain system and lighter than permanent magnet direct drive generator (PMG) systems. AML seeks to identify the tower mass savings and LCOE improvement arising from reduced drivetrain mass and the higher electrical system efficiency of their FSG concept compared to a PMG system.

DTU has created a 10-MW, 9.6-rpm reference turbine utilizing a new, light weight rotor design with the balance of tower head mass scaled-up from the NREL 5 MW reference turbine properties. NREL proposes that loads developed in the DTU 10MW reference turbine project be utilized by AML for the purposes of their concept design. The DTU drivetrain is, by concept definition, a medium speed gearbox with PM generator system (discreet drivetrain masses are not allocated by the DTU paper for components, only a "nacelle" mass is provided).

In the DTU 10-MW description document the designing tower base moment combined loading event is fully described. This loading condition, in combination with various tower head masses (THM), may be used as the design basis for optimization of the tower according to varying THM. With respect to tower design optimization, and in order for the loads to be deemed valid for differing THM, the system frequency response, first fore-aft bending mode of the tower inclusive of THM, must be maintained within 5 percent of the DTU baseline. The above systems compare as follows:

	Generator	**Rotor**	**Nacelle**	
	Mass	Mass[3]	Mass[4]	THM
FSG	183 MT[1]	229 MT	319 MT	548 MT
PMG	243 MT[2]	229 MT	379 MT	608 MT
DTU MS[3]	NA	229 MT	446 MT	647 MT

[1.][25], [2.][26], [3.][27], [4.][28]

AML would like to leverage NREL to support predicted turbine system LCOE reductions arising from the use of a 10-MW FSG compared to a comparable PMG and MS systems. Given the same design loads basis, the total expected mass for the balance of nacelle components; mainframe, rotor shaft and bearings, yaw system, etc. is assumed to be similar and for the purposes of the tower mass study is assumed to be 136 MT for both FSG and PMG systems. Due to budget and time constraints, no effort will be made to improve upon the balance of "nacelle" estimated masses. NREL deems these mass estimates to be reasonable.

Proposed Approach for NREL Work in BP2

NREL proposes to use the DTU 10-MW reference turbine data for the purposes of performing the work requested by AML in BP2. A complete description document for the 10MW turbine is available for use by NREL. NREL shall employ its systems engineering (SE) analytical modeling tool to develop tower designs based on the DTU external loading condition and the prescribed tower head masses.

Input assumptions and work scope:

1. The DTU reference turbine will be used for tower loads, baseline hub height, rotor mass and tower foundation stiffness (assume rigid) and tower response criteria. Note that the DTU reference turbine assumes installation on land; this assumption shall be maintained for all point designs.
    a. Tower top height h=115.63 m
    b. Horizontal force F=4605 kN
    c. Bending moment M=17851 kNm
    d. Tower Modes 1,2 f= 0.25 Hz
    e. Tower Top Diameter 5.5 m
    f. DTU Tower Base Diameter 8.3 m (Ref. DTU report, section 4.2.2, pp. 59 [27])
    g. Tower shell diameter shall taper linearly from top to bottom.

2. The DTU turbine configuration shall be modeled using the NREL SE tool to determine the tower mass as a cross-check of the mass developed by DTU, 628, 442 kg.
    a. The DTU-NREL tower will be developed by NREL to achieve strength, buckling and response criteria (design for fatigue will not be considered).
    b. Frequency response criteria to be maintained from DTU design +/- 5%.
    c. The tower mass derived by the NREL SE tool will serve as the basis for mass comparisons for the purpose of this study.
3. The tower head mass of the DTU turbine will be modified according to the mass of the PMG system and modeled in the NREL SE tool.
    a. The PMG tower will be developed by NREL to achieve strength, buckling and response criteria (design for fatigue will not be considered).
    b. Frequency response criteria to be maintained from DTU design +/- 5%.
4. The tower head mass of the DTU turbine will be modified for the FSG system in the NREL SE tool
    a. The FSG tower mass will be developed by NREL to achieve strength, buckling and response criteria (design for fatigue will not be considered).
    b. Frequency response criteria to be maintained from DTU design +/- 5%.
5. AEP calculations shall be performed using the shaft power of the DTU rotor (see table 3.3 of [27], above) and drivetrain efficiency assumptions for the purposes of LCOE calculation. AML has indicated 98.9% peak efficiency for the FSG (Table 1.2.1 of BP1 final report [28]). AML to provide the electrical system efficiency curve. The PMG shall be assumed 92% peak efficiency.

6. AML to provide capital costs and O&M costs for the FSG. The PMG systems' capital and maintenance costs shall be provided by NREL as inputs to the LCOE model.
7. The PMG systems' capital and maintenance costs shall be provided by NREL as inputs to the LCOE model.
8. Tower mass changes will provide variable cost inputs to the LCOE models for the capital cost of the two systems.
    a. The baseline, 116 m tall, DTU turbine tower cost, developed from its mass times a cost/kg of rolled-plate steel, will serve as the baseline tower cost.
9. NREL to complete LCOE analysis of the PMG and FSG systems accounting for the following system changes:
    a. Tower head masses resulting in varying tower mass
    b. Drivetrain capital costs
    c. AEP differences arising from drivetrain efficiency
    d. O&M cost and failure rate data for FSG provided by AML
    e. Consideration of the installation and service method required for each configuration, specifically whether the generator may be installed/removed independently of the rotor blades. For example, typical PMG designs require de-blading prior to completing drivetrain removal, inclusive of the hub, for generator servicing. The single-pick mass break point for typical, jack-up installation vessels is 800 MT. Crane picks up to 2,000 MT may be performed with a floating barge which is sea-state limited for operation.
10. NREL to document work outcomes in a final report to AML.

3.2.2.2.2 NREL Final Report, Levelized Cost of Energy (LCOE) Analysis for the AML Fully Superconducting Drivetrain Study, October 2014

A summary of the NREL levelized cost of energy (LCOE) analysis for the Advanced Magnet Lab's fully superconducting drivetrain study is provided in Appendix A: Advanced Magnet Lab's Fully Superconducting Drivetrain

3.2.2.2.3 Clarification of Cost Assumptions: BP1 vs. BP2

After a quick review of the BP1 and BP2 LCOE numbers, there are a number of clear reasons for the increase in LCOE, but the overarching culprit comes down to a more thorough accounting for all costs related to an offshore wind installation. As shown in the table below, costs for BOS and O&M have more than doubled and Soft Costs have been included in BP2 numbers. Although the Turbine costs and AEP have improved, the substantial increase in BOS, O&M, and Soft Costs have a greater impact on LCOE.

	BP1 ($/kW)	BP2 ($/kW)
Turbine Capital Cost	1,527	1,024
BOS	1,364	2,723
Soft Costs	0	541
Annual O&M	30	67

The increase in BOS, O&M and Soft Costs can be attributed to the source of BP1 vs BP2 costs: BP1 costs for BOS (and the non-existing Soft Costs) come from an old NREL 'model' [20] which are not detailed and are quite out of date. The new BOS and Soft Cost numbers are from our recently developed Offshore BOS model which is based on detailed data collected from installed projects in Europe and estimates for planned projects in the US.

An in-depth description of the BP1 O&M analysis notwithstanding, the BP2 analysis was done using the ECN O&M model which is regarded as the leading model in the offshore wind industry. Additionally, the BP2 numbers were based on published O&M estimates for direct-drive turbines and modified for the superconducting configuration. It is probable that the BP1 O&M estimates are lower than the BP2 estimates, since they do not include all O&M-based costs, there being a general underestimating of the true cost of offshore O&M.

All of this said, the true comparison that should be looked at is not the BP1 vs BP2 estimates, it should be the baseline (PMDD in this case) to the FSG configuration. And when looking at this comparison, the LCOE analysis in both budget periods indicates that the FSG configuration appears competitive. At this stage of 10-MW turbines in general though, simplified LCOE analyses such as this can only provide insight into a technology potential, and demonstration units must be installed to gather more reliable information for true lifetime costs and LCOE. It should also be noted that the $0.18/kWh for the FSG configuration is still lower than recent offshore wind LCOE estimates of $0.225/kWh [29].

3.2.3 Task 6.0 – De-Risking Experiments

Results of Task 6 de-risking experiments are presented by sub-task as detailed quarterly work progress reports delivered to the DOE, with the exception of Quarter 1. During this reporting period, primary activities for all tasks were related to project planning of the tasks and initiating contractual engagements with various sub-awardees and contractors, as listed below.

3.2.3.1 Report Period: July 1, 2012 to September 30, 2012 (Q1)

Overall Program Planning

- Detailed program financial plan developed, submitted and approved by DOE
- Internal controls and checklists developed to ensure program compliance in all areas
- Statement of Work developed and negotiated with all major sub-recipients
- Purchase Order released to Emerson Electric (Kato)
- Purchase Order pending for Columbus Superconductor and University of Houston (in final discussions)

Task 6.1 MgB_2 Mini-cable

- Program planning started (meeting schedules, work plan, controls/checkpoints/milestones)
- Technical program details in process
- Kickoff expected by early November 2012

Task 6.2 Composite Analysis

- Program planning underway (SOW for collaborators)
- Composite expert/center of excellence identified and active collaboration has commenced
- Purchase Order placed with agreed to Statement of Work

Task 6.5 AC Loss Measurement

- Significant work performed on technical solution/system. Team has converged on a specific approach.
- Meetings have occurred with various subject matter experts
- Test laboratory has been identified and budget/scope is being negotiated
- Detailed system design will commence at end of October 2012

Plans for Next Quarter

Task 6.1 MgB_2 Mini-cable

- Program will be kicked off
- Regular meeting/update logistics to be established
- Wire /Cable specifications to be agreed upon
- Preliminary design of the wire/cable to be completed
- Initial discussions of test plan to be underway

Task 6.2 Composite Analysis

- First phase of composite analysis to be completed
- Objectives/Specifications for test coupons to be completed
- Test facility to be identified

- Test plan to be detailed

Task 6.5 AC Loss Measurement

- Preliminary design of AC loss measurement apparatus to be completed
- Procurement of major subcomponents to be completed

Negotiations with test facility to be completed and contract to be in place.

3.2.3.2 Task 6.1 – MgB_2Mini-Cable Build and Test

The aim of Task 6.1 has been the validation (construction and test) of the mini-cables suitable to be implemented in the wind turbine generator. Two different wire configurations (37 and 61 filaments) were developed and produced following the design requirements. Using these wires, the mini-cable concept was proved.

The mini-cable configuration, the so-called “six around one” Figure 6.5.1.Figure 6.2.1.Figure 6.1.24, presents six MgB_2 round wires (the strands) cabled with a certain twist pitch around another MgB_2 wire, or around a copper strand with the same diameter.

The main efforts during the R&D program have been related to this “single-strand wire,” in particular, to:

- Develop and optimize round superconducting wires for the DC rotor field coil;
- Develop and optimize wires to minimize the AC losses.

After the studies on the single strand wire, activities were focused to develop procedures to assemble and test the mini-cable.

The starting point was a generic round wirepreviously developed at Columbus, but with a diameter of about 1.5 mm and powders suitable for self-field application. Efforts were focused to satisfy the main requirements of the generator design to:

- Improve the critical current in-field performance using special MgB_2 powders;
- Reduce the diameter of the wire down to 0.78 mm, fulfilling the design requirements and enhancing the minimum bending radius;
- Enhance the number of MgB*2* filaments in the wires, reducing the filament size as much as possible.

Special powders obtained with a synthesis at low temperature, together with a sieving process,were implemented to improve the critical current in the wire and also the workability of the small filament size. A new process was also developed for using these different powders with the small-diameter filament. Improvements were proved first at a diameter of 1.5 mm (see paragraph 0, Report period: October 1, 2012 to December 31, 2012 (Q2)), then to the final 0.78 mm (see paragraph 0, Report period: April 1, 2013 to June 30, 2013 (Q4).Changes in the Ic performance have been also evaluated as a function of the deformation steps, in particular, the swaging vs. drawing effect.

A 61-filament wire was then developed and characterized for the new process to solve the 37-filament wire issues related to breakage between small filaments and to reach a good critical current in field performance (details in 0, Report period: January 1, 2014 to March 31, 2014 (Q7)).

Figure 6.1.1 compares the main physical characteristics of the new wires.

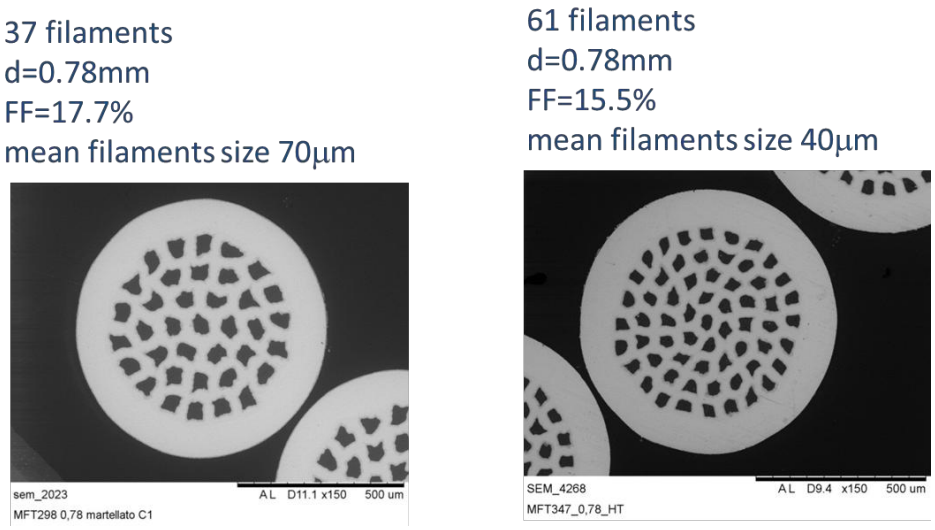

Figure 6.1.1. Comparison between physical characteristics of 37- and 61-filament wires

Other trials to reduce the filament size wereperformed, including a 91-filament wire configuration and a re-stacking approach using 7 wires with 19 filaments each. No definitive results have been reached for these new configurations, but much information has been obtained and a possible method to reach the target of 10-micron filaments has been outlined. This will require the optimization of a new "milling machine" just arrived in Columbus that is able to guarantee a controlled powder granulometry with a mean particle size lower than 5 microns (see 0, Report period: July 1, 2014 to September 30, 2014 (Q9)).

The The 37- and 61-filament wires have been characterized to define the critical bending radius, with no degradation for bending at 100 mm, and a 15% degradation for bending at 75 mm (0, Report period: July 1, 2013 to September 30, 2013 (Q5)). These numbers have determined some of the characteristics of the mini-cable assembly, in particular, the 10-cm twist pitch.

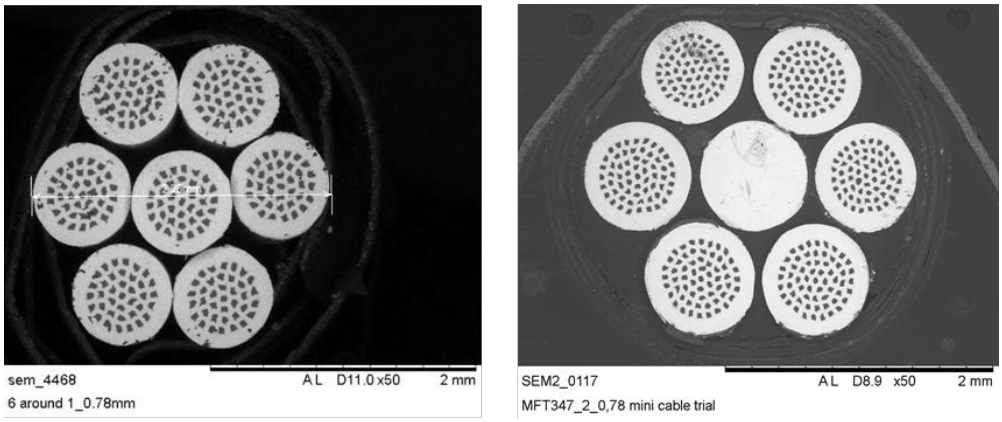

Figure 6.1.2. The37- and 61-filament wires reach at least six times the critical current of the strands with the same critical bending radius characteristics.

During the research program, a cable with un-sintered and sintered wires was manufactured and characterized (0, Report period: July 1, 2013 to September 30, 2013 (Q5)). Better results were obtained using cabling with pre-reacted wire,instead of trying to react the whole cable assembled 0, Report period: October 1, 2013 to December 31, 2013 (Q6)). Both the 37- and 61-filament wires, shown in Figure 6.1.2 have proven the mini-cable concept, reaching at least 6 times the critical current of the strands with the same critical bending radius characteristics.

3.2.3.2.1 Report period: October 1, 2012 to December 31, 2012 (Q2)

Major Activities

These two months have been dedicated to experimental activities related to:

- Powder improvements
- Fabrication of round wires with a diameter of 1.5 mm.

Activities Related to Specific Objectives

A. Technological improvement for the application of the MgB2 wire into DC rotor field coils

Critical current improvements in the magnetic field range of 2-3 T

Implementation of a sieving process

The first step of this task has been the implementation of fine powders with controlled grain size in the production process of wires. To do this, a new step of sieving was introduced in the manufacturing process. This arose from the need of the optimization of the filament size and homogeneity. From the superconducting point of view, an enhancement of the critical current has been expected because finer powders, and a more controlled particle size, lead to an improvement of the connectivity between grains. This could also lead to an increase of the grain boundary pinning and enhancement of the critical current performance at high fields [30].
The study presented below has been performed on two multi-filamentary wires (Samples G1 & G2).
Sample G1 (Figure 6.1.3 is a multi-filamentary wire produced without any sieving step. The longitudinal images obtained by Scanning Electron Microscopy (SEM) show some sample areas with abnormal large particles, which could produce breakage, both in the filaments and the wire and inhomogeneity in the superconducting properties.

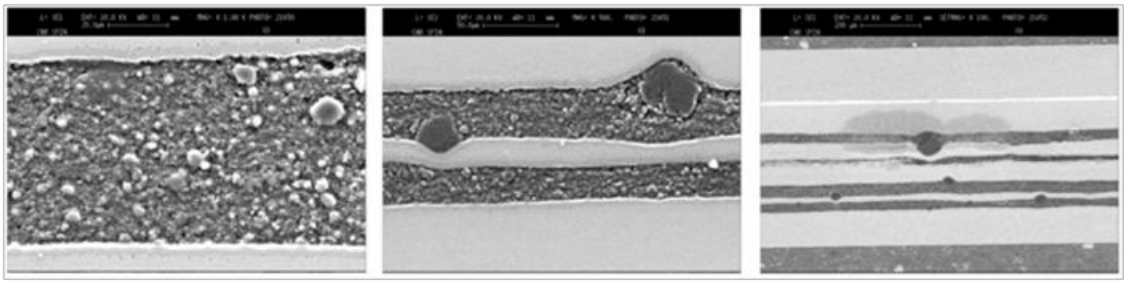

Figure 6.1.3. Longitudinal SEM images of sample G1 with powder without sieving process

Sample G2 has the same layout and the same production process of G1, but the new sieving process has been applied. Figure 6.1.4 shows longitudinal SEM images of the sample.

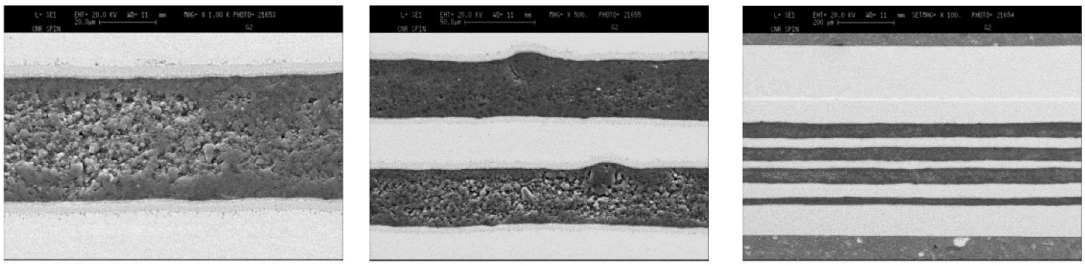

Figure 6.1.4. Longitudinal SEM images of sample G2 with sieving process added

The same visual inspection shows not only the absence of abnormal large particles but also a more uniform particle size distribution. This leads to denser filaments and, as a consequence, to a higher connectivity and enhanced critical current density. The sieving step has been already introduced in the production process of every wire related to the DOE project.

Implementation of "special powders" and optimization of reaction temperature

To enhance the critical current in field performance of MgB_2 wire at intermediate fields, rather than doping, which decreases the critical temperature, special powders can be produced working on the synthesis temperature [31]. As explained in Ref [30], the Jc versus magnetic field behavior of wire obtained with this "low temperature powders" is better than standard powder (ST) due to the presence of some amount of unreacted B and Mg, which can act as fluidifying for the MgB2 grains. The final thermal treatment at the end of the production process, a sort of sintering process, will ensure stoichiometry the complete reaction for the not reacted precursor. As presented in the publication the achievable Jc depends on temperature and a relatively low reaction temperature yields the highest critical current density.

It is worth noting that the implementation of this kind of powder is not only a substitution of powder in a well-established processing route for the production of a wire with a certain layout (final design and materials constituting the wire): powder characteristics will determine the optimum annealing step, with different temperatures, during the cold working deformation process. These special powders (ST) have been implemented in the round wires developed for this task.

- Mechanically reinforced sheaths (to reduce strain and bending sensitivity)

  Starting from Columbus Superconductors' know-how, a round wire configuration with 37 nickel-encapsulated filaments and Monel as reinforced sheath is the first wire-layout used to study the wire architecture suitable for the AML application in the DC rotor field coils.
  The round wire has been produced with a final diameter of 1.5 mm and the production process includes the sieving step mentioned in the previous paragraph.

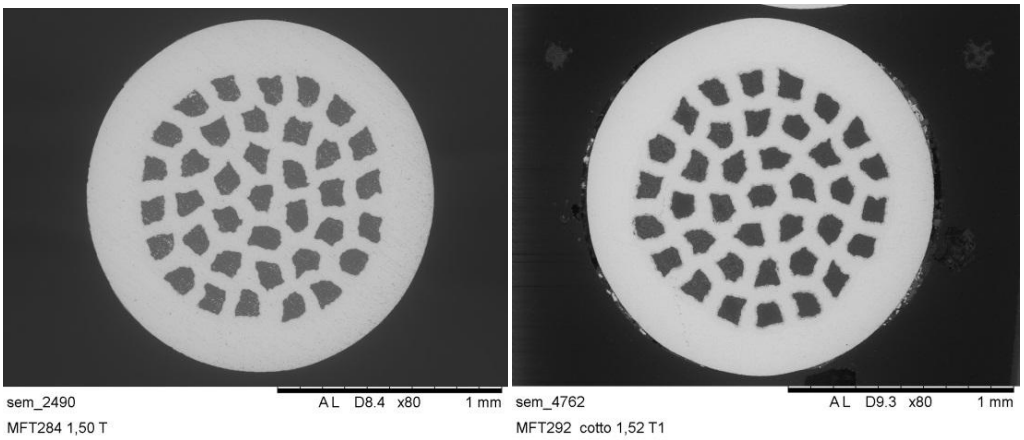

Figure 6.1.5. Cross-section of round wire with a diameter of 1.5mm
a. MFT284 with ST powder b. MFT292 with LT powders

Figure 6.1.5.a shows the SEM image of the cross-section of MFT284 wire. The filling factor is 20%. Powders used in this wire are standard (ST).

Figure 6.1.5.b shows the sample MFT292 with the same layout of the MFT284 but with LT powders. The filling factor is 20%. Using a thinner Ni tube for the monofilaments and hence reducing the materials at the interface between them could enhance this value. This possibility should be qualified, because it is not an obvious issue in terms of quality of the cross-section and consequently of the wire.

B. Characterization of wire performance around 2.5 T in the 15 K to 20 K temperature range.

Preliminary critical currents versus magnetic field measurements at different temperatures (from 16 K to 30 K) have been performed to characterize MFT284 (Figure 6.1.6) and MFT292 (Figure 6.1.7) wires.

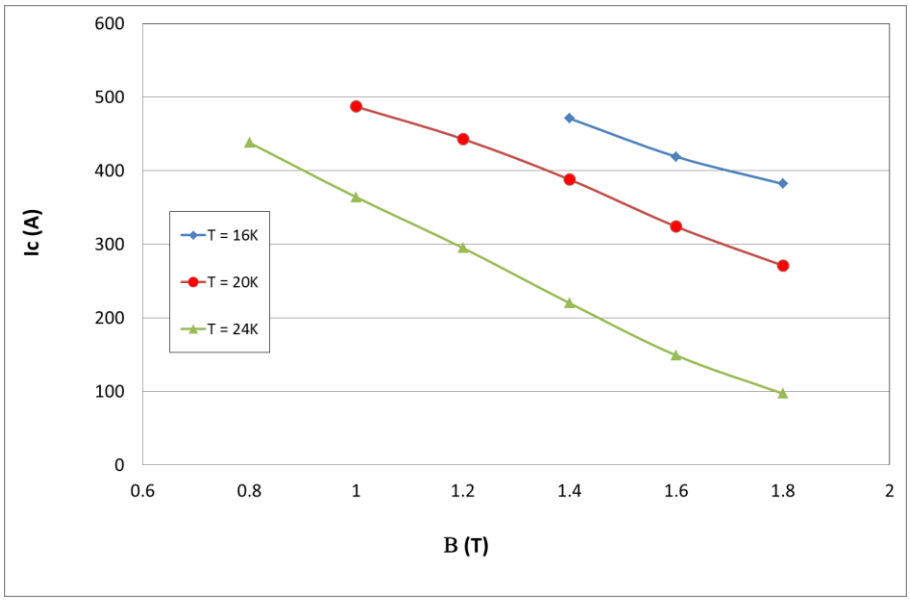

Figure 6.1.6. Critical current measurements of MFT284 round wire

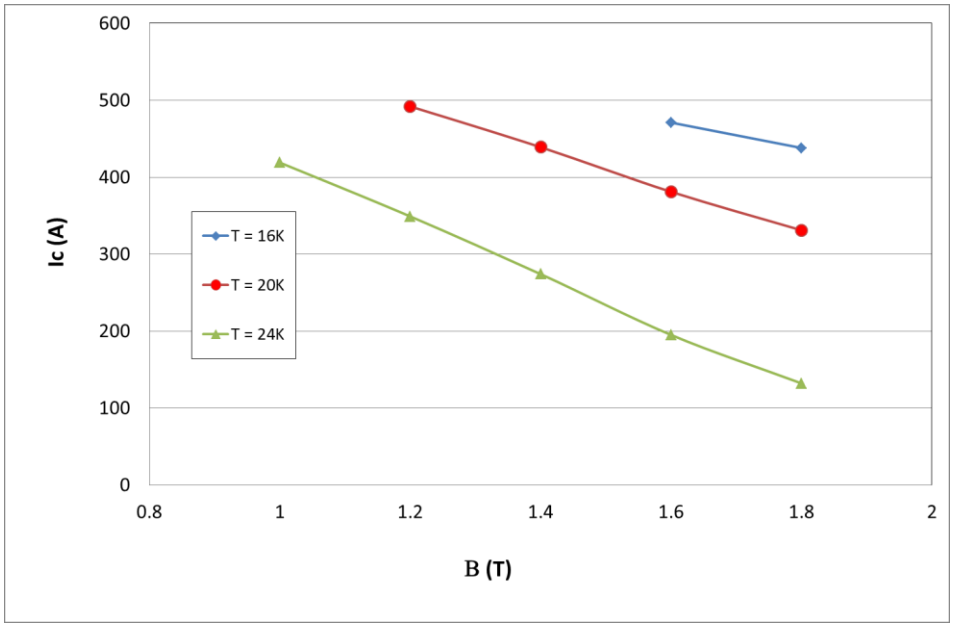

Figure 6.1.7. Critical current measurements of MFT292 round wire

Figure 6.1.8 shows the comparison between critical currents of the two wires. The results clearly show better performance of MFT292 wires in respect to MFT284 and the effect of LT powders to enhance the critical current of the wire.

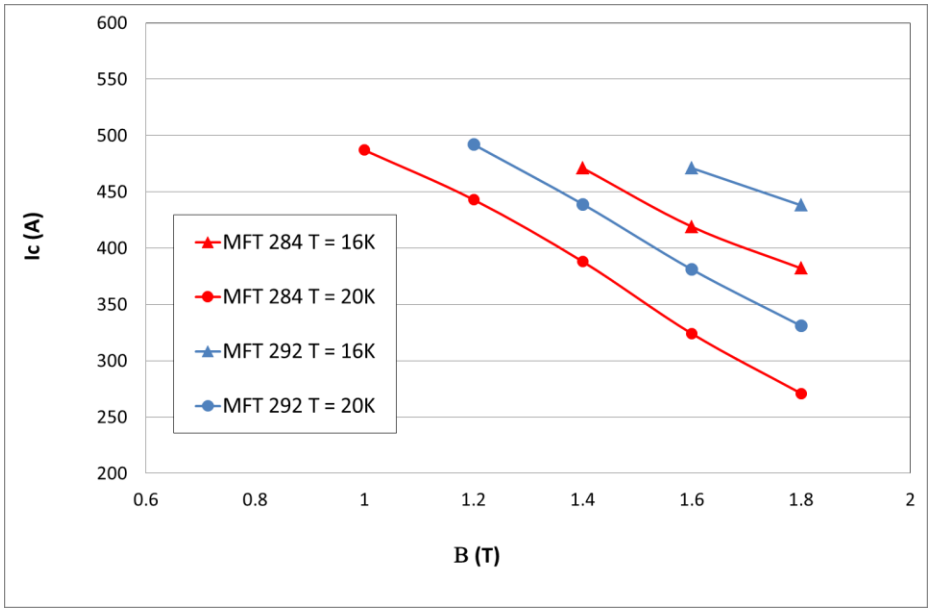

Figure 6.1.8. Comparison between critical current measurements of MFT284 (red) and MFT292 (blue) at T=16K and T=20K

Key Outcomes

- A sieving step has been introduced in the production process of round wire in order to improve grain uniformity and avoid abnormally large MgB_2 grains within the filaments. Results have shown more uniform and dense filaments. Thanks to this new step, the critical current has been enhanced through a better connectivity.
- A new synthesis process for the production of MgB_2 powder has been studied to improve the in-field electrical performance of wire without doping. Powders produced with this new process (LT powders) have been used for the fabrication of a round wire.
- A layout for a round wire has been developed to start studies for the AML application in the DC rotor field coils. Two different powders have been used in these design configurations to enhance the performance in magnetic field range as in the DC rotor application.
- Through the introduction of the "special powders," the electrical performance has been improved. As highlighted above, the behavior of the 2nd sample (MFT292) has a higher critical current density in the relevant field range than MFT284.

Plans for Next Quarter

- The activity on the two samples (MFT284 – MFT292) will be extended:
    - Both samples will be worked to reduce the diameter to 1.00 mm;
    - The thinner samples will be tested to verify an expected increase in engineering critical current density;
    - Tests will performed to determine the minimum bending radius in the out-of-plane on the four samples listed below:

1. MFT284 – Ø1.52 mm
2. MFT284 - Ø1.00 mm
3. MFT292 - Ø1.52 mm
4. MFT292 - Ø1.00 mm

- These four samples will be characterized in terms of Physical Properties (thermal conductivity, thermal coefficient of expansion, Young's modulus, shear modulus, compressive stress limit, tensile stress limit) in an appropriate laboratory. This activity is strictly connected to availability of a qualified laboratory that can perform these measurements;

- The activity related to the research and development of the most suitable wire for the application of the stator coils depends on the availability of a titanium grade 1. The search for a supplier is currently being pursued;
- In case of negative response, the cabling process for the required 6-around-1 cables for the rotor part coils will be started.

3.2.3.2.2 Report period: January 1, 2013 to March 31, 2013 (Q3)

The activities included in the previous report focused on two main topics:

- Powder improvements;
- Fabrication of round wires with a diameter of 1.5 mm.

With respect to the powder improvements, the implementation of the sieving process has led to a better control of particle's size distribution while the implementation of special powders (Low temperature powders - LT) has led to an improvement of the critical current (I_c) performance at intermediate magnetic field.

With respect to the wire's design, a fabrication process has been developed to produce round wires with small diameter. The process has been optimized for both the powders.

Since the wire characteristics for the stator and the rotor of the AML generator could be different, the aim of these activities is to have a good understanding about the possibility for Columbus to produce wires suitable for the generators in terms of dimension and superconducting, thermal, electrical and mechanical properties. These experimental results, together with activities related to the use of different precursors (i.e., high purity amorphous boron) will be the starting point that will lead reasonable projections of wires performance and costs for the next years.

Major Activities

These three months have been devoted to experimental R&D activities related to:

- Fabrication of round wires with a diameter below 1.5 mm;
- Design and fabrication of a wire suitable for the stator.

Other activities have been devoted to the study of Columbus preliminary results on

- Stress-strain behavior and bending radius of round wires;
- Improvement of I_c in field performance using different B precursors.
- These studies will be deeper discussed, together with experimental results, in the report related to next quarter.

Activities Related to Specific R&D Objectives

A. Technological improvement for the application of the MgB2 wire into DC rotor field coils

Both the samples MFT284 (normal powders) and MFT292 (LT powders) have been drawn down to a diameter of 1mm. In Figure 6.1.9, SEM images of the two wires show good cross-sections.

Samples have been characterized from 16 K to 30 K in magnetic field up to 1.8T and results of the critical current are reported in Figure 6.1.10 (MFT284) and Figure 6.1.11 (MFT 292).

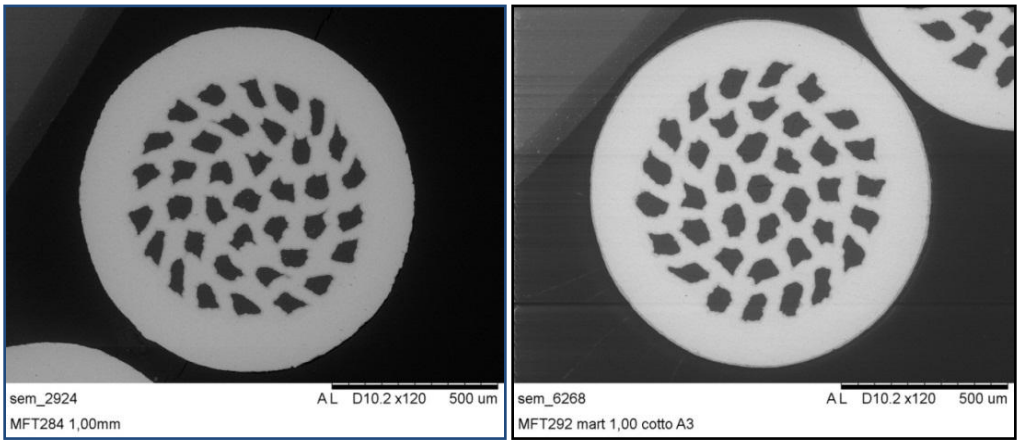

Figure 6.1.9. Cross-section of round wire with a diameter of 1 mm

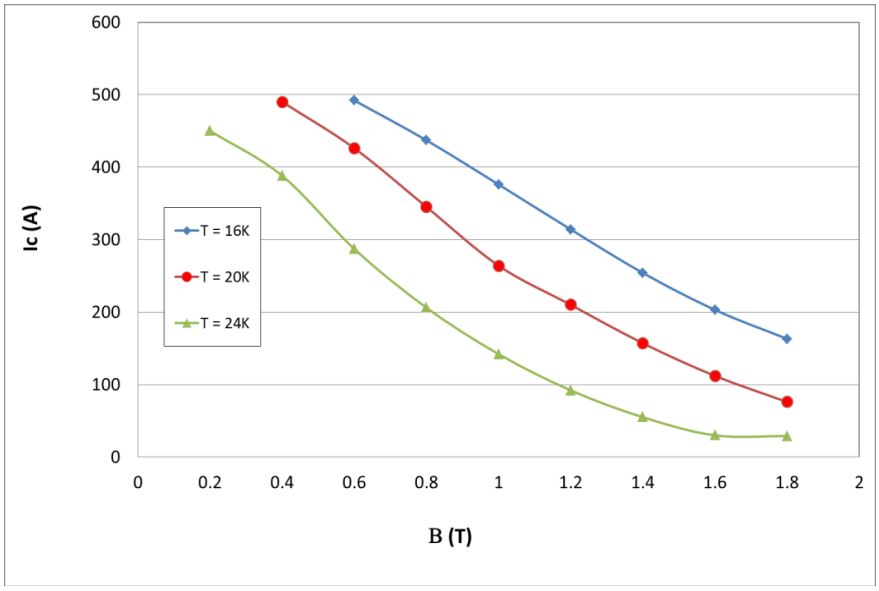

Figure 6.1.10. Critical current of MFT284 round wire (diameter 1mm)

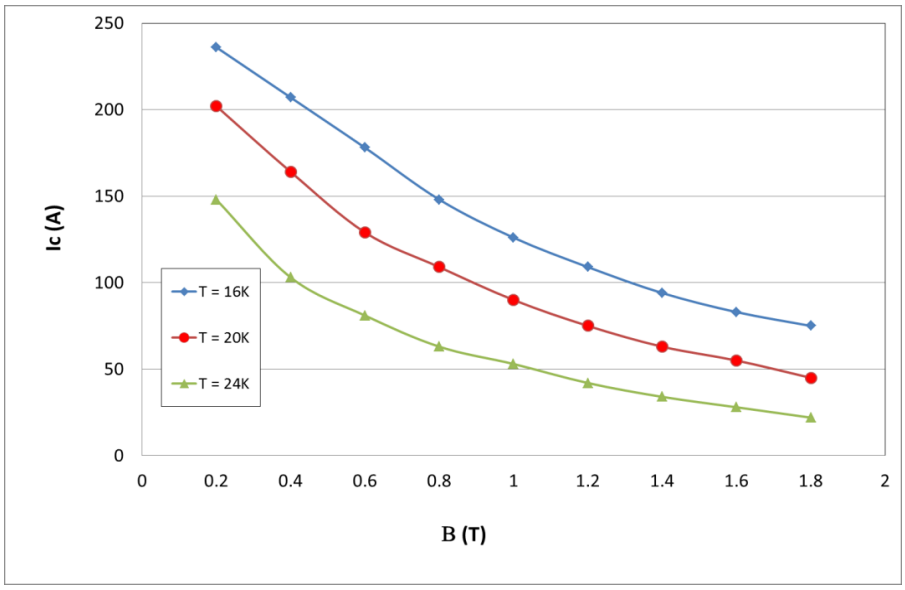

Figure 6.1.11. Critical current of MFT292 round wire (diameter 1 mm)

A direct comparison of the critical current at 16K and 20K for the MFT284 samples at different diameter show a reduced current for the lower diameter, but if we look at the engineering critical current density we can see that the sample with the lower diameter has higher value, although this is true only at low field.

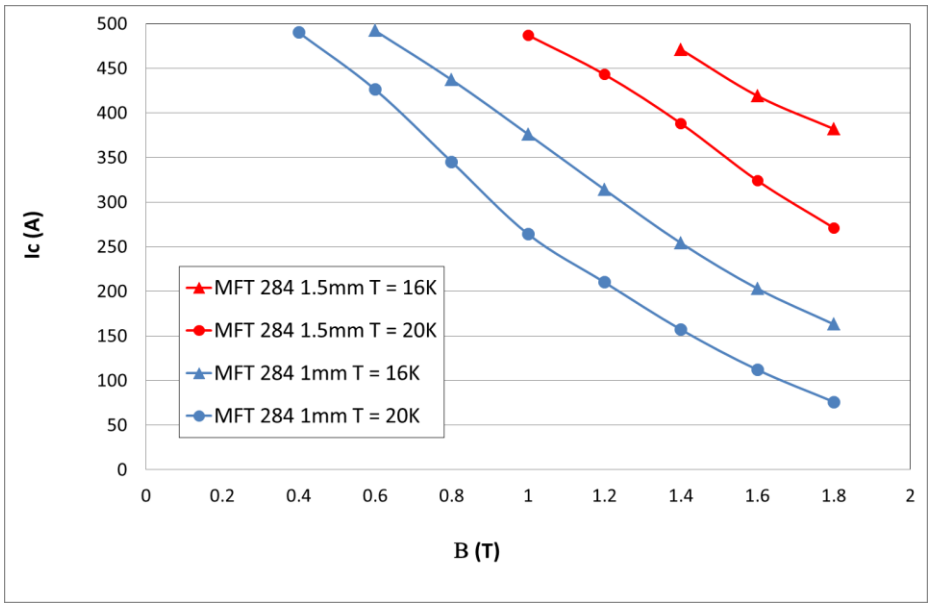

Figure 6.1.12. Critical current of MFT284 round wires: comparison between 1.5- and 1-mm diameter samples

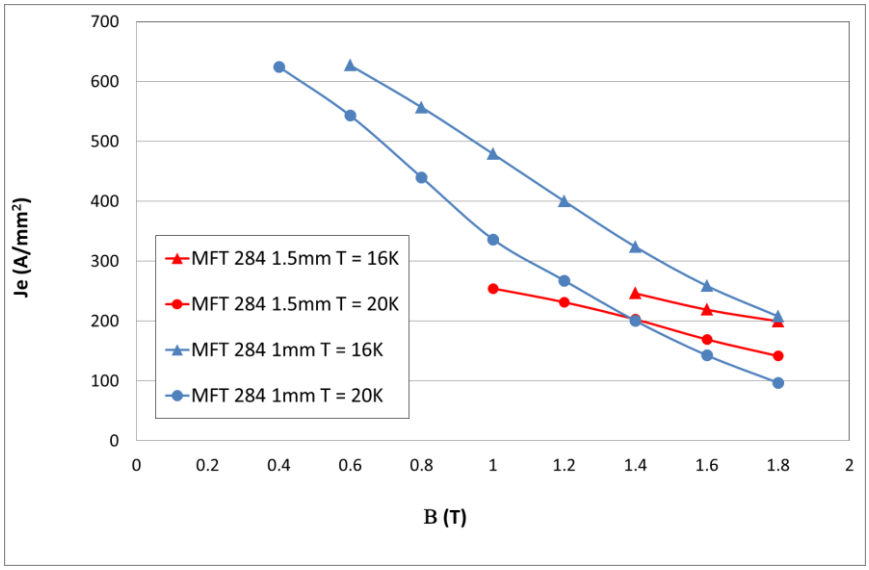

Figure 6.1.13. Engineering critical current density of MFT284 round wires: comparison between 1.5- and 1-mm diameter samples

The comparison between diameter 1.5 mm and 1 mm of the MFT294 in Figure 6.1.13 shows a very low critical current for the lower diameter sample (Figure 6.1.14) that cannot be explained by the diameter reduction. This result can be explained only by a degradation of the wire, probably due to some problem related to the short batch used for this first trial or by an optimization related to the use of the LT powders that are much more sensible to the process and to the heat treatment used.

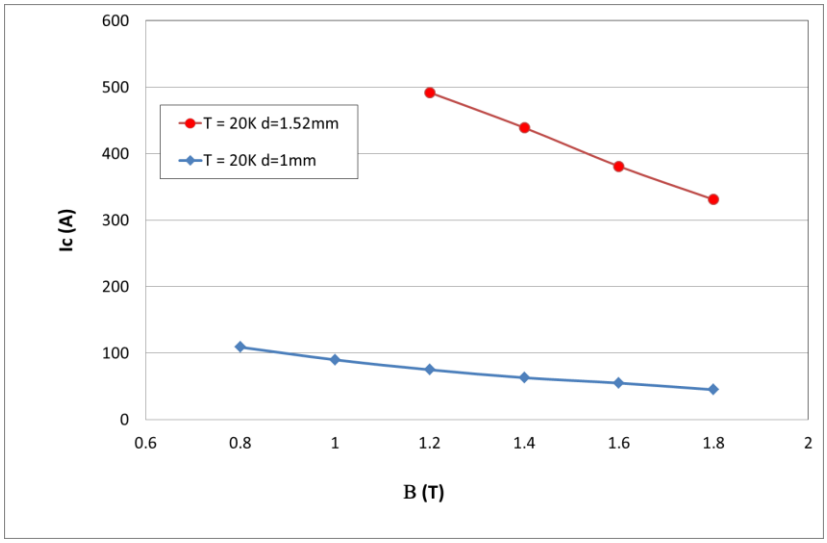

Figure 6.1.14. Critical current of MFT292 round wires: comparison between 1.5- and 1-mm diameter samples

The fabrication of a new sample with the same layout and with LT powders has started with the aim of producing a new wire with a diameter of 1 mm, but also to further reduce it to 0.78 mm.

New equipment is necessary to reach these diameters and to optimize the process. At the moment of writing this report, the wire is at 1.65 mm. In Figure 6.1.15, the cross-section of the wire is shown during intermediate steps of cold working.

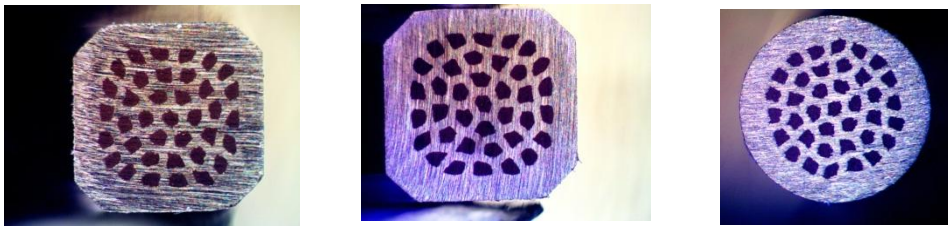

Figure 6.1.15. Cross-section of the new wire at intermediate step of production process

B. Research and development on MgB_2 wire with the goal of minimizing the AC losses

The wire most suitable for the stator application will be designed not only to reduce AC losses, but also to have a current limiting behavior. This means that the wire should have small filaments, not magnetic materials and a high resistivity matrix.

During these months, much effort has been devoted to the study of a new processing route to work with stainless steel (SS) tube. This material would reach not only the goal related to magnetic and electrical issues, but also it would improve the mechanical properties. The main issues in the development of the processing route will be the intermediate heat treatment (HT) needed by the material to sustain cold working because this HT could have a large impact on the MgB2 powder. The big issue will be to find a compromise on temperature and time that doesn't introduce degradation on the powder with enough workability for cold deformation.

Using a starting tube different both in diameter and thickness, we succeeded in the cold working of the SS monofilament and in the assembling of a 14-filament wire with Monel as external sheath (Figure 6.1.16).

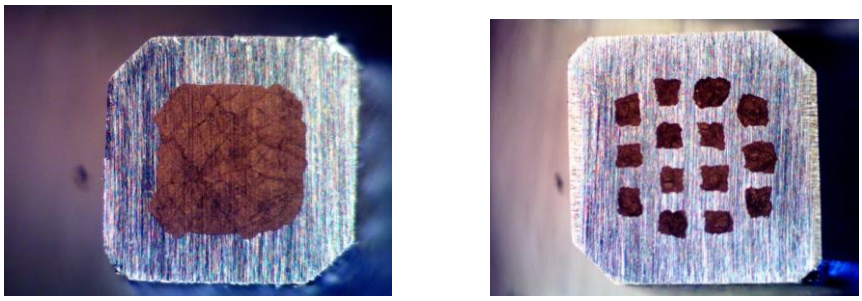

Figure 6.1.16. Cross-section of the SS monofilament and of the first multi-filamentary wire architecture with 14 SS monofilaments and Monel as external sheath

This wire has been successfully drawn at first to a final shape of a tape (3 mm, 0.5 mm thick) to check the critical current performance and to have information about powder degradation. Figure 6.1.17 shows the SEM image of the final cross-section and I_c data from characterization.

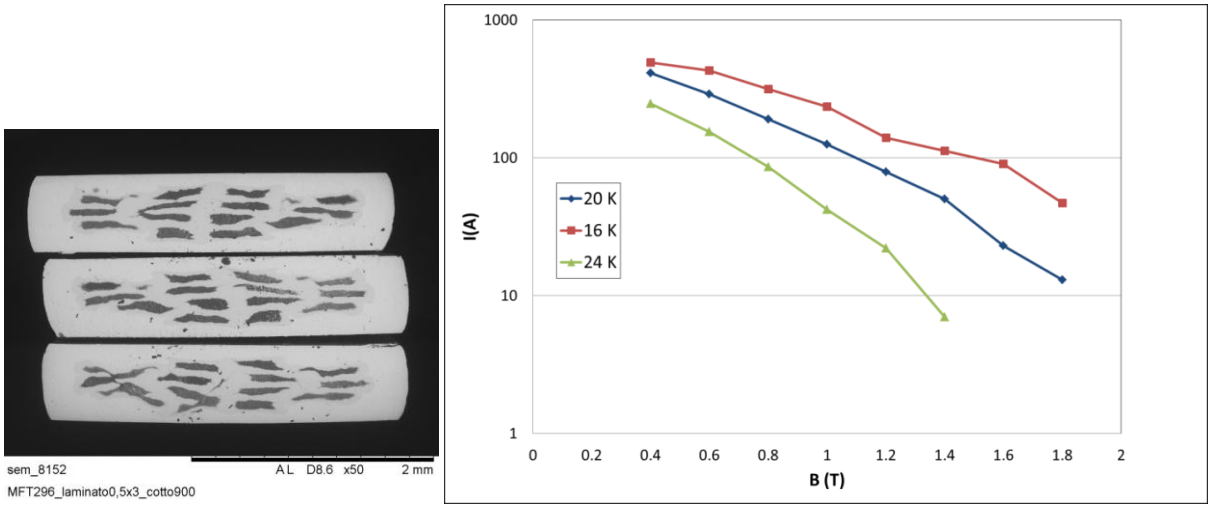

Figure 6.1.17. Cross-section of the 3 x 0.5-mm2 tape with SS filaments

The data is very promising, and in the next months the development will be devoted to improving the wire design and to reach the round configuration necessary for cabling activities.

Task 6.1 Plans for Next Quarter

- Define the final step of the process to produce a wire with the same characteristics of the MFT292 (1.5 mm) to reach the 0.8 mm diameter without degradation and start the cabling-related activities
- Design the wire for the stator and define the process to increase the number of filaments and to reach the round configuration to clarify the possibility to use SS for the monofilaments.

3.2.3.2.3 Report period: April 1, 2013 to June 30, 2013 (Q4)

In the previous report, the activities related to the implementation of special MgB_2 powders in round wires with small diameters have been discussed. We have obtained good results relatively to a diameter of 1.5mm, but the trials to go down to 1 mm have shown some superconducting performance degradations at a diameter of 1 mm.

During this quarter, several efforts have been made to optimize the wire processing to reach a diameter of 0.78 mm; the achievement of the round configuration at 0.78 mm in diameter has allowed the start of the cabling activities.

The critical bending radius of this wire has been evaluated, giving the information needed to fix the starting characteristics of the mini-cable.

Task 6.1 Activities Related to Specific R&D Objectives

- **Sub-task 6.1: Technological improvement for the application of the MgB_2 wire into DC rotor field coils**

A new, long sample called MFT298 has been produced to study a process to obtain a wire diameter of about 0.8 mm. New equipment, and its implementation has been necessary to avoid degradation of the superconducting performances like in the trials related to the previous quarter.

- The main issue has been the swaging process: the optimization of the dies design and the process characteristics. There are a lot of parameters relevant for the swaging process:
    - Speed
    - Pressure
    - Angle of the cone and length of the straight part of the dies

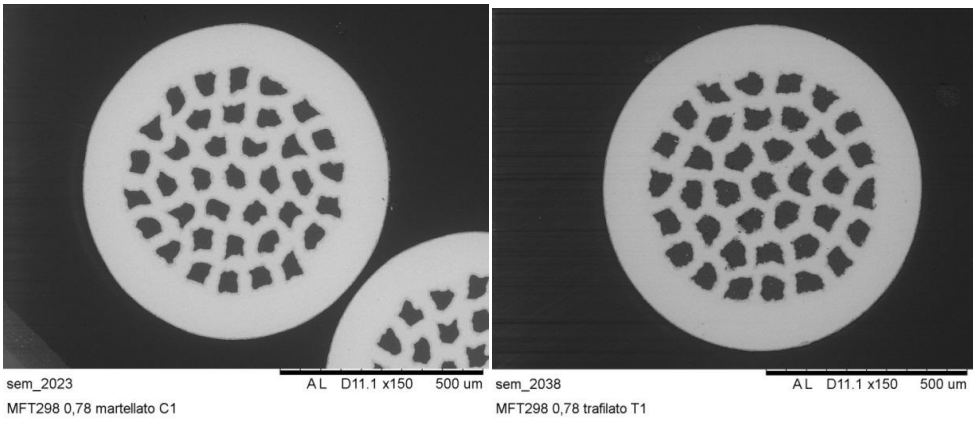

Figure 6.1.18. Cross-section of the new wires with a diameter of 0.78 mm

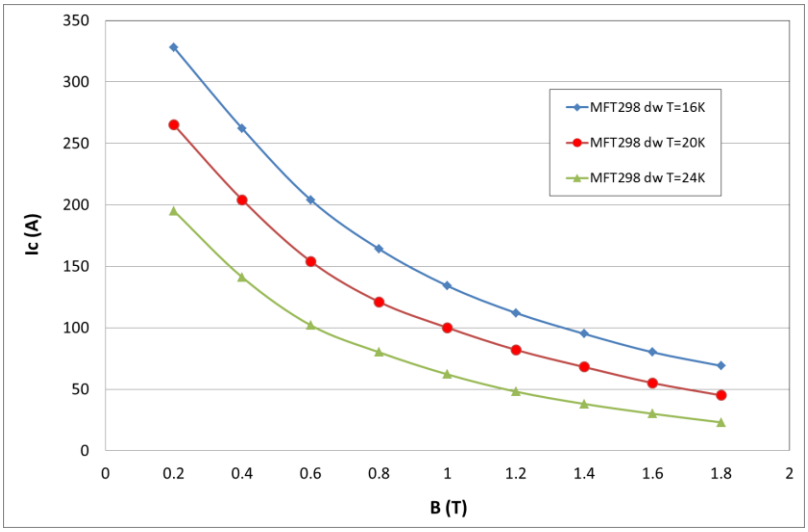

Figure 6.1.19. Critical current of MFT298_dw round wire (drawing process, diameter 0.78 mm)

The two wires have been characterized and critical currents are collected for the drawing process, and three for the wire obtained with the swaging process (Figure 6.1.19 and Figure 6.1.20).

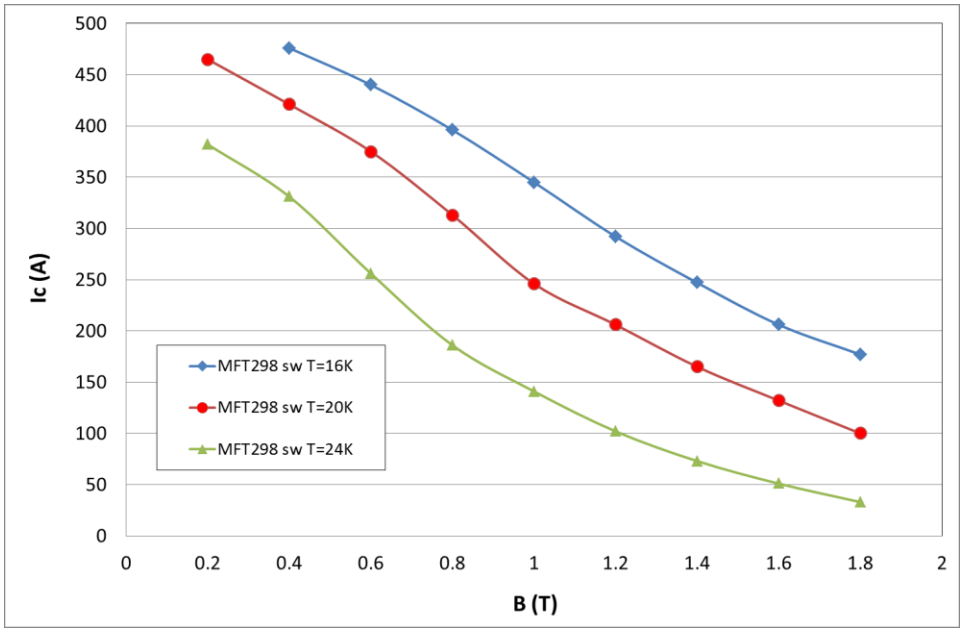

Figure 6.1.20. Critical current of MFT298_dw round wire (drawing process, diameter 0.78 mm)

It is clear that the wire obtained with the optimized swaging process has higher critical current with respect to the wire obtained with the drawing process, due to better compacting of the MgB_2 powder inside the wire. This is also revealed by the difference in filling factor values between them.

Figure 6.1.21 and Figure 6.1.22 show a comparison at 20 K between the 1.52-mm wire and these last two samples. The plot in Figure 6.1.21 shows the critical current values, while the plot in Figure 6.1.22 shows the critical current densities.The critical current of the 1.52-mm wire is higher than the smaller wires, but the critical current densities of the smaller and swaged wire is clearly much higher due to better compacting.

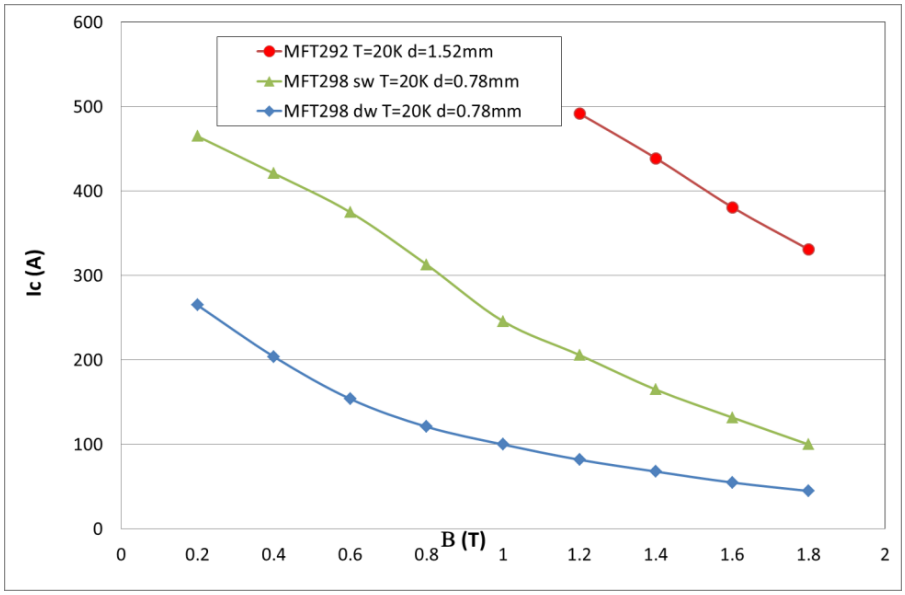

Figure 6.1.21. Comparison at 20K of the I_c and J_c of the 1.52-mm and 0.78-mm wires.

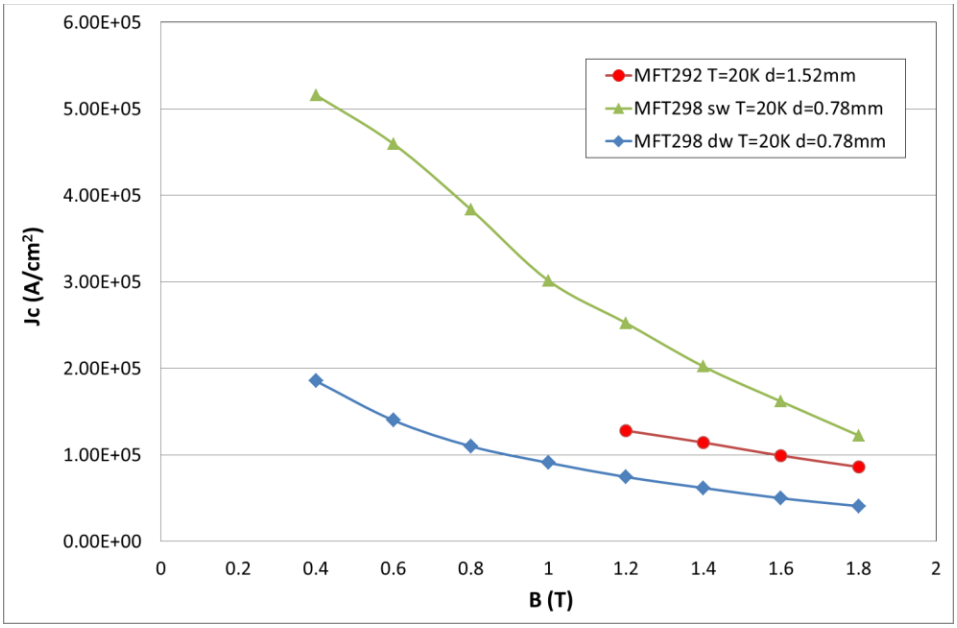

Figure 6.1.22. Comparison at 20 K of critical current densities

Results are very good and promising, since the feasibility of a 37-filament wire with a diameter of 0.78 mm has been proved,and an optimization of the filling factor of the swaged wire could be reached, for example, through a reduction of the thickness of the outer Monel sheath.

This page removed due to Intellectual Property/Distribution Limitations

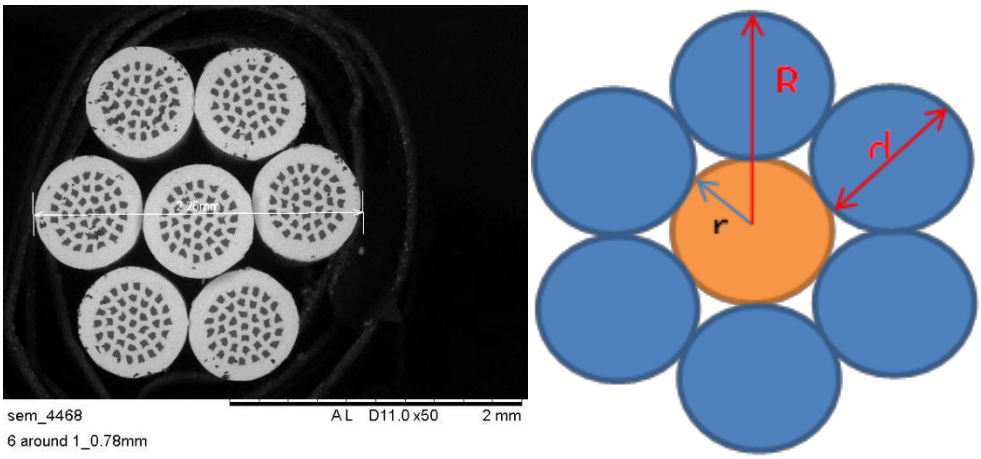

Figure 6.1.24. The 6-around-1 Configuration for the MgB_2 Mini-Cable

- Perform the critical current characterization of the mini-cable
- Define the configuration of the wire for the AC stator field coil to comply with requirements related to the other task activities.
    - Low AC losses
    - High resistivity
    - CTE.

3.2.3.2.4 Report period: July 1, 2013 to September 30, 2013 (Q5)

Introduction

In the previous report, results cocerning the characteristics of round wires with diameter of 0.78 mm were discussed in terms of the relationship between the superconducting performance (I_c versus B at different temperatures) and fabrication process (drawing versus swaging).

During this quarter, the critical bending radius of the round wires has been evaluated giving information to define the characteristics of the mini cable. According to the single strand characteristics, two mini cables have been prepared at Columbus to start the characterization activities.

Task 6.1 Activities Related to Specific R&D Objectives

- **Sub-task 6.5: determination of the critical bending radius without reaching detectable degradation**

The wire with the lowest diameter and with the process related to the highest critical current (the swaging process) has been characterized to determine the critical bending radius.

From Columbus' experience, a strain between 0.2% and 0.4% could be responsible for I_c degradation. Taking into account the radius (Figure 6.1.25, y~260 μm) of the outer ring of filaments, the more subjected to strain during bending, the critical bending radius should be in the range of 60 - 120 mm.

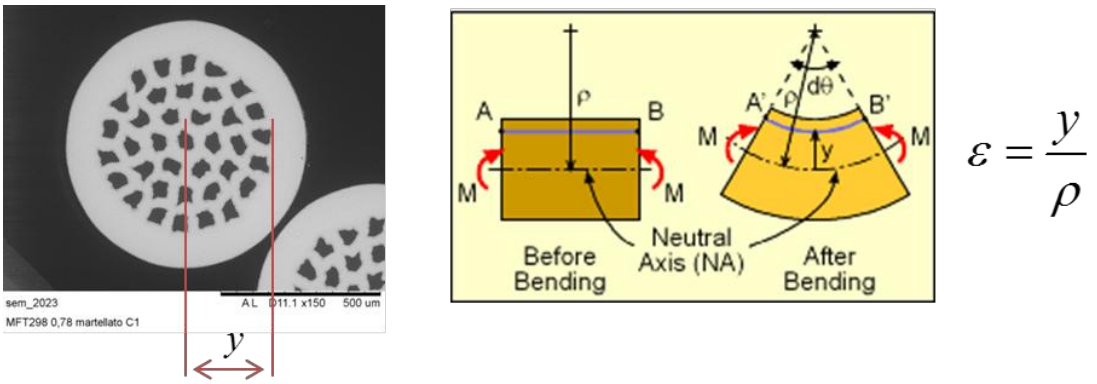

Figure 6.1.25. Cross-section of the 0.78-mm round wire and relationship between the strain ϵand the distance of the filaments with respect to the neutral axis

Two tests were performed, bending the wire on a radius of 100 mm and 75 mm:

I_c characterization has been performed on a straight sample holder. Figure 6.1.26 and Figure 6.1.27 show the I_c versus B at different temperatures.

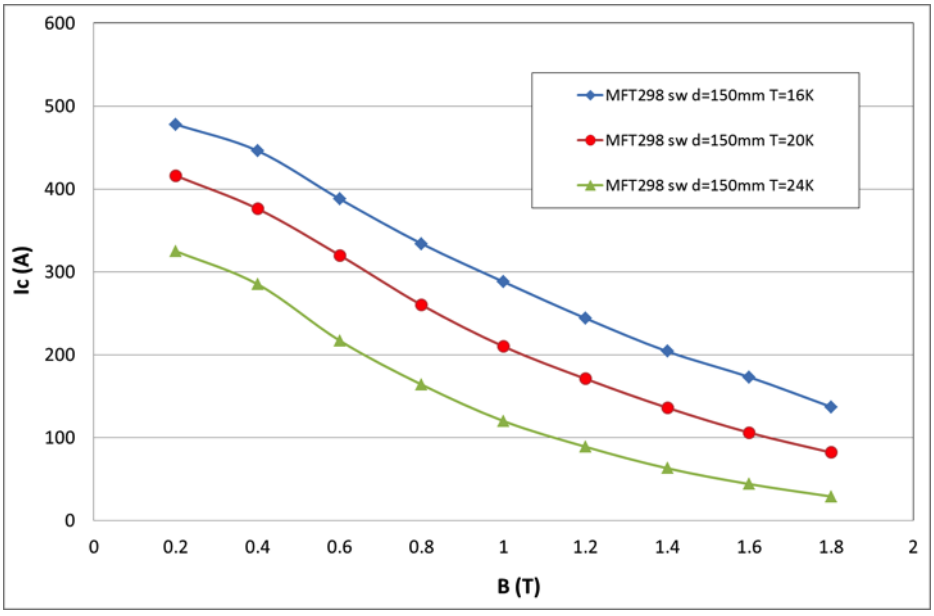

Figure 6.1.26. Critical current of MFT289_sw round wire bent on a radius of 75 mm

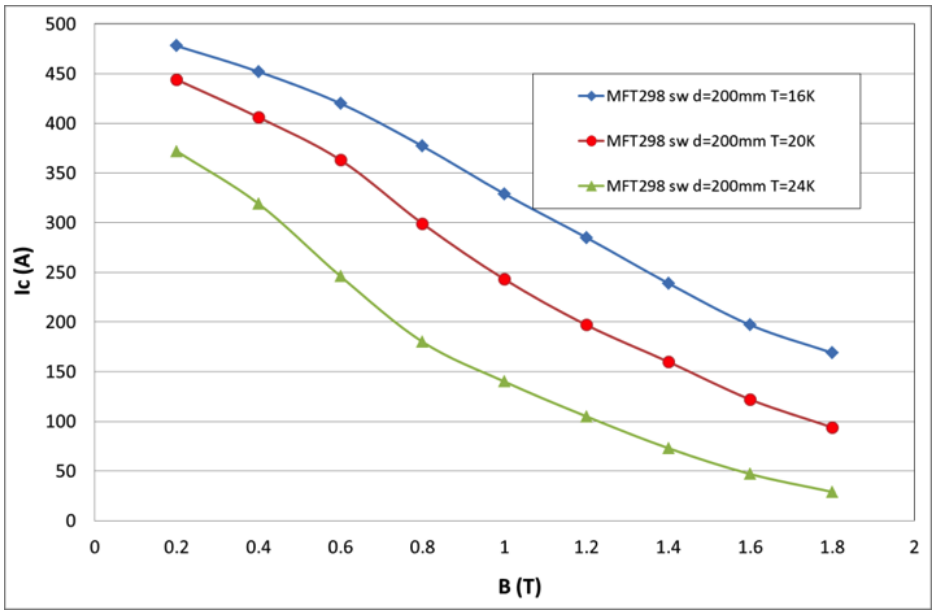

Figure 6.1.27. Critical current of MFT289_sw round wire bent on a radius of 100 mm

Bending the wire with the radius of 75 mm has led to a degradation of about 15-20%, while the radius of 100 mm has led to no degradation of the SC performance. Figure 6.1.28 and Figure 6.1.29 show comparisons at 20 K and at 24 K, respectively, between the wire not bent, or subjected to bending.

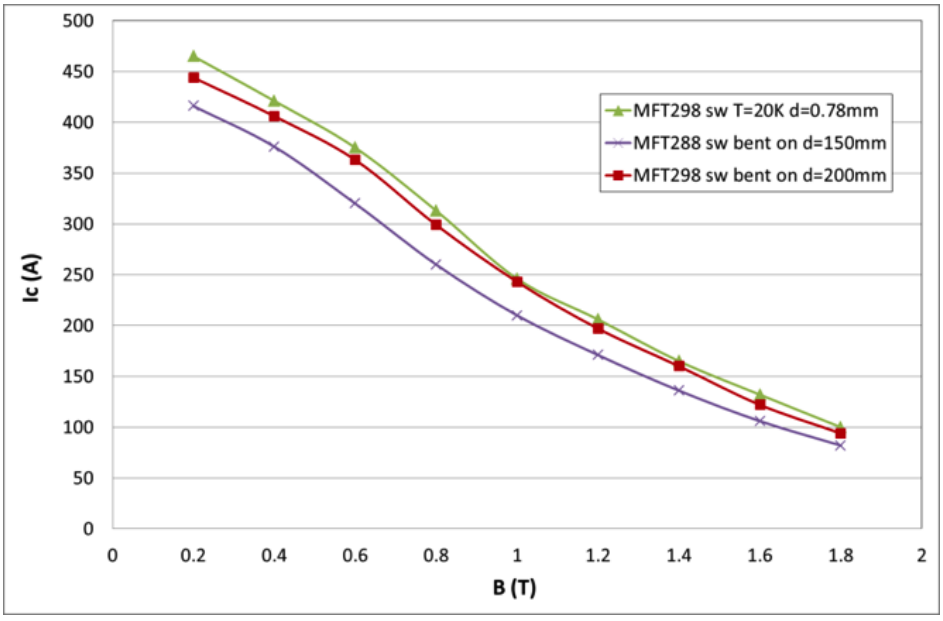

Figure 6.1.28. I_c comparison at T=20 K between the wire not bent, bent on radius of 75 mm, and 100 mm

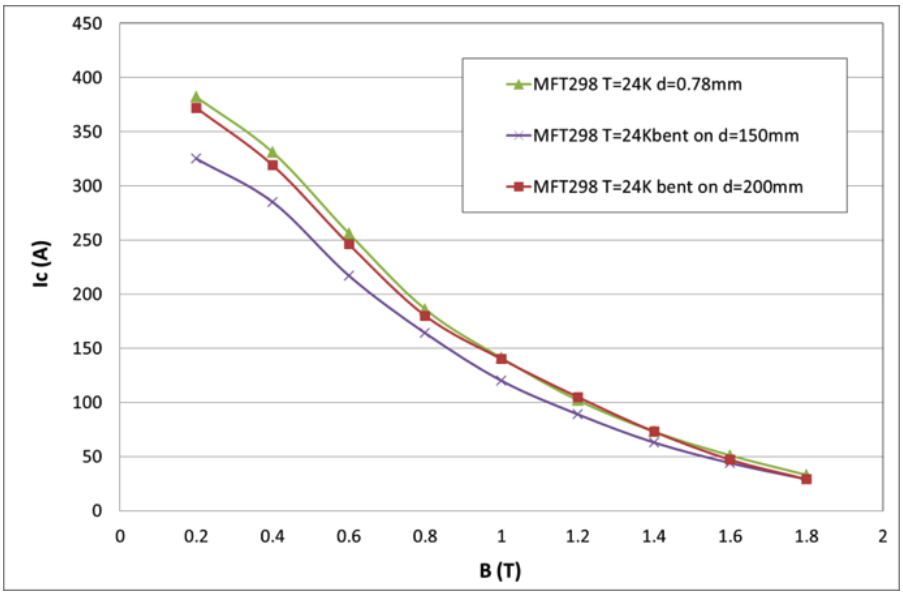

Figure 6.1.29. Ic comparison at T=20 K between the wire not bent, bent on radius of75 mm and 100 mm

Taking into consideration the relationship between the strain and the distance of the filaments from the neutral axis, as in Figure 6.1.25, the bending radius of 100 mm led to an equivalent critical strain of 0.26%.

- **Sub-task 6.6: Cabling of the developed conductor into six-around-one cable**

A first prototype cable has been assembled at Columbus according to the single strand characteristics. In particular, the "critical twist pitch" of the cable has been evaluated, starting from the critical strain.

Figure 6.1.30 shows the geometrical parameter in the helicoidal arrangement of a wire strand in a cable, which is then used for the evaluation of strain introduced due to the twist pitch.

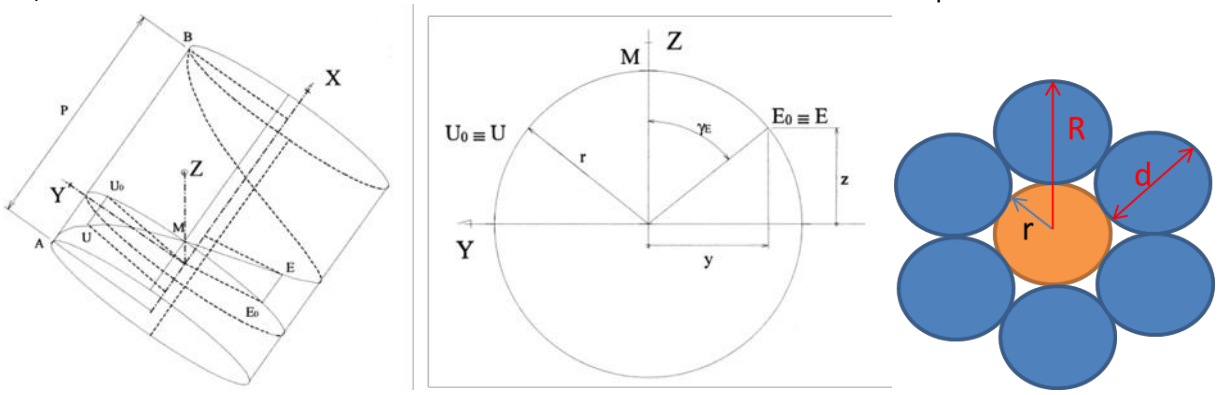

Figure 6.1.30. Geometrical parameters related to the helicoidal arrangement and the 6-around-1 configurationof the cable

Using 0.78mm for the diameter of the wire, in the cable configuration of Figure 6.1.30, a twist pitch of 55 mm results in a strain of 0.26%. In this way, a twist pitch of 100mm could be reasonable as a first approach to cabling.

Seven pieces of about two meters have been cut and located in the rotating assembling device shown in Figure 6.1.31 following the 6-around-1 wire configuration. The wires are pulled at constant speed through a die with a diameter of about 2.5 mm necessary to maintain the configuration. During this movement, the assembling machine rotates at fixed speed resulting in a 10-cm twist pitch. Figure 6.1.32 shows some images of two cables assembled using unreacted (Cable 1, upper picture) and reacted (Cable 2, lower picture) wire.

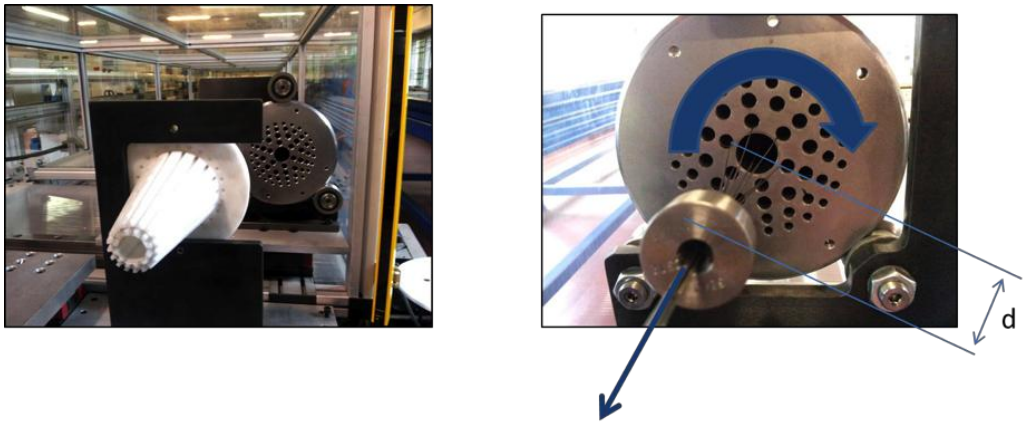

Figure 6.1.31. Cable Assembly Machine at Columbus

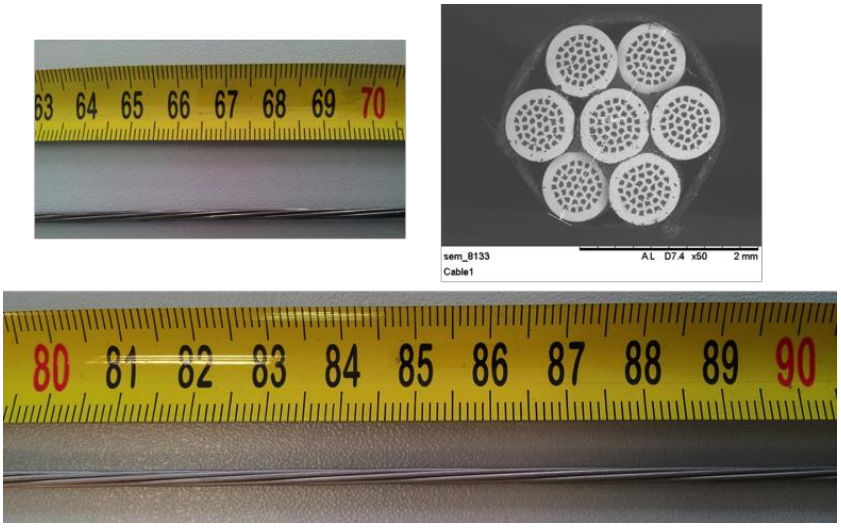

Figure 6.1.32. Two assembled cables using unreacted and reacted wire

Task 6.1 Plans for R&D Activities in the Next Quarter

In the next quarter, the two assembled cables will be characterized using the test facility at Columbus: temperature from 16K to 30K in field up to 1.8 T.

A sample holder 33 cm long will be used (Figure 6.1.33). The current injection terminals are 12 cm long. This distance is sufficient for current transfer to all strands of the twisted cable.

Figure 6.1.33. Sample holder in the test facility at Columbus

Wire configuration with more than 37 filaments will be also developed for AC losses issues. Configurations with 61 or 91 filaments were developed in the past as short samples, and in the next months, samples for cabling will be fabricated.

3.2.3.2.5 Report period: October 1, 2013 to December 31, 2013 (Q6)

Introduction

In the previous quarter, two mini cables for the DC rotor application have been assembled in the six-around-one configuration using the 0.78-mm, 37-filament round wire. Cabling parameters, like the twist pitch, were evaluated starting from the single-strand characteristics.

In this quarter, the mini-cables were characterized with critical current measurements. Results showed the most suitable procedure for the cabling and a reasonable reliability concerning bending properties that closely approximate those of the single strand.

During this quarter, activities for the development of a round wire suitable for the AC rotor coils led to a 61-filament round wire. Despite the fact that the I_c is lower than that of the 37-filament wire, the configuration seems feasible,even at a small diameter, and preliminary results show there is room for improvement.

- **Sub-task 6.7. Characterization of cable performance at 2.5 T at temperatures of 15 K and 20 K.**

Two cables have been characterized:

- **Cable 1**, one-around-six unreacted wire (Figure 6.1.34, upper)
- **Cable 2**, one-around-six reacted wire (Figure 6.1.34, lower)

Cables have been prepared in the Columbus test facility sample holder (Figure 6.1.35). The long current injection terminal(~ 13 cm) ensures the best current transfer into each strand.

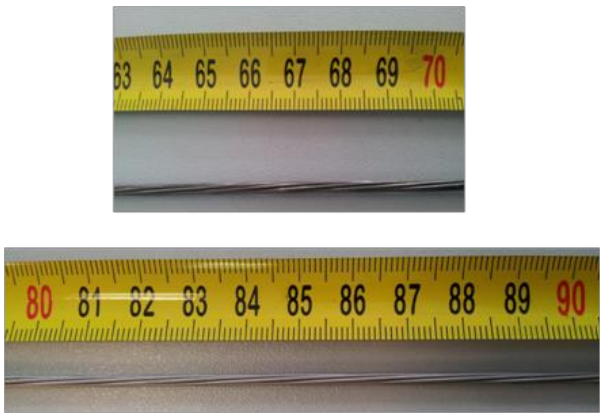

Figure 6.1.34. Images of cables with unreacted (upper) and reacted wire (lower)

Figure 6.1.35. Mini cable prepared in the sample holder for I_c measurements

Figure 6.1.36 shows I_c versus B at different temperatures for Cable 1. Figure 6.1.37 is a comparison between the critical current of the single strands and the I_c of the cable at 16 K and 20 K.

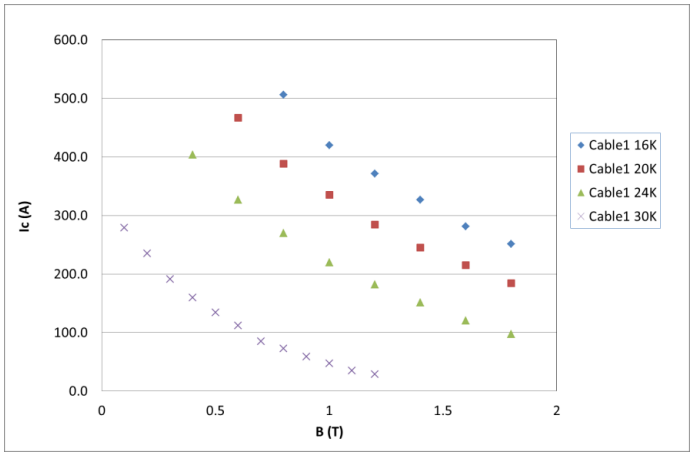

Figure 6.1.36. I_c versus B at different temperatures of Cable 1

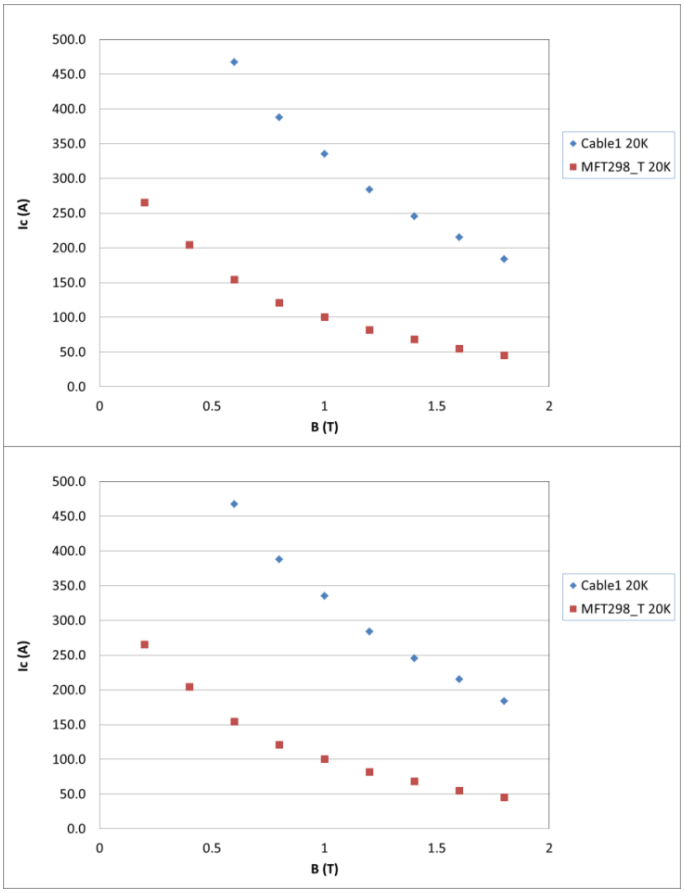

Figure 6.1.37. Comparison at 16 K and 20 K between the I_c values of Cable1 and the single strands

The values that we expected for the critical currents of a six-around-one mini-cable are around 6-7 times the Ic of the single strands, so it is clear that the expected values have not been reached, since the maximum Ic values are less than 4 times that of the single strands. This is clearly a degradation of the single-wire performances that probably occurred during the final heat treatment of the cable. In fact, since the wires are heat-treated together in the assembled configuration, they are not subjected to a uniform treatment, as is shown in Figure 6.1.36.

Results for Cable 2 are different. Figure 6.1.38 shows the Ic characteristics of Cable 2, while Figure 6.1.39 shows the plots for values of the single strands.

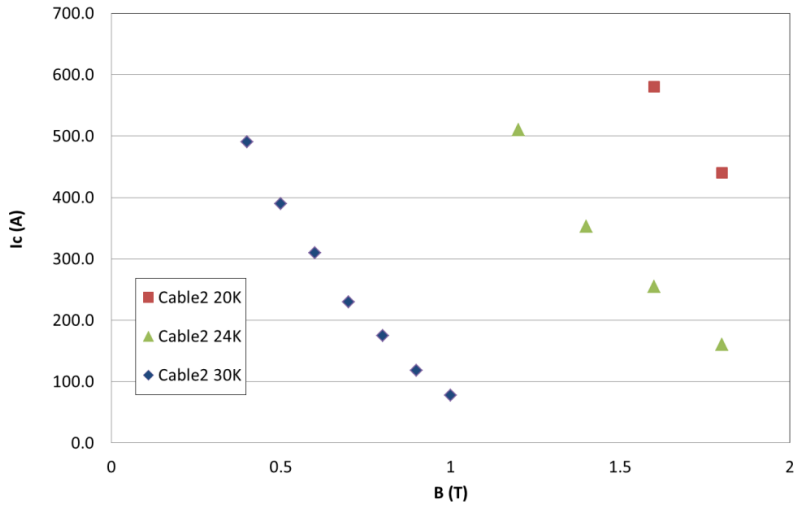

Figure 6.1.38. I_c versus B at different temperatures of Cable 2

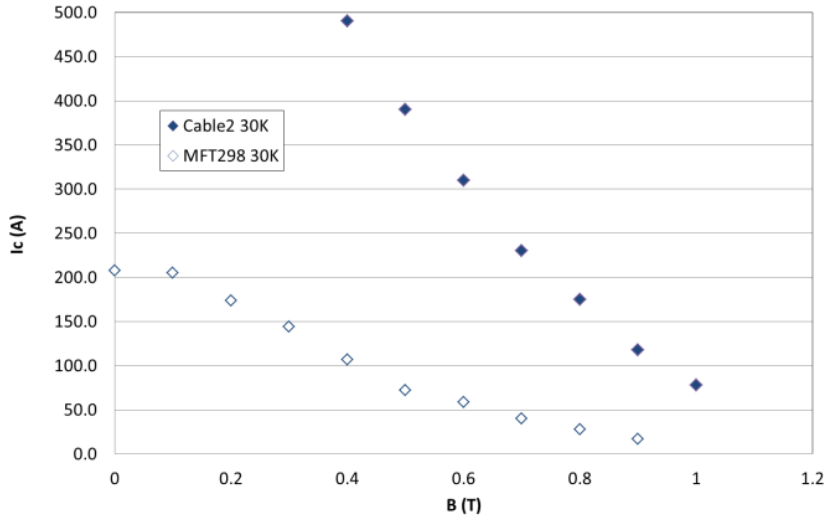

Figure 6.1.39. Comparison at 20 K, 24 K and 30 K between the I_c values of Cable 2 and the values of the single strands

The I_c value of the cable at 20 K, 1.8 T is about 4.4 times the I_c of each strand. At 24 K, the I_c is 5 times and at 30 K more than 6 times. Further analysis will try to explain this behavior, but it should be related to a not completely uniform current injection in each of the seven strands.
Results are promising and are also confirmed by a further test on a mini-cable bent on a diameter of 250 mm. Figure 6.1.39 compares the bent sample with the unbent sample showing no degradation, but a slightly better performance.

- Sub-task 6.2. Research and development on MgB_2 wire with the goal of minimizing the AC losses

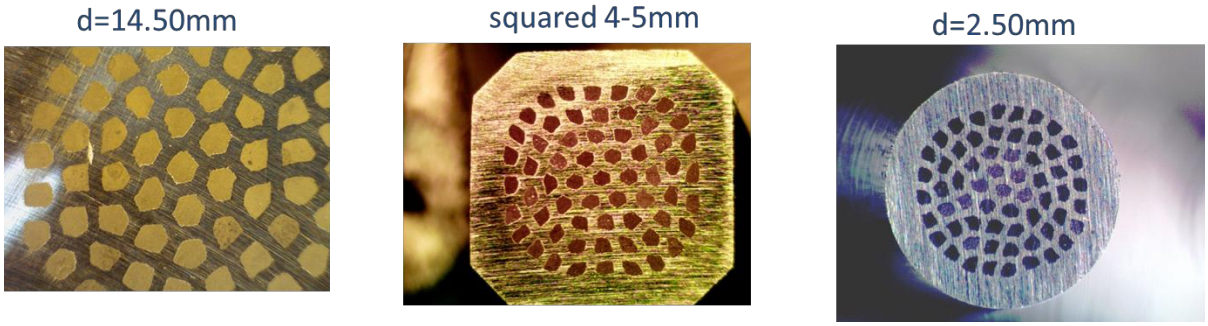

Figure 6.1.40. Cross-section of samples with 61 filaments at different dimensions during the deformation process

A new process has been developed to reach the diameter of 0.78 mm in a wire architecture with 61 filaments. Figure 6.1.40 shows samples at different dimension collected to show the behavior of the cross-section during the fabrication process.

The final diameter has been reached, working with the optimization of the last swaging steps and trying also to optimize the final heat treatment.

Figure 6.1.41 shows the cross-section of the wire with a detailed view of the filament size in the range between 30 μm and 40 μm. The MgB2 filling factor is approximately 15.5%.

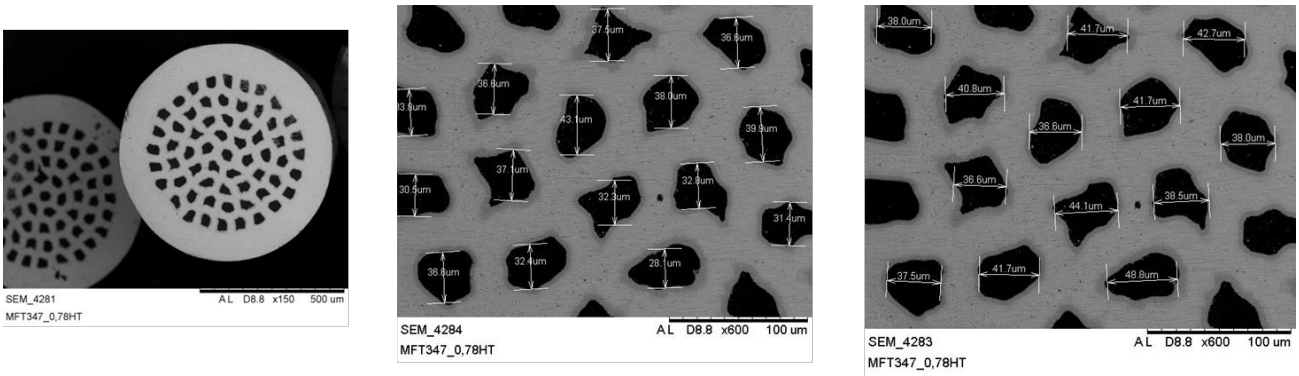

Figure 6.1.41. Final cross-section of samples with 61 filaments

Despite the I_c of this wire not being as high as that of the 37-filament configuration (Figure 6.1.42), there is room for improvement, which will be explored in the activities of the next quarter.

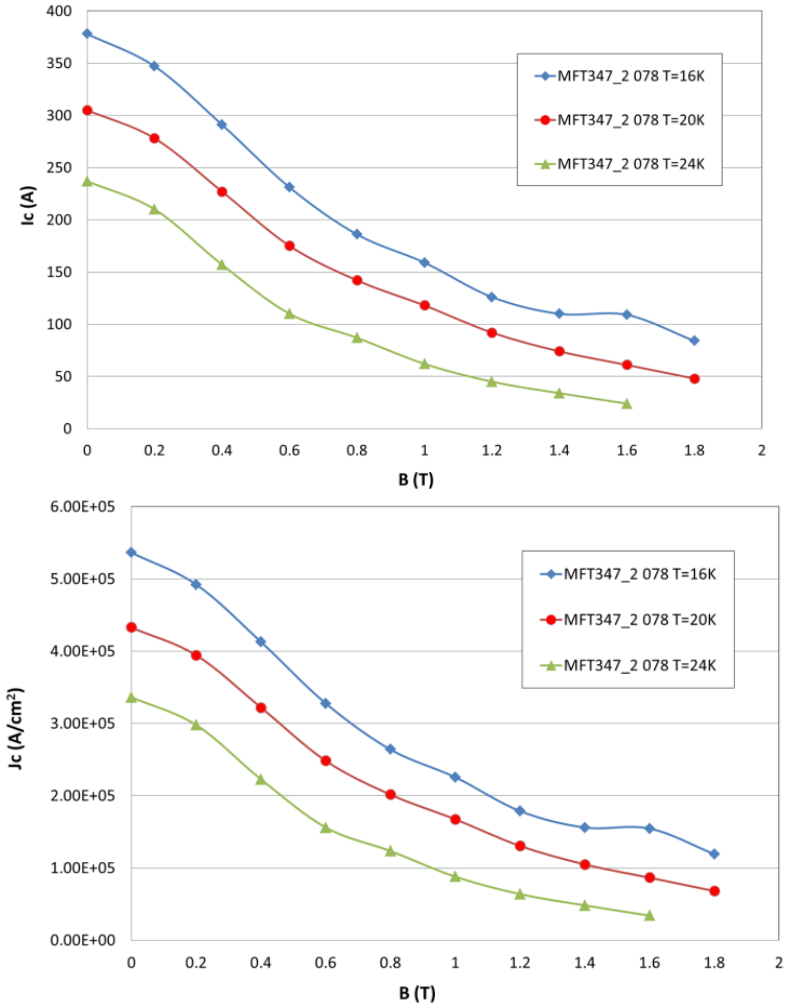

Figure 6.1.42. I_c and J_c characterization at different fields and temperatures of the first 61-filament round wire

Task 6.1 Plans for R&D Activities of Next Quarter

The performance of the 61-filament wire will be analyzed, working for improvement, and a mini-cable will be assembled and characterized.

The possibility of further reducing the filament size, and increasing the number of filaments will be explored in a new wire configuration.

This page removed due to Intellectual Property/Distribution Limitations

This page removed due to Intellectual Property/Distribution Limitations

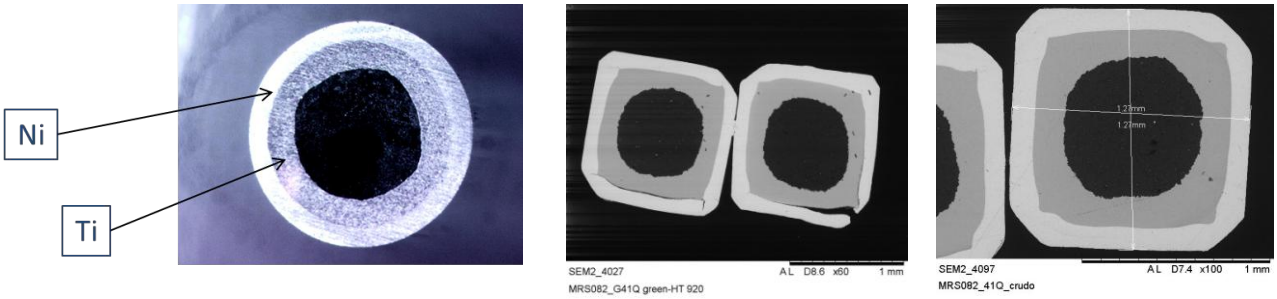

Figure 6.1.46. Structure of the MgB_2 monofilament with Ni and Ti barrier, with example of the main issue addressed during the R&D activity, the breakage of the outer Ni sheath.

Figure 6.1.47. Restacking of the 91 monocore wires into the Monel outer sheath

The monofilaments are reduced in diameter and brought to a circular cross-section for restacking into a Monel tube with a diameter of about 25 mm. The restacked configuration shown in Figure 6.1.47 is the starting point for wire manufacturing.

Several heat treatments are needed during the deformation steps and the shape changes in cross-section (round-square-round). Figure 6.1.48 shows an intermediate step with a squared wire of about 4 mm, and Figure 6.1.49 shows the wire in the final round configuration at 1.7 mm, 1.2 mm and 1.0 mm.

This page removed due to Intellectual Property/Distribution Limitations

The table and images of Figure 6.1.51 are a comparison of the main characteristics between the 37-, 61- and 91-filament wires developed to this point. The 91-filament wire still needs to be reduced in diameter, and an optimization of the temperature profile in the in-line furnace for sintering is required before an I_c characterization can be accomplished.

- **Sub-task 6.6. Cabling of the developed conductors into-six around-one configuration.**
- **Sub-task 6.7. Characterization of cable performance at 2.5 T at temperatures of 15 K and 20 K.**

A cable prototype (Cable 3) has been prepared at Columbus using the MFT347_2 wire strands with the same twist pitch and procedures as for Cable 1 and Cable 2 (see previous quarterly reports).

Final diameter (mm)	N° of filaments	Monel outer sheath	Type of filaments	FF (%)	Filaments mean dimension (μm)
0.78	37	Thick	Ni-MgB2	17.7	70
0.78	61	Thick	Ni-MgB2	15.5	40
0.85	91	Thin	Ni-Ti-MgB2	19.4	35
0.78	91	Thin	Ni-Ti-MgB2	?	?

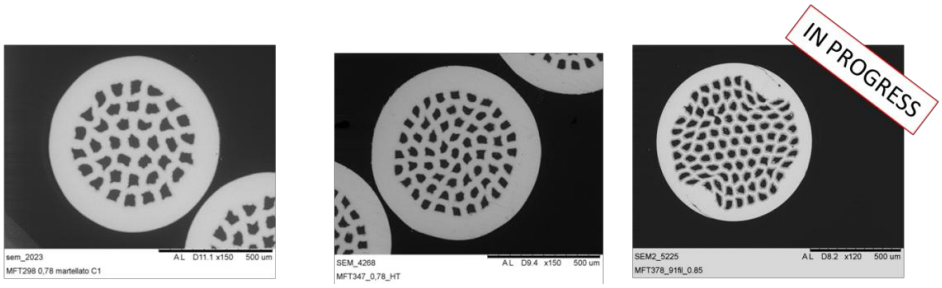

Figure 6.1.51. Images and main characteristics of the 37-, 61- and 91-filament round wires

The cable configuration has been changed in comparison to the previous ones using an OFHC copper wire at the center of the configuration with the aim of improving thermal stability of the conductor (Figure 6.1.52).

The critical current (I_c) of the cable has been measured, and the results presented in Figure 6.1.53 show that the current carrying capability of the cable is six times that of a single strand, proving that the six-around-one cable configuration shows no cabling degradation.

This page removed due to Intellectual Property/Distribution Limitations

This page removed due to Intellectual Property/Distribution Limitations

This page removed due to Intellectual Property/Distribution Limitations

This page removed due to Intellectual Property/Distribution Limitations

This page removed due to Intellectual Property/Distribution Limitations

This page removed due to Intellectual Property/Distribution Limitations

This page removed due to Intellectual Property/Distribution Limitations

This page removed due to Intellectual Property/Distribution Limitations

3.2.3.3 Task 6.2 –Structural Composite Analysis

3.2.3.3.1 Introduction/Summary

As the FSG concept developed in BP1, new, fundamental philosophies became keys to the success of the FSG design. Cryogenic operation temperatures between 15 and 20 degrees Kelvin combined with a manufacturing (zero stress) temperature at over 300 degrees K creates a very large temperature range for the electromagnetic active section. Many different materials are used in the component assemblies. Differential thermal expansion/contraction for materials having different expansion properties can easily develop damaging high stresses if not properly addressed. The first key philosophy developed for the FSG was: All active section materials need to be thermal expansion matched.

The FSG is cooled using a cryocooler. Even though the FSG design is very efficient with unprecedented low loss performance, the AC losses and heat leak through the structure push the cryocooler capability to the edge. To keep these losses to a minimum, non-magnetic metal is used for the rotor torque tube and cooling tubes. The stator active section sees AC fields, so even the non-magnetic metal for the torque tube would cause too much loss. It needs to be composite. The cooling tubes remain non-magnetic metal. The local cooling of the windings is by conduction to the cooling tubes which have helium gas forced convection inside the tubes. The winding support composite needs to have high thermal conductivity for improved cooling, but be not be electrically conductive.

A superconductor can carry much more current in a much smaller conductor than copper-based designs. The local forces developed are therefore much higher than copper based machines. The required support of the superconductors create the need for a dielectric, non-magnetic, non-conductive, high thermal conductive material strong enough to support the superconductor at cryogenic temperatures, without allowing potential quench causing micro-movements.

A concept of Compliant Composite (CC) material to thermally match the metal structures with the lowest possible Young's modulus composite material was developed. The metals could then expand or contract with minimal structural stress occurring from differential thermal expansion/contraction.

Search of available materials showed no existing composite materials match the FSG needs. Extensive FEA is needed to assess the behavior and capability of the structures involved. Structural behavior over the approximate 280 degrees Kelvin temperature range from room temperature to operating temperature changes dramatically for many material properties. This generated need for composite development and specific material testing to supply needed FEA material property inputs.

The rotor torque tube is made from 300 series stainless steel. The rotor torque tube material was chosen due to its ability to maintain ductility and strength at FSG cryogenic operating temperatures. Since the rotor also has the winding (mainly copper nickel) and cooling tubes (also 300 SS) bonded to composite, the thermal expansion properties of 300 SS becomes the basis for all composite thermal matching in the FSG configuration. The rotor "build" has four distinct radial situations:

1. Rotor torque tube – The 300 SS torque tube is the backbone of the rotor and the primary structure. It transfers temperature and torque from the bonded CC material at operating temperature to the room temperature center shaft. Re-entrant ends are used to minimize heat leak.
2. Cooling layer – Helical wound cooling circuits, imbedded in CC material are made up of hollow, 300 SS cooling tubes arranged for AC loss cancelling by using an out and return bifilar winding arrangement.
3. Winding layer – Insulated windings are imbedded in CC material.

4. Retention layer – A layer of filament wound composite with alternating weave build that thermal matches the behavior of 300 SS. This higher strength material captures the weaker CC material and provides extra restraint against the electromagnetic loading of the windings.

The stator "build" is very similar to the rotor, except the torque tube must also be composite and the cooling tubes moved radially outside the windings. Thermal intercepts are used on each end of the stator torque tube to improve the cooling efficiency against heat leak. The ends are supported with re-entrant supports to further minimize heat leak.

Costs of making even small-scale test assemblies would be prohibitive, leading to the plan of coupon testing for developed composite properties and design limits. This method would allow virtual de-risking of any structural configuration requiring only the cost of the modeling and FEA.

The goals of Task 6.2 were to develop the necessary composites, obtain mechanical properties and establish design limits to facilitate FEA risk assessment of various FSG design configurations.

Accomplishments

Task 6.2 was very successful. Initial thinking was that five different composites may be necessary; in the end, only two were needed. The retention layers for rotor and stator was shown successful made of the same material as the stator torque tube material.

TT Material

The tested TT material thermal behavior is very close to matching 304 SS in the transverse direction, with the axial total expansion falling short of 304 SS (Figure 6.2.1).

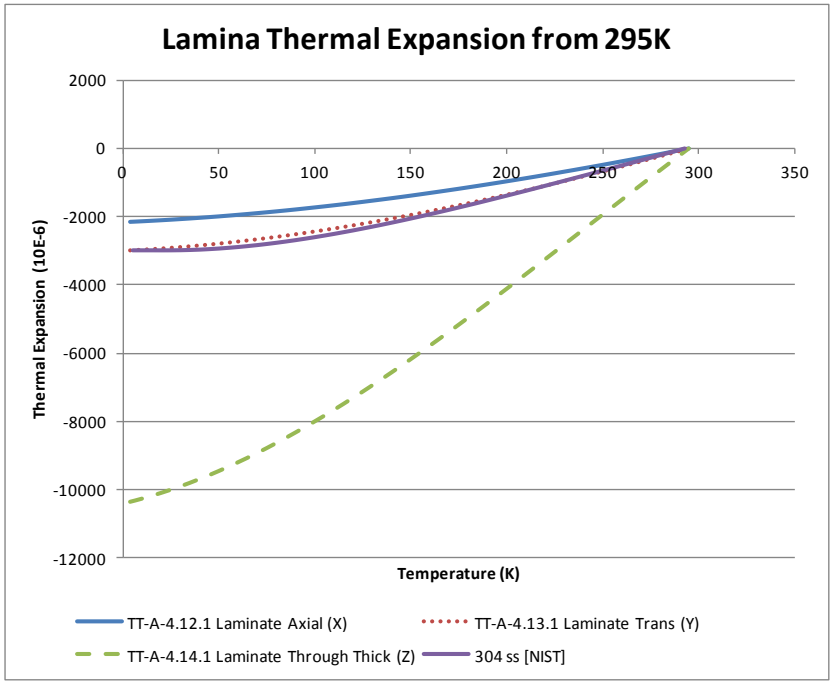

Figure 6.2.1. TT Material Test Data

TT Material Test Data

ANSYS Finite Element Analysis (FEA), using the lowest expansion measured during test, showed elevated thermal stresses in the CC material due to the differential expansion between the TT and CC material. A tweak of the TT material to reduce the fiber fraction was examined for effect (Figure 6.2.2). The resulting TT material significantly improved the stresses in the active section assembly. The plan moving forward will be to use the reduced fiber fraction in an increased thickness torque tube. The results will be a stronger assembly with better thermal match to 304 SS.

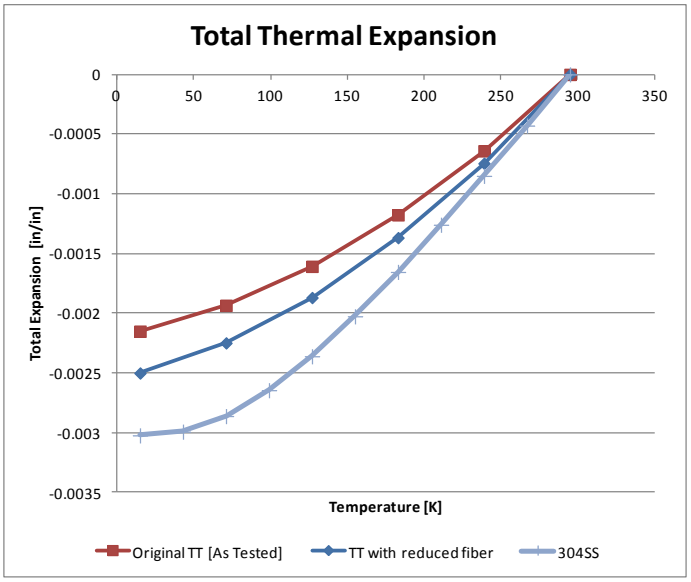

Figure 6.2.2. Tweaked TT Material with reduced fiber

The ultimate strength of the TT material is quite high, providing great comfort that the torque tube should not fail catastrophicallyTo be conservative; however, the design static stresses are kept below the first ply failure level, when possible, to avoid potential resin cracking (Figure 6.2.3).

TT Material Laminate Data by Test			
Temperature [K]	*4.2*	*90*	*295*
Tensile Strength (ultimate, laminate axial dir, ave, psi)	27,000	25,500	26,630
Tensile Strength (ultimate, laminate Transverse dir, ave, psi)	58,130	42,000	28,880
Tensile Modulus (laminate axial dir, ave, psi)	3,664,000	3,190,000	2,883,000
Tensile Modulus (laminate Transverse dir, ave, psi)	3,664,000	3,190,000	2,883,000
Poisson's Ratio (ave)	0.3177	0.3336	0.3766

TT Material Laminate Data by Test			
Temperature [K]	*4.2*	*90*	*295*
Tensile Strength (First Ply, laminate axial dir, ave, psi)	7,690	9,570	4,930
Tensile Strength (First Ply, laminate Transverse dir, ave, psi)	11,470	14,350	7,510
Compressive Strength (First Ply, laminate axial dir, ave, psi)	-33,280	-30,580	-16,730
Compressive Strength (First Ply, laminate Transverse dir, ave, psi)	-24,010	-28,610	-13,080
Shear Strength (First Ply, laminate in plane shear dir, ave, psi)	7,690	9,570	4,930
Tensile Modulus (laminate axial dir, ave, psi)	3,664,000	3,190,000	2,883,000
Tensile Modulus (laminate Transverse dir, ave, psi)	3,664,000	3,190,000	2,883,000
Poisson's Ratio (ave)	0.3177	0.3336	0.3766

Figure 6.2.3. TT Material Test Data

CC Material

The CC material thermal properties closely match both the rotor and stator torque tube thermal behavior (Figure 6.2.4).

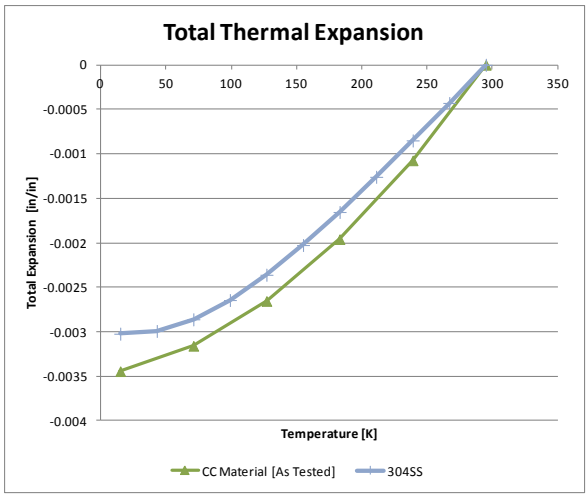

Figure 6.2.4. CC Material Match to 304 SS

The CC material successfully reduces the thermal stresses at operating temperature, leaving adequate stress margin for the electromagnetic loading (Figure 6.2.5).

CC Material Data by Test			
Temperature [K]	***4.2***	***90***	***295***
Compression Strength (ave, psi)	**83,300**	**85,319**	**18,519**
Maximum shear stress (ave, psi)	**10,600**	**7,717**	**5,764**
Tensile Strength (ave, psi)	**19,670**	**19,500**	**7,654**
Tensile strain at Maximum Load (%)	**0.45**	**0.50**	**0.78**
Tensile Modulus (ave, psi)	**4,350,000**	**3,900,000**	**2,201,600**
Poisson's Ratio (ave)	**0.31**	**0.33**	**0.29**

Figure 6.2.5. CC Material Data from Test

Summary

The data collected for the two developed composites used in the FSG design has been used for FEA for Task 4.0 to assess the design success. Reaching the desired thermal expansion matching has been largely successful and the thermal stresses reduced. The materials in both composites are electrically non-conductive.

The Young's modulus of the CC material is much lower than the conductor, cooling tubes and rotor torque tube. The calculated CC material thermal conductivity by rule of mixtures is high. The CC material is dielectric and strong enough to provide support for the superconducting windings. The concept of Compliant Composite has been achieved.

Task 6.2b Goals and Accomplishments

Goals

When the FSG Compliant Composite CC material definition neared completion, the team discussed Task 6.4 and the complexity of thermal cycle testing at 15 K. The team determined a basic, simple test should be implemented first. A low-cost, thermal cycling test regimen using an LN2 dipping procedure was determined to provide substantial validation of the CC material, without extreme complexity. This testing became a subtask of Task 6.2, called Task 6.2b.

The goals of Task 6.2b are:

1. Determine if CC material will encounter micro cracking from cryogenic shock during the dipping process.
2. Determine if the heat transfer within a sample assembly degrades from thermal cycling for an insulated conductor imbedded in the CC material.

Approach

An assembly with the insulated conductor and thermocouples was designed to allow measurement of the temperature distribution within the CC material. A method of performing a heat run on the assembly was devised. Power would be applied to the conductor causing the conductor to heat. A dedicated circuit with a non-temperature sensitive reference resistor was developed to facilitate determination of the wire temperature rise by resistance (Figure 6.2.6).

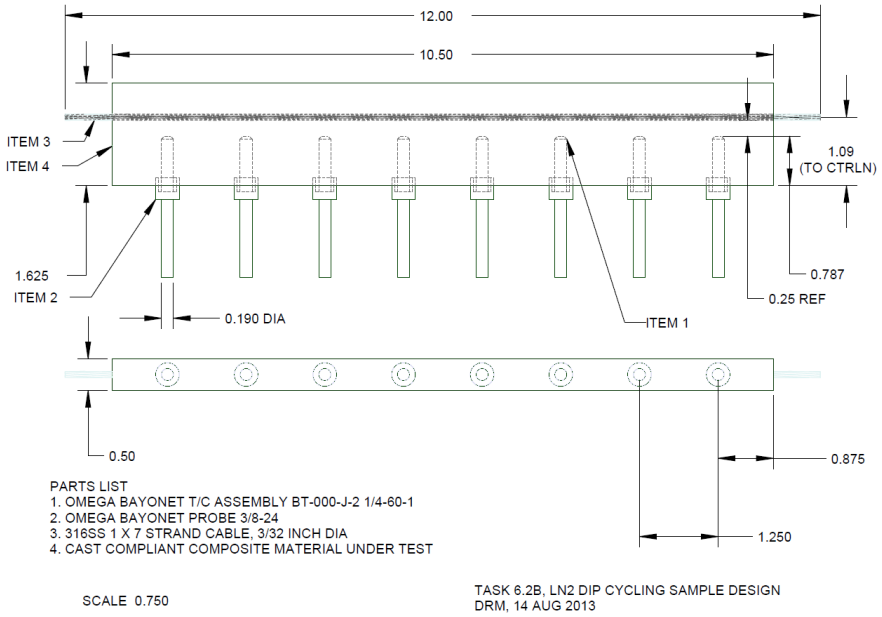

Figure 6.2.6. Geometryfor CC Sample Thermal Test

A conductor emulating the planned Kapton-insulated 6-around-1 cable, as in the FSG, was used.

During the team meeting, the conductor sheath material was planned to be migrated to 316 SS as a better choice for thermal expansion matching to the other materials, so a 316 SS mechanical cable was selected for the testing. The cable was hand-insulated with Kapton.

The difficulties in measuring accurate, precise temperatures proved challenging for this subtask. The test setup and correction factor development for ambient temperature and input power level proved successful (Figure 6.2.7).

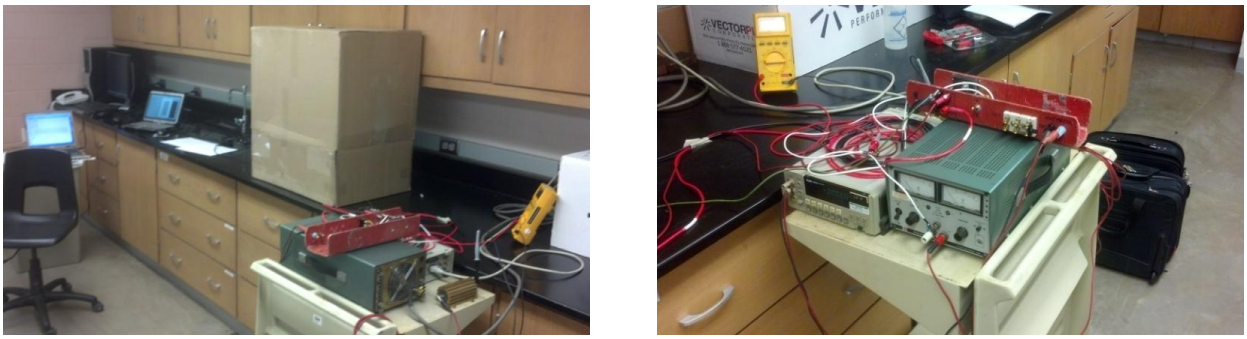

Figure 6.2.7. Task 6.2b Test Setup

Accomplishments

Using corrections for ambient temperature and input power level, the average thermocouple data repeated within 1.1% of the baseline data (Figure 6.2.8).

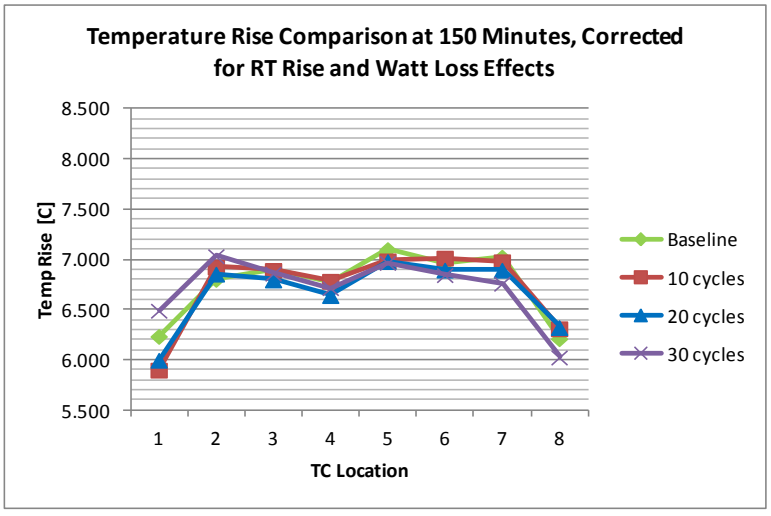

Figure 6.2.8. Thermocouple data showing variances from baseline

The conductor rise varied more with a maximum variation from the baseline of -10.5% [improved cooling] (Figure 6.2.9).

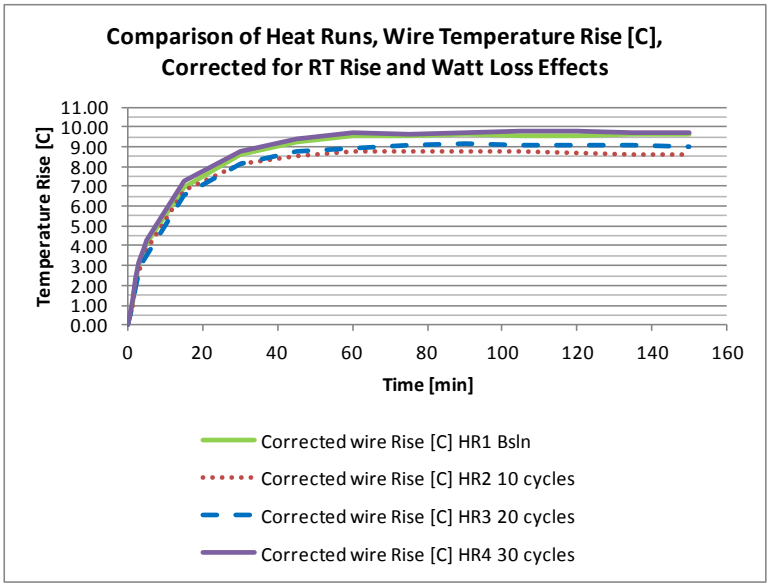

Figure 6.2.9. Conductor Temperature Rise Data

The microscopy comparisons (Figure 6.2.10) showed no micro cracking or any visual signs of composite damage after 60 thermal cycles (Figure 6.2.11).

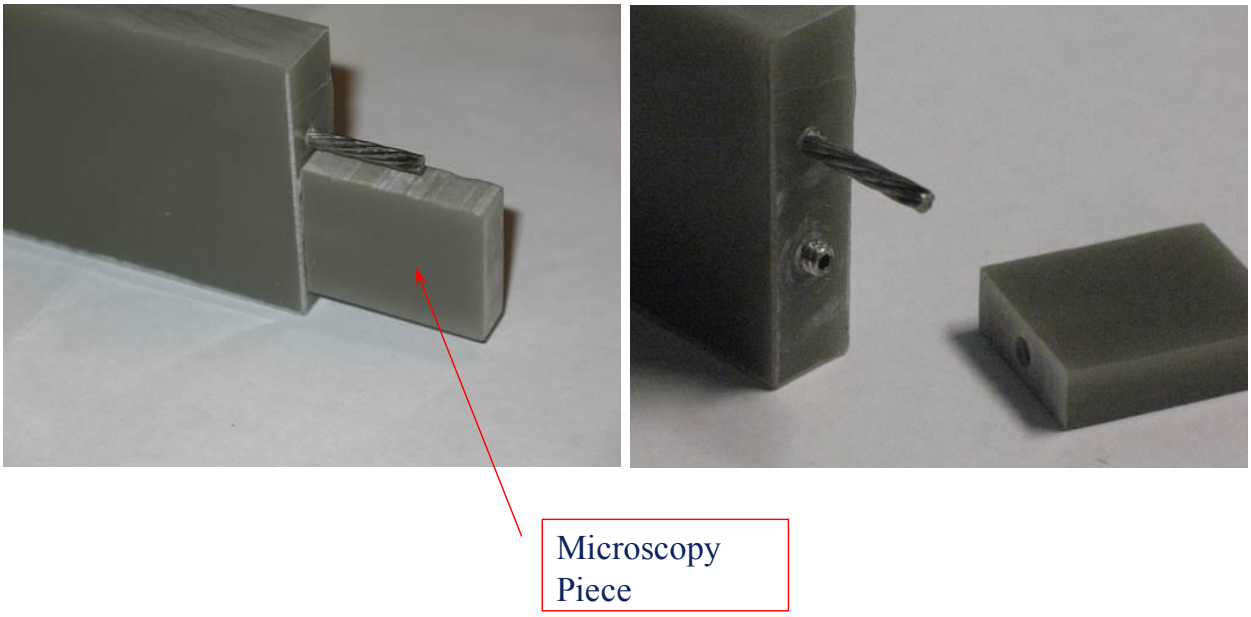

Figure 6.2.10. Microscopy Comparison

This page removed due to Intellectual Property/Distribution Limitations

- Methods for analyzing the structure using FEA software with orthotropic properties as input to composite analysis software were established.
- Testing procedures for the composite material were documented.
- Composites expertise to assist the project were found and added.
- Initial acceptance limits were established as simply no resin cracking allowed. Detailed acceptance criteria, including load relaxation effect needs to be determined.
- Initial composite materials were designed and analyzed for effect on thermal stresses. Several stator thermal stress sensitivity analyses were performed to determine effects from many design areas. These areas include Retention Layer (RL) thickness, RL preload (application of the RL with reinforcement pretension), Compliant Composite (CC) material changes, cooling tube material changes and the use of Corrugated Stainless Steel Tubing (CSST).
- Initial rotor thermal stress analyses were also performed.

Task 6.2 Specific Objectives

- **Composite Material Development and Test.**

  The specialized composites for cryogenic service in a Fully Superconducting Generator (FSG) need to be fully designed and validated as part of Task 6.2.

- **Get composites expertise in place.**

  Find a composites design expert to assist in the design of the desired composites, someone to build samples of the designed composites and someone to test the priority properties of the composites.

- **Develop small, detailed FEA models for fast answers.**

  Composite Designs for the stator and rotor need to be determined. Using detailed, model FEA results with various materials and geometries will lead to the composite requirements.

- **Develop method for structural FEA results to be used for useful composite stress results.**

  Kato is using ANSYS FEA software with orthotropic properties for composite materials. COMTEC uses CompositePro composites analysis software. A method to understand the structural results using meaningful composite stresses and failure modes is needed.

- **Develop potential composite material designs for the FSG application.**
  - Iterate using the composite material design properties and FEA results to optimize the composite materials for the FSG application.
  - Use composite design philosophies and methods to develop more realistic composite material properties.
  - Where needed, use early laboratory validation of undocumented constituents.
- **Develop stress limits and failure philosophies.**
  - The composites fail in several different modes. In normal, non-cryogenic applications, failures escalate from resin cracking (a degradation of the composite overall capability

performance) to the ultimate (complete) failure of the composite structure. In most cases, a design with some resin cracking is considered acceptable.
    - For the FSG application, where practically the only heat transfer is by conduction within the composite, resin cracking represents a degradation of the cooling capability that is crucial to the FSG success.
    - A review of the FSG design for meaningful acceptance criteria is still needed.

- **Determine testing requirements.**

  The primary material properties for the developed composites need to be validated by test. The actual test methods, number of samples, etc. needs to be defined to determine how and by whom the composites will be validated.

Task 6.2 Significant Results

- **Composites expertise**
    - We were fortunate to find Composite Material Technology Center (COMTEC), an Industry-University Partnership at Winona State University in Winona, Minnesota. Dr. Keith Dennehy has extensive composite design experience and COMTEC has the capability to make the necessary composite samples for Task 6.2. As we generated the testing requirements in more detail we determined shortfalls in low temperature testing. With an addition of a new environmental chamber, we were able to extend their test capability down to 89 K. They cannot do thermal conductivity or specific heat measurements.
    - Composite Technology Development, Inc. was found to perform tests at 4 K. They, however, cannot test thermal conductivity or specific heat measurements.
    - Southern Research Institute was found to perform the thermal conductivity and specific heat measurements.
- **Small, detailed FEA models for fast answers.**
    - Thus far, only thermal stress has been analyzed. With the cabled conductors under development, force loads based on single strand wires for the winding will be misleading. Detailed models of the stator and rotor have been developed.
- **Method for structural FEA results to be used for useful composite stress results.**
    - A method for plugging in FEA (ANSYS) results into the composite software (CompositePro) to obtain failure modes and safety factors was determined.
    - Local stresses defined by ANSYS, are plugged into CompositePro. Failure modes and safety factors are outputs.
- **Potential composite material designs for the FSG application.**
    - Three new compliant composites, not including G10CR and speculative estimates, were studied for effects. Two new stator torque tube composites were studied. Three new RL composites were studied.
- **Testing requirements**
    - Composite test requirements were defined. The first thermal stress analysis based on detailed FEA models was that the cooling tubes were encountering very high

compressive stress from heavy hoop loading. Analyses verified the symmetry boundary conditions for a complete hoop adequately simulate the helically placed tube.
    - Hoop stresses (thermal stress only) for the cooling tube arrangements with 304 SS are very high.
    - Available material properties need verification.
    - Thicker straight wall tubing improves tubing stress, but increases compliant composite (CC) stress
    - Corrugated Stainless Steel Tubing (CSST) improves the tubing stresses, but increases CC stress, introduces higher pressure losses and is prohibitively larger, reducing cooling circuits
    - Cooling tube stresses and CC stresses are greatly reduced with silicon bronze (Yet to be examined for electrical, magnetic suitability)

- Studies show the CC material needs to be at the lowest possible Young's modulus and with the closest possible CTE match to the conductors, cooling tubes and torque tube.
- Stator composites using COMTEC TT and COMTEC CC-1 were found possibly acceptable, but CC-1 is using a resin CTE that is possibly not available. CC-2 is a material that would be available, but shows higher CC stresses. CC-3 will be a new CC material with properties more similar to CC-1, but using readily available material and have more fibers in the radial direction for improved radial CTE and strength.
- Initial Stator torque tube (TT) stresses with COMTEC TT are looking acceptable, depending on the acceptance limits to be established.

Task 6.2 Other Significant Results

- Changes to the stator torque tube material properties mainly affect the cooling tube stresses.
- The retention layer (RL) can likely be the same as the TT.
- Pretension of the RL can help reduce CC stresses, but increases the tubing stress.
- Designs for the stator torque tube, retention layers are close to ready.
- Several compliant composite configurations were determined and analyzed.
- High CC stresses are local to the conductors and cooling tubes.
- Rotor thermal stresses are much worse than for the stator.
- A PO has been issued by Kato for Creare consulting for the BP2 work.
- A Creare quote for the de-risking cryocooler has received

Task 6.2 Key Outcomes, Milestones and other Achievements

Several key outcomes for Task 6.2 were accomplished:

- Composite expertise was located capable of assisting the composite development process.
- Composite test definitions were documented.
- Composites testing suppliers capable of full temperature range material properties are located.
- Stator thermal stresses were reduced to estimated acceptable levels (with single strand windings)
- Detailed examination of the cooling arrangement (not completed in BP1 conceptual design) showed surprisingly high compressive stresses in the cooling tubes.

- Produced a recommendation to examine silicon bronze material for the cooling tubes. (half the modulus with similar electrical behavior)
- We determined load relaxation behavior may change the allowable stress limits.

Task 6.2 Plans for Next Quarter

We will continue to refine the designs to reduce the thermal stresses.
Plans include:

- Re-examine the stator with the latest compliant composite CC-3 (trying the match CTE with 304 SS in three directions)
- Examine rotor and stator thermal stresses using the smaller bend radius conductors
- Examine rotor and stator electromagnetic force effects with the thermal stresses
- Establish composite limits with load relaxation in mind.
- Get approval to begin manufacture and testing of composites to validate estimated properties.
- Test polyester fiber properties for possible improvements
- Obtain the winding configuration for the cable conductor configuration and examine thermal stresses.
- Examine rotor and stator windings for Lorentz and magnetic loading.
- Receive environmental chamber to extend COMTEC testing capability to 89 K.

3.2.3.3.3 Report period: January 1, 2013 to March 31, 2013 (Q3)

Task 6.2 Major Activities

As part of Task 6.2, the composites needed for a successful Fully Superconducting Generator (FSG) design need to be examined in detail and designed for successful local stress behavior. The FSG concept revolves around a successful compliant composite support of the winding and cooling arrangements. The 280 Kelvin temperature swing from room temperature cure (295 K, 21.7 C, 71 F) to operating temperature (15 K, -258.2 C, -432.7 F) with several different materials bonded together led to a focus on differential thermal expansion as the highest potential risk and the primary area of focus for the design.

Detailed thermal stresses primarily in the rotor were examined in this quarter. Detailed models for the conductors and cooling tubes, based on BP1 data for the single conductor (non-cabled) winding configuration are used. The conductor configurations and winding configurations for the known single strand configuration were used here for composite design analyses.

COMTEC (Dr. Dennehy) determined projected material properties and first ply failure limits for the conventional 2D composites used and provided some guidance for non-conventional 3D composites. COMTEC also supported the technical requirements for the environmental chamber needed to extend their testing to below 89 K. COMTEC has begun to build and preliminary test samples in support of our project.

Eleven major stress studies were performed this quarter. Analyses of the rotor structure using ANSYS FEA software with orthotropic properties as input to composite analysis software were used.

The list of studies follows:

- **Micro model use** – showed similar thermal stress magnitudes, but not global effects. They did show that low modulus metals, like silicon bronze for the cooling tube may help.
- **Rotor winding study** using a 2-degree slice model for thermal stresses showed high Compliant Composite (CC) stress, high Torque Tube (TT) stress and increased Retention Layer (RL) and conductor stresses, compared to stator.

- **Hoop intercepts** using a half-pole model – the hoop behavior of the compliant composite was thought to cause constriction related thermal stress. This study showed the effect of placing deep radial grooves filled with something like impregnated Dacron felt, with lower Young's modulus. It was meant to break up the tangential hoop behavior of the laminated CC. It proved ineffective at thermal stress reduction.
- **Rotor Half-pole study** – this study examines the thermal stresses without the hoop interrupts. It showed unacceptable CC levels, stress concentrations at the transition from windings to pole body.
- **Rotor half-pole model with winding location effect** – the previous study was performed with the windings offset for a hoop intercept. This study sought to determine if the high thermal stresses are affected by winding location. The winding relocation to "as designed" had little effect on stress magnitudes.
- **Cabling effects** – a micro model using a length of different pitch, fully bonded cabling with a representative single conductor amount of composite was used to determine if stresses improve with cabling. They did not.
- **Slip plane effects** – a micro model with full bonded ends only was used to determine if stresses improve with a slip plane. They did not.
- **CTE correction study** – Frustration with the higher rotor stresses led to a revisit of the fundamentals. Separate cylinder models for each material, compared to published thermal linear expansion behavior led to a CTE input correction for the metal materials, which reduced the calculated thermal stresses. Still above failure levels in some conditions, but better.
- **CTE optimization study** for the rotor using a 2-degree model – Several CC materials with varied Young's modulus and CTE were run to show thermal stresses for the different CTEs. A "sweet spot" was clearly shown, where all stresses were reduced to below the estimated failure levels. This showed Compliant Composite Support is possible. It also showed how to optimize the CTE matching.
- **Revised CTE optimization with CC-4 and full-pole model** – a conventional 2D laminated composite for CC was designed matching the optimum CTE in the tangential /axial directions and examined for thermal stress. This orthotropic material with a through thickness CTE high due to resin domination in that direction, show high thermal stress locally at the conductors and cooling tubes. It showed conventional laminated composite cannot be successful as a compliant composite.
- **Preliminary conductor loading study with rotor full pole**– this study puts forces on the conductors for a pole per inputs from AML. The raw data was reduced to the appropriate load magnitude and angles for several rotor offset angles to the stator. The values for the peak torque offset angle were then scaled to rated conditions. A two-stage FEA calculation with thermal and thermal plus conductor loading was made for three different CC materials. The thermal load cases were subtracted from the thermal plus loading load cases to segregate just the conductor loading induced stresses. The magnitude of the resulting stresses were found significant, but with proper CC material development, manageable**.**

Task 6.2 Specific Objectives

- **Composite Material Development and Test**
  - The specialized composites for cryogenic service in a Fully Superconducting Generator (FSG) need to be fully designed and validated as part of Task 6.2.
- **Develop small, detailed FEA models for fast answers**
  - Composite Designs for the stator and rotor need to be determined. The extreme component count and size variations within the complex geometries won't allow full geometry models. Appropriate detail models to investigate the details of the design are needed. FEA results with various materials and geometries lead to the composite requirements.
- **Develop potential composite material designs for the FSG application**
  - Iterate using the composite material design properties and FEA results to optimize the composite materials for the FSG application.
  - Use composite design philosophies and methods to develop more realistic composite material properties.
  - Where needed, use early laboratory validation of undocumented constituents.
- **Develop stress limits and failure philosophies**
  - The composites fail in several different modes. In normal, non-cryogenic applications, failures escalate from resin cracking (a degradation of the composite overall capability performance) to the ultimate (complete) failure of the composite structure. In most cases, a design with some resin cracking is considered acceptable.
  - For the FSG application, where practically the only heat transfer is by conduction within the composite, resin cracking represents a degradation of the cooling capability which is crucial to the FSG success.
  - Failure limits based on first ply failure theories has been utilized. (Note: these limits apply to conventional 2D composite designs only.)
- **Determine testing requirements**
  - The primary material properties for the developed composites need to be validated by test. The actual test methods, number of samples, etc. needs to be defined to determine how and by whom the composites will be validated.
- **Validate winding and cooling arrangement support philosophy based on compliant composite.**

  Perform necessary studies to show that compliant composite can be successful. Show what is needed for success.
- **Determine the magnitude of the conductor magnetic loading induced stresses**
  - In operation, the components will see both thermal and magnetic loading. The failure limits will have to accommodate both. For successful design we need to know the stress magnitude from the magnetic loading to verify satisfactory safety factor exists for the design.

Task 6.2 Significant Results

- **Small, detailed FEA models for fast answers**
    - Thermal and loading induced stresses have been analyzed for the BP1 windings. Detailed models of the stator and rotor have been developed.

- **Develop potential composite material designs for the FSG application**
    - Many new compliant composites (theoretical only) were studied for stress optimization. The studies showed compliant composite theory could be successful with an isotropic material behavior. Target compliant composite properties were determined to achieve minimal thermal stress. A new conventional composite material was designed based on the optimization study. It showed **conventional 2D laminated composite cannot deliver the CTE match need for successful compliant composite application**.
- **Testing requirements**
    - Composite test requirements were defined.
    - Studies show the CC material needs to be at the lowest possible Young's modulus and with the closest possible CTE match to the conductors, cooling tubes and torque tube.
    - CTE measurements at cryogenic temperatures are now validated at COMTEC.
- **Validate winding and cooling arrangement support philosophy based on compliant composite.**
    - An optimization study using various isotropic CTE and Young's modulus materials was used to determine a "sweet spot", where thermal stresses at operating conditions were minimized for all Young's moduli examined. The thermal stresses reduced to well below estimated failure levels for all components. The materials examined, however, were using isotropic behavior, which doesn't represent the conventional 2D laminated construction. A conventional laminate designed based on the optimization study findings **verified isotropic behavior is needed for the necessary CTE matching to allow compliant composite philosophy to be successful.**
- **Determine the magnitude of the conductor magnetic loading induced stresses**
    - A preliminary study was completed to estimate the stresses induced from the loading for the conductors. AML provided values of load magnitude and vector angle for the straight part of the active section. The data was not for rated conditions and needed to be scaled to rated conditions. The study will be repeated with values calculated for rated conditions. The preliminary stresses show the forces cause significant, but with proper material development, manageable levels.

Task 6.2 Other Significant Results

- Several compliant composite configurations were determined and analyzed.
- Highest CC stresses are local to the conductors and cooling tubes.

Task 6.2 Key Outcomes, Milestones and other Achievements

- Several key outcomes for Task 6.2 were accomplished:
- Compliant composite support philosophy has been shown to be possible by analyses.
- We've shown an isotropic 3D reinforced composite is needed to be successful.
- The analyses show conventional 2D composite methods cannot achieve success.
- Internet searching shows 3D cloths exist that potentially could provide near isotropic behavior.
- COMTEC has made a mold to allow casting samples for faster initial mechanical testing of composites.
- Sample constituent material procurement has begun.
- Initial testing for composite materials has begun.
- Detailed acceptance criteria, based on first ply failure theories are established for two of the compliant composite materials examined.
- A preliminary study of magnetic loading for the conductors was completed to determine the rough magnitude of the stresses.

Task 6.2 Plans for Next Quarter

We will continue to refine the designs and materials to reduce the thermal stresses.
Plans include:

- Obtain the winding configuration for the cable conductor configuration and examine thermal stresses.
- Find 3D reinforcement materials for CTE matching in three directions
    - Determine availability of 3D materials
    - Procure samples for testing
    - Determine design methods
    - Determine manufacturing process impacts
- Perform CTE matrix study for the stator to determine target stator CTE CC material behavior needed
- Re-run some FEA studies with the metal material CTE correction (cabling, stator, etc.)
- Receive BEMKO environmental chamber that extends COMTEC mechanical properties testing down to a temperature of 89 K.
- Receive testing supplies, such as resin and reinforcements for sample creation.
- Make samples and test appropriate materials.
- Pretest materials to determine optimum choices for 4-K testing (to minimize $$, only successful prescreened materials will be tested at 4 K)
- Establish CTE/temperature behaviors for select materials to "tune" CTE for metals used in the rotor and stator assembly
- Curve overlay onto 304 SS to estimate net CTE
- Curve overlay onto Titanium to estimate net CTE
- Examine rotor and stator electromagnetic force effects with the thermal stresses
- Establish composite limits with load relaxation in mind.

3.2.3.3.4 Report period: April 1, 2013 to June 30, 2013 (Q4)

As part of Task 6.2, the composites needed for a successful Fully Superconducting Generator (FSG) design need to be examined in detail and designed for successful local stress behavior. The 280 Kelvin temperature swing from a room temperature cure (295 K, 21.7 C, 71 F) to operating temperature (15 K, -258.2 C, -432.7 F) with several different materials bonded together led to a focus on differential thermal expansion as the highest potential risk and the primary area of focus for the design. The FSG concept revolves around a successful Compliant Composite (CC) support of the winding and cooling arrangements. The concept premise is lower stiffness composite with matching thermal expansion to its surroundings for minimized thermal stress.

Task 6.2 Plans from Last Quarter

- Find 3D reinforcement materials for CTE matching in three directions

  Several material combinations have been examined, ever closer to the CTE (coefficient of thermal expansion) target performance. A room temperature target of 18 PPM/C for the Compliant Composite (CC) was determined based on stator and rotor FEA results using NIST 304 SS RT CTE data and earlier resin material estimates. We just found that the NIST data for 304 SS shows a room temperature CTE of 15.4 PPM/C. A web literature search lists 16.6 to 17.3 PPM/C for 304 SS. We have a sample of 304 SS with certification coming to better establish our CTE target. This may help the situation if the sample matches the literature values. We would then be closer to the target.

- Determine availability of 3D materials
  - Email discussions with 3Tex, a prominent maker of 3D woven cloths were had and 3D cloths were found unable to meet the CTE needed with isotropic behavior. The required isotropic behavior reduced the volume fraction (Vf) of the fibers to less than needed to reach the CTE target. Their existing machine is too small for the FSG (Fully Superconducting Generator) physical size of 2 m diameter by 4 m long. A new machine and the associated dollars would be needed.
  - Serious manufacturing issues would exist with 3D cloth, such as, handling of the inevitable seam, resin infusion with high Vf, dimensional control and potential in situ sag.
  - Due to the inability to reach the CTE target, we chose to pursue filled resin systems, instead.

- Procure samples for testing

  Cloth and resin for the Torque Tube (TT) material have been received. Many material combinations have been procured and TMA tested for the CC material.

This page removed due to Intellectual Property/Distribution Limitations

This page removed due to Intellectual Property/Distribution Limitations

This page removed due to Intellectual Property/Distribution Limitations

Dr. Dennehy received input stresses from Kato to run their CompositePro software and established safety factors for the TT material. He also helped define direction and specific needs for the CC materials. He searched for and obtained CC material samples for TMA testing.

Task 6.2 Major Stress Studies Performed This Quarter

Stator CTE Optimization for stator active section

Lowest stator CC stresses occur at 17.5 PPM/C using 15.4 PPM/C for 304 SS (NIST) (Figure 6.2.15). We found that isotropic behavior is needed, so laminated composite will not work. Low Young's Modulus performed better, showing a slower stress increase with CC CTE away from optimum CTE.

Figure 6.2.14. Bemco Environmental Chamber at COMTEC

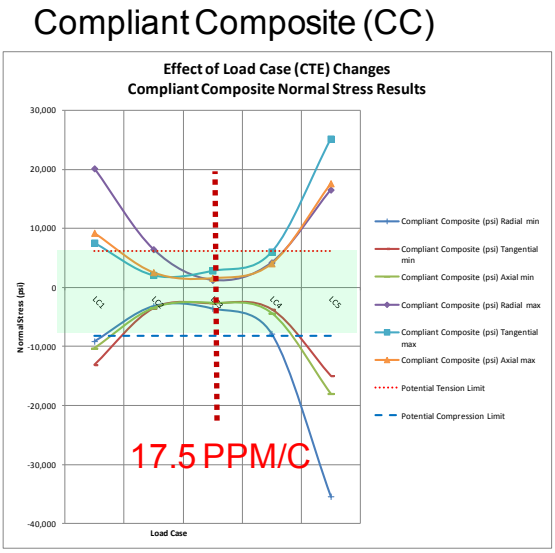

Figure 6.2.15. Stator CTE Optimization

- **Torque Tube Stresses for Rated Conditions**

  This study used detailed FSG Geometry with the 60 K heat interrupt included. A steady-state thermal analysis was performed and the temperature distribution imported. Rated loading was applied and stresses obtained. These stresses were provided to COMTEC for composite FEA developed safety factors (Figure 6.2.16).

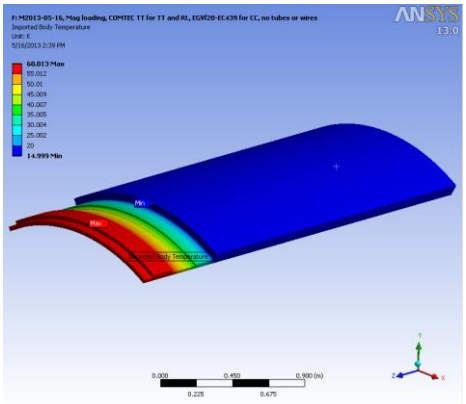

At Max Normal Stress Location	
Radial stress, Sx	2843
Tangential stress, Sy	**3381**
Axial stress, Sz	**5456**
Shear stress radial-tangential, Sxy	1835
Shear stress tangential-Axial, Syz	**-4904**
Shear stress radial-Axial, Sxz	-1645

Figure 6.2.16. Torque Tube Temperature and Rated Stresses

- **Stator Compliant Composite Stresses for Rated Conditions**

  This study examined thermal and magnetically induced stresses. The latest forces from AML were used to determine fatigue loading. The study showed the electromagnetic fatigue stress as small, relative to thermal stresses (Figure 6.2.17).

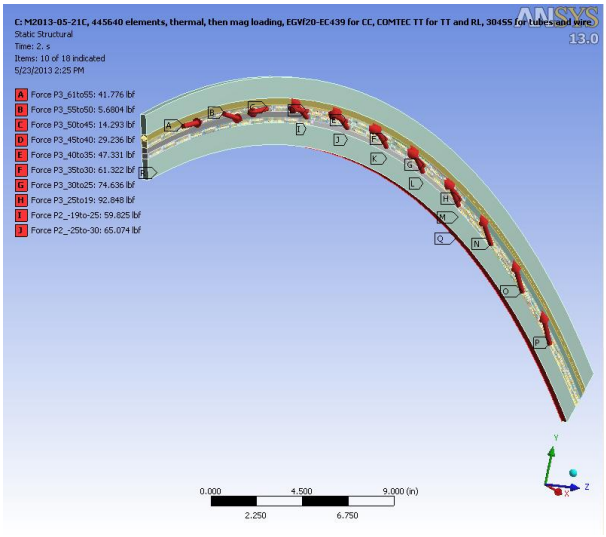

Figure 6.2.17. Stator Electromagnetic Loading Model

- **Rotor CTE Optimization for rotor active section**

  This study showed lowest CC stresses near 20 PPM/C using 15.4 PPM/C for 304 SS (NIST); also that isotropic behavior is needed. It showed low Young's modulus performs better (Figure 6.2.18).

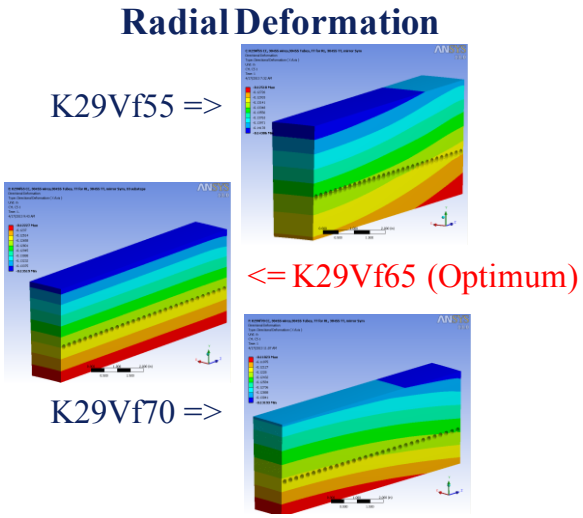

Figure 6.2.18. Radial Deformation Changes with CTE Changes

- **Rotor CTE Optimization with E Glass Short Random Fibers and Low CTE Resin**

  This study, based on projected filled resin properties from published data, showed isotropic CC material with matched CTE to 304 SS reduces CC stress. CTE test data for the milled E glass showed the composite to be non-isotropic using short fibers of milled E glass. Found supplier

data error as the cause. Their product bulletin showed filled resin CTE in a table for unfilled properties. Thermal performance was examined using comparisons of linear expansion plots.

- **Rotor Active Section Composite Design FEA Magnetic Loading Summary**

  This study examines both thermal and magnetic stresses. It used the latest forces from AML. The study determined the stresses for rated condition DC loading. It was shown that the magnetically induced stresses are small, relative to thermal stress (Figure 6.2.19).

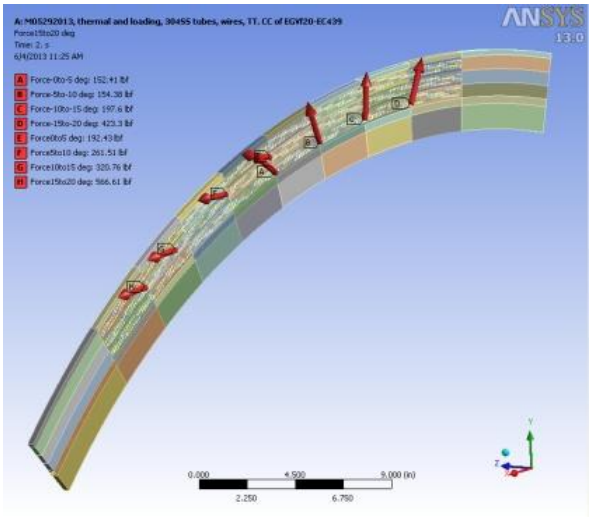

Figure 6.2.19. Rotor Electromagnetic Loading Model

- **TMA CTE Summary for Epoxicast 1082/EH-21**

This study examined Test data vs. published data for the Epoxyset product. Their published CTE is well below our CTE target value. The cured sample testing was to be used as verification that our target CTE was achievable. The sample tested much higher than published and above our CTE target value. It was the lowest-tested CTE yet and showed near isotropic behavior. The ROM estimate almost matches the tested values (Figure 6.2.20).

Task 6.2 Specific Objectives from Last Quarter

- **Develop small, detailed FEA models for fast answers**

  Composite designs for the stator and rotor are being determined, using these small, detailed models. The extreme component count and size variations within the complex geometries won't allow full geometry models. Appropriate detail models to investigate the details of the design are being used. FEA results with various materials and geometries show composite requirements. Many models have been developed to examine specific design issues, like thermal stresses, magnetic loading, and torque related loading. These models have helped to determine development direction and measure progress.

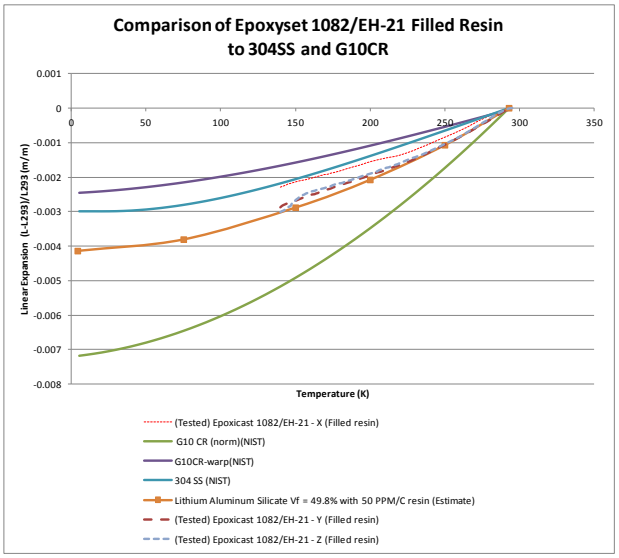

Figure 6.2.20. TMA CTE Results for Epoxyset's Epoxicast EC-1082/EH-21 Resin System

  The concept of compliant composite has been further validated in Q2 with these FEA studies. Large stress reductions from closer CTE matching and further reduction with lower CC Young's modulus are predicted. The search for material combinations that fulfill needed thermal/mechanical performance continues with several possible fillers found to improve the resin system thermal performance.

- **Develop potential composite material designs for the FSG application**

  In Q2, we have iterated using the new composite material properties and FEA results to improve the composite materials for the FSG application. Composite design tools and methods have been used for the stator torque tube and retention layer to develop projected composite material properties. Initial testing for the TT material has not shown any surprises.

  Where needed, we have used early laboratory validation of potential resin systems. Using this method we have found two examples of erred data for two manufacturers. The preliminary testing data allows us to change direction faster, allowing more possibilities to be examined. Time to obtain samples of potential constituents has been the longest delay.

- **Develop stress limits and failure philosophies**

  For the FSG application, where practically the only heat transfer is by conduction within the composite, resin cracking and debonding represent degradation of the cooling capability which is crucial to the FSG success. In Q2, FEA examinations related to Task 6.4, Sub-scale Torque Tube

This page removed due to Intellectual Property/Distribution Limitations

In Q2, improved force values were developed for the rated condition (1 MW at 10 rpm). The forces per length with their respective directions were incorporated into short, detailed rotor and stator models to isolate the magnetic loading-related stresses.

Task 6.2 Significant Results

Results for the torque tube material using FEA stresses for rated conditions show good safety factors.

In Q2, the compliant composite (CC) development direction has shifted based on findings from FEA and preliminary CTE results at COMTEC. The progression of CC development is described below:

- **Low stiffness polyester mat CC configuration**

  This was the prevailing concept at the end of BP1. While the stiffness of the polyester reinforcement is low (Low Young's modulus), the expansion properties are higher than the resin leading to a large CTE mismatch between the CC and the surrounding metals. That causes high local stresses.

- **Laminated CC**

  This type of material was found to be orthotropic with matched CTE possible only in the plane of the reinforcement cloth. A CTE mismatch is caused in the through thickness (radial) direction.

- **3D cloth composite CC**

  Discussions with 3Tex, a prominent supplier of 3D cloth, determined that not enough volume fraction of fiber is obtained in all directions with near isotropic behavior for CTE matching the desired CTE target. Perceived machining difficulty exists with the low CTE fibers like Kevlar. Perceived manufacturing/process difficulties with the large physical size, resin fill and cylindrical geometry (seam) also exist.

- **Short random fiber CC**

  This configuration was examined to improve through thickness strength and allow CTE tuning with altering the volume fraction of the filler. The short fibers were chosen to minimize flow alignment and reach near isotropic behavior. This casting process requires a pourable mixture, limiting the volume fraction of filler in the mixture to a fixed viscosity. The filler volume fraction limits using CTD-521 and short fibers of carbon fiber and E glass was found limited to about 27% and the CTE at those fractions to be too high. The isotropy of these samples was relatively poor, with large CTE variations in the three directions.

- **Filled resin system CC**

  Based on the low volume fractions obtained for the short fibers, a search for a lower CTE, unfilled resin, which would require less filler to reach a lower mixed CTE was made. This would allow easier CTE tuning and casting with a lower mixture viscosity. This search culminated in testing a low exotherm resin with published resin CTE values that would achieve the desired behavior. Unfortunately, the data published was shown by test to be wrong. The data for a filled

This page removed due to Intellectual Property/Distribution Limitations

This page removed due to Intellectual Property/Distribution Limitations

This page removed due to Intellectual Property/Distribution Limitations

This page removed due to Intellectual Property/Distribution Limitations

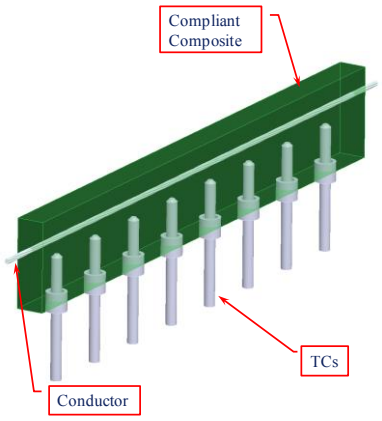

Figure 6.2.23. Thermal Conductivity of CC Material

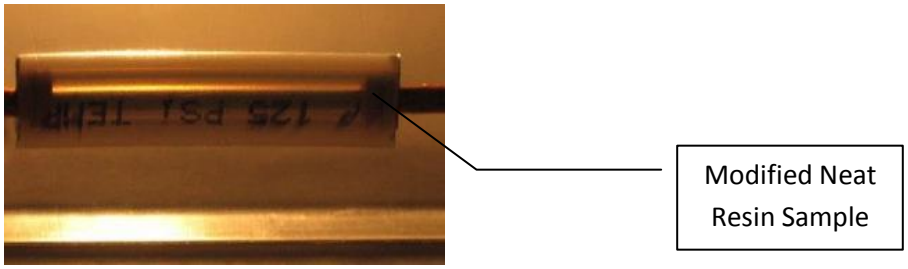

Figure 6.2.24. CC Effect on Sensed Temperature

The geometry consists of a single pass of 316 SS 6-around-1 cable insulated with Kapton film. The first sample uses adhesive backed Kapton. Non-adhesive backed Kapton is on order (Figure 6.2.25).

Thermal cycling with LN2 is used to quickly examine possible degradation effects of thermal shock and thermal cycling. The Room Temperature (RT) assembly is submerged in a Dewar containing LN2 (77K) and warmed to RT for each thermal cycle. Strategic heat runs are performed before the first cycle, after 10, 20 and 30 cycles. The heat run is a test where a fixed DC current is applied to the conductor for internal heating of the conductor. The test is continued until stable temperatures are reached.

Comparison of temperature results for the heat runs show thermal performance degradation, if any.
A separate micro cracking specimen is also attached to the test assembly and examined during each heat run, using microscopy.

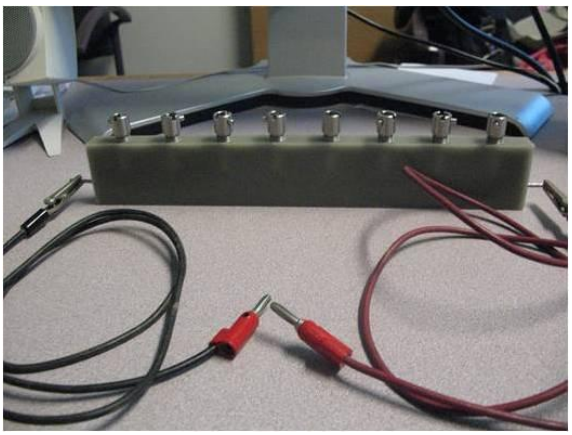

Figure 6.2.25. Cable Geometry

FEA Task 6.2b

Task 6.2B LN2 Thermal Cycling Test Sample Temperature Analyses

This study looks at sample assembly temperatures for the unmodified and modified samples (Figure 6.2.26). The modification includes a trapped air cavity using a sealed piece of tubing surrounding the conductor. The air has a thermal conductivity much lower than the composite, adding substantial local thermal resistance. The effect is to reduce the local thermocouple reading and increase the adjacent readings.

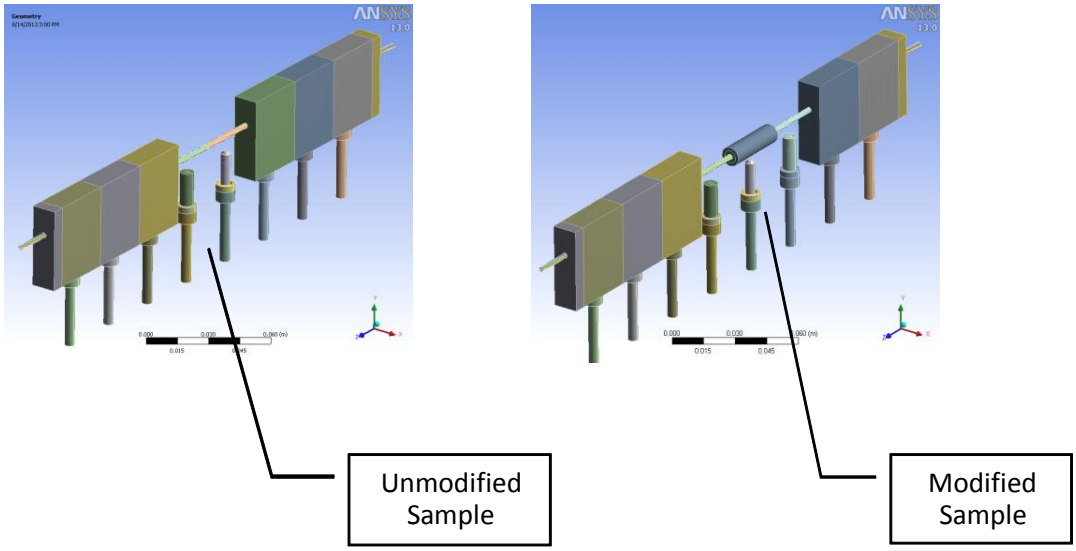

Figure 6.2.26. Assembly Temperatures for Unmodified and Modified Samples

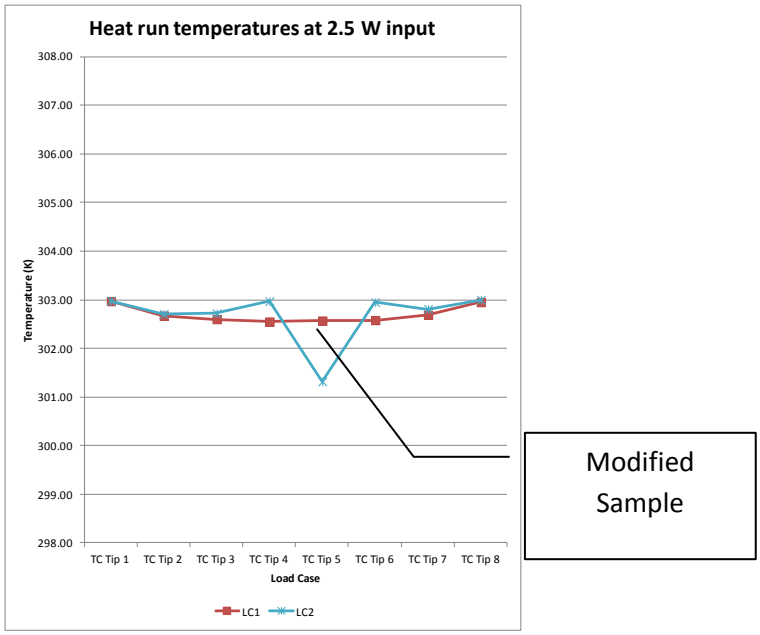

Figure 6.2.27. Heat Run Temperatures at 2.5 W Input

At 0.25-inch separation between conductor and TCs, 6 to 8 K temperature rise at the TCs is expected with 2.5 W heating of the conductor (Figure 6.2.27).

The effect of 0.071 radial dead air space between the Kapton and composite is a change from 7.57 K rise to 6.32 K rise, or a change of 1.25 K rise at TC number 5 next to an addition of 0.071 inch of dead air.

Task 6.2B LN2 Thermal Cycling Test Sample Design Analyses

This study shows the resulting stresses within the test sample due to 77K temperatures and during the RT heat run, where 2.5 W heating occurs in the insulated conductor (Figure 6.2.28).

The 77 K results (Figure 6.2.29) show low composite stresses, except at the ends of the sample. The 77 K results show similar results for the Kapton material, except the focus is even greater on the sample ends.The conductor heating stresses at 2.5 W are much lower than the 77 K thermal stresses.

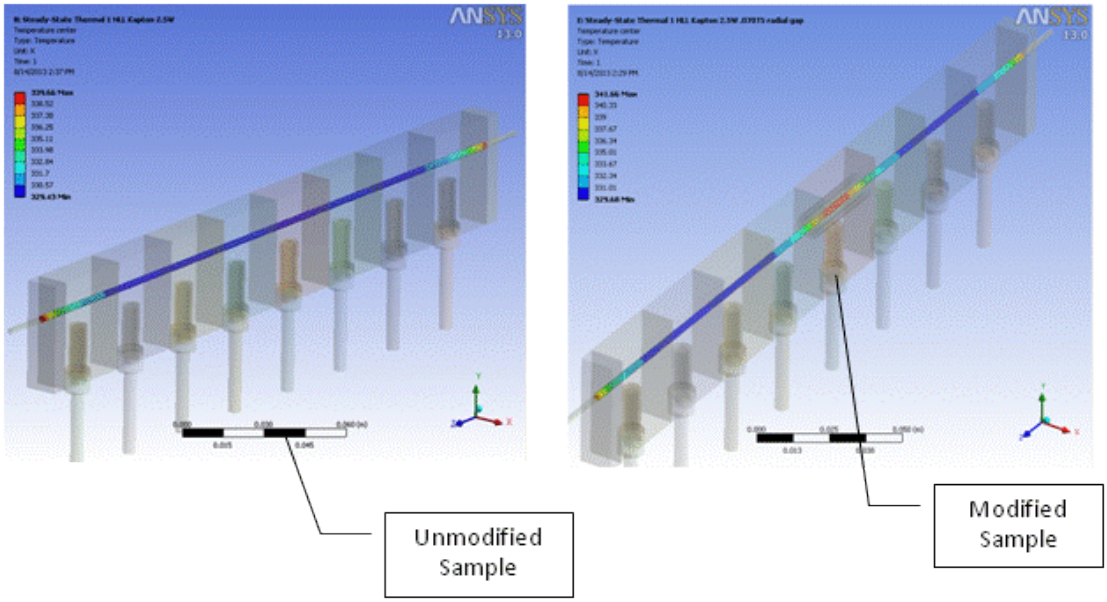

Figure 6.2.28. Thermal Cycling Results

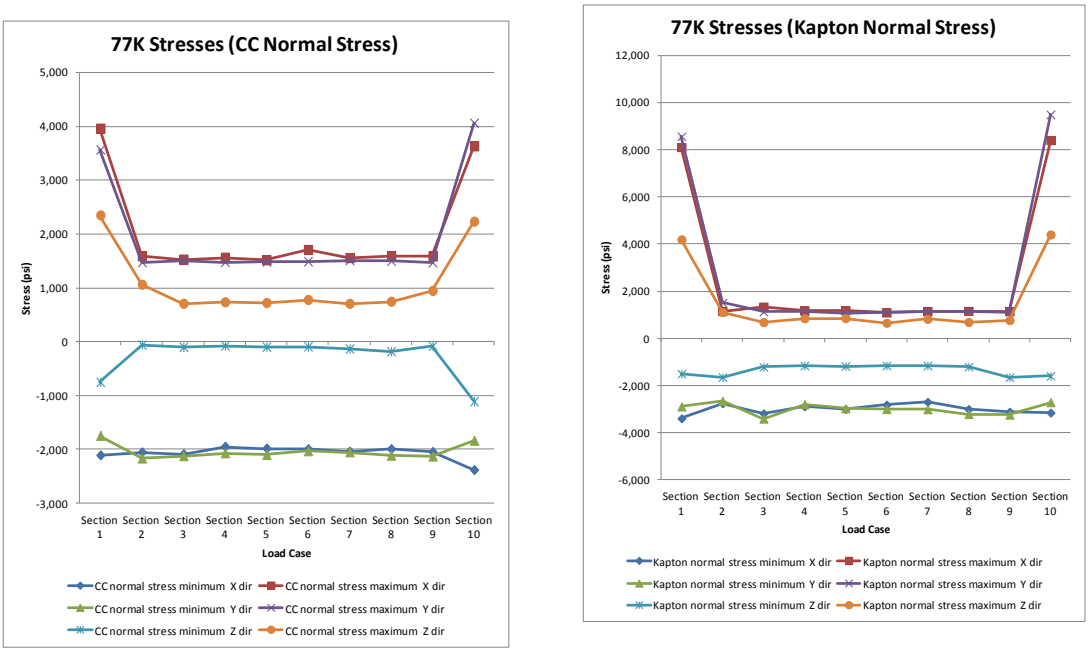

Figure 6.2.29. Thermal cycling test comparison of CC and Kapton samples at 2.5 W

Results of the Study

At 77 K (steady state):

This study uses an assumption that the materials are completely bonded and the Kapton behaves like an isotropic solid. The Kapton is actually a adhesive backed film with 5 discrete layers. Delamination from axial thermal loading is a good possibility.

- The local stresses for the wire interfaces at the ends of the composite are quite pronounced, but are lower than the current tested room temperature stress capability of the CC.
- The composite stresses are greatly reduced in the center sections of the sample with the added Kapton insulation layer. This study assumes complete bonding cable to Kapton and Kapton to composite. With allowed movement within the Kapton layers, the developed stresses for the composite and conductor should further reduce.
- Unless the thermal shock amplifies the transient stresses, it appears damage from the LN2 thermal cycling may be limited to the very ends of the sample assy.

Thermal results from heat generation:

- Temperatures are greatly influenced by convection on the external surfaces. This study uses 5 W/m^2 K. That's at the bottom of the usual range for free convection.
- Wire end conduction/convection will greatly affect the local end effects on temperatures. Since baseline comparison is our method to determine heat transfer change, consistency in methods will be imperative.
- The stresses at 2.5 W from conductor internal heating are much less than the 77 K thermal stresses.

Task 6.2b LN2 Dip Test Sample Transient Analyses

This study shows the predicted time/temperatures within the sample (Figure 6.2.30) during a dip into LN2 and the corresponding thermal stresses during the cool down (Figure 6.2.31). The assumptions for the analysis are:

Geometry using 5 layers of 0.001-inch thick Kapton on a 304 SS cable. The Kapton is assumed isotropic.

TCs are removed for the dip. All contact surfaces are assumed bonded.

Boiling LN2 convection coefficients are used.

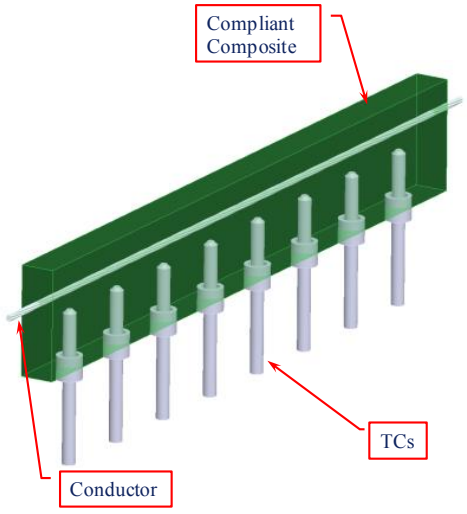

Figure 6.2.30. LN2 Dip Test Sample

Results of the Study

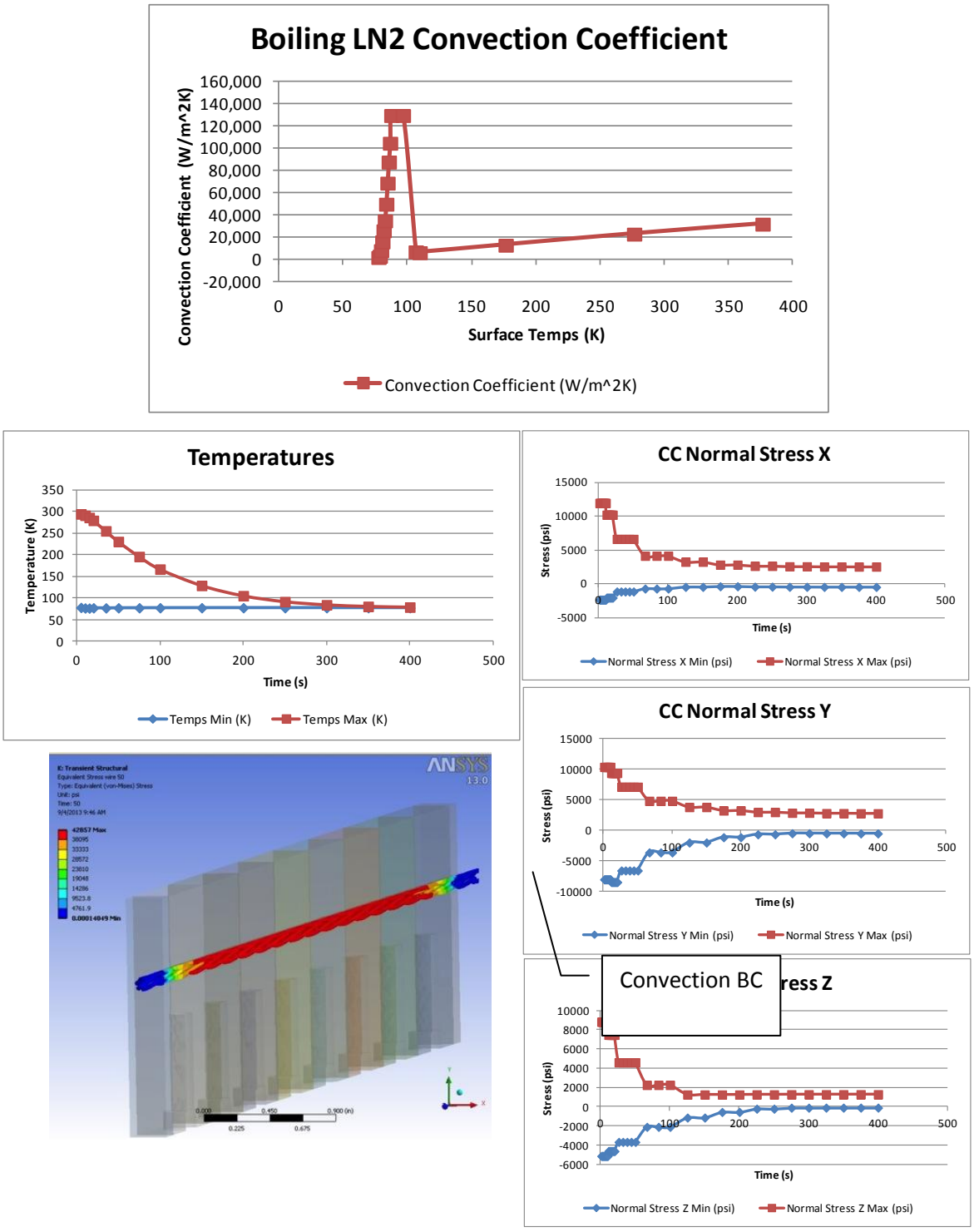

Figure 6.2.31. LN2 Dip Test Results

Thermal results from LN2 Dip:

- Temperatures are within 1.5 K of LN2 temperature in 7 minutes.
- The peak stresses develop almost immediately and composite maximum normal stress can exceed 7 times the stresses after reaching LN2 temperature.
- The peak stresses are primarily concentrated at the ends of the sample.
- The maximum principal strain reached 0.5% in the CC material.
- The peak normal stresses during cool down for the CC material temporarily exceed room temperature tested strength values. High shear stresses and high normal stresses exist at the sample ends.
- Potentially damaging stress levels can be reached per this study, but depending on the actual bond strength capabilities of the assembly and laminated behavior of the Kapton, it is doubtful these stresses will be fully reached. The Kapton layers will likely absorb the differential movement between the CC and conductor.
- The strains for the materials are generally quite low, indicating probable local de-bonding may occur at the ends, if at all.

Rev 1:

- NIST data for 304 SS and 316 SS are identical! The NIST linear expansion behavior agrees with literature information for 316 SS.
- Very similar results with the 316 SS study peak stresses slightly elevated from the 304 SS study.
- Results should represent expected behavior for a 316 SS-sheathed superconductor.

Task 6.2b LN2 Dip Trial Heat Run Data Review

This review examines the data for the first 6.2b trial part (used to establish the mold tooling and casting success) for a baseline heat run, LN2 dip, and a second heat run.

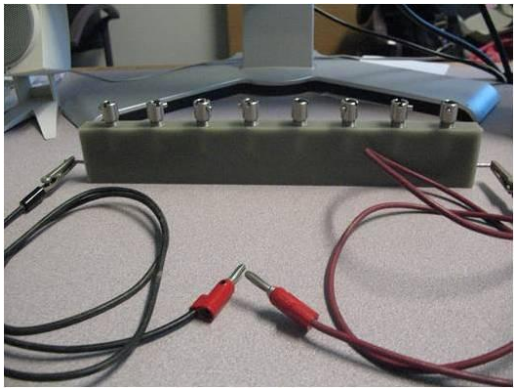

This review also examines the data for the first 6.2b trial part for a second pair of heat runs. The test setup was changed for these runs to separate the 1-ohm resistor and power supply from the sample to eliminate possible extraneous heat transfer into the test sample. Note: the resistor gets hot during the heat run and was sitting directly on the test bench for the previous runs. The power supply has an exhaust fan that was potentially heating the air near the sample.

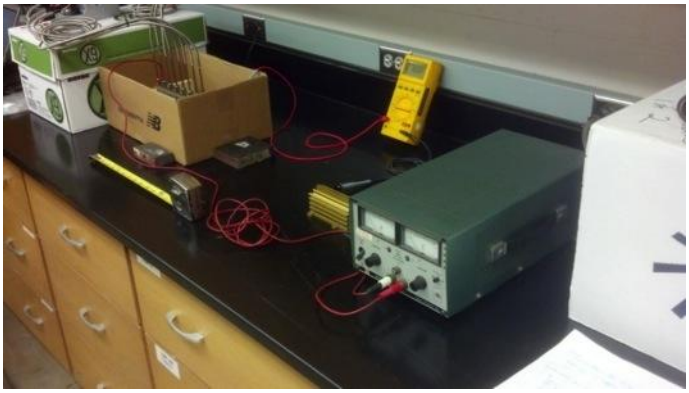

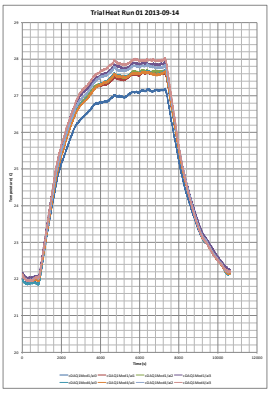

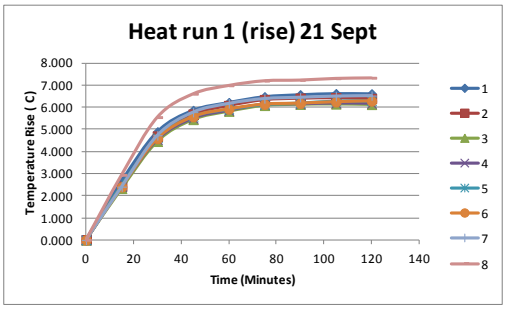

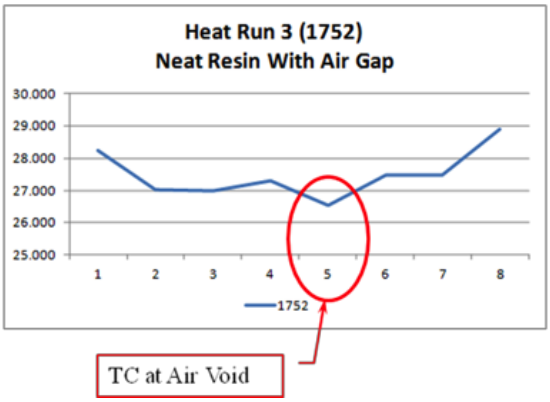

A third, partial heat run was also performed with a neat resin sample made to prove the sealing for a trapped air void introduced to provide a known heat transfer effect.

Testing at Southern Research Stopped

At the Team meeting, the team agreed that the high cost of the testing for specific heat and thermal conductivity measurements did not provide sufficient de-risking for the expense. The decision was made to use that money more efficiently.

At the time of the decision, the test coupons were complete. A clarification and updated quotation was received. The cost was nearly double the original quotation.

This page removed due to Intellectual Property/Distribution Limitations

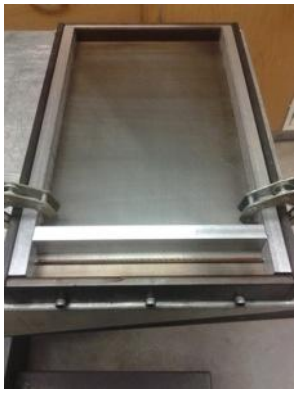

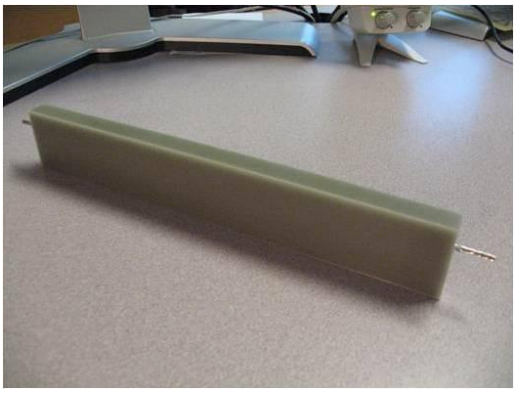

- The test instrumentation (thermocouples and data acquisition system) for 6.2b temperature measurements was procured.
- Instrumentation sensor calibration/sensitivity validation was performed.

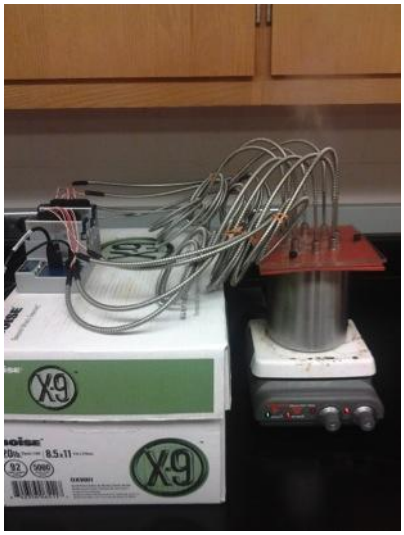

Calibration		
TC #	**Cold**	**Hot**
1	0.162256	99.36759
2	0.16115	99.44676
3	0.16169	99.43711
4	0.186591	99.42675
5	0.029239	99.31365
6	0.078254	99.36245
7	0.148811	99.33542
8	0.098441	99.33366
Average =	**0.128304**	**99.37793**
Min =	0.029239	99.31365
Max =	0.186591	99.44676
StdDEV =	***0.053951***	***0.051919***
Median =	**0.154981**	**99.36502**
Range =	***0.157352***	***0.133115***

- Details of the sample modification (air cavity) for 6.2b were developed.
- Task 6.2b test (thermal cycling and heat run) procedures were co-developed with Emerson.
- Microscopy methods for 6.2b (looking for micro-cracking) were developed.

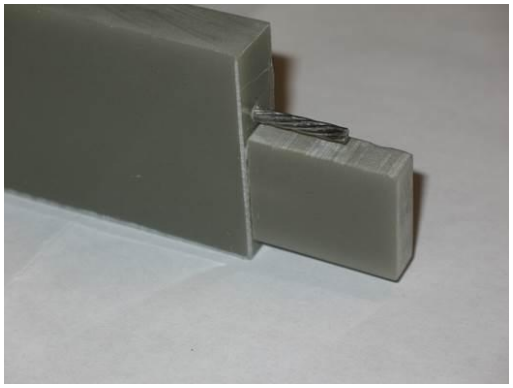

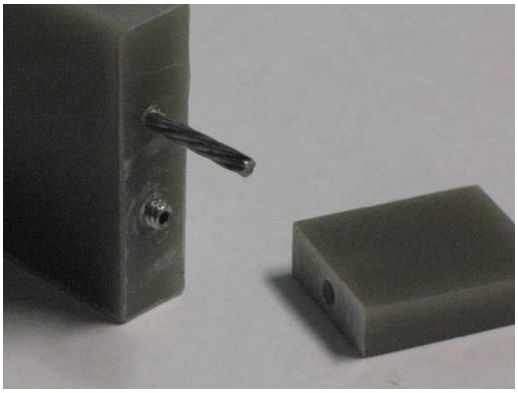

This page removed due to Intellectual Property/Distribution Limitations

This page removed due to Intellectual Property/Distribution Limitations

- **Make and test Task 6.2b thermal cycling samples.**

  Two different sample configurations were examined. The first Task 6.2b sample configuration used 5 thicknesses of 0.001-inch-thick, adhesive-backed Kapton applied to a 6-around-1, 316 stainless steel cable. Near the end of the testing of Configuration 1, it was pointed out that adhesive-backed Kapton was not used by superconducting collider magnets, so a second configuration using a single, half-lapped layer (two thicknesses) of non-adhesive-backed, 0.001-inch-thick Kapton was made and tested

  Two samples for each configuration, one modified with an added air void next to the conductor and one without modification were made (4 samples were tested, total).

  The testing was divided into two elements, one to compare modified and unmodified behavior, and one to determine the effect of thermal cycling from RT to 77 K back to RT using an immersion process into LN2.

  Testing for the first configuration (adhesive-backed Kapton) only utilized thermocouples placed equidistant to the conductor. During the heat run testing, improvements to the methods were continually added, improving the accuracy and consistency for the setup. Unfortunately, since these needed changes affected the results, comparisons of results with meaningful conclusions for the first configuration testing was not possible.

  An area of concern for cryogenic application of composites is the possibility of micro cracking. Damaging stresses within the composite matrix can develop from the extreme temperature ranges, causing separation of the resin from reinforcement or fillers, creating cracks in the composite. A method was developed to include a microscopy sample to the testing to assess the developed Compliant Composite (CC) material resistance to this phenomenon.

  The original Task 6.2b concept had only thermocouple measurements to assess the thermal performance effects from immersion into the cryogen. The primary risk addressed by the thermal cycling testing is to determine the effect of heat transfer degradation with respect to cooling the conductor. After considerable thought, a breadboard circuit was developed to allow accurate determination of conductor temperature rise during the heat runs. Methods for correcting the data for ambient temperature changes and varied current inputs for each test were added to greatly improve comparison capability. The initial test arrangement for Sample 1 is shown below.

Modified Sample, tubing with air under TC 5

Unmodified Sample

Task 6.2 Major Activities

Task 6.2b

Sample Configuration 1:

The geometry for Sample Configuration 1 consists of a single pass of 316 SS 6-around-1cable insulated with about 5 thicknesses of adhesive-backed Kapton film (Figure 6.2.32). Right, an early testing circuit used for power application.

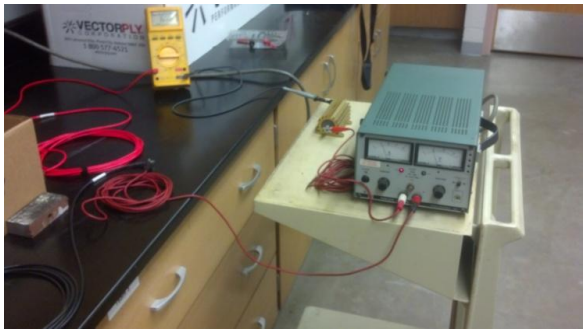

Test circuit used for baseline

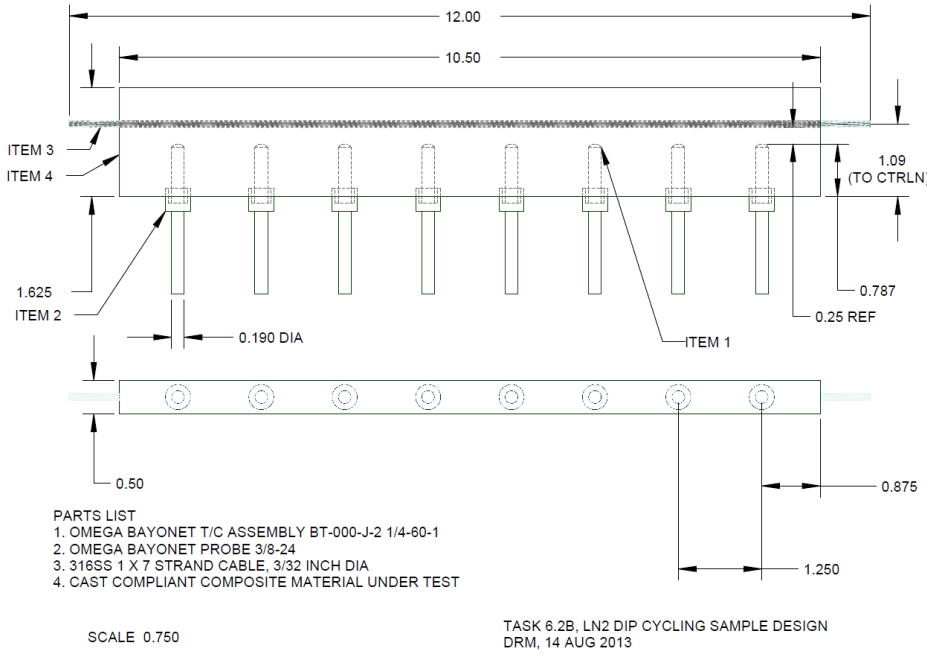

Figure 6.2.32. Geometry for Unmodified Sample

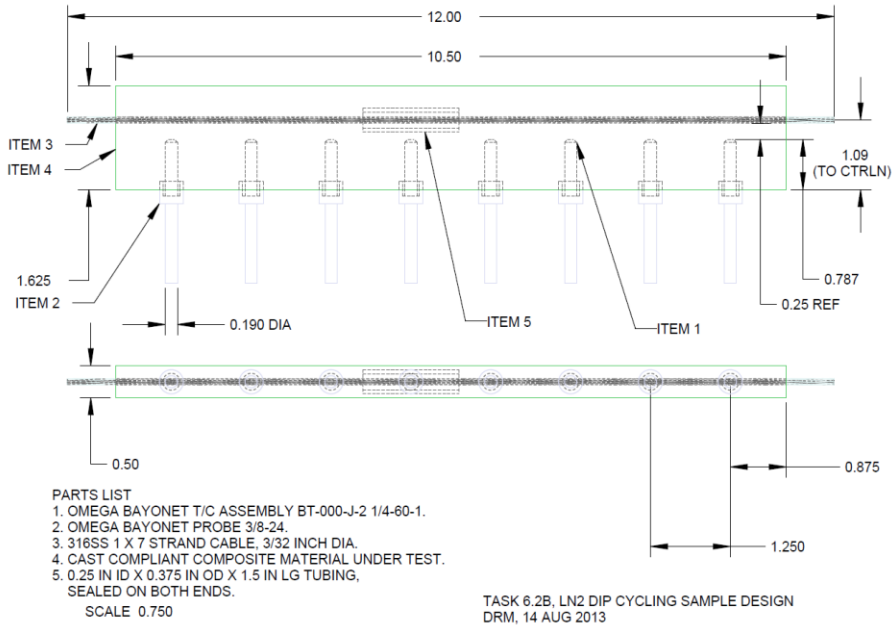

Figure 6.2.33. Geometry for Modified Sample

Element 1 testing includes a baseline heat run on the modified (Figure 6.2.33) and unmodified (Figure 6.2.32) samples to show the effect of the modification on the thermal behavior of the samples (Figure 6.2.34).

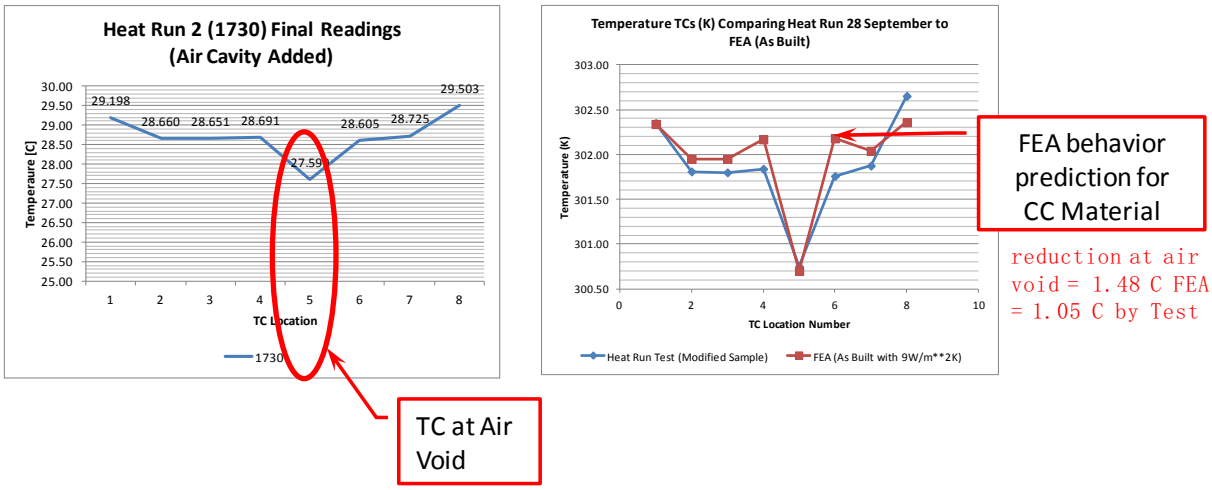

Figure 6.2.34. Effect of the modification is close to the FEA prediction.

Difficulties in stabilizing temperatures at the end of the previous heat runs prompted the use of a complete enclosure over the test setup. A box measuring 18-in. deep x 24-in. wide x 27.6-in. high with a 4-in. x 4-in. opening at the top was placed over the sample, probe cables and chassis assemblies (Figure 6.2.35).

Figure 6.2.35. Test Setup Enclosure

The addition of the system enclosure was used following the 20th thermal cycle. The heat run data was very smooth without the stability/fluctuation issues seen previously. A thermometer capable of 0.1-degree accuracy was added to measure ambient enclosure temperatures for the heat runs.

Average Temp Rise		Delta from bsline	Min	Max	Range	% ave Delta
Baseline	6.13	0.00	5.87	6.33	0.47	0.0%
10 Cycles	6.08	-0.05	5.76	6.25	0.50	-0.7%
20 Cycles	6.43	0.30	6.24	6.68	0.45	4.9%
30 Cycles	6.53	0.41	6.20	6.83	0.63	6.6%

Note: With Enclosure

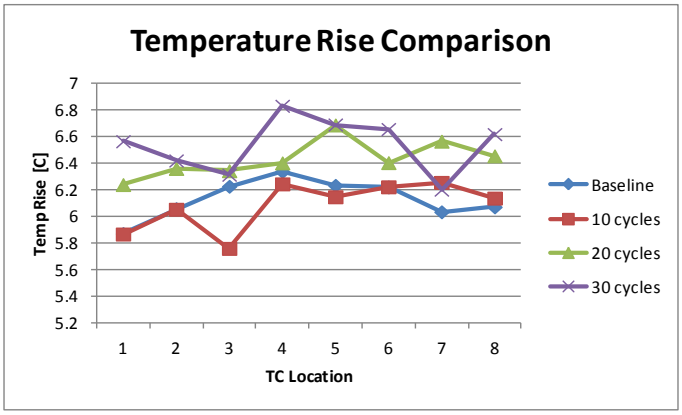

Figure 6.2.36. Unmodified Sample 1 Test Results

The results of the unmodified Sample 1 (Figure 6.2.36) were inconclusive, due to variations in the testing methods and results. During final testing, following thirty thermal cycles, it was apparent the electrical connections to the conductor, using alligator clips onto crimps, as well as loose crimps, were responsible for significant performance variance. Two heat runs without changes, other than simple reconnection, showed different results.

A separate micro cracking specimen is also attached to the test assembly and examined during each heat run, using microscopy (Figure 6.2.37).

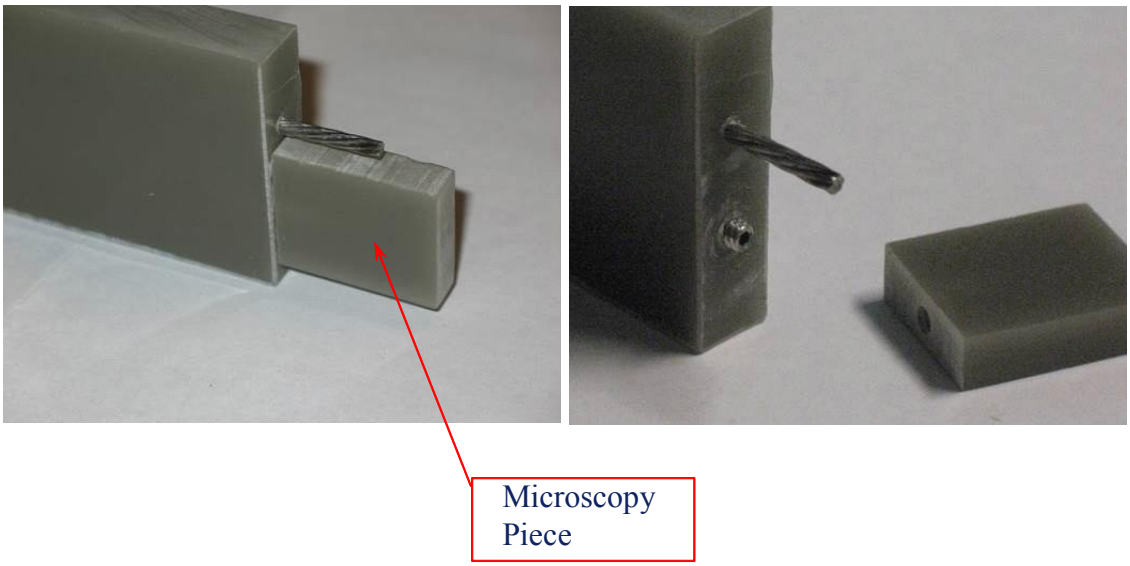

Figure 6.2.37. Protective piece used to prevent axial loading on the exposed conductor doubles as the microscopy sample.

This page removed due to Intellectual Property/Distribution Limitations

This page removed due to Intellectual Property/Distribution Limitations

The conductor information addresses the thermal risks more directly. The risk examined with Task 6.2b is detrimental effects to the heat transfer capability from environment thermal cycling. Ultimately, the fundamental risk is the conductor may lose the capability to remain superconducting if its temperature is not properly maintained with adequate cooling. The thermocouples give the ability to see variances in the heat transfer along the length with changes in developed adjacent temperatures. They do not show the effect on the conductor temperature.

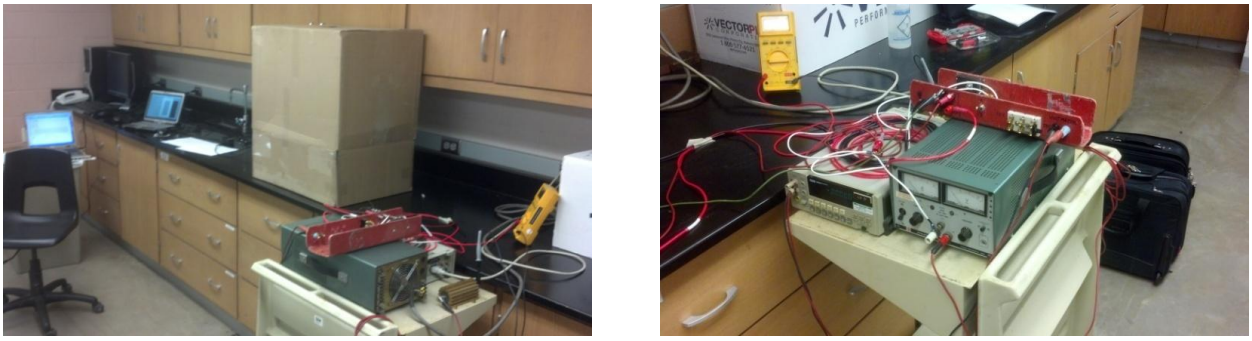

Figure 6.2.38. Test Circuit Used for Baseline

The method for determining the conductor temperature relies on the resistivity of the material changing with temperature and the use of a precision resistor with low temperature coefficient of resistivity.

A DC current is passed through the conductor to raise its temperature. The resistance will be measured by comparing the voltage drop across the specimen with the voltage drop across a precision resistor with low temperature coefficient of resistivity. The starting conductor temperature is taken from the average of the thermocouple temperatures. The corresponding resistivity for the conductor material is taken from a curve of resistivity vs. temperature for that material. The conductor resistance is extrapolated back from timed readings to determine the starting resistance. The calculated conductor resistance change ratio will be used to calculate the resistivity change and then the final conductor temperature is determined from a curve of temperature vs. resistivity.

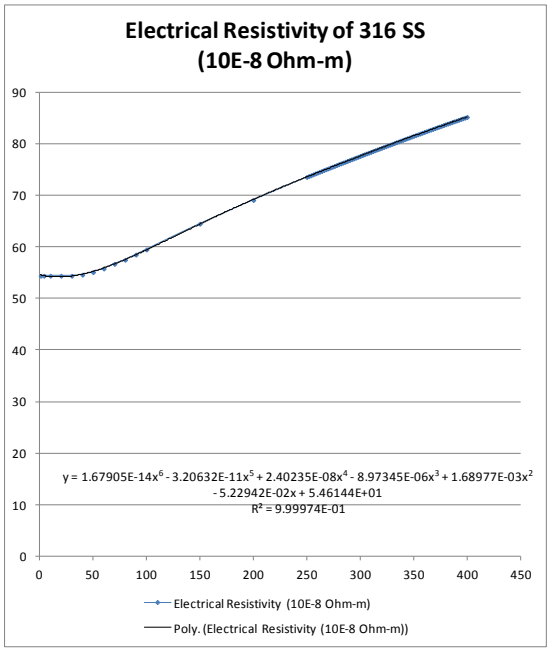

Resistivity vs. Temperature

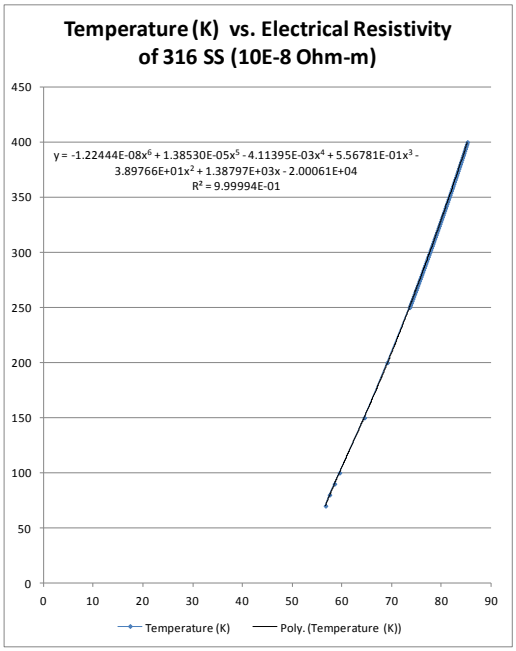

Temperature vs. Resistivity

Element 1 testing on the modified sample again showed good correlation to the earlier FEA results. Two heat runs on the modified Sample 2 showed good repeatability for the readings, as well.

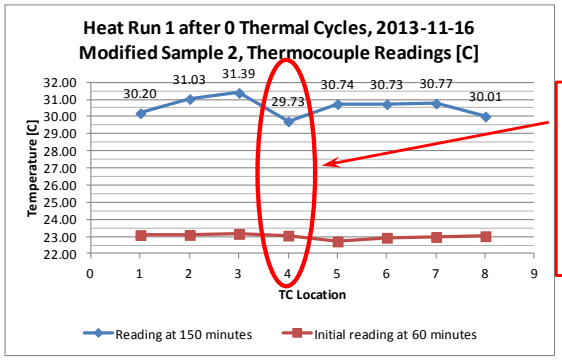

TC 4 over the Sealed Air cavity

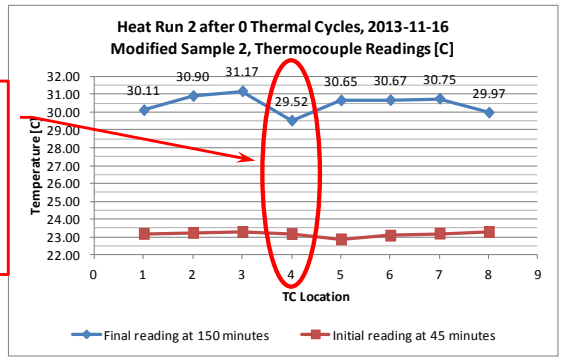

HR1 Air Cavity Delta
Temperature drop out = 1.34 C*

HR2 Air Cavity Delta
Temperature drop out = 1.39 C*

* Air cavity TC reading subtracted from the average of the two adjacent TC readings

Repeatability Testing of Modified Sample 2

Due to the variability shown in the Sample 1 testing results, repeatability testing of a non-thermal cycled modified Sample 2 was added to the testing scope.

Four heat runs of the modified Sample 2 were performed at separate times to establish the consistency of the results. Unfortunately, the data for the first conductor temperature measurement were not usable due to initial timing errors during the data taking. The subsequent heat runs, however, show the capability of the method. In addition to the test technique improvements, corrections for the ambient temperatures within the enclosure and for the variance of power supplied were determined and applied to the data.

Element 2 Testing of the Unmodified Sample 2

The corrections and improvements to the testing techniques discovered/developed during Sample 1 testing were incorporated during the testing of Sample 2. The results were smoother and more consistent (Figure 6.2.39 and Figure 6.2.40). A threaded screw clamp was used for more consistent electrical connections, as well.

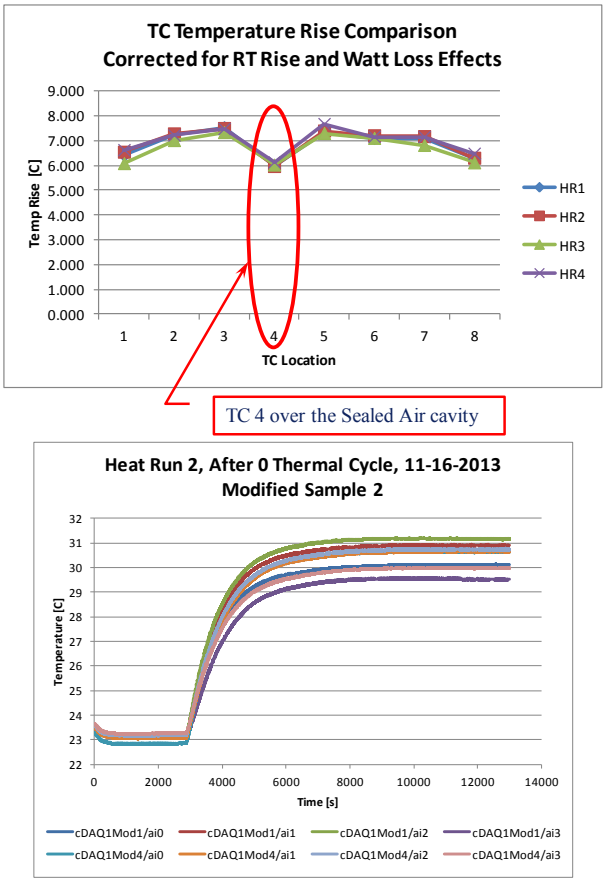

Figure 6.2.39. Plots of Thermocouple Results for Modified Sample 2

Corrected for Room Temperature Rise and Loss									
TC Temp rises [@ 150 min](RT effect)					TC Delta Temp rises [@ 150 min]				
RT Rise [C]	0.7	0.4	0.6	0.8					
Watts Loss	2.22605	2.22459	2.26767	2.22253					
TC	HR1	HR2	HR3	HR4	TC	HR1	HR2	HR3	HR4
1	6.409	6.537	6.076	6.622	1	0.000	0.128	-0.333	0.213
2	7.228	7.278	7.007	7.212	2	0.000	0.050	-0.221	-0.016
3	7.528	7.495	7.329	7.475	3	0.000	-0.033	-0.199	-0.053
4	5.962	5.960	6.017	6.131	4	0.000	-0.002	0.055	0.169
5	7.321	7.393	7.292	7.674	5	0.000	0.072	-0.029	0.353
6	7.089	7.202	7.095	7.155	6	0.000	0.113	0.006	0.066
7	7.086	7.168	6.810	7.149	7	0.000	0.082	-0.276	0.063
8	6.282	6.294	6.106	6.473	8	0.000	0.012	-0.176	0.191
AVE	6.863	6.916	6.717	6.987	AVE	0.000	0.053	-0.147	0.123
					% delta from HR1	0.0%	0.8%	-2.1%	1.8%

Figure 6.2.40. Thermocouple temperature rises were within 2.1 % of the baseline.

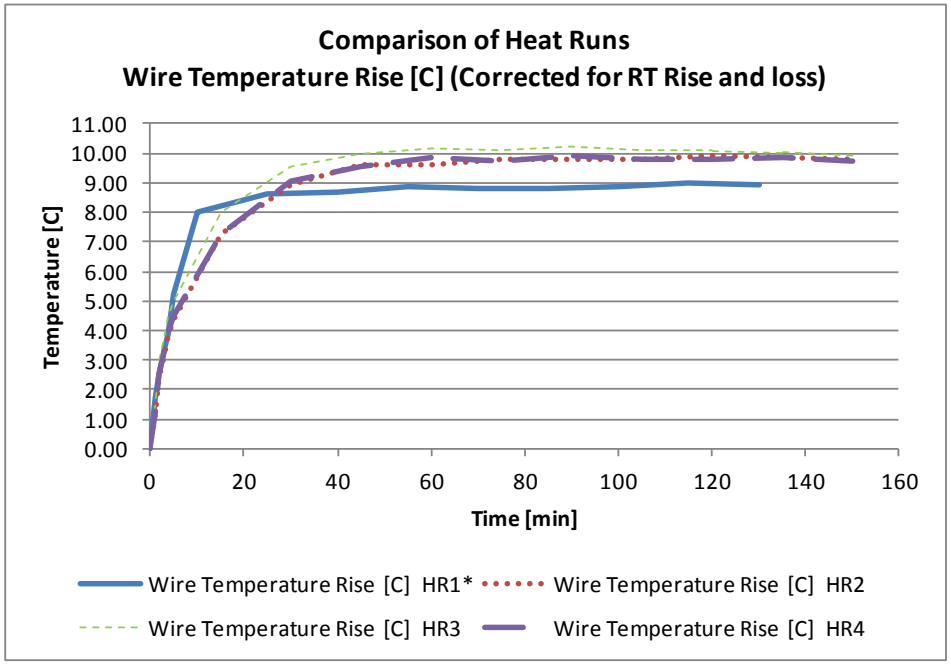

Figure 6.2.41. Conductor Temperature rises showing errant HR1 results

Figure 6.2.41 is the plot of conductor temperature rises showing the errant HR1 results.

Corrected for RT Rise and Watt Loss				
Average Conductor Rise at 150 minutes				
Watts	2.22605	2.22459	2.26767	2.22253
Test	HR1*	HR2**	HR3	HR4
Rise [C]	8.922	9.768	9.908	9.759
Delta from HR2		0.000	0.140	-0.009
Delta from HR2		0.00%	1.43%	-0.09%
*using initial resistance reading, only 130 minutes long				
**Used as baseline for conductor readings				

Figure 6.2.42. Conductor Temperature Rise Results

The conductor temperature rise results varied less than 2 % from the baseline (Figure 6.2.42). Note that the baseline was changed to Heat Run 2, due to timing errors on the first heat run.

The repeatability testing performed on the modified Sample 2 clearly showed the testing capability to capture the thermal behavior of the sample.

Thermal Cycle Testing of Unmodified Sample 2

Element 2, thermal cycling testing of the unmodified Sample 2, was performed with the improved heat run test techniques and conductor temperature rises. A baseline and heat runs after 10, 20 and 30 cycles were planned, but an additional 10 thermal cycles were added (Figure 6.2.43).

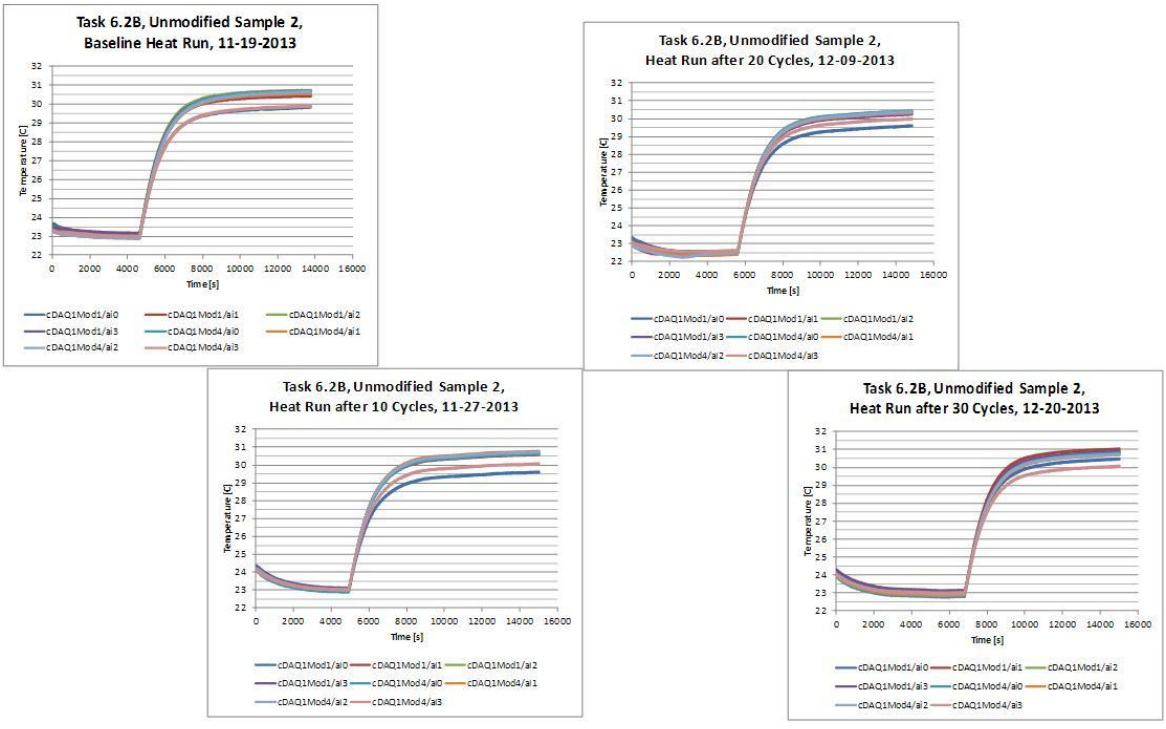

Figure 6.2.43. Thermocouple Uncorrected Raw Data

Uncorrected										
		TC Temp rises [C] [@150 min]					Temp Rise Deltas from Baseline			
		Baseline	10 cycles	20 cycles	30 cycles		Baseline	10 cycles	20 cycles	30 cycles
Loss [W]		2.22033	2.25574	2.21658113						
RT Rise [C]		0.7	0.6	1	0.9					
TC										
1		6.936	6.595	6.989	7.573		0.000	-0.341	0.053	0.637
2		7.503	7.637	7.844	8.13		0.000	0.134	0.341	0.627
3		7.591	7.602	7.786	7.952		0.000	0.011	0.195	0.361
4		7.467	7.493	7.631	7.804		0.000	0.026	0.164	0.337
5		7.800	7.699	7.969	8.062		0.000	-0.101	0.169	0.262
6		7.662	7.727	7.884	7.937		0.000	0.065	0.222	0.275
7		7.725	7.690	7.883	7.849		0.000	-0.035	0.158	0.124
8		6.913	7.013	7.314	7.095		0.000	0.100	0.401	0.182
	Ave	**7.450**	**7.432**	**7.663**	**7.800**		**0.000**	**-0.018**	**0.213**	**0.351**
				%Delta from Baseline			**0.0%**	**-0.2%**	**2.9%**	**4.7%**

Figure 6.2.44. Uncorrected thermocouple data shows 5% variance.

The uncorrected thermocouple data shows a variance of almost 5% from the baseline (Figure 6.2.44).

In Figure 6.2.45,the uncorrected thermocouple data for the final readings show variance locations.

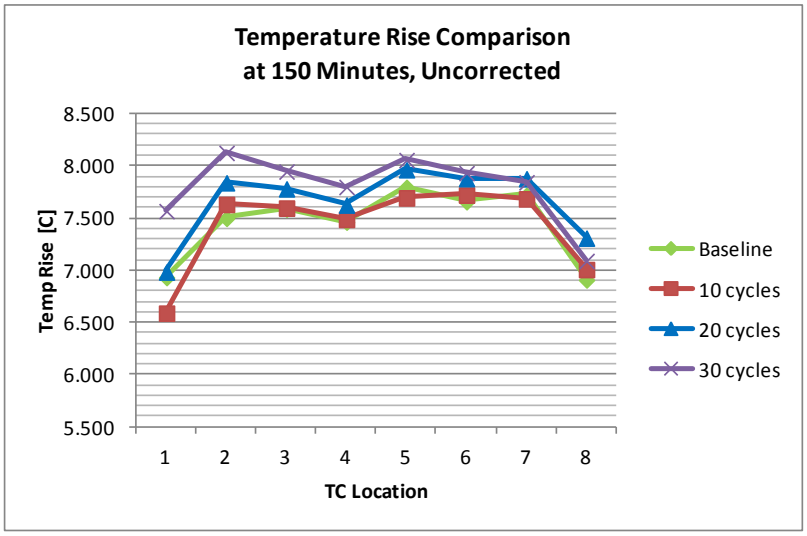

Figure 6.2.45. Uncorrected Thermocouple Data showing Variance Locations

Corrected for RT Rise and Loss										
		TC Temp rises [C] [@150 min]					Temp Rise Deltas from Baseline			
		Baseline	10 cycles	20 cycles	30 cycles		Baseline	10 cycles	20 cycles	30 cycles
Loss [W]		2.22033	2.25574	2.21658113	2.28225071					
RT Rise [C]		0.7	0.6	1	0.9					
TC										
1		6.236	5.901	5.999	6.492		0.000	-0.335	-0.237	0.256
2		6.803	6.927	6.856	7.034		0.000	0.124	0.053	0.231
3		6.891	6.892	6.797	6.861		0.000	0.001	-0.094	-0.030
4		6.767	6.785	6.642	6.717		0.000	0.018	-0.125	-0.050
5		7.100	6.988	6.981	6.968		0.000	-0.112	-0.119	-0.132
6		6.962	7.015	6.896	6.846		0.000	0.053	-0.066	-0.116
7		7.025	6.979	6.895	6.760		0.000	-0.046	-0.130	-0.265
8		6.213	6.312	6.325	6.027		0.000	0.099	0.112	-0.186
	Ave	**6.750**	**6.725**	**6.674**	**6.713**		**0.000**	**-0.025**	**-0.076**	**-0.037**
				%Delta from Baseline			**0.0%**	**-0.4%**	**-1.1%**	**-0.5%**

Figure 6.2.46. Corrected Thermocouple Data shows 1.1% variance

The corrected thermocouple data showa variance of only 1.1 % from the baseline (Figure 6.2.46).

In Figure 6.2.47, the corrected thermocouple data for the final readings shows variance locations.

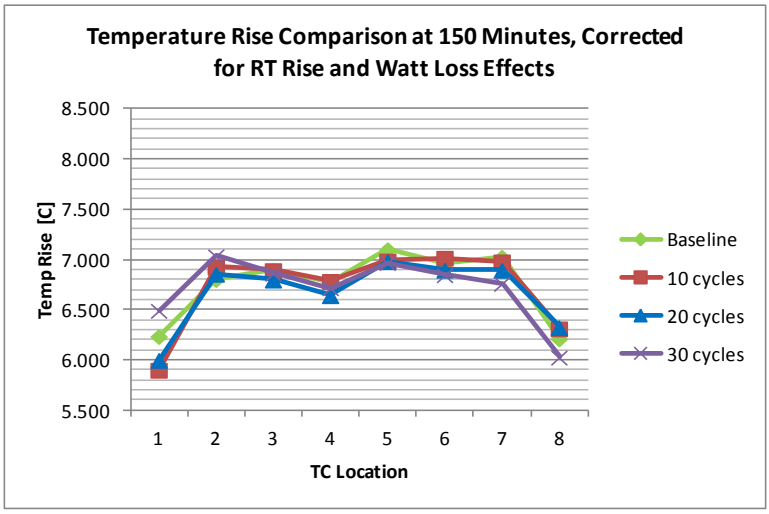

Figure 6.2.47. Corrected Thermocouple Data Showing Variance Locations

Figure 6.2.48 shows corrections made for ambient temperature changes in the enclosure over the sample.

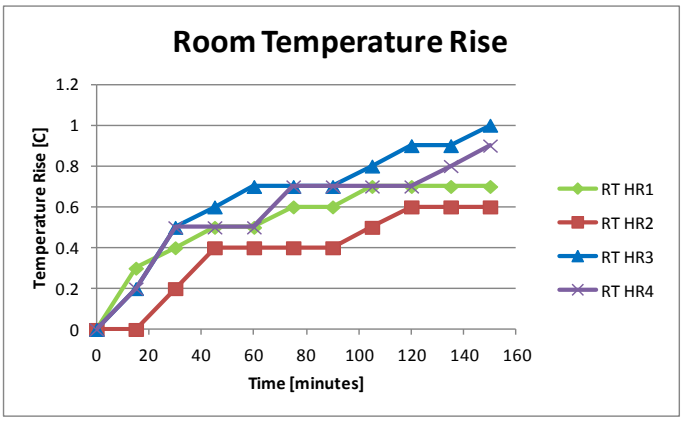

Room Temp Rise [C]		
Time	150 min	Percent Increase
RT HR1	0.7	0.0%
RT HR2	0.6	-14.3%
RT HR3	1	42.9%
RT HR4	0.9	28.6%

Figure 6.2.48. Corrections made for ambient temperature changes

Figure 6.2.49 shows corrections made for power changes into the sample. The conductor temperature rise varied almost 11% (improved cooling) (Figure 6.2.50).

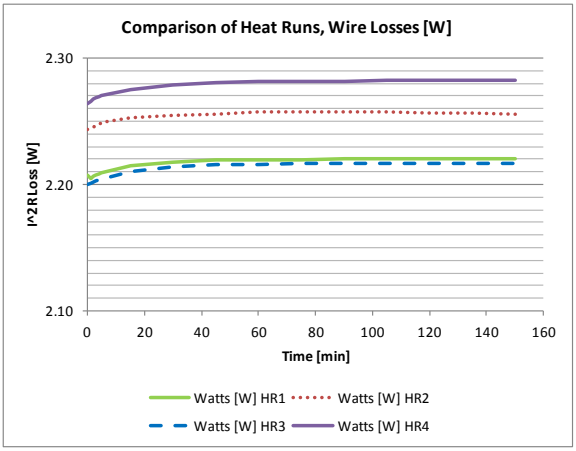

Conductor Loss at 150 minutes				
Test	HR1	HR2	HR3	HR4
Thermal Cycles	0 Cycles	10 Cycles	20 Cycles	30 Cycles
Rise [C]	2.2203	2.2557	2.2166	2.2823
Delta from Baseline	0.0000	0.0354	-0.0038	0.0619
Delta from Baseline	0.00%	1.59%	-0.17%	2.79%

Figure 6.2.49. Corrections made for power changes

Corrected for RT Rise and Loss										
		Conductor Temp rises [C] [@150 min]					Temp Rise Deltas from Baseline			
		Baseline	10 cycles	20 cycles	30 cycles		Baseline	10 cycles	20 cycles	30 cycles
Loss [W]		2.22033	2.25574	2.216581	2.282251					
RT Rise [C]		0.7	0.6	1	0.9					
Wire Rise {C]		9.609	8.596	9.032	9.710		0.000	-1.014	-0.577	0.101
				Delta from Baseline			**0.000**	**-1.014**	**-0.577**	**0.101**
				%Delta from Baseline			**0.0%**	**-10.5%**	**-6.0%**	**1.0%**

Figure 6.2.50. Corrected conductor temperature rise varied almost 11%.

Figure 6.2.51 shows corrected conductor temperature rise data, and Figure 6.2.52 shows the percent change in conductor temperature rise with thermal cycles.

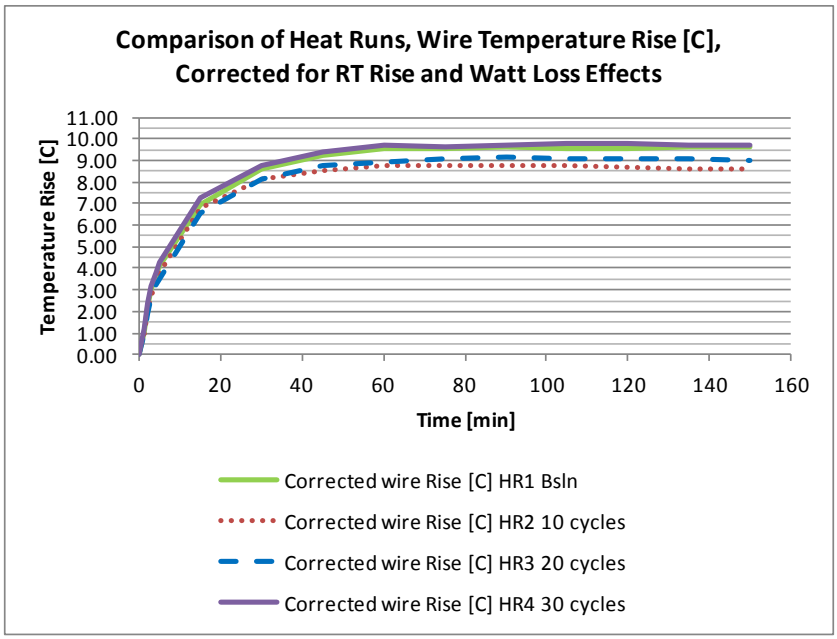

Figure 6.2.51. Corrected Conductor Temperature Rise Data

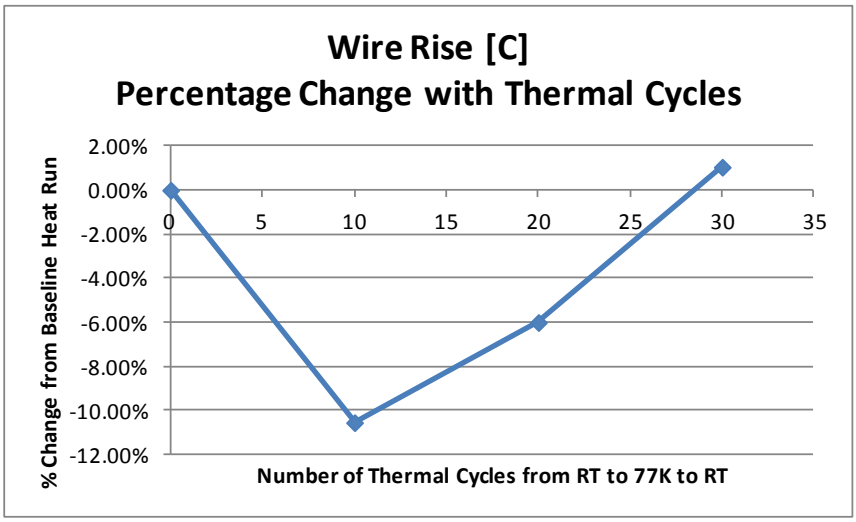

Figure 6.2.52. Percent change in conductor temperature rise with thermal cycles

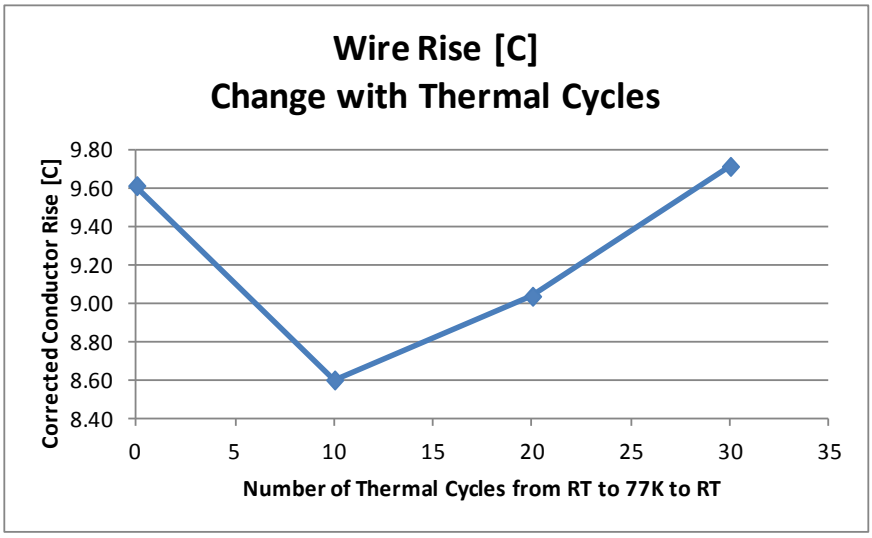

Figure 6.2.53. Change in conductor temperature rise with thermal cycles

Figure 6.2.53 shows the change in conductor temperature rise with thermal cycles. The maximum change is 1.014 C from the baseline for about 2.2 W losses in 10.5 inches of length (0.2095 W/inch). This compares to the FSG's AC loss of 400 W for a 28,750-m stator winding length (0.0003534 W/inch), roughly 600 times less.

Task 6.2b testing at the completion of all planned thermal cycles shows thermal performance is affected by thermal cycling in this configuration.

Although the conductor temperature rise was affected, compared to the baseline, the thermal performance changes in this testing were in a direction helpful to the thermal performance of the sample. Sample thermal performance eventually returned to the original behavior by the end of the planned number of thermal cycles.

The changes in thermal performance seem to be occurring at the outboard ends of the sample, based on the thermocouple results. This makes sense with the sample design. There is no restriction to "poke out" on the sample ends, with the design relying solely the inter-laminar shear strength of the 1 HLL of non-adhesive-backed Kapton. The Kapton behaves as a slip plane with no direct bonding of the Kapton to the conductor. There would only be a geometry-locking effect, dependent on tension-related insulation shape between adjacent cable strands. (How much the Kapton sucks into the valleys between the adjacent strands.)

With the axial symmetric configuration of the sample, maximum differential thermal movement would reach maximum at the ends of the sample, explaining the observed behavior.

The FSG, with its much longer length and restricted winding motion only at the extreme ends of the winding, will behave quite differently, making it difficult to interpret Task 6.2b results with regards to FSG risk.

Overall, Task 6.2b shows the Kapton insulation behaves like a slip plane, unable to restrict thermal movement of the conductor within. It shows that thermal performance of the insulation interfaces are affected in a very short length sample, compared to the much longer winding length proposed for the FSG. It reinforces the importance of precisely matching the thermal expansion/contraction of the conductor and composite.

COMTEC Activity

TT (Torque Tube) Material Testing

- Room temperature testing at COMTEC is complete; 4-K testing at CTD is complete.

Still needed

- Perform 90 K-mechanical testing at COMTEC.
- Use all test data with CompositePro software to provide FEA material properties.
- Assemble test summaries and write the report.

CC (Compliant Composite) Material Testing

- CC test coupons with the optimized thermal expansion/contraction properties were made for preliminary mechanical strength testing.
- Tensile tests were performed at 3, 5 and 7 days to determine room temperature.
- Cure needs 7 days to develop full strength.
- Since The CC material is not typical laminated composite, a new test matrix was needed to obtain the proper strength data.
- A test matrix for a filled composite was created, and a PO issued for the testing.

- Once the cure schedule was determined, manufacturing CC test coupons for further strength testing was completed and samples sent to CTD for 4-K testing.

No.	Test Description	ASTM Standard	Test Data Temperature Range (K)	# of Specimens	Sample Designation	Test Lab	Specimen Width mm (in)*	Specimen Length mm (in)*	Specimen Configuration
4.1	CC Material: tensile modulus, strength, and Poisson's ratio; E (Pa), S (Pa), NU.	D 638	295K	5 specimens	CC-4.1.1 to CC-4.1.5	COMTEC	19 (0.75)	165 (6.5) minimum	type I
4.1	CC Material: tensile modulus, strength, and Poisson's ratio; E (Pa), S (Pa), NU.	D 638	90K	1 specimen	CC-4.1.6	COMTEC	19 (0.75)	165 (6.5) minimum	type I
4.1	CC Material: tensile modulus, strength, and Poisson's ratio; E (Pa), S (Pa), NU.	D 638	4K	3 specimens	CC-4.1.7 to CC-4.1.9	CTD	19 (0.75)	165 (6.5) minimum	type I
4.2	CC Material: compression strength; -S (Pa).	D 6641	295K	5 specimens	CC-4.2.1 to CC-4.2.5	COMTEC	12 (0.5)	140 (5.5)	
4.2	CC Material: compression strength; -S (Pa).	D 6641	90K	1 specimen	CC-4.2.6	COMTEC	12 (0.5)	140 (5.5)	
4.2	CC Material: compression strength; -S (Pa).	D 6641	4K	3 specimens	CC-4.2.7 to CC-4.2.9	CTD	12 (0.5)	140 (5.5)	
4.3	CC Material: in-plane shear strength; SS (Pa).	D 3846	295K	5 specimens	CC-4.3.1 to CC-4.3.5	COMTEC	12.7 (0.5)	79.5 (3.13)	notched
4.3	CC Material: in-plane shear strength; SS (Pa).	D 3846	90K	1 specimen	CC-4.3.6	COMTEC	12.7 (0.5)	79.5 (3.13)	notched
4.3	CC Material: in-plane shear strength; SS (Pa).	D 3846	4K	3 specimens	CC-4.3.7 to CC-4.3.9	CTD	12.7 (0.5)	79.5 (3.13)	notched
4.4	CC Material: coefficient of thermal expansion, x-direction; CTEx (mm/mm/C).	**	4K to 295K	1 specimen	CC-4.4.1	CTD	38 (1.5)	38 (1.5)	
4.5	CC Material: coefficient of thermal expansion, y-direction; CTEy (mm/mm/C).	**	4K to 295K	1 specimen	CC-4.5.1	CTD	38 (1.5)	38 (1.5)	
4.6	CC Material: coefficient of thermal expansion, z-direction; CTEz (mm/mm/C).	**	4K to 295K	1 specimen	CC-4.6.1	CTD	38 (1.5)	38 (1.5)	
* mm to inch conversion is not consistent in the ASTM Standards, specimen sizes are taken directly from each ASTM Standard									
** Uses a CTD comparative strain gage method									

COMTEC supported 6.2b testing, making the test samples, performing the thermal cycles with immersion into LN2, providing the testing space for 6.2b, as well as assisting in data collection.

A larger degassing chamber was purchased and is now being used (Figure 6.2.54). The larger sample sizes for Task 6.4 testing requires preparing larger quantities of CC material in the same length of time.

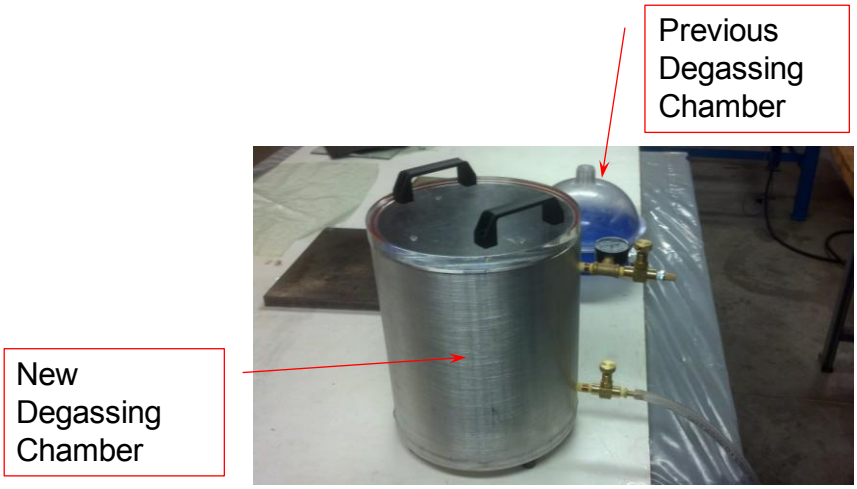

Figure 6.2.54. New degassing chamber in front of the previous chamber

This page removed due to Intellectual Property/Distribution Limitations

Task 6.2b

The test procedure for thermal cycling using LN2 has been perfected in testing of Sample 1 configuration, using 5 thicknesses of adhesive-backed Kapton. As testing processes were improved, the result changes only due to thermal change effects were deemed impossible to determine.

The improvements to the test methods developed on Sample 1 and the ability to determine the conductor temperature rise by resistance were used on Sample 2 containing 1 HLL of non-adhesive-backed Kapton. The thermocouples showed steady temperatures throughout the testing, while the conductor thermal behavior changed significantly. The conductor change was initially for the better, eventually returning to the original behavior.

Additional heat run tests for the modified Sample 2 (never thermal cycled) showed excellent repeatability for the test method when corrected for ambient temperature in the enclosure and power level applied.

Primary Conclusions from Task 6.2b:

- The Kapton insulation interface is responsible for the conductor thermal changes.
- The Kapton acts like a slip plane, unable to restrict conductor thermal movement.
- Readings support thermal change occurring mostly at the ends of the sample.
- Thermal expansion/contraction matching importance is shown. The conductor used for Task 6.2b is 316 SS. The expansion/contraction match may need to be even closer for the FSG.

Task 6.2 Plans for Next Quarter

- Obtain mechanical test data at 90 K for TT material.
- Obtain mechanical test data at RT, 90 K and 4 K for CC material.

3.2.3.3.7 Report period: January 1, 2014 to March 31, 2014 (Q7)

Task 6.2 Plans from Last Quarter

- Obtain mechanical test data at 90 K for TT material.

  Mechanical testing of the Torque Tube (TT) material is still on the task list. The focus was directed towards the Task 6.2b thermal cycle testing. This quarter, the focus was primarily on supporting Task 6.4 sample creation. 90 K data at COMTEC remains to be taken. Using the test data in CompositePro software to validate property values and a final material summary report also remain. The room temperature and 4 Kelvin data have provided enough comfort that there should be no surprises in the 90-K data.

- Obtain mechanical test data at RT, 90 K and 4 K for CC material.

  The coupons for the 4 Kelvin data were tested at CTD and results returned. The testing for room temperature is almost complete, save one remaining test and 90-K Kelvin testing has been planned.

Task 6.2 Major Activities

Task 6.2

Testing of the Compliant Composite (CC) material was completed at CTD (Composite Technology Development, Inc., 2600 Campus Drive, Suite D, Lafayette, CO 80026). The final report showed dramatic strength increase with sizable ductility reduction.

A low temperature stress-strain plot at 4 K is shown in Figure 6.2.55. A comparable room temperature stress-strain plot is shown in Figure 6.2.56.

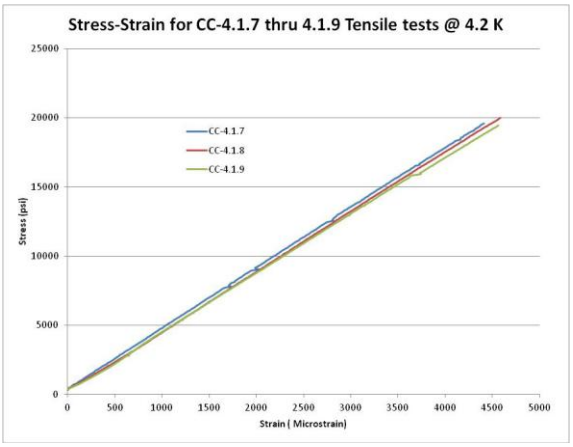

Figure 6.2.55. Low Temperature Stress-Strain Plot at 4 K

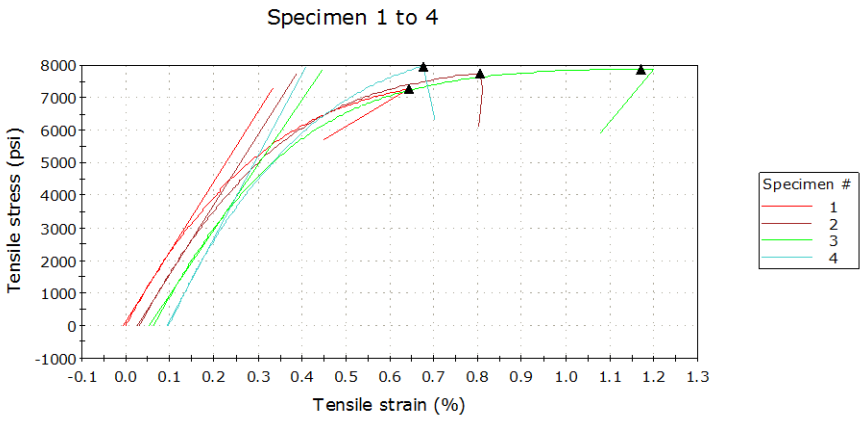

Figure 6.2.56. Room Temperature Stress-Strain Plot

Besides the strength testing, thermal expansion testing was performed showing nearly isotropic behavior and relatively good matching (within 23%) to 316 series stainless steel.

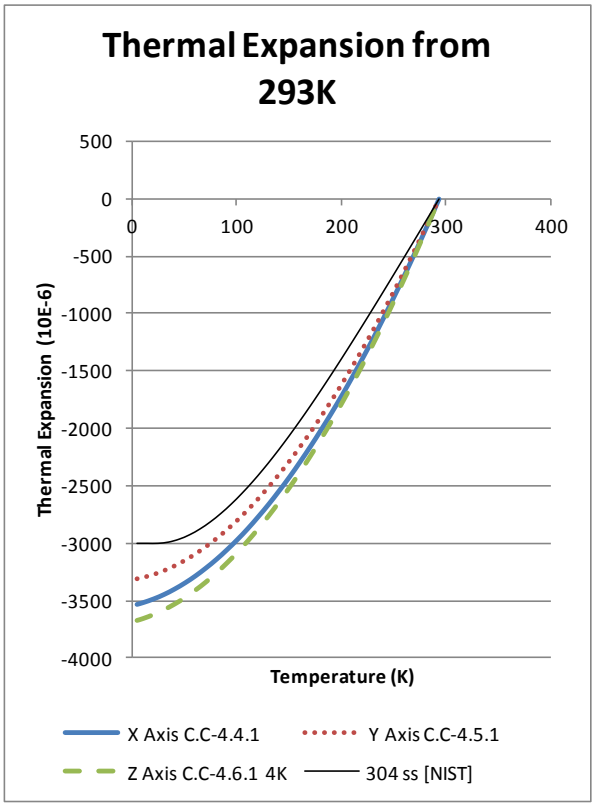

A summary of the results obtained through this quarter is shown below:

- Information for the CC material by test:

CC Material Data by Test			
Temperature[K]	**4.2**	**90**	**295**
Compression Strength (ave, psi)	83,300		18,519
Maximum shear stress (ave, psi)	10,600		5,764
Tensile Strength (ave, psi)	19,670		7,718
Tensile strain at Maximum Load (%)	0.45		0.78
Tensile Modulus (ave, psi)	4,350,000		2,201,600
Poisson's Ratio (ave)	0.31		

- The corresponding information for the TT material (Torque Tube):

TT Material Laminate Data by Test			
Temperature[K]	**4.2**	**90**	**295**
Compression Strength (laminate fiber dir, ave, psi)	128,300		51,793
Compression Strength (laminate Transverse dir, ave, psi)	31,100		10,874
Maximum shear stress (ave, psi)	20,000		5,089
Tensile Strength (laminate fiber dir, ave, psi)	166,000		84,296
Tensile Strength (laminate Transverse dir, ave, psi)	6,100		3,200
Tensile Modulus (laminate fiber dir, ave, psi)	5,700,000		5,887,082
Tensile Modulus (laminate, Transverse dir, ave, psi)	2,900,000		1,872,437
Poisson's Ratio (laminate fiber dir, ave)	0.29		0.318

TT Material Laminate Data by Test			
Temperature[K]	**4.2**	**90**	**295**
Tensile Strength (laminate axial dir. ave, psi)	**39,500**		**36,100**
Tensile Strength(laminate transverse dir, ave, psi)	**52,400**		**32,097**
Tensile Modulus (laminate axial dir, ave, psi)	**3,400,000**		**2,816,633**
Tensile Modulus (laminate transverse dir, ave, psi)	**3,200,000**		**2,816,633**
Poisson's Ration (ave)	**0.31**		**0.378**

COMTEC Activity

TT (Torque Tube) Material Testing

- Room temperature testing at COMTEC is complete.
- 4-K testing at CTD is complete.

Still Needed

- Perform 90-K mechanical testing at COMTEC.
- Use all test data with CompositePro software to provide FEA material properties.
- Assemble test summaries and write the report.

CC (Compliant Composite) Material Testing

- Room temperature testing at COMTEC is one sample short of complete.
- 4-K testing at CTD is complete.

Still needed

- Perform 90-K mechanical testing at COMTEC.

CC Material Technology Transfer

On 28 February, Gerry Stelzer and Jamison Farrell from AML traveled to COMTEC to learn the details for making CC Material. A trial sample for the Task 6.4 thermal cycle testing was made during the training, given by Dr. Dennehy. The images below show highlights from the meeting:

Discussing mold design

Discussing conductor insulation method

Demonstrating mixing method

Oven viscosity control

Composite degassing

Loading dispenser tube

Filling mold

Ready for cure

Check out of parts for Task 6.4 assembly

This page removed due to Intellectual Property/Distribution Limitations

operating temperature. The increased modulus means the thermal matching needs to be even closer to the much stronger metals in the structure.

- The loss of ductility (strain capability) is bad for the design since the allowed distortions at failure will be reduced and the brittle nature of any failure could cause extreme composite damage instantly. To avoid failures of this type, more conservative design limits are needed.

Task 6.2 Plans for Next Quarter

- Finish the 90-K testing.
- Establish design material limits for Task 4.0.

3.2.3.3.8 Report period: April 1, 2014 to June 30, 2014 (Q8)

Task 6.2 Plans from Last Quarter:

- Finish the 90-K testing.

  Mechanical testing of the Torque Tube (TT) material is complete. The tested data was combined with calculations from CompositePro software to provide FEA properties for use during Task 4.0.

  The CC material testing was also completed this quarter. The finalized CTD report is expected soon.

- Establish design material limits for Task 4.0.

  Testing results show failure limits for both materials. The tested values represent the catastrophic failure limits, with complete failure of all coupon layers occurring. For operation, the single ply failure criteria, when the first crack is predicted in the TT material, may be a better, more conservative limit.

Task 6.2 Major Activities

- Testing of the Compliant Composite (CC) material was completed. A spreadsheet of the tested values was generated. The CTD results are labeled preliminary, pending receipt of the final report for the 90-K data. A summary of the results is shown below:

compliant composite test results

material property	test designation	295 K (room temp)							90 K							4 K						
		test lab	units	avg	st dev	units	avg	std dev	test lab	units	avg	st dev	units	avg	std dev	test lab	units	avg	st dev	units	avg value	std dev
Tensile Modulus	4.1	COMTEC	ksi	2201.6	223.7	Pa	1.518E+10	1.542E+09	CTD	ksi	3900.0	n/a	Pa	2.689E+10	n/a	CTD	ksi	4350.0	70.0	Pa	2.999E+10	4.826E+08
Tensile Strength	4.1	COMTEC	ksi	7.654	0.307	Pa	5.277E+07	2.119E+06	CTD	ksi	19.500	n/a	Pa	1.344E+08	n/a	CTD	ksi	19.670	0.270	Pa	1.356E+08	1.862E+06
Poisson's Ratio	4.1			0.290	n/a				CTD		0.330	n/a				CTD		0.310	0.010			
Compressive Strength	4.2	COMTEC	ksi	18.519	0.331	Pa	1.277E+08	2.282E+06	COMTEC	ksi	85.319	n/a	Pa	5.883E+08	n/a	CTD	ksi	83.300	5.300	Pa	5.743E+08	3.654E+07
In-plane Shear Strength	4.3	COMTEC	ksi	5.764	0.049	Pa	3.974E+07	3.378E+05	COMTEC	ksi	7.717	n/a	Pa	5.321E+07	n/a	CTD	ksi	10.600	1.100	Pa	7.308E+07	7.584E+06
CTE x-direction	4.4	CTD				m/m/C	2.10E-05	n/a	CTD				m/m/C	8.60E-06	n/a	CTD				m/m/C	2.40E-06	n/a
CTE y-direction	4.5	CTD				m/m/C	1.97E-05	n/a	CTD				m/m/C	8.00E-06	n/a	CTD				m/m/C	1.80E-06	n/a
CTE z-direction	4.6	CTD				m/m/C	2.19E-05	n/a	CTD				m/m/C	8.90E-06	n/a	CTD				m/m/C	2.60E-06	n/a

rule of mixtures estimate:
(0.65)(0.23)+(0.35)(0.40) = 0.2895
at 293 K
CTD preliminary results
specimen CC-4.2.7 well below other two 4K specimens (77.4, 87.5, 85.1) driving avg below 90K result

A summary of results for the TT material was combined with calculations from CompositePro software to produce material properties suitable for structural FEA:

torque tube laminate material properties

material property	test designation	295 K (room temp)								90 K								4 K							
		CompositePro				test lab	units	avg	std dev	CompositePro				test lab	units	avg	std dev	CompositePro				test lab	units	avg	std dev
		units	value	units	value					units	value	units	value					units	value	units	value				
Ex	4.10-B	psi	2.883E+06	Pa	1.988E+10	COMTEC	psi	2.652E+06	3.306E+05	psi	3.190E+06	Pa	2.200E+10	CTD	psi	4.300E+06		psi	3.664E+06	Pa	2.527E+10	CTD	psi	3.400E+06	2.000E+05
Ey	4.11-A	psi	2.883E+06	Pa	1.988E+10	COMTEC	psi	2.974E+06	2.244E+05	psi	3.190E+06	Pa	2.200E+10	CTD	psi	3.400E+06		psi	3.664E+06	Pa	2.527E+10	CTD	psi	3.200E+06	2.000E+05
Ez		psi	1.994E+06	Pa	1.375E+10					psi	2.572E+06	Pa	1.773E+10					psi	3.114E+06	Pa	2.147E+10				
Gxy		psi	1.047E+06	Pa	7.219E+09					psi	1.196E+06	Pa	8.247E+09					psi	1.390E+06	Pa	9.587E+09				
Gxz		psi	4.827E+05	Pa	3.328E+09					psi	1.009E+06	Pa	6.953E+09					psi	1.167E+06	Pa	8.043E+09				
Gyz		psi	4.827E+05	Pa	3.328E+09					psi	1.009E+06	Pa	6.953E+09					psi	1.167E+06	Pa	8.043E+09				
NUxy	4.10-B		3.766E-01			COMTEC		3.780E-01	5.279E-02		3.336E-01		3.336E-01	CTD	psi	4.300E-01			3.177E-01		3.177E-01	CTD	psi	3.100E-01	3.000E-02
NUyx	4.11-A		3.766E-01			COMTEC		3.610E-01	4.644E-02		3.336E-01		3.336E-01						3.177E-01		3.177E-01				
NUxz			2.848E-01								3.674E-01		3.674E-01						3.485E-01		3.485E-01				
NUzx			1.970E-01								2.962E-01		2.962E-01						2.962E-01		2.962E-01				
NUyz			2.848E-01								3.674E-01		3.674E-01						3.485E-01		3.485E-01				
NUzy			1.970E-01								2.962E-01		2.962E-01						2.962E-01		2.962E-01				
CTEx	4.12-A	in/in/F	6.865E-06	m/m/C	1.236E-05	CTD	m/m/C	1.11E-05		in/in/F	3.076E-06	m/m/C	5.538E-06	CTD	m/m/C	5.8E-06		in/in/F	1.384E-06	m/m/C	2.492E-06	CTD	m/m/C	2.6E-06	
CTEy	4.13-A	in/in/F	6.865E-06	m/m/C	1.236E-05	CTD	m/m/C	1.57E-05		in/in/F	3.076E-06	m/m/C	5.538E-06	CTD	m/m/C	8.0E-06		in/in/F	1.384E-06	m/m/C	2.492E-06	CTD	m/m/C	2.9E-06	
CTEz	4.14-A	in/in/F	1.647E-05	m/m/C	2.964E-05	CTD	m/m/C	4.23E-05		in/in/F	6.720E-06	m/m/C	1.210E-05	CTD	m/m/C	3.16E-05		in/in/F	3.278E-06	m/m/C	5.900E-06	CTD	m/m/C	1.42E-05	
Kx		Btu/hr/ft/F	1.855E-01	W/m/K	3.209E-01					Btu/hr/ft/F	8.310E-02	W/m/K	1.438E-01					Btu/hr/ft/F	1.596E-02	W/m/K	2.760E-02				
Ky		Btu/hr/ft/F	1.855E-01	W/m/K	3.209E-01					Btu/hr/ft/F	8.310E-02	W/m/K	1.438E-01					Btu/hr/ft/F	1.596E-02	W/m/K	2.760E-02				
Kz		Btu/hr/ft/F	0.000E+00	W/m/K	0.000E+00					Btu/hr/ft/F	0.000E+00	W/m/K	0.000E+00					Btu/hr/ft/F	0.000E+00	W/m/K	0.000E+00				
Den		lb/in3	7.048E-02	g/m3	1.951E+06					lb/in3	7.048E-02	g/m3	1.951E+06					lb/in3	7.048E-02	g/m3	1.951E+06				
Sx	4.10-B	psi	4.930E+03	Pa	3.399E+07	COMTEC	psi	3.610E+04	2.070E+02	psi	9.570E+03	Pa	6.598E+07	CTD	psi	4.270E+04		psi	7.690E+03	Pa	5.302E+07	CTD	psi	3.950E+04	1.400E+03
		psi	2.663E+04							psi	2.550E+04							psi	2.700E+04						
Sy	4-11-A	psi	7.510E+03	Pa	5.178E+07	COMTEC	psi	3.350E+04	1.141E+03	psi	1.435E+04	Pa	9.894E+07	CTD	psi	5.940E+04		psi	1.147E+04	Pa	7.908E+07	CTD	psi	5.240E+04	1.700E+03
		psi	2.888E+04							psi	4.200E+04							psi	5.813E+04						
-Sx		psi	-1.673E+04	Pa	-1.153E+08					psi	-3.058E+04	Pa	-2.108E+08					psi	-3.328E+04	Pa	-2.295E+08				
-Sy		psi	-1.308E+04	Pa	-9.018E+07					psi	-2.861E+04	Pa	-1.973E+08					psi	-2.401E+04	Pa	-1.655E+08				
Sxy		psi	4.140E+03	Pa	2.854E+07					psi	8.280E+03	Pa	5.709E+07					psi	6.730E+03	Pa	4.640E+07				

CompositePro value is for first ply failure.
CompositePro value is for ultimate failure (for comparison to test value).
CTD preliminary results

- The corresponding information for the CC material (Compliant Composite):

CC Material Data by Test			
Temperature[K]	**4.2**	**90**	**295**
Compression Strength (ave, psi)	83,300	85,319	18,519
Maximum shear stress (ave, psi)	10,600	7,717	5,764
Tensile Strength (ave, psi)	19,670	19,500	7,718
Tensile strain at Maximum Load(%)	0.45	0.50	0.78
Tensile Modulus (ave, psi)	4,350,000	3,900,000	2,201,600
Poisson's Ratio (ave)	0.31	0.33	0.29

TT Material Laminate Data by Test			
Temperature[K]	**4.2**	**90**	**295**
Tensile Strength (ultimate, laminate axile dir, ave, psi)	**27,000**	**25,500**	**26,630**
Tensile Strength (ultimate, laminate Transverse dir, ave, psi)	**58,130**	**42,000**	**28,880**
Tensile Modulus(laminate axial dir, ave, psi)	**3,664,000**	**3,190,000**	**2,883,000**
Tensile Modulus(laminate Transverse dir, ave, psi)	**3,664,000**	**3,190,000**	**2,883,000**
Poisson's Ratio (ave)	**0.3177**	**0.3336**	**0.3766**

- The corresponding information for the TT material (Torque Tube):

TT Material Laminate Data by Test			
Temperature[K]	**4.2**	**90**	**295**
Tensile Strength (First ply, laminate axial dir, ave, psi)	7,690	9,570	4,930
Tensile Strength (First ply, laminate Transverse dir, ave, psi)	11,470	14,350	7,510
Compressive Strength (First ply, laminate axial dir, ave, psi)	-33,280	-30,580	-16,730
Compressive Strength (First ply, laminate Transverse dir, ave, psi)	-24,010	-28,610	-13,080
Shear Strength (First ply, laminate in plane shear dir, ave, psi)	7,690	9,570	4,930
Tensile Modulus (laminate axial dir, ave, psi)	3,664,000	3,190,000	2,883,000
Tensile Modulus (laminate Transverse dir, ave, psi)	3,664,000	3,190,000	2,883,000
Poisson's Ratio (ave)	0.3177	0.3336	0.3766

COMTEC Activity

CC (Compliant Composite) and TT (Torque Tube) Material Testing

90 K testing was performed at COMTEC:

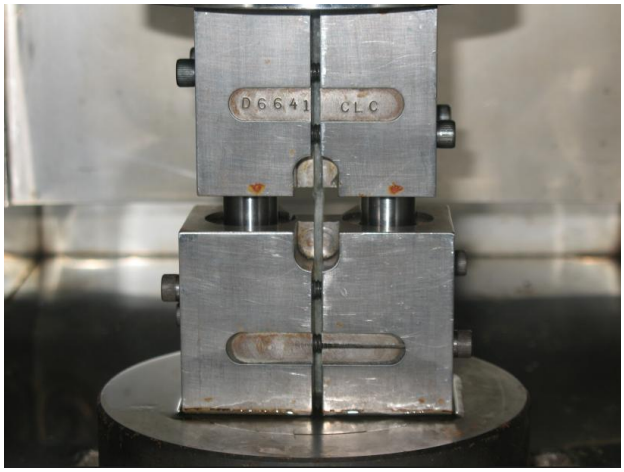

This page removed due to Intellectual Property/Distribution Limitations

References

[1] "A National Offshore Wind Strategy: Creating an Offshore Wind Energy Industry in the United States," U.S. Department of Energy, February 2011.
[2] "Critical Materials Strategy," U.S. Department of Energy, December 2011.
[3] "Electromagnetic Optimization of Direct-Drive Generators," D. Bang and H. Polinder, UpWind Project, October 2010.
[4] Technical presentation by Columbus Superconductor, October 2011.
[5] Hypertech Private Conversation
[6] http://ecmweb.com/market_trends/electric_path_least_resistance_2/)
[7] "DOE Technology Readiness Assessment Guide," DOE G 413.3-4A, U.S. Department of Energy, September 15, 2011.
[8] "Optimal Rotor Tip Speed Ratio," M. Ragheb, 2011.
[9] Modeling and Analysis of Variable Speed Wind Turbines with Induction Generator during Grid Fault," Sigrid M. Bolik, Institute of Energy Technology, Aalborg University, 2004.
[10] Goodzeit, Carl. Re-entrant shaft. U.S. Patent 7,791,229, Washington, D.C.: U.S.
[11] "Behavior of a 14-cm Bore Solenoid with Multifilament MgB2 Tape," M. Alessandrini, et al., ASC 2006, Seattle, August 2006.
[12] "Fabrication and transport properties of superconducting MgB2 cables", T Hol´ubek et al., Supercond. Sci. Technol. 22 (2009) 055011.
[13] "Winding and Testing of Large Bore Solenoids and Study of Quench Propagation in Short Coils Made With Multifilament MgB2 Tape," M. Alessandrini, et al., IEEE Transactions on Applied Superconductivity, Vol. 18, No. 2, June 2008.
[14] http://www.htess.com/hepak.htm
[15] "Robust Multilayer Insulation for Cryogenic Systems," J. E. Fesmire, S. D. Augustynowicz, and B. E. Scholtens, AIP Conf. Proc. 985, 1359 (2008).
[16] "Development of helium transfer coupling of 1 MW-class HTS motor for podded ship," E. Kosuge, Y. Gocho, K. Okumura, M. Yamaguchi, K. Umemoto, K. Aizawa, M. Yokoyama, and S. Takao, Journal of Physics: Conference Series Vol. 234, 2010.
[17] http://www.ferrolabs.com/en/products/full/31/
[18] "Maintenance-free alternatives to brush-based electrical transfer systems capable of increased power handling across a rotary interface", Michael T Howard, Diamond-Roltran, April 10, 2009.
[19] "Design, Construction and Tests of MgB2 Coils for the Development of a Cryogen Free Magnet", M. Modica et al., IEEE Transactions on Applied Superconductivity, Vol. 17, No. 2, June 2007.
[20] "Wind Turbine Design Cost and Scaling Model," L. Fingersh, M. Hand, and A. Laxson, National Renewable Energy Laboratory, December 2006.
[21] "Comparative Assessment of Direct-Drive High Temperature Superconducting Generators in Multi-Megawatt Class Wind Turbines," B. Maples, M. Hand, and W, Musial, National Renewable Energy Laboratory, October 2010.
[22] "Executive Summary WP4: Offshore Foundations and Support Structures," T. Fischer, UpWind Project, January 2011.
[23] "O&M Aspects of the 500 MW Offshore Wind Farm at NL7," L. W. M. M Rademakers and H. Braam, DOWEC Project, July 2002.

[24] "Technology Improvement Opportunities for Low Wind Speed Turbines and Implications for Cost of Energy Reduction," National Renewable Energy Laboratory, February 2008.
[25] DOE Status Mtg. Presentation 13, 6/9/14: slide 22, 2- bearing configuration including: FSG, converter, cryocooler, excitation
[26] AML BP1 final report, A.2.6.1
[27] DTU 10-MW Reference Turbine Report (MS: geared, medium-speed drivetrain)
[28] BP1 final report, A.2.6.1. Nacelle mass, for FSG and PMG, assumes generator mass plus 136 MT for balance of 'nacelle', based on 'PMDD' masses.
[29] "2011 Cost of Wind Energy Review," S. Tegen, E. Lantz, M. Hand, B. Maples, A. Smith, and P. Schwabe, Technical Report NREL/TP-5000-56266, March 2013.
[30] "Effect of grain refinement on enhancing critical current density and upper critical field in undoped MgB2 ex-situ tapes," A. Malagoli, V. Braccini, M. Tropeano, M. Vignolo, C. Bernini, C. Fanciulli, G. Romano, M. Putti, C. Ferdeghini, E. Mossang, A. Polyanskii, D.C. Larbalestier, Journal of Applied Physics, 104, 103908 (2008).
[31] "High-Energy Ball Milling and Synthesis Temperature Study to Improve Superconducting Properties MgB2 Ex-situ Tapes and Wires," G.Romano, M.Vignolo, V.Braccini, A.Malagoli, C.Bernini, M.Tropeano, C.Fanciulli, M.Putti, and Carlo Ferdeghini, IEEE Transactions on Applied Superconductivity, Vol. 19, No 3, June 2009.

Appendix A: Advanced Magnet Lab's Fully Superconducting Drivetrain Levelized Cost of Energy Study

NREL
NATIONAL RENEWABLE ENERGY LABORATORY

Advanced Magnet Lab's Fully Superconducting Drivetrain – Levelized Cost of Energy Study

E. Warner

With contributions by B. Maples

Produced under direction of AML Superconductivity and Magnetics by the National Renewable Energy Laboratory under Work for Others Agreement number TSA 14-645 and Task No WTJG.1000.

Work for Others Report

NREL/TP-5000-62844

NREL
NATIONAL RENEWABLE ENERGY LABORATORY

Advanced Magnet Lab's Fully Superconducting Drivetrain – Levelized Cost of Energy Study

Prepared under Task No. WTJG.1000

NREL is a national laboratory of the U.S. Department of Energy, Office of Energy Efficiency & Renewable Energy, operated by the Alliance for Sustainable Energy, LLC.

National Renewable Energy Laboratory
15013 Denver West Parkway
Golden, CO 80401
303-275-3000 • www.nrel.gov

Work for Others Report

NREL/TP-5000-62844
Contract No. TSA 14-645

NOTICE

Cover Photos: (left to right) PIX 16416, PIX 17423, PIX 16560, PIX 17613, PIX 17436, PIX 17721

Printed on paper containing at least 50% wastepaper, including 10% post consumer waste.

List of Acronyms

AEP_{net}	Net Annual Energy Production
AML	Advanced Magnet Lab
BOS_{cc}	Balance of System Capital Cost
DOE	Department of Energy
DR	Discount Rate
FSG	Fully Superconducting Generator
hrs	Hours
IWF	Insurance, Warranty and Fees
ICC	Initial Installed Capital Cost
km	Kilometer
kWh	Kilowatt-hours
LCOE	Levelized Cost of Energy
m	Meter
mil	Million
O&M	Levelized O&M Cost
PMDD	Permanent Magnet Direct-drive
Sc	Soft Costs
T	Effective State and Federal Tax Rate
TUR_{cc}	Turbine Capital Cost
year	Year

Table of Contents

List of Figures

List of Tables

1. Review of Project Objectives

The following documentation is intended to serve as a summary of the levelized cost of energy (LCOE) analysis for the Advanced Magnet Lab's (AML's) fully superconducting drivetrain study.

The Wind and Water Power Program within the U.S. Department of Energy's (DOE) Office of Energy Efficiency and Renewable Energy is interested in developing next-generation drivetrain technologies. Developing these technologies could reduce the cost of energy produced by wind turbines. DOE's release of Funding Opportunity Announcement (FOA) 439 seeks to help develop a next-generation wind turbine drivetrain through industry partnerships (DOE 2011).

AML has a 10-MW fully superconducting generator (FSG) turbine concept for offshore wind. AML's FSG was developed as part of the DOE innovative drivetrain FOA 439. AML's proposed generator concept is predicted to be lighter than the mass of a conventional geared drivetrain system or a permanent-magnet direct-drive (PMDD) turbine.

This report details the levelized cost of energy (LCOE) of a hypothetical 300-MW offshore wind farm using a baseline 10-MW PMDD turbine and AML's novel 10-MW FSG turbine concept. LCOE is used to evaluate the cost savings of AML's proposed next-generation drivetrain technology with respect to the baseline PMDD turbine. AML seeks to identify the tower mass savings and LCOE improvement arising from reduced drivetrain mass and the higher electrical system efficiency of their FSG turbine concept compared to a PMDD turbine. AML also seeks to understand the cost savings from a service-removable generator, which would avoid the removal of the turbine rotor in the event of a generator replacement.

NREL's work focused on:

- Developing tower designs using NREL's systems engineering analytical modeling tool and based on the DTU external loading condition and the prescribed tower head masses to estimate tower mass savings
- Estimate balance-of-system (BOS) costs using NREL's offshore BOS tool (Maples et al. forthcoming)
- Estimate net annual energy production (AEP_{net}) and operation and maintenance (O&M) costs of the FSG turbine using drivetrain efficiency assumptions provided by AML
- Reviewing and updating AML's turbine component costs

2. Methods

NREL used the LCOE equation provided by DOE (2011) to calculate the cost of energy for the baseline PMDD turbine and AML's novel FSG turbine concept. The LCOE reductions of AML's novel FSG turbine concept are shown by comparing hypothetical wind farms of thirty 10-MW turbines using the FSG turbines versus conventional PMDD turbines. An alternative nacelle configuration with a service removable generator for quicker generator exchanges is also presented (FSG – Alternative).

2.1 LCOE Equation

The LCOE analysis approach provides an all-inclusive, cradle-to-grave analysis of costs and energy production related to a power production facility. LCOE analysis permits the evaluation of the total cost of an offshore wind project, including capital investment costs (including installation), O&M costs, finance costs, and estimated energy production. The LCOE analysis approach does not consider policy incentives such as the production tax credit, the impacts of underlying economic conditions such as an economic recession, and project-support costs such as transmission lines and grid integration.

The inputs to the LCOE model are as follows:

$$LCOE = \frac{(DR + IWF) * ICC + O\&M(1 - T)}{AEP_{net}}$$

Where:	LCOE		=	Levelized Cost of Energy ($/kWh) (constant dollars)
	DR		=	Discount Rate (1/yr) = **7%**
	IWF		=	Insurance, Warranty, and Fees (1/yr) = **1%**
	ICC		=	Initial Installed Capital Cost ($)
		ICC	=	TUR_{cc} + BOS_{cc} +S_c
		TUR_{cc}	=	Turbine Capital Cost ($)
		BOS_{cc}	=	Balance-of-System Capital Cost ($)
		S_c	=	Soft Cost ($)
	O&M		=	Levelized O&M Cost ($/yr)[1]
	T		=	Effective State and Federal Tax Rate = **40%**
	AEP_{net}		=	Net Annual Energy Production (kWh/yr)

[1] Includes levelized replacement/overhaul costs

The LCOE model provided by DOE (2011) has five major inputs. The inputs ICC, O&M, and AEP enable an estimation of system-level impacts from design changes. Sections 4 through 8 develop or document estimates for these major LCOE input components for three scenarios. The costs of financing inputs in the above equation—DR and IWF—represent assumptions about finance charges, debt or equity repayment, and the cost of capital. DR and IWF are provided by DOE (2011).All costs, unless otherwise noted, represent 2009 U.S.$ to maintain consistency with the data provided by AML (2014a).

2.2 Models

LCOE estimates for offshore wind project scenarios were developed by applying NREL's BOS and ECN's O&M models to estimate the cost of relevant components as well as system performance.

2.2.1 Offshore Wind BOS Model

NREL's offshore BOS model estimates capital expenditures associated with installation activities and other BOS costs (Maples et al. unpublished). The model was built on data provided to NREL by GL Garrad Hassan (see GL Garrad Hassan [2012] unpublished and Elkinton et al. [2012]) in a report investigating the major contributions to U.S. offshore wind-project BOS costs. This data covered the key cost drivers and trends and provided typical values, expected ranges, and assumptions made based on 2010 technology and best practices. GL Garrad Hassan drew from active participation in offshore wind projects in Europe, along with its experience in the onshore wind industry in the United States.

The model is capable of calculating budgetary-level estimates related to:

- Development costs such as project management, engineering, permitting, and site assessment
- Ports and staging costs such as storage rental, crane rental, and port entrance and docking fees
- Support structure costs such as for primary steel, secondary steel, and the transition piece
- Electrical infrastructure costs such as for array cable, export cable, and the offshore substation
- Vessel costs such as for a heavy-lift vessel, jack-up vessel, or offshore barge
- Decommissioning such as cable removal and scour removal

The BOS model does not estimate exact periods of weather downtime. The model instead assumes that all installation vessels are contracted for the entire length of the construction period. Weather downtime is, however, calculated to demonstrate its relative impact on offshore installation operations by establishing a non-exceedance distribution based on wind and wave restrictions for each vessel and operation. Based on the non-exceedance distribution and the restriction of the vessel or operation, an average waiting time is assigned and added to the overall installation time. This non-exceedance methodology likely underestimates waiting time because it does not 1) look at correlated wind wave distributions (e.g., for a given weather window the wind limit might appear acceptable, but the wave limit might be exceeded); 2); account for "workable" weather windows (e.g., some weather windows might be too short to perform any meaningful work); or 3) account for dependencies among procedures.

2.2.2 ECN Offshore Wind O&M Tool

ECN's offshore wind O&M software Version 4 (Obdam et al. 2011) was used to model O&M costs for project scenarios. The ECN model was developed to estimate the long-term annual average costs and downtime of an offshore wind farm. ECN has the only software validated worldwide for analyzing offshore wind O&M, and in 2007 the tool received a validation statement from Germanischer Lloyd (ECN Wind Industrial Support 2012).

The tool uses long-term average data provided by the user as input (failure rates, wind and wave statistics, costs of vessels and spare parts, lead time of vessels and spare parts, etc.) and generates long-term average values as output (costs, downtime, and required resources). Modified to represent U.S.-specific vessel capabilities, costs, and met ocean data, the tool can be used to estimate the O&M requirements of offshore wind projects. The model outputs most relevant to this analysis are the O&M costs and the associated downtimes of the wind turbines and the BOS. The O&M tool is most appropriate when used in the planning phase of a wind farm. The ECN O&M tool's major limitation is lack of available offshore wind data. The cost and downtime estimates for corrective wind turbine maintenance are therefore uncertain.

The level of effort required for O&M activities over the life of a wind plant can typically be characterized by a common bathtub curve, as shown in Figure 1. The shape of the bathtub curve is derived from the high level of corrective maintenance required both during the commissioning or break-in period and again approaching the end of design life for the wind plant and the relatively steady amount of preventive maintenance throughout the lifespan of the wind plant. The ECN O&M tool, however, estimates the long-term average annual corrective and preventive maintenance costs and produces a flat average cost over the lifetime of the wind plant. The tool also calculates the average annual downtime associated with corrective and preventive maintenance. This is used to calculate wind plant availability in addition to the long-term average annual maintenance cost.

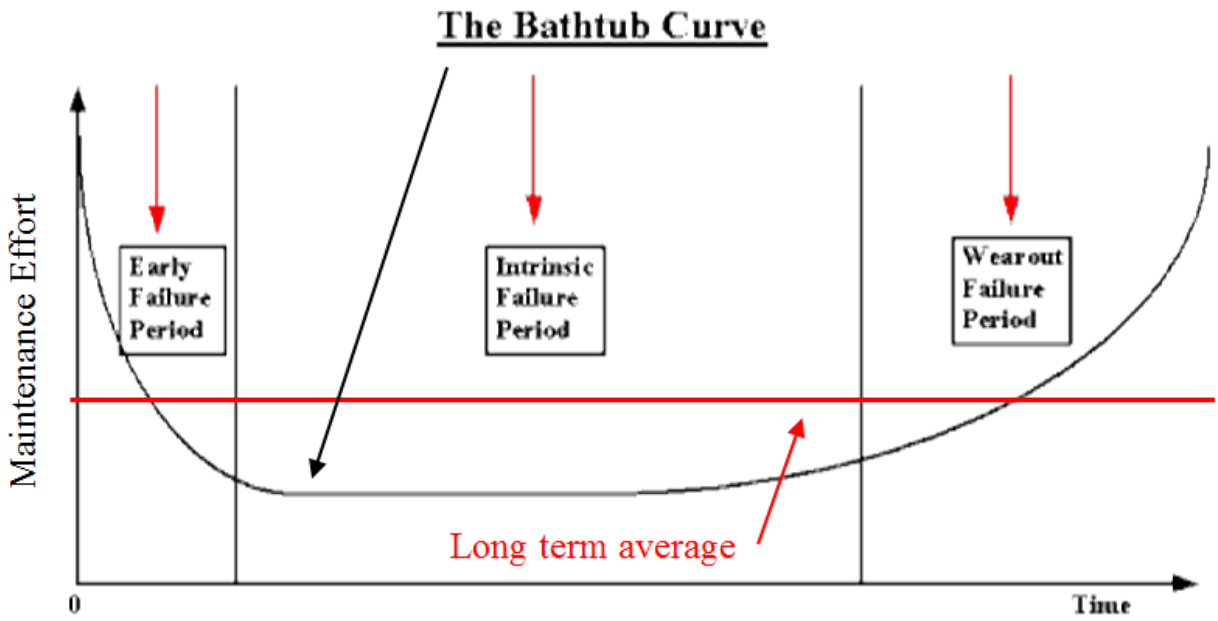

Figure 1. Example of estimated O&M efforts over the life of a wind turbine plant using the ECN O&M tool Source: Hembree et al. (2010)

3. Operating Parameters

Table 1 summarizes the operating parameters for the wind farms investigated, which consist of 30 10-MW turbines located in the Virginia wind energy area at a water depth of 28.5 m and 46 km distance from shore. The nearest port that is accessible for large vessels is the Port of Virginia, at an approximate distance of 86 km; it will serve as both the installation and O&M port facility. Power production estimates were calculated using a mean hub-height wind speed of 8.6 m/s, assuming a Weibull wind speed probability distribution and a 1/7-Power Law wind shear profile.

Table 1. Operating Parameters for Baseline Turbine and Wind Farm

Category	Baseline 500-MW Farm
Wind Plant Rating (MW)	300
# of Turbines	30
System Design Life (years)	20
Turbine Rating (kW)	10,000
Rotor Diameter (m)	172
Hub Height (m)	116
Drivetrain Type	PMDD, FSG
Substructure Type	Jacket
Distance to Shore (km)	46
Distance to Port (km)	86
Water Depth (m)	28.5
Wind Speed at HH (m/s)	8.63
Weibull K	2
Wind Shear	0.14
Air Density (kg/m^3)	1.225

The only long-term available data set with high recovery rates for correlated wind and wave measurements is the Wavewatch III hindcast wind and wave data for grid point 63198, covering the period from 01-Jan-2000 through 31-Dec-2009. This data set was used in the BOS and O&M cost models to calculate available installation and maintenance weather windows. Measured data from the Chesapeake Bay Light Tower (CHLV2) and buoy station 44099 correlate well to the hindcast data.

4. Turbine Capital Cost (TUR_{cc})

Turbine costs were estimated based on data provided by AML (2014a, 2014e). Several costs changes were made that are related to establishing consistency in the LCOE analysis and updating old data. Turbine costs are summarized in Table 2.

Marinization costs for the turbine were removed because they are no longer applicable to TUR_{cc} estimates because turbines are now designed specifically for the offshore environment instead of modifying land-based turbines. Support structure costs are included in BOS costs in Section 5. Tower costs were estimated by applying a $/kg value to the mass estimates conducted by NREL. It should be noted that the tower analysis was conducted for a land-based turbine, and results may be different for offshore applications.

Table 2. Summary of Turbine Capital Costs

Component	PMDD Turbine (US_{2009}$/turbine)	FSG Turbine - Baseline (US_{2009}$/turbine)
Rotor	3,027,372	3,027,372
Drivetrain, nacelle	8,090,942	5,671,332
Tower	1,539,697	1,541,986
Total	**12,658,011**	**10,240,690**

5. Balance of System Capital Costs (BOS_{cc})

BOS costs were estimated using NREL's offshore BOS model and are summarized in Table 3. The major cost difference between the PMDD and FSG turbine is related to the substructure. Substructure costs for the FSG turbine are lower due to the lighter generator, which translates to a roughly 10-tonne lighter substructure. This substructure mass reduction is in contrast to the findings of the tower study, which indicated no significant tower mass reduction for the FSG turbine due to the applied frequency constraints. The substructure cost model is based on turbine rating, hub height, water depth, and tower top mass, but it does not take into account frequency constraints. Therefore, the model concluded that the lower mass FSG would translate to a lighter substructure. Had the model incorporated frequency constraints, it is possible the FSG turbine would require a heavier substructure. To estimate the costs in Table 3, BOS modeling assumed a piecewise turbine installation (tower, nacelle, hub, Blade 1, Blade 2, Blade 3) due to the large component masses and the methods in wide use in industry. Typically, this method is also the lowest cost option.

Larger, purpose-built turbine installation vessels—such as the Deepwater Installer, Pacific Orca, and Pacific Osprey, which are capable of lifts in the range of 1,500 tonnes—are in the process of being commissioned and deployed. Due to the assumption of use of new, large turbine installation vessels combined with a piecewise installation method, maximum lift capacity of the cranes will not be a constraint for this analysis.

Table 3. Summary of Balance-of-System Capital Costs

Category	PMDD 300 MW Farm ($/kW)	FSG 300 MW Farm ($/kW)
Development	291	291
Substructure	678	671
Ports and Staging	17	17
Turbine and Substructure Installation	487	487
Electrical Infrastructure and Installation	1,257	1,257
Total	**2,729**	**2,723**

6. Soft Costs (Sc)

Soft costs include non-construction costs incurred before project commissioning and are mainly related to the cost of financial vehicles, including:

- Insurance—insurance to protect against damage to components, accidents, and liability during construction. 1% of total Installed Capital Cost
- Surety Bond (Decommissioning)—3% of ICC as specified by Appendix D of FOA 439
- Contingency—15% of total ICC
- Construction Financing—5.5% of ICC

Table 4 includes a summary of the soft costs. Differences result from the assumption that soft costs are based on a percentage of the ICC, which differs between the two wind plant configurations as described earlier.

Table 4. Summary of Baseline Soft Costs

Category	PMDD Turbine (mil US$$_{2009}$$)	FSG Turbine - Baseline (mil US$$_{2009}$$)
Insurance	23.1	22.1
Surety Bond	69.3	66.3
Contingency	346.5	331.5
Construction Financing	127.0	121.5
Total	566.0	541.4

7. Operation and Maintenance Costs(O&M)

O&M costs are highly dependent on the failure frequency of turbine and BOS components. O&M costs of the 300-MW wind farms were calculated in the ECN tool (Obdam et al. 2013) and are summarized in Table 5.

Failure rates, vessel costs, and weather assumptions were taken from Maples et. al. 2013 and were modified as necessary to estimate O&M costs of AML's FSG turbine and the reference PMDD turbine. The primary modifications were based on the following:

- PMDD and FSG TUR_{cc}(see Table 1)
- Thirty 10-MW turbines (AML 2014b, AML 2014c, AML 2014e)
- Generator costs (AML 2014a, AML 2014e).See Table 4.
- Labor hours for generator replacement (AML 2014c). See Table 5.

TUR_{cc} are used to estimate replacement part costs. The difference between the O&M costs of the wind farm using the PMDD turbine and the FSG turbine is mostly due to TUR_{cc} influence on material costs for repairs.

The difference between the O&M costs of the wind farm using the baseline FSG turbine and FSG turbine—alternative (in which the generator is service removable) is mostly due to the generator replacement costs due to the quicker replacement of the FSG turbine—alternative generator. The lower O&M cost for the alternative FSG configuration is strictly due to the lower replacement times for the generator.

Generator costs are a specific replacement cost applicable to the FSG turbine— baseline and alternative scenarios only. Labor hours are used to modify the time required for replacement of the generator. Fewer hours spent on the replacement repair means lower repair vessel and crew costs. The impact of the lower repair time is small, because only about 200 hours of repair time for the entire wind farm would be reduced annually.

Table 5. Operations and Maintenance Costs of the 300-MW Wind Farm

Category	Unit	300 MW PMDD Wind Farm	300 MW FSG - Baseline Wind Farm	300 MW FSG - Alternative Wind Farm (US_{2009}$/turbine)
Generator Replacement Cost	US_{2009}$/ generator	4,764,771	2,323,088	2,323,088
Generator Replacement Time	Labor hrs	144	144	56
O&M Costs Pre-Tax Deduction (O&M)	US_{2009}$/yr	23,787,000	20,177,000	20,149,000

8. Net Annual Energy Production (AEP_{net})

AEP_{net} was calculated in the ECN tool (Obdam et al. 2013) and is summarized in Table 6. To model the AEP_{net} of the PMDD turbine, the ECN tool was modified to use a turbine power curve and efficiency losses from the NREL Cost and Scaling model. To model the AEP_{net} of the FSG turbine, the power curve was modified based on data provided by AML (AML 2014d). The different efficiency curves for the two wind turbine generator concepts resulted in differences in estimated AEP_{net}. The ECN tool calculates capacity factors (without availability),which are shown in Table 6.

Availability and AEP_{net} were then calculated in the ECN tool based on O&M assumptions documented in Section 7. Results are shown in Table 6. The FSG turbine—alternative operates for an additional ~200 hours due to the lower number of labor hours required for generator replacement repairs. AEP_{net} is otherwise unchanged.

Table 6.Net Annual Energy Production of the 300 MW Wind Farm

Category	Unit	300 MW PMDD Wind Farm	300 MW FSG - Baseline Wind Farm	300 MW FSG - Alternative Wind Farm
Capacity Factor (w/o Availability)		42.1%	43.4%	43.4%
Availability		93.0%	93.0%	93.0%
Capacity Factor (w/Availability)		39.2%	40.4%	40.4%
Net Annual Energy Production	kWh/yr	1,015,754,000	1,049,423,000	1,049,629,000

9. Summary of Levelized Costs of Energy

LCOE for all three hypothetical 300-MW offshore wind farms is summarized in Table 7. In the LCOE equation, TUR_{cc} and BOS_{cc} are annualized using the DR of 7% and IWR of 1%. O&M has a tax deduction (T) of 40%. Annualized TUR_{cc} and BOS_{cc} costs along with post-tax deduction O&M are divided by AEP_{net} to generate the data shown in Table 7.

Table 7. Levelized Cost of Energy of a 300-MW Wind Farm

Category	Unit	300-MW PMDD Wind Farm	300-MW FSG—Baseline Wind Farm	300-MW FSG—Alternative Wind Farm
Turbine Capital Cost	$/kWh	0.0299	0.0234	0.0234
Balance of System Cost	$/kWh	0.1075	0.1038	0.1038
Operations & Maintenance Cost	$/kWh	0.141	0.0115	0.0115
Soft Costs	$/kWh	0.0446	0.0413	0.0413
Levelized Cost of Energy	$/kWh	0.1960	0.1800	0.1800

The wind plant concept with FSG turbines results in a lower LCOE estimate due to the following:

- Lower drive system cost, which affects turbine cost and O&M replacement costs
- Lower substructure cost due to lower drive system weight, which affects balance-of-system costs
- Increased energy capture based on drive-system efficiency as a function of wind speed

As shown in Table 7, there is a very small difference in LCOE between the FSG—baseline and FSG—alternative. In this analysis, there was no change in TUR_{cc} between the two; whereas in reality the two configurations would most likely not have identical capital costs.

Further design analysis is needed to verify that the drive system weight differences translate into reduced mass substructure designs for all expected load conditions over the life of the wind plant. O&M costs and energy production estimates will vary with geographic location due to weather patterns, wind resource strength, and distances from port. Additional analysis could provide insight into the magnitude and range of differences in LCOE between the two turbine concepts for more general applications.

References

AML. 2014a. DOE BP1 final report COE comments 081414.pdf

AML. 2014b. COE Model AML Combined - DR2 - PMDD.xlsm

AML. 2014c. COE Model AML Combined - DR2 - FSG.xlsm

AML. 2014d. Energy Model 022912 - DR2 - All turbines.xlsm

AML. 2014e. DOE BP2 Task 5.0 Costs_2014-10-02_rev0.pdf

DOE. 2011. U.S. Wind Power: Next Generation Drivetrain Development. DE-FOA-0000439. Washington, D.C.

ECN Wind Industrial Support. (2012). Retrieved January 24, 2013, fromhttp://www.ewis.nl/fileadmin/ecn/units/wind/docs/EWIS/SP-310_OM_Tool_Brochure.pdf

Elkinton, C.; Clayton, J.; Maples, B. (2012).Offshore Wind Balance of Station Costs in the US. GL Garrad Hassan. AWEA Offshore Windpower Conference & Exhibition. October 9-11, Virginia Beach, VA.

Hembree, B.; Prins, J.; Spagon, P.; Tobias, P.; Zey, C. (2010). "8.1.2.4. Bathtub Curve."NIST/SEMATECH e-Handbook of Statistical Methods. Accessed May 2013: http://www.itl.nist.gov/div898/handbook/apr/section1/apr124.htm.

GL Garrad Hassan. (2012). Expected Offshore Wind Farm balance of Station Costs in the United States.Forthcoming.

Maples, B.; Saur, G.; Hand, M.; van de Pieterman, R.; Obdam, T. (2013). Installation, Operation, and Maintenance Strategies to Reduce the Cost of Offshore Wind Energy. 106 pp.; NREL Report No.TP-5000-57403.

Maples, B.; Elkington, C.; Clayton, J.; Garrett, C.; Castillo, N.; Crivella, E. (unpublished).Expected Offshore Wind Farm Balance of Station Costs in the United States. NREL/SR-5000-55082. NREL. 2014.

NREL Statement of Project Objectives (SOPO) in Support of Advanced Magnet Lab's Innovative Drivetrain DOE Award for Budget Period 2. Golden, CO.

Obdam, T. S., Braam, H., & Rademakers, L. (2011).User Guide and Model Description of ECN O&M Tool Version 4.

FSG Final Scientific/Technical Report - Budget Period 2

Part II - Tasks 6.3–8.0

Federal Agency: DOE EERE – Wind & Water Power Program

Award Number: DE-EE0005140

Recipient: Advanced Magnet Lab, Inc. DUNS Number: 94-374-8681

Project Title: A Lightweight, Direct-Drive, Fully Superconducting Generator for Large Wind Turbines

Project Period: 10/1/2011 to 3/31/2015

Principal Investigators:
Dr. Rainer Meinke, Senior Scientist
rbmeinke@amlsm.com (321) 728-7543
Mr. Darrell Morrison, Senior Principal Mechanical Engineer
Darrell.Morrison@Emerson.com (507) 345-2881
Report Submitted by:
Mr. Vernon Prince, Director
vprince@amlsm.com (321) 728-7543

Date of Report: March 31, 2015
Covering Period: October 1, 2012 to December 31, 2014

Working Partners:
Argonne National Laboratories, Dr. Jerry Nolen (630) 252-6418
Center for Advanced Power Systems (CAPS), Dr. Sastry Pamidi (850) 644-1447
Columbus Superconductor SpA, Dr. MatteoTropeano, Tel. 39.010.869.8100
Composite Material Technology Center (COMTEC), Dr. Keith Dennehy (507) 457-5276
Creare Inc., Dr. Tony Dietz (603) 643-3800 ext. 2310
Emerson Inc., Mr. Mike Sieberg (507) 345-2731
National Renewable Energy Lab (NREL), Mr. Derek Petch (303) 384-7012
University of Houston, Dr. Philippe Masson (713) 743-4605

Table of Contents - Part II

Tasks 6.3–8.0

List of Figures

Task 6.3

Task 6.5

Task 6.6

Task 7

List of Tables

3.2.3.4 Task 6.3 – Conductor Containment Fatigue Analysis

3.2.3.4.1 Task Summary/Achievements

The superconducting windings in the rotor and stator coils have to sustain strong Lorentz forces which are caused by the self-field of the windings and more importantly by the torque transfer between rotor and stator. During machine operation these forces are constantly varying, which could lead to fatigue of the coil support structure, i.e., the compliant composite developed during BP2. Additionally, the acting forces have to sustain fault conditions, under which the acting forces can increase by as much as a factor of two. The constantly changing forces acting on the windings could lead to delamination of the bonding between the conductor and the surrounding composite. Such delamination would allow the conductor to move relative to the composite, which due to friction would lead to heating of the conductor or due to flux changes experience by the moving conductor would introduce an additional voltage into the moving conductor elements. Both effects could lead to premature quenching of the conductor. For the stator winding, a good contact between the conductor and the surrounding composite is furthermore of utmost importance to guarantee good heat transfer between the conductor and composite. Any weakened contact or gap between the conductor and the composite would hamper the transfer of heat, generated by AC losses in the superconductor, to the cooling tubes and an increase in the operational temperature of the conductor.

A superconducting test coil made with the newly developed compliant composite has been built, and the windings of the coil have been exposed to Lorentz forces which are representative of the peak forces seen in the rotor and stator winding. By operating the test coil in a strong external magnetic field and changing the transport current through the test coil rapidly changing Lorentz forces were generated and the coil was exposed to a significant number of such load cycles. The coil critical current monitored during this test did not show any decrease and a search for micro cracks after the completed experiment also did not show any deterioration of the material.

At room temperature, a fatigue testing with a large number of load cycles was performed, which proved that the coil support based on the compliant composite meets the fatigue requirements.

3.2.3.4.2 Report period: July 1, 2013 to September 30, 2013 (Q5)

At the team meeting in July, the method for monitoring sample condition was determined. The applied current during the testing will be near the critical current of the conductor. This makes the conductor resistance very sensitive to the local temperatures. Even micro movements within the sample will cause friction heating that can be seen in the input signals. These will be monitored for indications of adequacy of the conductor containment and potential degradation over time.

- Contact with the National High Magnetic Field Laboratory (NHMFL) was made and time for testing in their Cell #4 requested.
- Details of cryostat loading/support capability were not forthcoming from NHMFL, so AML personnel visited their site to take measurements and obtain details of the Cell #4 geometry to facilitate support analysis.
- The obtained information showed that the Task 6.3 concept in play at the time would produce moment loading not properly supported by the Cell #4 geometry.
- The situation was discussed in length in an AML/Emerson meeting which developed a new concept with a winding design that self cancels the forces within the test sample, minimizing the loading on the cell's cryostat and supports.

Task 6.3 Major Activities

In situ degradation sensing method established. Operation will be near conductor critical current to heighten sensitivity to friction causing micro movements. Monitoring inputs will show movement-related spikes due to movement. Production of these spikes represents poor conductor support. Increasing spike counts or spike amplitudes will indicate degradation (thermal resistance change, such as interface de-bonding or cracking.

Finite Element Analysis (FEA)

High Magnetic Field Concept 1 Summary

This study looks at a simplified approach to producing winding forces capable of generating similar composite stress behavior to the full-size unit at rated conditions using applied current within a high external DC magnetic field. This uses the High Magnetic Field Lab generated flux fields, but with a greatly reduced AC current input and a simplified test sample.

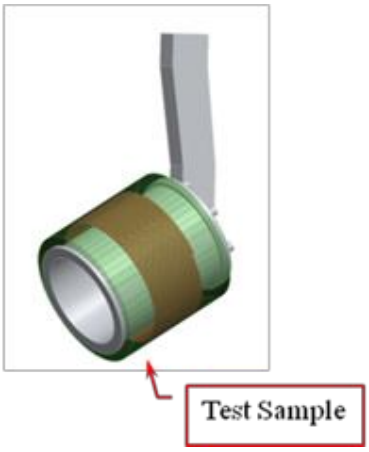

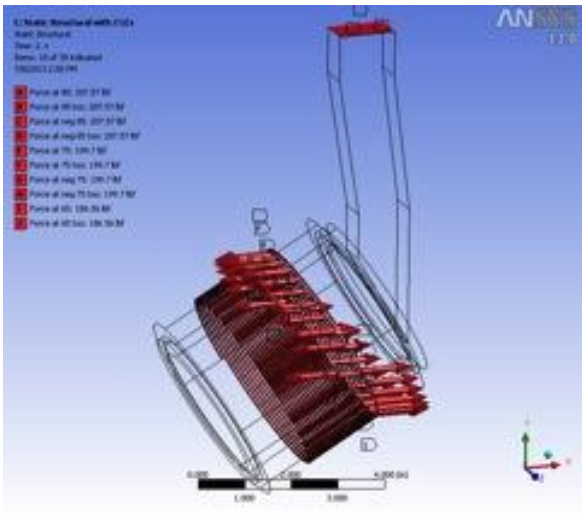

Results of this study

- This analysis shows the support structure heavily stressed with high deflections under load for these loading conditions. Full mounting geometry information is needed to properly design the system. To match the appropriate stresses, the loading will likely need reduction, making this less of an issue.
- The chosen angle of 30 degrees provides too much lateral (tangential in the machine) stress compared to the radial stresses. The angle should be changed to a steeper angle and the current reduced to provide a match for the operational stress levels.
- The desired test stress levels, relative to the operational needs to be determined.

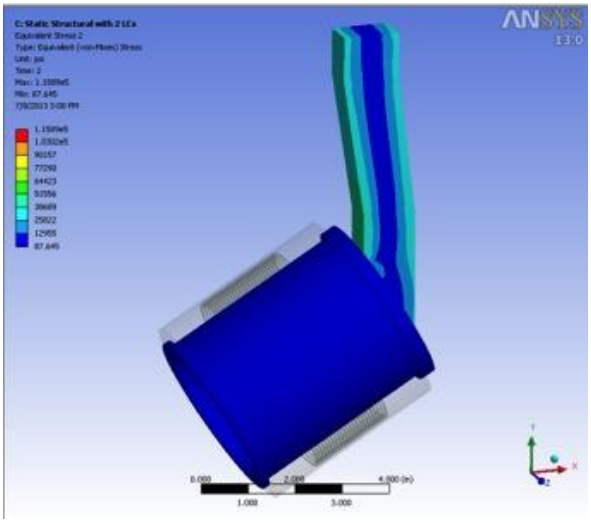

Task 6.3 Specific Objectives

- Determine test sample configuration.
  - Underway.

Task 6.3 Significant Results, Including Major Findings, Developments or Conclusions (Positive or Negative)

FEA showed significant moments produced with the solenoid winding concept, potentially damaging to the Cell #4 geometry, which wasn't designed for lateral loads. This finding led to a self-cancelling winding approach now underway.

Task 6.3 Plans for Next Quarter

- Obtain the winding design for the self-cancelling concept.
- Perform FEA of the sample to baseline the stresses, design the sample and mounting geometry.
- Provide support for AML.

3.2.3.4.3 Report period: October 1, 2013 to December 31, 2013 (Q6)

This task was examined further in this quarter:

- Previously, obtained information showed that moment loading would not be supported by the Cell #4 geometry.
- The situation was discussed in length in an AML/Emerson meeting which developed a new concept with a winding design that self cancels the forces within the test sample, minimizing the loading on the cell's cryostat and supports.
- AML is devising a winding that would produce significant local conductor loading, but be self-cancelling, eliminating the global moment that could potentially damage Cell #4.
- The test concept provides a limited number of alternating current cycles, remaining in the low cycle fatigue range. It cannot provide useful FEA fatigue design limit information. It can, however, determine if the AC forces on the strands of the conductor experience friction related movement. Similar windings for accelerator magnets see DC loading. DC loading would not create friction movements upon reaching the design point. The FSG stator winding, however will see AC force fluctuations continually.
- By operating in superconducting mode close to the critical current and monitoring the inputs, even slight movements causing heat generating movements inside the conductor can be seen.
- The successful testing outcome for Task 6.3 would be the absence of detectable movements during operation with AC currents. These movements could be between the cable strands or at the Kapton insulation interfaces.
- A second part of Task 6.3 was added to obtain fatigue design limits, using test coupons to obtain a rudimentary stress-life curve for the CC material.

Task 6.3 Major Activities

- AML has been working on the winding concept for a self-cancelling winding.
- Coupon fatigue testing and design limit determination methods were determined. Between CTD, Kato Engineering and COMTEC, a plan to develop fatigue design limits was developed. A rudimentary S-N Curve at room temperature will be determined. Two high stress points on the S-N curve will be repeated at lower temperatures to verify the S-N curve at RT is conservative. This would establish conservative design criteria for a lower risk design at a reasonable cost.
- Coupons for the fatigue testing have been made and sent to CTD.

Task 6.3 Specific Objectives

- Determine test sample configuration. Underway.

Task 6.3 Significant Results, Including Major Findings, Developments or Conclusions (Positive or Negative)

- None, yet.

Task 6.3 Plans for Next Quarter

- Obtain the winding design for the self-cancelling concept.
- Perform FEA of the sample to baseline the stresses, design the sample and mounting geometry.
- Provide support for AML.

3.2.3.4.4 Report period: January 1, 2014 to March 31, 2014 (Q7)

This task was examined further in this quarter. This task is now divided into two parts. The first part is the originally planned testing at the NHMFL. The second part is developing fatigue design limits using coupon testing for the CC material, similar to material property testing in Task 6.2.

Part 1, Testing at NHMFL

Previously, obtained information showed that lateral moment loading from a test sample could not be supported by the Cell #4 geometry.

The winding design concept that self cancels the forces within the test sample, minimizing the loading on the cell's cryostat and supports is shown in Figure 6.3.1

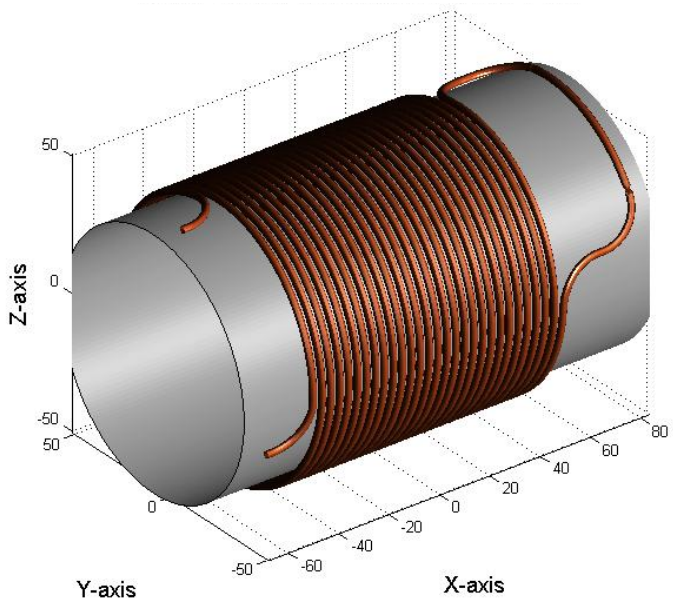

Figure 6.3.1. Bifilar Helical Winding for Fatigue Test

This winding produces significant local conductor loading, but is globally self-cancelling, eliminating the global moment loads that could potentially damage Cell #4.

The testing at NHMFL uses high current, which has a relatively low rate of change that provides a limited number of alternating current cycles within the test window, remaining in the low cycle fatigue range. It cannot provide useful composite FEA fatigue design limit information.

It can, however, determine if the AC forces on the strands of the cabled conductor experience friction-related movement. Similar windings for accelerator magnets see DC loading. DC loading would not create friction movements upon reaching the design point. The FSG stator winding, however will see AC force fluctuations continually.

By operating in superconducting mode close to the critical current and monitoring the inputs, even slight movements causing heat generating movements inside the conductor can be seen.

The successful testing outcome for Task 6.3 would be the absence of detectable movements during operation with AC currents. These movements would likely be between the cable strands or at the Kapton insulation interfaces.

Part 2, Coupon Fatigue Testing at CTD

The second part of Task 6.3 was added to obtain tested fatigue design limits, using test coupons. The costs for a full stress-life curve at 15 K would be prohibitive, due to the high cost of cryogen. Instead, a conservative fatigue stress-life curve was determined at room temperature with the high stress loading points retested at 90 K and 15 K to verify the room temperature values are conservative.

Task 6.3 Major Activities

- Part 1: AML has fully developed the winding concept for a self-canceling winding and begun sample design.
- Part 2: Coupon fatigue testing is complete. Conservative fatigue design limits have been developed. The room temperature stress-life curve is shown in Figure 6.3.2

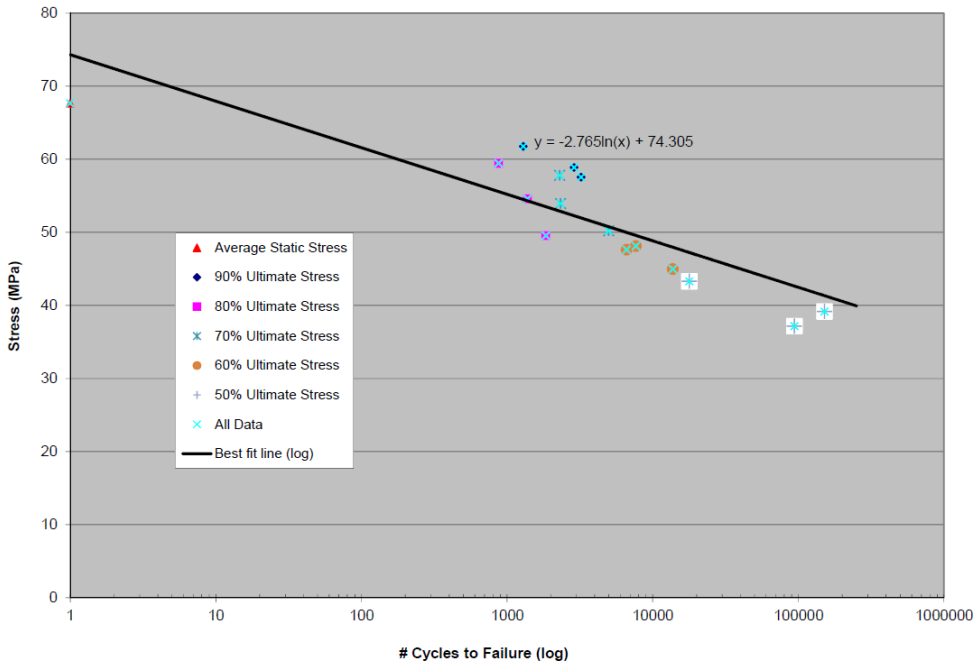

Figure 6.3.2. Tension Fatigue @ 295 K for Kato Emerson

At room temperature, the 80% loading failed at 200 cycles or less. Life testing at 90 K and 15 K for the 80% ofRT ultimate strength were performed. Both samples exceeded 1,000,000 cycles, verifying the room temperature data to be quite conservative.

Task 6.3 Specific Objectives

- Part 1: Determine test sample configuration. The configuration was decided, sample designed and preparations for sample manufacture made.
- Part 2: Determine fatigue design limits. All planned testing was completed.

Task 6.3 Significant Results, Including Major Findings, Developments or Conclusions (Positive or Negative)

- Part 1: Sample construction can begin.
- Part 2: Based on the RT fatigue testing, Task 4.0 will start with a fatigue limit of 5,100 psi for fatigue type loading on the CC material. Indications are that the actual limit could be higher from the benefits of strength increase at lower temperatures.

Task 6.3 Plans for Next Quarter

- Perform FEA of the sample to baseline the stress and deflections within the conductor cable.
- Build and test the Bifilar helical-based sample at NHMFL.
- Provide support for AML.

3.2.3.4.5 Report period: April 1, 2014 to June 30, 2014 (Q8)

A Kapton-wrapped, 6-around-1, MgB_2mini-cable constitutes the superconductor for the rotor and stator windings of the FSG. This cable is embedded in grooves of a compliant composite, which transfers the acting Lorentz forces to the rotating shaft and respectively to the stator support of the generator. High strength bonding of the Kapton-wrapped cable in the composite support grooves is important to avoid movements of the conductor inside of the grooves, which would deposit frictional energy into the conductor, leading to heating and premature quenches of the superconductor. Additionally, for the stator winding, good thermal contact between the conductor and the composite matrix material is of utmost importance, since the heat generated by AC losses in the conductor needs to be effectively conducted to heat absorbing cooling tubes also embedded in the composite coil support structure.

The strong Lorentz forces acting in the rotor and stator windings of the machine are constantly changing in size and directions during operation of the machine. Accordingly, fatigue of the bonding between the conductor in the supporting grooves are a potential issue. A delamination between the Kapton overwrap and the surrounding groove walls could lead to frictional energy deposition and at the same time hamper the heat transfer needed for removing energy deposition due to AC losses in the superconductor. Task 6.3 will analyze, if delamination between the mini-cable and the support grooves due to fatigue will occur.

In order to determine if fatigue caused by repeated load changes will affect the performance of a superconducting winding that is representative of the FSG, a small test coil has been built for testing. The coil consists of a bifilar, solenoidal winding; the design is shown in Figure 6.3.3. The coil will be operated in the bore of a superconducting solenoid magnet at the National High Magnetic Field Laboratory in Tallahassee, Florida. Within a constant background field of about 5 Tesla, the test coil will be able to operate at an excitation current of more than 3000 A, generating Lorentz forces acting on the

mini-cable of at least 150 Newton per cm of conductor length. Due to the bifilar winding no net force will act, when the test coil is supported inside of the external superconducting solenoid. However, strong shear forces act between adjacent turns of the bifilar winding, which are about 20% higher than the peak forces acting on the stator windings of the FSG. Due to operating in a high background field of 5 Tesla and the bifilar winding of the test coil, the flux density seen by the conductor in the test are almost completely independent of the current in the mini-cable. Accordingly, energy deposition due to flux changes seen by the conductor are insignificant.

For the fatigue test, the critical current of the test coil will be determined at the beginning of the test. The coil will then be exposed to a constant up and down ramp of the excitation current in the constant background field of the external solenoid. If a delamination of the mini-cable occurs after several hundred excitation cycles of the test coil, the mini-cable will start to move inside the support grooves under the effect of the changing Lorentz forces. Such movements will affect the critical current of the test coil and premature quenching of the test coil will occur. A corresponding lowering of the critical current therefore indicates fatigue of the mini-cable bonding. In order to detect any developing quench in the test coil, the coil is monitored by a sensitive quench protection system during the test.

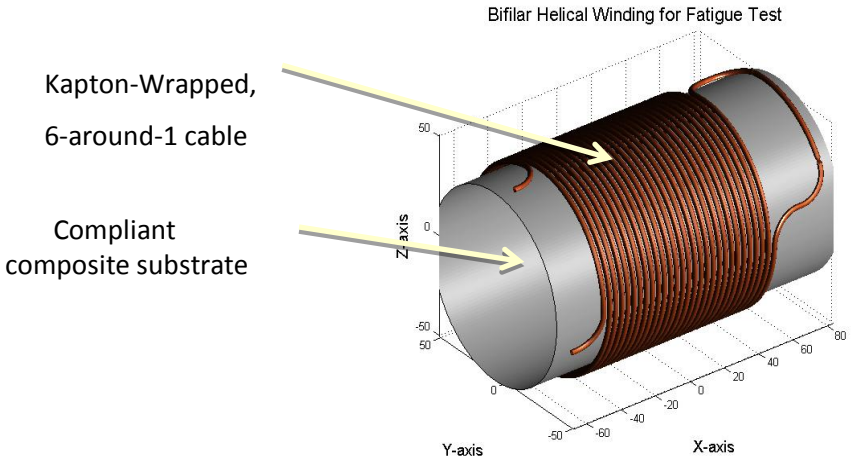

Figure 6.3.3. Design of Bifilar Solenoid Coil

The test coil is built with the same compliant composite that has been developed for the FSG, which constitutes the best match in CTE between the conductor and the composite coil support structure. For the manufacturing of the test coil, a support cylinder of the compliant composite has been built as indicated in Figure 6.3.4. For this purpose the composite, which has the viscosity of a paste is slowly filled into the transparent cylinder shown in the figure. A transparent material has been chosen for the outside wall to allow detection of any potential voids in the poured material.

Figure 6.3.5 shows resulting support cylinders for the test coil after machining off the outer transparent container. In the first attempt, shown at the top of Figure 6.3.5, several voids occurred on the outer machined surface of the compliant composite. Such voids might compromise the performance of the test coil under strong Lorentz forces. The process was therefore improved, and in the second attempt, the composite was applied in several steps with heating of the composite slurry before the

pouring and setting the container on a vibrating table. As can be seen in the lower part of the figure, the voids on the machined circumference are almost completely eliminated.

A support groove for the mini-cable for the bifilar solenoid winding is machined into the surface of the support cylinder. The resulting support structure is shown in Figure 6.3.6. The groove at the right side of the support structure is needed to accommodate the required minimum bending radius of the rather stiff mini-cable.

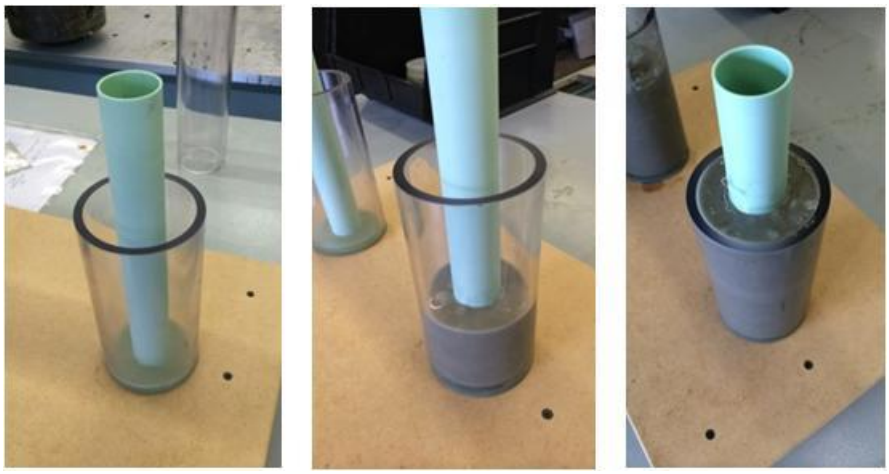

Figure 6.3.4. Transparent container for manufacturing the support cylinder of the test coil

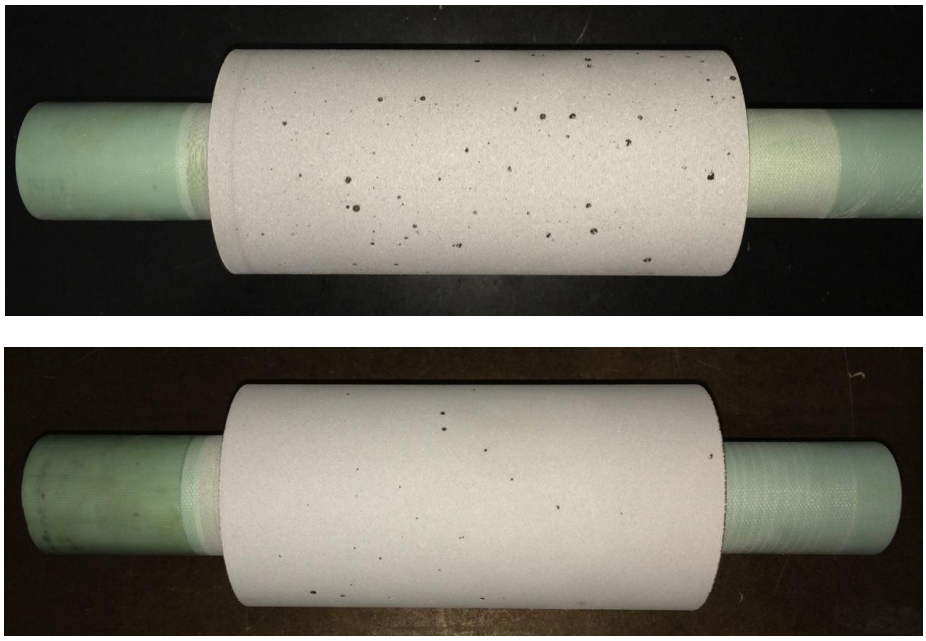

Figure 6.3.5. Top: First attempt of support cylinder manufacturing with numerous voids on the outer machined surface. Bottom: Second improved cylinder with a significantly reduced number of voids

Figure 6.3.6. Support groove for the bifilar solenoidal winding machined into the support cylinder

The Kapton-wrapped mini-cable has been manufactured at AML from a NbTi superconductor. For this purpose, 6 individual NbTi strands with a diameter of 0.85 mm each are wrapped around an additional strand in the center of the resulting 6-around-1 cable, which is then wrapped with Kapton tape (Figure 6.3.7). Due to the rather short length of mini-cable required for the test coil, less than 10 m, a manufacturing run on a large cabling machine would have been cost prohibitive.

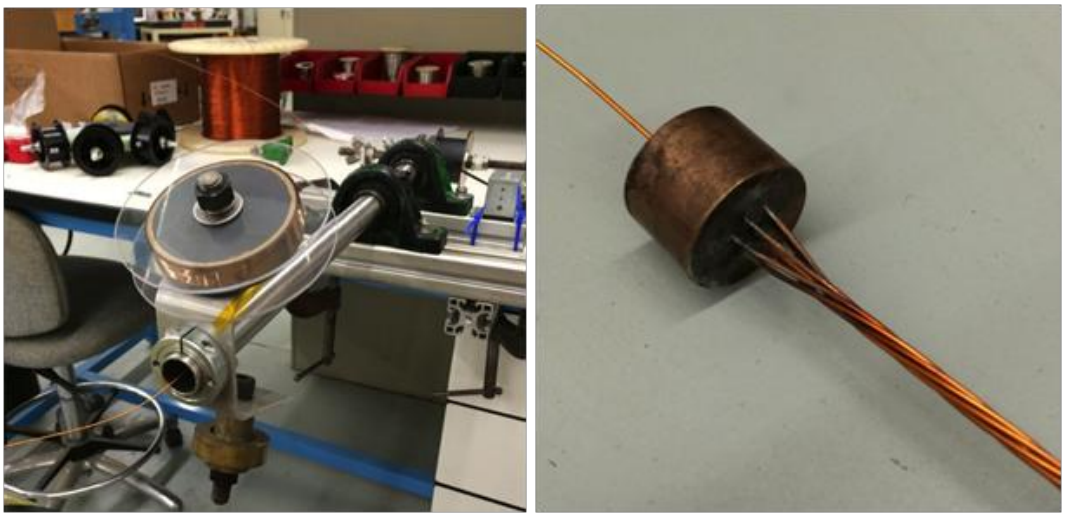

Figure 6.3.7. Setup for manufacturing of the Kapton-wrapped mini-cable

The resulting Kapton-wrapped, 6-around-1 NbTi cable is shown in Figure 6.3.8 (left). The right side of this figure shows how the cable fits into the machined support grooves. The manufacturing process of inserting and bonding the mini-cable into the machined support grooves is schematically shown in Figure 6.3.9. As indicated in the figure, a small amount of the slurry is painted into the bottom of the machined grooves. Then, the mini-cable is wound onto the support structure by inserting it into the

grooves. The grooves are the filled completely with additional slurry and finally the outer surface is machined to a smooth surface with nominal outer dimensions.

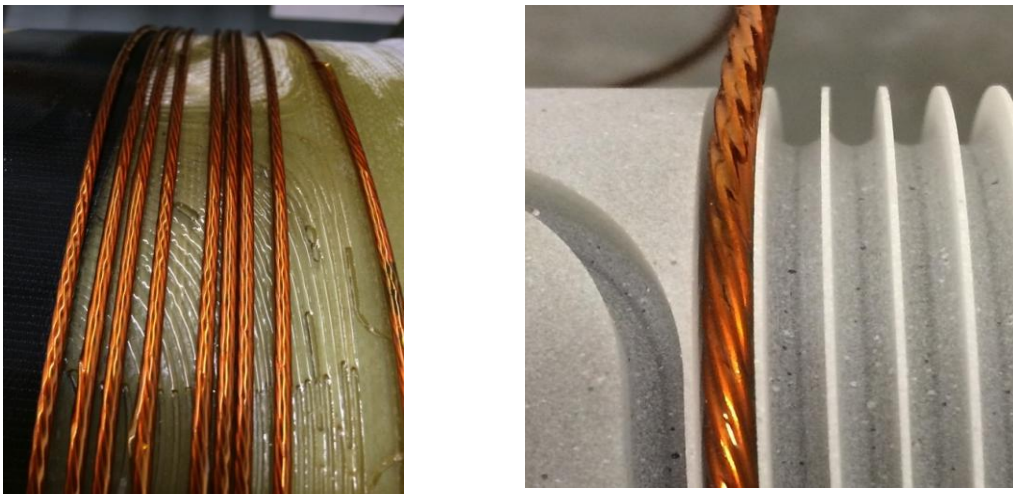

Figure 6.3.8. Left: Manufactured Kapton-wrapped, 6-around-1 mini-cable. Right: Cable placed in groove of support structure

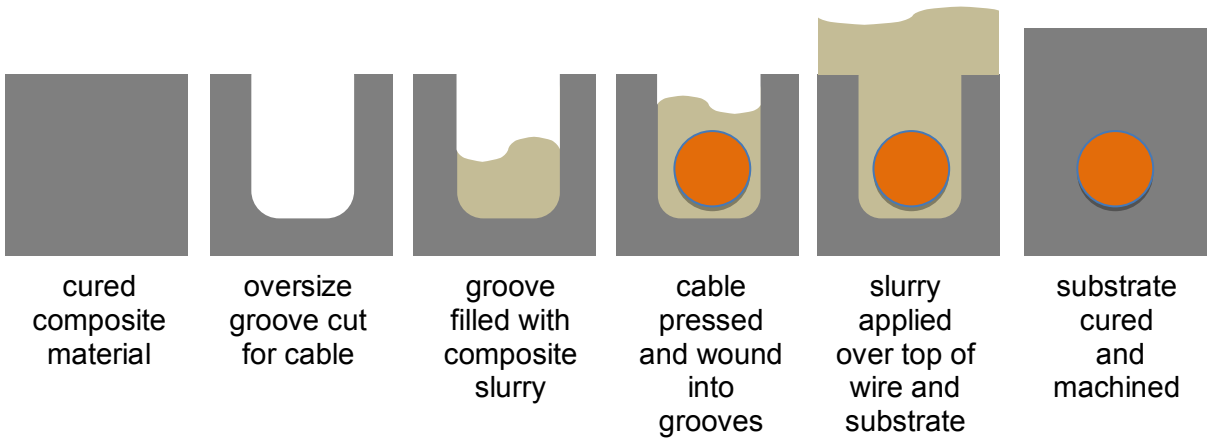

Figure 6.3.9. Test coil winding procedure of mini-cable in schematic form

The coil for the fatigue test at the National High Magnetic Field Laboratory has been completed. The test has been scheduled for the 3rd week of September. The required test coil support needed for the experiment has been designed and the current leads needed for the test have been received by AML for test preparations. A detailed test plan for the fatigue test is currently being prepared.

This task is now divided into two parts. The first part is the originally planned testing at the NHMFL. The second part is developing fatigue design limits using coupon testing for the CC material, similar to material property testing in Task 6.2.

Part 1, Testing at NHMFL

- This activity and the associated preparations have been described in the previous section.
- The successful testing outcome for Task 6.3 would be the absence of detectable movements during operation with AC currents. These movements would likely be between the cable strands or at the Kapton insulation interfaces.

Part 2, Coupon Fatigue Testing at CTD

- Fatigue coupon testing was completed first quarter, 2014.

Task 6.3 Major Activities

- Part 1: Described in previous section.
- Part 2: Coupon fatigue testing is complete. A conservative fatigue design limit of 5,100 psi will be used for Task 4.0 assessment.

Task 6.3 Specific Objectives

- Part 1: Described in previous section.
- Part 2: Complete.

Task 6.3 Significant Results, Including Major Findings, Developments or Conclusions (Positive or Negative)

- Part 1: Described in previous section.
- Part 2: Based on the RT fatigue testing, Task 4.0 will start with a fatigue limit of 5,100 psi for fatigue type loading on the CC material. Indications are that the actual limit could be higher from the benefits of strength increase at lower temperatures.

Task 6.3 Plans for Next Quarter

- Perform FEA of the sample to baseline the stress and deflections within the conductor cable. (Kato)
- Build and test the Bifilar helical based sample at NHMFL.

3.2.3.4.6 Test Coil Autopsy

After completion of the cryogenic test, an autopsy of the test coil has been performed to check for any development of micro-cracks or delamination that might have developed in the compliant composite due to the strong Lorentz forces acting on the Kapton-wrapped mini-cable.

As a first test, a visual inspection of the outside of the test coil was performed. An example of these inspections is shown in Figure 6.3.10. Particular emphasis was put on areas where small voids exists in the surface of the composite that encapsulates the coil winding. These small voids resulted from the manufacturing process of the coil caused by small air bubbles. It can be assumed that in such areas, where the composite does not form a continuous layer, the strength of the material is compromised, and the probability of cracking in the material is enhanced. The red square shown in Figure 6.3.10 is an area with such a void, which is shown in an enlarged view in Figure 6.3.11.

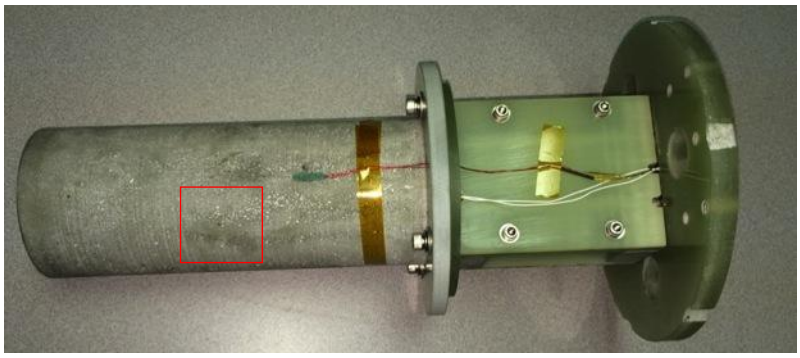

Figure 6.3.10. Test coil returned from fatigue test. The red square indicates an area of detailed surface inspection.

The area in the square of Figure 6.3.11 was further inspected under a microscope with various magnifications. The magnified views are shown in Figure 6.3.12.

Figure 6.3.11. Enlarged view of the square shown in Figure 6.3.10, which contains a small void in the surface.

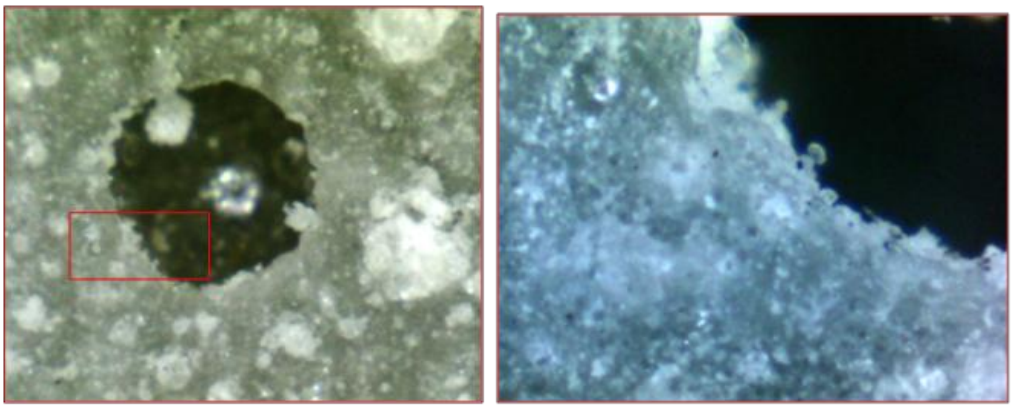

Figure 6.3.12. Enlarged view of the squares shown in Figures 6.3.10 and 6.3.11. The right side shows the highly magnified view of the area in the rectangle on the left.

No indications of any micro-cracks or defects other than those from the manufacturing process were found on the outer surface.

In order to check for micro-cracking on the inside of the composite, the test coil was cut diagonally as shown in Figure 6.3.13. It could be assumed that in particular close to the embedded conductor, which experienced strong forces during the excitation cycles, delamination of the conductor or micro-cracking of the composite has been developed.

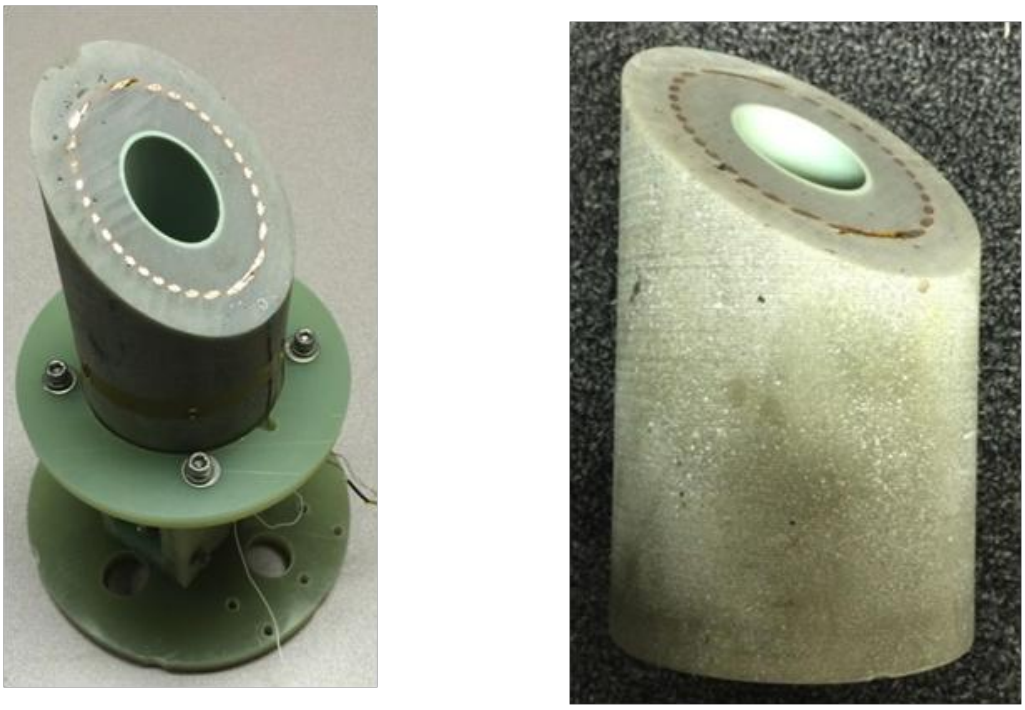

Figure 6.3.13. Exposed area of the inside of the test coil showing the embedded conductors of the bifilar mini-cable winding.

An example of the performed inspections is shown in Figure 6.3.14. The rectangle surrounding one of the mini-cables was analyzed under a microscope and is shown on the right-hand side of Figure 6.3.15. Since the test coil was cut under an angle of about 45 degrees relative to the coil axis, the round cross-section of the Kapton-wrapped mini-cable becomes oval shaped as shown in the figure on the left. The brown line surrounding the seven wires of the cable is the Kapton tape, which was wrapped around the wires. As seen in the figure on the right, the Kapton wrap left voids where it bridges the outer rim of two adjacent wires.

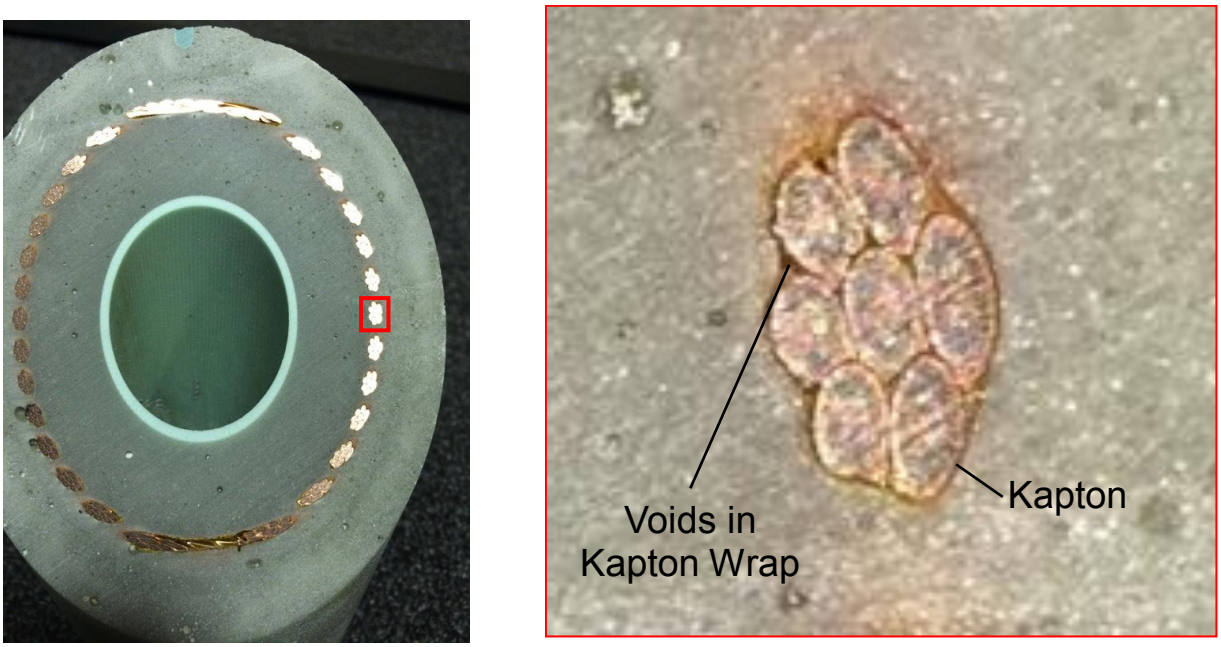

Figure 6.3.14. Left: Surface of the diagonal cut through the test coil. Right: Microscopic view of the area inside of the rectangle on the left.

No indications of any delamination of the Kapton-wrap from the surrounding composite nor any micro-cracks were found. Figure 6.3.15 and Figure 6.3.16 show additional examples of the performed inspections. Neither one shows any delamination or micro-cracking.

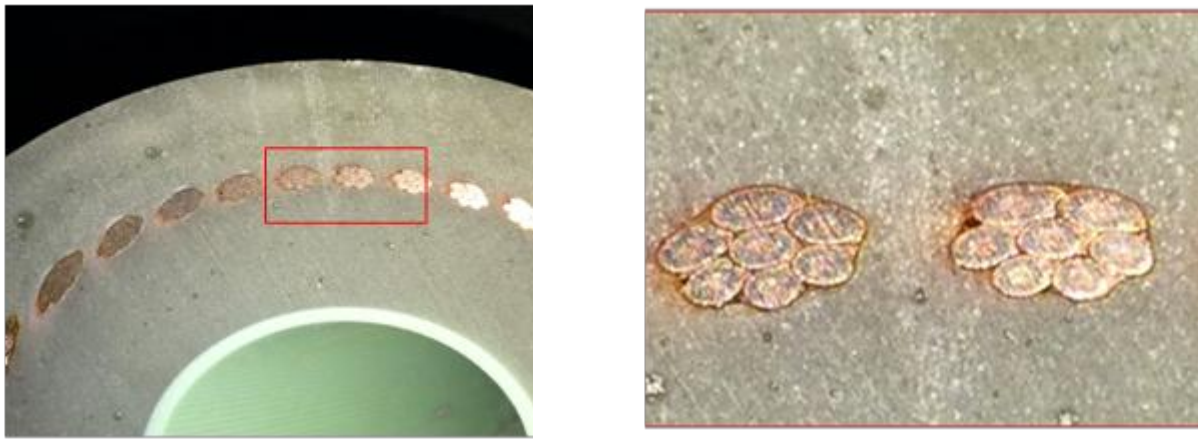

Figure 6.3.15. Left: Surface of the diagonal cut through the test coil. Right: Microscopic view of the area inside of the rectangle on the left.

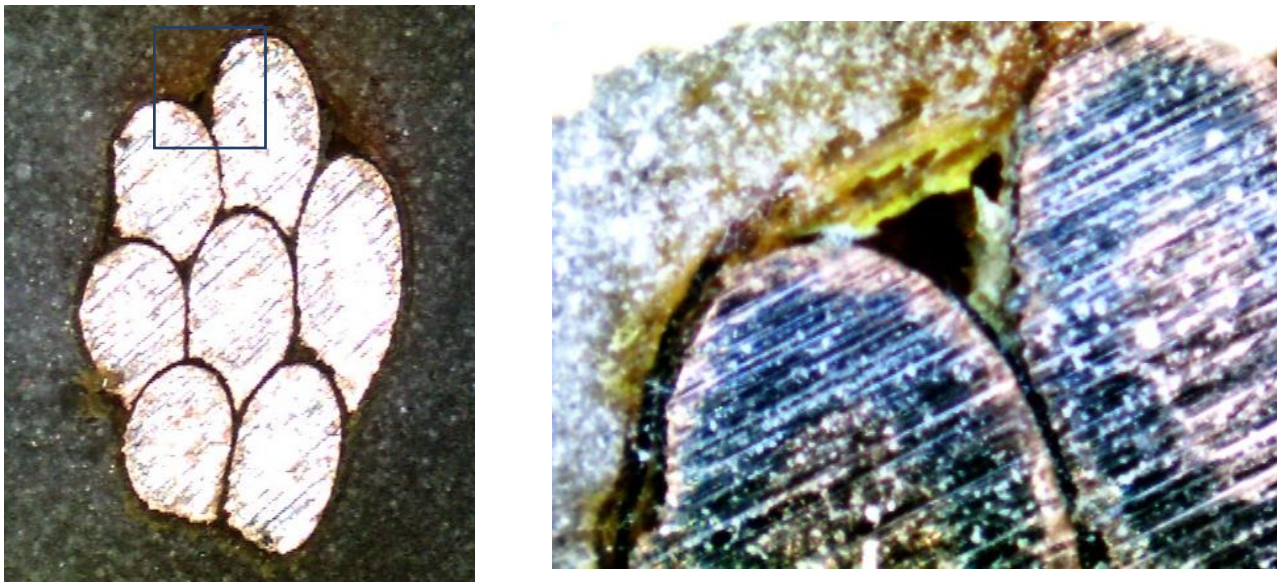

Figure 6.3.16. Left: Microscopic view of an embedded mini-cable. Right: Highly magnified area of the rectangle on the left.

In summary, it can be said that no indications of any stress-related damage were found in the autopsy of the test coil after the multiple load cycles sustained by the test coil during cryogenic testing. The conductors embedded in the compliant compsite are able to withstand the maximum forces acting during FSG operation.

3.2.3.5 Task 6.4 – Sub-scale Torque Tube Temperature Cycling

3.2.3.5.1 Summary

Task Goals

The FSG relies heavily on continual, successful active section cooling by conduction from the windings through composite and its associated bonds to cooling tubes with internal convection with gaseous helium. During BP1 conception design, it was realized this behavior is crucial to FSG success. With low tolerance for conductor temperature increases in operation, high quantity of insulated superconductors with internal losses, large surface area for the cooling tubes and their associated bonds, it was deemed to be a significant risk to be investigated in BP2.

The most prominent stress causing loads are due to the thermal expansion differences of the many materials utilized in the FSG configuration. These are primarily driven by the large temperature range between operation and room temperature. The number of complete cool down/warm up cycles in the life of the FSG is expected to be relatively low. For this study, a possibility of once a year was examined. Wind turbines have traditionally been designed for a 20- to 25-year life.

Task 6.4 was developed with the goal to assess the FSG capability to withstand the rigors of cool down and warm up between operation at 15 K and room temperature of 295 K.

The goals for task 6.4 became:

1. Assess the thermal cycling risk to the FSG design by completing 25 thermal cycles between room temperature of 295 K to 15 K and back to room temperature.
2. Design a representative test sample to allow proper risk assessment.
3. Establish a representative process for cool down and warm up that provides acceptable transient thermal stresses.
4. Establish a method to measure thermal behavior in the sample.
5. Determine the effect of thermal cycling from RT to 15 K on heat transfer within a representative sample. Compare subsequent heat runs to a baseline run to assess change.
6. Document sample visual inspection results after testing.

Accomplishments

Task 6.4 was very successful, achieving 25 thermal cycles from room temperature (295 Kelvin) to 15 K and back to room temperature with stable thermal behavior and no visible signs of damage.

Costs of making full size test assemblies are prohibitive, leading to sample design by FEA. The FEA shows thermal stresses develop in a very short length, allowing a much smaller sample. The weakest component in the configuration is the conductor insulation. It is multilayered which may make it behave as a slip plane along the conductor length while the racetrack coil shape limits the total conductor end movements.

Initially, the direction was to use the intended FSG superconductor. A method to assess heat transfer, however, was elusive. Rather than using a superconductor with its associated complexity and the lack of electrical resistance heating, a non-superconductor of a material similar to the primary mechanical member of the proposed superconductor was selected. At the time of Task 6.4 sample design, a superconductor based on 316 SS was in the plan. A mechanical cable made of strands (6-around-1) of 316 SS was chosen for Task 6.4.

Several configurations were examined. The sample configuration was ultimately designed to provide a meaningful length without end restriction to provide the worst case for conductor movement within the insulation. The thought being more differential movement would create more heat transfer change effect.

The final sample configuration was the outcome of team discussion. A configuration with a single pass of conductor and cooling tube with equidistant temperature sensors was selected (Figure 6.4.1).

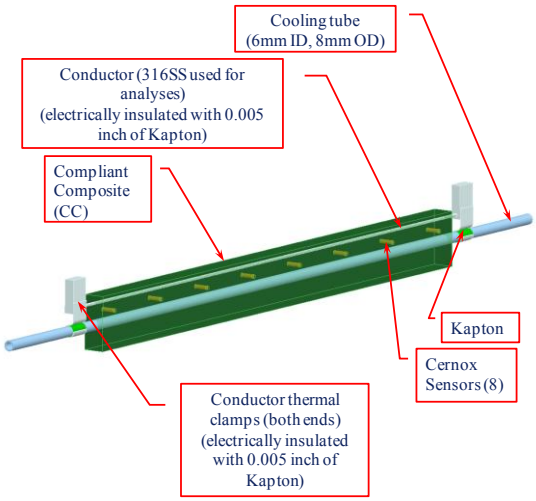

Figure 6.4.1. Task 6.4 Model Geometry

The strategic placement of the temperature sensors between a single pass conductor and the cooling tube allows determining a behavior change, as well as the likely change source location, i.e., if the cooling tube bond degrades, the sensor will read hotter, because less heat is removed (Figure 6.4.2). If the conductor interfaces degrade, the sensor will read cooler, because less local heat is getting to the composite.

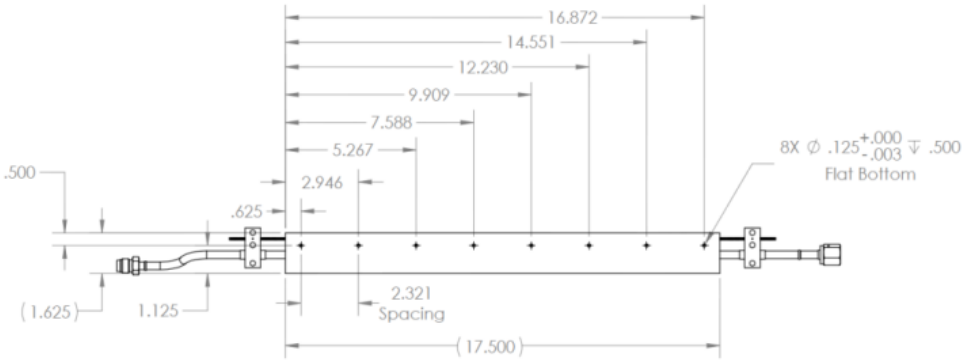

Figure 6.4.2. Task 6.4 Sample Drawing [inch]

Prior to Task 6.4, concerns for possible micro cracking for a newly developed composite prompted the introduction of a preliminary, less costly thermal cycling task, Task 6.2b. This simplified testing was simply to prove the compliant composite was capable of cryogenic operation without catastrophic results and provide insight into what lie ahead for Task 6.4. The conductor temperature rise by resistance test method was developed in Task 6.2b and used here in Task 6.4.

The rise by resistance uses the known conductor material resistivity change with temperature data. Resistivity data for 316 SS is shown in Figure 6.4.3. For each test, the sample is left to stabilize to the initial temperature. The temperatures for the TCs are recorded and current applied. The conductor resistance readings are extrapolated back to the initial application of current. The temperature of the conductor will be that of the TCs at the start of the test, yielding the resistivity for that temperature. As the conductor heats from the applied current, the resistance changes proportionally. At the end of the test, the temperature will level off to a final stable temperature. The final resistance reading will be used for a resistance ratio from the start to the finish of the heat run. This resistance ratio times the initial resistivity will provide the final resistivity which can be used to determine the final conductor temperature.

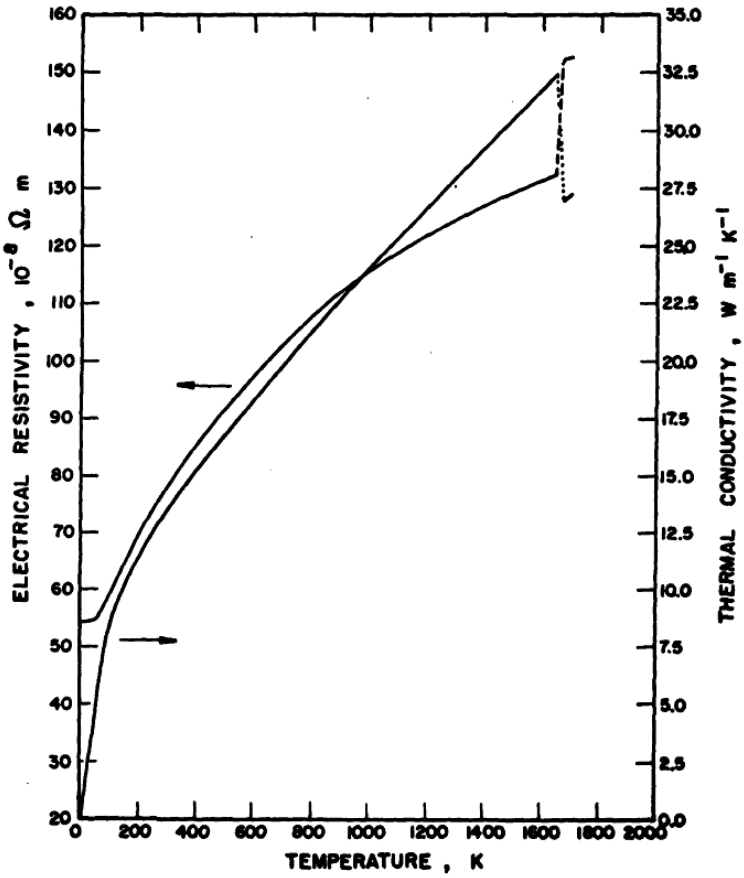

Figure 6.4.3. Electrical Resistivity and Thermal Conductivity of AISI 316 Stainless Steel

The temperature of the heat run needs to be as low as possible for maximum thermal stress during a heat run. The 316 SS material resistivity, which allows measurement of the wire rise by resistance during application of current, flat lines below 60 K, however, forcing heat runs to start at 70 K with acceptable resistivity margin.

A test configuration using an existing Argonne National Lab Dewar was designed. An initial “dummy” sample was used for preliminary set up and thermal cycle check out (Figure 6.4.4).

It showed successful ability to reach the desired temperature range. Following the preliminary thermal cycle, the “dummy” sample was replaced by the official sample. Visual inspection of the “dummy” sample following a single cycle showed no sign of thermal distress (Figure 6.4.5 and Figure 6.4.6).

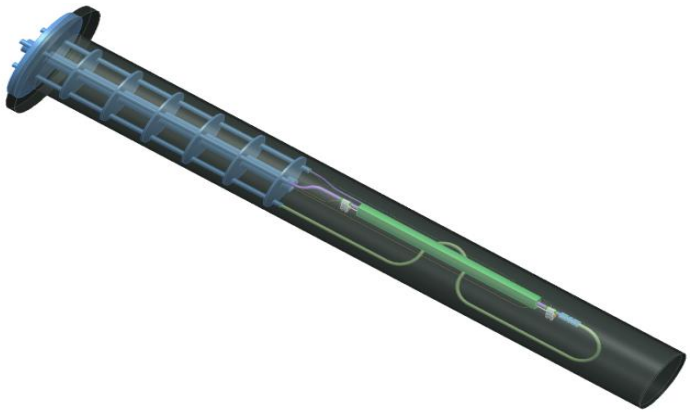

Figure 6.4.4. Task 6.4 Sample Modeled inside Dewar

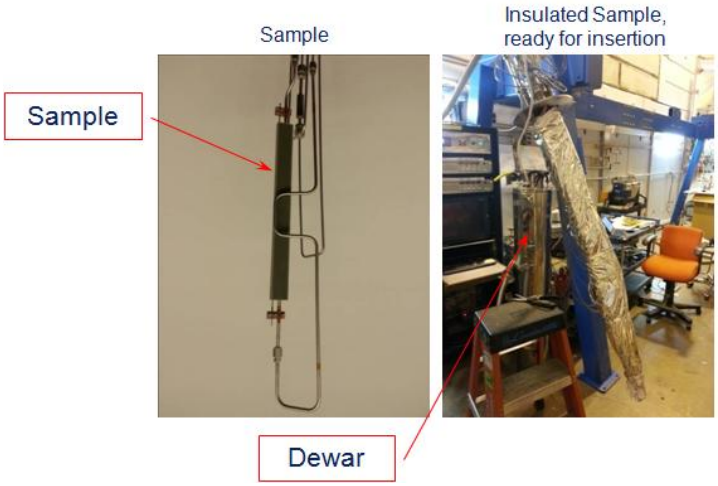

Figure 6.4.5. Task 6.4 Sample Prior to Testing

Figure 6.4.6. Dr. Nolen Prepping for Test

The gas temperature for the inlet gaseous helium is controlled by controlled mixing of 5 K and room temperature helium. Manual mixing proved to be inadequate both for steady state and for cool down/warm up temperature control. This forced the addition of automatic, computer controlled mixing valves (Figure 6.4.7).

The cooling for the sample with gaseous helium was affected by flow rate, as well. A precision flow controller was added to the setup to better control the gas (Figure 6.4.8).

Following the modifications to the cooling controls, repeatability of the heat run results was acceptable.

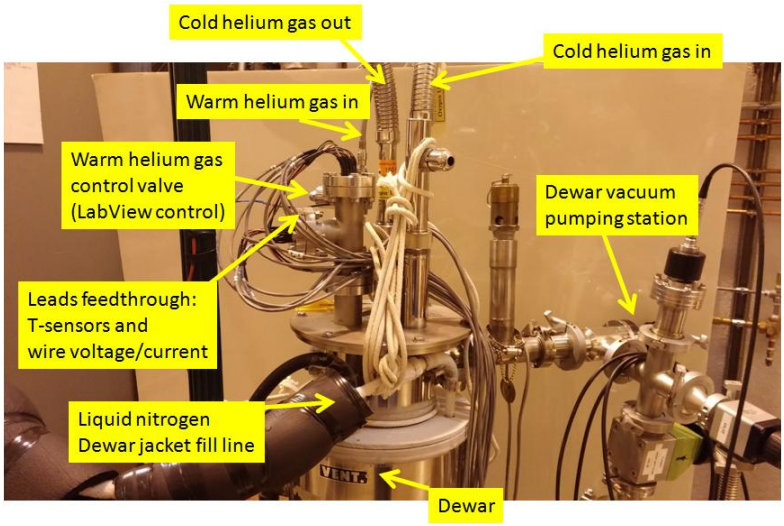

Figure 6.4.7. Argonne Test Setup Details

Test Description

Heat transfer consistency assessment was the measurement of success for this testing. Comparative results from several heat runs performed before, during and after thermal cycles were used to show stability of the internal heat transfer interfaces. End temperature changes from a heat run, with controlled cooling and fixed applied current indicate heat transfer behavior changes within the sample.

Thermal Cycle

Temperature was cycled between 295 Kelvin and 15 Kelvin. 15 K is planned to be the coldest operation temperature within the FSG (Figure 6.4.9).

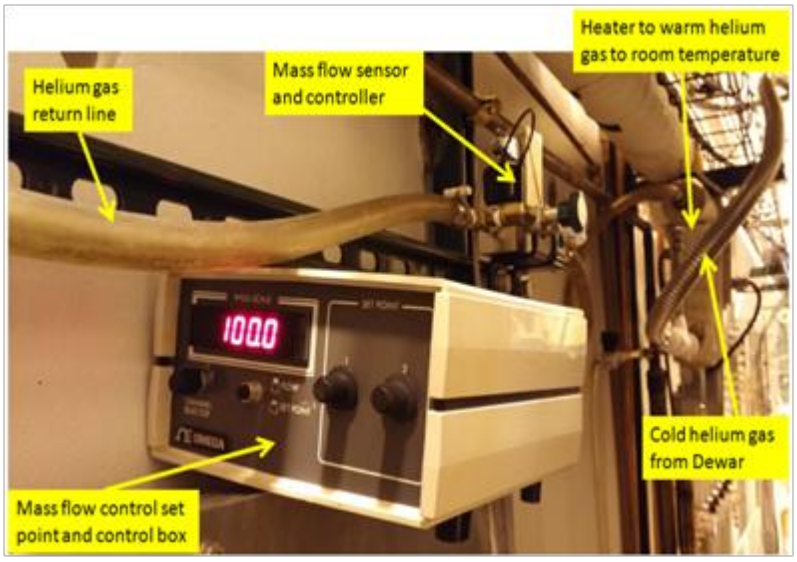

Figure 6.4.8. Flow Control Setup

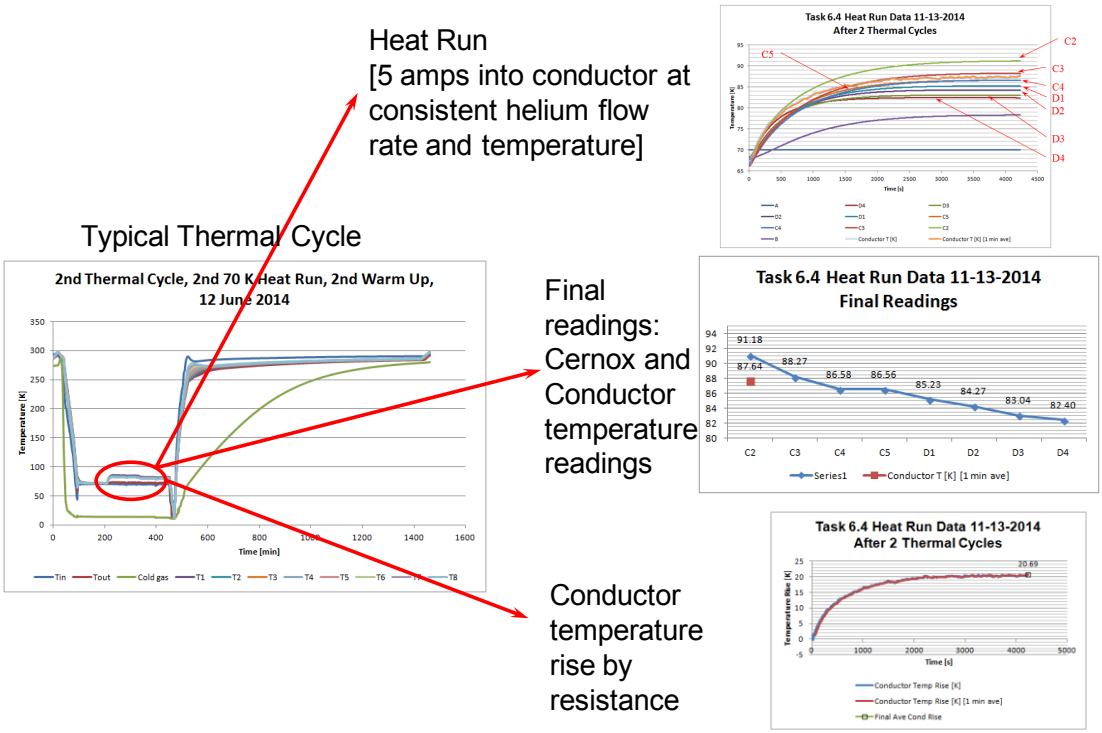

Figure 6.4.9. Thermal Cycle Data Taken

Heat Run

The heat run testing consisted of documenting the temperatures from the Cernox sensors, as well as the calculated temperature rise by resistance for the conductor, starting from 70 Kelvin with consistent cooling gas temperature and flow (Figure 6.4.10).

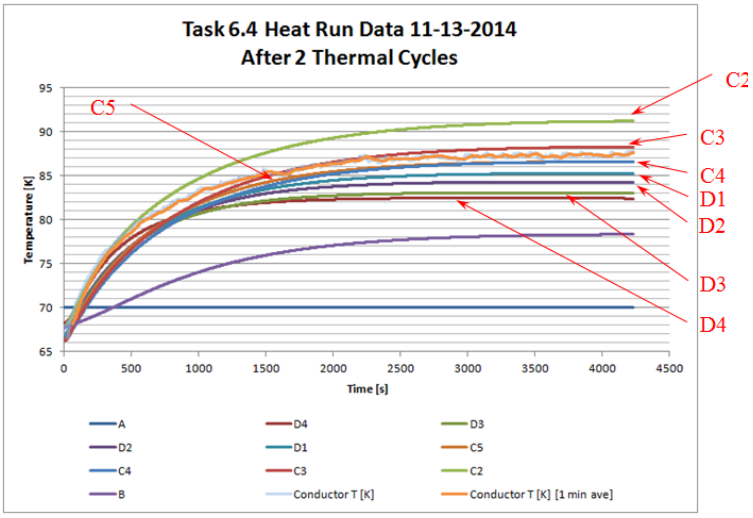

Figure 6.4.10. Early Heat Run Data

Summary

Runs on 11/13/2014 and 12/12/2014 were run with less gas flow [flow controls not yet in place]. Cold and hot gas temperatures were very consistent at 10, 15 and 25 thermal cycles (Figure 6.4.11).

Cernox readings were very consistent 10 through 25 cycles [worst case 0.6 K for one sensor]. Conductor calculated temperatures not as consistent with 1.6-K variation (Figure 6.4.12).

The consistency of Cernox readings indicate the heat transfer is remaining intact with minimal effects from thermal cycling.

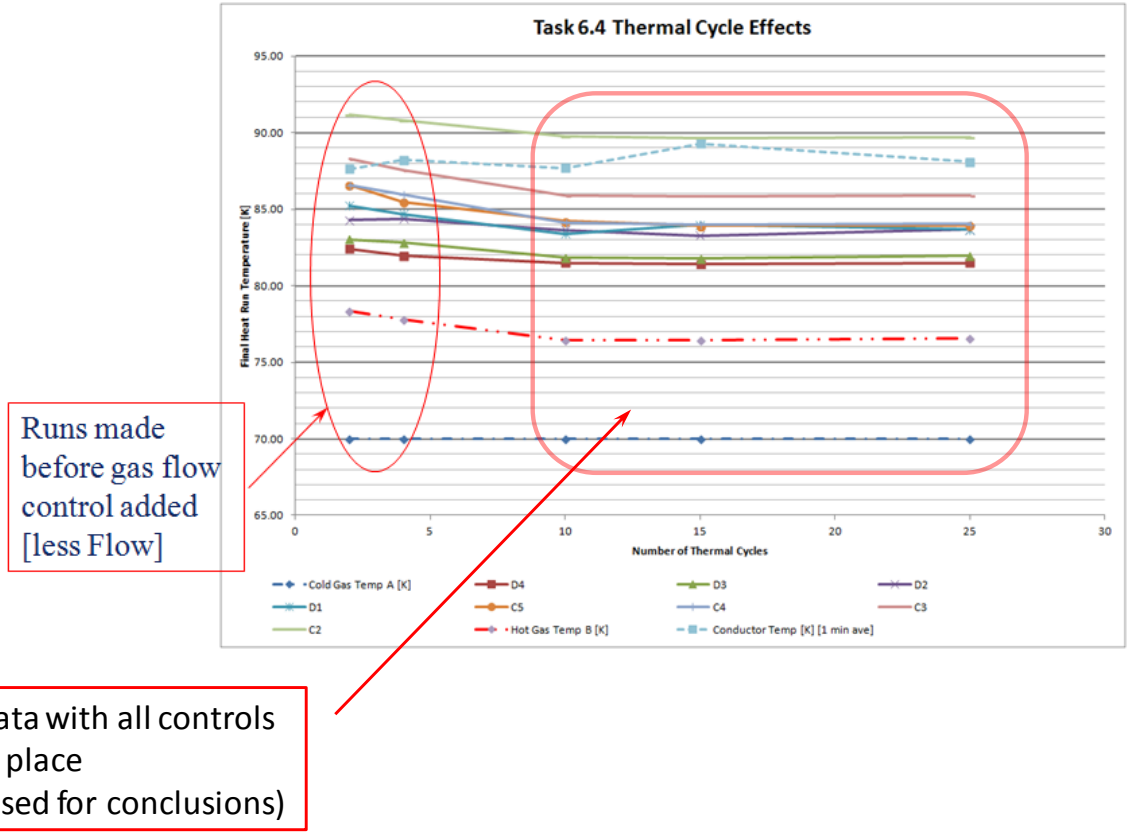

Figure 6.4.11. Comparison Data from all Runs

The electrical loss per inch in this test is 300 times the expected AC losses per inch in FSG operation. The FSG temperature rise would therefore be 1/300 of the observed results:

- 1.6-K conductor temperature delta would be 0.005 K from thermal cycling.
- 0.6-K Cernox delta would be 0.002 K from thermal cycling.

The results indicate thermal cycling should not cause significant system degradation in operation.

The conductor Kapton layer for this experiment was non-adhesive-backed Kapton hand wrapped onto the conductor. The reduced Kapton tensioning may have contributed to behavior variation at the conductor/Kapton interface.

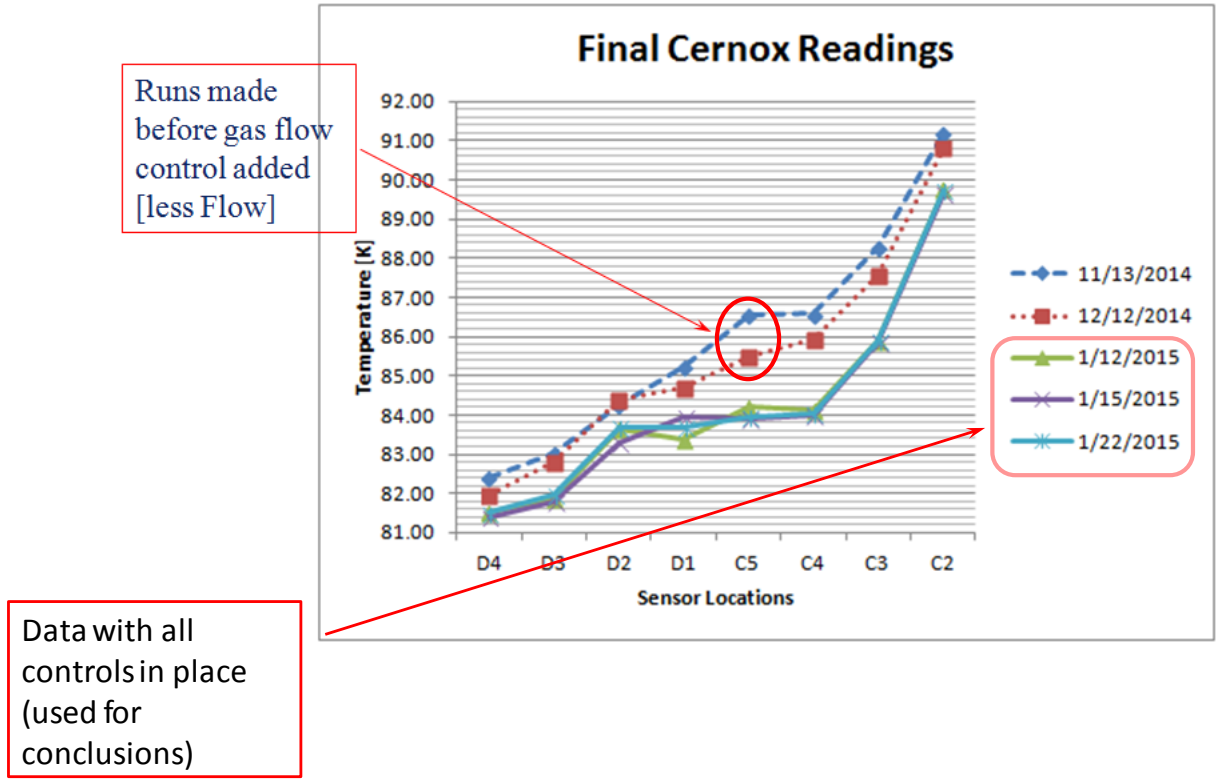

Figure 6.4.12. Final Cernox Readings from all Runs

Visual Inspection

Following the Argonne testing, the sample was removed and visually examined. The sample was pristine, with no evidence to suggest conductor poke out movement or de-bonding between the composite and cooling tube (Figure 6.4.13 through Figure 6.4.20).

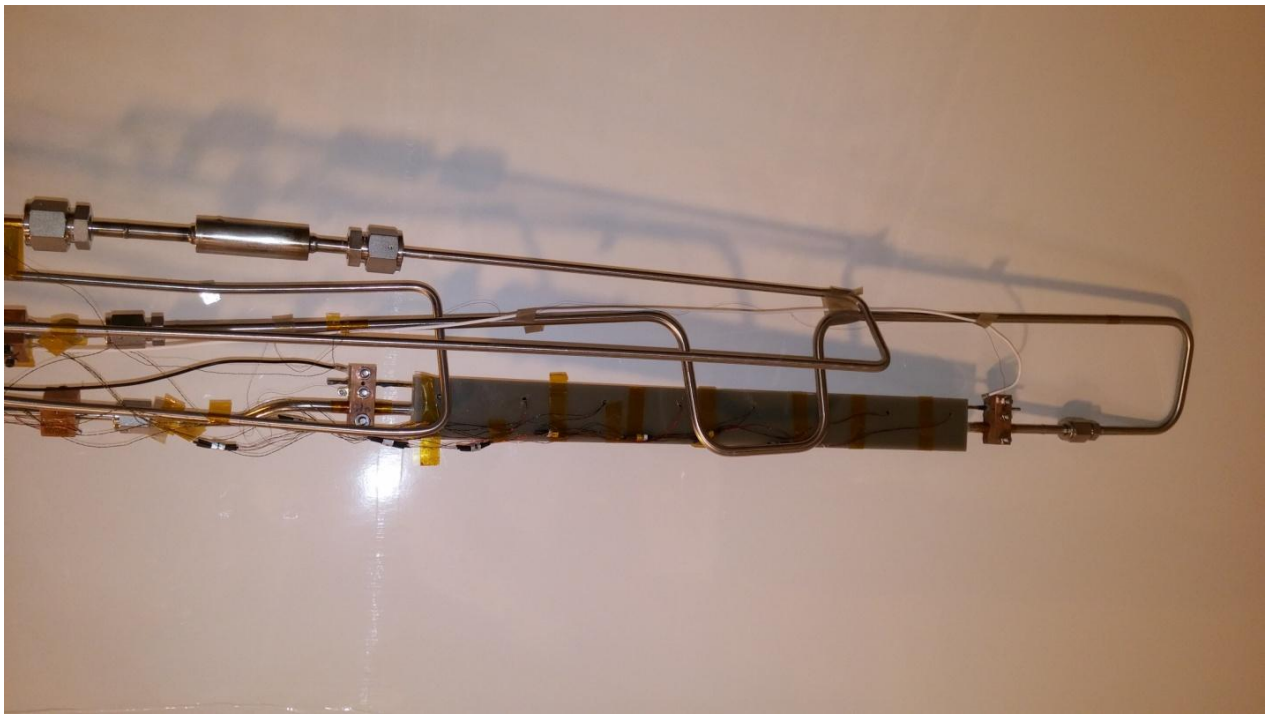

Figure 6.4.13. Task 6.4 Sample after all Testing

Figure 6.4.14. Task 6.4 Sample Disconnected after all Testing

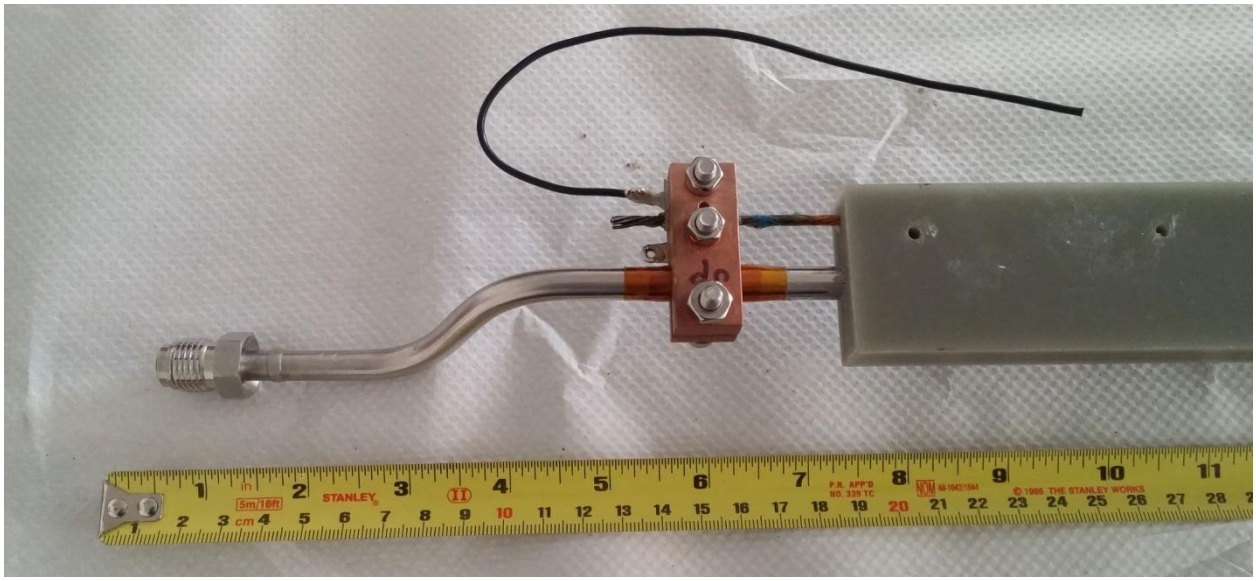

Figure 6.4.15. Task 6.4 Sample, Top End

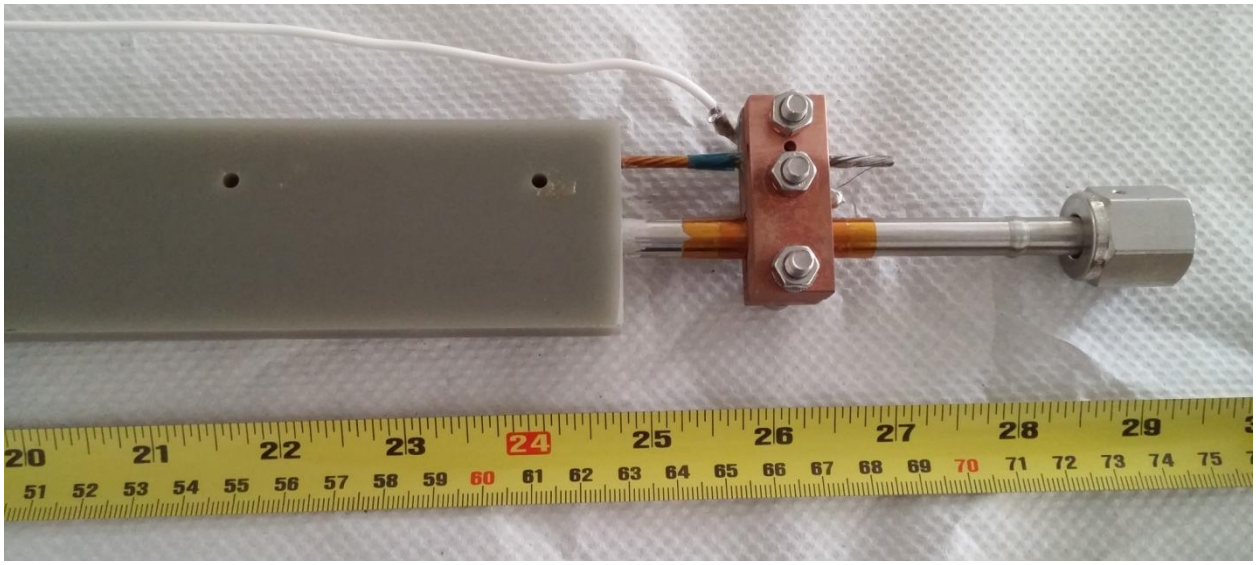

Figure 6.4.16. Task 6.4 Sample, Bottom End

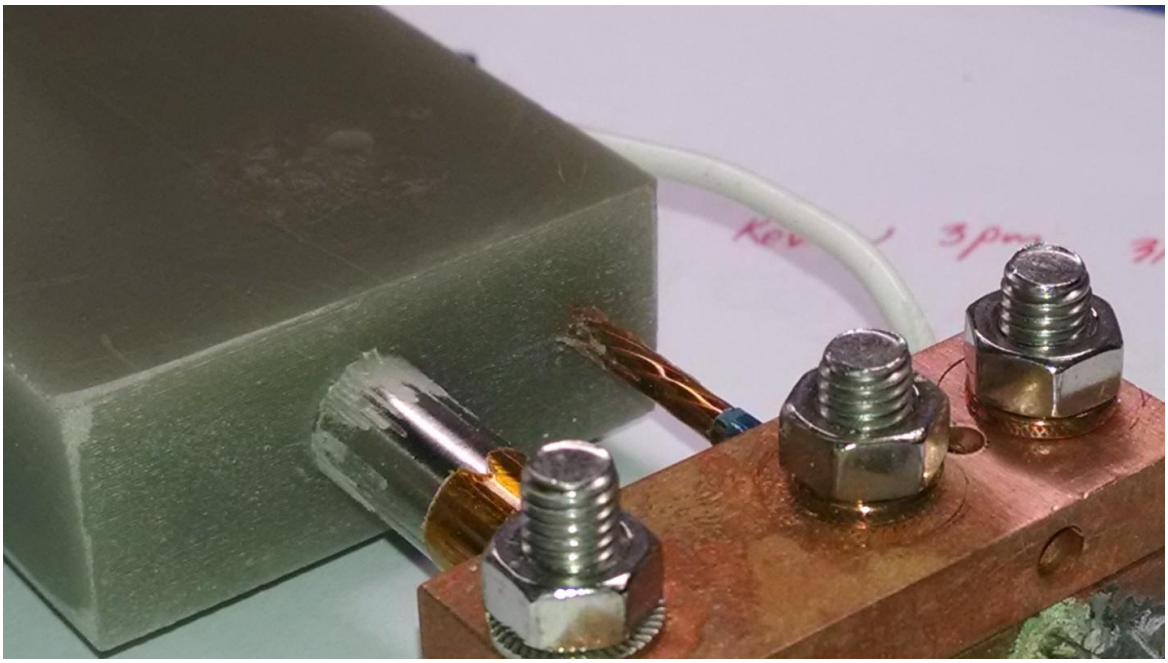

Figure 6.4.17. Task 6.4 Sample after Testing, Bottom Detail

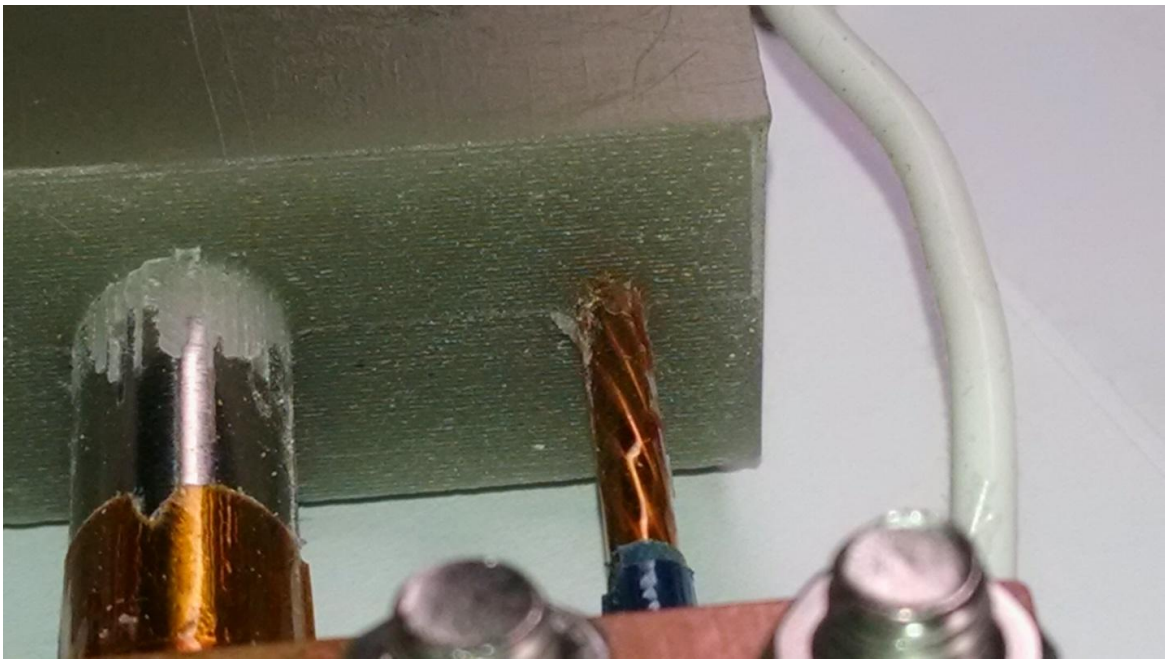

Figure 6.4.18. Task 6.4 Sample after Testing, Bottom End Detail 2

Figure 6.4.19. Task 6.4 Sample after Testing, Top End Detail

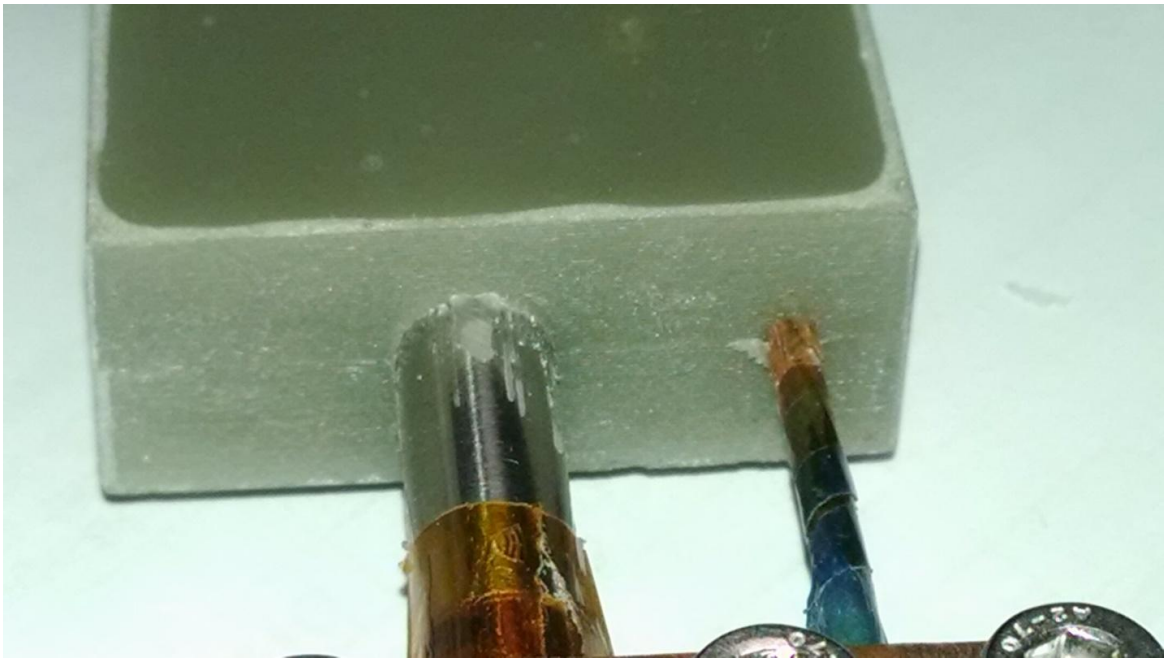

Figure 6.4.20. Task 6.4 Sample after Testing, Top End Detail 2

3.2.3.5.2 Report period: July1, 2013 to September 30, 2013 (Q5)

Plans from Last Quarter:

- Obtain cryostat details from ANL
- Rough size and geometry information has been received.
- Other tasks remaining
  - Optimize length for full thermal stress development
  - Determine/document heat run procedure
  - Make components
  - Test

Major Activities

Thermal Cycling Loading Summary

Following the Team meeting in July, a simple concept using a single pass for a cooling tube and conductor was defined. Cernox temperature sensors are placed midway between the cooling tube and conductor (Figure 6.4.21). Thermal performance of the system is verified intermittently in the thermal cycling regimen using heat runs similar to those developed for Task 6.2b. Heat transfer degradation is seen with sensor temperature changes relative to the baseline heat run. As an interface degrades, the thermal resistance increases. If there is degradation at the conductor, the sensor temperature will reduce. If there is degradation at the cooing tube, the sensor temperature will increase. Several sensors along the sample show relative condition of the system and will lead to better autopsy focus, should degradation occur.

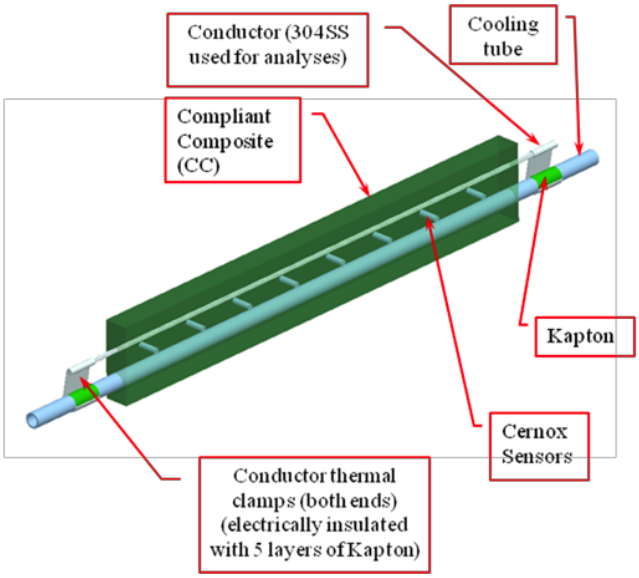

Figure 6.4.21. Thermal Testing Concept Design

Finite Element Analysis (FEA)

Test Sample Design (Heat Transfer Degradation Temperature Effects)

This study shows the resulting temperature distribution within the two test sample configurations (with and without thermal clamps at the sample ends) from a heat run with about 2.5W conductor heating at 15-K helium temperature at the tube ID with:

- Expected heat transfer
- Contact segments between the tube and composite completely disabled (NO heat transfer)

- Contact segment completely disabled (NO heat transfer) between the Kapton insulation and composite.

Results of this Study:

This study shows the heat generation within the exposed ends of the conductor will affect the experimental data curve shape. See the nominal curve shape for with and without the thermal clamps on the conductor ends (Figure 6.4.22).

Comparison to subsequent heat runs should clearly indicate local variations in thermal behavior within the sample.

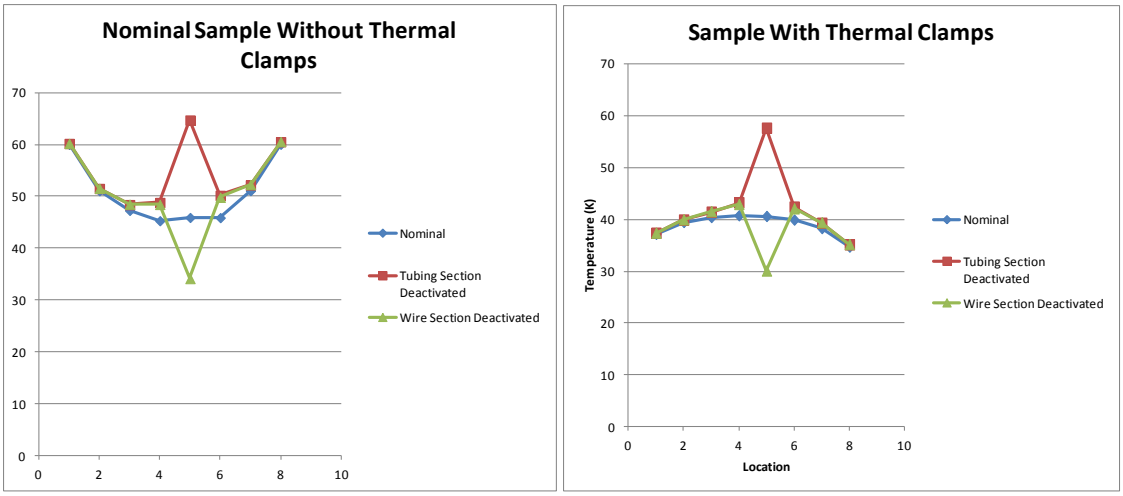

Figure 6.4.22. Temperature distribution differences within two test sample configurations

The local heat transfer changes not only show temperature change, but also indicate whether heat transfer is degraded at the conductor or cooling tube interfaces (Figure 6.4.23).

Thermal clamps at conductor ends are needed. Temperatures at the conductor ends are greatly influenced by the thermal clamps.

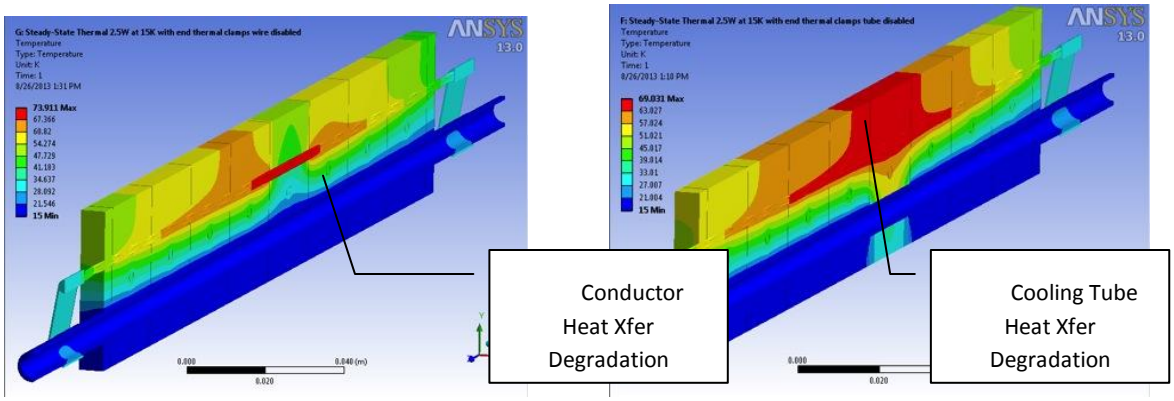

Figure 6.4.23. Heat Transfer Degradation

Test Sample Cool-Down Transients

This study shows the resulting transient temperatures and stresses within the test sample from a cool down from RT (295 K) to 15 K with 300 W/[m^2 K] at the ID of the cooling tube. The helium temperature is 15 K throughout the cool down for this analysis. The actual process will likely include a stair step reduction in gas temperature with a limited separation of sample temperature and gas temperature.

Results of this Study:

The sample will take about 3 hours to cool down to 15 K using a helium flow producing 300 W/[m^2 K] convection at the ID of the cooling tube. Subsequent input from Argonne is a convection coefficient between 500 and 1000 W/[m^2 K] is more realistic.

The Cernox sensors with the thermal end clamps will indicate with a maximum temperature spread of about 3.25 K in the middle of the cool down, but will recover to be within 1 K of each other by the end of the cool down. The thermal clamp sizing and thickness may be "tuned" to balance the end effects on temperature.

Different convection levels should be examined to determine the minimum safe time possible for Task 6.4.

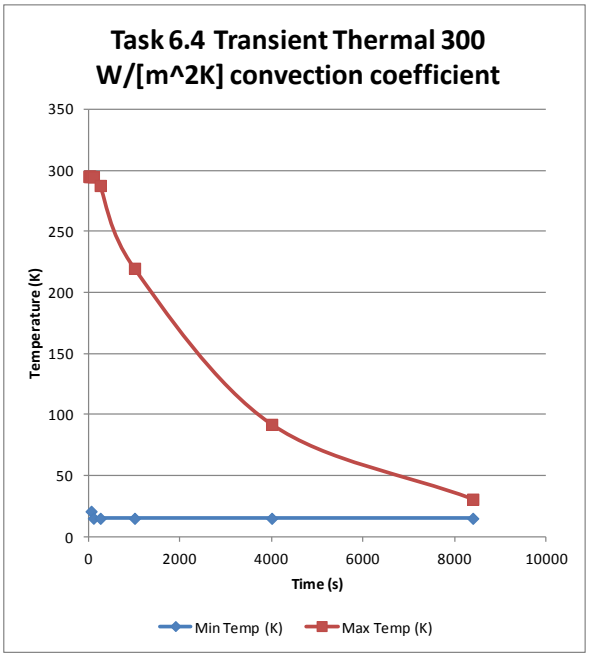

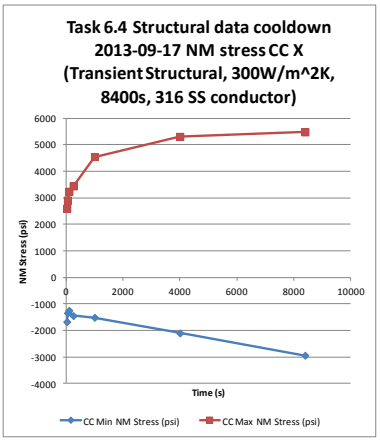
Task 6.4 Structural data cooldown 2013-09-17 NM stress CC X (Transient Structural, 300W/m^2K, 8400s, 316 SS conductor)
NM Stress (psi)
Time (s)
CC Min NM Stress (psi)
CC Max NM Stress (psi)

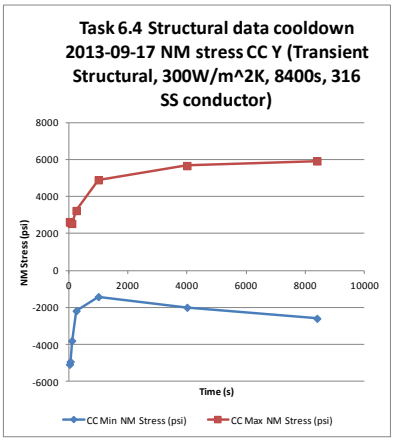
Task 6.4 Structural data cooldown 2013-09-17 NM stress CC Y (Transient Structural, 300W/m^2K, 8400s, 316 SS conductor)
NM Stress (psi)
Time (s)
CC Min NM Stress (psi)
CC Max NM Stress (psi)

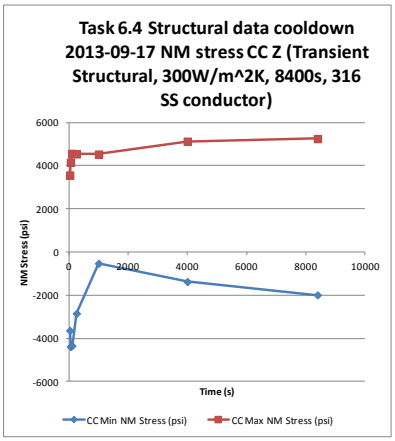
Task 6.4 Structural data cooldown 2013-09-17 NM stress CC Z (Transient Structural, 300W/m^2K, 8400s, 316 SS conductor)
NM Stress (psi)
Time (s)
CC Min NM Stress (psi)
CC Max NM Stress (psi)

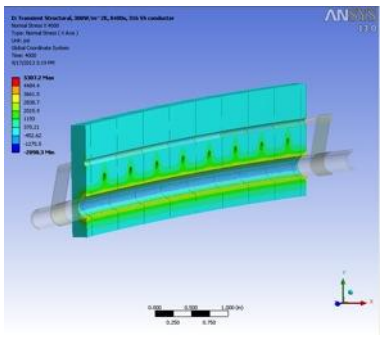

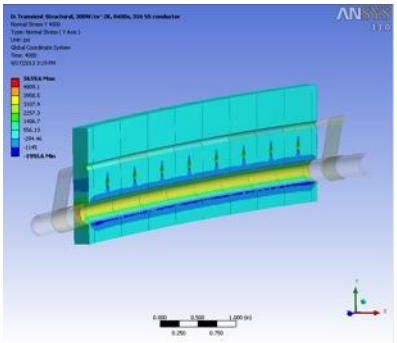

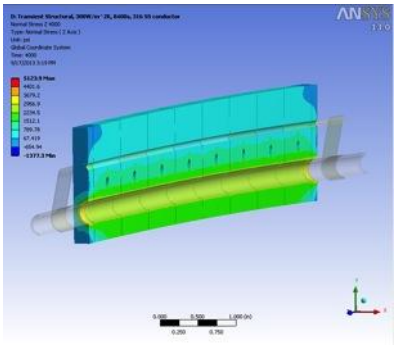

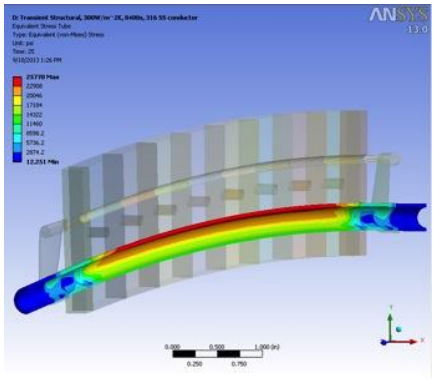

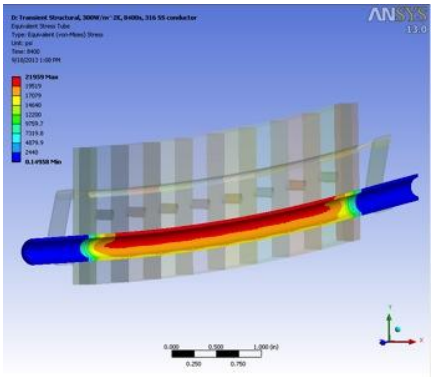

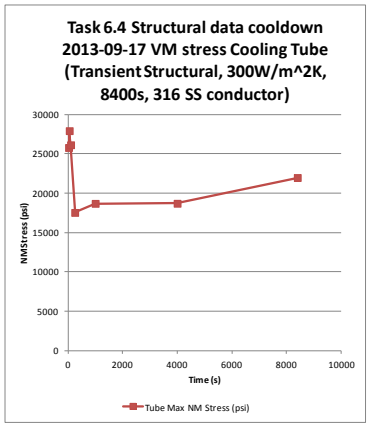
Task 6.4 Structural data cooldown 2013-09-17 VM stress Cooling Tube (Transient Structural, 300W/m^2K, 8400s, 316 SS conductor)
NMStress (psi)
Time (s)
Tube Max NM Stress (psi)

Task 6.4 Specific Objectives

- Develop experiment and detailed test plan for the build and test of a subscale torque tube at cryogenic temperature for the purpose of understanding:
  - The mechanical performance of the composite torque tube under multiple thermal cycles.
  - The thermal and mechanical performance of cooling tubes, integrated into the torque tube.
  - The thermal performance of conductors embedded into the torque tube

Task 6.4 Significant Results, Including Major Findings, Developments or Conclusions (Positive or Negative)

- The test sample configuration has been revised to allow better understanding of the thermal performance. The sensor location between the conductor and cooling tube provides probable degradation location, as well as whether it has happened.
- The need for thermal clamps on the conductor ends was shown.
- The thermal behavior for heat transfer changes was shown.
- The initial transient stresses can be high with a low Helium gas temperature throughout the cool down of the sample. A stair step cooling gas temperature approach is needed.
- The cooling tube was too far from the sample assembly neutral axis, causing sample bending during the cool down.
- Argonne National Laboratory (ANL) provided a convection coefficient range to use, going forward.

Task 6.4 Plans for Next Quarter

- Obtain cryostat details from ANL
- Optimize length for full thermal stress development
- Determine cool down and heat up procedure
- Determine/document heat run procedure
- Make components.

3.2.3.5.3 Report period: October 1, 2013 to December 31, 2013 (Q6)

Task 6.4 Plans from Last Quarter

- **Obtain cryostat details from ANL**

  ANL provided details and photographs of the planned cryostat. The photographs, combined with key dimensions from ANL, enabled a Task 6.4 thermal cycling design to be developed (Figure 6.4.24). Figure 6.4.25 shows a model of the existing top plate with the thermal cycling sample inside the modeled interior of the cryostat to ensure proper fit.

Figure 6.4.24. ANL Photographs of Planned Cryostat

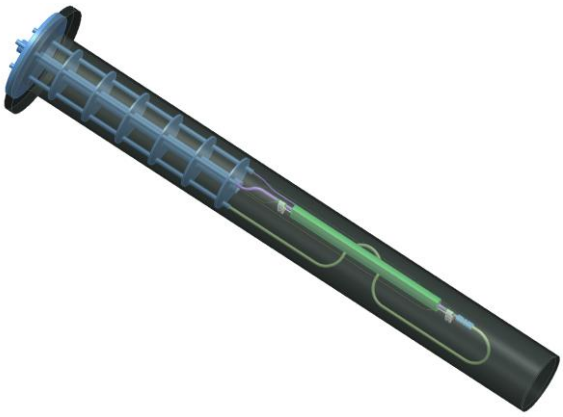

Figure 6.4.25. Model of the existing Top Plate with Thermal Cycling Sample

Figure 6.4.26 shows a model of the sample assembly attached to the existing top plate assembly. Figure 6.4.27 shows a model of Task 6.4 geometry sent to AML for detail design, cooling tube and conductor assembly manufacture in preparation for the casting process.

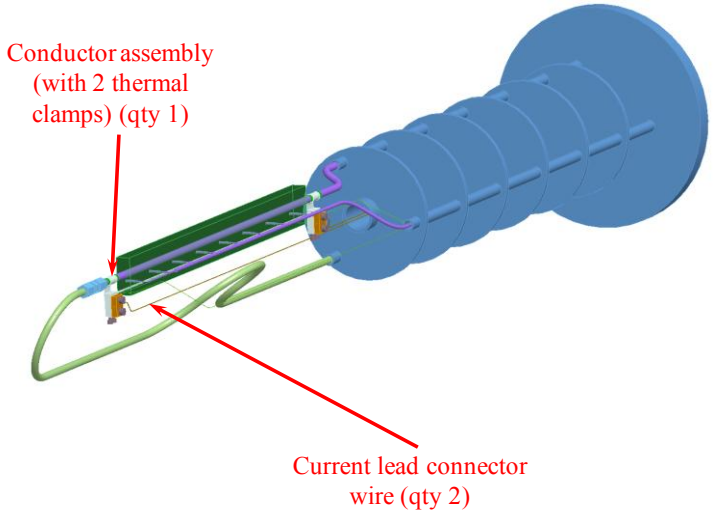

Figure 6.4.26. Model of Sample Assembly

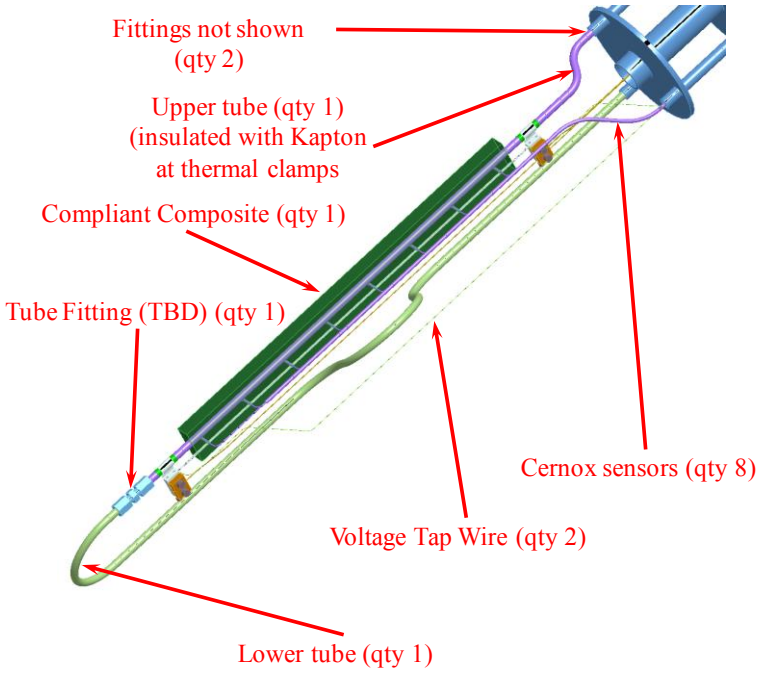

Figure 6.4.27. Task 6.4 Geometry sent to AML

- **Optimize length for full thermal stress development**

  Stress calculations of three different lengths showed similar stress levels to show the stress relatively independent of length. Based on using the longest possible sample still able to use the existing molds at COMTEC and minimizing the rework/cost, a length of 17.5 inches was selected.

- **Determine cool-down and heat-up procedure**

  FEA transient studies of the proposed sample based on process suggestions from Jerry Nolen, Argonne National Lab, have produced a recommended cool-down procedure (and heat-up procedure) for Task 6.4.

- **Determine/document heat run procedure**

  A preliminary heat run process was generated and sent out for review.

- **Make components**

  The mold modification and casting process are almost ready for trial casting.

- **Test**

  A trial cast sample will be needed before the actual samples for the ANL testing will be made.

Task 6.4 Major Activities

Determination of sample length came from a series of steady-state structural thermal studies at 10.5, 15.75 and 21 inches long (Figure 6.4.28).Similar stress ranges were seen for all three examined lengths. Based on that, the decision was to use the longest sample possible with existing molds at COMTEC.

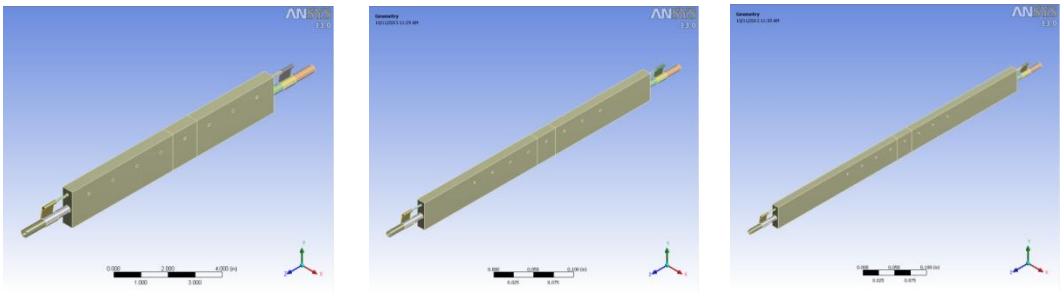

Figure 6.4.28. Model Geometries Examined

Cooling Tube VM Stress (psi) at 15K			
Length (inch) =>	10.5	15.75	21
VM Stress Cooling Tube min	0	0	0
VM Stress Cooling Tube max	25,718	25,721	25,769
VM Stress Cooling Tube min at CTR	23,819	23,802	23,807
VM Stress Cooling Tube max at CTR	25,718	25,716	25,711

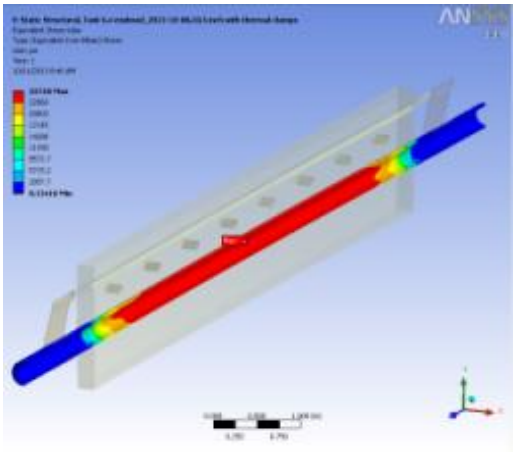

Above are results for the cooling tube stresses.

Cable VM Stress (psi) at 15K			
Length (inch) =>	10.5	15.75	21
VM Stress Cable min	29	29	66
VM Stress Cable max	31,846	31,880	31,942
VM Stress Cable min at CTR	26,822	26,833	26,843
VM Stress Cable max at CTR	27,494	27,493	27,526

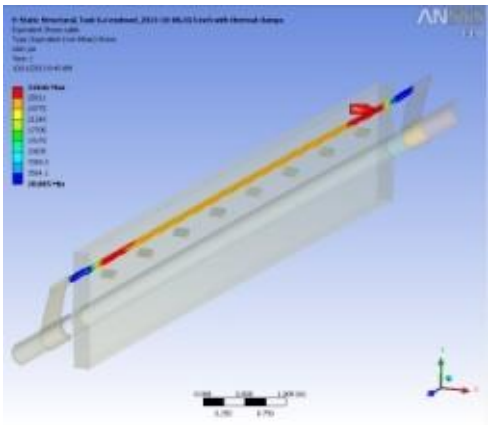

Above are results for the conductor stresses.

Compliant Composite Stress (psi) at 15K			
Length (inch) =>	10.5	15.75	21
NM Stress CC X min	-5,541	-5,400	-5,579
NM Stress CC X max	7,549	7,215	7,113
NM Stress CC X min at CTR	-5,541	-1,562	-1,587
NM Stress CC X max at CTR	7,549	3,306	3,336
NM Stress CC Y min	-3,497	-3,349	-3,386
NM Stress CC Y max	9,399	9,123	9,050
NM Stress CC Y min at CTR	-1,804	-1,821	-1,752
NM Stress CC Y max at CTR	3,831	3,837	3,846
NM Stress CC Z min	-1,410	-1,387	-1,563
NM Stress CC Z max	6,198	6,320	6,243
NM Stress CC Z min at CTR	1,243	1,244	1,242
NM Stress CC Z max at CTR	2,501	2,494	2,501
SH Stress CC XY min	-4,215	-4,452	-4,339
SH Stress CC XY max	4,541	4,493	4,443
SH Stress CC XY min at CTR	-2,725	-2,727	-2,682
SH Stress CC XY max at CTR	2,737	2,723	2,697
SH Stress CC YZ min	-4,104	-4,487	-4,222
SH Stress CC YZ max	4,410	4,017	4,409
SH Stress CC YZ min at CTR	-43	-26	-33
SH Stress CC YZ max at CTR	47	29	23
SH Stress CC XZ min	-4,198	-4,121	-4,603
SH Stress CC XZ max	4,276	4,048	4,403
SH Stress CC XZ min at CTR	-32	-39	-*
SH Stress CC XZ max at CTR	26	39	-*
* Missing Plot			

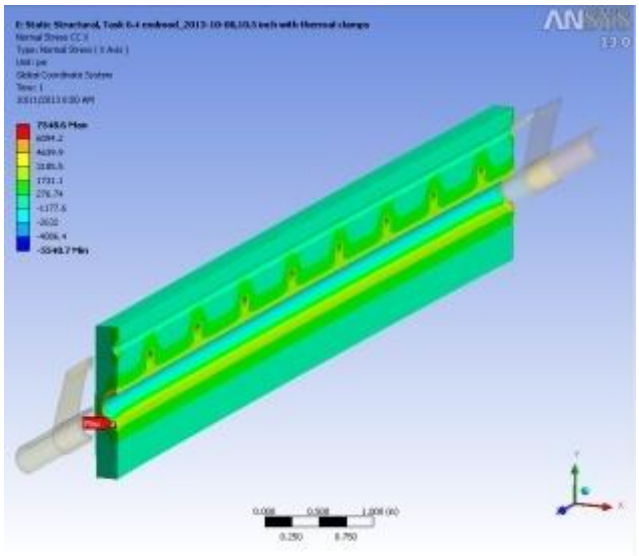

Above are results for the compliant composite stresses.

Kapton Stress (psi) at 15K			
Length (inch) =>	10.5	15.75	21
NM Stress Kapton X min	-2,139	-2,199	-2,449
NM Stress Kapton X max	5,145	5,123	4,636
NM Stress Kapton X min at CTR	-1,501	-1,437	-1,480
NM Stress Kapton X max at CTR	1,501	1,499	1,430
NM Stress Kapton Y min	-2,448	-2,375	-2,390
NM Stress Kapton Y max	4,876	4,780	4,806
NM Stress Kapton Y min at CTR	-1,353	-1,316	-1,316
NM Stress Kapton Y max at CTR	1,606	1,429	1,504
NM Stress Kapton Z min	-1,563	-2,164	-2,170
NM Stress Kapton Z max	3,800	4,350	4,088
NM Stress Kapton Z min at CTR	50	117	73
NM Stress Kapton Z max at CTR	957	920	948
SH Stress Kapton XY min	-1,866	-1,950	-1,705
SH Stress Kapton XY max	1,489	1,752	1,888
SH Stress Kapton XY min at CTR	-824	-936	-847
SH Stress Kapton XY max at CTR	992	851	935
SH Stress Kapton YZ min	-4,985	-5,121	-5,044
SH Stress Kapton YZ max	5,237	5,235	5,198
SH Stress Kapton YZ min at CTR	-34	-60	-42
SH Stress Kapton YZ max at CTR	31	57	43
SH Stress Kapton XZ min	-5,182	-5,277	-5,207
SH Stress Kapton XZ max	4,827	4,857	4,833
SH Stress Kapton XZ min at CTR	-33	-62	-39
SH Stress Kapton XZ max at CTR	30	63	40

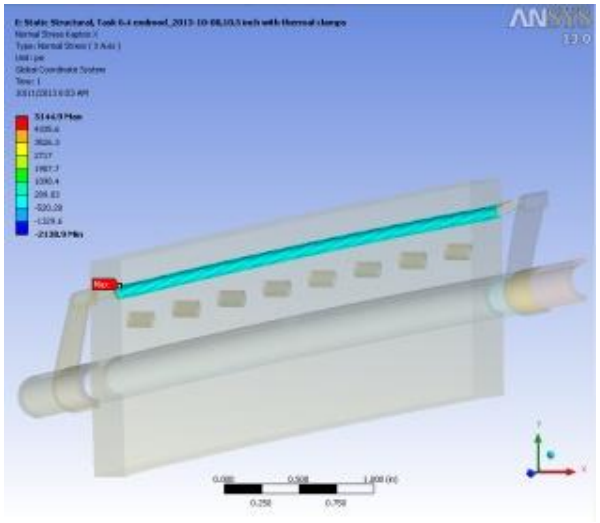

Above are results for the Kapton stresses.

Cool-down procedures were determined by comparison of a direct cool down compared to a stepped cool down, which limits the maximum temperature spread within the sample. The direct cool down used a constant source of 15 C helium passing through the cooling tube (Figure 6.4.29). The stepped process limited the maximum temperature step to approximately 50 K. The process of analysis performed multiple studies modifying the step size and timing of the temperature boundary conditions until the desired process was achieved.

Direct Cool Down with Initial Geometry

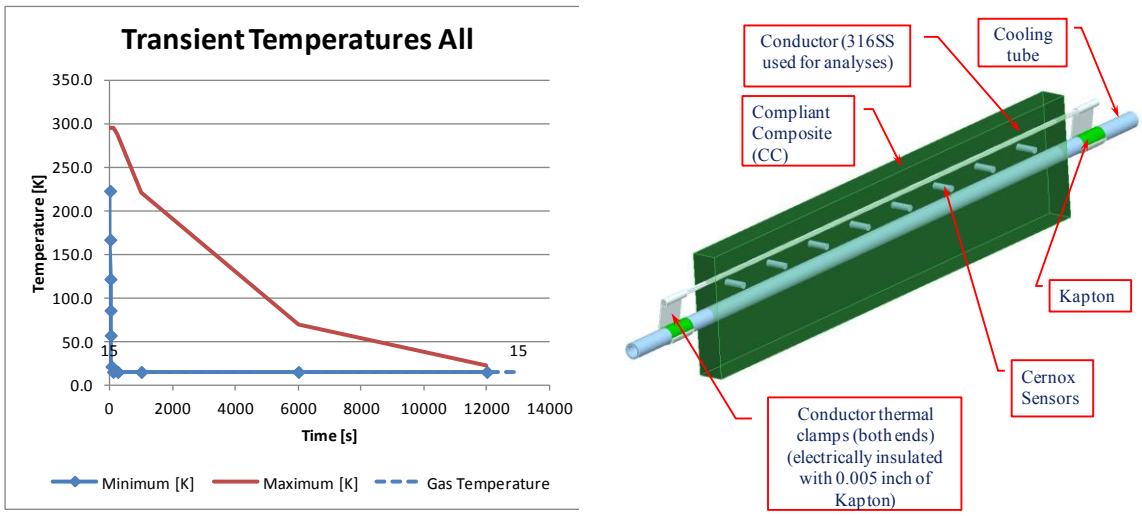

Figure 6.4.29. Direct Cool-Down Temperatures and Geometry

Figure 6.4.30 shows in the direct method, extreme peak stresses develop in the beginning of the cool down.

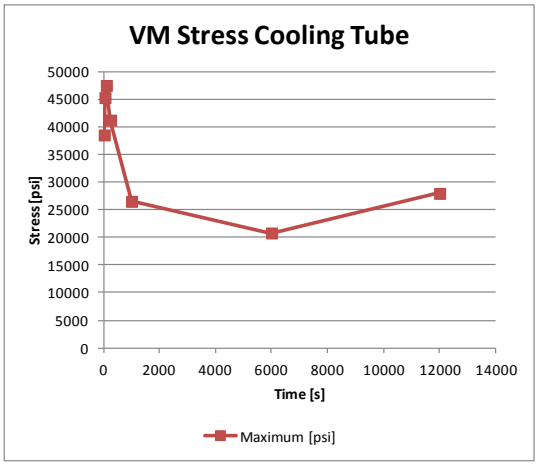

Figure 6.4.30. Peak stresses develop in the beginning of the cool down.

Figure 6.4.31 shows the stepped cool-down geometry and temperatures.

Stepped Cool Down with Final Geometry

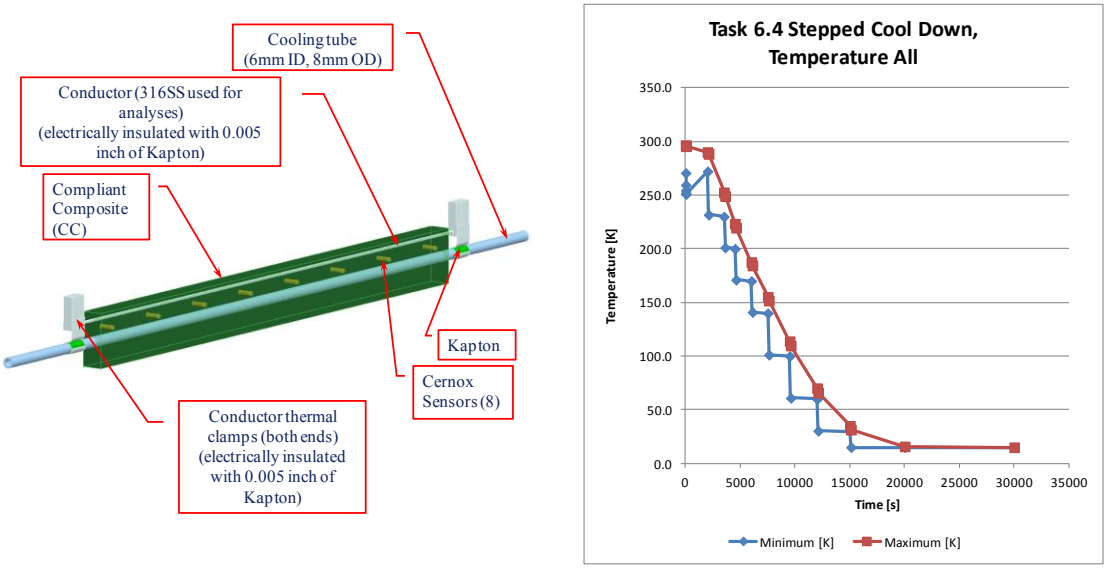

Figure 6.4.31. Stepped Cool-Down Temperatures and Geometry

Figure 6.4.32 shows that peak stress for the cool down using the stepped process occurs at the final temperature.

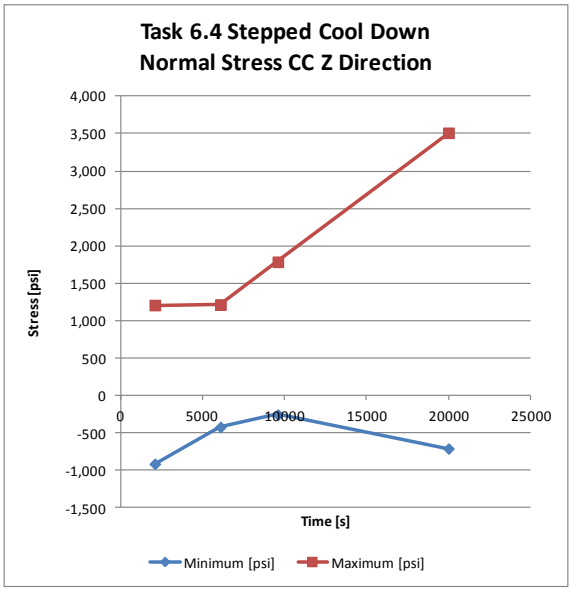

Figure 6.4.32. Peak stress develops for cool down at final temperature.

The time for cool down is increased roughly by 2.5 hours by a stepped approach, but stresses remain acceptable throughout the process.

Task 6.4 Sample Design

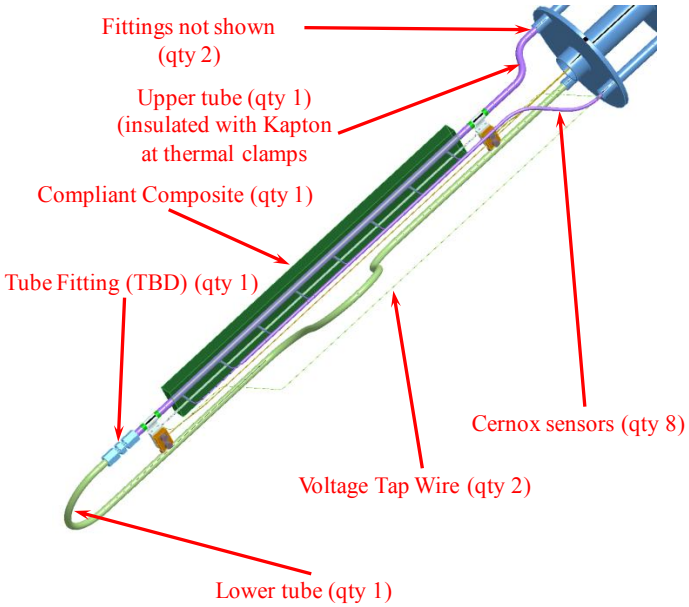

Figure 6.4.33. Final Model Geometry Sent to AML

Figure 6.4.33 shows the final model geometry sent to AML

AML is detailing the component designs for the sample. The conductor and cooling tube assemblies will be premade and sent to COMTEC for the sample casting process. They are being premade to avoid any post casting high temperature operations, such as soldering, welding, brazing, etc. High temperatures beyond 100 C risk damage to the sample integrity.

Task 6.4 Significant Results, Including Major Findings, Developments or Conclusions (Positive or Negative)

Based on AN-provided cryostat geometry, test sample geometry was established. The test sample configuration has been finalized and components are now being manufactured.

The initial transient stresses will be too high with a constant, low Helium gas temperature direct cool-down approach. Details of an acceptable stair step cooling gas temperature approach have been studied. An approach using a maximum temperature differential between the cooling gas and the Cernox temperature sensors of less than 50 K should yield acceptable stresses during the cool-down and heat-up processes. To support the stair-step cool-down process, ANL will add a second cryostat with the function of temperature control.

The heat run start temperature of 70 K was determined as the minimum to allow determination of the conductor (316 SS) temperature rise by resistance. The resistivity of 316 SS flattens below 60 K.

Task 6.4 Plans for Next Quarter

- Document cool-down and heat-up procedures
- Document heat-run procedure
- Make components
- Test

3.2.3.5.4 Report period: January 1, 2013 to March 31, 2014 (Q7)

Task 6.4 Plans from Last Quarter

- **Document cool-down and heat-up procedure/Document heat-run procedure**

  A draft procedure for the ANL testing was distributed for feedback. The document covers the methods for cool down and warm up of the sample using cooling gas during the thermal cycling, as well as the heat-run procedures to determine heat transfer changes caused by thermal cycling.

- **Make components**

  A trial sample and the test sample are complete and at ANL. ANL is using the trial sample for checkout of the test system set up.

- **Test**

  A tentative test window is scheduled for the week of 19 May.

Task 6.4 Major Activities

Task 6.4 thermal cycling sample design has been developed. Figure 6.4.34 shows a solid model of the existing top plate with the thermal cycling sample inside the modeled interior of the cryostat to ensure proper fit.

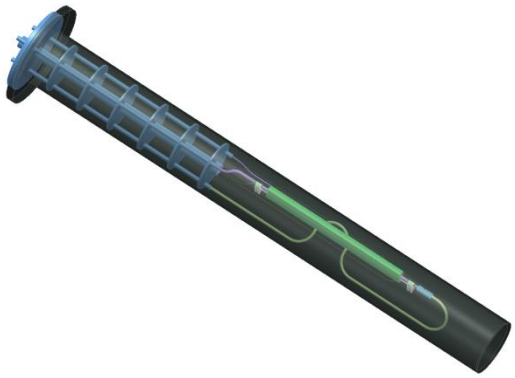

Figure 6.4.34. Thermal Cycling Sample Design

The sample configuration and mold details came together and are shown in Figure 6.4.35. Prototype mold components made using a 3D printer are fully functional in about one hour; maintaining conductor tension during casting operations.

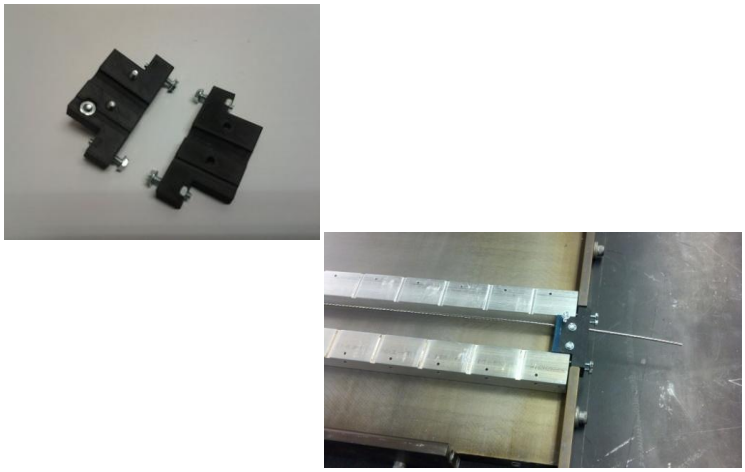

Figure 6.4.35. Prototype Mold Components made using 3D Printer

A trial pour was made successfully, leading to the final sample (Figure 6.4.36).

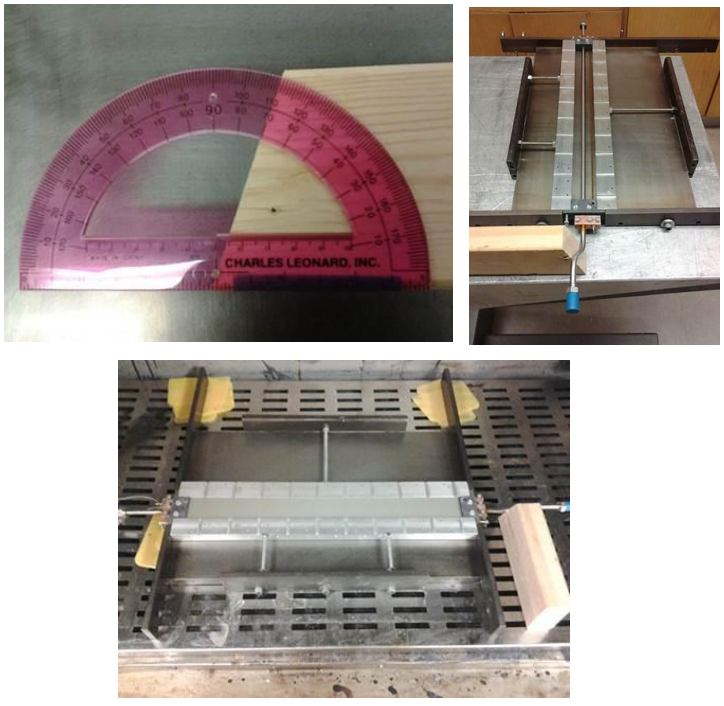

Figure 6.4.36. Successful Trial Pour

The resulting final Task 6.4 sample (Figure 6.4.37) was then sent to AML for machining and final preparations for testing at Argonne National Laboratory (ANL).

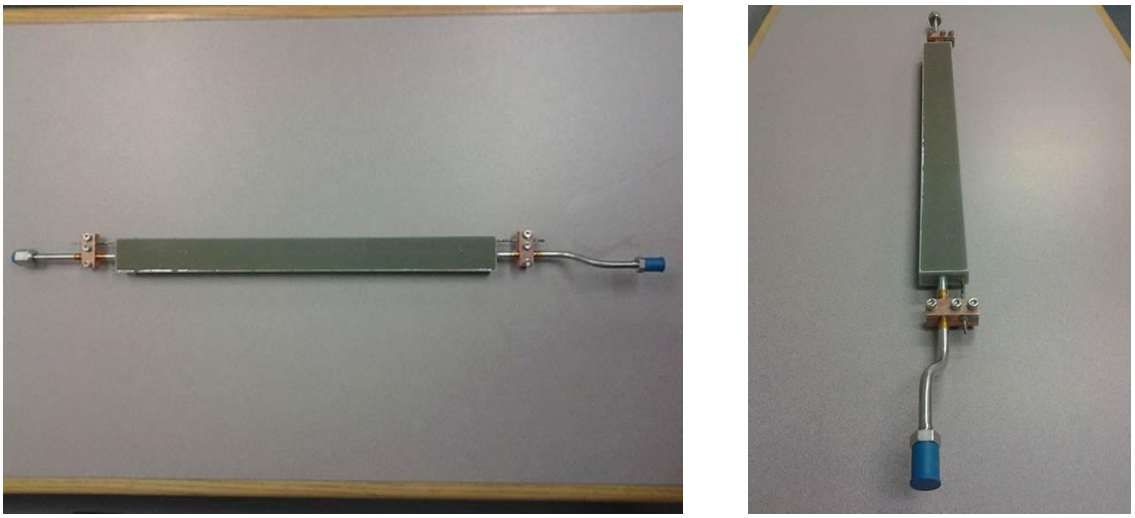

Figure 6.4.37. Final Task 6.4. Sample

Task 6.4 Significant Results, Including Major Findings, Developments or Conclusions (Positive or Negative)

- The casting process for the CC material based samples was fully developed, leading to a successful test sample.

Task 6.4 Plans for Next Quarter

- Make final preparations for running the experiment and perform testing.

3.2.3.5.5 Report period: April 1, 2012 to June 30, 2014 (Q8)

Task 6.4 Plans from Last Quarter:

- **Make final preparations for running the experiment and perform testing.**

  Testing is now underway.

Task 6.4 Major Activities

A dummy sample was made, mounted and tested to check the capability for controlling the mixed inlet gas temperature. After a successful pre-test, the official sample was assembled into the setup and testing started (Figure 6.4.38).

Figure 6.4.38. Dummy Sample Pre-test and Official Test Setup

Following the pre-testing, Darrell Morrison, Kato Engineering, and Jerry Nolen, Argonne National Laboratory, met at ANL to begin the Task 6.4 testing. Prior to beginning the first cryogenic cool down, a "practice" heat run at room temperature was performed to validate the procedure. There were minor changes needed to the data collection worksheets. Following the week of testing, the test procedure was rewritten to include all testing improvements discovered. The testing setup is shown in Figure 6.4.39 and Figure 6.4.40.

Figure 6.4.39. Filling LN2

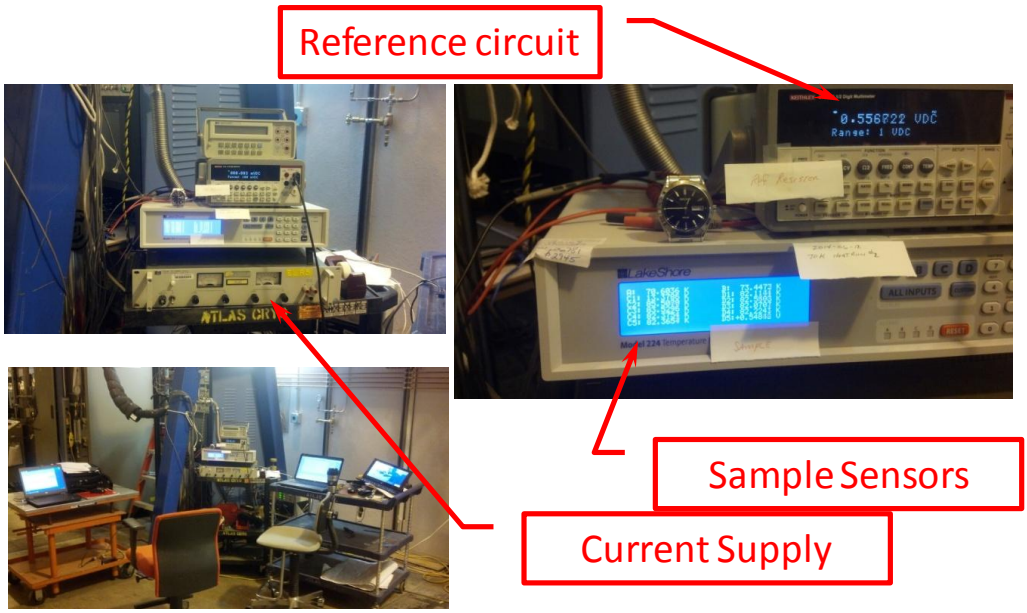

Figure 6.4.40. Testing Setup

The sample includes eight Cernox temperature sensors along the length of the sample, placed equidistant between the conductor and cooling tube. Additional Cernox sensors measure the temperatures for the cold gas, mixed inlet gas and gas out of the sample. Voltage drop for the conductor and reference resistor are also recorded during the heat runs. The data acquisition system recorded 8 sample temperatures, 3 gas temperatures and the sample voltage continuously.

Example data from a complete thermal cycle are shown in Figure 6.4.41.

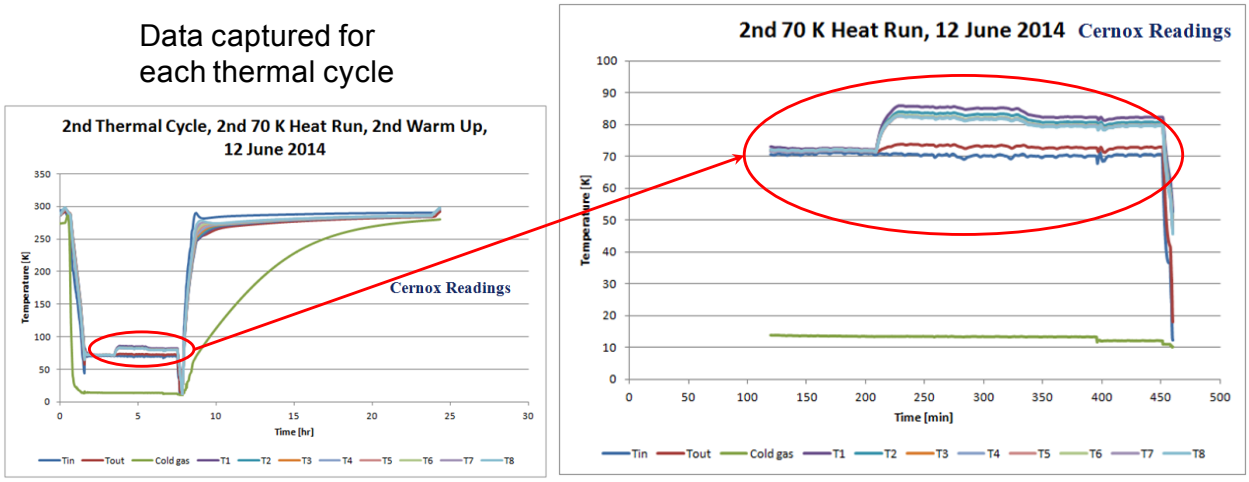

Figure 6.4.41. Example data from a complete thermal cycle

During a heat run, about 5 amps are used to heat the 316 SS conductor. This current level provides about 13 K rise in wire temperature and about 9 K rise for the Cernox sensors in the sample. The data was manually taken at the prescribed timing using a camera, transferred to a spreadsheet and analyzed.

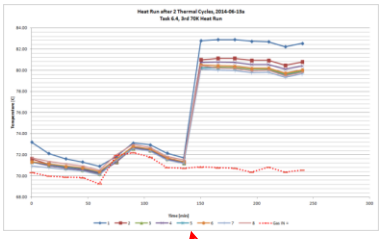

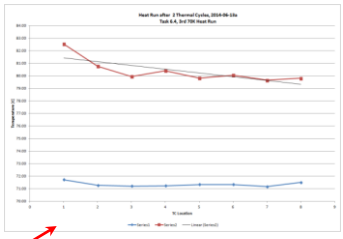

Heat run, 2014-06-12a (Task 6.4), 70K, 2nd ht run

											0	15	30	45	60	75	90	105
Time =>	10:30	10:45	11:00	11:15	11:30	11:45	12:00	12:15	12:30		12:45	13:00	13:15	13:30	13:45	14:00	14:15	14:30
TC#	0	15	30	45	60	75	90	105	120		135	150	165	180	195	210	225	240
1	73.184	72.109	71.606	71.324	70.912	71.798	73.112	72.942	72.147		71.720	82.788	82.884	82.891	82.735	82.694	82.210	82.535
2	71.617	71.116	70.829	70.659	70.304	71.290	72.641	72.472	71.679		71.271	80.982	81.115	81.100	80.930	80.921	80.461	80.767
3	71.372	70.981	70.730	70.570	70.208	71.326	72.595	72.399	71.595		71.207	80.230	80.295	80.273	80.083	80.114	79.645	79.947
4	71.306	70.979	70.735	70.584	70.230	71.307	72.618	72.422	71.617		71.220	80.742	80.760	80.726	80.547	80.549	80.088	80.396
5	71.323	71.096	70.849	70.703	70.336	71.536	72.753	72.525	71.705		71.323	80.238	80.203	80.162	79.962	79.990	79.518	79.820
6	71.359	71.153	70.926	70.772	70.393	71.567	72.795	72.553	71.728		71.338	80.505	80.434	80.385	80.186	80.201	79.730	80.036
7	70.944	70.787	70.601	70.473	70.097	71.436	72.590	72.339	71.515		71.166	80.088	80.000	79.959	79.757	79.807	79.338	79.649
8	71.721	71.390	71.140	70.957	70.535	71.996	72.976	72.686	71.838		71.496	80.441	80.191	80.157	79.915	80.001	79.475	79.801
max-min =	2.2394	1.3215	1.0058	0.8508	0.8147	0.7061	0.5226	0.6024	0.6312		0.5535	2.7009	2.8842	2.9327	2.9782	2.887	2.8721	2.8857
Gas IN =	70.336	69.994	69.892	69.851	69.250	71.948	72.209	71.796	70.804		70.725	70.842	70.783	70.737	70.358	70.840	70.370	70.561
Sensors Average =			70.927	70.755	70.377	71.532	72.760	72.542	71.728		71.343	80.752	80.735	80.707	80.514	80.535	80.058	80.369
Gas OUT =	71.3858	70.7785	70.590	70.474	70.062	71.606	72.646	72.328	71.501		71.146	72.817	73.004	73.004	72.740	72.983	72.542	72.769
Gas Flow [SCFM] =	90	90	90	90	90	90	90	90	90		90	90	90	90	90	90	90	90
Gas delta Temperature =	1.050	0.784	0.698	0.623	0.811	-0.343	0.437	0.532	0.697		0.422	1.975	2.221	2.267	2.382	2.143	2.172	2.208

During each heat run, the initial voltage readings are used to extrapolate back to time equals zero to determine the start resistance for the conductor. And the test start, the average temperatures of the Cernox sensors are used to establish the conductor start temperature. The resistivity for that temperature is used with the change in resistance during the test to determine the temperature rise of the wire. The wire temperature rise results for the first three heat runs, corrected for changing inlet gas temperature and for power level, are shown below:

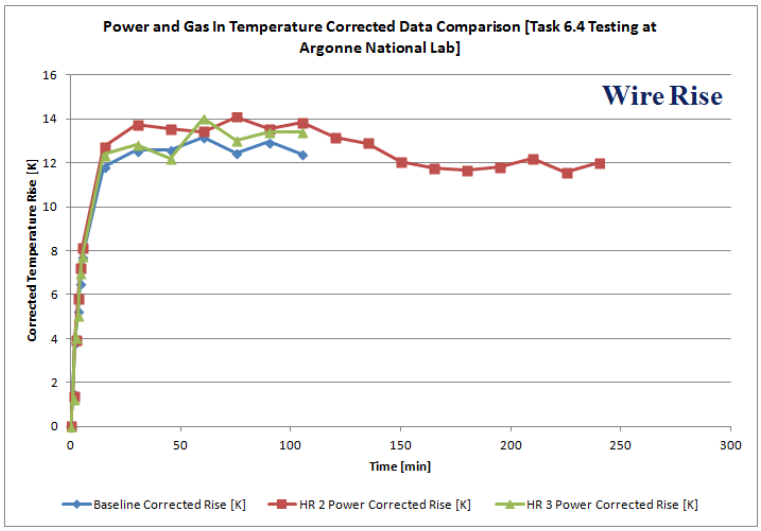

During the first two thermal cycles, it became apparent that something in the refrigeration cycle creates a time variation in the temperature of the input gas that presents difficulty in measuring small changes in temperature. The variation in supply gas temperature prevents stable, repeatable sample temperatures to the precision desired for accurate temperature rise determination.

It also creates difficulty in determining when temperatures have stabilized at the start and end of a heat run. Servo controlled valves with temperature feedback should minimize the temperature float seen for the inlet gas during these first three heat runs.

Even with the inlet gas stability issue, two complete thermal cycles were completed of the thirty planned. A baseline heat run for the first time at 70 K was performed. Heat runs after the first and second thermal cycles were performed. During Task 6.2b, the second heat run was performed after 10 thermal cycles. Significant change in behavior was apparent, but the timing of the change was questionable. For Task 6.4, a more detailed look at the thermal behavior during the initial thermal cycles was deemed necessary. Heat runs after the first and second thermal cycles will be followed by heat runs after the 5th, 10th, 20th and 30th thermal cycles.

The thermal performance changes will be detected by comparison of successive heat run results to the baseline run.

Corrected Conductor Rise

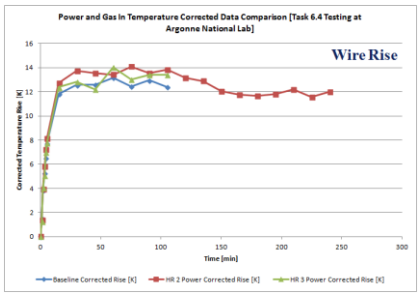

Corrected Cernox Rise at Locations

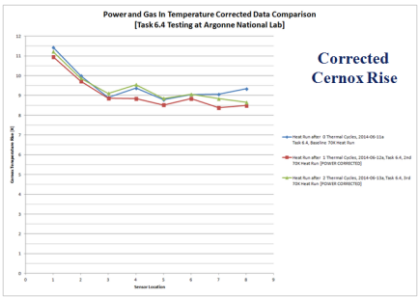

Corrected Cernox Rise vs. Time

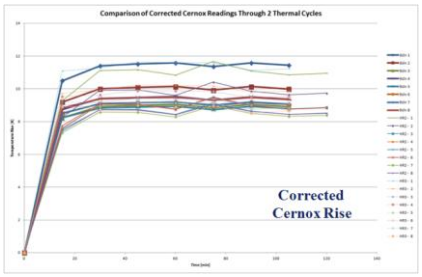

Manual cold gas and room temperature gas mixing led to 4 incidents during thermal cycling where the imposed limit of no more than 50 K separation of the inlet gas temperature and sample Cernox readings was exceeded. Servo valves with temperature feedback are planned to avoid high thermal stresses from temperature spreads within the sample for upcoming testing.

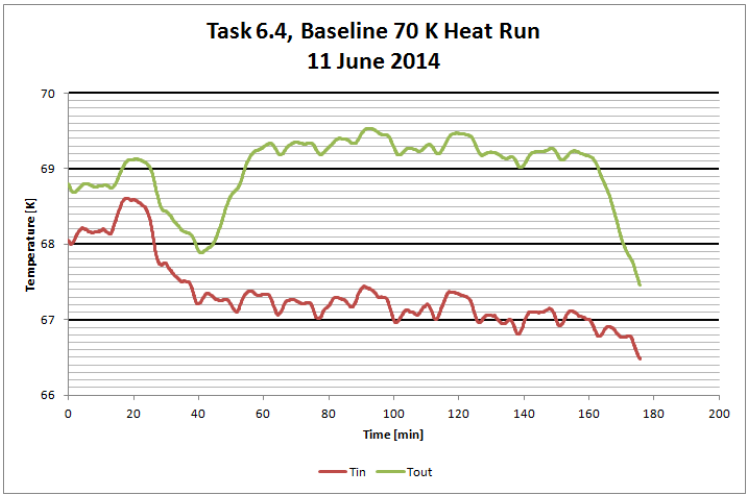

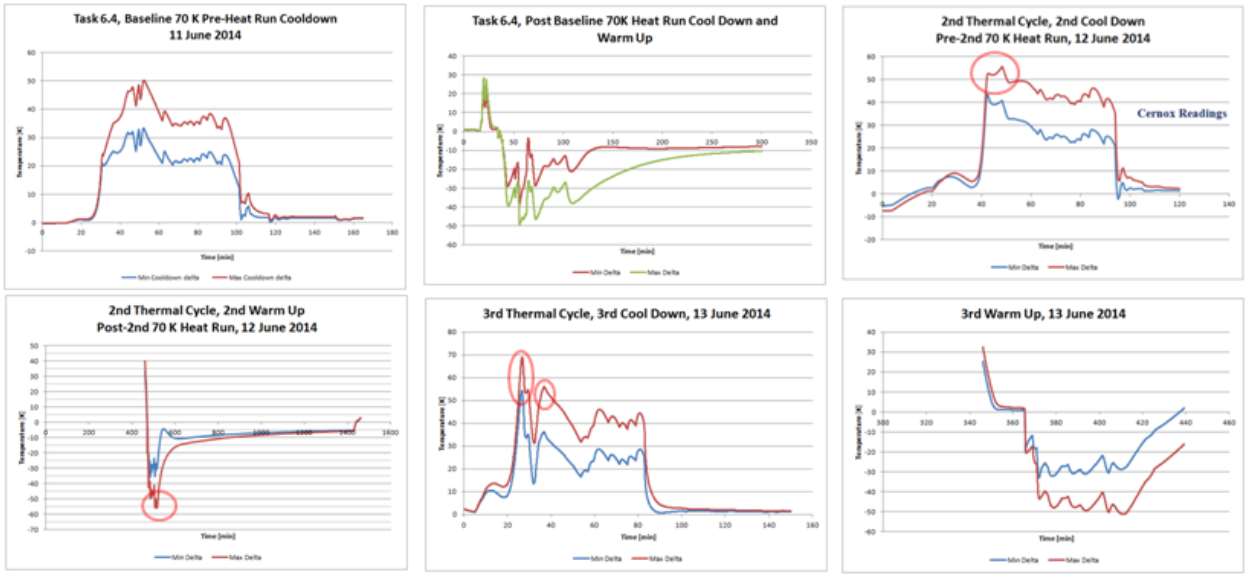

Task 6.4 Significant Results, Including Major Findings, Developments or Conclusions (Positive or Negative)

The initial three heat runs during the first two thermal cycles has shown an issue with the ability to maintain a stable inlet gas temperature. The input gas temperature has more "float" than the level of reading change expected from heat transfer degradation. This will be corrected using a valve control with feedback.

The results, after two thermal cycles of 30 planned, do not indicate major changes in sample behavior.

Task 6.4 Plans for Next Quarter

- Make necessary gas temperature control changes to the setup.
- Continue thermal cycle testing.

3.2.3.6 Task 6.5 – Characterization of AC losses in MgB2 Superconductor

3.2.3.6.1 Overview

Fully superconducting synchronous machines offer major advantages for future electrical machines. Potential applications include high-power wind generators and turbo-electric propulsion systems for future aircrafts. Such electrical machines with superconducting rotor and stator windings will be much lighter and smaller than existing normal conducting or partially superconducting versions of such machines therefore offering major advantages or even enabling technology.

While the rotor windings in synchronous machines are excited with DC currents and maintain these currents without losses while superconducting, the stator windings have to sustain AC currents, which lead to unavoidable losses and resulting heating of the superconducting stator coils. These AC losses are caused by three sources: Under AC excitation superconductors get magnetized, and the resulting change in magnetization direction absorbs energy and leads to losses. Furthermore, losses result from eddy currents that are induced in the normal conducting matrix, which is part of any practical, composite superconductor. An additional loss is caused by coupling between the superconducting filaments that are embedded in the normal conducting matrix.

The losses are dependent on many operational and material-based parameters, which include frequency of the AC, total variation of the magnetic field, operational temperature, critical current of the superconductor at the given temperature and field, filament diameter of the superconductor, conductivity of the matrix material, and transport current in the conductor and its phase relationship with the magnetic field. Based on complex correlations between the contributing parameters, the multiple sources of the losses and the particular variation of the magnetic field seen by the stator windings in synchronous machines, an estimate of AC losses under these conditions is prone to significant uncertainties. The ideal solution for determining the AC losses would require to actually build a prototype of a given machine configuration and empirically determine the resulting losses. But even this approach might not produce the needed results, since the machine might not be operational at all due to unacceptable losses. It is therefore planned to develop a flexible test system which allows performing AC loss measurements on potential superconductors under the particular conditions that exist in a synchronous machine.

The conductors that will be used for future, fully superconducting machines currently do not exist. In fact, major improvements in conductor performance are expected before actual systems will be built. It therefore seems necessary to develop and implement a test setup that enables a most economic test operation and will be available for the foreseeable future. Based on these two requirements, i.e., economic operation and long-term availability, AML decided to develop and built a versatile test system that accommodates all foreseeable needs and make this system available to the superconducting community.

A versatile test system that allows AC loss measurements for various applications is significantly more complicated and costly than a test system that would accommodate only one particular conductor test. AML was able to combine the funding of two projects to afford such a general test setup. To make such a test setup available to the larger superconductor community, AML decided to have the system located at a well-established and highly qualified facility.

The Center of Advanced Power Systems (CAPS) has agreed to become the custodian of the system and will actually perform the required tests of currently available MgB2 conductors under a subcontract from AML. The data on AC losses obtained from these measurements will be parameterized by AML and personnel from the University of Houston (Dr. Philippe Masson and his group) andcompared with model

calculations for AC losses in fully-superconducting synchronous machines. The enhanced understanding of the AC losses occurring in superconductors will enable much more accurate predictions of these losses in future superconducting machines and facilitate their application.

Dr. Sastry Pamidi, who leads the conductor test group at CAPS, together with his team, has many years of experience in AC loss measurements of superconductors and is therefore best qualified to do these complex measurements. CAPS also offered to make major components of its existing test equipment available for the planned test setup. This generous offer also helped significantly to make the system affordable with the given budget constraints. Furthermore, AML has built over several years special magnets for AC excitations of superconductors for Dr. Pamidi's group. Very similar excitation coils as those already existing at CAPS will be used for the currently planned system, and existing power supplies and various other components needed for such measurements are therefore available.

System Description–General System Requirements

To simulate the AC losses experienced in synchronous machines in a controlled environment of a test setup, the following components are needed.

- **A test chamber for the superconductor sample, for which the AC losses should be determined under controlled conditions.** This sample test chamber should be at a controlled temperature as needed for the operation of the superconductor under test, an alternating background field, with a well-determined frequency that supplies a rotating as well as pulsating magnetic flux density, which simulates the conditions in a synchronous machine. The energy deposited by the AC losses into the sample chamber should be precisely measurable.
- **A cooling system** that supplies cold helium gas to the sample chamber. The temperature range of the gas cooling the superconductor in the test chamber should be as low as 15 K, and the system should be able to accommodate AC losses of close to 10 Watts.
- **A calorimetric measuring system**, which enables to measure the energy deposited by AC losses in the superconductor. This requires a precise measurement of the helium flow rate through the sample chamber plus a measurement of the inlet and outlet temperature. Given the helium flow rate in grams per second and the temperature increase of the helium gas, the energy deposited by AC losses in the superconductor can be determined.
- **A controlled magnetic background field** which induces AC losses into the superconducting test sample. The amplitude of flux density and its frequency should be adjustable over the maximum possible range. For low frequencies in the range of 1 Hz the maximum flux density should reach a value of about 0.5 Tesla. Unavoidably the maximum flux density at which loss measurements can be performed will decrease with frequency of the background field. The limitation in frequency is determined by the available power supplies for the magnets, the inductive voltage occurring across the terminals of the field generating coil, and by the capacity of the cooling system, since the heat generated by AC losses increases with the square of the frequency. In order to simulate the flux-changing conditions of the stator windings in a synchronous machine, the background field should generate a rotating as well as pulsating magnetic flux density at the superconducting sample.

3.2.3.6.2 AC loss modeling in multi-filament MgB2 conductors

3.2.3.6.2.1 Introduction

To properly design cooling systems and optimize superconducting devices such as rotating machines or transformers accurate estimations of the losses, depending on the frequency and both the local field configuration and electrical superconductor behavior are paramount. Various methods can be used to assess the losses: i) Analytical formulae relying on strong assumptions and simplifications (critical state model), ii) Time-consuming numerical simulations (few tens of hours for some of the simulations performed in this paper), and iii) Scaling laws consisting of semi-analytical fit expressions based on numerical simulations. The latter is as fast as analytical calculations and requires weaker assumptions. The only compromise lies in the accuracy of the analytical expressions proposed to fit the data. The present study deals with such a method to estimate magnetization losses in superconducting filaments under transverse elliptical field.

In the framework of the development of a code to design fully superconducting electrical rotating machines, investigation of AC losses in superconducting stators is needed [36]. A first step in such a code development is the estimation by means of semi-analytical formulae of the magnetization losses generated by elliptical field transversally applied to superconducting round wires. In the present paper, an elliptical field is defined as a combination of an alternating field and a rotating field that can be seen as the two extreme configurations of the elliptical field. So far, most of the studies providing analytical expression of the losses rely on the well-known critical state model [32], [37] ,[38], [39]. Rhyner [40] proposed a model and analytical formulae of magnetization losses generated by an alternating field in a superconductor slab with a smooth current-voltage characteristic. This very study was further developed for round wires and briefly described by Kajikawa, et al. [41]. Compared to our expressions, the results of the latter reference present some discrepancy with the numerical data reported in Appendix B and, in addition, are only valid for a purely alternating field. As a first step in our investigation, a dimensional analysis is applied to the system and a set of dimensionless variables is proposed. The analysis leads to the discovery that the introduction of a fundamental variable c_n built on those dimensionless parameters allows for the development of a scaling law for losses generated by a purely alternating field. That scaling law is compared to the critical state model to validate our method. A similar approach is presented for the other extreme configuration of the elliptical field, i. e., the purely rotating field. Based on those two results, a scaling law for any elliptical field is finally proposed.

3.2.3.6.2.2 Numerical model description

The scaling laws proposed in the present paper rely on loss data coming from a 2D finite element model developed on the commercial software (COMSOL®). The circular filament is represented by a disk of radius r within a square domain that defines the outer boundary of our system (Figure 6.5.1).

The H-formulation is used to simulate the induced currents in the superconductor. This method has been extensively used in the past and is a reliable method to numerically estimate the losses [33], [34],

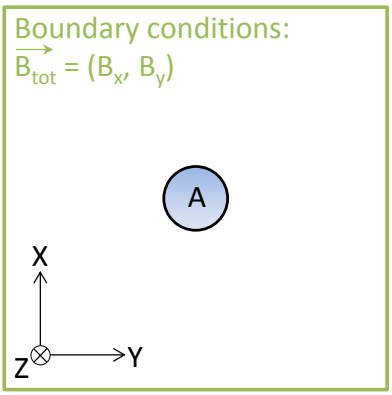

Figure 6.5.1. Geometry of the Model

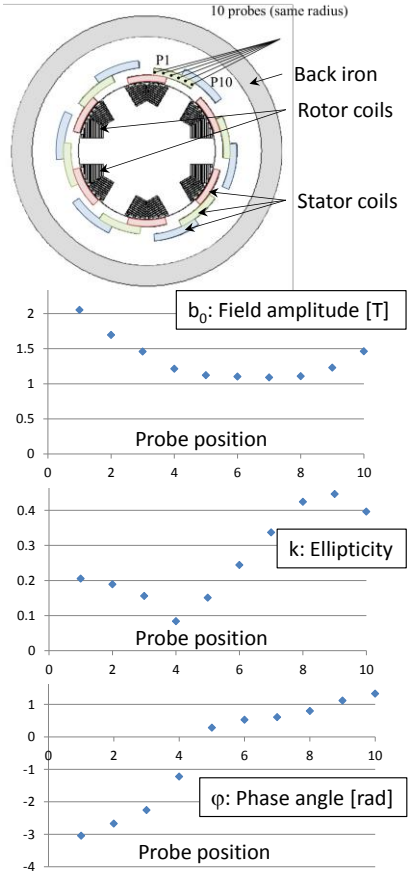

Figure 6.5.2. 2D cross-section of a superconducting machine and magnetic field configuration of conductors due to the rotor and all three stator phases over one coil of the middle stator phase at a given radius for 10 different angular locations. The relative position of the stator coils to each other has a huge influence on the ellipticity k of the field

The electrical behavior of the superconductor is described by a smooth-power law as follows:

$$\vec{E} = E_c \left(\frac{|\vec{J}|}{J_c} \right)^n \frac{\vec{J}}{|\vec{J}|} \qquad (1)$$

E is the electric field [V.m-1] with only one component Ez along the z-axis (2D model). J is the current density in the superconductor [A/m2] with only one component Jz. The electric field criterion Ec = 10-4 V.m-1 allows for defining the critical current density Jc [A.m-2]. n is the so called dimensionlessn-value (n = 1 in the normal resistive state and n $\rightarrow +\infty$ in the critical state model).

The magnetic flux density is applied to the wire by defining suitable conditions on the boundaries of the outer square domain as follows:

$$\vec{B}_{tot} = \begin{cases} B_x = kb_0 \sin(\omega t) \\ B_y = kb_0 \cos(\omega t) + (1-k) b_0 \cos(\omega t + \varphi) \end{cases} \quad (2)$$

b_0 is the magnitude of the magnetic flux density [T], k is a parameter that belongs to [0,1] and describes the *ellipticity* of the magnetic flux density (k = 0 for a purely alternating field and k = 1 for a purely rotating field). φ is the phase angle between those two components of the field [rad]. It is worth noticing that the parameterization has been developed in the framework of the design of a superconducting electrical rotating machine where it is relevant to decompose the external magnetic flux density into alternating and rotating components.

Figure 6.5.2 shows b_0, k and φ in one coil of a superconducting rotating machine stator at a given radius, due to the combined fields of the rotor and all three stator phases. The one objective of Figure 6.5.2 is to demonstrate that each conductor is in a unique magnetic configuration and, therefore, to support the validity of our system description. To understand the ruggedness of the curves, it is worth noticing that the first four probes are just above the inner phase coil and the last four probes are just below the outer phase coil. It can be added that the gap between the backiron and the stator coils strongly impacts the field configuration, too. As it can be seen in Eq. (2), only the fundamental of the temporal variation of the magnetic field is taken into account in our study. In the case of tape-shape superconductors, some interesting studies have been made on the impact of the field harmonics on AC losses [42], [43].

The pulsation of the field is $\omega = 2\pi f$ [rad.s^{-1}] where f is the frequency [Hz]. The output of the model is the magnetization loss Q per unit length of conductor **per cycle** [J/m/cycle] and may be expressed as:

$$Q = \oint dt \iint_A E_z J_z dA \quad (3)$$

One can get the volume losses density [J/m^3/cycle] by dividing Q by the cross-section area $A = \pi r^2$ of the filament. In our model J_c and n are constant throughout a cycle and do not depend on the local field (nor the temperature). Before using the semi-analytical expressions of this paper, the reader will have to pick, from experimental works, the values of n and J_c based on the magnitude of the field applied to the filament. For MgB_2 materials some values can be found in [44] where n varies from 10 to 50 for magnetic fields from 2 T to 6 T. As presently defined, the model assumes that the magnetic flux density generated by the induced superconducting currents must be negligible on the outer domain boundaries. To ensure that the results are correct, two simulations with different outer domain sizes are carried out every time and the results are assumed to be right if there is no discrepancy in terms of calculated AC losses.

3.2.3.6.2.3 Dimensional analysis

A dimensional analysis is applied to the system in order to determine the number of parameters needed to describe our model. This is done by using a proper set of dimensionless variables. So far, our system is represented by a hypothetical equation g(Jc, μ0, r, Ec, Q, b0, f, φ, k, n) = 0, where all the parameters are defined in Table 6.5.1. The Vaschy-Buckingham theorem (also called the π-Theorem) states that our system involving 10 variables, which units can be expressed from 4 independent units – e.g., kilogram, meter, second, ampere (Table 6.5.1) –, can be reduced to an equation involving only 10 - 4 = 6 non-unique dimensionless parameters.

Table 6.5.1. Variable units of our system in kilograms, meters, seconds and amperes

Var.	Name	Usual unit	[kg]	[m]	[s]	[A]
J_c	Critical current density	$A.m^{-2}$	0	-2	0	1
μ_0	Vacuum permeability	$H.m^{-1}$	1	1	-2	-2
r	Wire radius	m	0	1	0	0
E_c	Electrical field criterion	$V.m^{-1}$	1	1	-3	-1
Q	Losses per cycle per unit length	$J.m^{-1}$	1	1	-2	0
b_0	Magnetic field amplitude	T	1	0	-2	-1
f	Frequency	Hz	0	0	-1	0
ϕ	Phase angle	Rad	0	0	0	0
k	*Ellipticity*	N/A	0	0	0	0
n	n-value	N/A	0	0	0	0

Therefore, the system could be totally described by G(π1, π2, π3, π4, π5, π6) = 0 where πi would be 6 dimensionless variables (Table 6.5.2). In the initial system, 3 parameters are already dimensionless - φ, k, n (Table 6.5.1), so one just needs to define 3 additional π-parameters. One dimensionless quantity seems to be physically meaningful: b* = b0/Bp where Bp is the magnetic flux density leading to full current penetration of the filament as defined in the critical state model (Bp = 2μ0Jcr/π). Then, a reduced loss can be defined as q*=Q/Q1 with Q1 = μ0Jc2r4. We arbitrarily defined the last dimensionless parameter, a reduced frequency, as f*= f/f1 with f1 = Ec/(μ0Jcπr2). Therefore, the equation for our system becomes

$$G(b^*, f^*, q^*, \varphi, k, n) = 0 \qquad (4)$$

Instead of a reduced frequency, it is worth noticing that one could have described the system, for example, by means of a reduced length r*= r/r1 with r1 =(Ec/(μ0Jcf))0.5 , which expression is similar to that of skin depth in normal resistive conductors, Jc/Ec being a conductivity.

Table 6.5.2. Dimensionless Variables of the System						
Variable	**b^***	**f^***	**q^***	**φ**	**k**	**n**
Expression	$\frac{b_0\pi}{2J_c\mu_0 r}$	$\frac{fJ_c\mu_0\pi r^2}{E_c}$	$\frac{Q}{\mu_0 J_c^{\,2} r^4}$	φ	k	n

To estimate AC losses in a wire produced by a purely alternating field (k = 0) or a purely rotating field (k = 1) only 4 parameters b*, f*, n, q* are necessary. The next sections are dedicated to these two limiting cases. Thereafter, k and φ are introduced to take into account any kind of elliptical field in an attempt to provide practical semi-analytical formulae allowing for easy estimation of the magnetization losses when the superconductor is driven by a power-law current-voltage characteristic (see Eq. 1). Since the formulae are based on an analytical fit, a domain of validity needs to be defined.

3.2.3.6.2.4 Magnetization losses under alternating or rotating magnetic field

Alternating field losses

Two specific cases: n = 10 and n = 20

To simulate losses generated by a purely alternating field (k = 0 in Eq. 2), one needs to take into account only 3 parameters b^*, f^*, n. As a first step, let n be equal to 10 or 20. A few simulation results are shown in Figure 6.5.3 in a semi-log scale. The loss function $\Gamma = q^*/b^{*2}$ that represents somehow the ratio between the energy loss and the magnetic energy in vacuum is used to described the data [46]. That is the ratio between the dissipated and available energies [45].

It is possible to go one step beyond in the representation of the losses by applying a transformation to the abscissa. Dividing the abscissa by b^* to the power of 9 (n = 10) or 19 (n = 20) allows for revealing a **continuous scaling law** (Figure 6.5.4). This is one of the main results of this paper.

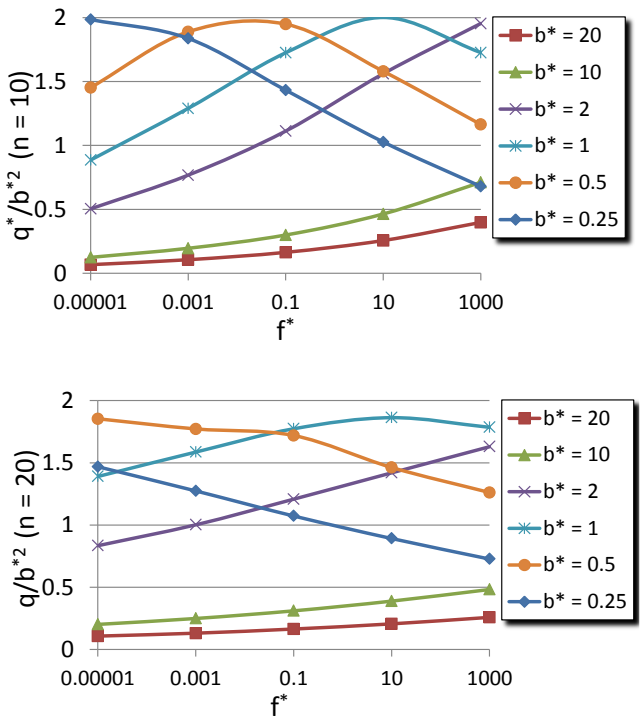

Figure 6.5.3. Losses q^*/b^{*2} versus f^* for various b^* (n = 10 upper and n = 20 lower)

- General case

The previous method has been tested and can be applied for any n-value. The important quantity to describe the ratio q*/b*2 is always f*/b*n-1.This very interesting result is then used to define semi-analytical expressions of the losses.

It is worth noticing that when n = 1 (normal conductor), the loss per cycle q* depends on b*2 and f* (Indeed Eddy current losses per cycle are proportional to the frequency times the square of the magnetic field). When n $\rightarrow\infty$, the losses per cycle q* must depend only on the magnetic field as can be shown by the critical state model (see Eq. 5) [37]. Therefore, the quantity f*/b*n-1 is raised to the power -1/n in order to fit with the critical state model and is called cn (see Eq. 6).

$$\frac{q^*}{b^{*2}} = \begin{cases} \frac{16}{3\pi} b^* (2 - b^*) & (b^* \le 1) \\ \frac{16}{3\pi} b^{*-1} (2 - b^{*-1}) & (b^* \ge 1) \end{cases}$$

[37](5)

$$c_n = \left(\frac{b^{*n-1}}{f^*} \right)^{\frac{1}{n}} = \frac{b_0 \pi}{2\mu_0 j_c r} \left(\frac{2E_c}{b_0 f \pi^2 r} \right)^{\frac{1}{n}}$$

(6)

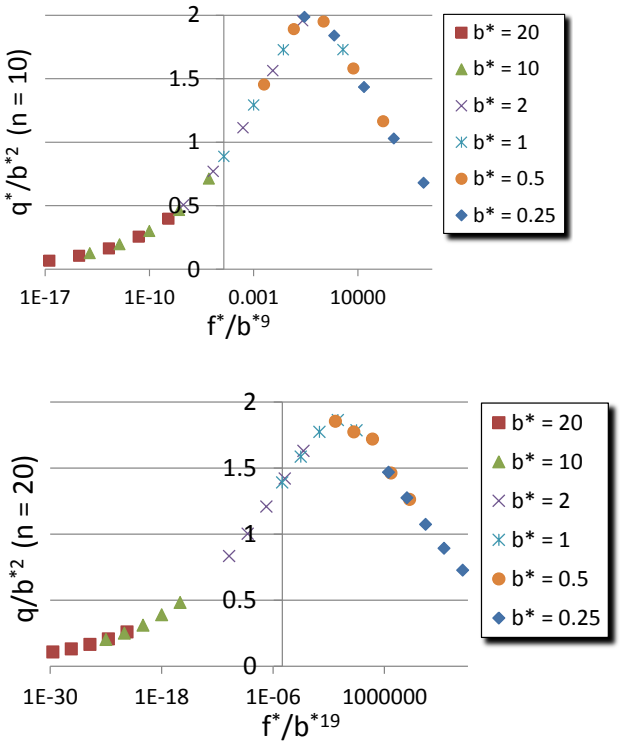

Figure 6.5.4. Losses q^*/b^{*2} versus f^*/b^{*n-1} for various b^* (n = 10 or 20)

The comparison with normal and critical states lends legitimacy to our method and the variable c_n. No attempt is made to give a phenomenological meaning to the variable cn. From a macroscopic point of view, cn can be seen as the balance between the magnitude of the magnetic field and the penetration length of the field through the superconductor. If the penetration length is small (high frequency), a higher field is needed to generate the same amount of losses that would be generated for a larger penetration (low frequency), the relationship between the field and the penetration length (or the frequency) being driven by the flux creep mechanism, i. e., the n-value. When n = 2, the weight of the frequency is as much as the weight of the magnetic field in terms of AC losses since c2 = (b*/f*)0.5, dividing the field magnitude by a factor of 2 is the same as multiplying the frequency by a factor of 2. **Reduced losses can be described for each n-value by a scaling law Γ of only one universal variable c_n:**

$$q^* = b^{*2} \Gamma(c_n)$$

(7)

Figure 6.5.5 shows the results for n = 2, 3, 5, 10, 20, 40 and 50 as well as the Critical State Model as limit. The peak values of the curves occur when c_n is between 0 and 1 and the higher n is, the closer to 1 is the maximum of c_n. In the critical state model $c_n = b^*$ and the peak occurs for $b^* = 1$. According to the simulation results, the peak values represent the transition from partial current penetration to full current penetration state.

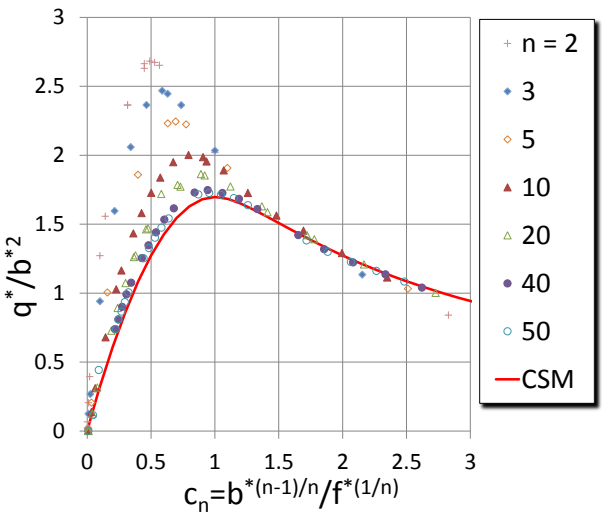

Figure 6.5.5. Alternating field: losses q^*/b^{*2} versus $(b^{*n-1}/f^*)^{1/n}$ for various n-values and comparison with the Critical State Model (CSM or n →∞)

One can try to merge all the curves into one by scaling the peak value of each curve to (1,1), to do so, the losses q*/b*2 are normalized with respect to their own maximal value for each n-value, namely max(n) (see Eq. 8), and are called Q*. The coefficients (α1, α2) = (1.648, 0.716) are fit coefficients based on the numerical simulation data; the coefficient 16/(3π) comes from the limit provided by the critical state model (see Eq. 5 with b* = 1). The variable cn is divided by x(n) (see Eq. 9) and is called X*. The coefficients (α3, α4) = (0.757, 0.582) are fit coefficients based on the numerical simulation data, in Eq. 10, the coefficient 1 comes from the limit provided by the critical state model. Figure 6.5.6 shows the results after such a transformation is performed.

$$max(n) = \frac{16}{3\pi} + \frac{\alpha_1}{n^{\alpha_2}} \qquad (8)$$

$$x(n) = 1 - \frac{\alpha_3}{n^{\alpha_4}} \qquad (9)$$

According to our numerical data, it appears that all the curves merge nearly into just one. Actually, the data do not merge to a perfect single curve and the accuracy of the fit reflects this. Nevertheless, a fit of this single curve can provide a good estimation of the magnetization losses in a circular superconducting filament with a power-law electrical behavior when subjected to an alternating field. The fit accuracy is discussed at the very end of the paper. One suggests fitting the curve as follows:

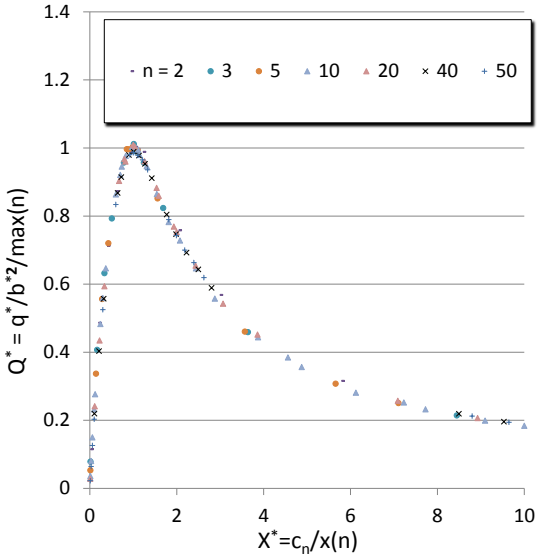

Figure 6.5.6. Alternating field: losses $Q^* = q^*/b^{*2}/max(n)$ versus $X^* = c_n/x(n)$ for various n-values

$$Q^* = \begin{cases} X^*(2-X^*) & (X^* \le 1) \\ X^{*-1}(2-X^{*-1}) & (X^* \ge 1) \end{cases} \quad \text{with } X^* = \frac{1}{x(n)}\left(\frac{b^{*n-1}}{f^*}\right)^{\frac{1}{n}} \text{ and } Q^* = \frac{1}{max(n)}\frac{q^*}{b^{*2}} \qquad (10)$$

It can be seen that this expression is similar to the one of the critical state model provided in [37] (see Eq. 5) but the normalized c_n variable, namely X*, is substituted for the reduced field b*. **Indeed, the critical state model is a special case of expression (10), since when n →∞, X*→ b* and Eq. (10) → Eq. (5).** Based on Eq. 8, 9 and 10 and Table 6.5.2, the reader can easily work out the fit formula to get the losses in [J/m/cycle] that depends on the amplitude of the magnetic field $\mathbf{b_0}$, the frequency of the field **f**, the radius of the filament **r** as well as the **n**-value and the critical current density $\mathbf{J_c}$ defining the electrical behavior of the superconductor. The next three figures (Figure 6.5.7 throughFigure 6.5.9) represent the fit and the numerical data for different ranges of the parameter X^*.

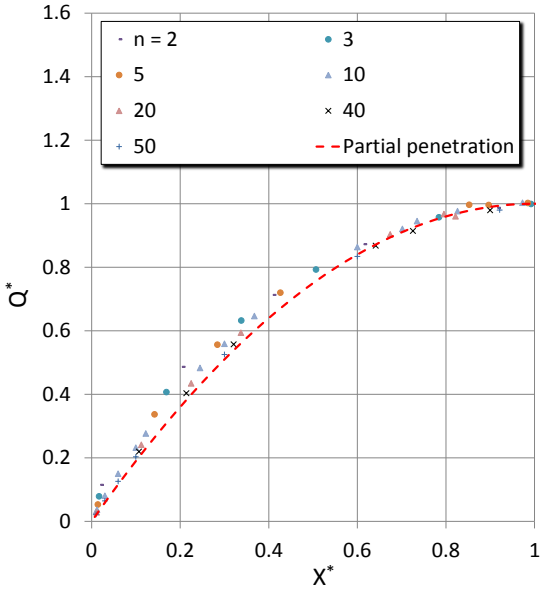

Figure 6.5.7. Alternating field: fit and numerical data in partial penetration (X^* = 0 no penetration; X^* = 1 full penetration)

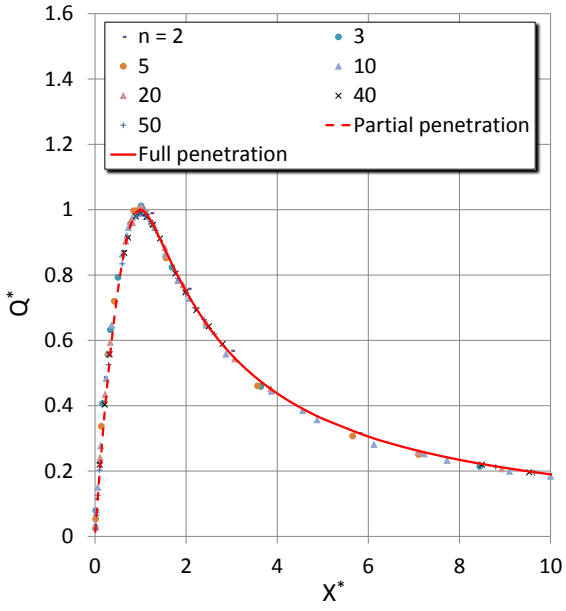

Figure 6.5.8. Alternating field: fit and numerical data around the full penetration (X^* < 1 partial penetration; X^* > 1 full penetration)

- Example and error

Let us describe the method for the following set of parameters: b0 = 2 T, f = 50 Hz, r = 25 µm, Jc(Ec = 10-4 V.m-1) = 1000 A.mm-2 and n = 15. According to Table 6.5.2, one can get b* = 100, f* = 1.2337 then Eq. 9 and 10 provide X* = 86.0 (with x(n = 15) = 0.843) which means that, based on Eq. 10, the reduced losses Q* = 0.02312. According to Eq. 8 and Eq.10, the reduced losses q* = 447.3 (with max(n = 15) = 1.935) which means that, based on Table 6.5.2, the losses per unit per cycle Q = 0.0002196 [J/m/cycle]. A numerical simulation with the same parameters was performed and provides Q = 0.0002167 [J/m/cycle], i.e., a 1.3 % discrepancy.

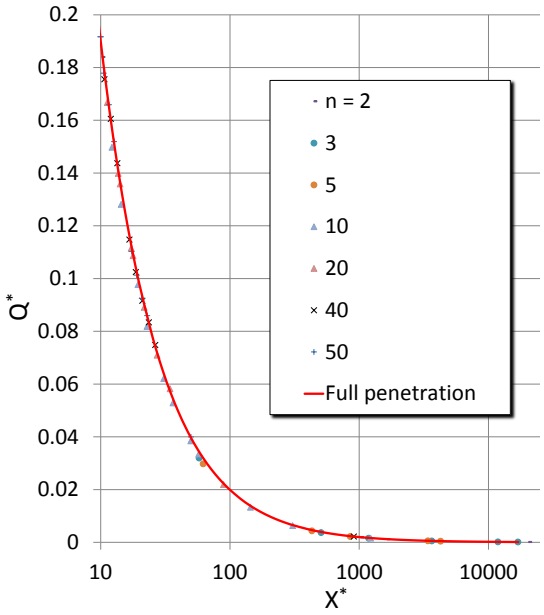

Figure 6.5.9. Alternating field: fit and numerical data in full penetration in a semi-log scale

Rotating field losses

In order to simulate the losses generated by a purely rotating field (k = 1 in Eq. 2), one needs to take into account the same 3 parameters b^*, f^*, n as previously. As rotating field loss is less common in scientific literature [38], [39] than alternating field loss, the screening current distributions in the superconductor in the event of an external purely rotating field are shown in Figure 6.5.10 as illustration.

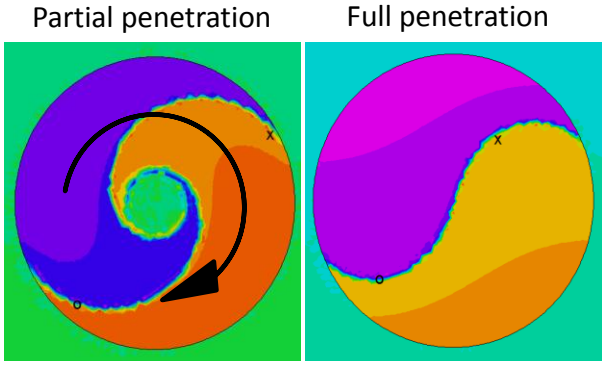

Figure 6.5.10. Illustration of the distribution of the magnetization currents generated in a round superconducting filament when subjected to an external rotating field. The black arrow describes the clockwise circular progression of the magnetic field direction.

The same method as previously described for a purely alternating field can be applied to the numerical data. Eq 8 and 9 become Eq.11 and 12 with (λ_1, λ_2) = (0.651, 0.339) and (λ_3, λ_4, λ_5) = (3.647, 2.675, 0.578). Figure 6.5.11 is the counterpart of Figure 6.5.6 for rotating field losses.

$$max_{rot}(n) = \lambda_3 + \frac{\lambda_4}{n^{\lambda_5}} \qquad (11)$$

$$x_{rot}(n) = 1 - \frac{\lambda_1}{n^{\lambda_2}} \qquad (12)$$

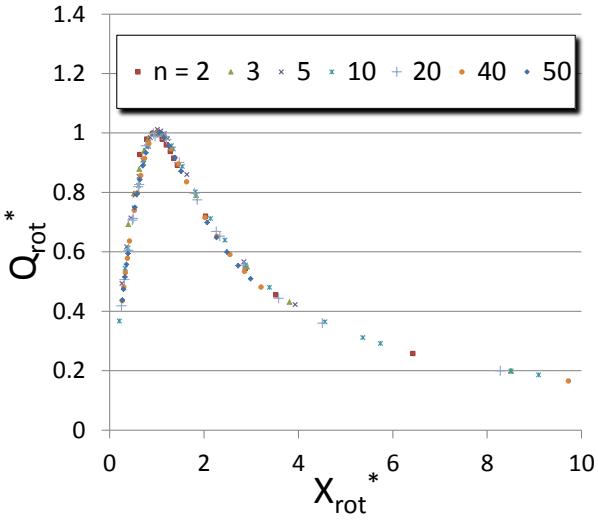

Figure 6.5.11. Rotating field: Losses $Q_{rot}^* = q^*/b^{*2}/max_{rot}(n)$ versus $X_{rot}^* = c_n/x_{rot}(n)$ for various n-value

Similarly to the magnetization losses generated by an alternating field, the reduced losses produced by a rotating field merge approximately into only one curve. One suggests fitting the numerical data with only one formula over the whole range of variation (Eq. 13) with (β_{in},β_{out}) = (2.784, 0.718). The fit is compared to the numerical data in Figure 6.5.12 through Figure 6.5.14.

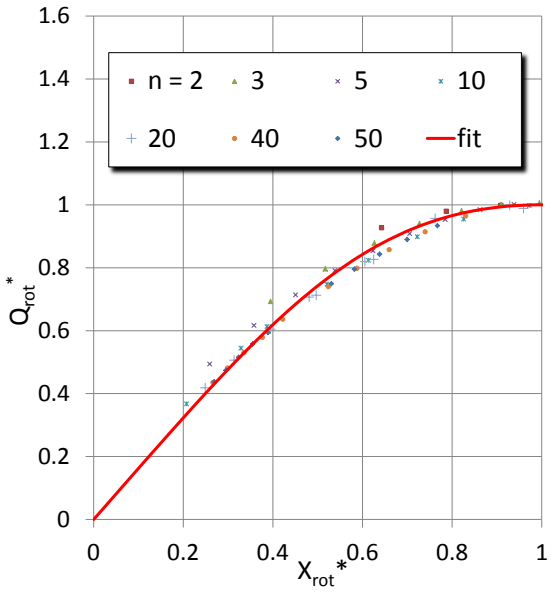

Figure 6.5.12. Rotating field: Fit and numerical data in partial penetration ($X_{rot}^* = 0$ no penetration; $X_{rot}^* = 1$ full penetration)

$$Q_{rot}^{*} = \frac{X_{rot}^{*}}{\left[0.5(1+X_{rot}^{*\beta_{in}})\right]^{\beta_{out}}} \text{ with } X_{rot}^{*} = \frac{c_n}{x_{rot}(n)} \text{ and } Q_{rot}^{*} = \frac{q^{*}}{b^{*2}\max_{rot}(n)} \quad (13)$$

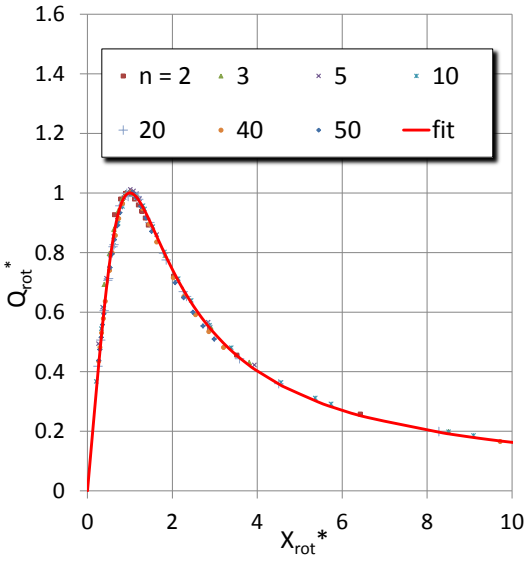

Figure 6.5.13. Rotating field: Fit and numerical data around the full penetration ($X_{rot}^{*} < 1$ partial penetration; $X_{rot}^{*} > 1$ full penetration)

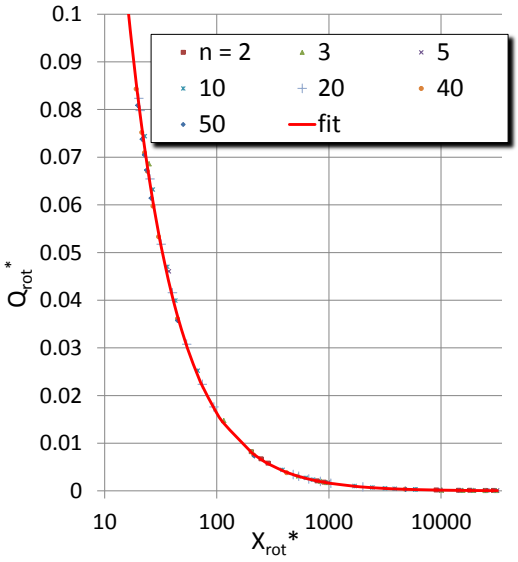

Figure 6.5.14. Rotating field: Fit and numerical data in full penetration in a semi-log scale

- Example and error

Let us describe the method for the same set of parameters as previously done for the alternating field losses: b_0 = 2 T, f = 50 Hz, r = 25 µm, $J_c(E_c = 10^{-4}$ V.m$^{-1}) = 1000$ A.mm^{-2} and n = 15. According to Table 6.5.2, one can get $b^{*} = 100$, $f^{*} = 1.2337$ then Eq. 12 and 13 provide $X_{rot}^{*} = 98.0$ (with $x_{rot}(n = 15) = 0.740$) which means that, based on Eq. 13, the reduced losses $Q_{rot}^{*} = 0.01687$. According to Eq. 11 and Eq. 13 the reduced losses $q^{*} = 709.5$ (with $\max_{rot}(n = 15) = 4.206$) which means, according to Table 6.5.2, that the losses per unit per cycle Q = 0.0003483 [J/m/cycle]. A numerical simulation was performed and provides Q = 0.0003502 [J/m/cycle], i.e., a 0.6% discrepancy.

3.2.3.6.2.5 Magnetization losses under Elliptical field

In this section, we treat the general situation in which an elliptical magnetic field, as described in Eq. 2, is applied to the superconducting filament. Two extra-variables k and φ must be taken into account with respect to the previous section: k is the ellipticity of the field between 0 and 1 with k = 0 defining a purely alternating field and k = 1 a purely rotating field, φ is the phase angle between the

alternating and rotating components of the field. Firstly, the phase angle φ is set to zero and additional numerical sets of data are generated for various values of k between 0 and 1 (k = 0.25, 0.5 and 0.75). For each k-value, the data are processed following the very same steps as before. Then, the effect of the phase angle φ - varying from -π to π - is taken into consideration. Finally, in an attempt to validate our practical fit expression, a hundred numerical simulations are performed with variables randomly taken in the whole range of variation (see Appendices C and D),and the resulting losses are compared to the losses coming from our general semi-analytical loss expression. Previous work has been performed on an elliptical applied field but without taking into account the frequency dependency of the losses [35].

No phase angle: φ=0

The above data transformation is applied to the 3 additional sets of data (k = 0.25, 0.5 and 0.75). For each k-value, i. e., magnetic field configuration, the quantity q^*/b^{*2} is plotted versus c_n for different values of n. A second step leads to the normalization of the data, q^*/b^{*2} is divided by $max_{ell}(n,k)$ and c_n is divided by $x_{ell}(n,k)$ in an attempt to merge all the curves in one. The results of the transformation can be seen in Figure 6.5.15 through Figure 6.5.19.

$$Q^* = \frac{q^*}{b^{*2}\,\max_{ell}(n,k)} \tag{14}$$

$$X^* = \frac{c_n}{x_{ell}(n,k)} \tag{15}$$

It is worth noticing that the normalization functions (Eq. 16 and 17) depend on the n-value as well as k. They can be expressed as follows,

$$x_{ell}(n,k) = 1 - \frac{\alpha_1(k)}{n^{\alpha_2(k)}} \tag{16}$$

$$\max_{ell}(n,k) = \alpha_3(k) + \frac{\alpha_4(k)}{n^{\alpha_5(k)}} \tag{17}$$

where $\alpha_1(k)$, $\alpha_2(k)$, $\alpha_3(k)$, $\alpha_4(k)$, $\alpha_5(k)$ are functions depending only on the magnetic field *ellipticity*. Those functions have simple expressions (18) with coefficients p_{ji} displayed in Table 6.5.3.

$$\begin{cases} \forall i \in \{1,2,3,4\}, \alpha_i(k) = p_{1i}k^2 + p_{2i}k + p_{3i} \\ \alpha_5(k) = p_{15} + p_{25}\cos(k\pi) \end{cases} \tag{18}$$

Figure 6.5.15 through Figure 6.5.19 show the normalized data as well as the fit curves coming from expression (20). It is worth noticing that the general expression (20) is working as well for k = 0 with β_{in} = 2 and β_{out} = 1 (Figure 6.5.15). Actually, the fit expression previously suggested for k = 0 (Eq. 10) was used to check the validity of our method by comparing it to the critical state model expression given in [37]. Nonetheless, to find a general fit formula, an expression with a similar form must be used for each set of data (k = 0, 0.25, 0.5, 0.75 and 1) where some of the coefficients are functions of the *ellipticity* and can vary continuously from one value of k to another. The latter are exponents $\beta_{in}(k)$ and $\beta_{out}(k)$ defined in

Eq. 20 with m_i constants given inTable 6.5.3. Figure 6.5.20 shows the discrepancy between such a fit expression and the 593 data points that have been generated to create it.

$$Q^* = \frac{X^*}{\left[0.5\left(1 + X^{*\beta in(k)}\right)\right]^{\beta out(k)}} \quad (19)$$

$$\begin{cases} \beta_{in}(k) = m_1 k^2 + m_2 k + m_3 \\ \beta_{out}(k) = 1 - (1 - m_4)k \end{cases} \quad (20)$$

Table 6.5.3. Coefficients p_{ji} in (18) and Coefficients m_i in (20)

i=	1	2	3	4	5
p_{1i}	-0.5541	-0.8583	1.9114	0.9325	0.6470
p_{2i}	0.4553	0.6216	0.0515	0.0637	0.0685
p_{3i}	0.7544	0.5781	1.6929	1.6673	
m_i	0.2480	0.5350	2.0000	0.7180	

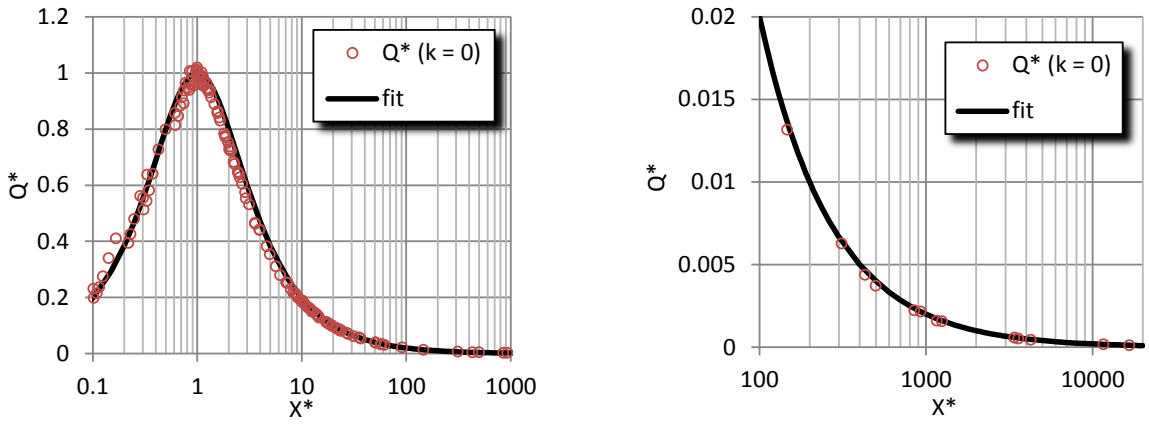

Figure 6.5.15. Normalized data and fit (see Eq. 10) for k = 0 (purely alternating field) in a semi-log scale

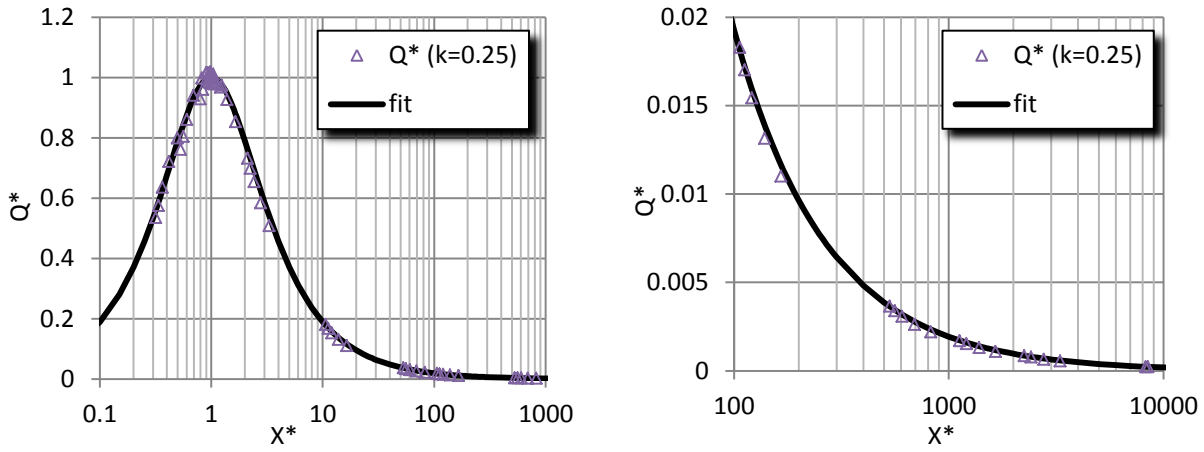

Figure 6.5.16. Normalized data and fit for k = 0.25 (elliptical field) in a semi-log scale

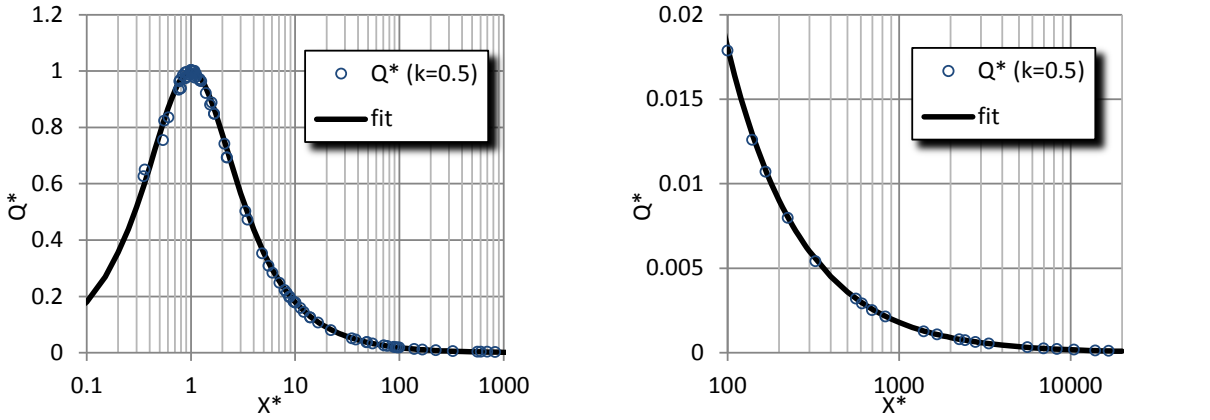

Figure 6.5.17. Normalized data and fit for k = 0.5 (elliptical field) in a semi-log scale

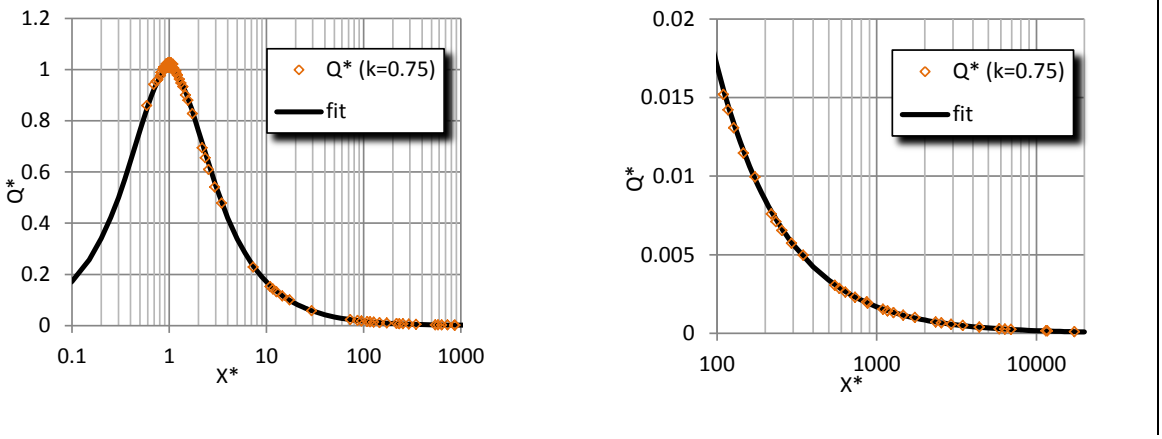

Figure 6.5.18. Normalized data and fit for k = 0.75 (elliptical field) in a semi-log scale

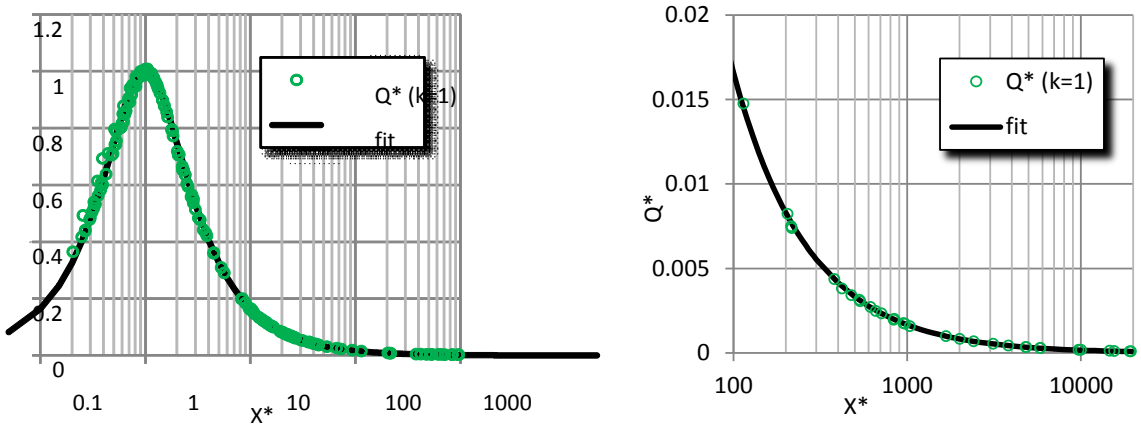

Figure 6.5.19. Normalized data and fit for k = 1 (purely rotating field) in a semi-log scale

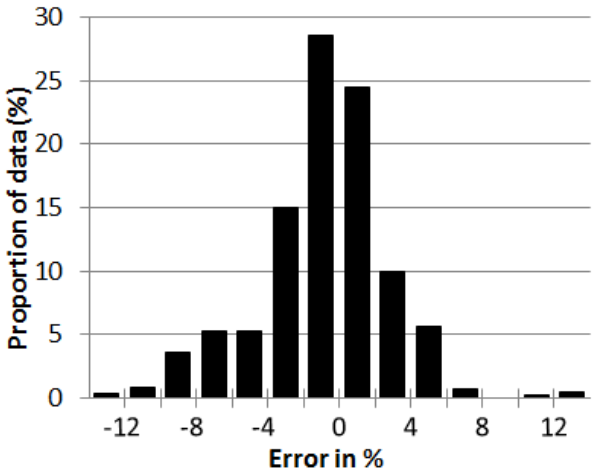

Figure 6.5.20. Error over the 593 data used to generate the fit expression. The relative error in (%) can become significant (25%) when the losses are low (half penetration of the magnetization currents) where the absolute losses are almost negligible.

With phase angle φ

To obtain the loss variation due to the phase angle in the fit expression, the method described in [35] is applied. This method applied to our study states that for a given set of variables (c_n, n, k, φ) the ratio between **absolute magnetization losses** with and without phase angle can be approximated by a cosine of the phase angle φ,

$$\frac{Q(c_n,k,n,\varphi)}{Q(c_n,k,n,\varphi=0)}=\frac{(1-\lambda)}{2}(1+\cos\varphi)+\lambda \qquad (21)$$

where the coefficient λ is defined as follow,

$$\lambda=\frac{Q(c_n,k,n,\varphi=\pi)}{Q(c_n,k,n,\varphi=0)} \qquad (22)$$

Two simulations were performed to illustrate such an assumption (see Figure 6.5.21). The coefficient λ needs to be known, in other words **absolute** losses $Q(c_n, k, n, \varphi=\pi)$ must be calculated. Indeed, absolute losses for a phase angle φ = π are similar to absolute losses for a phase angle φ = 0 with a different ellipticity and a different magnitude of the magnetic field [35] - (k_1, b_1, φ=0) instead of (k, b_0, φ=π) (see expressions (24)) - and can therefore be estimated from the results of the previous section where the phase angle is zero. This means that coefficient λ is known.

$$\begin{cases} if \quad 0<k<\dfrac{1}{3} \quad ,k_1=\dfrac{k}{1-2k}, \quad b_1=(1-2k)b_0 \\ if \quad \dfrac{1}{3}\le k\le 1 \quad ,k_1=abs\left(\dfrac{1-2k}{k}\right), \quad b_1=kb_0 \end{cases} \qquad (23)$$

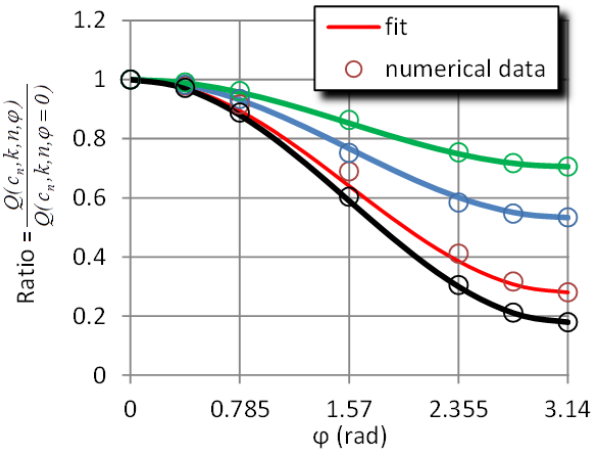

Figure 6.5.21. Simulations illustrating the cosine variation with respect to the phase angle ϕ of ratio between losses generated by an elliptical magnetic field with and without phase angle (see Eq. 21)

Verification of the fit expression

To check the validity of our general fit expression, 100 new simulations were performed with variables (c_n, n, k, φ) randomly taken in the domain of variation defined in Appendix D, Table D.1. Then, the results of the numerical simulations were compared with our semi-analytical expression (see Figure 6.5.22). A table with the comparison of the fit expression with the numerical results is given in Appendix C for more details. In the domain of variation, the fit expression seems to work pretty well according to the results plotted in Table C.1 (within ±15%). Therefore, if a set of parameters (J_c, b_0, r, f) leads to a value of c_n less than $5000*20.265^{1/n}$, our expression of the fit can be used. Nothing can be said for values of c_n beyond this value. As for the n-value, the fit is shown to be good if n is between 3 and 50, but it may be valid for higher values of n, too.

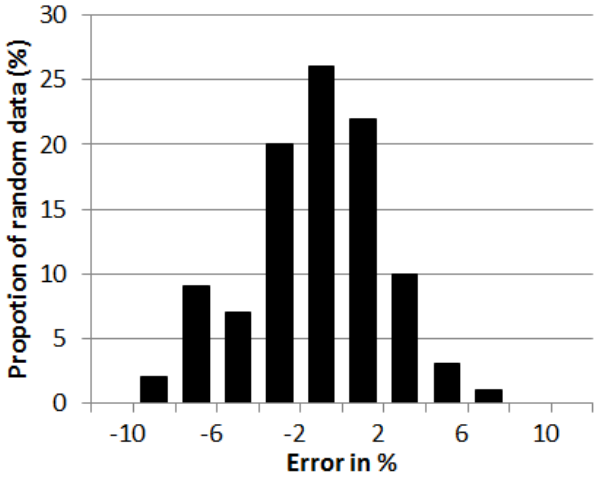

Figure 6.5.22. Error on the 100 data used to verify the fit expression. All data are reported in Appendix C.

Implementation of full model

This section shows how to easily implement the model. Firstly, the expressions of βin, βout, α1, α2, α3, α4, α5 (see Eq. 18 and 20) need to be calculated for the value of k with the constants provided in Table 6.5.3. Then, X* must be evaluated using Eq. 15, 16 and 6. One can now find the value of Q*(φ=0) based on Eq. 19. In parallel Q*(φ=π) can be calculated by substituting into the previous expression of Q*(φ=0) the value of k to k1; and b0 to b1 (see Eq. 23); the value of cn is changed since b0 becomes b1 as well as the ones of βin, βout, α1, α2, α3, α4, α5 since k becomes k1. Now the reduced losses q* can be calculated for both cases - q*(φ=0) and q*(φ=π) - by means of Eq. 14, 17 and Table 6.5.2. Once the reduced losses are known, Table 6.5.2 allows for the calculation of the absolute losses Q in [J/m/cycle]. The coefficient λ can therefore be obtained by dividing Q(φ=π) by Q(φ=0). Finally, the ratio (22) is known and the absolute losses Q(cn, k, n, φ) can be obtained by multiplying Q(φ=0) by the ratio (22). The absolute losses Q in [J/m/cycle] can be divided by the cross-section area of the filament πr2 to get the losses in [J/m3/cycle]. Figure 6.5.23 provides some predicted losses as a function of the n-value that come from our semi-analytical expression with a comparison with the critical state model of a purely alternating field. Figure 6.5.23 shows i) how the n-value affects the losses; ii) how large n must be to approach the critical state asymptote.

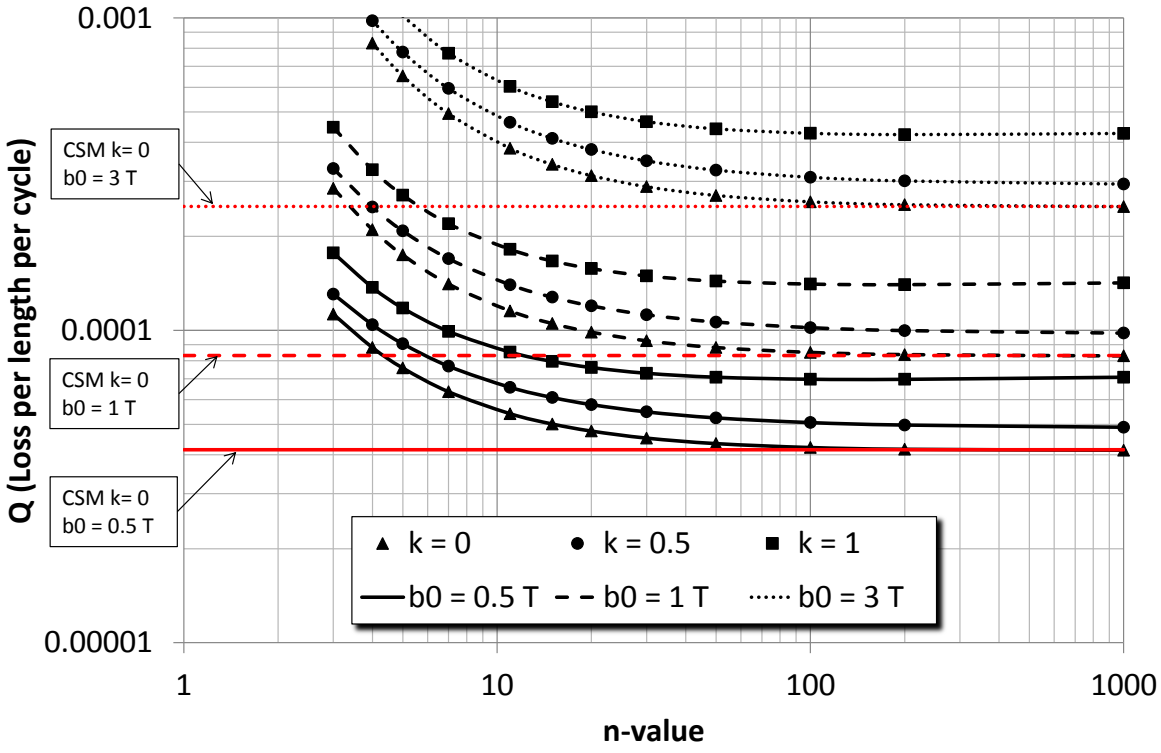

Figure 6.5.23. Loss estimation versus n-value for a radius r = 25 µm, a current density J_c = 1000 A.mm^{-2}, 3 field configurations (k = 0, k = 0.5, k = 1), 3 different field magnitudes (b_0 = 0.5 T, b_0 = 1 T, b_0 = 3 T) without phase shift (φ = 0) at a frequency f = 50 Hz

3.2.3.6.2.6 Losses with transport current

Adding the transport current requires 2 additional parameters to be considered: i* which represents the ratio of the transport current and over the full penetration current and θ the phase shift between the transport current and the AC field. In this model, the transport current, rotating field and AC field are assume to vary with the same frequency. With SL(b*,f*,n,k,φ) the scaling law presented in the previous section, the total losses with transport current and elliptical field can be estimated using the following equation:

$$Losses(b^*, f^*, i^*, n, k, \varphi, \theta) = SL(b^*, f^*, n, k, \varphi) + \left[MF(b^*, f^*, i^* = 1, n, k, \varphi, \theta) - SL(b^*, f^*, i^*, n, k, \varphi)\right] i^{*2}$$

(24)

Where MF(b*,j*,i*=1,n,k,φ,θ) is an analytical fit of the losses at the transport current. The total losses are then assumed to vary with the square of the transport current as shown in equation 25.

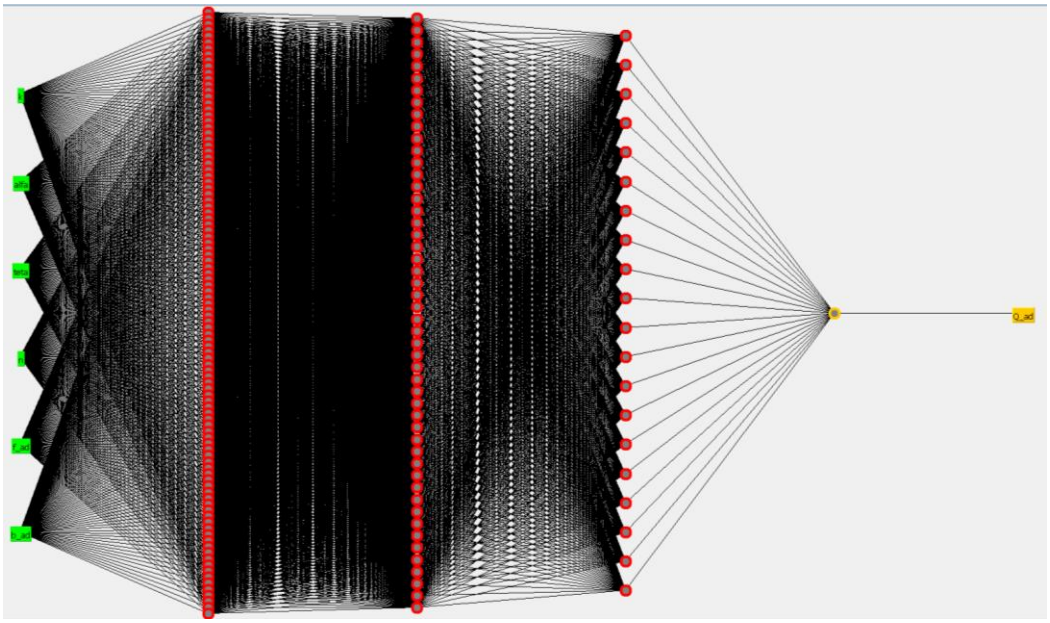

Figure 6.5.24. Neuron network used to create an estimator for the function MF(b,j*,i*=1,n,k,φ,θ)*

An estimator of the function MF(b*,j*,i*=1,n,k,φ,θ) was created using over 2500 data points generated on a supercomputer running finite element analysis. The estimator was generated by using neural networks with 3 layers of neurons (100, 50 and 20 neurons) as shown in Figure 6.5.24.

The neuron network is taught the data and able to estimate the results from the finite element analysis within about 10% as shown in Figure 6.5.25, the estimator has been tested on over 600 randomly chosen points.

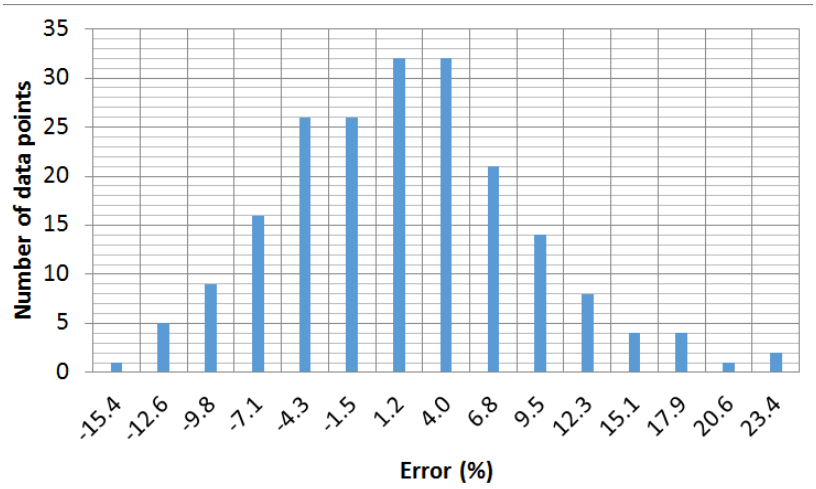

Figure 6.5.25. Error distribution of the estimation of the function MF(b,j*,i*=1, n, k, φ, θ) using a neural network*

3.2.3.6.2.7 Implementation

The calculation of AC losses in a superconducting stator requires analysis on each conductor of a single pole. A simulation of a rotation at full load allows for calculation of the normal and tangential components of the magnetic flux density on each conductor of the stator and then the calculation of the AC losses model parameters. The process is illustrated in Figure 6.5.26.

3.2.3.6.2.8 Conclusion

An investigation was conducted of the magnetization losses generated by a transverse elliptical magnetic field and transport current in an isolated circular superconducting wire with a power-law current-voltage characteristic. The investigation revealed a universal variable c_n that lead to a scaling law for magnetization loss under any applied elliptical field:

$$c_n = \frac{1}{\mu_0 j_c}\left(\frac{b_0\pi}{2r}\right)^{\frac{n-1}{n}}\left(\frac{E_c}{f\pi r^2}\right)^{\frac{1}{n}} = \frac{b_0\pi}{2\mu_0 j_c r}\left(\frac{2E_c}{b_0 f\pi^2 r}\right)^{\frac{1}{n}}$$

Based on this variable, semi-analytical fit formulae are proposed to estimate magnetization losses from data numerically obtained. Those formulae are valid for a large range of radius **r** of the filament, critical current density $\mathbf{j_c}$, magnitude of the magnetic field $\mathbf{b_0}$, frequency of the applied field **f** and n-value **n** of the power-law resistivity.

The analytical scaling law presented in this paper provides a practical, accurate and very fast way of estimating the magnetization losses in round superconducting filaments. (Some of the numerical

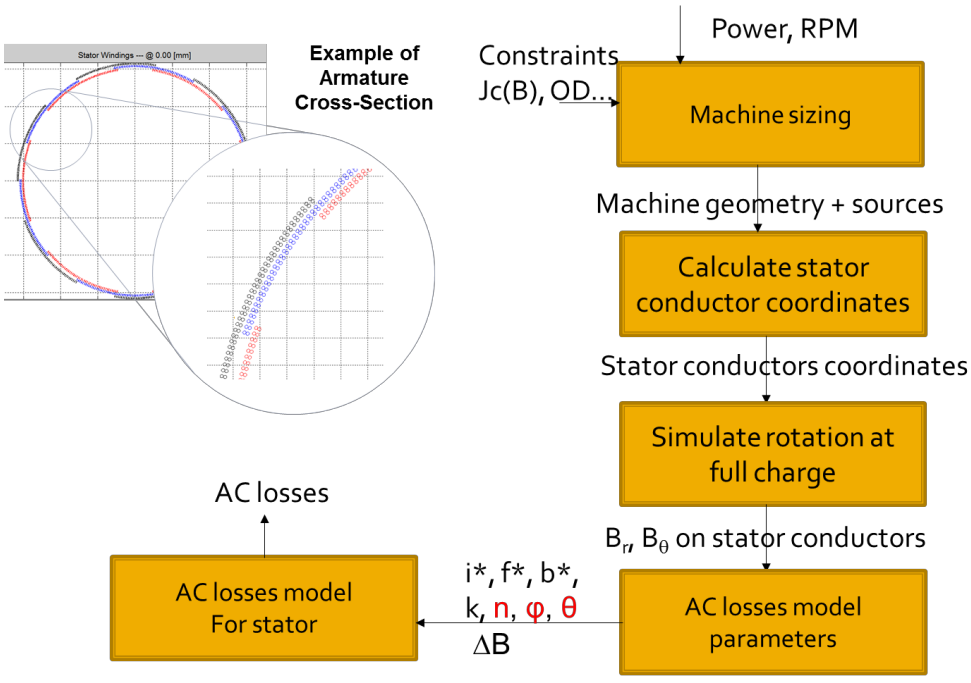

Figure 6.5.26. Process implemented to calculate the AC losses in superconducting stators

simulations that were performed took few tens of hours especially for high n-value for which the convergence is very slow). In the case of a twisted multifilament conductor, readers have to keep in mind that both the n-value and the critical current density must be picked depending on the magnitude of the local magnetic field (for each filament) since our expression does not take into account the field-dependency of those quantities. It might be noted that in a composite conductor with metal matrix, the situation becomes extremely complicated. The coupling currents can modify the field amplitude and direction to varying degrees, depending of the degree of penetration of the shielding coupling currents. The hysteresis results calculated for isolated filaments apply only to the asymptotic situations of very low frequency or for a multifilament conductor with a twist pitch short enough that the coupling penetration depth is negligible compared to the wire diameter. For only "partial penetration" the coupling currents in the filaments become part of the problem, interacting with the transport currents to complicate the situation. Nevertheless, work is ongoing to expand the present method to take into account the transport current in the case of an isolated filament.

The model developed is unique and of much higher fidelity than the conventional models currently used based on the critical state model. The full model was implemented in python and coupled to an electromagnetic solver allowing for more accurate computations of the AC losses. A 3D model is being developed to include a resistive matrix and the impact of large filament twist pitch on the AC losses.

3.2.3.6.3 Report period: October 1, 2012 to December 31, 2012 (Q2)

Background

For system general description and requirements, see previous reports in paragraphs 3.2.3.6.1 and 3.2.3.6.2.

Thermal losses due to AC current in the stator windings represent a key parameter of the Fully Superconducting Generator (FSG) since it defines the majority of thecooling load requirements for the cryogenic cooling system. Our ability to characterize, model and quantify these losses will be critical to the FSG design. As a result, as part of the de-risking of the FSG, a test system is being built to be able to experimentally characterize these losses.

Such a test system will need to simulate the magnetic, electrical and thermal conditions experienced by a superconducting wire/cable in the stator much in the same way they are exhibited in the actual machine.

Task 6.5 Major Activities

A. Conceptual design of the AC Loss Measurement System (ALMS)

A conceptual design was made of the ALMS. The design was driven by the test requirements, which needed to simulate the conditions a superconducting armature coil would experience during actual operation. In addition, since superconductors that will ultimately be used for machines such as the FSG are still being developed, the test system needed to have enough flexibility to reasonably accommodate future conductors or machine configurations.

The various losses developed in the coils being tested are all manifested as an increase in temperature. As a result, the decision was made to perform a measurement of the temperature increase of the cooling gas that is used to cool the test sample, at a known flow rate, to determine the losses. This method of energy loss measurement was also a key driver of the system design.

Figure 6.5.27 shows the main components of the AC Loss Measurement System. Item 1 is the system cryostat. This cryostat is a vacuum-walled vessel that will contain liquid nitrogen at a temperature of 77

Kelvin. Liquid nitrogen is used to cool the excitation coils (item 2) and the current leads supplying power to the test coil assembly (item 3) and also provides a thermal shield for the gas Helium lines going into the test coil assembly (item 3).

Item 2 is the excitation coil assembly. The purpose of the excitation coil is to provide a magnetic field onto the test coil assembly simulating the magnetic field generated by the rotor in the actual superconducting generator. The excitation coil has the following key specifications:

- Copper wound coil cooled by liquid nitrogen at 77 K
- Field: 0 to 0.5 Tesla
- Frequency: DC to few Hz
- Physically rotatable relative to test coil in 5-10 degree increments

Item 3 is the test coil assembly. This assembly consists of a cryostat that is sealed and submerged into the liquid nitrogen bath. The inside of this cryostat is cooled with gaseous helium to a temperature of about 15K. The cryostat constructed out of composite material to avoid any induced eddy currents that will interfere with the measurements.

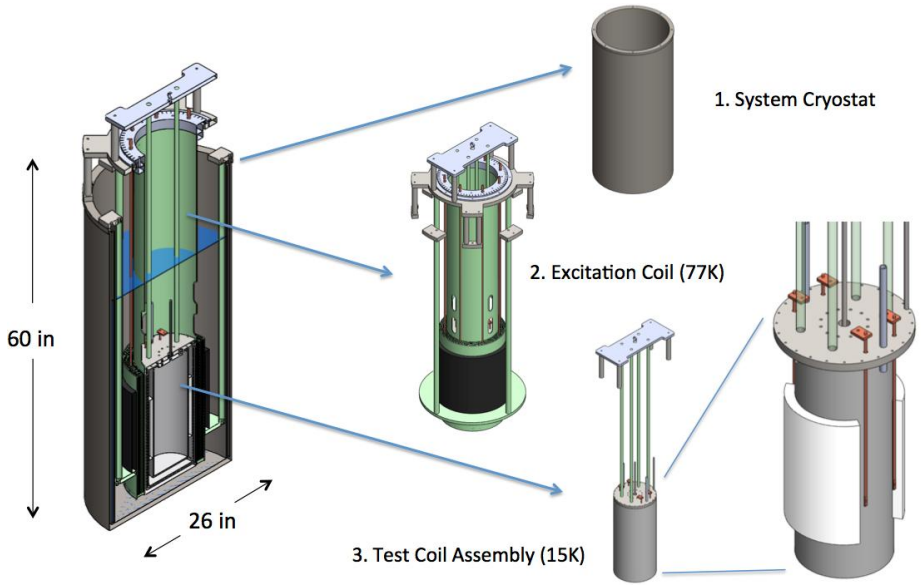

Figure 6.5.27. AC Loss System Components

The cryostat is designed to accommodate wound coils with up to two sets of current leads or straight wires. In addition to being subjected to the magnetic field from the excitation coils, a transport current source ranging from 0 to 100 Amps can be connected to the test coil. The phase difference between the test coil current and the external magnetic field can also be controlled.

B. Conceptual Design of cryogenic cooling and measurement system

A cryogenic cooling system has been designed by Creare Inc. for the specific requirements of the ALMS. Since the initial conductors to be tested are MgB2, the cooling temperature is in the range of 15-18K; the critical temperature of MgB2 at the current levels of interest.

In addition to cooling down the test sample with gaseous helium, the system also has to precisely measure the difference between the entrance and exit temperatures of the cooling gas. Together with the gas flow rate this information is used to determine the losses in the test coil.

A diagram of the cooling system is shown in Figure 6.5.28, along with a table of the key parameters of the system in Table 6.5.4.

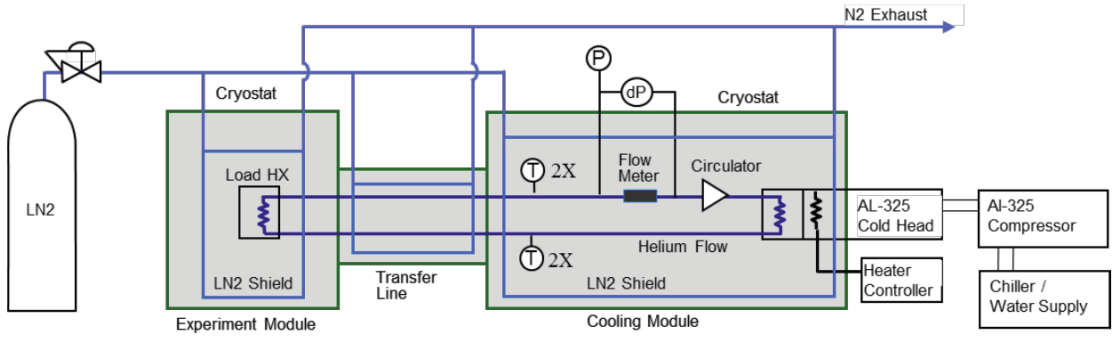

Figure 6.5.28. Cryogenic Cooling and Measurement System

Table 6.5.4. Key Parameters for Cryogenic Cooling System

Parameter	Value	Unit
Cooling Load	1	W
Gas	He	
Mass Flow Rate	0.2	g/s
Flow Tube Diameter	0.125	in
Equipment Inlet Temperature	15	K
Temperature Rise Through Experiment	1	K
Cryocooler Cold Head Temperature	12.9	K
Cryocooler Cooling Power	8.2	W
Circulator Heat Load	5.7	W
Budget for Other Parasitic Heat Loads (not including LN2)	1.5	W

C. Identification of a test facility for ALMS with proper infrastructure and support personnel

It will be highly desirable to use the ALMS as a test facility for superconductors well beyond the life of the currently funded DOE program. For this reason the AML team decided to approach the Center for Advanced Power Systems (CAPS) in Tallahassee, Florida to participate as a team member on this sub-task and to provide a home for this system.

Scientists at CAPS have a broad base of experience in the testing of superconductors and have specifically performed testing of AC losses in YBCO conductors at this facility. Not only does this team have experience in performing these tests, but they also have the infrastructure requirements (power, cooling fluids and gasses, safety procedures, trained support personnel) in place to support this type of testing.

AML has provided magnets to CAPS in the past for use in many of their experiments and has a great working relationship with the team.

Dr. Sastry Pamidi and other team members at CAPS have provided valuable guidance to the design team for ALMS and will continue to participate in design reviews and next stages of the project.

D. Development of process for making MgB2 test coils

The ALMS will be focused on the testing of MgB_2 test coils and MgB_2 wires. Due to the large minimum bending radii of reacted MgB_2 wire an alternate process called “wind-and-react” has to be pursued. With this process, MgB_2 coils consisting of unreacted wire can be formed with small bend radii. Subsequently these coils are heat-treated to react the wire into superconducting MgB_2. The reaction process occurs at elevated temperatures (about 700°C) and therefore requires the substrate that is used to form the wire into a coil to be made out of a heat resistant material such as ceramic.

AML has ordered ceramic substrates and has initiated machining tests of these substrates leading to the formation of coils.

Plans for Next Quarter

- Complete design for ALMS
- Procure components
- Start assembly and integration
- Start design of MgB_2 test coils (wind and react process in ceramic coils)
- Complete design of cryogenic cooling and measurement system
- Procure long lead items
- Finalize contract and purchase order with CAPS
- Write detailed test plan.

3.2.3.6.4 Report period: January 1, 2013 to March 31, 2013 (Q3)

Background

For system general description and requirements, see previous reports in sections 3.2.3.6.1 through 3.2.3.6.3.

Test Cryostat Design for Test Sample

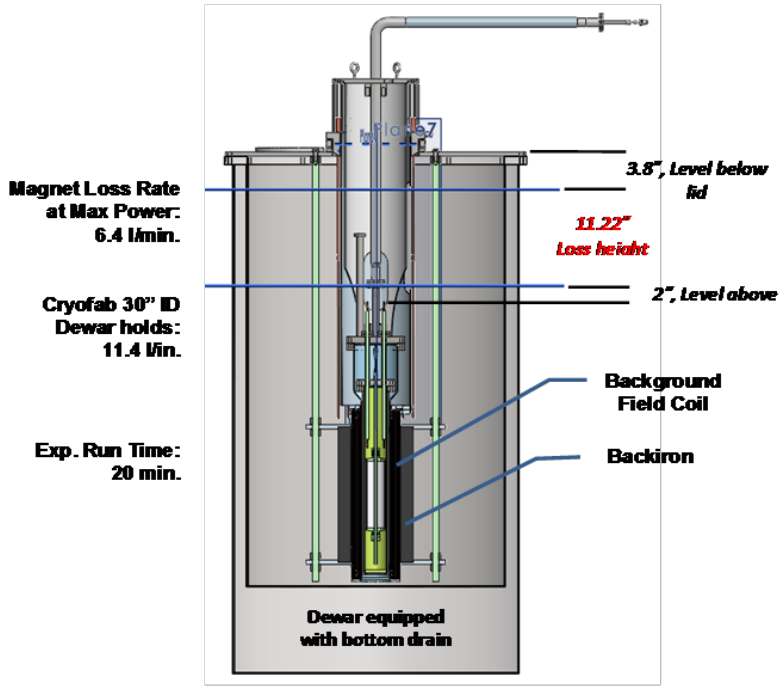

Figure 6.5.29. Cryostat assembly for the experimental setup. Immersed into a large outer LN2 cryostat is the sample cryostat for the AC loss measurement. The sample cryostat is surrounded by the coil for the background field and backiron to shape the flux density.

The cryostat for the experimental setup is shown in Figure 6.5.29. As indicated the system consists of a large outer LN2 cryostat, which holds the liquid nitrogen needed for cooling the background field coil. Immersed into this cryostat is the background field coil, which is surrounded by an iron yoke. The sample cryostat for the superconducting AC losses with its helium transfer line is located in the center of the background field coil. More detailed drawings of all components are given below.

The background field coil described in more detail below is normal conducting and generates a significant amount of heat during its operation. To maintain the operational temperature of this coil (77K) about 6.4 liter of LN2 evaporates per minute. With the given height of this cryostat the system can be operated for about 20 minutes without a refill of LN2. To allow longer operational periods between fillings of LN2, the cryostat is equipped with a bottom drain, which can be connected to a second external cryostat as shown in Figure 6.5.30.

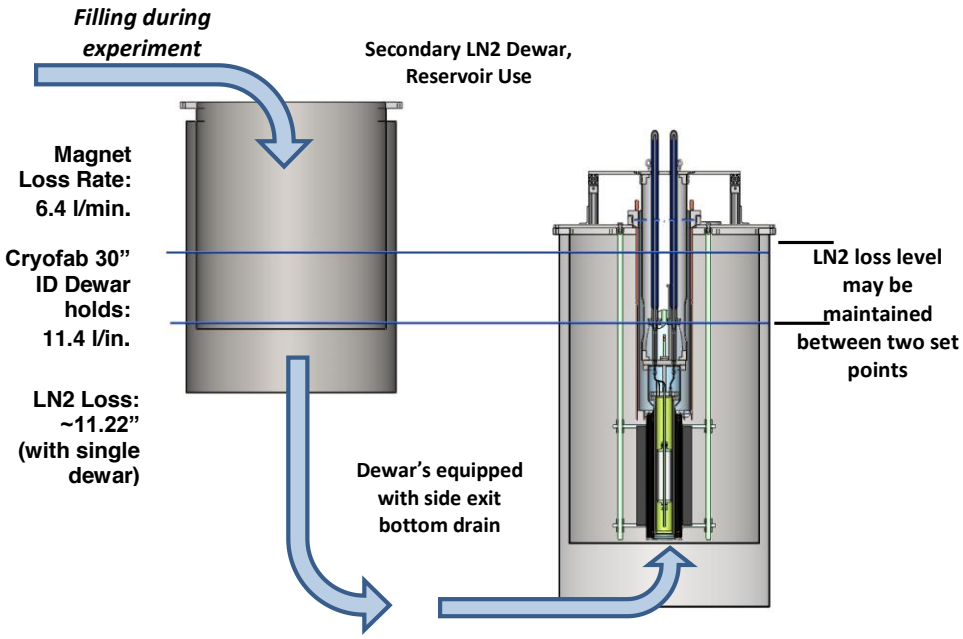

Figure 6.5.30. LN2 main cryostat with secondary cryostat for uninterrupted use without LN2 refills

Refilling LN2 in the secondary dewar will not interrupt the measurements performed in the main LN2 cryostat.

An exploded view of the test setup cryostat with its components is shown in Figure 6.5.31. From left to right the figure shows the main LN2 cryostat followed by the support system for the backiron, which is hanging from a large flange. This is followed by the background field coil, which is described in more detail below. Next in line are a hanging stand and the actual sample cryostat for the AC loss measurement. Figure 6.5.32 indicates how the components of the test setup are inserted into each other.

Figure 6.5.33 shows in more detail the support flange for the backiron. Located on the same flange is a bearing that allows rotating the background dipole field coil around its axis. This rotation is needed for the following reasons. To simulate the flux seen by the stator windings in a synchronous machine, the field coil of the test setup can be placed at different orientations about its axis. At each angular location a measurement of the resulting AC losses will be performed and each location represents a possible relative angular orientation between the rotor and stator in a synchronous machine. Performing these static measurements at each angular orientation is much simpler for the required experimental setup than a field coil that could rotate with a given rpm.

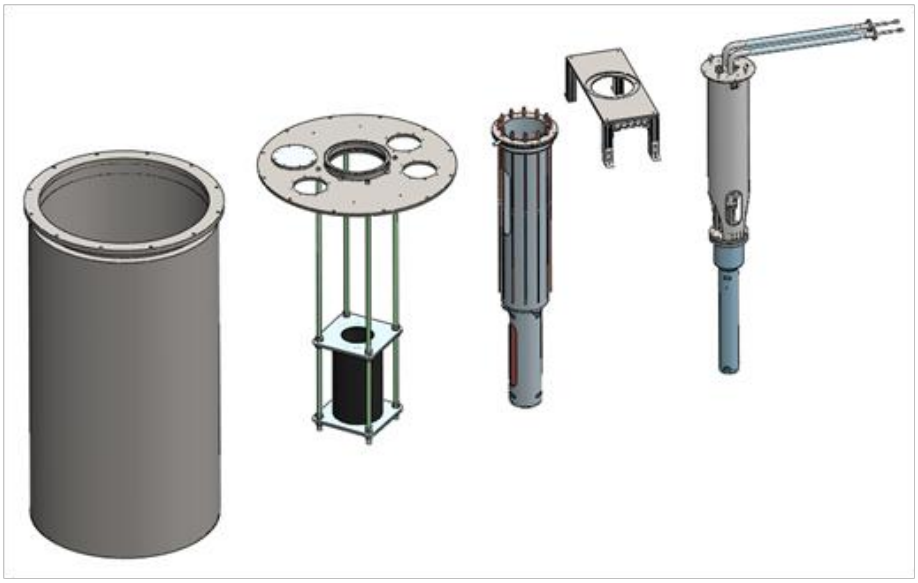

Figure 6.5.31. Exploded view of components of the LN2 cryostat. Showing from left to right the main LN2 cryostat, the flange supporting the backiron of the field coil, the multi-layer field coil, a support stand for the sample cryostat, and the sample cryostat.

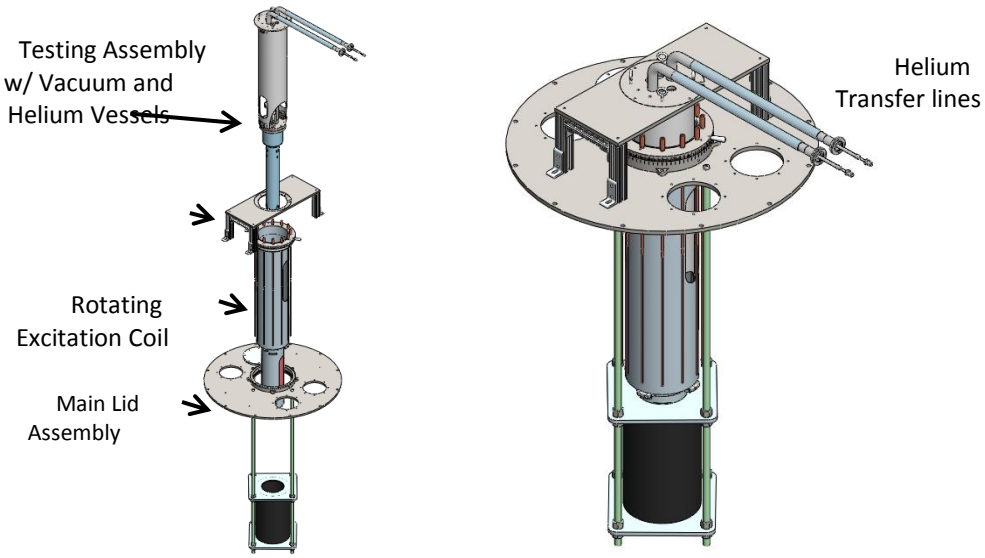

Figure 6.5.32. Exploded view of LN2 cryostat components indicating how they fit into each other.

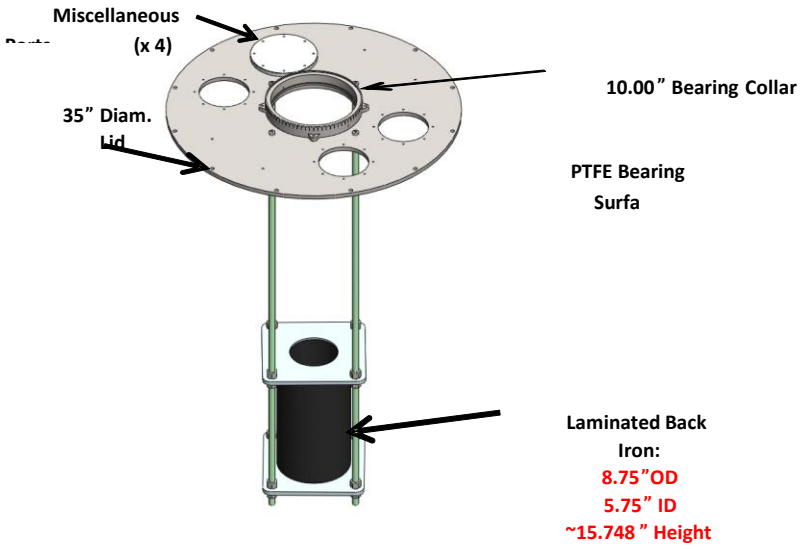

Figure 6.5.33. Support flange for the backiron with bearing for the rotation of the background field coil.

However, while these static measurements are much simpler than a rotating field coil, they only simulate a pulsing magnetic flux density and not a rotating magnetic field, which also exists for the case of rotor and stator in a synchronous machine. To simulate the conditions and losses that result from a rotating field, the following options is integrated in the design of the measuring setup. The background field coil consists of a total of 8 layers. For the static measurements at fixed angular orientation all 8 layers will be electrically in series, generating the highest flux density possible for the setup. By rotating 4 layers of the 8 layers of the dipole background field coil (Figure 6.5.34) and exciting the two sets with independent power supplies with an appropriate phase relationship, a rotating flux density seen by the test sample can be generated. The maximum flux density generated for the rotating field will however, by lower than for the static measurement.

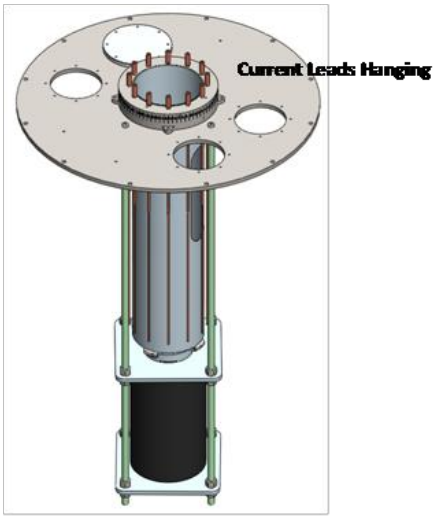

Figure 6.5.34. Current leads for the individual layers of the background field coil

Independent current leads for the layers of the dipole background field coil are required to allow the two modes of operation for pulsed and rotating magnetic fields. These leads can be seen in Figure 6.5.35. The necessary connections of these current leads to the top flange are shown in Figure 6.5.35.

Figure 6.5.36 shows the sample cryostat with the input and output helium leads inserted into the background field coil. The sample cryostat is vacuum insolated since it is inserted into the LN2 of the main cryostat. Without this vacuum insulation a large background heat load would be present. The details of the vacuum insulation, in particular the insulation vacuum on the top flange are shown in Figure 6.5.36.

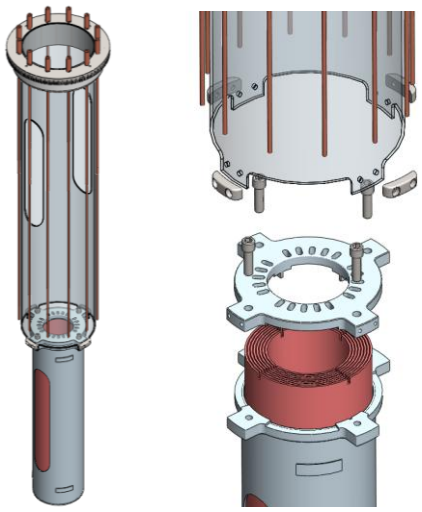

Figure 6.5.35. Details of the current lead connections to the top flange for the individual layers of the dipole background field coil.

As shown in Figure 6.5.36, the vacuum-insulated sample cryostat ishanging from a lid flange on top.AnInput and output helium line is running from the top flange of the main cryostat to the sample volume. Two HTS current leads are present to supply the sample coil under test with an AC current.

The amplitude and phase relationship of this current relative to the excitation of the background

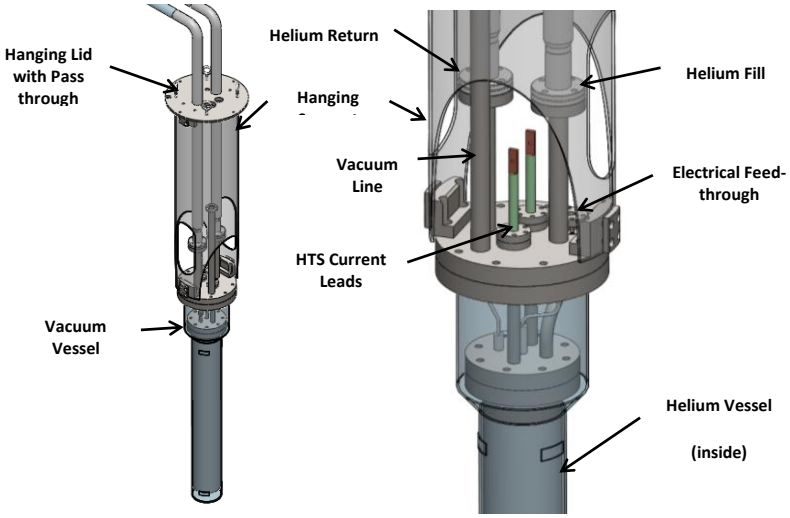

Figure 6.5.36. Details of the support and its connections of the sample cryostat

field can be adjusted to simulate various operational conditions of a synchronous machine. Additionally, a vacuum line is supplied, which allows evacuating the insulation vacuum.

Furthermore, a multi-pin electrical feed-through is supplied, which is needed to read various electrical sensors that are needed inside the cold helium volume of the sample cryostat. The internal details of the sample cryostat are shown in Figure 6.5.37.

The sample cryostat has an inner diameter of 2.5 inches. This diameter was dictated by the maximum possible diameter and field volume of the background field coil (see below). The sample cryostat itself and the sample coil inside are equipped with radial supports of low thermal conductivity (not shown) that prevents movements caused by the AC excitation.

The sample cryostat is made of non-conductive composite material to avoid eddy current losses in this material. The top flange, which consists of stainless steel to guarantee leak tightness, is sufficiently far away from the field of the background coil that eddy currents in this material are insignificant.

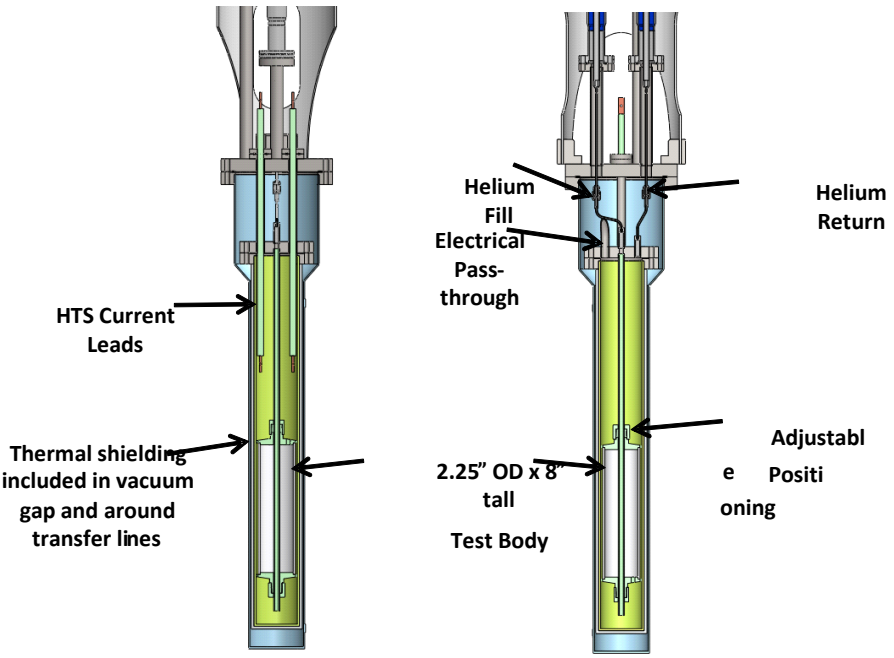

Figure 6.5.37. Details of sample cryostat

Background Field Coil

The required background field coil has been optimized to produce the highest possible flux density at the location of the sample coil. Experience with similar coils built in the past by AML has shown that the maximum achievable flux density for such a coil is about 0.5 Tesla. Such a field requires current densities in copper of about 200 A/mm2 and highly efficient LN2 cooling of the conductor is necessary. The design of this coil is based on patented AML technology that enables epoxy-free coil windings. Due to the direct contact between the LN2 cooling and the conductor the required current densities become feasible.

The winding configuration of the coil is based on 8 layers, 35 turns per layer, in a cosine-theta type saddle coil. The applied coil configuration (AML patent) achieves pure cosine-theta current density distribution over the complete length, including the coil ends. The overall length of the excitation coil is 0.42 meters, which is considerably less than a previous design that was based on double-helix winding configuration. The reduced length led to a significantly reduced inductance and resistance and therefore to manageable operational voltages for higher frequency as well as cooling requirements.

The coil design was optimized for field uniformity and manufacturing requirements. The layout of the optimized design is show in Figure 6.5.38. The resulting dipole field strength and uniformity as well as the higher-order harmonics are shown in Figure 6.5.39 and Figure 6.5.40. As shown in Figure 6.5.38 to Figure 6.5.40, the coil configuration produces a very uniform dipole field with a maximum flux density of about 0.5 Tesla.

The achievable operating range in flux density and frequency for the AC loss measurements based on currently available power supplies at the CAPS are shown in Figure 6.5.42.

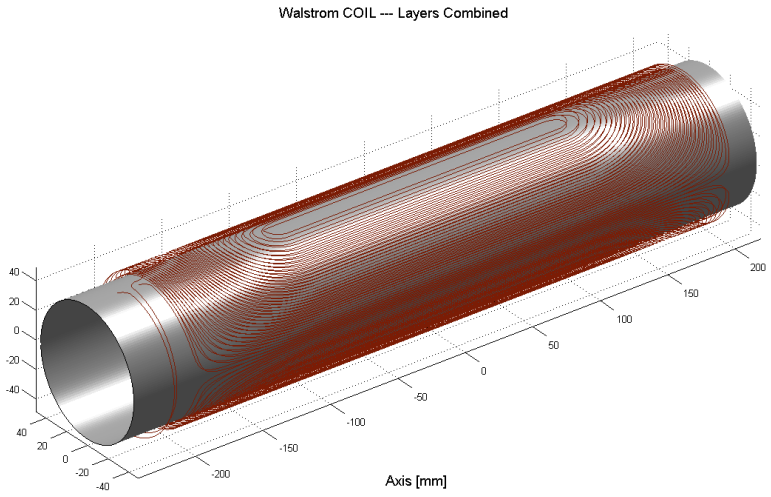

Figure 6.5.38. Layout of excitation coil. For clarity, only one layer is shown.

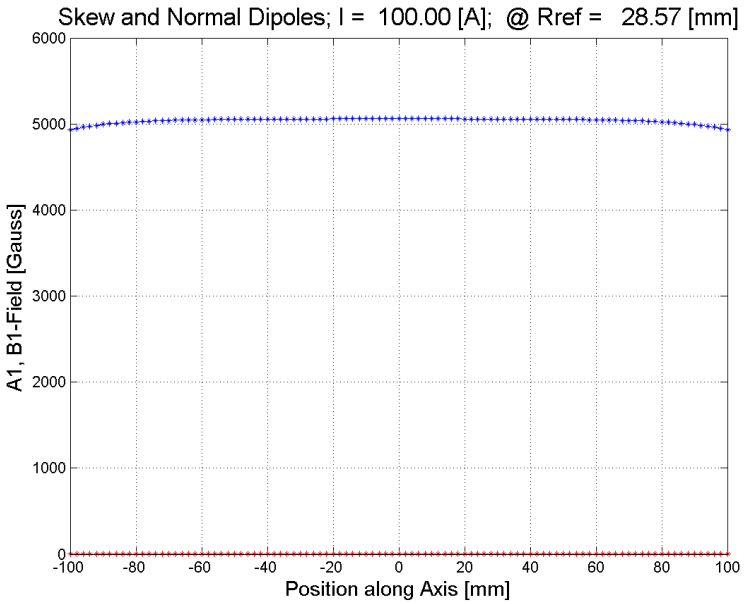

Figure 6.5.39. Figure shows dipole field over the region of interest. Variation in dipole field is less than 3% over the region of interest +/-100 [mm], as specified by design requirements.

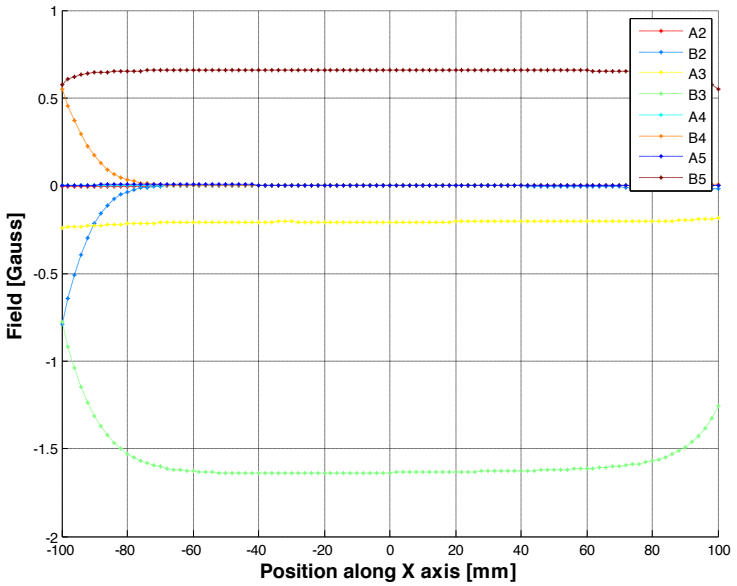

Figure 6.5.40. Figure shows first few high order harmonics in the field in the region of interest.

Figure 6.5.41. The contribution of the high order components is extremely small compared to the dipole field.

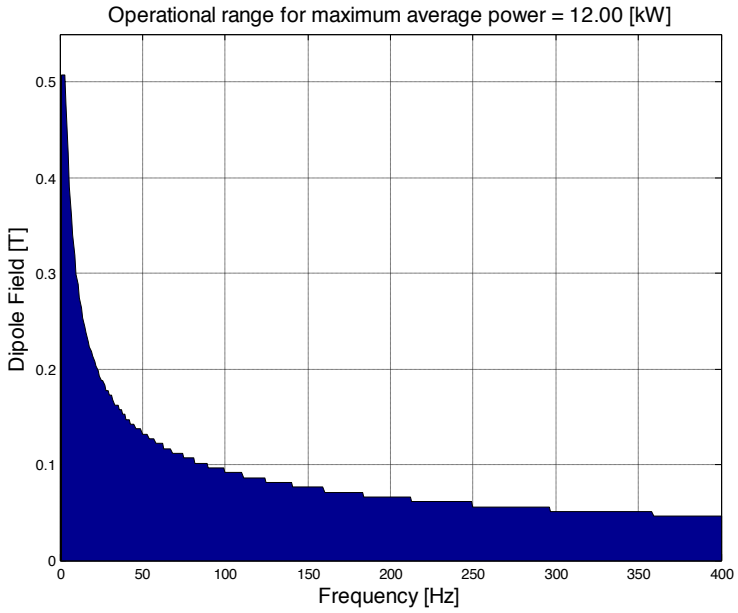

Figure 6.5.42. Operating range of experiments possible with the new excitation coil assuming 12 kW power supply.

As can be seen from Figure 6.5.42, the maximum frequency at which a flux density of about 0.5 Tesla is possible is limited to a few Hz, but rather large frequencies up to at least 400 Hz are feasible with reduced flux density.

MgB2 Sample Coils

It is currently planned that the MgB2 sample coils will be manufactured in collaboration with HyperTech. AML will produce the required coil windings with unreacted conductor, and HyperTech will perform the reaction cycle. The detailed design of these coils is currently TBD.

Cryogenic Cooling System

Introduction

This is the first Informal Monthly Report for Creare's Consulting Contract with Advanced Magnet Laboratory per Creare Proposal P-10072/AML P.O. 11481. This report covers the period March 5, 2013, through April 5, 2013.

Objective

The overall objective of this project is to develop a superconducting generator for large-scale (10 MW) wind turbines. The generator will be cooled using cycle gas from a Creare turbo-Brayton cryocooler and transferred to the rotor via a rotating cryogenic coupling.

The objective of the work proposed for Budget Period 2 is to conduct a number of de-risking experiments to answer critical questions pertaining to the superconducting generator design.

The specific objective of Creare's work proposed here is to support the program, including cooling system design, and technical interactions with the project team.

Technical Progress during the Reporting Period

Our efforts during the reporting period were focused on the design of the cooling system for the AC-loss experiment.

System Requirements

The requirements for the cooling system for the AC loss experiment are listed in Table 6.5.5.

Table 6.5.5. AC-Loss Experiment Cooling System Requirements

Parameter	Value	Unit
Maximum Heat Load (at 15 K)	< 10	W
Operational Temperature	> 15	K
Maximum Temperature Increase in Coil	1.5	K
Test Gas	He	

System Configuration

A schematic of the cooling system approach is shown in Figure 6.5.43. The cooling module and the experiment module are housed in separate vacuum-insulated cryostats. Helium flow, driven by a Cryozone circulator, is cooled by a pair of AL-325 GM cryocoolers with interface heat exchanges mounted onto each cold head. The flow passes through a vacuum-insulated transfer line to the experimental module, where it cools the test coil. The losses in the test coil will be determined from the product of the heat capacity of the gas, the mass flow rate, and the temperature difference between the inlet and outlet flows. The temperature will be measured by redundant temperature sensors mounted in the inlet and outlet flow tubes to the experiment. The mass flow rate will be determined from the pressure difference across a calibrated venturi flow meter installed in the cooling module. The uncertainty associated with these two measurements drives the uncertainty of the heat load measurement. All cold components and tubing will be insulated with multilayer insulation (MLI).

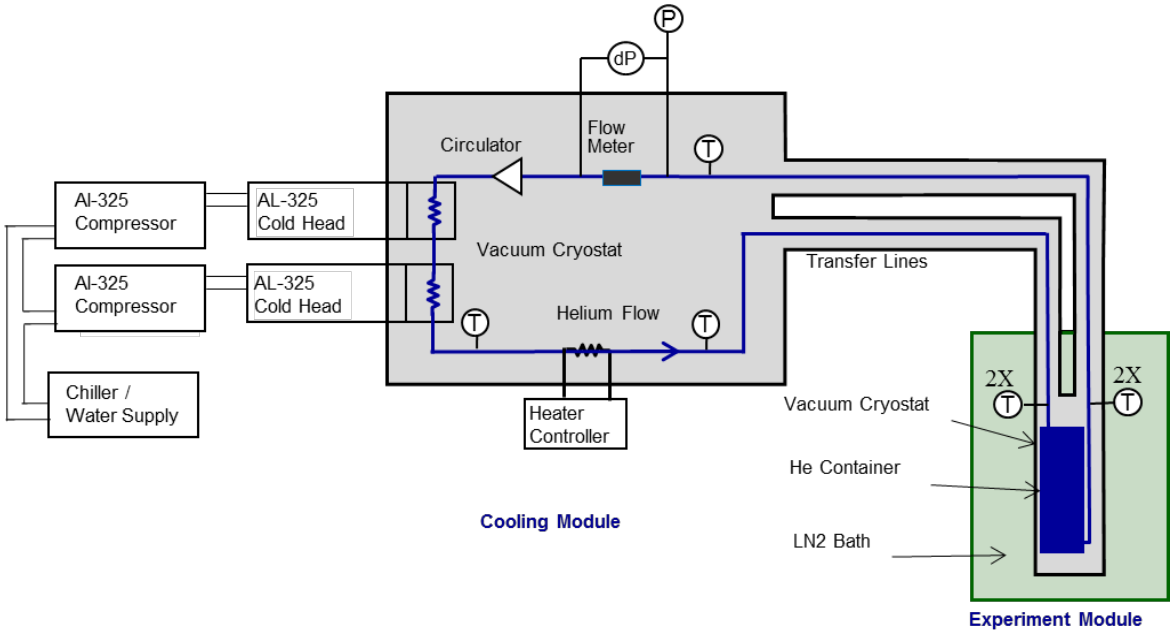

Figure 6.5.43. Cooling System Schematic

The general layout and relative size of the cooling module and the experiment module are shown in 3-D models pictured in Figure 6.5.44. The modules are positioned to minimize the length of the transfer line and so minimize the thermal losses associated with this line. The cooling module is also positioned to minimize the head room above the experiment module, as there is limited roof clearance in the laboratory where the experiment will be installed.

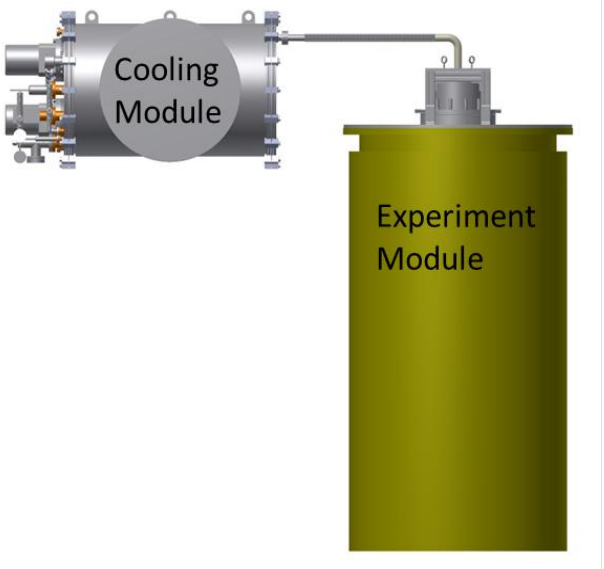

Figure 6.5.44. Models of Cooling Module and Experiment Module

System Components

The primary system components are listed in Table 6.5.6.

Table 6.5.6. System Components

Parameter	Value	Unit
Cryocooler	AL32510	Cryomech
Interface Heat Exchangers		Cryozone
Circulator	Noordenwind	Cryozone
Cryostat	Custom	TBD
Transfer Line	Custom	Precision Cryogenics

System Design

A solid model of the system design is shown in Figure 6.5.45. We selected a tee configuration for the cryostat. All of the components are mounted on one flange of the tee, and the two transfer line pass-throughs are mounted on the opposing flange. The central flange in the tee provides access to allow the transfer line to be disconnected inside the cryostat. This approach avoids the use of bayonet fittings, which would introduce unacceptable heat loads. The layout of components inside the cryostat is shown in Figure 6.5.46.

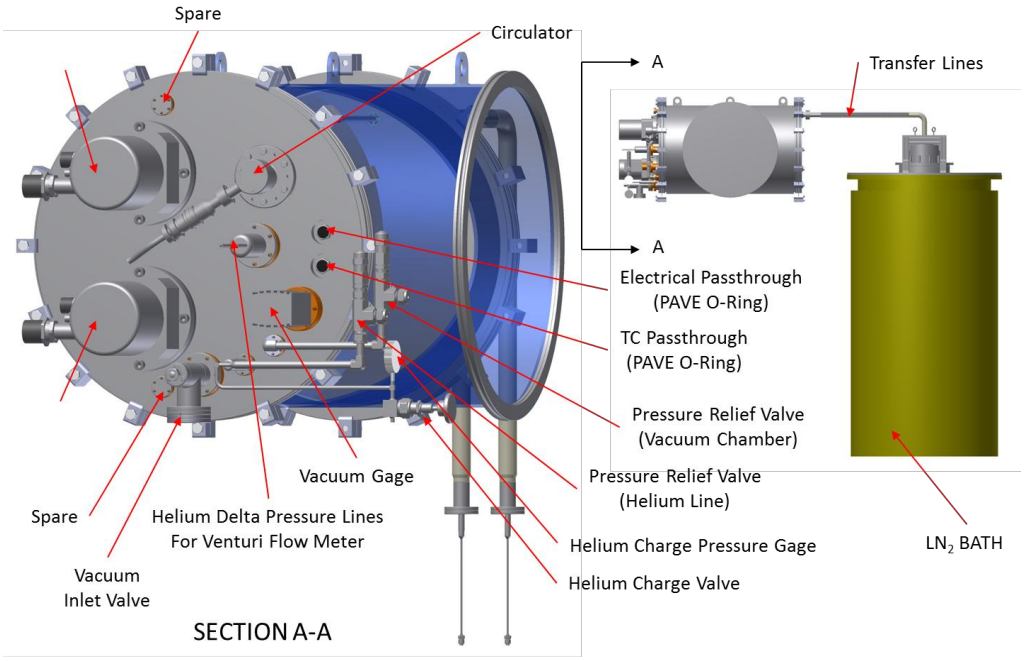

Figure 6.5.45. System Design showing Component Layout in Cryostat Base Plate

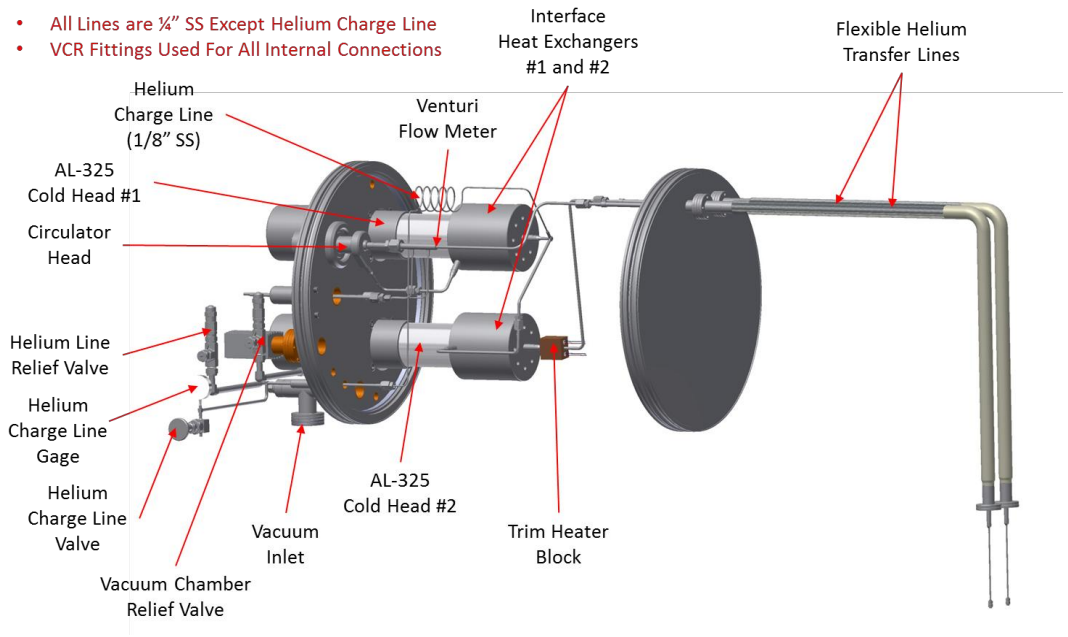

Figure 6.5.46. System Design Model showing Component Layout within Cryostat

System Pressure Drop and Fan Selection

A key requirement in the design of the cooling system is to provide sufficient cooling to keep the temperature increase in the test coil below 1.5 K. In our design, we assumed a temperature increase of 1 K in the helium flow across the experiment. The helium mass flow required can then be determined. A 10-W load requires a mass flow of 1.7 g/s to provide a 1 K temperature difference across the experiment (Cp of helium at 15 K and 690 kPa is 5.8 kJ/kgK). For a specified mass flow rate, the pressure drop through the system will depend on the system pressure. This dependence is shown in Figure 6.5.47 for mass flows corresponding to 5-W and 10-W experiments. The performance characteristics of two sizes of Cryozone fans are also included in the figure. The results show that the smaller Cierzo fan cannot provide sufficient flow rate for the 10-W experiment until the system pressure is increased to 110 psi. The larger Noordenwind fan provides sufficient flow at a system pressure of 70 psi.

Although the Noordenwind fan has a higher static heat load than the Cierzo fain (5.5 W versus 3.75 W), the higher system pressure required by the smaller fan may not be possible as the ability of the experiment helium cryostat to take higher pressures is uncertain. Furthermore, as the additional penalty of 1.75 W of cooling may be provided by increasing the cold head temperatures by approximately 0.1 K, the advantages of the greater head and lower system pressures possible with the Noordenwind fan outweigh the increased static thermal loading.

The 1 psi pressure margin at 100 psi system pressure provides some headroom for pressure losses in the experiment, which have been assumed to be small in this analysis. Additional pressure losses may be introduced in the helium flow distribution components in the experiment.

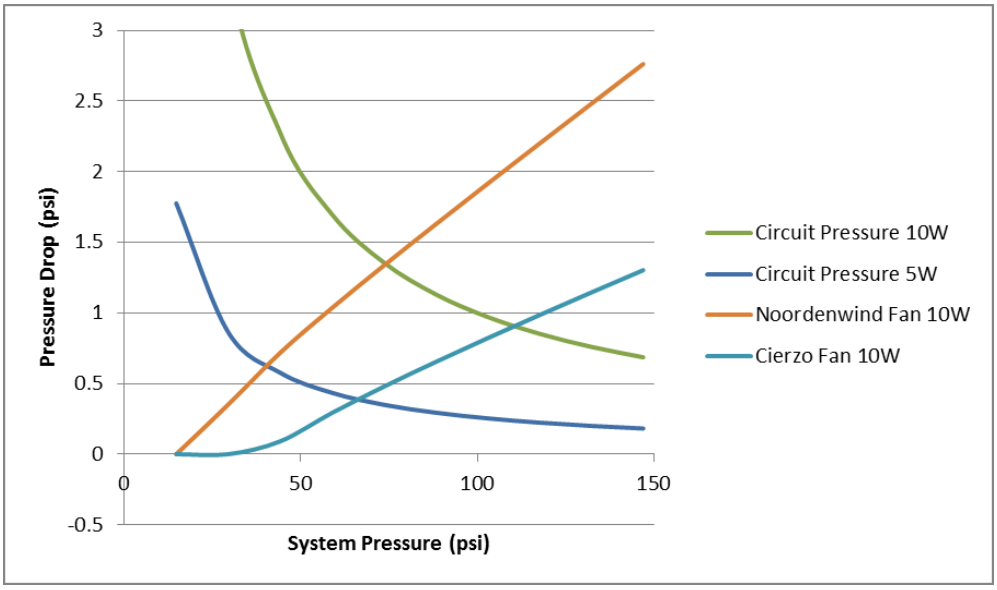

Figure 6.5.47. Circuit Pressure Drop and Available Fan Pressure Head Plotted Against System Pressure

The component pressure drops are summarized in Table 6.5.7 for the 10-W case. The largest pressure drop in the system is associated with the flexible transfer line. The large pressure associated with the flexible transfer line is due to the corrugated tubing used in this line. If this proves to be an issue, we may be able to insert a liner into the tube to reduce these losses.

Table 6.5.7. Component Pressure Drop at 100-psi System Pressure

Parameter	ID (in)	Length (in)	Pa	psi
Tubing: Circulator Outlet to Cold Head #1	0.18	8	344	0.05
GM Cold Head Heat Exchanger #1			249	0.04
Tubing: GM Cold Head #1 to GM Cold Head #2	0.18	13	474	0.07
GM Cold Head Heat Exchanger #2			249	0.04
Tubing: GM Cold Head #2 to Venturi	0.18	14	484	0.07
Venturi Line	0.13	12	952	0.14
Tubing: Flexible Transfer Line	0.24	53	3166	0.46
Tubing: Straight Transfer Line	0.31	71	145	0.02
Tubing: Cover to Circulator	0.18	24	752	0.11
Tubing: Rigid Line in Experiment	0.18	20	652	0.09
Total			6814	0.99

Thermal Loads

Thermal Load Summary

Table 6.5.8 summarizes the heat load estimates for the cooling module and the experiment module. The bases for these estimates are described in the subsections that follow.

Table 6.5.8. Heat Loads

Parameter	Value	Unit
Transfer Line	3.1	W
Cooling Module Cryostat	0.8	W
Current Leads	TBD	W
Pressure Taps	0.15	W
Fill Tube	0.24	W
Cooling Module Instrumentation	0.18	W
Experiment Cryostat	0.003	W
Experiment Module Instrumentation	.07	W
Circulator Static Heat Load	5.5	W
Circulator Dynamic Heat Load*	3.2	W
Total	13.2	W

*Estimated for experiment heat load of 10 W requiring a mass flow of 1.7 g/s or volume flow rate of 0.29 m3/hr with fan providing a pressure head of 56 m (1 psi) at an efficiency of 0.4.

Transfer Line

The vacuum-jacketed transfer line is the largest heat load in the system. It will be supplied by Precision Cryogenics, which estimated the heat leak to be 0.96 W/m for the flexible section, 0.74 W/m for the straight section, and 0.66 W for each elbow. The length of the flexible section is approximately 1.3 m, which gives a heat load of approximately 1.3 W. The length of the straight section is longer than the flexible section, but much of the straight section is immersed in LN_2 or cold LN_2 boil-off gas. The straight section outside the LN_2 dewar is approximately 0.4 m long, with a heat load of 0.3 W. The length of the section within the dewar is approximately 1.0 m, which gives a heat load of 0.17 W if we assume the external temperature is 77 K and scale the warm loss factor assuming it is a conductive heat load. The total heat load of the transfer line is 3 W.

Cooling Module Cryostat Radiation Load

Thermal radiation will transfer heat from the warm vacuum enclosure surfaces to the cold components within them. We will use MLI to limit the heat transfer rate. The MLI will consist of

Dunmore DE-013 aluminized PET with a 1% open area perforation pattern, combined with Apex Mills B4A polyester scrim. We will attach 20 layers with a layer density of 19 layers/cm (48 layers/inches). We analyzed this configuration per Equation (1). We then increased the calculated heat transfer rate by 100% to account for practical considerations such as seams, penetrations, and surface area uncertainty. The resulting heat transfer rates for our estimated cold surface area of 0.5 m^2 is 0.80 W.

$$\dot{Q}'' = \frac{C_s \tilde{N}^a T_m}{N+1}(T_h - T_c) + \frac{C_r \varepsilon}{N}(T_h^{4.67} - T_c^{4.67}) \quad (1)$$

where:

$$\begin{aligned}
&\dot{Q}'' = \text{Heat flux rate (W/m2)} \\
&C_s = 73\text{E-}9 \text{ (empirical)} \\
&N = \text{Number of layers} \\
&\tilde{N} = \text{Packing density (layers/cm)} \\
&a = 2.63 \text{ (empirical)} \\
&T_m = \text{Mean temperature (K)} \\
&T_h, T_c = \text{Hot and cold surface temperatures (K)} \\
&C_r = 7.07\text{E-}10 \text{ (empirical)} \\
&\varepsilon = \text{MLI single layer emissivity (0.035)}
\end{aligned} \quad (2)$$

Current Leads

A pair of power leads will pass current to the test coil. These leads will be copper down to a 77-K intercept, and then HTS from 77 K to the experiment. We do not have an estimate for the heat load to the 15-K helium from the HTS leads.

Instrumentation Leads

The cooling module includes several instrumentation wires that pass between the cryogenic components and the warm enclosure. We have assumed there will be eight leads from temperature sensors in the cold module. We have assumed that the eight wires are 30 AWG copper, each wire is one meter long, electric current is zero, and the wire bundle is enclosed by a single layer of aluminized mylar (emissivity = 0.035) to reduce radiation heat transfer. These wires will contribute a radiation heat load of 0.1 W and a conductive heat load of a similar magnitude for a total heat load of 0.2 W.

The temperature sensor leads in the experiment module will be staked at 77 K. These leads will have a negligible radiation heat load and a conductive heat load of 0.1 W. The total heat load associated with the instrumentation leads at 15 K is therefore 0.3 W.

Evacuation and Fill Tube

The helium circuit includes a small tube that connects the cryogenic flow loop to an evacuation and fill port, a pressure gauge, a relief valve, and accumulator volume. Fill tube parameters are listed in Table 6.5.9. Assuming a tube length of 0.4 m and at least one layer of MLI, we estimate a heat load of 0.2 W.

Table 6.5.9. Assumptions and Results for Evacuation and Fill Tube Thermal Analysis

Parameter	Value	Unit
Warm End Temperature	300	K
Cold End Temperature	15	K
Tube Material	S31603	
Outer Diameter	6.4 (0.25)	mm (in)
Wall Thickness	0.71 (0.028)	mm (in)
Tube Length	0.4	m
Tube Emissivity (with aluminized mylar)	0.035	0.035
Heat Transfer to Cold End	0.2	W

Pressure Tap Tubing

A pressure tap is required on either side of the venture meter. Tap parameters are listed in Table 6.5.10. Assuming a tube length of 0.4 m and at least one layer of MLI, we estimate a heat load of 0.15 W.

Electric Heater

An electric heater may be included to provide control over the temperature of the cooling gas exiting the cryocoolers. This heater will also provide an alternate method to measure the helium mass flow rate. As the heater leads may be disconnected in cases where the cooling capacity is maximized, we did not include the heat leak of the heater leads in this analysis.

Circulator Fan

The dynamic loss associated with the fan was estimated based on an experiment heat load of 10 W.

Table 6.5.10. Assumptions and Results for Pressure Tap Tubing

Parameter	Value	Unit
Warm End Temperature	300	K
Cold End Temperature	15	K
Tube Material	S31603	
Outer Diameter	2.4 (0.09)	mm (in)
Wall Thickness	0.71 (0.02)	mm (in)
Tube Length	0.3	m
Tube Emissivity (with aluminized mylar)	0.035	0.035
Heat Transfer to Cold End	0.15	W

This load requires a mass flow of 1.7 g/s to provide a 1-K temperature difference across the experiment (Cp of helium at 15 K and 690 kPa is 5.8 kJ/kgK). This flow rate is equivalent to a volume flow rate of 0.29 m3/hr. At this flow rate, the pressure losses in the circuit are approximately 8.4 kPa (1.2 psi). This estimate is discussed in the next section. This is equivalent to a required head of 38 m. This operating point is shown on the fan characteristic in Figure 6.5.48. At this low flow rate, we assume an efficiency of 25% and calculate an isentropic enthalpy rise of 0.8 W and a dynamic loss of 2.4 W, giving a total enthalpy increase of 8.7 W associated with the fan.

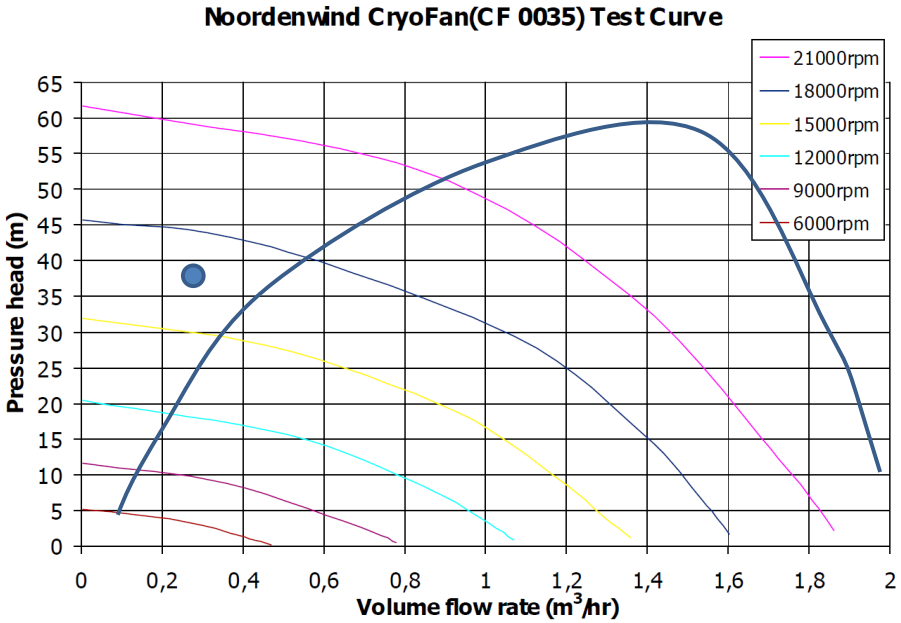

Figure 6.5.48. Cryozone Noordenwind Fan Characteristic

Refrigeration

To meet the system heat load of 13.2 W, plus an experiment heat load of 10 W at 15 K, we determined that two AL-325 cryocoolers would be required. The performance curve for this cryocooler is shown in Figure 6.5.49. Cryozone engineers estimate their cold head heat exchangers will provide gas at 2 K above the temperature of the cold head. Hence, to provide gas at 15 K, the cold head will operate at approximately 13 K. At this temperature, the AL-325 provides approximately 8 W refrigeration. Total refrigeration provided by two cold heads is 16 W, and the maximum heat load possible in the experiment is 3.2 W. However, the performance curve of the cryocooler offers an increase of about 8 W for each K increase in cold head temperature. Increasing the temperature of the experiment to 15.5 K increases the available cooling power to 24 W, which is sufficient cooling for a 10-W experiment.

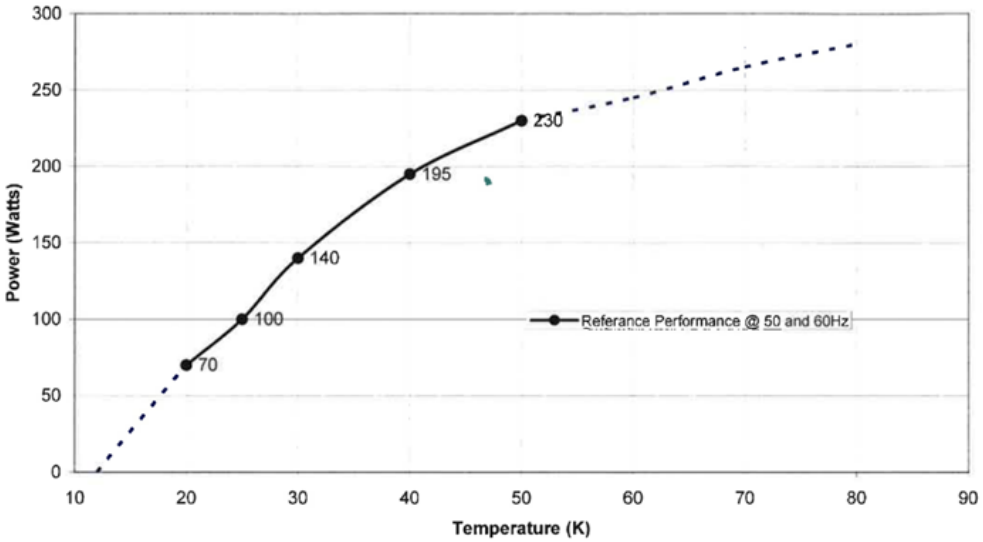

Figure 6.5.49. Cryomech AL-325 Performance Curve

Measurement Uncertainty

The heat load in the experiment will be determined from the product of the heat capacity of the gas, the mass flow rate, and the temperature difference between the inlet and outlet flows. The temperature will be measured by redundant temperature sensors mounted in the inlet and outlet flow tubes to the experiment. The mass flow rate will be determined from the pressure difference across a calibrated venturi flow meter installed in the cooling module. The uncertainty associated with these two measurements drives the uncertainty of the heat load measurement.

We plan to specify Cernox sensors from Lakeshore Cryotronics as the temperature sensors. The sensors are to be mounted inside the experiment inlet and exit tubes in the region submerged in LN2 in order to minimize any variable parasitic losses that might affect the measurement. Redundant sensors should be used for this critical measurement. Creare has previously demonstrated agreement between redundant temperature measurements that are within the ±9 mK uncertainty specified for these sensors by following a specific sensor mounting technique developed in house. The uncertainty associated with the temperature difference is ±18 mK, or 1.8% for a difference of 1 K.

The uncertainty associated with the mass flow measurement arises from the pressure measurement from which the mass flow is derived. For our uncertainty analysis, we assumed an orifice plate with a diameter ratio of 0.5 installed in a tube with an internal diameter of 0.18 inches. For the 10-W experiment, this orifice produces a pressure drop of 600 Pa. The uncertainty in the mass flow measurement is plotted in Figure 6.5.50 for a range of experiment heat loads from 1 W to 10 W for three different pressure transducers. The 3" H2O PX653-03D5V transducer from Omega has a full-scale range of 620 Pa and an uncertainty of 0.3% FS. It covers the full range of experiment heat loads but introduces excessive uncertainties at loads below 3 W. If the experiment load is below this value, a transducer with a smaller range should be used. Note that these pressure ranges are at the limit of measureable pressure ranges with reasonably priced commercial differential pressure transducers.

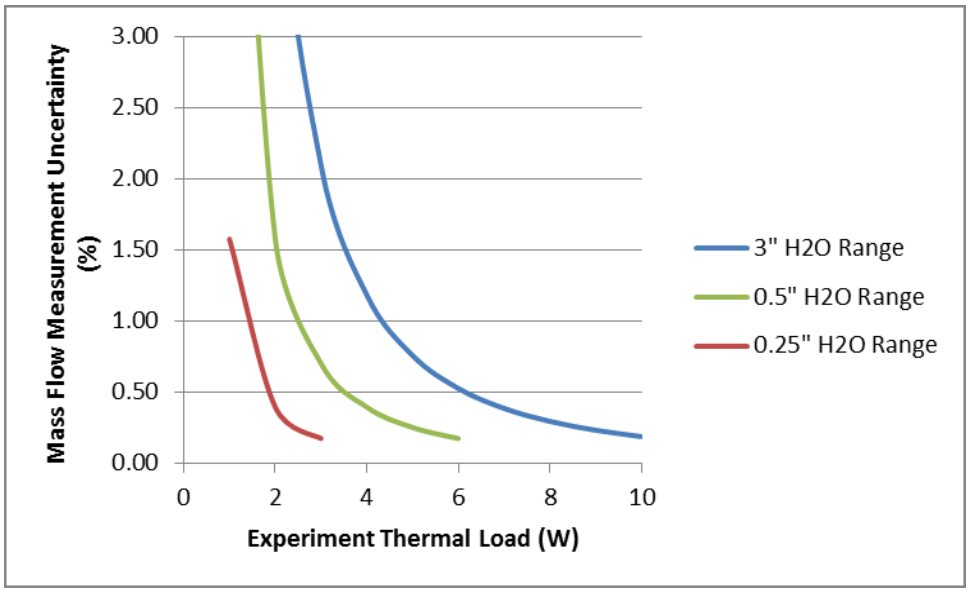

Figure 6.5.50. Uncertainty of the Mass Flow Measurements plotted against the Experiment Heat Load for Three Pressure Transducers with Different Ranges.

The measured differential pressure may be increased by reducing the size of the tube and so increasing the flow velocity. However, the cost is increased pressure drop in the tube.

Based on this analysis, we estimate that the total uncertainty in the heat load measurement will be of the order of 3%.

3.2.3.6.5 Report period: April 1, 2013 to June 30, 2013 (Q4)

Overview

For system general description and requirements, see previous reports in paragraphs 3.2.3.6.1 through 3.2.3.6.4.

Overall Status

- **Helium and Vacuum Cryostats**

  The helium and vacuum vessels and associated hermetic lids have been fabricated. The units are undergoing leak testing and will subsequently be shipped to Creare for testing with the cryogenic cooling system. The figures below show the vessels and associated lids.

- **Excitation Magnet System**

  The design for the excitation magnets is complete. Materials have been received at AML and manufacturing will commence shortly.

- **Cooling System**

  All major components for the cooling system have been received at Creare. They are in the process of assembling the system in preparation for testing with the helium and vacuum vessels (Figure 6.5.51 and Figure 6.5.52). Testing is scheduled to occur in September.

Figure 6.5.51. Vacuum and Helium Vessel

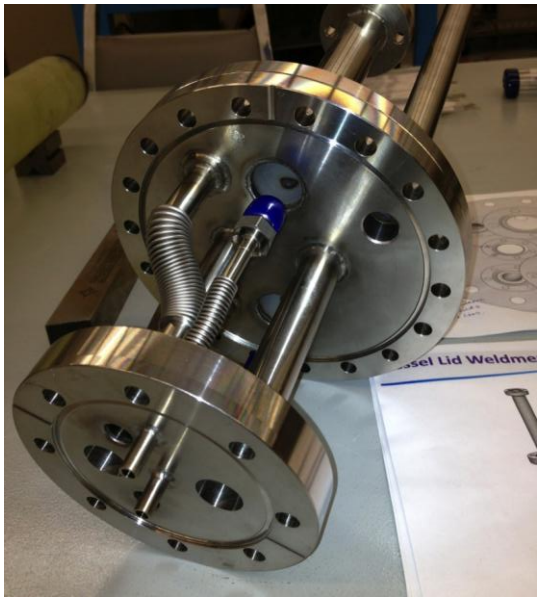

Figure 6.5.52. Vessel Lid Assembly

3.2.3.6.6 Report period: July 1, 2013 to September 30, 2013 (Q5)

For system general description and requirements, see previous reports in paragraphs 3.2.3.6.1 through 3.2.3.6.5.

MgB2 Sample Coils

It is currently planned that the MgB2 sample coils will be manufactured in collaboration with HyperTech. AML will produce the required coil windings with unreacted conductor, and HyperTech will perform the reaction cycle. A design of these coils is shown in Figure 6.5.53.

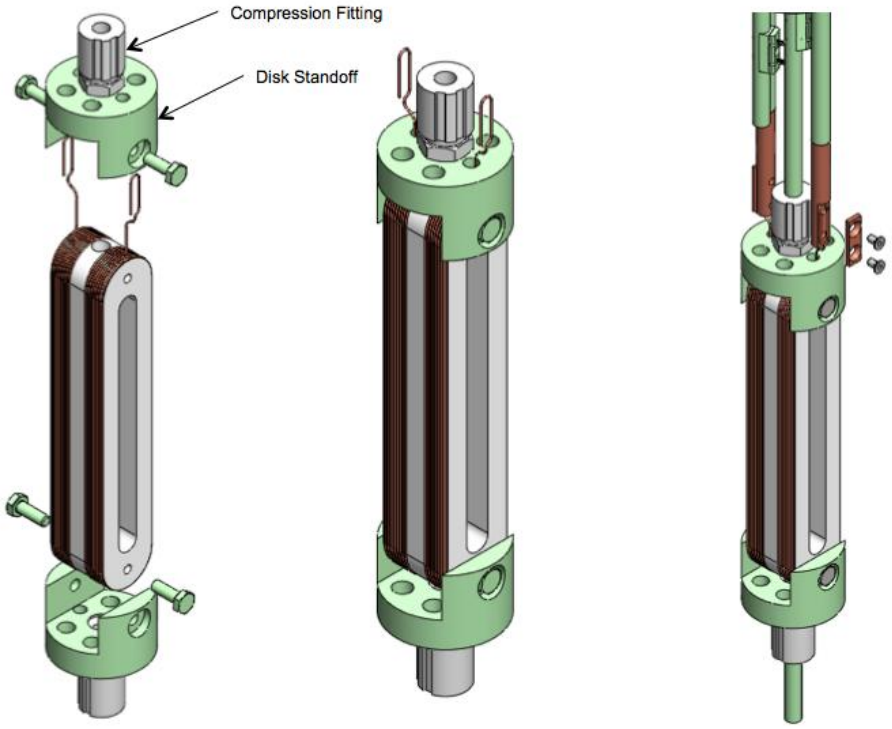

Figure 6.5.53. MgB2 saddle coil mounted to the current leads in the test cryostat

Task 6.5 Overall Status

Helium and Vacuum Cryostats

The helium and vacuum vessels and associated hermetic lids have been fabricated, leak tested and shipped to Creare for integration into the cooling module. Figure 6.5.54 shows the leak testing process. Figure 6.5.55 and Figure 6.5.56 show these two vessels and their stainless lids with pass-throughs.

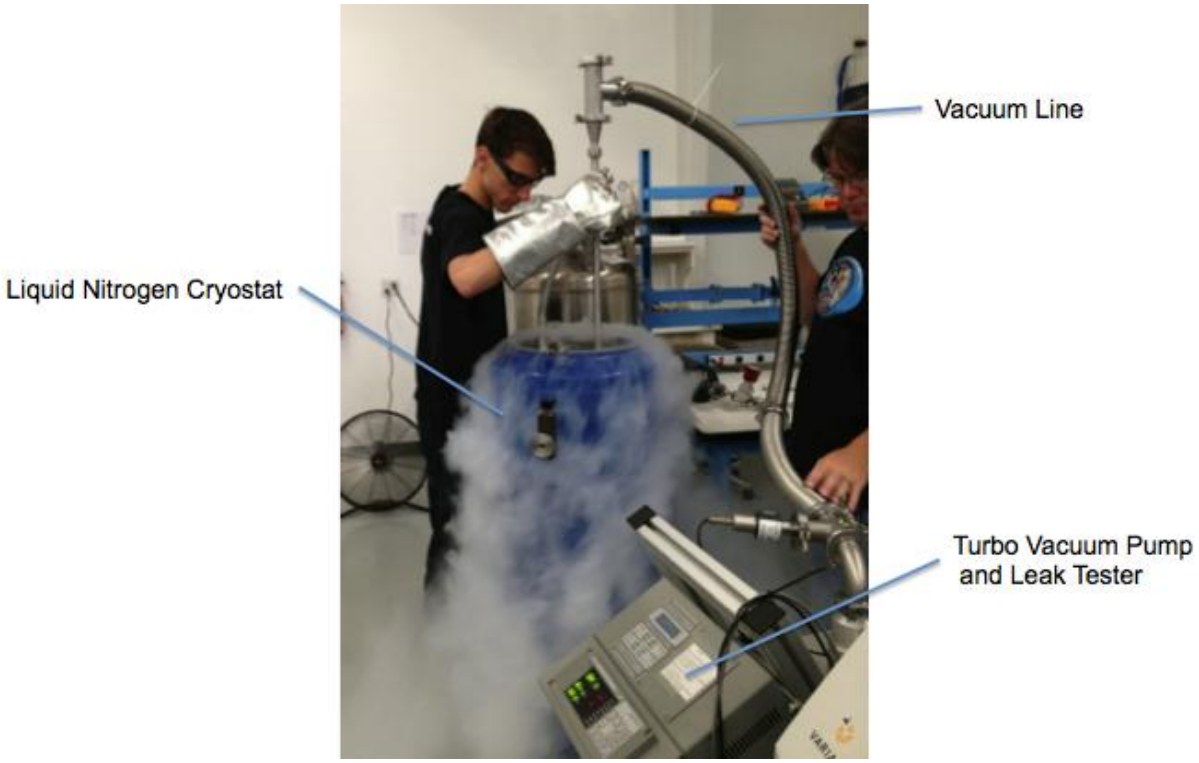

Figure 6.5.54. Leak testing of Vacuum and Helium Cryostats

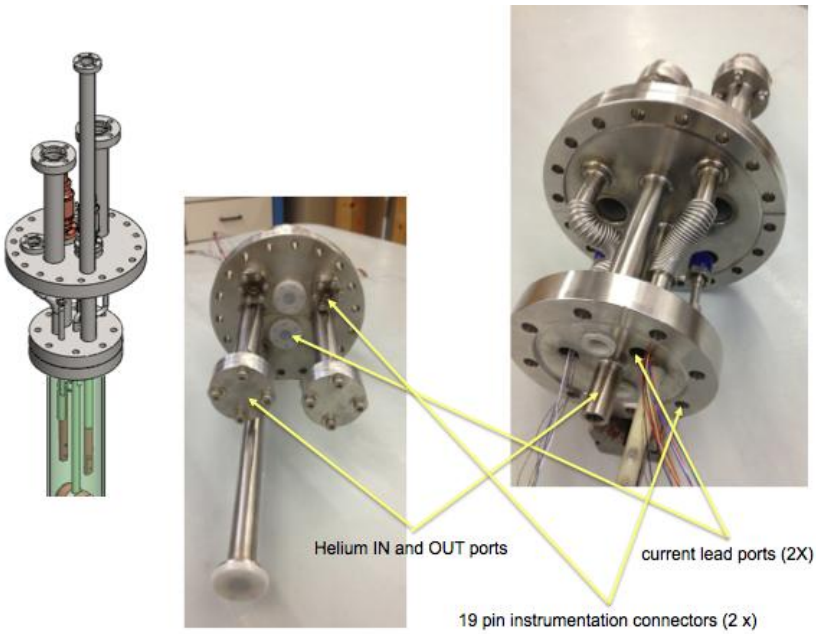

Figure 6.5.55. Vacuum and Helium Welded Lids

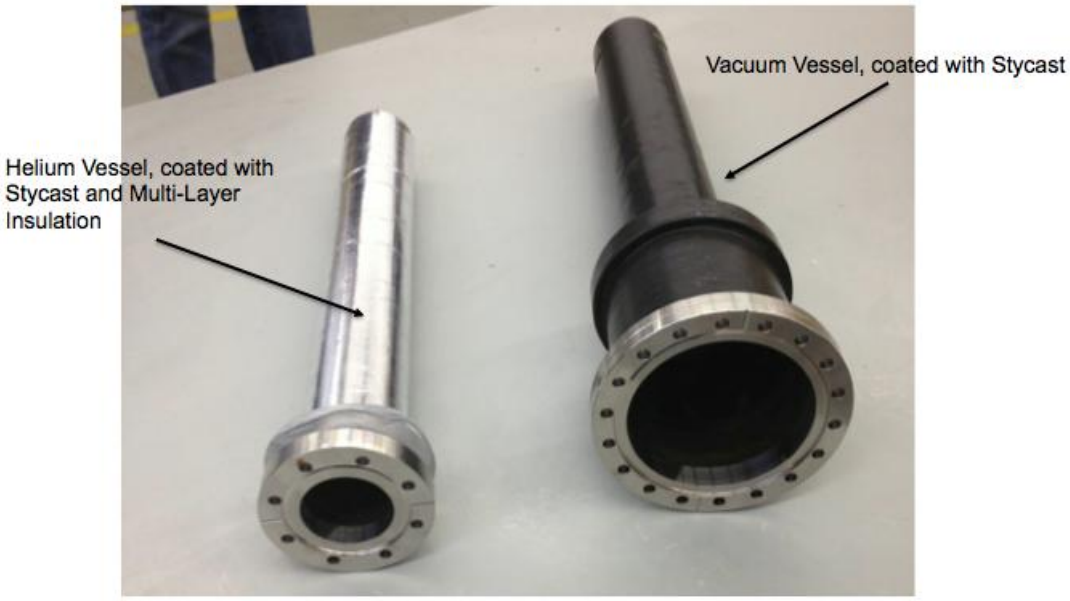

Figure 6.5.56. Vacuum and Helium Cryostat Vessels

Excitation Magnet System

The fabrication of the excitation magnet is in process. The backiron laminations are in house. The eight sub-coils which make up the excitation magnet assembly are completed and ready for integration. Figure 6.5.57 and Figure 6.5.58 show the various components of the excitation magnet assembly.

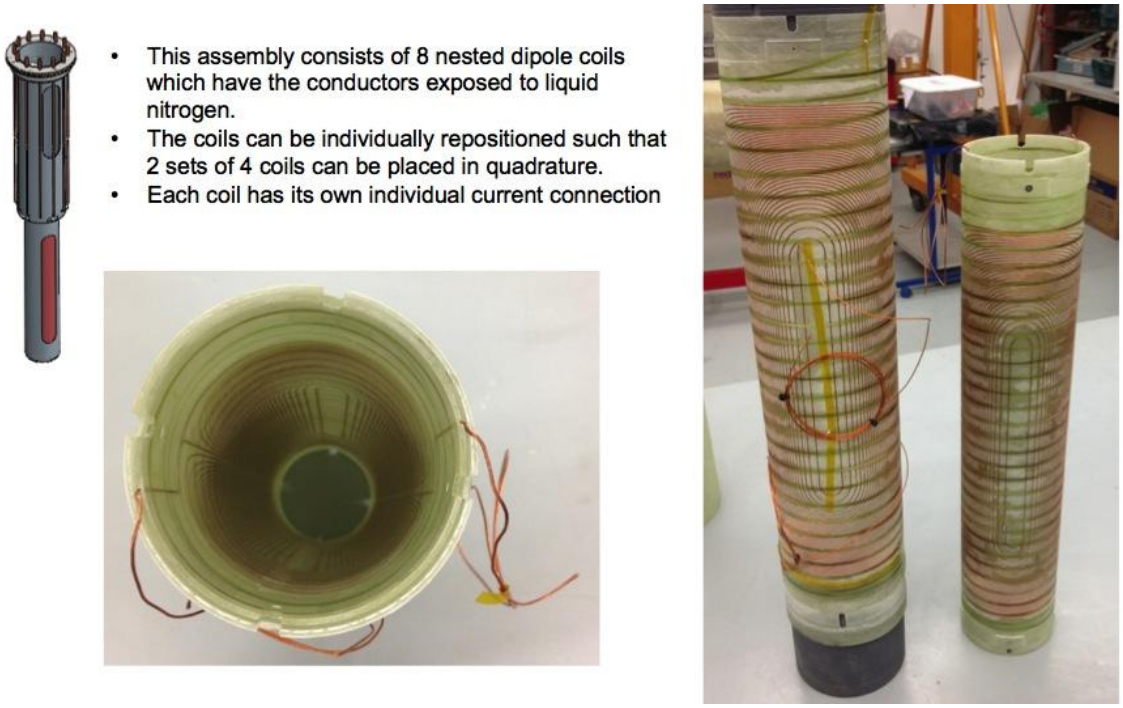

Figure 6.5.57. Excitation Magnet Coils

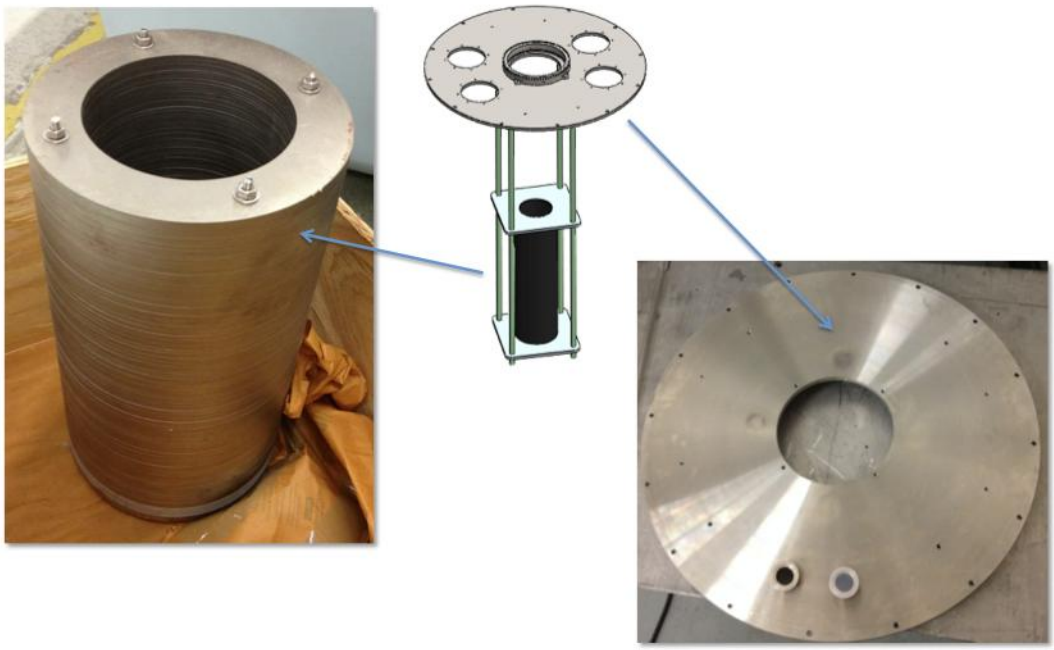

Figure 6.5.58. Backiron Laminations and Cryostat Top Plate

Calibration Heater and Test Coil Assembly

A dedicated calibration heater was fabricated which can generate up to 20 Watts of heat inside the experiment module (Helium Vessel). This calibration heater will be used to calibrate the calorimetric loss measurement system at Creare. Figure 6.5.59 shows the calibration heater.

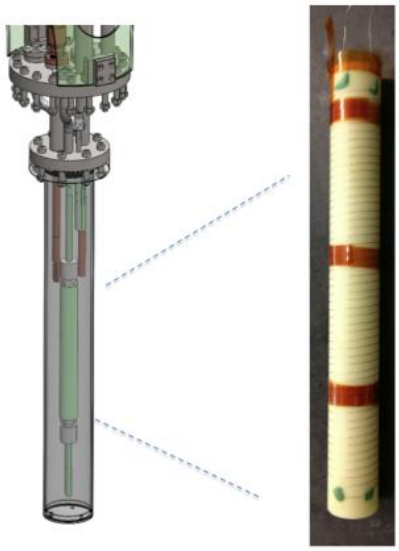

Figure 6.5.59. Calibration Heater Assembly

Subsequently, a test coil assembly consisting of a substrate and an MgB2 coil will be used to start characterizing AC losses in such conductors. Figure 6.5.60 shows the test coil assembly.

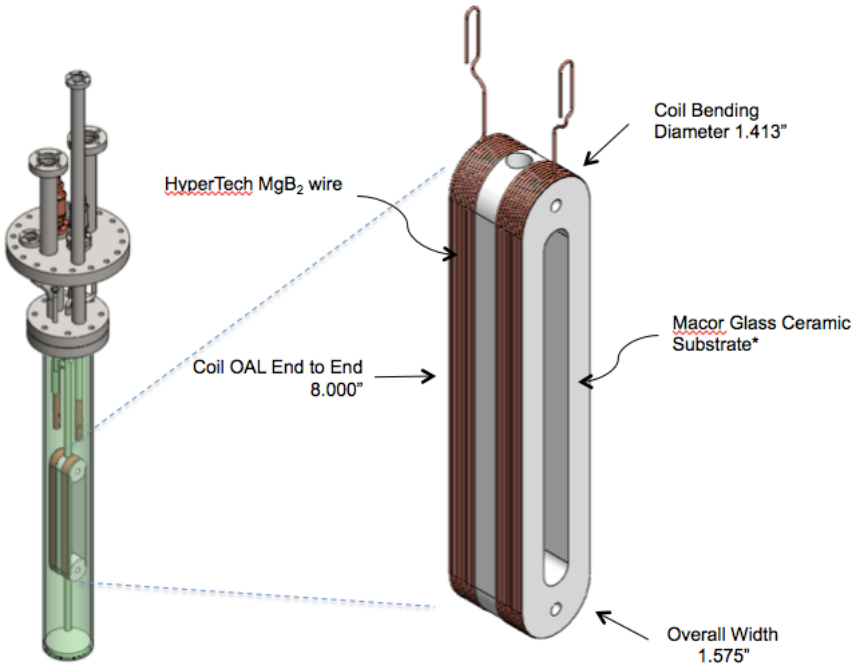

Figure 6.5.60. MgB2 Test Coil Assembly

Cooling System, Manufactured at Creare Inc., Hanover, NH

During the reporting period, the assembly of the cooling system was completed. The final step in this task was to wrap 12 layers of multilayer insulation (MLI) around all components inside the cooling module vacuum space. The insulated components are shown in Figure 6.5.61.

In this period, our work scope was increased to enable us to modify the calibration heater inside the experiment module and to add a temperature sensor to the heater surface. The modifications to the heater are shown in Figure 6.5.62. A further scope increase was also initiated to enable us to repair a leak in one of the cryogenic transfer lines. We successfully repaired this leak after a number of attempts and installed the transfer line onto the experiment module (Figure 6.5.63).

We mounted a dewar (Figure 6.5.64) beside the cooling module and installed the experiment module inside the dewar. We then connected and leak checked the complete system and obtained a satisfactory result, with a vacuum level (at the pump) of 7E-9 Torr in the cooling module and 7E-8 Torr in the experiment module.

At the end of the reporting period, we were preparing for system testing and calibration, which will be described in our next report.

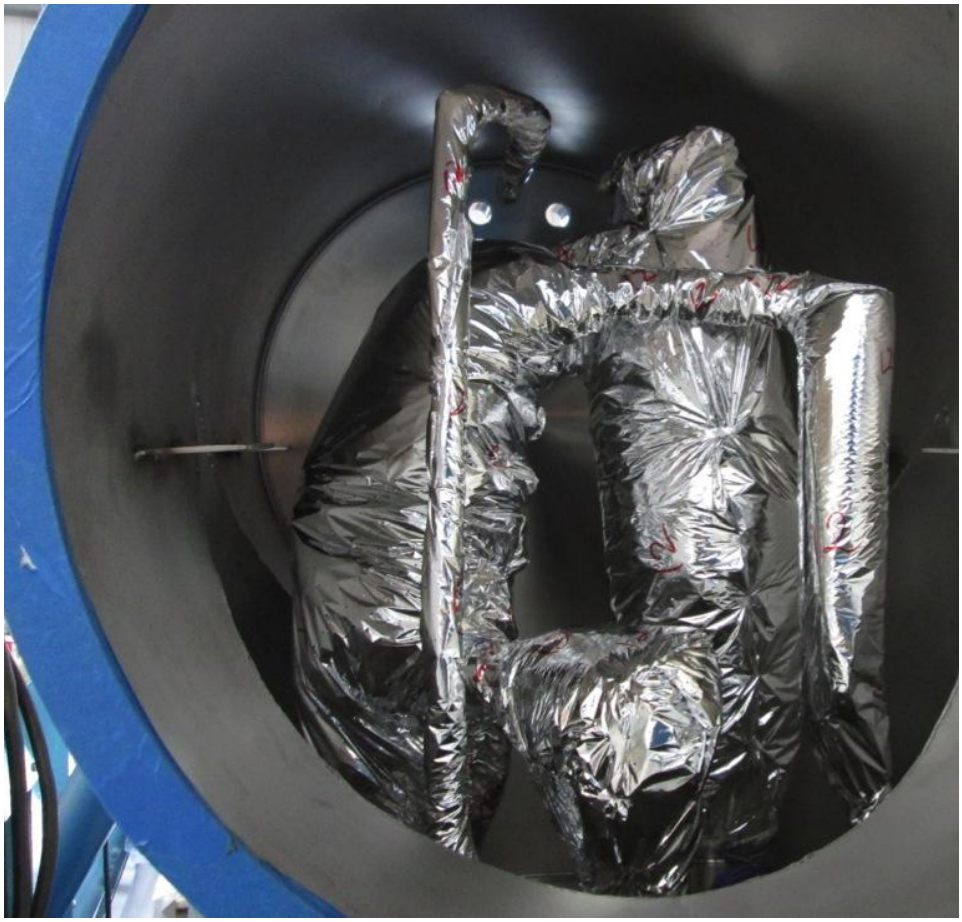

Figure 6.5.61. Cooling Module Insulation. All components inside the cooling module vacuum space are wrapped with 12 layers of multilayer insulation (MLI).

Figure 6.5.62. Calibration Heater Modification. A thin copper sheet was wrapped around the heater wire to ensure a uniform heater surface temperature. A Cernox™ temperature sensor was mounted on the copper surface to measure the heater surface temperature.

Figure 6.5.63. Cryogenic Transfer Line. The transfer line is shown installed on the experiment module.

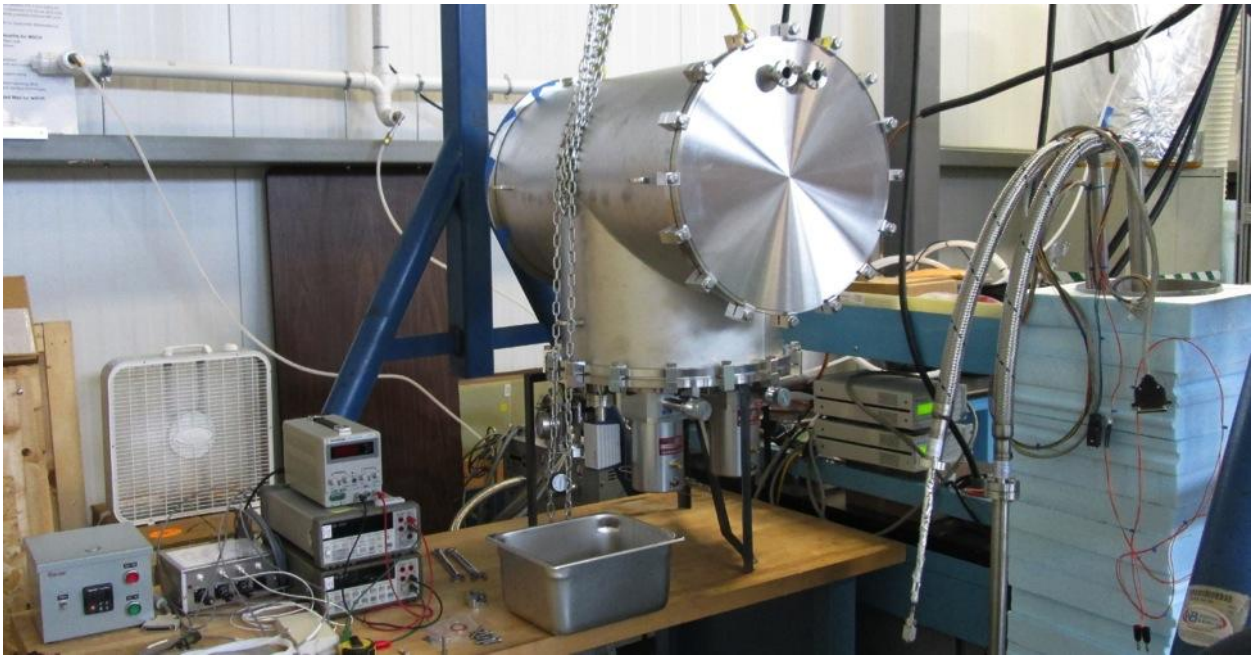

Figure 6.5.64. Test Setup. Cooling module is center; experiment module is on the right where it is installed inside an insulated dewar.

Task 6.5 Status

At the end of the reporting period, we had completed system assembly and were starting to prepare for system testing and calibration. AML is scheduled to visit Creare to perform a buy-off of the cooling system with the Helium and Vacuum cryostats on October 23rd, 2013.

3.2.3.6.7 Report period: October 1, 2013 to December 31, 2013 (Q6)

Overview

A complete overview of the system is provided in paragrahs 3.2.3.6.1 through 3.2.3.6.6.

Task 6.5 Overall Status

System Components

All system components have been manufactured, assembled and integrated. Testing and shakeout has occurred for each of the subsystems and all subsystems have been shipped to CAPS where all testing will take place. CAPS and AML have integrated all subsystems and have performed a preliminary testing of the system in anticipation of MgB2 coil testing. These tests are expected to start in February of 2014.

Task 6.5 Test Reports

The following are test reports produced by Creare and AML for the cooling system and the excitation coil assemblies, reproduced in their respective, original formats.

Creare Cooling Module Test Report #1

1 Introduction

This document describes testing of the Cooling Module developed by Creare for the Advanced Magnet Laboratory per Creare Proposal P-10072/AML P.O. 11481.

2 Objective

The objective of these tests was to characterize the performance of the Cooling Module and to calibrate the cooling load measurement system.

3 System Description

A schematic of the cooling system approach is shown in Figure 1. The cooling module and the experiment module are housed in separate vacuum-insulated cryostats. Helium flow, driven by a Cryozone circulator, is cooled by a pair of AL-325 GM cryocoolers with interface heat exchanges mounted onto each cold head. The flow passes through a vacuum-insulated transfer line to the experimental module, where it cools the test coil. The losses in the test coil are determined from the product of the heat capacity of the gas, the mass flow rate, and the temperature difference between the inlet and outlet flows. The temperature is measured by redundant temperature sensors mounted in the inlet and outlet flow tubes in the experiment. The mass flow rate will be determined from the pressure difference across a calibrated orifice-plate flow meter installed in the cooling module. All cold components and tubing are insulated with multilayer insulation (MLI).

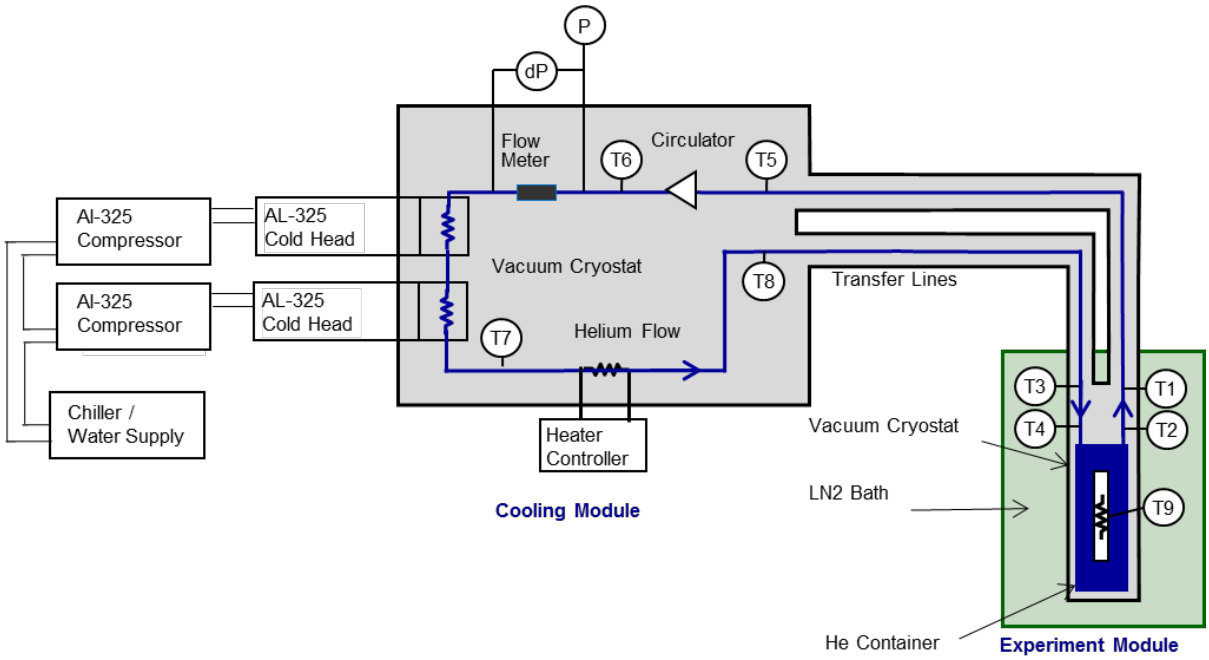

Figure 1. Cooling System Schematic

An instrumentation list for this test is given in Table 1.

Table 1. Instrumentation List

Measurement	ID	Range	Type
Heater Voltage	V	0-30 V	HP 34401A
Heater Current	I	0-3 amps	HP 34401A
Load Inlet	T1	1.4-325 K	CX-1050 SN X90343
Load Inlet	T2	1.4-325 K	CX-1050 SN X90344
Load Exit	T3	1.4-325 K	CX-1050 SN X90345
Load Exit	T4	1.4-325 K	CX-1050 SN X90346
Cooling Module In	T5	1.4-325 K	CX-1050 SN X90347
Flowmeter In	T6	1.4-325 K	CX-1050 SN X90348
Coldhead Exit	T7	1.4-325 K	CX-1050 SN X90349
Cooling Module Exit	T8	1.4-325 K	CX-1050 SN X90350
Heater Surface	T9	1.4-325 K	CX-1050 SN X90353
Flowmeter Inlet P	Pfm	0-100 psia	Sensotec FPA sn 1408980
Circ Delta Pressure	dPfm	0-5 “H2O	Sensotec FDW sn 1409152
Fan Speed	N	0-21 krpm	On-board
Vacuum Level	Pvac	1e-3 to 1e-8	Inficon BPG400

4 System Test Plan

Our system test and calibration procedure was as follows:

1. Evacuate flow loop, fill with helium, evacuate again and then fill with helium to 85 psia.
2. Evacuate both test module and cooling module vacuum spaces. Separate vacuum pumps were connected to each space.
3. Run fan at full speed (21,000 rpm).
4. Turn on both cryocoolers.
5. Top up flow loop as required to maintain 85 psia as system cools.
6. Stabilize at minimum temperature (15 K, mdot approx 0.3 g/s)
7. Take data point when drift rate dT < 10mK/min)
8. Increase heater power in steps, stabilizing and taking data points after each increase (heater resistance is 82.5 Ω).
9. Repeat for reduced fan speed (11,000 rpm).
10. Calculate orifice discharge coefficient, K.

5 Test Results

Total cool down and test time was about 15 hours. Temperatures during cool down and testing are shown in Figure 2. The fan was not started until 75 minutes into the cool down, and there was a 65-minute period when the cryocoolers were shut down. Stable temperatures were reached at about 700 minutes elapsed time. Accounting for the delays, the total cool down time was approximately nine hours.

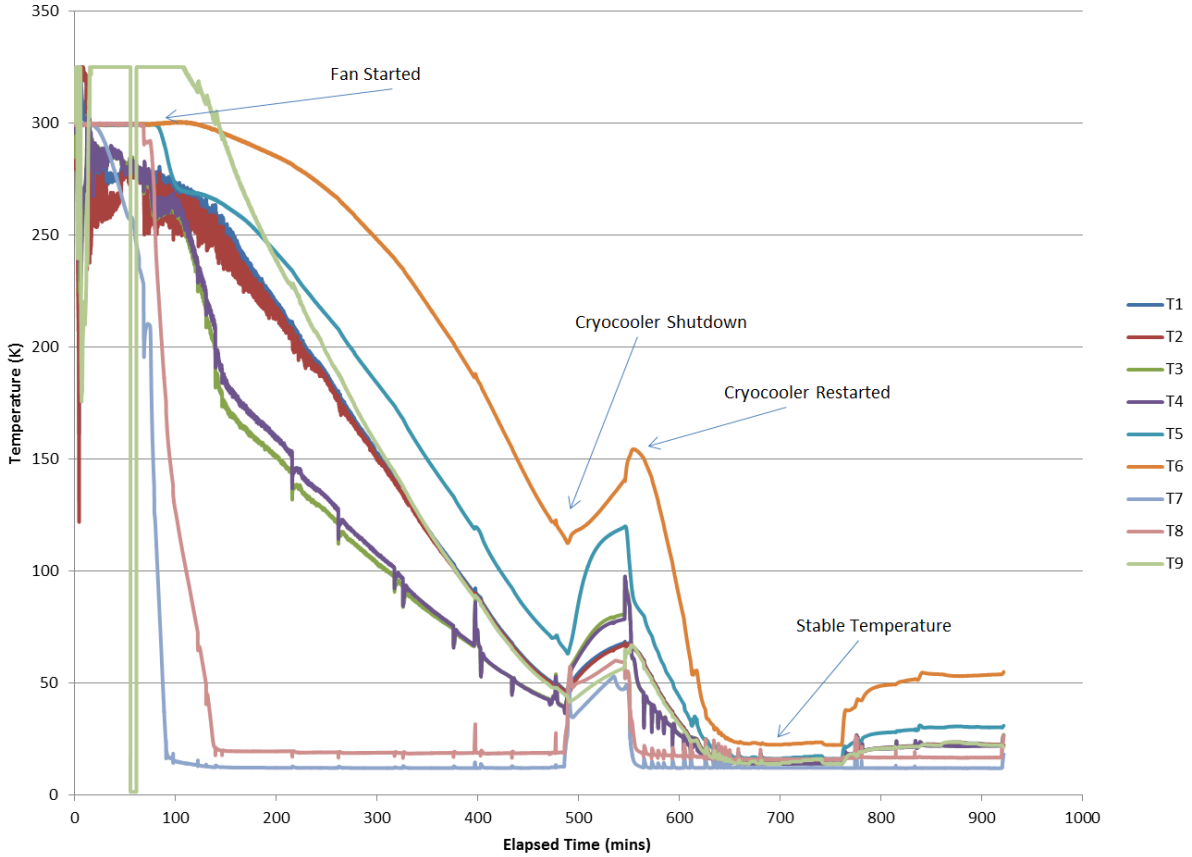

Figure 2. System Cool Down.

At maximum fan speed the system stabilized at 14 K. We increased the heat power in steps up to 2 W and stabilized at each intermediate heater power setting. The system took about 10 minutes to stabilize, with the drift rate in the temperature difference between the experiment inlet and outlet flows less than 10 mK/min by the end of the 10 minute period. Flow temperatures are plotted in Figure 3. The flow rate is determined from the input power to the heater, the temperature difference between the experiment inlet and outlet flows, and the flow heat capacity according to Equation 1.

$$q = \dot{m}Cp(\Delta T) \quad (1)$$

We calculated a mass flow value of 0.3 g/s for the max fan speed condition, with a parasitic heat load into the experiment of 0.19 W with no heater power. Unfortunately, we undersized the orifice for this flow rate and the differential pressure transducer we selected was out of range at this fan speed.

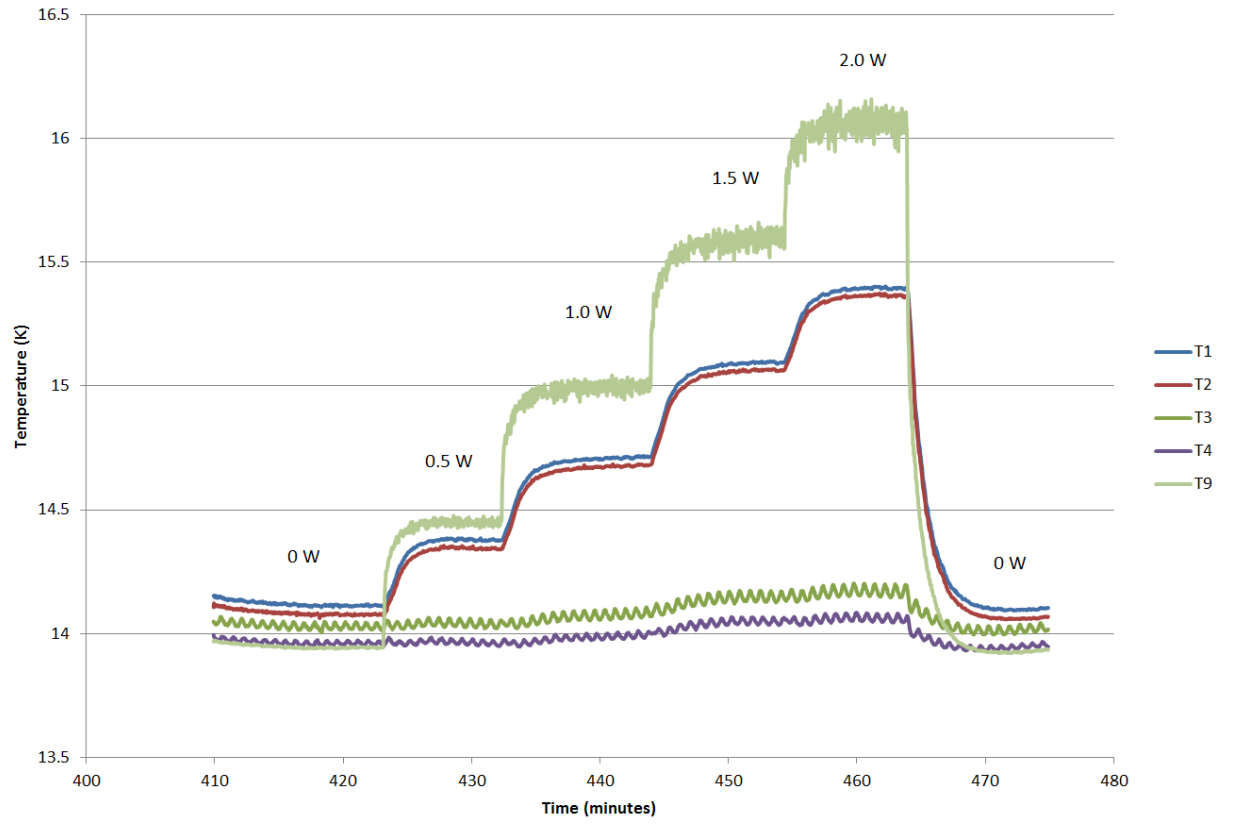

Figure 3. System Calibration at Maximum Fan Speed (21000 rpm)

To calibrate the orifice plate we ran the fan at half speed. The temperatures recorded during this test are plotted in Figure 4. The flow rate in this condition was 0.07 g/s and the parasitic heat load into the experiment was 0.18 W, which confirmed our previous value. At this flow rate, the temperature of the flow entering the experiment module was approximately 22 K. The pressure drop across the orifice plate flow meter was 3.61 "H2O. We determined a discharge coefficient for the orifice plate of 0.722 according to Equation 2.

$$\dot{m} = \frac{\pi d^2}{4} K \sqrt{2\rho \Delta P} \qquad (2)$$

Where d is the orifice plate diameter of 875 micron. This discharge coefficient may now be used to estimate the mass flow rate from the orifice plate differential pressure reading. At the maximum mass flow rate of 0.3 g/s, the differential pressure will be 47 "H2O. Hence, to operate at this flow rate with the current orifice meter a pressure transducer with a range of at least 50" H2O will be needed.

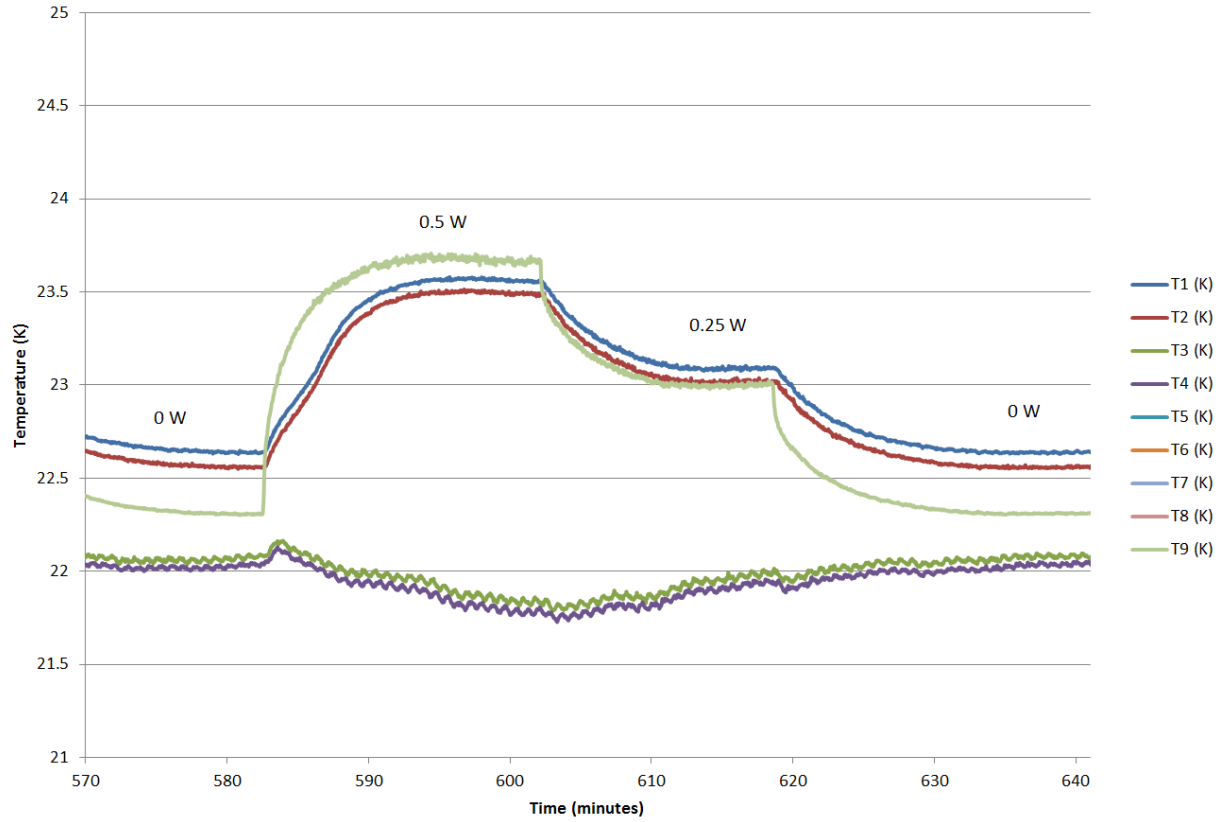

Figure 4. System Calibration at Half Fan Speed (11,000 rpm)

6 Conclusions and Recommendations

We have tested and calibrated the Cooling Module. Our tests demonstrated that the Cooling Module can supply a stable flow of cryogenic helium with a cooling capacity of 1 W at 15 K. The temperature rise in the cooling flow through the experiment was approximately 0.7 K and the temperature difference between the sample and the flow exiting the module was approximately 0.3 K. The discharge coefficient of the orifice plate flow meter was 0.72.

The current differential pressure transducer with a range of 5" H2O will need to be replaced with a transducer with a range of at least 50" H2O in order to operate the system at maximum flow rate with the current orifice plate. Alternatively, a larger diameter orifice plate may be installed. We recommend this alternative as a larger size orifice plate will reduce the flow restriction, enabling a higher mass flow at maximum fan speed, which will reduce the system cool down.

Creare Cooling Module Test Report #2

1 Introduction

This document describes follow-on testing of the Cooling Module developed by Creare for the Advanced Magnet Laboratory per Creare Proposal P-10072/AML P.O. 11481.

2 Objective

The objective of these tests was to characterize the performance of the Cooling Module and to calibrate the cooling load measurement system after revisions to the system.

3 System Description

A schematic of the cooling system approach is shown in Figure 1. The cooling module and the experiment module are housed in separate vacuum-insulated cryostats. Helium flow, driven by a Cryozone circulator, is cooled by a pair of AL-325 GM cryocoolers with interface heat exchanges mounted onto each cold head. The flow passes through a vacuum-insulated transfer line to the experimental module, where it cools the test coil. The losses in the test coil are determined from the product of the heat capacity of the gas, the mass flow rate, and the temperature difference between the inlet and outlet flows. The temperature is measured by redundant temperature sensors mounted in the inlet and outlet flow tubes in the experiment. The mass flow rate will be determined from the pressure difference across a calibrated orifice-plate flow meter installed in the cooling module. All cold components and tubing are insulated with multilayer insulation (MLI).

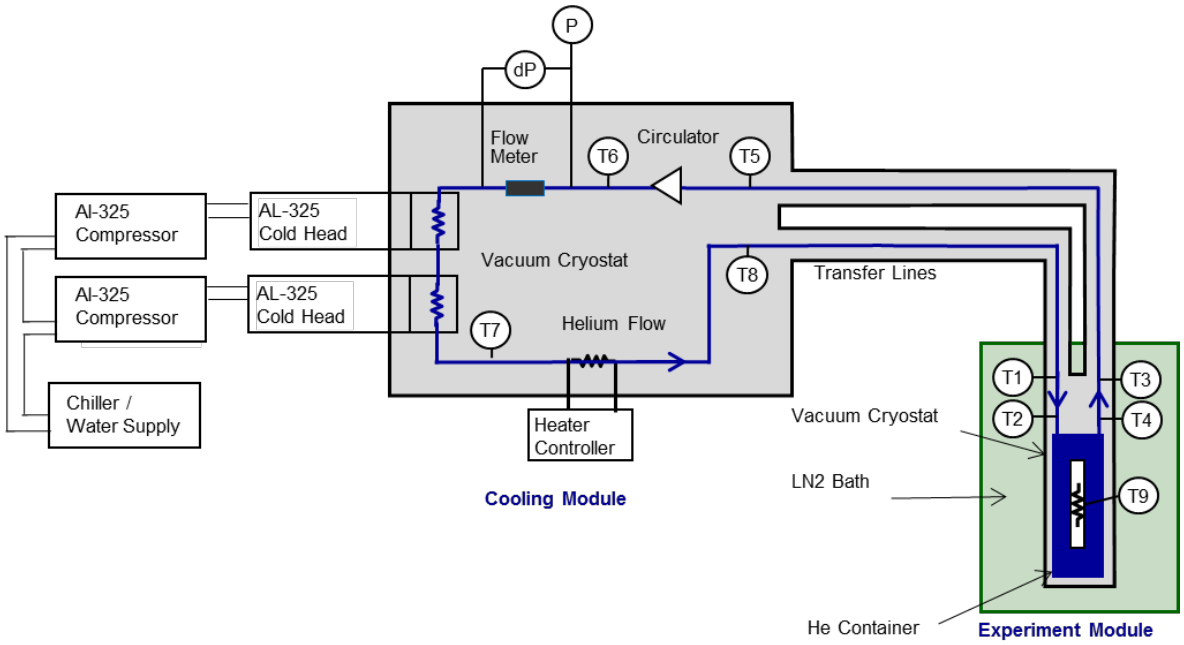

Figure 1. Cooling System Schematic

An instrumentation list for this test is given in Table 1.

Table 1. Super FSG Instrumentation List

ID	Measurement	Range	Type
V	Heater Voltage	0-30 V	HP 34401A
I	Heater Current	0-3 amps	HP 34401A
T1	Load Inlet	1.4-325 K	CX-1050 SN X90343
T2	Load Inlet	1.4-325 K	CX-1050 SN X90344
T3	Load Exit	1.4-325 K	CX-1050 SN X90345
T4	Load Exit	1.4-325 K	CX-1050 SN X90346
T5	Cooling Module In	1.4-325 K	CX-1050 SN X90347
T6	Flowmeter Inlet	1.4-325 K	CX-1050 SN X90348
T7	Coldhead Exit	1.4-325 K	CX-1050 SN X90349
T8	Cooling Module Exit	1.4-325 K	CX-1050 SN X90350
T9	Heater Surface	1.4-325 K	CX-1050 SN X90353
Pfm	Flowmeter Inlet P	0-100 psia	Sensotec FPA sn 1408980
dPfm	Circ Delta Pressure	0-5 “H2O	Sensotec FDW sn 1409152
N	Fan Speed	0-30 krpm	On-board
Pvac	Vacuum Level	1e-3 to 1e-8	Inficon BPG400

4 System Revisions

Two key revisions were made to the system following the last test. The diameter of the flow meter tubing was increased from 1/8" tube with 35-mil walls and an internal diameter of 0.18" to ¼" tube with 28-mil walls and an internal diameter of 0.194", and the orifice diameter was increased from 875 micron to 1778 micron. The second revision we made was to swap the inlet and outlet lines into the experiment. These were initially connected so that the inlet line was the short tube leading into the experiment module and the outlet line was the long tube that ran through the center of the heater. The long tube is now the inlet line, and the short tube is the outlet. This configuration is shown in Figure 1.

5 System Test Plan

Our system test and calibration procedure was as follows:

1. Evacuate flow loop, fill with helium, evacuate again and then fill with helium to 85 psia.
2. Evacuate both test module and cooling module vacuum spaces. Separate vacuum pumps were connected to each space.
3. Run fan at full speed (21,000 rpm).
4. Turn on both cryocoolers.
5. Top up flow loop as required to maintain 85 psia as system cools.
6. Stabilize at minimum temperature
7. Reduce fan speed till flow meter pressure transducer is within range (7,000 rpm)
8. Take data point when drift rate dT < 10mK/min)
9. Increase heater power in steps, stabilizing and taking data points after each increase (heater resistance is 82.5 Ω).
10. Repeat for reduced fan speed (5,000 rpm).
11. Calculate orifice discharge coefficient, K.

6 Test Results

System temperatures during cool down are plotted in Figure 2. The time to reach a stable temperature below 15 K was three hours. This is a considerable improvement over the nine hours required for cool down before we modified the system to open up the flow meter.

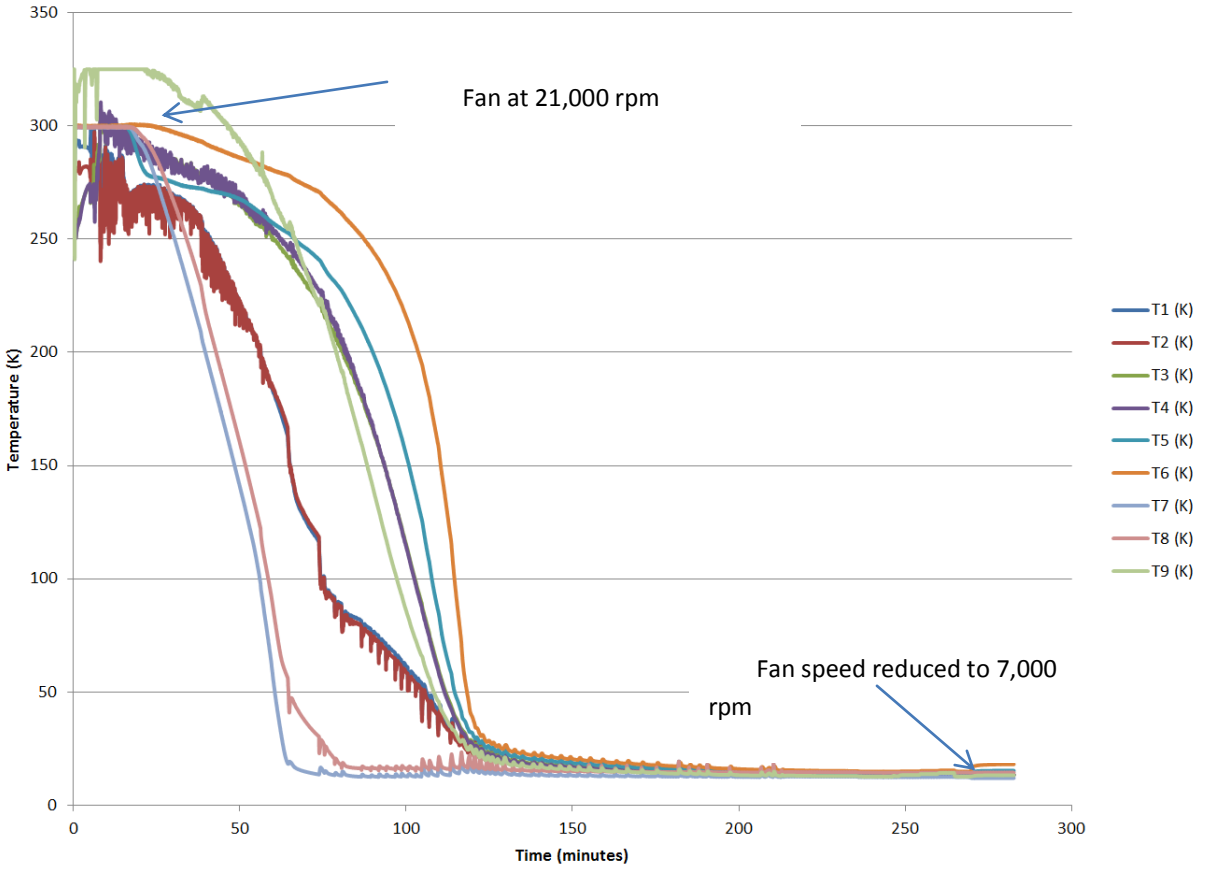

Figure 2. System Cool Down.

At maximum fan speed the experiment stabilized at approximately 13.5 K. We decreased the fan speed to reduce the flow rate until the pressure drop across the flow meter orifice was with the pressure transducer's full scale range. This occurred at a fan speed of 7,000 rpm. We then increased the heater power to 0.5 W and then 1 W and waited for the temperatures to stabilize at each heater power setting. The system took about 1.5 minutes to stabilize, with the drift rate in the temperature difference between the experiment inlet and outlet flows less than 10 mK/min by the end of this period. Temperatures in the experiment module are plotted in Figure 3. The temperature difference across the experiment (dT) is referenced to the secondary vertical axis. The temperature rise across the experiment was approximately 0.2 K for each 0.5 W increase in heater power.

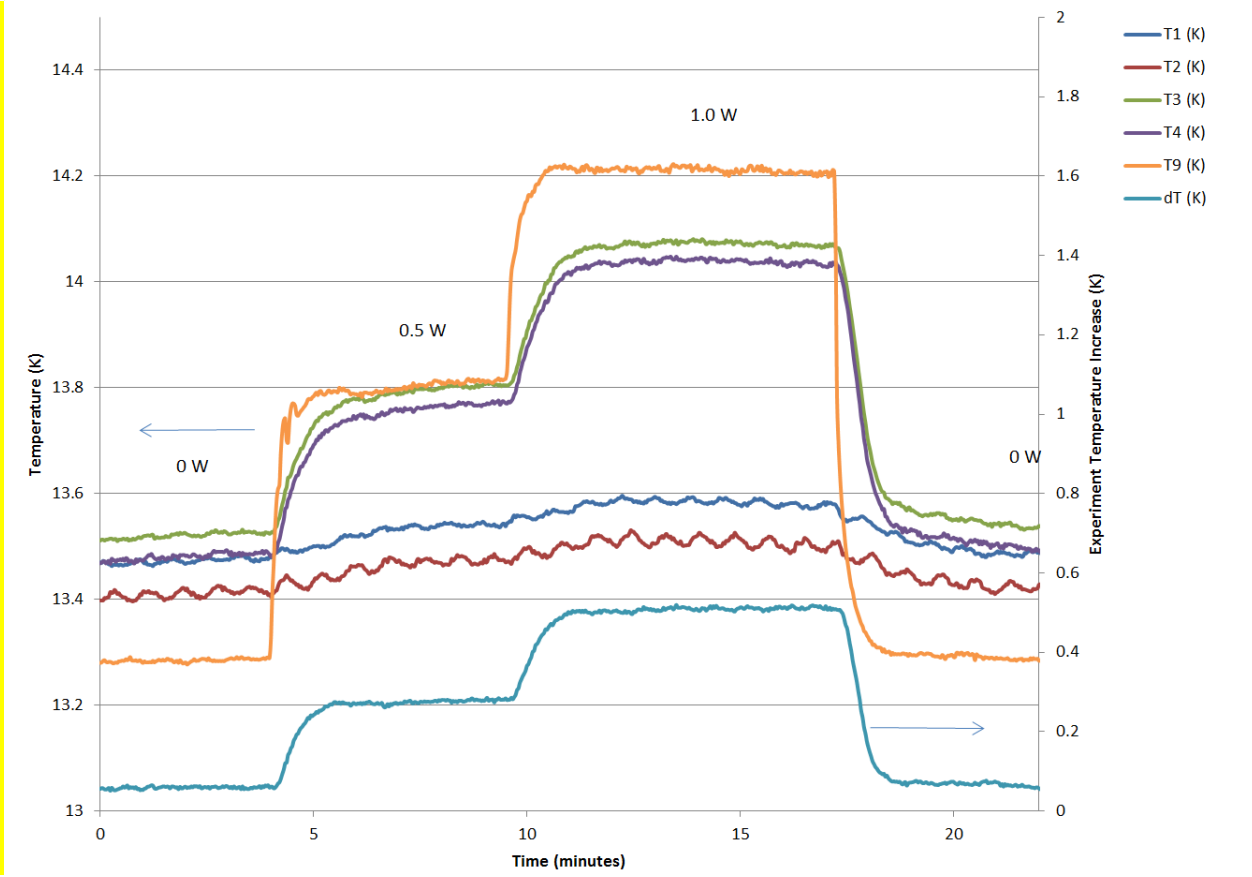

Figure 3. System Calibration at Fan Speed of 7,000 rpm. Experiment temperatures are referred to the primary vertical axis, and the temperature difference across the experiment (dT) is referred to the secondary axis.

We repeated this exercise at a reduced fan speed of 5,000 rpm (Figure 4). The temperature rise across the experiment at this flow rate was approximately 0.5 K.

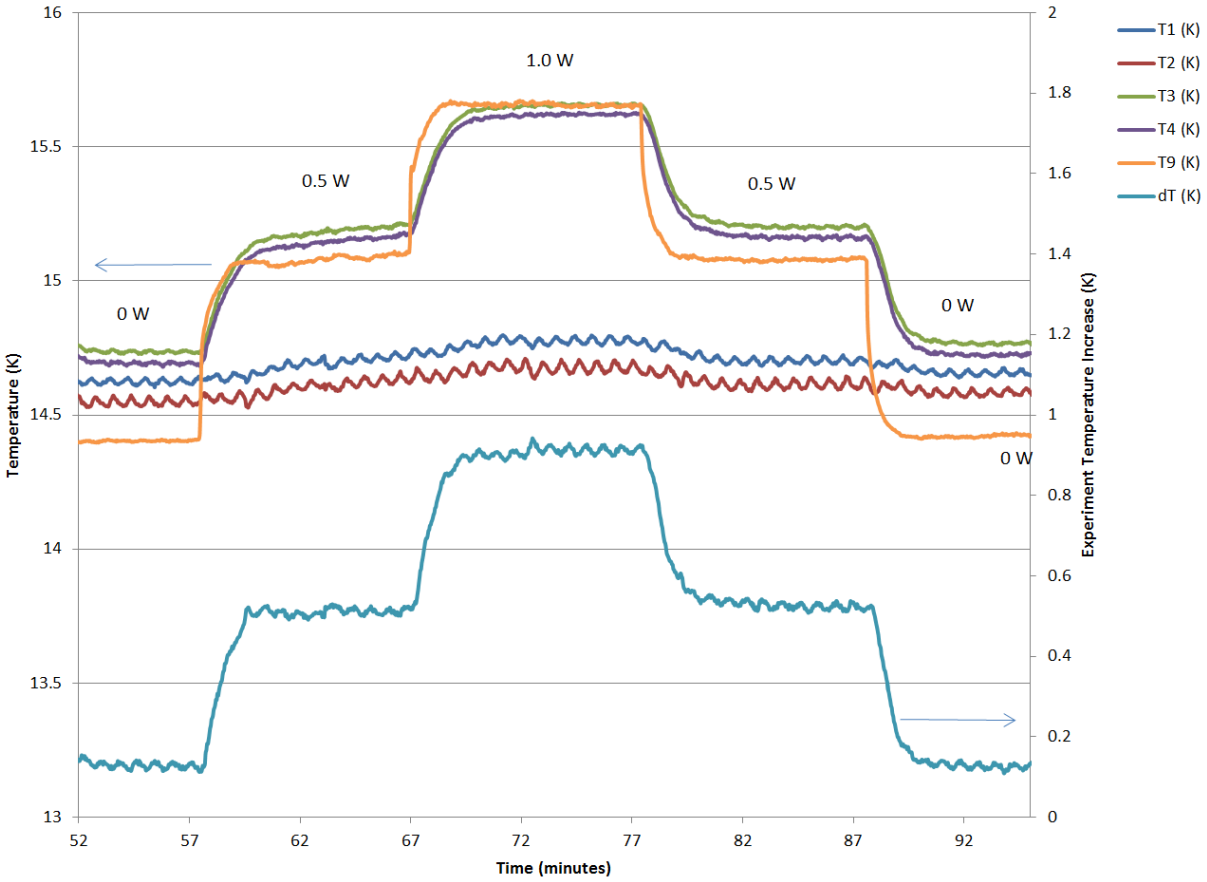

Figure 4. System Calibration at Reduced Fan Speed 5,000 rpm)

The flow rate through the experiment was determined from the input power to the heater, the temperature difference between the experiment inlet and outlet flows, and the flow heat capacity according to Equation 1.

$$\dot{m} = \frac{q}{Cp\Delta T} \quad (1)$$

where q is the heat input into the experiment, Cp is the heat capacity of the gas and ΔT is the temperature difference between the outlet and inlet streams. The flow rate measured by the flow meter is calculated according to Equation 2.

$$\dot{m} = K\left(\frac{\pi d^2}{4}\right)\sqrt{2\rho\Delta P} \quad (2)$$

where ΔP is the pressure drop across the flow meter orifice, ρ is the flow density upstream of the orifice, d is the diameter of the orifice (1778 micron) and K is the flow meter flow coefficient. Combining these two equations gives the relation between the heat input into the experiment and the measured pressure drop across the flow meter as shown in Equation 3.

$$q_c = KCp\Delta T\left(\frac{\pi d^2}{4}\right)\sqrt{2\rho\Delta P} - q_0 \qquad (3)$$

Where q_c is the power to the calibration heater in the experiment module and q_0 is the parasitic heat into the experiment module. The discharge coefficient may be determined from this relation, as shown in Figure 5. The flow coefficient, K, estimated from these data is 0.8 and the parasitic heat estimate is 0.16 W. The discharge coefficient, C, given by Equation 4, was 0.793.

$$C = K\sqrt{1-\beta^4} \qquad (4)$$

where β (0.36) is the ratio of the orifice diameter, d (0.070”), to the upstream line diameter, D (0.194”).

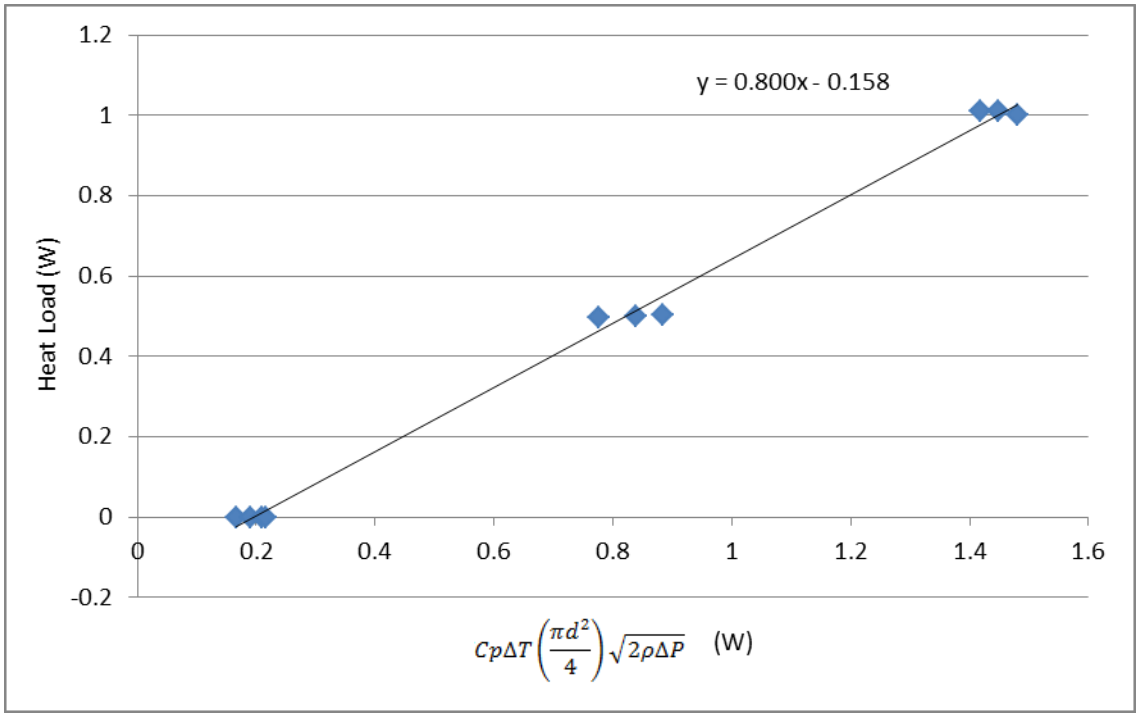

Figure 5. Flow Meter Calibration Regression

7 Conclusions

We have tested and calibrated the Cooling Module. Our tests demonstrated that the Cooling Module can supply a stable flow of cryogenic helium with a cooling capacity of 1 W at 15 K. The temperature rise in the cooling flow through the experiment was approximately 0.4 K at this heater power rand the temperature difference between the sample and the flow exiting the module was approximately 0.2 K. The calibrated value for the flow coefficient of the orifice plate flow meter was 0.8.

AML Excitation Field Coils Test Report

The excitation field coils were tested on 11/22/13 at AML prior to shipment to CAPS. These tests were performed in a liquid Nitrogen bath. The backiron was not used during the tests. Given the resistance of each sub-coil and the available power supplies at AML, our measurements were limited below the full capability of the coils. All tests are performed at DC.

The following is a summary of the tests performed:

1. Resistance at 77 K

The resistance of each sub-coil was measured and recorded after the coil has been submerged in LN2.

Coil Set	Measured Resistance (Ohm) (@ 298 K) (manufacturing check, 10/13)	Predicted Resistance (Ohm) (@ 77 K)[1]		Measured Resistance (Ohm) (@ 298 K) on 11/21/13 (after assembly)	Measured Inductance (mH) (@ 298 K) on 11/21/13 (after assembly)	Measured Resistance (Ohm) (@ 77 K) 0n 11/22/13	Ratio of room temperature and 77K values
1&2	2.80	0.35		2.78	2.25	0.305	9.11
3&4	3.34	0.43		3.34	3.10	0.336	9.94
5&6	3.72	0.48		3.72	3.69	0.435	8.55
7&8	4.23	0.54		4.23	4.61	0.508	8.32
All		1.80					

[1]Resistivity at 293 K for copper: 1.678 nOhm m

Resistivity at 80 K for copper: 0.215 nOhm m

1

Figure 1: Excitation Coils submerged in Liquid Nitrogen

2. Individual coil pair power-up

Each coil pair was powered up individually. This gives us the ability reach the highest possible current capable with the power supply.

Measurement#	Voltage/Current	Coil 1&2	Coil 3&4	Coil 5&6	Coil 7&8
1	Voltage			4.83	5.56
	Current			10.6	10.41
2	Voltage		12.62	14.05	16.01
	Current		30.20	30.3	30.21
3	Voltage			19.00	21.70
	Current			40.67	40.68
4	Voltage		21.64	24.04	27.54
	Current	50	51.20	51.21	51.14
	Calculated Resistance		0.420	0.466	0.535

3. Series configuration power-up

The coils were connected in series and powered up as one unit. Given the maximum voltage of the power supply of 60 Volts we can reach a maximum current of approximately 33 Amps.

Test#	Voltage/Current	Coils
1	Voltage (V)	44.07
	Current (A)	25.12
2	Voltage (V)	60.4
	Current (A)	34.29

The calculated resistance at 77 K, based on the measured data, is approximately 1.76 Ohms.

4. Magnetic field Measurement

At a known coil current, the magnetic field inside the coil bore was measured.

Figure 2 A GMW Associates Hall probe is used to measure the magnetic field. A warm bore was inserted into the coil assembly for the hall probe.

At a known coil current, the magnetic field inside the coil bore was measured. The field measurements were taken for individual coil pairs as well as with all coils connected in series. A GMW Associates Hall probe was rotated within the bore until the maximum field was observed.

Coils	Voltage (Volts)	Current (Amps)	Max Bore Field (mTesla)
1&2	8.75	25.11	0.020
3&4	10.47	25.08	0.021
5&6	11.67	25.11	0.020
7&8	13.25	25.08	0.020
All	44.07	25.12	0.082

The measurements confirm that the total field equals the sum of the fields for the individual coils. Note that these fields were produced without the backiron in place.

3.2.3.6.8 Report period: January 1, 2014 to March 31, 2014 (Q7)

Introduction/Overview

A complete overview of the system is provided in paragraphs 3.2.3.6.1 through 3.2.3.6.7.

Task 6.5 Overall Status

The complete system has been installed at CAPS and integrated into their existing system of AC power supplies and measuring equipment. The installation is shown in Figure 6.5.65.

Figure 6.5.65. AC Loss Measurement Installation at CAPS

The cryogenic calibration tests originally performed at Creare have been successfully repeated at CAPS using a LabView program. For the test at CAPS, the background field magnet with its iron yoke manufactured at AML was installed.

Some electrical noise observed in the temperature measurement system has been eliminated with better twisting of the lead wires.

The background field magnet developed at AML consists of 8 individual layers. Originally, all 8 layers were installed in the system with the same orientation to achieve the highest possible background field (~.5 Tesla).

The orientation of the coils has been rearranged in such a way that 4 layers are rotated by 90 degrees relative to the other 4 layers. This modification has the advantage that not only a pulsating

field can be generated, but also a rotating field by powering the two coil sets with separate power supplies and a 90-degree phase shift of the AC currents.

With the help of a special pick-up coil (Figure 6.5.66), built at AML, it has been confirmed that a rotating field can actually be generated. It was also confirmed that the mutual inductance between the two sets of background field coils is insignificant small, so that the coils can be exited without interference.

Figure 6.5.66. Support structure for pick-up coil for measurements of rotating magnetic field

A significant boil-off from the LN2 is observed during operation of the background field coils, which limits the maximum current and field level that is currently achievable. The AC loss measurement system is installed at CAPS in a lab area with limited ventilation, which augments the problem.

A solenoidal MgB_2 test coil (Figure 6.5.67) has been built and is mounted in the AC loss measurement system for initial tests of AC loss measurements. The coil has been built with the wind-and-react technology, using a wire with 0.85-mm diameter from HyperTech. The unreacted wire is placed in a machined groove in a Macor ceramic cylinder, and the whole assembly is then heat treated. The required heat treatment (~900 C) was performed at HyperTech.

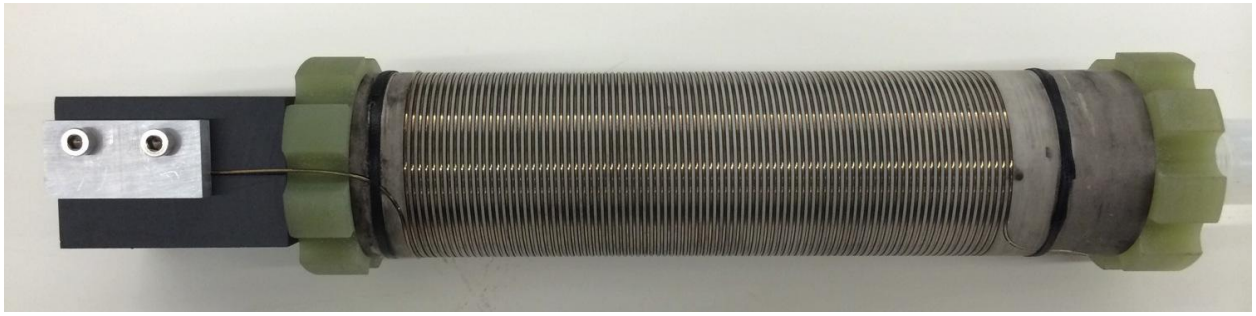

Figure 6.5.67. Solenoidal MgB2 test coil for initial tests of AC loss measurement system

Two coils are currently being built at AML for actual measurements of AC losses. One coil has a racetrack configuration (Figure 6.5.68). This coil will be built with a HyperTech conductor of the same diameter as the solenoid coil, using a Macor ceramic support structure and using the wind-and-react technology.

The second coil configuration consists of a bundle of individual, straight conductors without any electrical interconnection (Figure 6.5.70). These coils are being built by Columbus conductor with various numbers of filaments (see Part I, section 3.2.3.2). For the unconnected wires, no transport current can be injected, but the losses in the superconductor for various background field levels and frequencies can be determined.

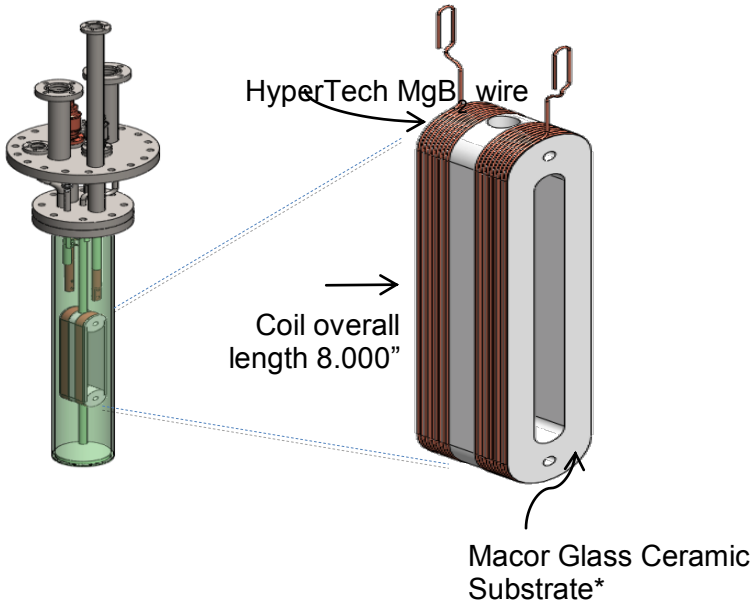

Figure 6.5.68. MgB_2 Racetrack Coil for AC loss measurements with installation

Figure 6.5.69. in the AC loss measurement test chamber

Figure 6.5.70. Bundle of MgB2 wires

3.2.3.6.9 Report period: April 1, 2014 to June 30, 2014 (Q8)

The AC loss measurement system, built by AML and Creare, has been installed at the Center for Advanced Power Systems (CAPS), integrated with their power electronics and data acquisition, has been calibrated, and is now fully functional. The complete system performance meets specifications.

A first test coil wound with MgB_2 superconducting from Hypertech wire has been built and its AC losses at different frequencies and flux densities of the background field have been measured and compared with model calculations performed by the University of Houston. A second test sample for straight wire samples has been built and tests of magnetization losses at different flux densities and frequencies have been started. A racetrack coil, which best matches the conductor orientation that is present in a synchronous machine is under construction by AML and Hypertech and will be ready for AC loss measurements within the next few weeks.

AC Loss Measurement Test Setup

A schematic diagram of the AC loss measurement system is shown in Figure 6.5.71. The test sample for AC loss measurements is inserted in a test chamber and cooled with gaseous helium from a cooling system to temperatures down to 15 K. Only the helium inlet and outlet lines are shown in the diagram. AC losses of the test sample are determined by a calorimetric measurement by measuring the inlet and outlet temperature of the helium gas and the helium flow rate. The test sample is housed inside of a background field magnet, which is excited by an AC current. The frequency of the current is defined by a signal generator, the required operational current for the field coil is produced by a high power Techron amplifier. The background field coil is normal conducting and cooled with LN2. The sample coil can be driven with an AC current, also generated by a signal generator and amplified by another power amplifier. The phase difference between the magnet excitation and the sample coil excitation can be adjusted and controlled. The maximum flux density of the background field magnet is currently limited by the boil-off rate from the LN2 cooling of the magnet coil.

The complete system installed at CAPS is shown in Figure 6.5.72. The T-shaped SS container shown on the left-hand side contains the cooling system developed and built by Creare. The large LN2 cryostat in the center contains the background field magnet with the test sample on its inside. The helium cryostat housing the test sample showed some leaks after the initial installation, which have been repaired at AML and the module has been re-installed at CAPS. The design of this test chamber has been improved to prevent leaks, and the system is fully functional.

Figure 6.5.73 shows a screen shot of the LabView control system that is used for performing the AC loss measurements. All readings of the temperature and pressure measurements are displayed on the graphical user interface.

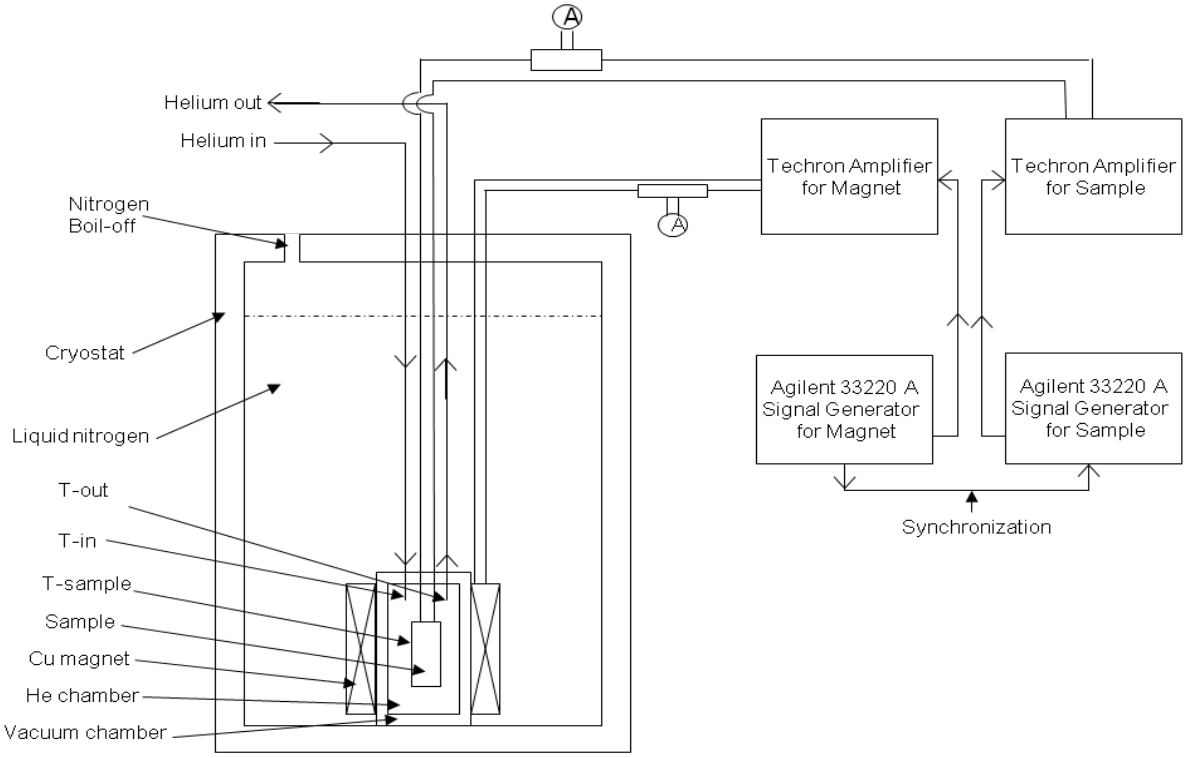

Figure 6.5.71. Schematic Layout of AC loss measurement system

Figure 6.5.74 shows the system during operation. A significant boil-off from the LN2 cryostat is clearly visible. The LN2 boil-off is currently limiting the maximum flux density of the background field to about 200 mT, although the background field magnet with its surrounding iron yoke is capable of producing a flux density of about 0.5 T.

The MgB_2 sample coils for AC loss measurements have to be built with a wind-and-react manufacturing process to accommodate the required small bending radii for coils that fit into the test chamber. A ceramic coil support structure is therefore needed to sustain the reaction temperature of the MgB_2 conductor of close to 700 C. AML developed support structures based on machinableMacor ceramic. The coil support structure is machined at AML,Hypertech is placing the MgB_2 conductor and performing the required heat treatment. The design of a solenoidal coil with the sample holder is shown in Figure 6.5.75. The actual manufactured coil is presented in Figure 6.5.76.

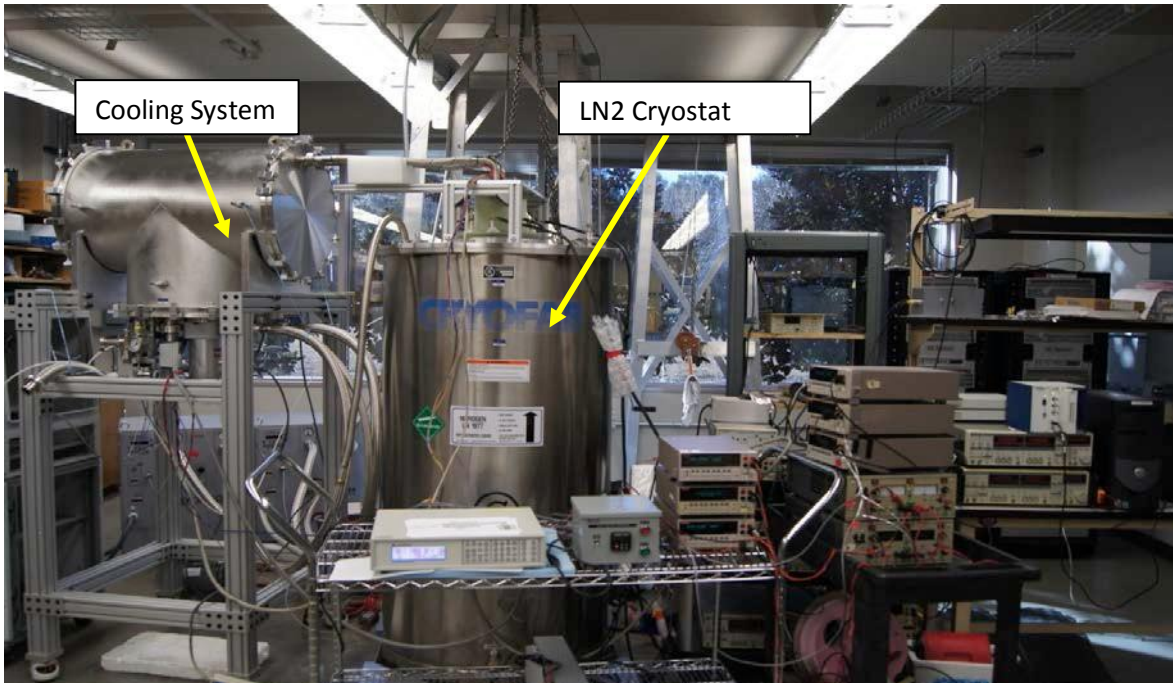

Figure 6.5.72. Complete AC Loss measurement system installed at the Center for Advanced Power Systems (CAPS) in Tallahassee, Florida

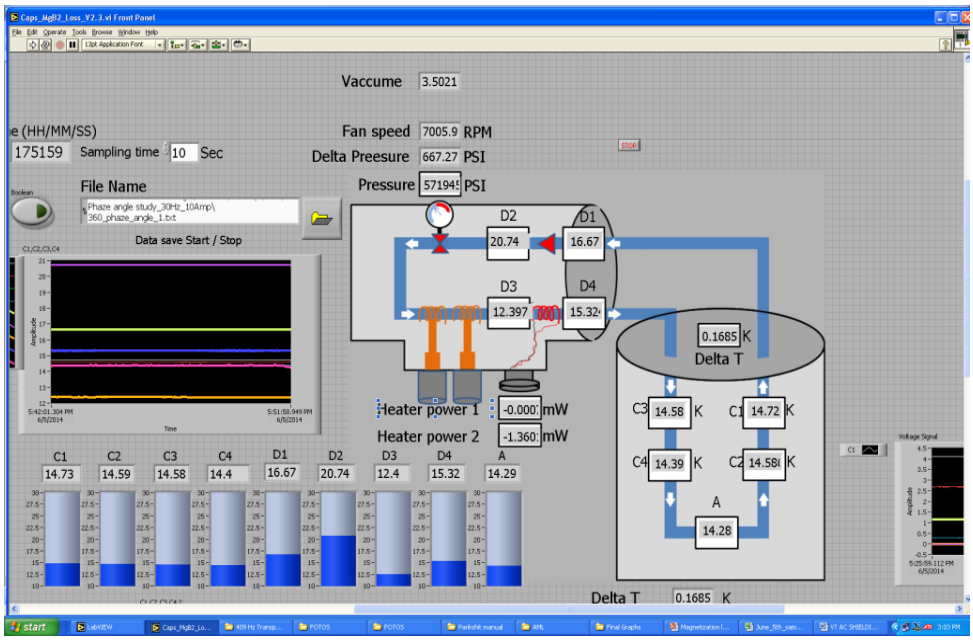

Figure 6.5.73. Screen Shot of LabView Control System

Figure 6.5.74. Operation of AC loss measurement system with LN2 boil-off

Figure 6.5.77 shows the solenoidal test coil ready for the installation in the test chamber. A resistive heater made with Nichrome wire has been added to the coil for calibration purposes. Based on the measured resistance of the heater, its heat load generated for a given excitation current is precisely known and can be used for a calibration of the calorimetric measurement procedure of the system. The calibration curve obtained with the help of the resistor is presented in Figure 6.5.78.

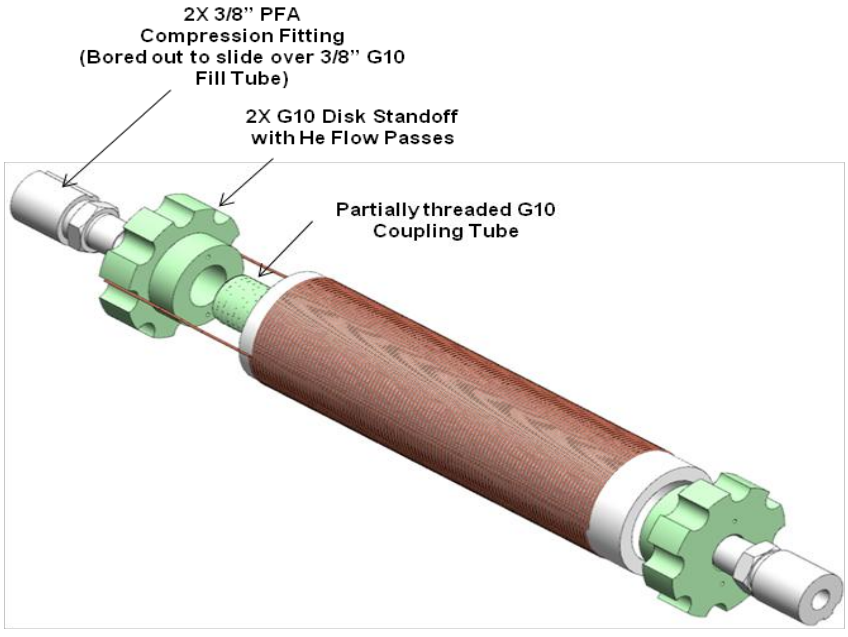

Figure 6.5.75. Design of sample holder for test coils

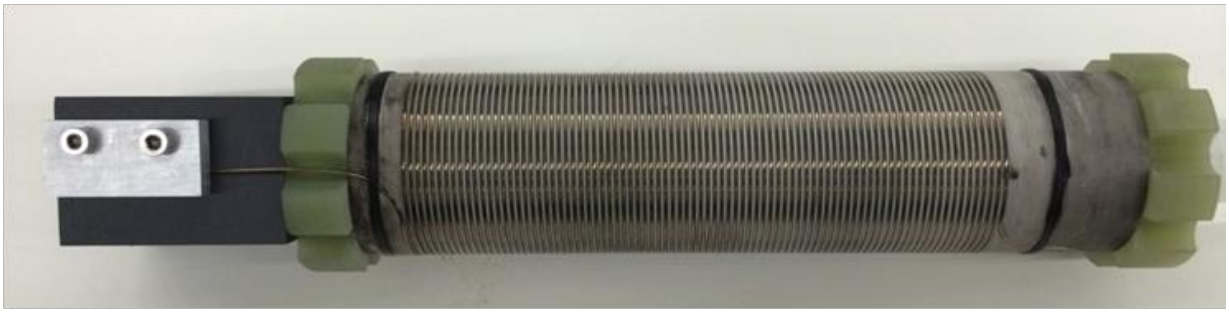

Figure 6.5.76. MgB_2 Test Coil

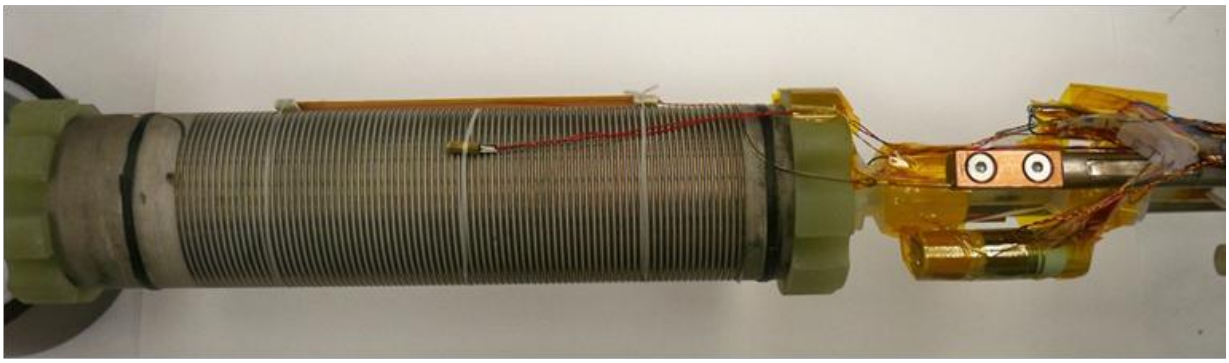

Figure 6.5.77. MgB_2 Solenoidal Test Coil ready for installation into the test chamber

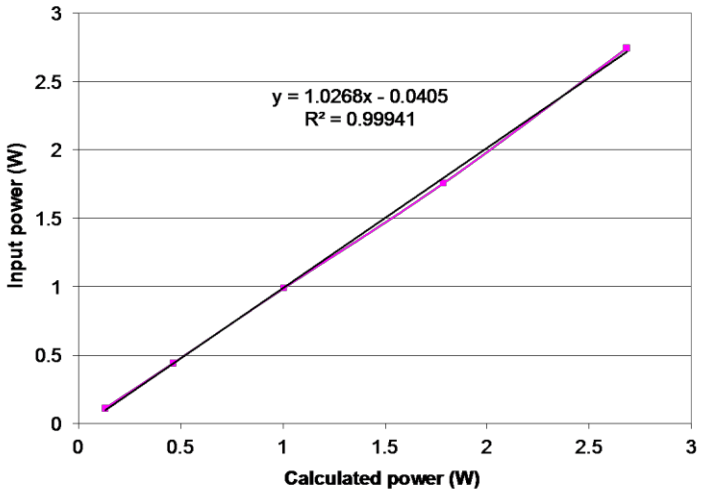

Figure 6.5.78. Calibration curve obtained with resistive heater

The temperature measurement of a typical AC loss measurement is shown in Figure 6.5.79. As can be seen, the Delta-T temperature increase caused by the energy deposition due to AC losses in the MgB2 conductor reaches a plateau in less than 10 minutes. The recovery after the background field has been turned off, the losses are removed and the operational temperature returns to its original value is even significantly faster and takes only about 5 minutes.

A resistance measurement of the MgB2 coil, presented in Figure 6.5.80, shows that the coil is superconducting. As can be seen in this figure, the resistance is practically zero and, as expected, near 39 K, a transition into the normal conducting state occurs.

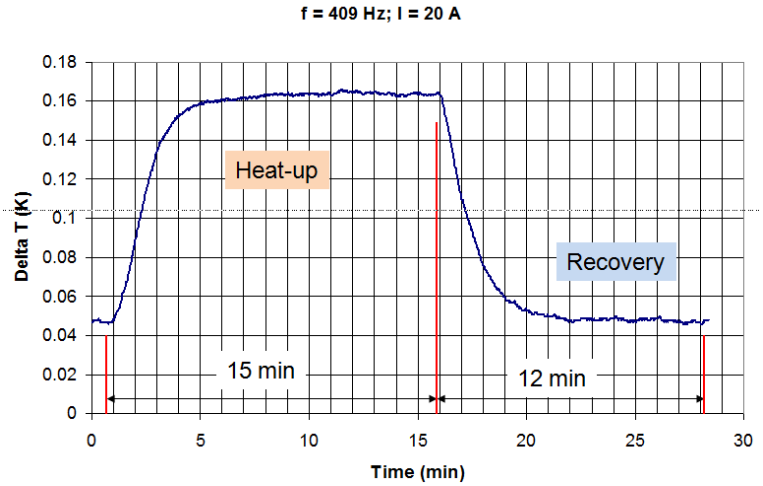

Figure 6.5.79. Typical heat load measurement showing heat-up and recovery

An actual measurement of the AC losses of the test coil is shown in Figure 6.5.80. The scale on the left side of the graph shows the measured increase in temperature Delta-T for the black curve. The actual temperature of the sample is shown by the purple curve with the corresponding scale on the right hand side. The fluctuations seen by this sensor are due to electrical noise, probably introduced by the background field excitation.

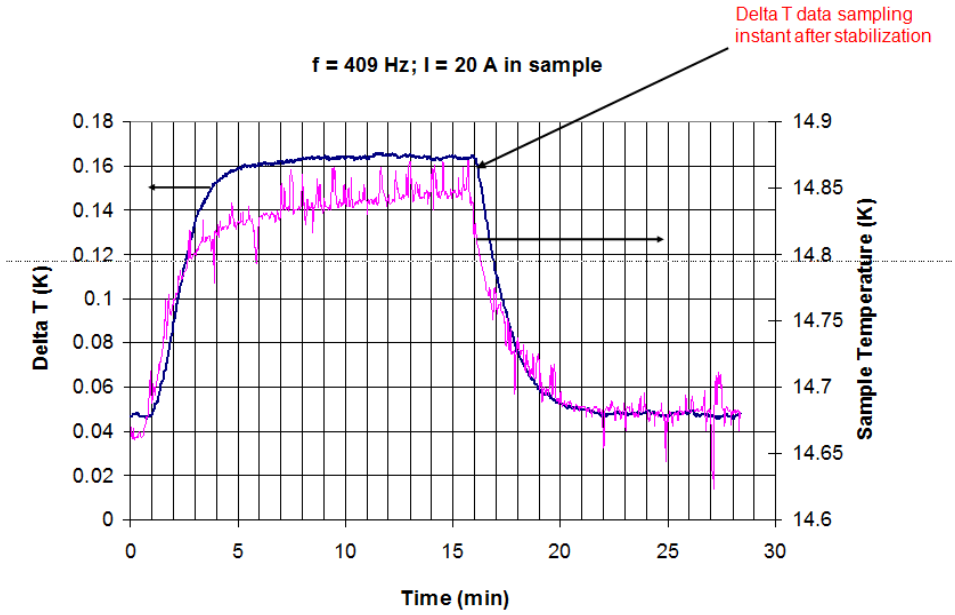

Figure 6.5.80. Temperature measurement versus time of the sample coil shown by the purple curve with the scale on the left. Delta-T measurement given by the black curve with the corresponding scale on the right.

Magnetization losses of the solenoidal coil for various flux densities of the background field and frequencies are presented in Figure 6.5.81. Transport current losses as a function of transport current for various frequencies are shown in Figure 6.5.82.

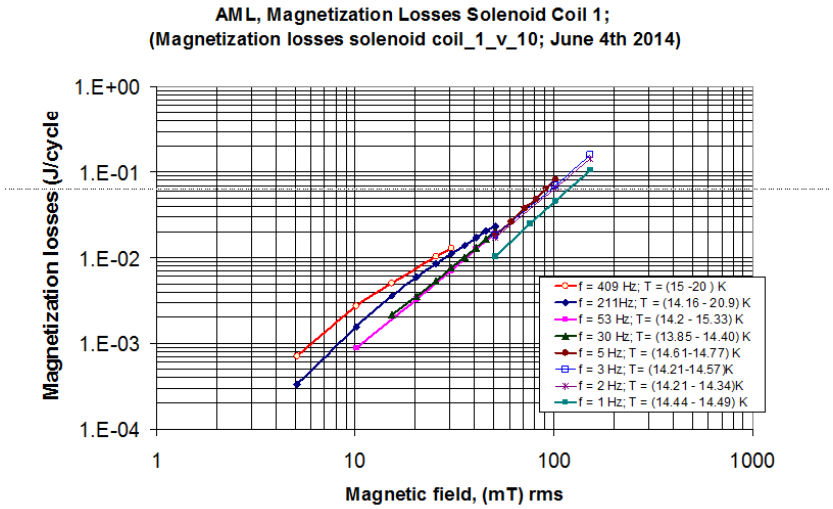

Figure 6.5.81. Magnetization losses of MgB_2 test coil versus magnetic field for different frequencies.

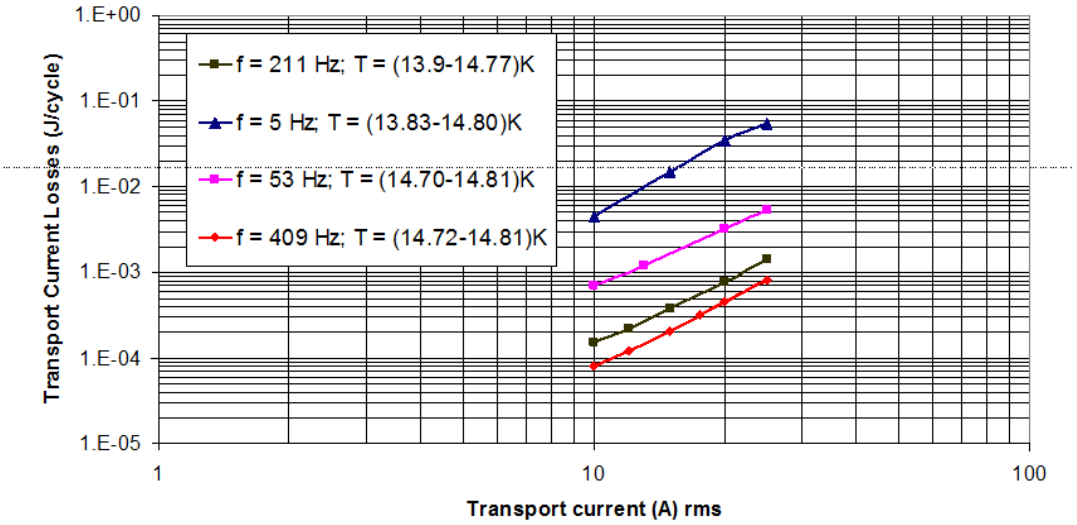

Figure 6.5.82. Transport current losses of MgB_2 test coil as a function of transport current for various frequencies.

A potential influence of the phase shift between the background field and the transport current through the test coil are shown in Figure 6.5.83.

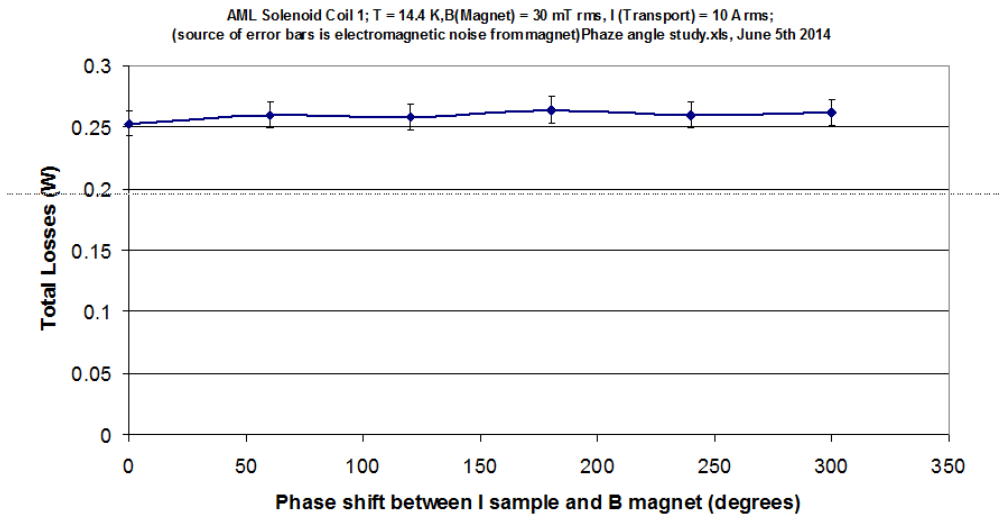

Figure 6.5.83. Total losses of MgB2 test coil as a function of phase shift between the background field and excitation current in test coil.

As an additional test, the critical current of the test coil has been performed by measuring the voltage across the coil as a function of excitation current. The resulting data are shown in Figure 6.5.84. Taking a threshold of 1.5 mV as the transition, the critical current of the coil is 17 A with an n-value of 2.7. These rather low values of the MgB_2 conductor are currently unexplained. It could be that the conductor performance was compromised due to bending during handling of the coil after reaction heat treatment.

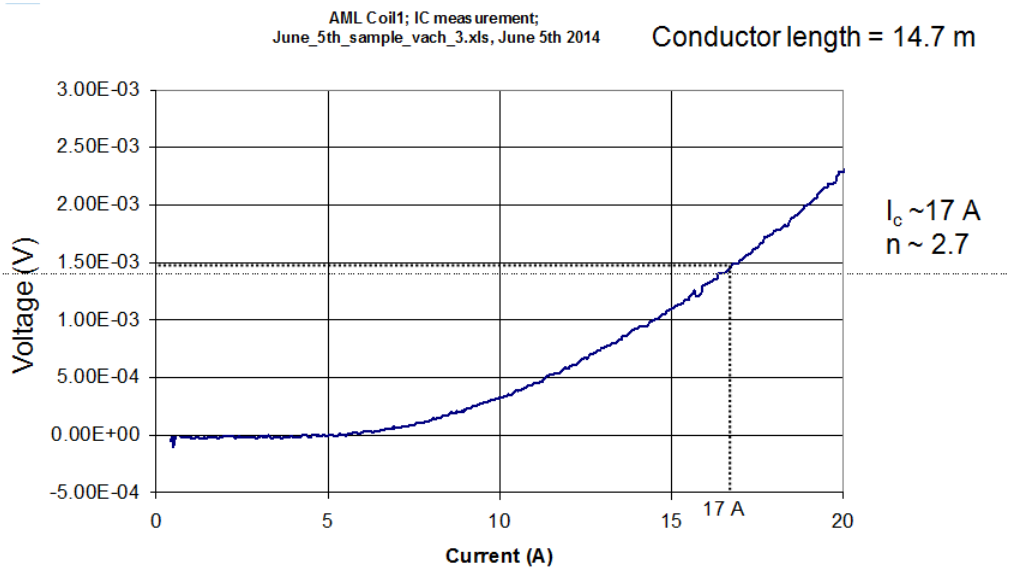

Figure 6.5.84. Critical current measurement of MgB_2

The measured data of AC losses have been compared with a model developed by the University of Houston. The comparison is shown in Figure 6.5.85 and Figure 6.5.86. As can be seen, good agreement between the measured data and the model predictions are already obtained. In a the stator winding of a synchronous machine, the magnetic field is perpendicular to the conductor, which is not the case for the solenoidal winding of the test coil. A correction factor is therefore needed in order to make the model applicable to the solenoidal configuration. This required correction factor has been estimated to be 4.5 and has been applied for the comparison. For the design of an FSG a reliable estimate of the expected AC losses in the stator winding under all possible operational scenarios is of utmost importance.

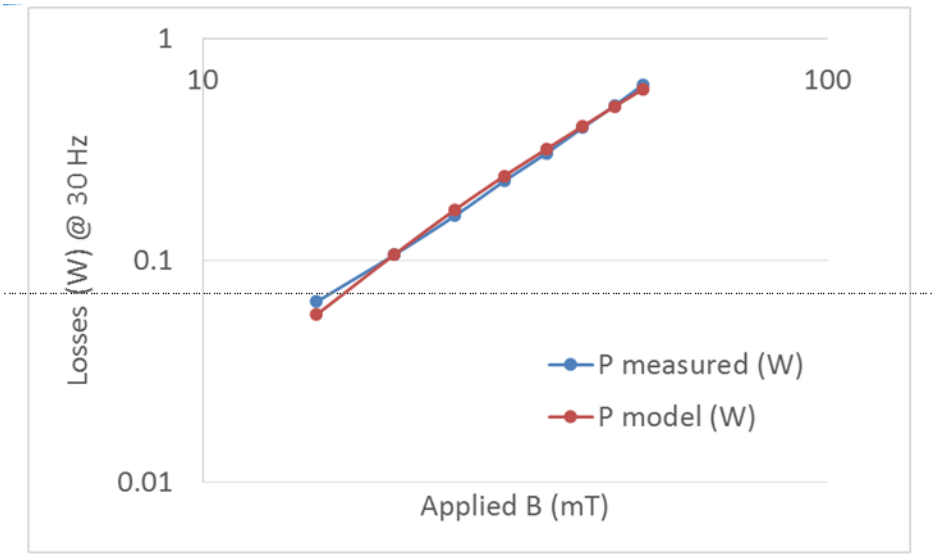

Figure 6.5.85. Comparison of model calculation and measurements for fixed frequency and different flux density.

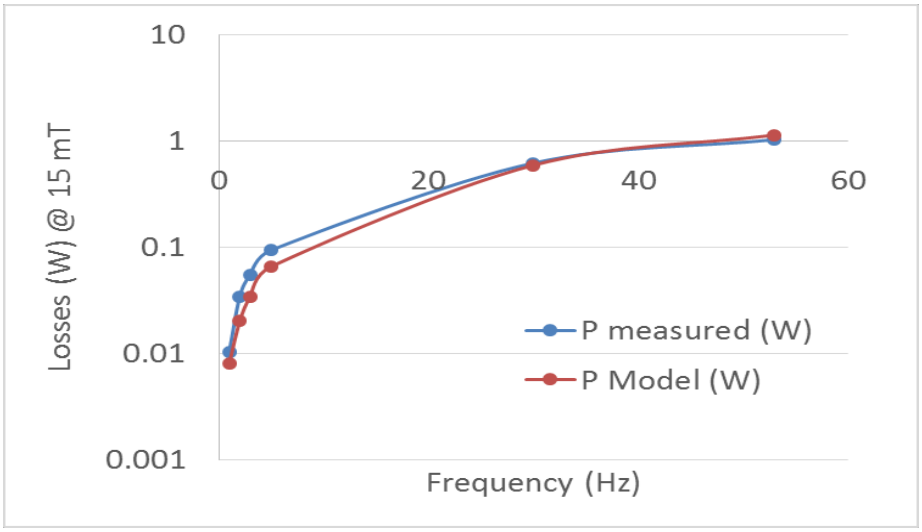

Figure 6.5.86. Comparison of model calculation with measurements for fixed flux density and different frequencies.

The MgB_2 conductor under development by Columbus in Italy is already reacted and the corresponding minimum bending radius does not allow building test coils with small bending radii. However, magnetization losses of such conductor can be measured with straight wire segments. A sample holder for such wire samples has been designed and built at AML. The design and the actual

samples are shown in Figure 6.5.87. The MgB2 wire samples supplied for these tests are presented in Figure 6.5.88. Columbus has produced to different wires with 37 and 61 filaments, respectively. The magnetization losses for the 37-strand wire for different flux densities of the external field and various frequencies are shown in Figure 6.5.89.

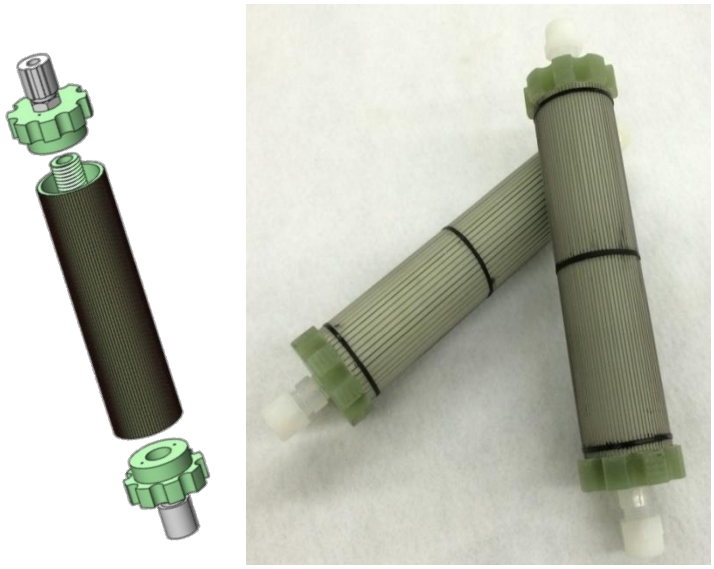

Figure 6.5.87. Left: Design of sample holder for magnetization losses of straight wire samples. Right: Actual sample holders containing Columbus MgB2 conductor with 37 and 61 filaments, respectively

Figure 6.5.88. Straight MgB2 wire samples used for magnetization loss measurements

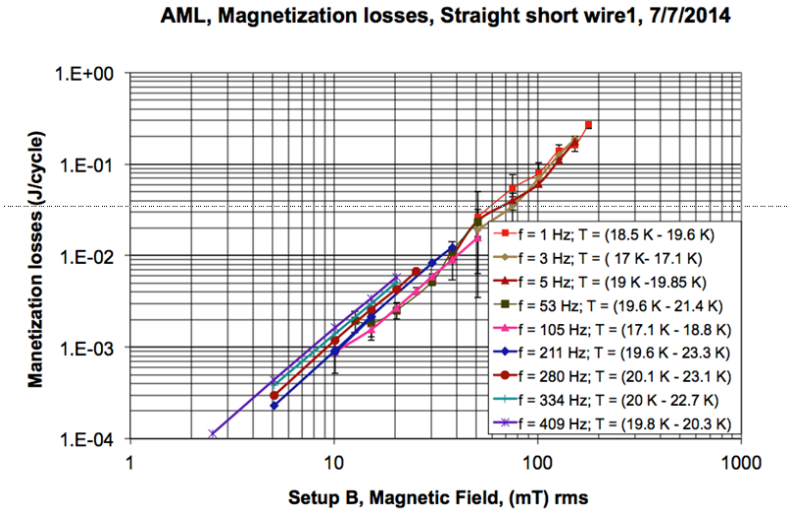

Figure 6.5.89. Magnetization losses of Columbus MgB_2 conductor versus flux density and frequency

To perform AC loss measurements with the correct conductor orientation as found in the synchronous machine, a racetrack coil is needed for the tests. The design of this coil has been developed at AML and the ceramic support structure has been built. The design is shown in Figure 6.5.90.

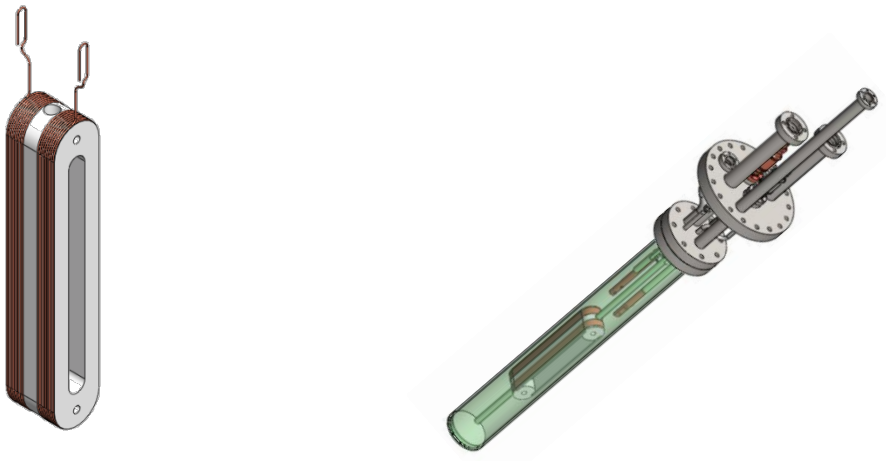

Figure 6.5.90. Left: Design of racetrack coil for AC loss measurements. Right: Racetrack coil mounted in test chamber for AC loss measurements.

The coil support structure machined out of Macor ceramic has been manufactured and the coil winding is currently being done at Hypertech. AC loss measurements under all possible conditions will be done at CAPS.

3.2.3.7 Task 6.6 – Fault Current Limitation Measurement

3.2.3.7.1 Introduction/task objectives

Fully superconducting generators typically present fairly low synchronous reactances in the 0.5 to 1 p.u. range. The lower reactance leads to large fault currents and torque in case of short circuit of 1 or more phases of the stator. While this would be an issue for copper wound stators which would experience very large short circuit currents (~8-10 p.u.), superconducting stators will naturally transition to the normal resistive state as soon as the phase current reaches the critical current of the conductor thus adding a large impedance in the circuit and limiting the fault current. The superconductor in the stator can be seen as two conductors in parallel; one representing the matrix material and the second representing the superconducting filaments.

The matrix resistivity needs to be high for effective limitation, i.e., NiCu alloy with a resistivity in the range of 6e-9 Ω.m. The superconductor has an equivalent resistivity which can be approximated from the E(J) characteristic of the material $E = Ec\left(\frac{J}{Jc}\right)^n$ with Ec the critical electrical field set at 1e-4 V/m and Jc the critical current density, n is the n-value characteristic of the superconductor. The resistivity of the superconducting filaments can then be written

$$\rho_{sc} = \frac{Ec}{Jc(B,T)}\left(\frac{J}{Jc(B,T)}\right)^{n-1}$$

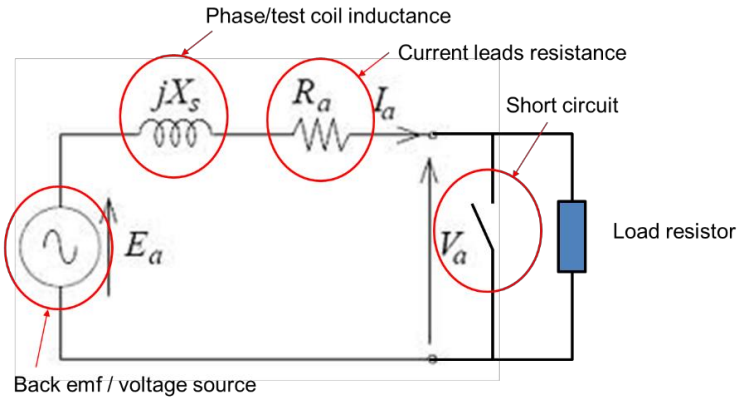

Figure 6.6.1. Single-phase equivalent circuit of a synchronous generator

The resistivity of the superconductor depends strongly on the temperature and the applied magnetic flux density.

Time domain simulations of fault current limitations have been performed in the first phase of the project (BP1) showing that the fault current could be limited to magnitudes lower than the nominal load current thanks to the very large impedance created in the circuit when a phase composed of kilometers of conductor transitions to the normal resistive state.

The objectives of this task are:

1. Mimic a phase of a superconducting machine subjected to an AC voltage source and manually create a short circuit;
2. Verify that the short circuit current is indeed limited by transition of the superconducting wire.

A small-scale superconducting coil made of MgB2 wire was fabricated to mimic a phase of a superconducting generator; the back e.m.f. created by the rotation of the rotor is represented by a voltage source and the load is represented by a resistor. The circuit is represented in Figure 6.6.1.

Xs represents the MgB2 coil reactance, Ra the current lead resistance connecting the coil at 15 K to the load resistor at room temperature. Ea is an AC voltage source.

3.2.3.7.2 Superconducting test coil

A superconducting coil was designed to demonstrate current limitation. The coil was fabricated by HyperTech Research with low Jc conductors and high matrix resistivity. The coil design is shown in Figure 6.6.2. The test racetrack coil is composed of 6.2 m of MgB2 conductors provided by Hypertech Research. The conductor was designed with a low Jc to match the limitations of the test facility (100 A HTS current leads). The conductor is composed of 54 filaments in a Cu10Ni matrix material exhibiting a matrix resistivity of about 4e-7 Ω.m. The conductor presents a very sharp transition and a large n-value.

The conductor specifications are shown in Figure 6.6.3.

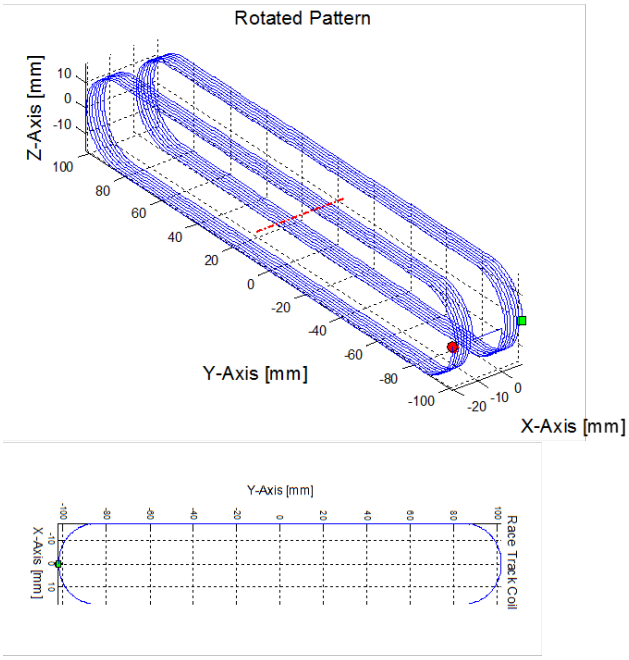

>>>>>>>>>> RACE TRACK COIL FOR AC LOSS MEASUREMENT <<<<<<<<<<
LXS: 170 Length of straight sections
LYS: 0
RArc: 17 Arc radius
NLayer: 1
NTurn: 7 Number of turns
WSpTT: 1.2400
WSpLL: 0
NPX: 100
NPY: 0
NArc: 100
AEnter: 0
LExit: 0

Total Number of Turns:	14
Wire Diameter:	0.840 [mm]
Remaining Gap:	0.400 [mm]
Width of Half-Pattern:	8.680 [mm]
Gap between Half Coils:	12.320 [mm]
Width of Whole Pattern:	29.680 [mm]

Estimated Conductor Length: 6267.73 [mm] ----- 246.76 [in]

Figure 6.6.2. Test Coil Geometry

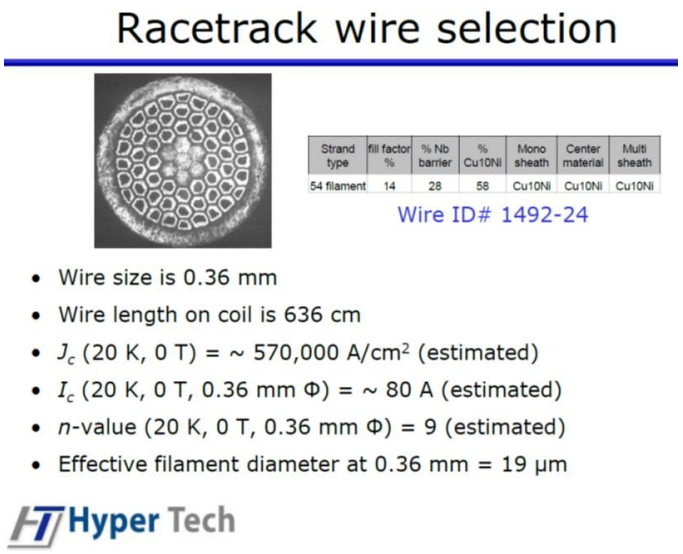

Figure 6.6.3. Wire Section and Properties

3.2.3.7.2.1 Experimental setup

The test coil is placed in the cryostat developed for AC losses measurements presented in an earlier section. The circuit shown in Figure 6.6.1 is cabled. The test coil is cooled by cold, gaseous helium-forced convection. The coil shown in Figure 6.6.4 has exposed conductor allowing for a good heat transfer with the helium flow. The current, voltage and coil temperature are monitored.

Ceramic resistors are used to load the circuit as shown in Figure 6.6.5. A mechanical switch is used to create a short circuit. Once the test coil is cooled down, a voltage is applied leading to a load current flowing in the circuit. A short circuit is created for a few seconds leading to transition of the test coil (quench) and current limitation. The current is recorded and acquired digitally.

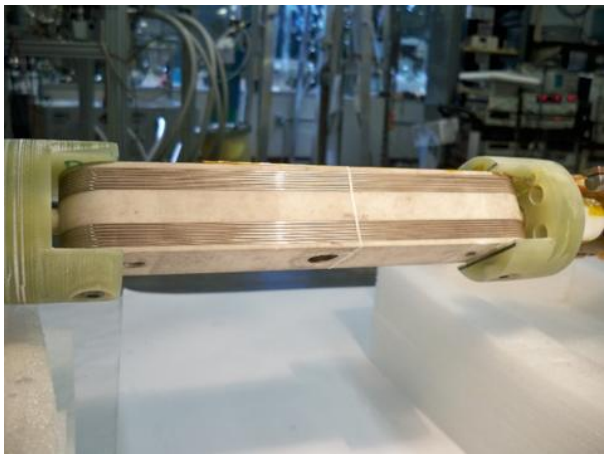

Figure 6.6.4. Test coil as mounted in the cryostat

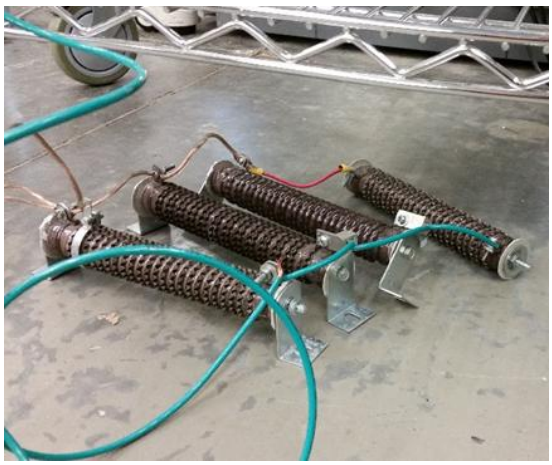

Figure 6.6.5. Load Resistors

Figure 6.6.6 shows the data acquisition system and the mechanical switch used to create the short circuit.

Figure 6.6.6. Data Acquisition System and Mechanical Switch

Figure 6.6.7 shows the test facility.

Figure 6.6.7. Test Facility

3.2.3.7.2.2 Results

A large number of tests were performed at different frequencies 100 Hz, 50 Hz, 10 Hz and 1 Hz. Current limitation was demonstrated for all frequencies. The results shown below were obtained at 50 Hz and are representative. It is to be noted that the test coil experienced a reduction of its critical current density after each test; the actual reason for the performance degradation is not known yet but might be due to thermal strain effects during the quench.

At 50 Hz, the critical current of the test coil was about 35 A. A series of short circuits were applied at different phase voltage and load current.

Test #	Load current (A)	Prospective current (A) /Peak current (A)	Peak temperature (K)	Comments
1 (Figure 6.6.8)	4 A	13 A / 13 A	14.5 K	Prospective current is lower than Ic – no quench/limitation
2 (Figure 6.6.9)	6 A	20 A / 20 A	15.5 K	Prospective current is lower than Ic – no quench/limitation A quench occurred because of temperature increase due to AC losses
3 (Figure 6.6.10)	12 A	42 A / 35 A	31 K	Current was limited to Ic
4 (Figure 6.6.11)	16 A	52 A / 35 A		Current was limited to Ic

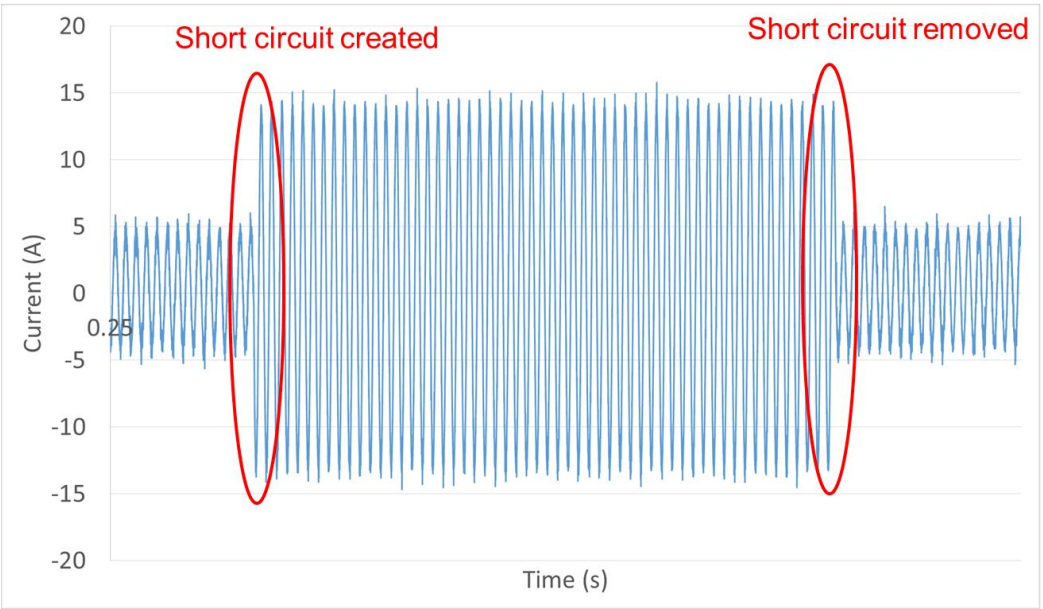

Figure 6.6.8. Test 1-Current in Circuit

Test 1 – Current in circuit

Test 1: the short circuit current is lower than the critical current and the temperature increase during the short circuit negligible, as a result, no quench was observed. The short circuit was maintained for about 2 seconds.

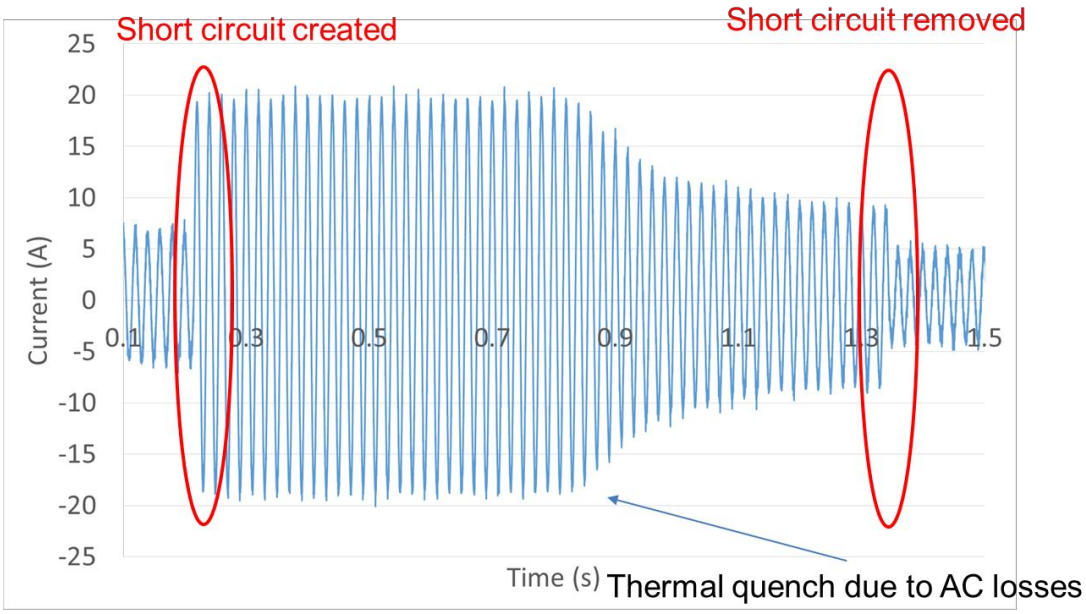

Figure 6.6.9. Test 2 – Circuit Current

Test 2 – Circuit Current

Test 2: the short circuit current was lower than the critical current of the coil and no over current transition was observed. However, the AC losses in the coil were high enough to induce an electro-thermal instability and a quench was observed after 0.7 s. The short circuit current was then reduced to about 10 A before the fault was eliminated. The shows that, while longer, fault current limitation can occur even when the short circuit current is lower than Ic which can be good in the case of partial short circuit during which the phase current is increased to values lower than Ic. During the quench, the coil temperature increased by 1 K from 14.5 K to 15.5 K.

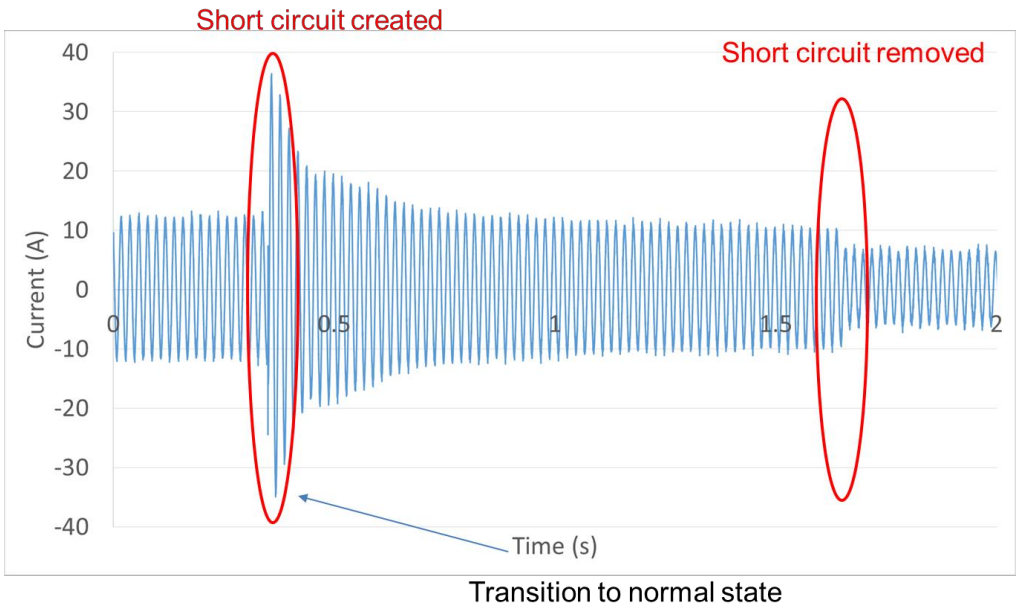

Figure 6.6.10. Test 3 – Circuit Current

Test 3 – Circuit Current

Test 3: the short circuit current was higher than the critical current of the coil. While the unlimited fault current should have been over 40 A a peak of 35 A was measured showing current limitation at the critical current of the coil. The current is limited at first peak and decreased right away with a final value of 11 A right before the fault is eliminated, which is lower than the original load current. During the current limitation, the temperature of the coil reached 31 K.

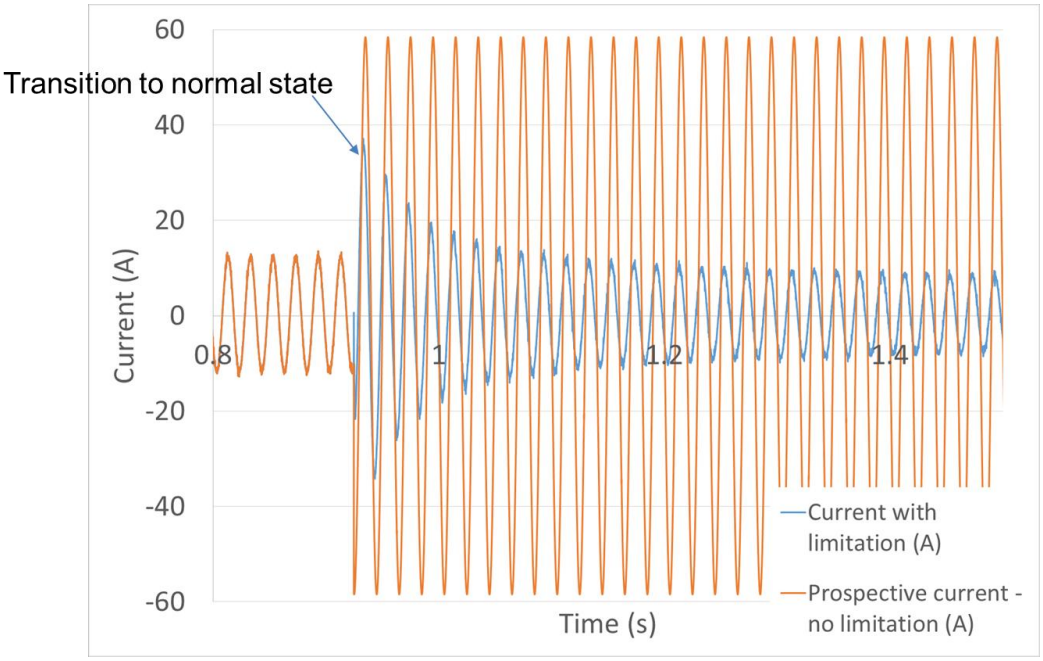

Figure 6.6.11. Test 4 – Circuit Current

Test 4 – Circuit Current

Test 4: the unlimited short circuit current was over 50 A, about 1.5 times higher than the critical current. The fault current was limited to the same value as during test 3: 35 A. The fault current is effectively limited to the Ic of the conductor. Figure 6.6.11 shows the unlimited current (calculated), after 0.2 s the current is about the same value as the nominal load current. The current was reduced to about 12 A right before the fault was eliminated. The temperature of the coil reached 31 K as shown in Figure 6.6.12.

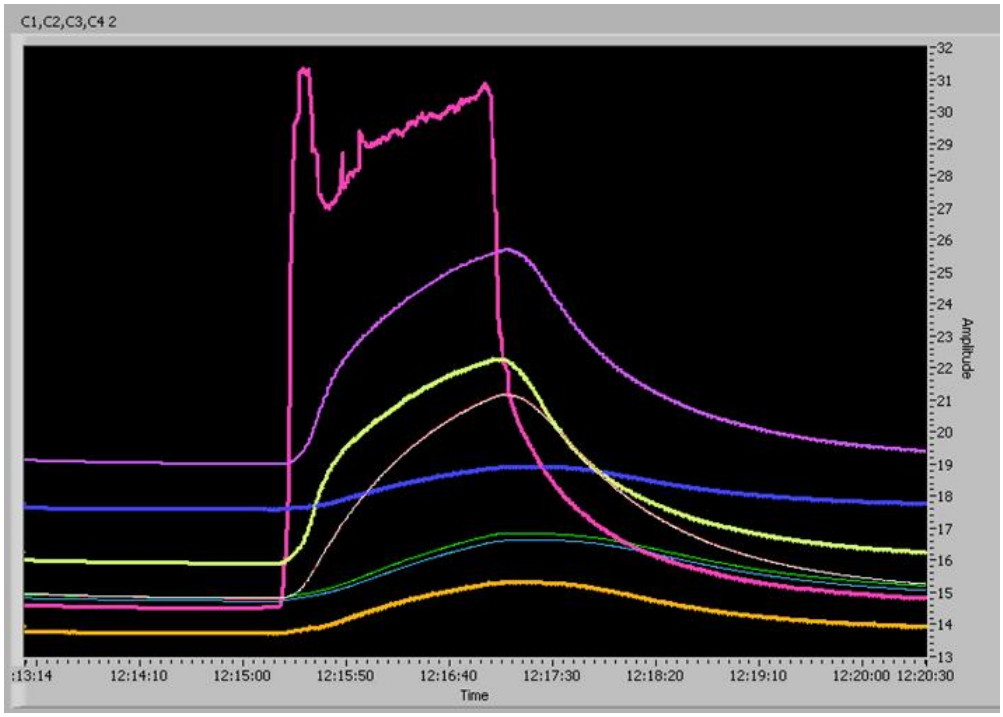

Figure 6.6.12. Temperature of the test coil during fault current limitation

3.2.3.7.2.3 Conclusion

We have successfully developed an experiment to simulate a short circuit in a phase of a superconducting stator using a MgB2 superconducting coil:

- The current limitation was successfully demonstrated
- A prospective fault current of ~50 A was limited to the Ic of the superconducting coil to about 30 A
- The current limitation happens very fast – within a few ms
- The temperature increase in the superconductor was reasonable to about 35 K

The experimental data confirmed that the short circuit current will effectively be limited to the critical current of the coil. The results were reproducible and the same behavior was observed for the different frequencies tested. It is important to make sure that the normal resistance of the superconducting coil is large enough to significantly increase the impedance of the circuit during a quench.

4 Task 7.0 – Commercialization Plan

4.1 Introduction

The fully superconducting generator (FSG) as envisioned in the concepts developed in BP1 and de-risked in BP2 is well matched to direct drive wind turbine technology of the future.

Key benefits of the FSG include:

- High specific torque capability allows direct drive turbines with reduced up tower weight potentially leading to lower turbine and infrastructure costs.
- The use of an inexpensive superconductor capable of AC current. The superconductor represents the highest cost component for both the rotor and stator. This FSG will have a lower capital cost.
- A stator designed to behave as a current limiter for faults or extreme gust loading conditions to limit the peak torque developed in operation. The stator and rotor structure strength requirement is therefore reduced for minimized capital cost. The remainder of system costs can also be reduced accordingly.
- Greatly reduced direct drive reflected inertia effects reduce the acceleration and deceleration associated torques.
- Active section heat leak is minimized by re-entrant heat path design. This minimizes the required cryocooler size and therefore reduces capital cost as well as cost of operation.
- A winding support design that greatly reduces thermal stresses for the extreme temperature difference between ambient and operating conditions (about 300 K). Reducing these stresses improves the FSG reliability for reduced operation costs. Winding support is achieved with a cast-in-place approach, minimizing the machining for winding placement and provides full support of the highly loaded conductors.
- High-capacity, long-life, high-reliability, high-efficiency cryocooler minimizes operating costs.
- Separate cryostats for rotor and stator to eliminate shaft vacuum seals for improved operating costs.

4.2 Commercialization Plan

The de-risking experiments performed for BP2 were successful in assessing the risks for BP1 highlighted aspects of the concept. None of the design aspects studied became showstoppers. These would represent design issues without solutions.

Instead, all experiments showed the highest perceived risk areas of the concepts developed in BP1 as relatively low.

BP2 success now leads to the next step in FSG development.

The next logical step in the FSG development is to make and test a complete subscale prototype machine.

The maximum knowledge gained from a prototype would be in a wind turbine application. A direct comparison of the critical parameters for the wind application could show expected performance results for the full-sized FSG. Several wind turbine generators in the 1.5-MW size exist.

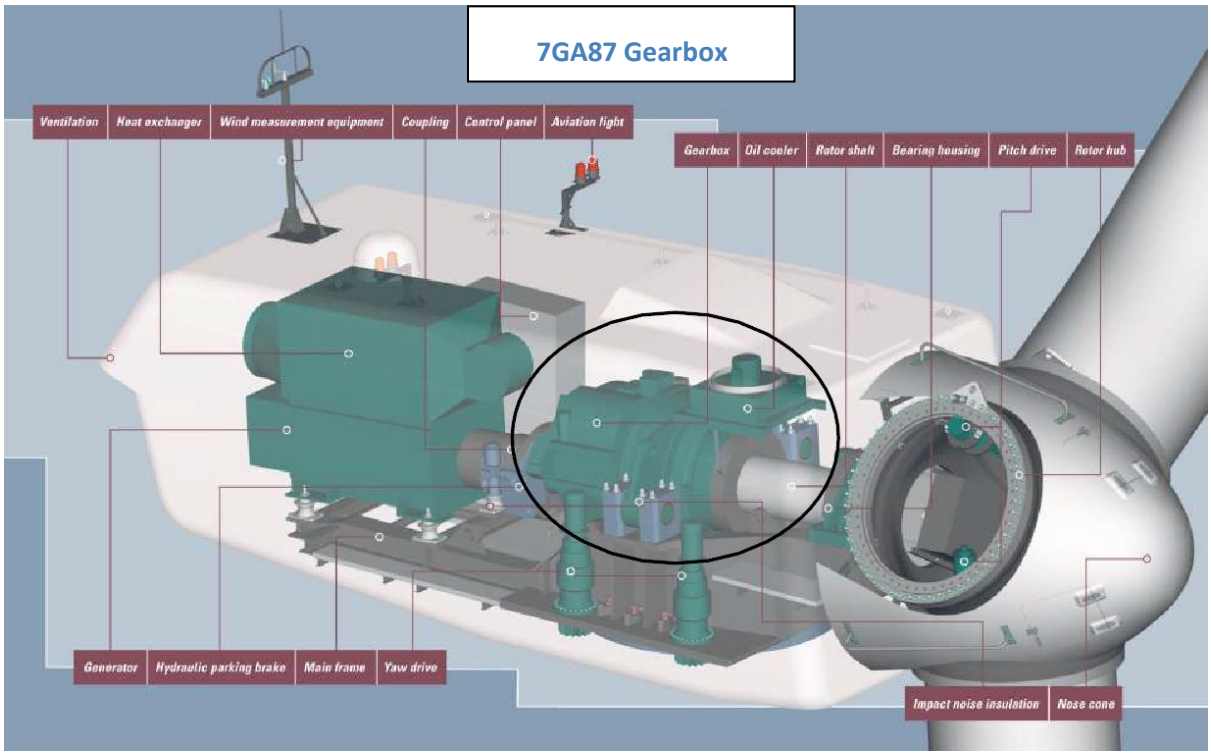

Figure 7.1. Existing GE 1.5-MW Nacelle

An internet search quickly shows that the GE 1.5-MW series wind turbines are the most popular machines with well over 15,000 turbines in the field. Many years of operational data exist, allowing easy comparison to the FSG results. The mainframe design allows design of a "drop in" replacement of the existing drivetrain components with a direct drive FSG of the same rating (Figure 7.1).

The prototype will have the following primary purposes:

- Develop manufacturing processes. Several aspects of the design are new to the generator industry, such as use of superconductors, cryogenics, vacuum containment, high composite structural content, etc.
- Develop in-process and final testing methods for fully superconducting machines.
- Secondary goals for the prototype would be use in a wind turbine application:
- Validate the projected cost of energy for the full sized FSG
- Show the benefits of direct drive for reduced blade loading.

Prototype details:

- The specifications for the prototype are:
  - 1500 kW, 690 V
  - 18.7 rpm.

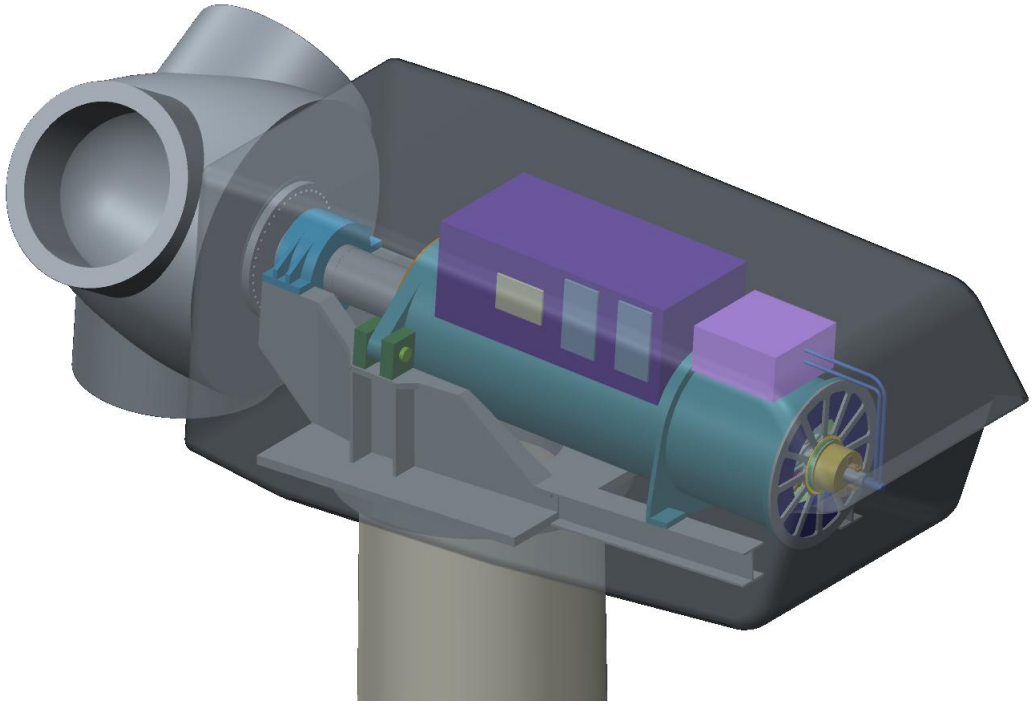

Figure 7.2. 1.5-MW FSG in GE 1.5-MW Nacelle

Some of the nacelle components could be reused, such as the main slow speed bearing and trunnion blocks. An early task would be to determine the appropriate prototype configuration.

Preliminary design of a 1.5-MW prototype has been performed to allow retrofit feasibility confirmation. Approximate nacelle/mainframe geometry was determined and used for the exterior envelope. These were used to develop a preliminary FSG design. The result was the prototype geometry shown in Figure 7.2. Integral power converter and cryocooler allows greater accessibility within the nacelle.

The preliminary prototype model was used to provide a price estimate for a single unit of $5.87 M, ready for test.

5 Task 8.0 – Project Management and Reporting

Project management reports for all Budget Periods and other deliverables have been provided in accordance with the Federal Assistance Reporting Checklist following the instructions included therein.

References

[32] "AC loss and macroscopic theory of superconductors," W. J. Carr, Jr., 2nd edition, ISBN: 0415267978, (2001).
[33] "Modelling HTc superconductors for AC power loss estimation," J. K. Sykulski, R. L. Stoll, A. E. Mahdi, and C. P. Please, IEEE Trans. on Magnetics, vol. 33, no. 2, pp. 1568–1571, Mar. (1997).
[34] "Numerical solution of critical state in superconductivity by finite element software," Z. Hong, A. M. Campbell, and T. A. Coombs, Supercond. Sci. Technol., vol. 19, no. 12, pp. 1246–1252, Dec. (2006).
[35] "Numerical analysis of the impact of elliptical fields on magnetization losses," C. Lorin, and P. J. Masson, IEEE Trans. on Applied Superconductivity, vol. 23, no. 3, 8201405, Jun. (2013).
[36] "Development of a 3D sizing model for all-superconducting machines for turbo-electric aircraft propulsion," P. J. Masson , K. Ratelle, P-A. Delobel, A. Lipardi, and C. Lorin, IEEE Trans. on Applied Superconductivity, vol. 23, no. 3, 3600805, Jun. (2013).
[37] "Energy dissipation in high temperature ceramic superconductors," M. Ciszek, A. M. Campbell, S. P. Ashworth and B. A. Glowacki Applied Superconductivity, vol. 3, no. 7-10, pp. 509-520, (1995).
[38] "Losses in Nb/Ti multi-filamentary composite when exposed to transverse alternating and rotating fields," C. Y. Pang, A. M. Campbell, P. G. McLaren, IEEE Transactions on Magnetics, vol. MAG-17, no. 1, pp. 134-137, (1981).
[39] "AC losses in superconducting wires in a rotating magnetic field. I. Low-frequency loss in a wire in a high transverse field," M. Noda, K. Yamafuji, Japanese journal of applied physics, vol. 20, no. 1, pp. 277-285, (1981).
[40] "Magnetic properties and AC-losses of superconductors with power law current-voltage characteristics," J. Rhyner, Physica C: Superconductivity, vol. 212, no. 3-4, pp. 292-300, (1993).
[41] "Theoretical expressions of magnetization losses in elliptic superconducting wires with voltage-current characteristics represented by power-law," K. Kajikawa, Y. Mawatari, T. Hayashi and K. Funaki, Applied Superconductivity, vol. 3, no. 7-10, pp. 509-520, (1995).
[42] "AC losses in thin coated conductors under non-sinusoidal conditions," M. Spektor, V. Meerovich, V. Sokolovsky and L. Prigozhin, Superconductivity Science and Technology, vol. 25, 025008, (2012).
[43] "Losses in superconductors under non-sinusoidal currents and magnetic fields," V. Sokolovsky, V. Meerovich, M. Spektor, G. A. Levin, I. Vajda, IEEE Transactions on Magnetics, vol. 19, no. 3, pp. 3344-3347, (2009).
[44] "Study of the MgB2 grain size role in ex situ multi-filamentary wires with thin filaments," A. Malagoli, V. Braccini, C. Bernini, G. Romano, M. Vignolo, M. Putti, C. Ferdeghini, Superconductor Science and Technology, vol. 23, 025032, (2009).
[45] "Superconducting magnets," M. N. Wilson, ISBN 0198548109, p. 163, (2002).
[46] "Magnetization and AC loss in a superconductor with an elliptical cross-section and arbitrary aspect ratio," B. Ten Haken, J-J. Rabbers, H.H.J. Ten Kate, Physica C, vol. 377, pp. 156-164, (2002).

Appendices

Appendix B: Kajikawa Model for Alternating Field Losses

The alternating field loss formula proposed by Kajikawa et al [41] is expressed with our notation and compared to our numerical data.The reduced losses can be expressed only using the variable cn, demonstrating the universality of this variable. In the partial penetration state reduced losses are,

$$w_1^* = \frac{q^*}{b^{*2}} = \frac{256}{\pi^3}\left(\frac{\pi^2}{128}\right)^{\frac{1}{n+1}} \frac{n}{3n+1} \frac{\Gamma(\frac{n}{n+1})^2}{\Gamma(\frac{2n}{n+1})} \left(1.33+3.11n^{-0.63}\right) c_n^{\frac{n}{n+1}}$$

and in full penetration,

$$w_2^* = \frac{q^*}{b^{*2}} = \frac{2}{\pi}\left(\frac{16}{\pi}\right)^{\frac{1}{n}} \frac{n}{(n+1)^2(3n+1)} \frac{\Gamma(\frac{1}{2n})^4}{\Gamma(\frac{1}{n})^2} \frac{1}{c_n}$$

Then reduced losses over the whole domain are expressed as,

$$Q^* = \frac{w_1^* w_2^*}{max(n)(w_1^* + w_2^*)}$$

The comparison with our data, calculated by the H-formulation, around the full penetration is shown in Figure B.1. In the asymptotic cases ($c_n << 1$ and $c_n >> 1$) the formula works well (for $X^* > 10$ the error is within±7%) which is no more true around the full penetration limit ($X^* = 1$).

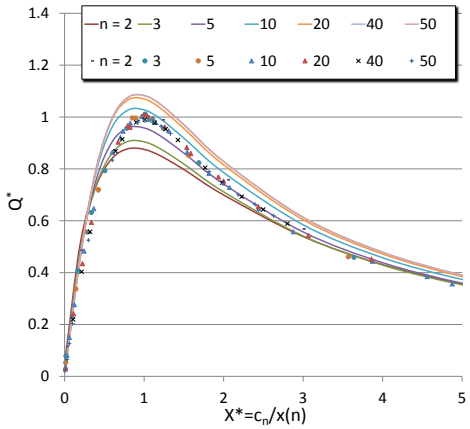

Figure B.1. Comparison between [41] formulae (continuous curves) and our numerical data (discrete points) around the full penetration for the case of a transverse alternating field.

Appendix C: Expression Validation

Table C.1. Tests of validation of the fit expression.

φ(rad)	k	n	cn	Q	fit	Error (%)
-2.45	0.3	18	4.5	7.01E-05	7.70E-05	-10
1.88	0.01	18	3.375	8.52E-05	9.25E-05	-9
-0.37	0.14	8	3	9.18E-05	9.87E-05	-8
0.24	0.05	18	1.6875	3.42E-05	3.68E-05	-8
-0.47	0.21	4	6000	4.56E+01	4.90E+01	-7
-2.23	0.17	8	8	2.48E-04	2.66E-04	-7
0.91	0.19	4	1660	5.01E+00	5.36E+00	-7
2.02	0.02	4	8440	7.62E+01	8.14E+01	-7
2.36	0	4	10510	1.13E+02	1.21E+02	-7
0.56	0.06	8	12	5.75E-04	6.10E-04	-6
2.08	0.03	4	200	1.47E-01	1.56E-01	-6
0.7	0.09	25	5	1.34E-04	1.42E-04	-6
-2.17	0.36	12	18	4.51E-04	4.76E-04	-6
1.9	0.16	12	1125	8.02E-02	8.43E-02	-5
1.12	0.13	8	750	1.14E-01	1.19E-01	-5
-0.75	0.12	8	60	4.61E-03	4.81E-03	-4
0.34	0.37	4	1130	3.07E+00	3.21E+00	-4
-3	0.59	3	110	1.42E-01	1.48E-01	-4
2.56	0.77	8	4	1.48E-04	1.54E-04	-4
-0.08	0.41	50	0.3	7.76E-07	8.04E-07	-4
2.93	0.86	25	2	6.10E-05	6.31E-05	-4
-2.45	0.32	50	720	1.44E-02	1.49E-02	-4
0.01	0.53	4	2	8.33E-05	8.62E-05	-4
0.8	0.04	12	2250	2.25E-01	2.33E-01	-3
-0.09	0.51	12	4.5	1.75E-04	1.81E-04	-3
1.59	0.13	12	1.2	1.73E-05	1.78E-05	-3
0.2	0.72	18	5.625	2.37E-04	2.45E-04	-3
-1.77	0.21	18	0.45	1.24E-06	1.28E-06	-3
2.9	0.68	18	0.675	3.27E-06	3.37E-06	-3
2.58	0.32	18	84.375	2.00E-03	2.06E-03	-3
22.8	0.17	18	4612.5	2.34E-01	2.40E-01	-3
1.71	0.11	18	843.75	4.19E-02	4.29E-02	-3
-2.53	0.01	12	75	4.01E-03	4.11E-03	-2
-1.35	0.32	4	5000	2.83E+01	2.89E+01	-2

2.42	0.82	25	12	4.52E-04	4.63E-04	-2
-1.07	0.92	18	13.5	6.96E-04	7.11E-04	-2
0.69	0.91	8	1.5	5.63E-05	5.75E-05	-2
-0.66	0.66	12	2.25	7.75E-05	7.92E-05	-2
-3.07	0.32	12	90	2.55E-03	2.59E-03	-2
0.23	0.75	18	67.5	3.92E-03	3.99E-03	-2
-0.47	0.77	25	0.5	4.73E-06	4.81E-06	-2
-2.31	0.93	8	5	2.77E-04	2.81E-04	-2
0.6	0.61	12	12	5.85E-04	5.95E-04	-2
1.78	0.95	12	7.5	4.05E-04	4.12E-04	-2
-0.34	0.89	18	3000	2.93E-01	2.98E-01	-2
1.41	0.98	18	90	6.07E-03	6.15E-03	-1
-1.6	0.08	25	750	3.09E-02	3.13E-02	-1
0.18	0.71	8	900	2.09E-01	2.12E-01	-1
2.38	0.86	8	50	4.79E-03	4.85E-03	-1
2.47	0.62	18	1.0125	8.24E-06	8.33E-06	-1
2.61	0.7	12	112.5	5.96E-03	6.03E-03	-1
-0.64	0.65	12	120	9.11E-03	9.21E-03	-1
1.17	0.39	4	20	3.13E-03	3.15E-03	-1
-2.47	0.9	12	6750	1.14E+00	1.15E+00	-1
2.33	0.04	50	100	2.91E-03	2.94E-03	-1
2.23	0.72	8	80	6.84E-03	6.89E-03	-1
2.72	0.76	12	6150	7.66E-01	7.69E-01	0
0.99	0.58	12	6	2.34E-04	2.35E-04	0
-0.6	0.95	8	75	9.84E-03	9.87E-03	0
-1.37	0.98	8	4100	1.71E+00	1.71E+00	0
-1.04	0.96	8	1500	4.63E-01	4.64E-01	0
0.95	0.33	18	0.9	1.11E-05	1.12E-05	0
2.36	0.76	12	1.35	2.84E-05	2.85E-05	0
2.72	0.26	50	3020	6.57E-02	6.57E-02	0
-2.31	0.75	12	4000	4.76E-01	4.76E-01	0
2.33	0.04	50	100	2.94E-03	2.94E-03	0
0.33	0.59	25	250	1.29E-02	1.29E-02	0
0.33	0.59	25	250	1.29E-02	1.29E-02	0
-0.88	0.97	25	1	2.98E-05	2.97E-05	0
0.63	0.07	8	0.9	1.25E-05	1.24E-05	1
-0.55	0.99	4	1000	3.75E+00	3.73E+00	1
-2.07	0.64	4	100	4.24E-02	4.21E-02	1
1.09	0.99	8	0.6	1.07E-05	1.06E-05	1

0.37	0.28	50	50	1.62E-03	1.61E-03	1
-2.07	0.4	12	0.6	1.80E-06	1.79E-06	1
0.48	0.27	8	0.4	1.66E-06	1.64E-06	1
-1.25	0.54	4	5	3.35E-04	3.31E-04	1
-2.33	0.73	4	1	1.59E-05	1.57E-05	1
-0.44	0.5	50	1610	6.69E-02	6.60E-02	1
2.18	0.68	50	10	2.72E-04	2.68E-04	1
0.88	0.41	18	5062.5	3.70E-01	3.65E-01	2
-1.6	0.58	12	0.9	1.07E-05	1.05E-05	2
-0.35	0.56	4	0.5	3.69E-06	3.63E-06	2
2.18	0.68	50	10	2.73E-04	2.68E-04	2
0.87	0.05	8	0.8	9.64E-06	9.47E-06	2
-1.77	0.61	4	2000	6.63E+00	6.51E+00	2
-1.15	0.6	18	1012.5	6.55E-02	6.41E-02	2
1.63	0.71	25	1.5	3.54E-05	3.46E-05	2
-2.86	0.32	50	0.8	1.43E-06	1.40E-06	3
0.3	0.11	8	4500	1.32E+00	1.29E+00	3
1.15	0.45	18	9	2.94E-04	2.86E-04	3
-1.76	0.62	12	1350	1.22E-01	1.18E-01	3
-2.83	0.14	4	0.5	1.42E-06	1.37E-06	3
2.04	0.66	50	1000	3.30E-02	3.20E-02	3
2.04	0.66	50	500	1.61E-02	1.56E-02	3
1.51	0.39	18	56.25	1.98E-03	1.91E-03	4
1.62	0.59	50	2	4.26E-05	4.04E-05	5
-2.16	0.47	18	1687.5	6.88E-02	6.50E-02	5
-2.16	0.47	18	1687.5	6.88E-02	6.50E-02	5
1.53	0.45	25	25	7.51E-04	7.01E-04	7

Appendix D: Range of Validity of Our Fit Expression

The study was initially carried out to better assess AC losses in MgB_2 stators of rotating machines. That is why round superconducting wires were analyzed. The range of variation for each of the dimensionless parameters is defined based on such application requirements (see Table D.1) [MAL09]. The semi-analytical formulae are valid in the full range of variation as defined in Table D.1. Moreover, it is worth noticing that losses generated by certain out-of-range sets of variables could still be estimated as shown in Table D.2 where losses for 4 sets of variables can be estimated using the formulae. Indeed, the only real limitation in Table D.1 comes from the value of the variable c_n that is defined later on (Eq 7). In Table D.2, example #1, the amplitude of the field is equal to 20 T – out of the range defined by Table D.1 - nevertheless, c_n is in the range defined in Table D.1 ($2019 < 5000 \times 20.165^{0.1}$); therefore, this set of variables is in the range of application of the formulae that are provided in the coming sections.

Table D.1. Range of variations of the parameters

	Min	**Max**	**Unit**
r	5	100	µm
J_c	100	2500	$A.mm^{-2}$
b_0	0.001	2	T
f	0.1	1000	Hz
μ_0	$4\pi x10^{-7}$		$H.m^{-1}$
E_c	10^{-4}		$V.m^{-1}$
φ	$-\pi$	π	
k	0	1	
n	3	50	
b*	**5×10^{-3}**	**5×10^{3}**	
f*	**10^{-5}**	**10^{3}**	
c_n	≈ 0	$\approx 5000 \times 20.265$	

Table D.2. Example of 4 additional "out-of-range" parameters

Var.	#1	#2	#3	#4	Unit
r	20	30	*250*	10	μm
J_c	300	*4000*	1000	750	$A.mm^{-2}$
b_0	*20*	0.5	2	*6*	T
f	50	50	50	*0.01*	Hz
n	10	40	21	15	
μ_0	$4\pi x10^{-7}$	$4\pi x10^{-7}$	$4\pi x10^{-7}$	$4\pi x10^{-7}$	$H.m^{-1}$
E_c	10^{-4}	10^{-4}	10^{-4}	10^{-4}	$V.m^{-1}$
b*	**4.17×10^3**	**5.21**	**10**	**10^3**	
f*	**2.37×10^{-1}**	**7.11**	**1.23×10^2**	**3×10^{-4}**	
c_n	**2091**	**4.8**	**7.1**	**1084**	
max(c_n)	**6755**	**5390**	**5770**	**6110**	

Appendix E: Biographies of Key Contributors

The following are biographies of the individuals who have been key contributors to the FSG development project.

Dr. Keith T. Dennehy

Winona State University

Short Biography

Dr. Dennehy has over 28 years' experience in the technology of composites engineering. A professor in the department of composite materials engineering, Winona State University, he provides instruction in the areas of design and manufacturing of composites and the development of laboratories for computer-aided engineering technologies. He developed LabVIEW-based data acquisition system for composites processing equipment for Ford Motor Company, and worked on the design and development of plastic/composite parts to replace metal parts at the Deere Technology Center-Moline, Illinois. He also worked on intranet-based web resource to promote information sharing across the worldwide Deere plastics/composites community of practice and developed a web-based introductory course in designing plastic parts.

Dr. Dennehy participated in the development of engineering design core curriculum and provided instruction in engineering design and other areas of engineering expertise for the Kanazawa Institute of Technology, Kanazawa, Japan. As an engineering consultant, Alliant Techsystems (ATK), Space Systems, he developed Excel software tools for analyzing mechanical joints in support of the James Webb Space Telescope, Primary Backplane Support Structure Program. Most recently, as a consultant for Kato Engineering, Dr. Dennehy provided composites design and process development assistance on a Department of Energy funded project to develop a 10-megawatt (MW) direct-drive fully superconducting generator for use in next-generation wind turbines. He also provides customized courses and seminars on composites modeling, manufacturing and testing.

Dr. Dennehy holds an MBA from the University of Utah, a Ph.D. in Civil Engineering from Rensselaer Polytechnic Institute, an M.S. in Civil Engineering from Youngstown State University, and a B.S. in Civil Engineering from Rensselaer Polytechnic Institute.

Education and Training

1989	MBA Executive Program, University of Utah, Salt Lake City, Utah
1985	Ph.D. in Civil Engineering, Rensselaer Polytechnic Institute, Troy, New York
1982	M.S., Civil Engineering, Youngstown State University, Youngstown, Ohio
1978	B.S., Civil Engineering, Rensselaer Polytechnic Institute, Troy, New York

Professional Experience

1995-current *Professor, Department of Composite Materials Engineering, Winona State University, Winona, Minnesota*

Associate Professor, August 1990 - August 1995 (tenured, August 1993)

- Provide instruction in the areas of design and manufacturing of composites

- Develop laboratories in computer-aided engineering technologies and composites manufacturing
- Participate in student recruiting, advising and placement

Director of Composite Materials Technology Center (COMTEC), December 1996 – July 2002

- Oversaw organization that uses Composite Materials Engineering Program resources (faculty, staff, students, facilities and equipment) to provide engineering services to industry
- Involved in marketing, quote preparation, technical consultation, program management, budget accountability, and staffing

Chairperson, August 1991 – August 1995

- Active in program start-up: staffing, facilities definition, equipment specification and procurement, curriculum development, and program accreditation
- Coordinated activities of academic department
- Oversaw department budget
- Interfaced with other university departments, industry and the community

June 2012–

August 2012 *Contract Engineer, Global Materials and Manufacturing Research and Innovation Center, Ford Motor Company, Dearborn, Michigan*

- -Developed LabVIEW-based data acquisition system for composites processing equipment

May 2006 - August, 2006

May 2004 - August, 2004

May 2003 - August, 2003

Contract Engineer, Materials Engineering & Technology - Plastics John Deere Technology Center-Moline, Deere & Company, Moline, Illinois

- Worked on the design/development of plastic/composite parts to replace current metal parts
- Co-inventor, US Patent #6668534, "Auger fingers for harvesting assemblies, and combines"
- Assessed new materials/processes with potential future application to Deere products
- Assisted in developing testing capabilities using the dynamic mechanical analysis instrument
- Worked on intranet-based web resource that promotes information sharing across the worldwide Deere plastics/composites community of practice
- Developed web-based introductory course, "Designing Plastic Parts"

August 1995–
November 1996 *Visiting Professor, Engineering Design Core, Kanazawa Institute of Technology, Kanazawa, Japan (leave of absence from Winona State University)*

- Participated in the development of engineering design core curriculum
- Provided instruction in engineering design and other areas of engineering expertise

April 1988–
August 1990 *Engineering Manager, EDO Corporation, Fiber Science Division, Salt Lake City, Utah (now part of ITT Exelis*)

- Directed and administered engineering department of a composite structures company
- Oversaw company research and development activities
- Coordinated selection of, installation of, and training on computer-aided drafting and design (CADD) and computer-aided engineering (CAE) systems

January 1986 –
April 1988 *Lead Engineer, Product Engineering, Composite Structures Design and Analysis, Hercules Aerospace, Magna, Utah (now part of Alliant Techsystems, also known as ATK)*

- Lead technical team member on composite space structures program
- Advanced development of analytical methods for characterizing low velocity impact damage in composites as Principal Investigator on an internal research and development project

May 1979 –
January 1981 *Assistant Track Supervisor, Consolidated Rail Corporation (Conrail), Youngstown, Ohio*

June 1978 –
May 1979 *Engineering-Management Trainee, Consolidated Rail Corporation (Conrail), Indianapolis, Indiana*

Consulting

Kato Engineering (an Emerson Electric company), North Mankato, Minnesota

- Provided composites design and process development assistance on a Department of Energy funded project to develop a 10-megawatt (MW) direct-drive fully superconducting generator for use in next-generation wind turbines, October 2012 – October 2014.

Mayo Clinic, Rochester, Minnesota

- Provided product design and process development assistance, July 2008 – November 2008.

Alliant Techsystems (ATK), Space Systems, Magna, Utah:

- Developed Excel software tools for analyzing mechanical joints in support of the James Webb Space Telescope, Primary Backplane Support Structure Program, June 2007 – October 2007.

Briggs and Morgan, Minneapolis, Minnesota

- Provided consulting/expert testimony on behalf of Miken Composites in a patent infringement case brought by Wilson Sporting Goods (judgment in favor of Miken Composites), January 2003 – February 2008.

LMK Enterprises, Ottawa, Illinois

- Designed/analyzed composite T-liner for sewer renewal system, April 2004.

Andersen (Windows) Corporation, Bayport, Minnesota

- Confidentiality agreements prevent disclosure of details, January 2002 – March 2002 and December 1994 – December 1995.

Innovative Skate Systems, Inc., Edina, Minnesota

- Developed composite (continuous reinforcement) frame for in-line skates, July 1995 – October 1995.

WinCraft, Inc., Winona, Minnesota

- Evaluated alternate processes and materials for the manufacture of novelty erasers, October 1994 – June 1995.

Coda Composites Company, Winona, Minnesota

- Involved in development of composite bows for string instruments, February 1993 – January 1995 (cofounder/owner, interest divested).

O'Rourke House, Rochester, Minnesota

- Assessed feasibility of using composite materials to repair a foundation wall that mistakenly had reinforcing steel left out, October 1994 – December 1994.

Customized Course/Seminar Instruction

- Ford, Dearborn, Michigan: composites overview, August 2014.
- John Deere (Des Moines Works), Des Moines, Iowa: carbon fiber composites overview, March 2014.
- Lockheed Martin, Eagan, Minnesota: composites overview, December 2007.
- MTS Systems Corp., Eden Prairie, Minnesota: testing of composite materials, October 2007.
- Composite Products Inc., Winona, Minnesota: plastics/composites overview, May 2002 – June 2002.
- Advanced Engineered Wood Composites Center, University of Maine, Orono, Maine: manufacturing of composite products, May 1997.
- Lucas Body Systems, Lake Center Industries, Winona, Minnesota: computer-aided drafting and solid modeling (SDRC I-DEAS), June 1995 – July 1995.
- Watlow Controls, Winona, Minnesota: solid modeling and finite element analysis (ANSYS), January 1993 – February 1993.

Dr. Anthony Dietz

Creare, LLC

Short Biography

Dr. Dietz received his undergraduate degree in Aeronautical Engineering from the University of Sydney and his doctorate from Oxford University. His graduate studies focused on gas-turbine research. After graduating, Dr. Dietz served with the Royal Australian Air Force at the Aircraft Research and Development Unit where he worked as a Flight Test Engineer. He directed a number of projects, the largest of which was a flight-loads trial on an F-18 aircraft. Dr. Dietz then worked in the Fluid Dynamics Laboratory at the NASA Ames Research Center, where he conducted basic fluid dynamics experiments on boundary-layer transition in both subsonic and supersonic wind tunnels.

At Creare, Dr. Dietz has led research and development projects on a variety of applications, including advanced airdrop technology, hearing protection, cryogenic turbomachinery, and superconducting systems. He is currently leading projects to develop improved head and hearing protection, innovative sensors and flow solutions for airdrop operations, and high temperature superconducting systems for power transmission.

Awards

1994 NRC Research Associateship

1987 Rhodes Scholarship

1987 First Class Honors and University Medal, University of Sydney, Aeronautical Engineering

Education and Training

1990 Ph.D., Mechanical Engineering, University of Oxford, UK

1987 B.Eng., Aeronautical Engineering, University of Sydney, Australia

Professional Experience

1999 – present *Engineer, Creare Incorporated, Hanover, NH.*

- Led research and development projects on a variety of applications, including cryogenic turbomachinery, superconducting power transmission, advanced airdrop technology, acoustic sensors, and hearing protection. Currently leading a NASA-funded project to develop a cryocooler for a superconducting electric aircraft, and a Navy-funded project to develop improved hearing protection for helicopter crews.

1997 – 1999 *Senior Research Scientist, MCAT, Inc., NASA Ames Research Center, Moffett Field, CA.*

- Designed and conducted an experiment in a supersonic wind tunnel with a cryogenic model to investigate the effects of temperature on boundary layer transition. Conducted an experiment that demonstrated the cancellation of 3D boundary-layer instability waves on a flat plate in a low-speed wind tunnel.

1994 – 1997 *National Research Council Research Associate, Fluid Mechanics Laboratory, NASA Ames Research Center, Moffett Field, CA.*

- Successfully completed a unique experiment that validated boundary-layer receptivity theories and increased understanding of receptivity to vorticity. Redesigned a low-speed wind tunnel to improve flow quality and to automate tunnel control, calibration and data acquisition. Developed an innovative hot wire temperature correction scheme.

1990 – 1993 *Flight Test Engineer, Royal Australian Air Force Aircraft Research and Development Unit, Edinburgh, Australia.*

- Planned and directed a number of flight trials including part of a multi-million dollar flight loads trial on an F-18 aircraft that provided vital data for Australian and Canadian fatigue tests. Led a team of engineers working on loads data reduction and analysis. Developed software that accelerated post-flight data reduction and instrumentation health checks.

1987 – 1990 *Turbo Machinery Research Group, University of Oxford, England.*

- Made original measurements of the unsteady pressure on a rotating turbine at engine representative conditions. Assisted in commissioning of a new transient flow facility, developed a technique for field balancing the turbine, developed innovative instrumentation for fast-response blade pressure measurements.

Synergistic Projects

Ongoing Projects

- Development of a 15-K Cooling Module that provides a measured flow of 15-K cryogenic helium gas for cooling superconducting magnets and other superconducting experiments.
  - Successfully delivered a system that provides 1-W of cooling at 15 K. Currently developing a system to provide 10-W cooling at 15 K.
- Preliminary development of the cryogenic cooling system for the first fully superconducting direct drive wind generator.
  - Completed sizing and scaling studies and cost analyses for the cryocooler. Completed a preliminary design of the cryogenic coupling.
- Development of an extremely lightweight, high performance cryocooler optimized for cooling superconducting devices in electric aircraft.

- Optimized a turbo-Brayton cryocooler design for this application. The system configuration includes two single-stage super-critical compressors, a novel recuperative heat exchanger, and a high performance turboalternator. The cryocooler requires 35 kW of input power at a heat rejection temperature of 320 K, weighs only 104 kg, has an efficiency of 31% relative to Carnot cycle, a specific mass based on input power of 3.0 kg/kWinput and a specific mass based on refrigeration of 52 kg/kWcooling. These specific mass values are far better than any cryocooler developed to date.
- Designed and fabricated an innovative recuperative heat exchanger, which is a critical cryocooler component. The heat exchanger is half the weight of the best competing technology.

❖ Development of an efficient, cost-effective cryocooler for cooling superconducting systems in Navy ships.
- Design and fabrication of a demonstration cryocooler has been completed. Assembly and testing is underway.

❖ Field-Serviceable Superconducting Cable Housing.
- Developing a cryostat design with field-applied fittings that allow the cryostat length to be adjusted during installation and provide for a viable means of field repair. The result is a hermetic superconducting cable housing assembly that is modular, easy to install, lightweight, possesses low heat leak, and is more cost-effective compared to currently available cable housing systems.

<u>Past Projects:</u>

❖ Superconducting power transmission for directed energy applications.
- Designed and optimized a superconducting power transmission system with a two-stage turbo-Brayton cryocooler proving cooling to a multi-stage current lead connected to power cables formed from twisted bundles of stacked high temperature superconducting tapes.
- The estimated system weight was 10% of a copper system and the estimated losses were 65% of a copper system.
- Built a test facility and installed a 50-K 5-kA cable and a 20-K 28-kA cable. Demonstrated 1-kA transmission through the 5-kA cable at 50 K and 6.25-kA transmission through the 28-kA cable at 40 K. Transmission current was limited by excessive joint resistance.

❖ High temperature superconducting (HTS) system components
- Developed a series of components for Navy HTS ship degaussing systems including: HTS cables mounted in a flexible cryostat, HTS quick-disconnect (HTSQD) connectors for the HTS cables, and a HTS junction box.

❖ Thermal management of superconducting electromagnets in VASIMR thrusters.
- Designed and built a thermal management system for HTS magnets, which are a key component in the Variable Specific Impulse Magnetoplasma Rocket (VASIMR) being developed by Ad Astra, a commercial spin-off from NASA Johnson. We designed and built a thermal isolation and structural support system and thermal interface heat exchangers for the magnet and performed a cooling demonstration with the magnet operating at its required operating temperature of 35 K.

Relevant Publications:

- Michael, P.C., Bromberg, L., Dietz, A. J., Cragin, K.J., and Gold, C., Design and Test of a Prototype 20 kAHTS DC Power Transmission Cable, accepted for publication in IEEE Trans. On Applied Superconductivity, 2014.
- Dietz, A. J., Audette, W. E., Barton, M. D., Hilderbrand, J. K., Marshall, W. S., Rey, C. M., Winter, D. S., and Petro, A. J., "Flow Cooling of Superconducting Magnets for Space Applications," Advances in Cryogenic Engineering: Transactions of the Cryogenic Engineering Conference (CEC), Vol. 53, American Institute of Physics, Melville, NY, 2008, pp. 291–298. AIP Conference Proceedings, Vol. 985, Part 1.
- Dietz, A. J., Audette, W. E., Bromberg, L., Minervini, J. V., and Fitzpatrick, B. K., "Resistance of Demountable Mechanical Lap Joints for a High Temperature Superconducting Cable Connector," IEEE J ApplSupercon, Vol. 18, No. 2, 2007, pp. 1171–1174.
- Zagarola, M. V., Dietz, A. J., Swift, W. and Davis, T., "35 K Turbo-Brayton Cryocooler Technology," Advances in Cryogenic Engineering: Transactions of the Crogenic Engineering Conference (CEC), (Anchorage, AK), edited by J. Waynert et al., Vol. 49B, Paper C4-C-07, American Institute of Physics, Melville, NY, 2004, pp. 1635–1642. AIP Conference Proceedings, Vol. 710, Part 2.
- Dietz, A. J., Coleman, C. P., Laub, J. A. and Poll, D. I. A., "Effect of Wall Temperature on Roughness Induced Attachment Line Transition," IUTAM Symposium: Laminar-Turbulent Transitions, (Sedona, AZ), Springer-Verlag, 2000, pp. 249–254.
- Dietz, A. J., "Local Boundary-Layer Receptivity to a Convected Disturbance," J Fluid Mech, Vol. 378, 1999, pp. 291–317.
- Dietz, A. J., "Boundary Layer Receptivity to Transient Convected Disturbances," AIAA J, Vol. 36, No. 7, 1998, pp. 1171–1177.

Dr. Philippe Masson

Advanced Magnet Lab, Inc.

Short Biography

Dr. Philippe Masson has been working in the area of electro-mechanical systems, power application of superconductivity and Multi-Physics modeling since 1999. He spent 6 years at the FSU-Center for Advanced Power Systems working on the development of high power density superconducting machine for aircraft propulsion as part of the NASA/DoD URETI on Aeropropulsion and Power and on electro-thermal instabilities in superconductors for the US Air Force Research Lab. At the same time, he was appointed by the FAMU-FSU College of Engineering as adjunct professor for the Department of Electrical Engineering. Dr. Masson was appointed to the Editorial board of IEEE Transactions on Applied Superconductivity and has been serving as Editor for Large Scale Applications since 2005. He joined the editorial board of the International Journal of Aerospace Engineering in 2009.

Dr. Masson is a Senior Member of IEEE and AIAA and a member of the Cryogenic Society of America. He received the "Outstanding Young Researcher Award" from NASA GRC in 2007 and the Boom Award from the Cryogenic Society of America in 2010. Dr. Masson has published over 40 journal papers and given more than 60 conference presentations in the area of Applied Superconductivity and Multi-Physics Modeling. He is a member of the program committee of the Applied Superconductivity Conference (ASC) since 2002 and has served as technical editor for ASC 2004, 2006, 2008, 2010 and Magnet Technology 21. He has been elected to the board of director of the Applied Superconductivity Conference in 2014.

Dr. Masson received a Ph.D. in Electrical Engineering from the Université Henri Poincare, Nancy, France. His work included the design, realization and testing of a superconducting inductor for synchronous machine based on a novel topology.

Awards

2010 Cryogenic Society of America Roger W. Boom Award 2010
This award was created by the Cryogenic Society of America to be given to a young professional (under 40 years of age) who "shows promise for making significant contributions to the fields of cryogenic engineering and applied superconductivity." The spirit of the R.W. Boom Award is to recognize young people for their pursuit of excellence, demonstration of high standards and clear communications.

2007 NASA/DoD URETI "Outstanding young researcher" award

2005 Appointed Editor for Large Scale Applications for the IEEE Transactions on Applied Superconductivity

Education and Training

2002 Ph.D. in Electrical Engineering (electric machines and applied superconductivity), G.R.E.E.N. Laboratory, University Henri Poincaré, Nancy 1, France

1999 D.E.A. - P.R.O.T.E.E. (Electrical Engineering). Advanced Research degree, University Henri Poincaré, Nancy 1, France

1998 M.S., Electrical Engineering, University Henri Poincaré, Nancy 1, France

1996 B.S., Electrical Engineering, University Henri Poincaré, Nancy 1, France

Professional Experience

2012 – current *Assistant Professor of Mechanical Engineering and Principal Investigator at the Texas Center for Superconductivity*
- Applied superconductivity, numerical modeling of superconductivity, multiphysics modeling

2008 – 2011 *Senior Scientist, Advanced Magnet Lab, Palm Bay, FL*
- Development of high specific power/torque electric motors and generator including the first 10 MW direct drive fully superconducting generator for wind turbines and superconducting machines for the N+3 aircraft.

2006 – 2008 *Adjunct Professor, FAMU-FSU College of Engineering, Tallahassee, FL*

2005 – present *Editor for Large Scale Applications, IEEE Transactions on Applied Superconductivity*

2003 – 2008 *Research Faculty at FAMU-FSU College of Engineering and FSU-Center for Advanced Power System, Tallahassee, Florida*.
- Multiphysics simulation of quench propagation in YBCO coated conductors and development of detection and protection schemes as part of US Air Force sponsored project
- Development of high power density superconducting rotating machinery for aircraft propulsion as part of the NASA/DoD sponsored University Research, Engineering & Technologies Institutes on Aeropropulsion, Power and Technology (joint program with Georgia Tech and Ohio State)

1999 – 2002 *Research Assistant, G.R.E.E.N. Lab, University Henri Poincaré, Nancy 1, France*
- Theoretical and experimental study of a novel HTS inductor configuration for synchronous motors.

1999 – 2002 *Teaching Associate, Department of Electrical and Computer Engineering, Technical Institute of Nancy, University Henri Poincaré, Nancy 1, France:*
- Member of faculty committee for B.S. in electrical engineering and computer sciences

Synergistic Projects

Ongoing Projects

- Design optimization of HTS wind generator using advanced YBCO-coated conductors (ARPA-e)
- Development of the first fully superconducting direct drive wind generator. (DOE)
- Development of experimentally validated models for superconducting rotating machines for NASA's N+3 aircraft turbo-electric propulsion. (NASA)

Past Projects:

- Development of a superconducting inductor for synchronous machines based on flux concentration
  - Development of a 3D electromagnetic simulation tools based on Markov Chains Monte Carlo methods and regularization (LP method)
  - Design, construction and testing of a prototype
  - Design and implementation of a quench protection system
  - Setup of a LHe cooling system
- Simulation of quench propagation in YBCO coated conductors and investigation of protection schemes as part of US Air Force Research Laboratory sponsored project
  - Resolution of non-linear, coupled multiphysics problems
  - Application to airborne superconducting generators
  - Simulation using FEA software COMSOL Multiphysics
- Development of high power density superconducting rotating machinery for aircraft propulsion as part of the NASA/DoD sponsored University Research, Engineering & Technologies Institutes on Aeropropulsion, Power and Technology (joint program with Georgia Tech and Ohio State)
  - Design of various motors for all-electric aircraft propulsion
  - 200 kW, 2700 RPM & 1.5 MW, 3000 RPM – novel configuration patented
  - Experimental validation of conduction cooling system
  - Safety torque generation system for HTS motors (failure mode)
  - 450 kW, 3000 RPM, axial flux using trapped flux magnets
  - Simulations with ANSOFT Maxwell-ePhysics-Optimetrics
- Development of a superconducting linear actuator for aircraft application for the BOEING Company
  - 2000 N linear motor, using YBCO coils and permanent magnets
  - Simulations with ANSOFT Maxwell-ePhysics-Optimetrics
- Development of design methods and physics-based electro-thermal sizing models for high temperature superconducting machines. The models are currently used at NASA Glenn Research Center, Georgia Institute of Technology and Empirical Systems Aerospace, LLC.

Relevant Publications:

- C. Lorin, D. Netter, P. J. Masson, "Scaling law for hysteresis losses in round superconductors magnetized by alternating, rotating or elliptical magnetic fields", I.E.E.E. Transactions on Applied Superconductivity, DOI: 10.1109/TASC.2014.2341255.
- P. J. Masson, K. Ratelle, P. Delobel, A. Lipardi, C. Lorin, "Development of a 3D Sizing Model for All-Superconducting Machines for Turbo-Electric Aircraft Propulsion", I.E.E.E. Transactions on Applied Superconductivity, Vol. 23, No 3, 10.1109/TASC.2013.2239471, 2013.

- C. Lorin, P. J. Masson, “Numerical Analysis of the Impact of Elliptical Fields on Magnetization Losses”, I.E.E.E. Transactions on Applied Superconductivity, Vol. 23, No 3, 10.1109/TASC.2013.2239347, 2013.
- C. A. Luongo, P. J. Masson, T. Nam, D. Mavris, M. Waters, D. Hall, H. D. Kim, G. V. Brown, “Next Generation Aircraft: A Potential New Application for High Temperature Superconductors”, I.E.E.E. Transactions on Applied Superconductivity, Vol. 19, No 3, June 2009, pp. 1055-1068.
- P. J. Masson, D. Soban, G. V. Brown, C.A. Luongo, "HTS Machines as Enabling Technology for All-Electric Airborne Vehicles", Superconductor Science and Technology, Vol. 20, No 8, August 2007, pp. 748-756.
- P. J. Masson, M. Breschi, P. Tixador, C. A. Luongo, “Design of HTS Axial Flux Motor for Aircraft Propulsion”, I.E.E.E. Transactions on Applied Superconductivity, Vol. 17, No 2, June 2007, pp. 1533-1536.
- P. J. Masson, J. E. Pienkos, C. A. Luongo, “Scaling Up of HTS Motor Based on Trapped Flux and Flux Concentration for Large Aircraft Propulsion”, I.E.E.E. Transactions on Applied Superconductivity, Vol. 17, No 2, June 2007, pp. 1579-1582.
- P. J. Masson, P. Tixador, J. C. Ordoñez, A. Morega, C. A. Luongo, “Electro-Thermal Sizing Model for HTS Motor Design”, I.E.E.E. Transactions on Applied Superconductivity, Vol. 17, No 2, June 2007, pp. 1529-1532.
- P.J. Masson, P. Tixador, C. A. Luongo, “Safety Torque Generation in HTS Propulsion Motor for General Aviation Aircraft”, I.E.E.E. Transactions on Applied Superconductivity, Vol. 17, No 2, June 2007, pp. 1619-1622.
- E. Ailam, D. Netter, J. Leveque, B. Douine, P. J. Masson, A. Rezzoug, “Design and Testing of a Superconducting Motor”, I.E.E.E. Transactions on Applied Superconductivity, Vol. 17, No 1, March 2007, pp. 27-33.
- P.J. Masson, C.A. Luongo, “High Power Density Superconducting Motor For All-Electric Aircraft Propulsion”, I.E.E.E. Transactions on Applied Superconductivity, Vol. 15, No. 2, June 2005, pp. 2226-2229.

Vernon G. Prince

Advanced Magnet Lab, Inc.

Short Biography

Vernon Prince has over 27 years' experience in the management and operation of high- technology corporations, successful retail franchises, and residential/commercial real estate enterprises. As general manager, AML Energy Advanced Magnet Lab, Inc., Palm Bay, FL, a technology company developing advanced and disruptive electromagnet technology for use in large markets such as energy, medical and power transmission, Mr. Prince oversees corporate strategy, technology and product development and marketing, the technology development roadmap, as well as fundraising strategies and operations plans, including the development of large-scale power generation systems for large wind turbines.

Mr. Prince has been founder and strategic business developer of a mobile marketing system for mobile WEB and Text Messaging (SMS); sensing systems for radiological dispersion devices (dirty bombs); global manufacturer of components and sub-assemblies for fiber optic telecom systems; state-of-the-art assembly technologies for the top telecommunications equipment manufacturers in the world; and a developer/manufacturer of automation equipment for the U.S. military, Intel, AMD, Seagate, Motorola, IBM, Delco, Bosch Automotive and other major micro-electronics manufacturers. He has also been a key advisor to automation and software companies in developing automation subsystems and software and revitalizing their engineering and business performance.

Vernon Prince holds B.S. and M.S. degrees in engineering and engineering management from the Florida Institute of Technology (Eastern Florida State College), Melbourne, Florida.

Education and Training

1987	M.S., Engineering Management, Florida Institute of Technology, Melbourne, Florida
1985	B.S., Computer Engineering, Florida Institute of Technology, Melbourne, Florida

Professional Experience

2008 – current *General Manager, AML Energy Advanced Magnet Lab, Inc., Palm Bay, F*L, a technology company developing advanced and disruptive electromagnet technology for use in large markets such as energy, medical and power transmission.

- Developed comprehensive business plan including technology development roadmap, fundraising strategies and operations plans. Plans include development of large-scale power generation systems for large wind turbines.
- Oversee operations of the company, including corporate strategy, technology and product development and marketing.

2006 – 2007 *Founder, CEO, Trimedia Publications, Melbourne, FL*, a Marketing company specializing in the creation of weekly publications, web-based content and unique mobile phone marketing concept for small and medium-sized clients. Business growth planned through franchising into metro areas.

- Oversee operations of the company, including corporate strategy, product development, creative content, software creation and support, and management of all departments.
- Developed complete mobile marketing system for mobile WEB and Text Messaging (SMS)

2005 – 2006 *Founder, Chairman, RDE Labs, Inc./Threat Sensing, Inc., Melbourne, FL*, developer of sensing systems for radiological dispersion devices (dirty bombs)

- Founded, planned company strategy, and developed advanced radiological sensing systems.
- Applied for two patents for unique technological products; one patent awarded.

2002 – present *Business Development/Entrepreneur, Melbourne, FL*; developed successful retail franchises and residential/commercial real estate.

- *Franchisee and Operator* of two (2) Cold Stone Creamery franchises, ranked in the top 5% of the company.
- *Owner and Developer* of Lakeside Centre, a retail and residential real estate development comprised of 20,000 square feet of retail space and 18 townhouse units.
- *Co-Owner and Developer* of 203 Nieman, a portfolio of commercial buildings located in Brevard County, Florida.

2001 – 2002 *CTO – Global Automation Division, JDS Uniphase, Melbourne, FL*, a Leading global manufacturer of components and sub-assemblies for fiber optic telecom systems.

- Managed the R&D activities of over 250 automation, packaging and photonics engineers.
- Coordinated the global automation of divisions of JDS Uniphase in the US, Europe and China.
- Completed seven major milestones as part of the sale of Optical Process Automation to JDS Uniphase.

1999 – 2001 *Co-founder, Vice President, Optical Process Automation, Melbourne, F*L, a manufacturer of automatic and semi-automatic equipment and processes for fiber-optic communication assemblies. Clients included JDS Uniphase, New Focus, Lucent and Intel Photonics.

- Recruited over 150 world-class automation and photonics engineers to develop state-of-the-art assembly technologies for the top telecommunications equipment manufacturers in the world.
- Established key partnerships with suppliers for integrated assembly lines and developed key accounts.

- Positioned the company to be acquired for over $400 million by JDS Uniphase.

1997 – 1999 *Co-founder, Vice President, APTEC, Melbourne, FL*, a consulting firm to automation and software companies.

- Provided expertise as a key advisor to automation and software companies in developing automation subsystems and software and revitalizing their engineering and business performance.

1992 –1997 *Co-founder, Vice President, AMTI/Zevatech Group / ESEC, Melbourne, FL*, manufacturer of automation equipment and assembly lines for Intel, AMD, Seagate, Motorola, IBM, Delco, Bosch Automotive and other major micro-electronics manufacturers.

- Developed product portfolio, oversaw engineering and forged lasting relationships with key suppliers.
- Grew company from start-up to $15 million in revenues and over 100 employees in three years.
- Positioned AMTI for a merger with Zevatech, a manufacturer of electronics assembly equipment.
- Coordinated sale to ESEC, a Swiss electronics assembly equipment company for $175 million.

1987 – 1992 *Vice President Software Engineering, WT AUTOMATION, Palm Bay, FL*, a developer/manufacturer of automation equipment for military and micro-electronics industries.

- Promoted from Software Engineer to Vice President in two years.
- Initiated strategic alliances with customers and developed key accounts for the company
- Spearheaded development of vision systems, databases and software platforms.

MatteoTropeano

Columbus Superconductors

Short Biography

Dr. Tropeano received his undergraduate degrees in Physics and his doctorate in Materials Science and Technology from the University of Genoa. His academic research activities focused on the experimental and theoretical properties of materials, including applied electronics, radioactivity, particle accelerators, nuclear physics, and superconductivity. Dr. Tropeano worked eight years as a researcher in the physics department of the University of Genoa and with the National Research Council (CNR), Italy. He also served as a visiting scientist at the National Physical Laboratories (NPL) in New Deli, India, where he specialized in the superconducting properties of materials (mainly magnesium diboride and Fe-based superconductors).

As a member of the R&D and Business Development team at Columbus Superconductors, Dr. Tropeano leads research in the development, optimization and characterization of superconducting MgB2 wires under contracts granted by the EC (European Community) and the DOE (Department of Energy, USA). These projects address the development of more efficient energy generation and power transmission through an innovative wind generator and superconducting cable.

Dr. Tropeano is author and co-author of more than 50 international publications, presentations, and lectures on the electronic, magnetic, and superconducting properties of materials and “de-risking experiments” in the wind energy sector.

Education and Training

2011	Ph.D., Materials Science and Technology, University of Genoa, Italy
2010	Science in High Magnetic Fields, 2nd EuroMagNET Summer School, Netherlands
2001	B.Eng., Physics, University of Genoa, Italy

Professional Experience

2011-present	*Permanent staff member at Columbus Superconductors SpA, Genoa, Italy.* Member of the R&D team with activities focused on the development, optimization and characterization of superconducting MgB2 wires. Several wires configuration and related fabrication process developed to fulfil or negotiate user and project requirements in terms of geometrical characteristics (dimension, shape, layout and length) and physical properties of the wire (electrical, thermal and mechanical characteristics).

Synergistic Projects

Ongoing Projects

- Member of technical committee TC90 of the IEC (International Electrotechnical Commission). Technical expert in working group WG13: General characteristics for practical superconducting wires.
- In the framework of TC90 technical commission, achieved an important step forward with the acceptance to start procedures to create international standards for the MgB_2 technology.

Past Projects

- Awarded contract for R&D-demonstrative projects granted by the EC (European Community) and the DOE (Department of Energy, USA).
- Granted two European FP7 projects, and managed from the proposal submission to the coordination of the technical and financial activities: Suprapower (Project n.308793) and Best Paths (Project n.61274). Aim of these projects was to address the need for more efficiency energy generation and power transmission through an innovative wind generator and superconducting cable.
- Another project granted by the DOE followed from the proposition stage and managed up to the completion of all the tasks. The project focused on "de-risking experiments" in the wind energy sector.

Relevant Publications:

- S. Sanz, T. Arlaban, R. Manzanas, M. Tropeano, R. Funke, P. Kováč, Y. Yang, H. Neumann, and B. Mondesert, *Superconducting light generator for large offshore wind turbines,* Journal of Physics: Conference Series 507 (2014) 032040.
- G. Prando, S. Sanna, G. Lamura, M. Tropeano, A. Palenzona, H. J.Grafe, B. Buchner, P. Carretta, and R. De Renzi, *Structural Phase separation at the magnetic-superconducting transition in* $La_{0.7}Y_{0.3}FeAs_{1-x}Y_x$, Phys. Status Solidi B, 1-4 (2013).
- M. Kulich, R. L. Fluckiger, C. Senatore, M. Tropeano, and R. Piccardo, *Effect of cold high pressure deformation on the properties of ex situ* MgB_2 *wires,*Supercond. Sci. Technol. 26 (2013) 105019.
- D Daghero, M. Tortello, G. A. Ummarino, V. A. Stepanov, F. Bernardini, M. Tropeano, M. Putti, and R. S. Gonnelli, *Effects of isoelectronic Ru substitution at the Fe site on the energy gaps of optimally F-doped SmFeAsO,* Supercond. Sci. Technol. 25 (2012) 084012.
- Pallecchi, M. Tropeano, G. Lamura, M. Pani, M. Palombo, A. Palenzona,and M. Putti, *Upper critical fields and critical current densities of Fe-based superconductors as compared to those of other technical superconductors,* Physica C 482 (2012) pp. 68–73.
- P. Bonfà, P. Carretta, S. Sanna, G. Lamura, G. Prando, A. Martinelli, A. Palenzona, M. Tropeano, M. Putti, and R. De Renzi, *Magnetic properties of spin-diluted iron pnictides from μSR and NMR in* $LaFe_{1-x}Ru_xAsO$, Physical Review B 85, 054518 (2012).
- Palenzona, A. Sala, C. Bernini, V. Braccini, M. R.Cimberle, C. Ferdeghini, G. Lamura, A. Martinelli, I. Pallecchi, G. Romano, M. Tropeano, R. Fittipaldi, A. Vecchione, A. Polyanskii, F. Kametani, and M. Putti, A new approach for improving global criticalcurrentdensity in Fe.Se0.5Te0.5 polycrystallinematerials, Supercond. Sci. Technol. 25 (2012) 115018.

- E.Bellingeri, I. Pallecchi, R. Buzio, A Gerbi, D. Marrè, M.R.Cimberle, M.Tropeano, M.Putti, A.Palenzona, S.Kaciulis,andC.Ferdeghini,*Critical temperature enhancement by biaxial compressive strain in $FeSe_{0.5}Te_{0.5}$thin film,* J.SupercondNovMagn (2011) 24:35-41.
- Yamamoto, J. Jiang, F. Kametani, A. Polyanskii, E. Hellstrom, D. Larbalestrier, A. Martinelli, A. Palenzona, M.Tropeano and M.Putti, *Evidence for electromagnetic granularity in plycrystalline Sm1111 iron-pnictides with enhanced phase purity,* Supercond. Sci. Technol. 24 (2011) 045010.
- Vajpayee, R. Jha, A. K. Srivastava, H. Krishan, M. Tropeano, C. Ferdeghini, and V. P. S. Awana, *The effect of synthesis temperature on the superconducting properties of n-SiC added bulk MgB_2 superconductor,* Supercond. Sci. Technol. 24 (2011) 045013.
- Pal, M. Tropeano, S. D. Kaushik, M. Hussain, H. Krishan, and V. P. S. Awana, *Intriguing complex magnetism of co inRECoAsO (RE=La, Nd and Sm),* Journal of Applied Physics 109, 07E121 (2011).
- G. Prando, P. Carretta, R .DeRenzi, S. Sanna, A. Palenzona, M. Putti, and M.Tropeano, *Vortex dynamics and irreversibility line in optimally doped $SmFeAsO_{0.8}F_{0.2}$ from ac susceptibility and magnetization measurements,* Physical Review B 83, 174514 (2011).
- Martinelli, A. Palenzona, M. Tropeano, M. Putti, C. Ferdeghini, G. Profeta, and E. Emerich, *Retention of the Tetragonal to Orthorhombic Structural Transition in F-Substituted SmFeAsO:A New Phase Diagram for $SmFeAs(O_{1-x}F_x)$,* Physical Review Letter 106, 227001 (2011).
- Pallecchi, M. Tropeano, C. Ferdeghini, G. Lamura, A. Martinelli, A. Palenzona, and M. Putti, *Pseudogap Analysis of Normal State Transport Behavior of 11 and 1111 Fe-Based Superconductors,* J Supercond Nov Magn (2011) 24:1751–1760.
- G. Prando, A. Lascialfari, A. Rigamonti, L. Romanò, S. Sanna, M. Putti, and M. Tropeano, *Superconducting phase fluctuations in SmFeAsO0.8F0.2 from diamagnetism at a low magnetic field above T_c,* Physical Review B 84, 064507 (2011).
- Pallecchi, F. Bernardini, M. Tropeano, A. Palenzona, A. Martinelli, C. Ferdeghini, M. Vignolo, S. Massidda, and M. Putti, *Magnetotransport in La(Fe,Ru)AsO as a probe of band structure and mobility,* Physical Review B 84, 134524 (2011).
- T.Shiroka, G. Lamura, S. Sanna, G. Prando, R. De Renzi, M. Tropeano, M. R. Cimberle, A. Martinelli, C. Bernini, A. Palenzona, R. Fittipaldi, A. Vecchione, P. Carretta, A. S. Siri, C. Ferdeghini, and M. Putti, *Long- to short-rangemagneticorder in fluorine-dopedCeFeAsO,* PhysicalReview B 84, 195123 (2011).
- A .Martinelli, A. Palenzona, M. Tropeano, C. Ferdeghini, M. Putti, M. R. Cimberle, T. D. Nguyen, M. Affronte, C. Ritter, *From antiferromagnetism to superconductivity in $Fe_{1+y}Te_{1-x}Se_x$ (0<x<0.20): Neutronpowderdiffractionanalysis,* PhysicalReview B 81, 094115 (2010).
- E.Bellingeri, I. Pallecchi, R. Buzio, A.Gerbi, D.Marrè, M. R. Cimberle, M. Tropeano, M. Putti, A. Palenzonaand C. Ferdeghini,*Tc=21K in epitaxial $FeSe_{0.5}Te_{0.5}$thin film with biaxial compressive strain,* AppliedPhysicsletters 96, 102512 (2010).
- G. Prando, P. Carretta, A. Rigamonti, S. Sanna, A. Palenzona, M. Putti and M. Tropeano, *^{19}F NMR study of the coupling between 4f and itinerant electrons in the pnictide superconductors $SmFeAsO_{1-x}F_x$ (0.15<x<0.2),* Physical Review B 81, 100508 (2010).
- M. Putti, I. Pallecchi, E. Bellingeri, M. R. Cimberle, M. Tropeano, A. Palenzona, C. Tarantini, A. Yamamoto, J. Jang, J. Jaroszynski, F. Kameani, D. Abraimov, A. Polyansky, J. D. Weiss, E. E. Hellstrom, A. Gurevich, D. C. Larbalestrier, R. Jin, B.C. Sales, A. S. Sefat, M .A. McGuire, D. Mandrus, P. Cheng, Y. Jia, H. H. Wen, C. B. Eom, *New Fe-based superconductors: properties relevant for applications,* Supercond. Sci. Technol. 23 (2010) 034003.

- M. Tropeano, I. Pallecchi, M. Putti, , M. R. Cimberle, C. Ferdeghini, G. Lamura, M. Vignolo, A. Martinelli, A. Palenzona, *Transport and superconducting properties of fe-based superconductors: a comparison between $SmFeAsO_{1-x}F_x$ and $Fe_{1+y}Te_{1-x}Se_x$,* Supercond. Sci. Technol. 23 (2010) 054001.
- M.Tropeano, M. R. Cimberle, C .Ferdeghini, G. Lamura, A. Martinelli, A. PalenzonaIPallecchi, A. Sala, I.Sheikin, F. Bernardini, M. Monni, and M. Putti, *Isoelectronic Ru substitution at the iron site in $SmFe_{1-x}Ru_xAsO_{0.85}F_{0.15}$ and its effect on structural, superconducting and normal-state properties,* Physical Review B 81, 184505 (2010).
- S. Sanna, R. De Renzi, T. Shiroka, G. Lamura, G.Prando, P.Carretta, M. Putti, A.Martinelli, M. R.Cimberle, M. Tropeano, and A. Palenzona, *Nanoscopic coexistence of magnetic and superconducting states within the FeAs layers of $CeFeAsO_{1-x}F_x$,* Physical Review B 82, 060508 (2010).
- G. Prando, P. Carretta, A.Lascialfari, A. Rigamonti, S.Sanna, L. Romanò, A. Palenzona, M. Putti, M.Tropeano, *Investigation of fluctuating conductivity and spin dinamics in $SmFeAsO_{1-x}F_x$ superconductors,* Advance in Science and Technology Vol.75 (2010) pp. 141-146.
- S. Kaciulis, A. Mezzi, C. Ferdeghini, A. Martinelli and M.Tropeano, *Chemical composition of superconducting SmFeAsO doped with fluorine,* Surface and Interface Analysis 2010, 42, 692-695.
- M. Tropeano, C Fanciulli, C Ferdeghini, D. Marrè, A S Siri, MPutti, A. Martinelli, M. Ferretti, A.Palenzona, M.R.Cimberle, C.Mirri, S.Lupi, R.Sopracase, P.Calvaniand A.Perucchi, *Transport and infrared properties of $SmFeAsO_{1-x}F_x$): fromSDW to superconducting ordering,* Supercond. Sci.Technol. 22 (2009) 034004.
- Pallecchi, C. Fanciulli, M. Tropeano, A. Palenzona, M. Ferretti, A. Malagoli, A. Martinelli, I. Sheikin,M. Putti, and C. Ferdeghini, *Upper critical field and fluctuation conductivity in the critical regime of doped SmFeAsO,* Physical review B 79, 104515 (2009).
- M.Tropeano, C. Fanciulli, F. Canepa, M. R. Cimberle, C.Ferdeghini, G.Lamura, A.Martinelli, M.Putti, M.Vignolo and A.Palenzona, *Effect of chemical pressure on SDW and superconductivity in undoped and 15% F-doped $La_{(1-y)}Y_{(y)}FeAsO$ compounds,* Physical Review B 79, 174523 (2009).
- S.Sanna, R.DeRenzi, G.Lamura, C.Ferdeghini, A.Martinelli, A.Palenzona, M.Putti, M.Tropeano, T.Shiroka, *Intrinsic Ferromagnetic Impurity Phases in $SmFeAsO_{1-x}F_x$Detected by μSR,*JSupercond Nov Magn (2009) 22: 585–588
- M.R.Cimberle,F.Canepa, M.Ferretti, A.Martinelli, A.Palenzona, A.S.Siri, C.Tarantini, M.Tropeano, C.Ferdeghini, *Magnetic characterization of undoped and 15% F-doped LaFeAsO and SmFeAsO compounds,* Journal of Magnetism and Magnetic Materials 321 (2009) pp. 3024–3030.
- A.Malagoli, M.Tropeano, V. Cubeda, C.Bernini, V.Braccini, C.Fanciulli, G.Romano, M.Putti, M.Vignolo, and C. Ferdeghini, *Study of the Superconducting and Thermal Properties of ex situ GlidCop-Sheathed Practical MgB_2 Conductors,* IEEE Transactions on Applied Superconductivity, Vol. 19, No 4, August 2009.
- M.Vignolo, G.Romano, A.Malagoli, V.Braccini, M.Tropeano, E. Bellingeri, C.Fanciulli, C.Bernini, V. Honkimäki, M.Putti, and C. Ferdeghini, *Role of the Grain Oxidation in Improving the In-Field Behavior of MgB_2 Ex-Situ Tapes,* IEEE Transactions on Applied Superconductivity, Vol. 19, No 3, June 2009.
- Ferdeghini, E. Bellingeri, C.Fanciulli, M. Ferretti, P. Manfrinetti, I. Pallecchi, M. Putti, C. Tarantini, M.Tropeano, A. Andreone, G. Lamura, and R. Vaglio, *Superconducting Properties of Vn_3Si Thin Films Grown by Pulsed Laser Ablation,* IEEE Transactions on Applied Superconductivity, Vol. 19, No 3, June 2009.
- G. Romano, M. Vignolo, V. Braccini, A. Malagoli, C. Bernini, M. Tropeano, C. Fanciulli, M. Putti, and C. Ferdeghini, *High-Energy Ball Milling and Synthesis Temperature Study to Improve Superconducting*

Properties MgB_2Ex-situ Tapes and Wires, IEEE Transactions on Applied Superconductivity, Vol. 19, No 3, June 2009.

- S. Sanna, R. DeRenzi, G. Lamura, C. Ferdeghini, A. Palenzona, M. Putti, M. Tropeano and T. Shiroka, *Magnetic-superconducting phase boundary of $SmFeAsO_{1-x}F_x$ studied via muon spin rotation:Unified behavior in a pnictidefamily,* Physical Review B 80, 052503 (2009).
- E. Bellingeri, R. Buzio, A Gerbi, DMarrè, S. Congiu, M. R. Cimberle, M.Tropeano, A.S. Siri, A. Palenzonaand, C. Ferdeghini, *High quality epitaxial $FeSe_{0.5}Te_{0.5}$ thin films grown on $SrTiO_3$ substrates by pulsed laser deposition,* Supercond. Sci. Technol. 22 (2009) 034004.
- Martinelli, A.Palenzona, M. Tropeano, C. Ferdeghini, M.R.Cimberle, C. Ritter, Neutron powder diffraction investigation of the structural and magnetic properties of (La1-yYy) FeAsO (y=0.10, 0.20 and 0.30), Physical Review B 80, 214106 (2009).
- Pallecchi, G. Lamura, M.Tropeano, M. Putti, R. Viennnois, E. Giannini, D. Van derMarel, *Seebeck effect in $Fe_{1+x}Te_{1-y}Se_{y,}$* Physical Review B 80, 214511 (2009).
- M. Vignolo, G. Romano, A. Malgoli, V. Braccini, C. Bernini, ,M. Tropeano, A. Martinelli, V. Cubeda, A. Tumino, M. Putti, C. Ferdeghini and A. S. Siri, *Development of MgB_2 Powders and Study of the Properties and Architecture of Ex-Situ PIT Wires,*IEEE Transactions on Applied Superconductivity, Vol. 18, No 2, June 2008.
- Martinelli, M. Ferretti, P. Manfrinetti, A. Palenzona, M. Tropeano, M.R. Cimberle, C. Ferdeghini, R. Valle, C. Bernini, M. Putti, C. Ferdeghini and A.S. Siri, Synthesis, crystal structure, microstructure, transport and magnetic properties of SmFeAsO and SmFeAs(O0.93F0.07), Supercond. Sci.Technol. 21 (2008) 095017.
- P. Brotto, M. Tropeano, C. Ferdeghini, P. Manfrinetti, A. Palenzona, E. GalleaniD'Agliano and M. Putti, *Experimental confirmation of the low B isotope coefficient of $MgB_{2,}$* Physical review B 78, 092502 (2008).
- M. Tropeano, A. Martinelli, A. Palenzona, E. Bellingeri, E. GalleaniD'Agliano, T.D. Nguyen, M. Affronte and M. Putti, *Thermal properties of $SmFeAsO_{1-x}F_x$ as a probe of the interplay between electrons and phonons,* Physical review B 78, 094518 (2008).
- Malagoli, V. Braccini, M. Tropeano, M. Vignolo, C. Bernini, C. Fanciulli, G. Romano, M. Putti, C. Ferdeghini, E. Mossang, A. Polyanskii, D.C. Larbalestier, Effect of grain refinement on enhancing critical current density and upper critical field in undoped MgB2 ex-situ tapes, Journal of AppliedPhysics, 104, 103908 (2008).
- Marini, C. Mirri, G. Profeta, S. Lupi, D. Di Castro, R. Sopracase, P. Postorino, P. Calvani, A. Perucchi, S. Massidda, G. M. Tropeano, M. Putti, A. Martinelli, A. Palenzona and P. Dore, The opticalphononspectrum of SmFeAsO, EPL, 84 (2008) 67013.
- V. Braccini, A. Malgoli, A. Tumino, M. Vignolo, C. Bernini, C. Fanciulli, G. Romano, M. Tropeano, A. S. Siri, and Giovanni Grasso, *Improvement of Magnetic Field Behavior of Ex-Situ ProcessedMagnesiumDiborideTapes,* IEEE Transactions on AppliedSuperconductivity, Vol. 17, No 2, June 2007.
- Gozzi, A. Latini, G. Capannelli, F. Canepa, M. Napolitano, M. R. Cimberle, M. Tropeano, Synthesis and magnetic characterization of Ni nanoparticles and Ni nanoparticles in multiwalled carbon nanotubes, Journal of Alloys and Compounds 419 (2006) pp. 32-39.
- Martinelli, M. Ferretti, C. Castellano, C. Mondelli, M. R. Cimberle, M. Tropeano, C. Ritter, Effect of Cr substitution on the crystal and magnetic structure of (Pr0.55Ca045) MnO3 :A neutron powder diffraction investigation, Physical review B 73, 064423 (2006).

- Guarino, R. Fittipaldi, A. Nigro, M. Gombos, A. Vecchione, R. Ciancio, S. Pace, M.R. Cimberle, M. Tropeano, D. Zola, M. Polichetti, *Structural and magnetic characterization of GdSr2RuCu2O8 films deposited by d.c.sputtering*, Phys. Stat. Sol. (c) 3, No. 9, pp. 3073–3076 (2006).
- Malagoli, G. Grasso, M. Vignolo, A. Tumino, V. Braccini, C. Bernini, M. Tropeano, A.S. Siri, D. Nardelli, M. Modica,*Long length MgB2 conductors for industrial applications*, Advances in Science and Technology Vol. 47 (2006) 238-245.
- Martinelli, M. Ferretti, C. Castellano, M.R. Cimberle, M. Tropeano, C. Mondelli, *Effect of Cr substitution on the crystal and manetic structure of* $(Pr_{0.55}Ca_{0.45})O_3$, Advances in Science and Technology Vol. 52 (2006) pp. 93-9.7
- Martinelli, M. Ferretti, C. Castellano, C. Mondelli, D. Martin y Marero, M. R. Cimberle, M. Tropeano, *Structure and magnetic properties of (Pr 0.55 Ca 0.45)(Mn1-y Cry)O3 (y = 0.00, 0.03, 0.06),* Journal of the European Ceramic Martinelli, M. Ferretti, C. Castellano, C. Mondelli,, M. R. Cimberle, M. Tropeano, *(La,Ca)(Mn,M)03 (M=Ni,Cr) compounds investigated by means of XRPD and DC magnetic measurements*, Journal of the European Ceramic Society 25 (2005) pp. 3037-3040.
- M. R Cimberle, M. Tropeano, M. Ferretti, A. Martinelli, C. Artini, G.A. Costa, *Effect of disorder on the passage from bulk superconductivity to spin glass behaviour in RuSr2GdCu2O8,* Superconductors Science and Technology. Volume 18 (2005) pp. 454-460
- Castellano, F. Cordero, O. Palumbo, R. Cantelli, R. Cimberle, M. Tropeano, A. Martinelli, M. Ferretti, *Local sructure and magnetic properties of Mn substitued manganites studied by EXAFS and DC magnetic measurements*, Solid State Communications 136 (2005) pp. 244-249.
- M. Salluzzo, G.M. de Luca, D. Marrè, M. Putti, M. Tropeano, U. Scotti di Uccio, R. Vaglio, *Thickness effect on the structure and superconductivity of Nd1.2Ba1.8Cu3OZ epitaxial films,* Physical review B 72, 134521 (2005).
- S. Agostinelli, J. Allison, K. Amako, M. Tropeano et al., *Geant 4- a simulation toolkit*, Nuclear Instruments and Methods in Physics Research, Section A: Accelerators, Spectrometers, Detectors and Associated Equipment. Volume 506, Issue 3, 1 July 2003, pp. 250-303.